

Developing computational protocols for
molecular spectroscopy that are able to
unravel the photophysical properties of
photoluminescent inorganic solid state and
organometallic materials

Dissertation
zur
Erlangung des Doktorgrades (Dr. rer. nat.)
der
Mathematisch-Naturwissenschaftlichen Fakultät
der
Rheinischen Friedrich-Wilhelms-Universität Bonn

vorgelegt von
Rami Ali Mohamed Shafei
aus
Kairo, Ägypten

Bonn 2024

Angefertigt mit Genehmigung der Mathematisch-Naturwissenschaftlichen Fakultät
der Rheinischen Friedrich-Wilhelms-Universität Bonn

1. Gutachter: Prof. Dr. Frank Neese
2. Gutachter: Prof. Dr. Thomas Bredow

Tag der Promotion: 20.06.2024

Erscheinungsjahr: 2024

To the memory of my beloved mother, Hadiya Hassan.

Summary

The aim of the thesis is to conduct a thorough examination of photoluminescent inorganic solid-state and organometallic materials through comprehensive theoretical and computational analyses. This involves unraveling the complexities of their electronic, structural, and optical properties. Motivated by the rich applications and our current state-of-the-art understanding of rare-earth (RE) and transition-metal (TM) materials, this thesis aims to contribute further insights to facilitate and guide the practical design of innovative materials with finely tuned photoluminescent properties. Commencing with the principles of computational chemistry and spectroscopy, and utilizing cutting-edge electronic structure methods including both DFT- and wavefunction-based methods, the study decodes the optical properties of Eu^{2+} -doped phosphors and chiral Re(I) complexes. The work encompasses the development of computational protocols, establishing systematic approaches that correlate optical features with structural and electronic characteristics. Furthermore, studies on excited-state dynamics allow for a thorough understanding of the effect of vibronic couplings on the electronic structure and various optical spectra.

At the core of the study, a multifaceted exploration of Eu^{2+} -doped phosphors unfolds, introducing a groundbreaking systematic computational protocol adept at predicting electronic structures, optical transitions, and ultimately spectral characteristics of optical bands. The present work demonstrates the powerful synergy between theoretical insights and practical applications, predicting optical properties and enhancing the emission properties of specific phosphors. The research results identify crucial structural, electronic, and magnetic parameters controlling the emissive relaxation and the spectral broadening mechanisms. The research work unravels the interplay between crystal structure effects, spin-orbit coupling, and vibronic coupling in fine-tuning of luminescence.

The study extends into chiral Re(I) complexes, specifically [*fac*- $\text{ReX}(\text{CO})_3\text{L}$] family, with circularly polarized luminescence, introducing a computational protocol predicting their photophysical and optical properties. The work unveils distinctive emission characteristics influenced by spin-vibronic coupling, expanding the horizons of the computational study into the chiroptical intricacies of photophysics in TM complexes.

Summary

In summary, the thesis weaves fundamental principles, luminescent systems, and innovative computational protocols into a comprehensive narrative. The implications extend beyond theoretical advancements, promising applications in energy-efficient lighting technologies and luminescent probes. Navigating the intersection of fundamental science and practical innovation, the research presented in this thesis could ultimately illuminate a path toward a future where tailored luminescent materials shape several technological landscapes and industrial progress.

Preface

The work presented in this thesis constitutes a five-year research project conducted between January 2019 and January 2024 at the Department of Molecular Theory and Spectroscopy, Max-Planck-Institut für Kohlenforschung, Mülheim an der Ruhr, Germany.

List of Publications

Published papers included in this thesis

1. Electronic and Optical Properties of Eu^{2+} -Activated Narrow-Band Phosphors for Phosphor-Converted Light-Emitting Diode Applications: Insights from a Theoretical Spectroscopy Perspective.
Rami Shafei, Dimitrios Maganas, Philipp Jean Strobel, Peter J. Schmidt, Wolfgang Schnick, and Frank Neese
J. Am. Chem. Soc., **2022**, 144(18), 8038-8053, DOI: 10.1021/jacs.2c00218
2. Theoretical spectroscopy for unraveling the intensity mechanism of the optical and photoluminescent spectra of chiral Re(I) transition metal complexes.
Rami Shafei, Ai Hamano, Christophe Gourlaouen, Dimitrios Maganas, Keiko Takano, Chantal Daniel, Frank Neese
J. Chem. Phys., **2023**, 159(8), 084102, DOI: 10.1063/5.0153742
3. A Theoretical Spectroscopy Study of the Photoluminescent Properties of Narrow Band Eu^{2+} -doped Phosphors Containing Multiple Candidate Doping Centers. Prediction of an unprecedented Narrow Band Red phosphor.
Rami Shafei, Philipp Jean Strobel, Peter J. Schmidt, Dimitrios Maganas, Wolfgang Schnick, and Frank Neese
Phys. Chem. Chem. Phys., **2024**, 26(7), 6277-6291, DOI: 10.1039/D3CP06039J

Publications in progress

1. A Combined Experimental and Computational Study on the Broadening Mechanism of the Luminescence Spectrum of Narrow Band Eu^{2+} -doped Phosphors
Rami Shafei, Philipp Jean Strobel, Peter J. Schmidt, Dimitrios Maganas, Wolfgang Schnick, and Frank Neese

Presentations

1. Developing a computational protocol for understanding Linear and Circular Polarized long-lived luminescence spectra in Chiral Re(I) Complexes
Oral presentation in *ANR CHIRON Workshop*, University of Strasbourg
21 March 2022, Strasbourg
2. Excited State Dynamics of Circularly Polarized Luminescence in Transition Metal-based Complexes
Oral presentation in *ANR CHIRON Workshop*, University of Rennes
5 April 2023, Rennes
3. Luminescence in Eu²⁺-doped Phosphors for High-efficient pc-WLEDs: Descriptors for Crucial Role of Eu-Ligand Covalency and Eu-Doping Probability
Poster presentation for *German Advisory Board visit (Fachbeirat)*, Max-Planck-Institut für Kohlenforschung
20 April 2023, Mülheim an der Ruhr

Acknowledgments

First of all, I am deeply grateful to Professor Dr. Frank Neese for his unwavering support and leadership, which afforded me the opportunity to embark on this research journey. His guidance and the collaborative atmosphere he cultivated were indispensable to the success of this project. I extend sincere thanks for his mentorship and the wealth of knowledge he generously shared, enriching my academic experience.

I express sincere appreciation to Dr. Dimitrios Manganas for his exceptional mentorship and support throughout this research. His dedication to elucidating complex scientific concepts equipped me with the necessary skills for this undertaking. I appreciate the autonomy he granted me to explore innovative approaches independently. Our daily discussions were not only intellectually stimulating but also played a crucial role in advancing the project. Furthermore, I am thankful for his efforts in maintaining a harmonious work environment, both scientifically and socially.

I would like to thank Professor Dr. Wolfgang Schnick and his team at the University of Munich (LMU), including Dr. Peter J. Schmidt and Dr. Philipp J. Strobel, for their collaborative spirit, insightful discussions, and valuable experimental contributions. I also would like to thank Professor Dr. Chantal Daniel and Dr. Christophe Gourlaouen, from the University of Strasbourg, their collaboration significantly enhanced the depth and breadth and extend the domain of my research.

I extend my sincere appreciation to Professor Dr. Thomas Bredow, from the University of Bonn, for supervising my Ph.D. work and to Professor Dr. Serena DeBeer for the invaluable opportunity to work at MPI CEC through our joint workspace with my home institute. Their support was crucial in fostering a dynamic research environment.

I would like to express deep thanks and gratitude to Dr. Eckhard Bill for his invaluable scientific discussions, assistance, support, encouragement, and enduring inspiration during my Ph.D. His influence remains impactful, resonating even after his passing.

Special recognition is extended to the entire ORCA and FACCTS teams. From ORCA team, particularly I would like to thank Dr. Dimitrios Liakos, Dr. Frank Wennmohs and Dr. Kantharuban Sivalingam for their guidance in calculations and adept problem-solving. From

Acknowledgements

FACCTS team, I am also grateful to Dr. Bernardo de Souza for his implementation in ESD and Dr. Christoph Riplinger for his work on the QMMM method for solids. Their guidance, support, discussions were instrumental in achieving this project.

I express gratitude to Professor Dr. Mihail Atanasov, Dr. Maurice van Gastel, and Dr. Daniel SantaLucia for their invaluable contributions through our thorough discussions of scientific ideas and results.

I would like to thank all my colleagues, especially Nicolas Foglia, Anneke Dittmer, Tiago da Costa, Pauline Colinet, Derek Rice, and Zachary Mathe. Their invaluable help, engaging discussions, diverse perspectives, and insightful contributions have greatly enriched the depth of my scientific experience.

I extend my appreciation to the Egyptian Ministry of Higher Education and Scientific Research for their financial support during the initial phase of this research. Additionally, thanks are due to the Max Planck Society for their instrumental financial backing, which has played a crucial role in the progression of this study.

A heartfelt thank you to my family for their unwavering love and support. I am genuinely thankful for Omneya and my precious daughters, Hadya and Hanna, for the enduring presence you bring into my life. Your love and support have made this journey possible and more meaningful.

Finally, I would like to express my gratitude to my Ph.D. committee members, Professor Dr. Frank Neese, Professor Dr. Thomas Bredow, Professor Dr. Sigurd Höger, and Professor Dr. Carsten Urbach, for their invaluable guidance and support.

Rami Shafei

Mülheim an der Ruhr, 2024

Contents

1	Introduction	1
PART I	Theory of Computational Spectroscopy for Unraveling the Electronic Structure and Photoluminescence	6
2	Introduction to PART I	7
3	Introduction to Spectroscopy (Light Matter Interaction)	9
3.1.	Introduction to Spectroscopy.....	9
3.2.	Photon Field (Maxwell's Equations).....	12
3.2.1.	Linear and circular polarization of Light.....	14
3.3.	Optical Processes and Experimental Schemes	15
3.3.1.	Transmission	16
3.3.2.	Reflection– band gap in semiconductors.....	16
3.3.3.	Refraction	17
3.3.4.	Diffraction and Crystallography	18
3.3.5.	Absorption, Emission and Luminescence	18
3.3.6.	Scattering and Raman Effect	22
3.3.7.	Polarization and Chirality.....	24
4	Electronic structure of molecules and Ions-doped in Crystals.....	25
4.1.	Optical Spectroscopy and Quantum Mechanics	25
4.1.1.	Schrödinger Equation.....	25
4.1.2.	Variational principle	27
4.1.3.	Perturbation Theory.....	28
4.2.	The Electronic Problem.....	29
4.3.	Adiabatic and Born-Oppenheimer Approximations	30
4.4.	Energies levels (Static interaction).....	31
4.4.1.	Atomic orbitals.....	32
4.4.2.	Crystal Field and Coupling Schemes (are Electrons in collective or individual Behavior?).....	33
4.4.3.	CF Splitting and CF States.....	35
4.4.4.	Covalency and chemical bonding (Ligand Field Theory)	36
4.4.5.	Effective Hamiltonian.....	38
4.4.6.	Spin-orbit Coupling on the Basis of Quasi Degenerate Perturbation Theory	39
4.4.7.	Spin Hamiltonian - Zero-Field Splitting for ground and excited multiplets.....	40

5	Electronic Structure Methods for Ground and Excited States	43
5.1.	Wavefunction Methods.....	43
5.1.1.	Hartree-Fock (HF) Method	43
5.1.2.	Correlation Energy	45
5.1.3.	Configuration Interaction (CI)	46
5.1.4.	Multiconfigurational self-consistent field methods (MCSCF).....	48
5.1.5.	Iterative-Configuration Expansion Configuration Interaction (ICE-CI).....	50
5.1.6.	Perturbation Theory Methods: MP2, NEVPT2 and QD-NEVPT2.....	50
5.1.7.	Coupled-Cluster (CC) methods: CCSD, DLPNO-CCSD	52
5.1.8.	Equation of Motion Coupled-Cluster Method (EOM-CC) and STEOM-DLPNO-CCSD Variant	54
5.2.	Density Functional Theory (DFT).....	55
5.2.1.	Hohenberg-Kohn Theory	56
5.2.2.	The Kohn-Sham Equations	57
5.3.	Time-Dependent DFT (TD-DFT)	60
6	Theory of Electronic Transitions and Spectroscopies	61
6.1.	Introduction	61
6.2.	Radiative vs non-Radiative Processes.....	62
6.3.	Vibronic Coupling effect on the optical Spectra	65
6.3.1.	Adiabatic approximation and Vibronic Coupling.....	65
6.3.2.	Frank-Condon approximation, Stokes Shift and Huang-Rhys parameters ...	67
6.3.3.	Herzberg-Teller Vibronic Coupling.....	71
6.3.4.	Jahn-Teller and Pseudo Jahn-Teller Effect.....	72
6.4.	Light Polarization, Natural and Induced Optical Activity.....	74
6.5.	Radiative Transitions and Spectroscopies	76
6.5.1.	Fermi's Golden Rule.....	76
6.5.2.	Optical Transition probabilities and oscillator strengths	76
6.6.	Fermi's Golden Rule and Path Integral	80
6.6.1.	Absorption and luminescence rates and spectra (ABS, PL)	80
6.6.2.	Circularly polarized absorption and luminescence rates and spectra (ECD, CPL) in chiral molecules.....	81
6.6.3.	Excited State Dynamics (ESD).....	82
6.6.4.	Thermal Statistical Mechanics.....	84
6.7.	Non-Radiative Transition Rates and Quantum Yields	84
6.8.	Spin-vibronic/phonon Coupling	85
6.8.1.	Spin Hamiltonian	85
6.8.2.	Spin-vibronic / Spin-Phonon Coupling Effects.....	86
7	Modelling of Photoluminescent Molecules and solids	88
7.1.	Molecular Models for Finite Molecules (Solvent Effect)	88

7.1.1. Explicit Solvation Models.....	89
7.1.2. Implicit Solvation Models.....	90
7.2. Clusters Models for Solid-State Materials.....	92
7.2.1. Free Cluster Model.....	92
7.2.2. Hydrogen-Saturated Cluster Model.....	93
7.2.3. Embedded Cluster Approach.....	93
7.3. Protocol to construct an Embedded Cluster Model for Inorganic Solid-state Eu ²⁺ -doped Phosphors.....	95
PART II Understanding the Electronic Structure and Photoluminescence in Solids : Eu²⁺-doped Phosphors as an Example	106
8 Introduction to PART II.....	107
8.1. Objectives and Overview of the forthcoming chapters.....	111
9 Electronic Structure of Free Eu²⁺ Ion and Doped in Perfect Cubic Ligand Field.....	114
9.1. Free Eu ²⁺ Ion.....	114
9.1.1. Calculations details	115
9.1.2. Electronic structure of Eu ²⁺ ion.....	117
9.2. Eu ²⁺ in cubic (inverted <i>O_h</i>) ligand field	118
9.2.1. Calculations details	119
9.2.2. Electronic structure of Eu ²⁺ in cubic (inverted <i>O_h</i>) ligand field.....	119
9.3. PJTE in Eu ²⁺ in prefect cubic Ligand Field.....	122
9.4. A qualitative analysis of Absorption and emission processes in Eu ²⁺ -doped phosphors	125
9.5. Conclusions.....	127
10 Luminescence in Eu²⁺-doped Phosphors for pc-WLEDs – Design the Computational Protocol and Define the Electronic Descriptors	129
10.1. Introduction	129
10.2. Study Set – Geometric Structure	130
10.3. Experimental Spectra.....	134
10.4. Computational Protocol and calculations details.....	136
10.5. Embedding Cluster Approach	138
10.5.1. Construction of the cluster models.....	138
10.5.2. Cluster size convergence	141
10.6. Absorption and Emission Processes: A Qualitative Electronic Structure Analysis .	143
10.7. A theoretical protocol for understanding the absorption and luminescence spectra in Eu ²⁺ -doped phosphors	145
10.7.1. Nitride phosphors	146
10.7.2. Oxynitride and oxide phosphors.....	151

10.8. Definition of geometrical versus covalency descriptors	154
10.9. Summary and Conclusions	157
11 Luminescence in Narrow-band Eu^{2+}-doped Phosphors bearing Multiple Candidate Eu^{2+} doping centers – Extending and Validation of the Proposed Protocol and Descriptors	159
11.1. Introduction	159
11.2. Study set of Phosphors and Geometrical Properties	161
11.3. Experimental Results	164
11.4. Electronic Structure Analysis. Insights into the Emission mechanism of multiple doping centers.....	167
11.5. Computational Details	171
11.5.1.Construction of the Cluster Models	172
11.6. Computational considerations.....	173
11.7. Finding the most doping probable site for Eu^{2+} (Doping Descriptor).....	175
11.7.1.Understanding the Eu^{2+} doping in the framework of DLPNO-CCSD(T)/LED analysis.....	177
11.8. Absorption and Emission Spectra	180
11.9. Validity of the Proposed Computational Protocol and Defined Descriptors Predicting Luminescence Properties of Solid-state Eu^{2+} -doped Phosphors	186
11.10. Summary and Conclusions	189
12 Eu^{2+}-doped Phosphors Engineered – Prediction of an Unprecedented Narrow-band Red-Emitting Eu^{2+}-doped Phosphor (CBLA)	191
12.1. Introduction	191
12.2. Collaborative Exploration: Bridging Experimental Insights with Theoretical Perspectives Towards Promising Eu^{2+} -doped Phosphors.....	191
12.2.1. Insights into the emission intensity mechanism of $\text{CLA}:\text{Eu}^{2+}$, $\text{SLA}:\text{Eu}^{2+}$, and $\text{CBLA2}:\text{Eu}^{2+}$ Phosphors.....	192
12.2.2. Insights into the emission intensity mechanism of $\text{RNLSO}:\text{Eu}^{2+}$, $\text{RNLSO2}:\text{Eu}^{2+}$, and $\text{CBLA2}:\text{Eu}^{2+}$ phosphor	193
12.3. Designing a $\text{CBLA}:\text{Eu}^{2+}$ -doped phosphor with potentially improved emission properties.	195
12.3.1. The impact of the host environment to the emission properties of the Eu^{2+} -doped phosphors.	195
12.3.2. Vibronic Coupling Effect along the tetragonal distortion pathway	198
12.3.3. CBLA an ‘ideal’ hypothetical host for a red Eu -doped phosphor with extraordinary emission properties	201
12.4. Conclusions.....	203
13 Broadening Mechanism of Luminescence in Narrow-band Eu^{2+}-doped Phosphors	204

13.1. Introduction	204
13.2. Study Set.....	207
13.3. Experimental Spectra.....	207
13.3.1. What defines the narrow band broadening in narrow band phosphors? ...	208
13.4. Theory	211
13.4.1. Zero-Field Splitting (ZFS) and Effective Spin Hamiltonian	211
13.4.2. Theory of photoluminescence relaxation times	212
13.5. Computational Details	215
13.6. Analysis of the Electronic and Magnetic Structure of Ground and Excited Emissive States.....	217
13.6.1. Non-Relativistic Limit.....	217
13.6.2. Relativistic Limit.....	220
13.7. Emission mechanism at the Static Limit. The role of the ground and excite state magnetic structures.....	226
13.8. Emission mechanism at dynamic limit	228
13.9. Relation of magnetic structure with the dynamic nature of the emissive process..	231
13.10. Luminescence Spectra.....	236
13.10.1. Luminescence Spectra in SLA:Eu ²⁺	237
13.10.2. Luminescence Spectra in SALON:Eu ²⁺ and SMS:Eu ²⁺	239
13.10.3. Luminescence Spectra in SLBO:Eu ²⁺	241
13.10.4. Luminescence Spectra in CBLA2:Eu ²⁺	243
13.11. Conclusions and Requirements for a narrow Eu-doped band phosphor	245
14 Concluding Remarks of PART II Towards Design and Tune of Solid- state Eu²⁺-doped phosphors Materials	246
PART III Towards Design and Control of Circularly Polarized (CP) Photoluminescent Materials with Long-lived Excited States	248
15 Introduction to PART III	249
16 Theoretical Spectroscopy of Circularly Polarized Absorption and Photoluminescence in Chiral Transition Metal Complexes. Chiral Re(I) complexes as Case Study	251
16.1. Introduction	251
16.2. Theoretical considerations	254
16.3. Choice of the Study Set – Geometric Structure	256
16.4. Experimental (Chiro-) Optical Properties and Photophysics	259
16.5. Computational Strategy.....	262
16.6. Absorption and Emission processes. A qualitative electronic structure analysis ...	264
16.6.1. Insights into the nature of the Emissive Excited State	267
16.7. Absorption and ECD spectra.....	269

16.7.1. Calibration of the TD-DFT protocol.....	269
16.7.2. Non-Relativistic Absorption and ECD spectra	271
16.7.3. Relativistically corrected Absorption, ECD and g_{abs} spectra.....	276
16.8. Phosphorescence Spectra and Excited State lifetimes.....	278
16.8.1. Non-heligenic NHC diastereomers	278
16.8.2. Heligenic diastereomers	283
16.9. Circularly polarized luminescence (CPL) spectra and CPL intensity mechanism..	286
16.10. Spin-vibronic Coupling	291
16.10.1. SA-CASSCF/QD-NEVPT2 Potential Energy Surfaces Scans	291
16.11. Summary and Conclusions	296
17 General Conclusion: A Journey through Photoluminescence Complexity	298
Appendixes	300
Bibliography.....	361

1 Introduction

Photoluminescence (PL) plays pivotal roles in various scientific, industrial, and technological applications.[1-4] In a surprising turn of events in 2014, both the Nobel Prizes in Physics and Chemistry were awarded for achievements closely tied to the field of photoluminescence.[5-9]

The Nobel Prize in Physics 2014 was awarded jointly to Isamu Akasaki, Hiroshi Amano and Shuji Nakamura "for the invention of efficient blue light-emitting diodes which has enabled bright and energy-saving white light sources".

The Nobel Prize in Chemistry 2014 was awarded jointly to Eric Betzig, Stefan W. Hell and William E. Moerner "for the development of super-resolved fluorescence microscopy".

Photoluminescent materials, spanning organic, organometallic, and inorganic solid-state domains, find essential roles in cutting-edge technologies such as optoelectronic devices,[10-14] light-emitting diodes (LEDs),[15-20] sensors, (bio)imaging probes,[3, 21-27] and photocatalysis.[28, 29] Among the diverse photoluminescent materials, those based on transition metals and rare earth elements, are pivotal in various applications owing to their distinct photophysical and photochemical characteristics. Furthermore, these materials not only provide a fascinating platform for fundamental research but also serve as building blocks for the development of innovative technologies with multifaceted applications.

Of particular interest are the lanthanides activated solid-state phosphor materials. These materials possess unique and tunable emission properties that are in high demand across a broad spectrum of applications. Moreover, they serve as fundamental building blocks for various solid-state devices, including energy-efficient phosphor-converted white LEDs (pc-WLEDs), solid-state lasers, liquid crystal displays, solar cells, and near-infrared detection technologies.[17-20, 30-52]

1 Introduction

Another fascinating class of photoluminescent materials is the circularly polarized (CP) photoluminescent materials. These materials exhibit not only ordinary photoluminescence but also distinct interactions with different polarization states of light. That opens up new avenues for applications across diverse domains[53] including 3D optical displays,[54-59] sensors,[56, 60, 61] photoelectric devices,[62-67] asymmetric synthetic photochemistry,[68] anti-counterfeiting,[69-71] and cryptography.[72, 73]

Tailoring and controlling the photoluminescent properties of these materials are essential for achieving specific functionalities to meet the evolving demands of technological applications. However, this task is often challenging due to the complex electronic structure inherent in these materials. Furthermore, the presence of intricate vibronic coupling and complex excited state dynamics poses significant challenges to predict and control their photoluminescent behavior. Conventional methods relied on chemical intuition and trial-and-error methods, which are time and resources intensive and not necessarily successful.[15, 74-78] Indeed, the quest for innovative luminescent materials with desired properties requires a comprehensive understanding of the structural, electronic and photophysical characteristics and their correlations. Such correlations extend beyond basic investigations to unravel the intricate interplay between electronic structures, transitions, and emission characteristics across both static and dynamic limits.[79, 80]

Molecular spectroscopy, a cornerstone in the study of materials, enables the non-invasive exploration of molecular systems. That allows the investigation of their structure, properties, and dynamics across various environments and chemical conditions. The utilization of diverse spectroscopic techniques, spanning different electromagnetic field ranges, and their synergistic application contribute to a more comprehensive understanding of the studied systems. Nevertheless, the increasing complexity of these experimental techniques necessitates computational chemistry for accurate interpretation.[81]

Computational molecular spectroscopy, initially developed within the realm of quantum chemistry to predict spectroscopic properties, has evolved into a specialized field. It now serves as a versatile tool, not only for theoretical researchers but also for those engaged in experimental studies. Leveraging theoretical and computational methods can provide a very powerful means to analyze, comprehend, and interpret spectroscopic features. In addition, the significant advancements in theoretical and computational methods, including DFT-based and WF-methods, enhance the accuracy of properties calculation, providing a powerful and productive tool. Designing systematic computational protocols contribute valuable insights

1 Introduction

into the electronic structure of studied chemical systems, bridging the gap between experiments and underlying physical properties. This synergy enables deeper understanding and identifying structural characteristics responsible for specific spectroscopic properties. Knowledge derived from computational spectroscopic models extends beyond individual molecules, offering insights into entire classes of compounds.[81, 82] Such a systematic protocol have proven instrumental in prediction and interpretation of electronic and various spectroscopic properties in diverse materials spanning molecules, complexes, and solids.[79, 80, 83-91]

The motivation behind this research lies in the imperative to overcome these challenges and contribute to a deeper understanding of photoluminescent f-block and d-block element-containing materials in molecular complexes, and solid-state materials. The task which can be achieved through a systematic developing of efficient computational protocols enables accurate prediction and interpretation of the optical properties of these materials. In addition to define structural and electronic descriptors of the underlying mechanisms of the photoluminescent spectra and photophysical properties. Through this work two classes of materials were investigated, the inorganic solid-states Eu^{2+} -doped phosphors and the chiral Re complexes.

The thesis is divided into three main parts. The first part, outlines the fundamental principles of computational chemistry and molecular spectroscopy, emphasizing their significance in analyzing the optical properties of transition and rare transition metal ions in molecular complexes and solid-state materials. These tools help interpret experimental optical properties, spectra, and electronic structures, facilitating the establishment of correlations between optical features and structural/electronic characteristics. This correlation serves as a valuable guide for designing new materials with specific targeted properties.

In the second part, the research aims to comprehensively understand the luminescent properties of Eu^{2+} -doped phosphors. The primary objectives include developing a computational protocol to explore the electronic structure, states, and optical transitions, alongside investigating the impact of vibronic coupling effects. Key to this exploration is the identification of essential structural, chemical, and electronic descriptors governing emission spectral features and the broadening mechanism. The study employs advanced techniques such as high-level electronic structure methods, spectroscopic analysis, and excited-state dynamics (ESD) to facilitate the design of phosphors with finely tuned luminescence properties for solid-state applications.

1 Introduction

Through a systematic approach, the research unfolds insights across various facets. Starting with a detailed analysis of the electronic structure of Eu^{2+} ions, emphasizing the intricate nature of excited states and the dominance of local ligand structures. Subsequently, we introduce a computational protocol that proves versatile, accurately predicting optical properties and emission features. This protocol's robustness and generality are demonstrated by successful application to more complex Eu^{2+} -doped phosphors, specifically phosphors with multiple candidates for Eu^{2+} doping. The study further exemplifies its findings through a detailed example of in-silico designed new Eu^{2+} -doped phosphor, showcasing unprecedented narrow band red emission. The collective insights contribute valuable guidelines for designing highly efficient and tailored Eu^{2+} -doped phosphors. This research not only advances our theoretical understanding but also offers a roadmap for innovative materials crucial in fields such as lighting, displays, and sensing technologies.

Finally, the third part introduces a groundbreaking computational protocol designed to predict the optical properties of chiral $\text{Re}(\text{I})$ complexes, focusing on the $[\text{fac-ReX}(\text{CO})_3\text{L}]$ family. We explore the diverse spectroscopies of these complexes which provide a nuanced understanding of the electronic and chiroptical characteristics. That includes computation and interpreting of absorption, emission, circular dichroism (CD) and circularly polarized luminescence (CPL) spectra.

The protocol navigates the challenges posed by electronic complexity, employing methods like TD-DFT, state-of-the-art wavefunction-based methods and ESD approaches. Rigorously calibrated against parameters with known error bars, the protocol achieves remarkable agreement between theoretical and experimental spectra. That allows a quantitative analysis of the experimentally observed spectral features, providing deeper understanding of chiroptical properties. Examining different diastereomers within the family, it uncovers that different type of charge transfer dominating the emission process can lead to different relaxation mechanisms. This distinction significantly influences photoluminescent properties, including spectral bands, spin-vibronic coupling, relaxation times, and quantum yields. Crucially, the study identifies spin-vibronic coupling as a key factor shaping the photophysics of $\text{Re}(\text{I})$ complexes.

In conclusion, the findings of this research contribute to the advancement of our understanding of the photophysical properties and underlying mechanisms governing photoluminescent materials. The developed computational protocols serve as powerful tools that can be extended to encompass a broader range of similar materials, offering insights into their optical behavior, and facilitating the exploration of novel luminescent systems. These

1 Introduction

results not only enhance our theoretical comprehension but also provide valuable guidance for experimental efforts aimed at designing innovative photoluminescent materials with tailored properties for specific applications. Ultimately, this research paves the way for the development of next-generation materials that meet the evolving demands of various technological fields, including lighting, displays, sensing technologies, and beyond.

PART I

Theory of Computational Spectroscopy for Unraveling the Electronic Structure and Photoluminescence

2 Introduction to PART I

This part provides an overview of the fundamental theories, methods, and concepts in computational chemistry and spectroscopy. They serve as powerful tools for computing and understanding the optical properties of transition and rare transition metal ions within both molecular complexes and solid-state materials. This framework facilitates the interpretation of experimental photophysical, optical properties and spectra in terms of electronic structure and dynamics effects. That also enables the establishment of correlations between optical properties and structural and electronic characteristics, which can be leveraged as a guiding map for the design of novel materials with targeted properties. Comprehensive discussions on these topics are covered in various authoritative textbooks and literature.[82, 92-114]

In **Chapter 3**, we introduce the fundamentals of spectroscopy, exploring the light-matter interaction and various optical processes, while shedding the light on specific experimental spectroscopic techniques. Moving to **Chapter 4**, the electronic structure of molecules and ions doped in crystals is demonstrated, focusing on the energy levels and the influence of molecular environments, including crystal/ligand field effects, and spin-orbit (SO) coupling. This chapter also introduces the calculation of zero-field splitting, of ground or excited SO states, utilizing the effective spin Hamiltonian formulation. **Chapter 5** provides a comprehensive overview of the electronic structure methods for studying ground and excited states, encompassing both wavefunction-based and DFT-based methods.

Chapter 6 establishes the theoretical foundations for electronic transitions and spectroscopies, encompassing radiative and non-radiative processes, as well as the effects of vibronic coupling on optical spectra. The calculation of excited states dynamics is explored, demonstrating the efficient treatment through Fermi's Golden Rule within the path integral formulation. This enables the computation of absorption and luminescence rates and spectra, extending to circularly polarized absorption and luminescence rates and spectra in chiral systems. Finally, in **Chapter 7**, the focus shifts to modeling photoluminescent molecules and

2 Introduction to PART I

solids, presenting computational strategies and models for both finite molecules and solid-state materials. Throughout the work, we consistently employ the embedded cluster approach for modeling computations of properties in solid-state materials.

3 Introduction to Spectroscopy (Light Matter Interaction)

3.1. Introduction to Spectroscopy

Spectroscopy is the study and monitoring of interaction of light and other radiation with matter, which result in spectra. Hence, more comprehensively, spectroscopy monitors the production, investigation, and interpretation of spectra. As illustrated in **Figure 3.1**, the electromagnetic spectrum spans over a wide range of energies. In principle, light exhibits a dual wave-particle nature. The wave nature (*classical picture*) of light is characterized by wavelength λ , and propagates through space (vacuum) with the speed $c = 1/\alpha \cong 137$, in atomic units where α is hyperfine constant.[94]

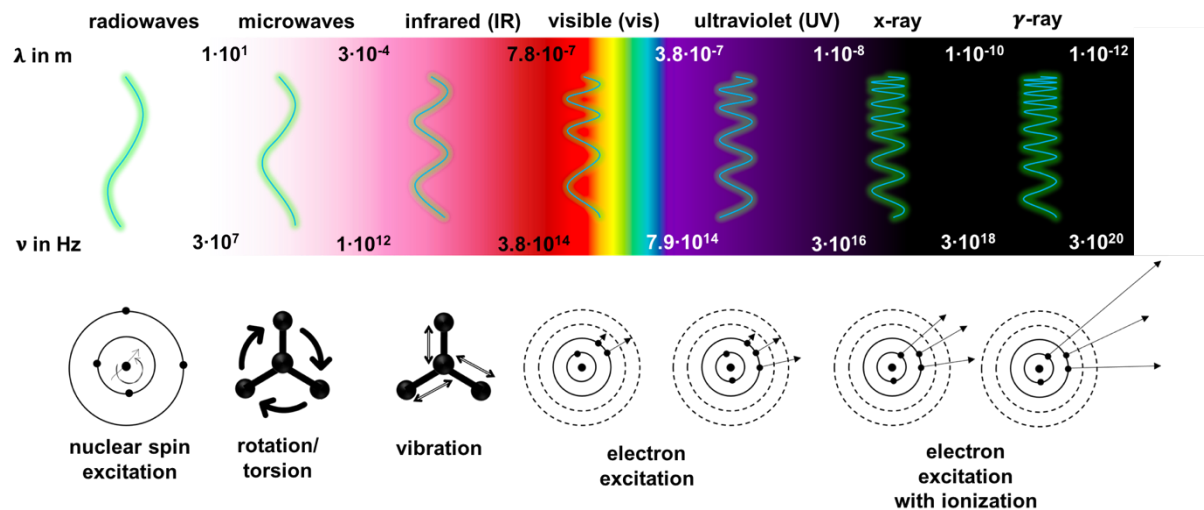


Figure 3.1. The electromagnetic spectrum and the types of excitations and the spectroscopies within the different spectral regions (adapted from Ref[115]).

Chemical systems encompass atoms, ions, molecules, and ion-doped in solids, exclusively exist in distinct energy states. Transitions between these quantized states, known as spectroscopic transitions, are characterized by the absorption or emission of energy quanta called photons (*quantum picture*). As introductory example, we discuss the two-level system given in **Figure 3.2**.

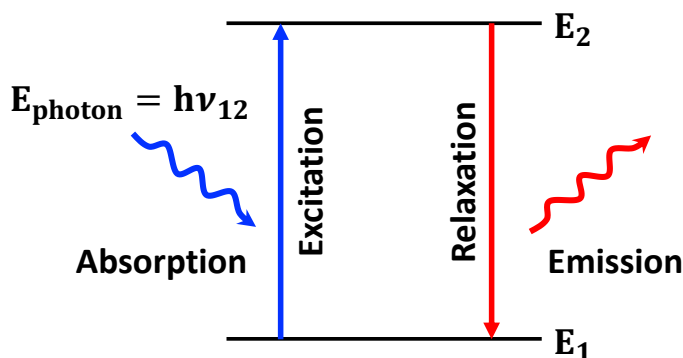


Figure 3.2. Possible transitions (absorption, emission) in a two-levels quantum system.

The energy (E_{photon}) and momentum (p) of the absorbed or emitted photon are quantized and can be expressed, and related according to the Bohr's and de Broglie's relations, by

$$E_2 - E_1 = E_{\text{photon}} = h\nu = \frac{hc}{\lambda} = pc \quad (3.1)$$

where, h is the Planck's constant and ν is the frequency of absorbed or emitted photon. E_1 and E_2 are the discrete energy levels. Photons possessing energy equal to the energy gap of the system exhibit the potential for interaction (*resonance condition*). This interaction precipitates the exchange of energy either into or out of the system, which manifests as the radiative processes of absorption or emission, respectively. In a broader sense, these energy exchanges can be quantified through spectroscopic techniques. The investigation and analysis of spectra give invaluable insights into the underlying chemical architecture, as well as the electronic and magnetic characteristics thereof.[81, 114]

Numerous spectroscopies and spectroscopic techniques are designed, basically based on, and classified according to how light and matter interact, causing reflection, refraction, diffraction, absorption, emission, or scattering, ... of radiation by matter (some are shown in

Figure 3.3) over a selected range of radiation energy. The diversity of electromagnetic radiation energy between the different spectral regions, leads to differences in their production, detection, interaction with matter. So, each spectral region can resonate with a specific type of transitions (excitations/decays) in atoms, molecule, or solids, leading to different type of spectroscopic techniques, as illustrated in **Figure 3.1**. [114]

In magnetic resonance spectroscopies (NMR and EPR), microwaves cause transition in (nuclear and electron) spin states, respectively which are resonating with external magnetic field. They give information about the molecular structure and local environment of paramagnetic ions, respectively. Radio- and IR regions are in the range of the molecular rotations and vibrations, helping to understand the vibrational behavior and normal modes of molecules and phonon structure in solids. Electronic structure and transitions can be studied by the absorption and emission of UV-Visible-NIR radiation by valence electrons, leading to optical spectroscopy. Core-electrons of atoms can be only treated by high energy X-rays, leading to various x-ray absorption (XRD, AEFS, EXAFS) and emission (XES) spectroscopies. These allow the investigation of local structure of targeted atoms and ions. [81, 114]

As a matter of fact, optical spectroscopy is an excellent tool to understand the electronic structure, energy levels and transitions of the absorbing and emitting centers in atoms, molecules, or activator ion doped in solids. In this work, which is mainly focused on the study of photoluminescent materials and their structure-property correlations, the optical spectroscopy and corresponding spectra are intensively used and studied.

Generally, the interaction between radiation (light) and matter can be approached in three different approximations: classical, quantum, and semi-classical. The classical approximation treats both radiation and matter classically, while the quantum approximation employs quantum mechanics to analyze their behavior. However, neither of these approximations is optimal for theoretical treatment in optical spectroscopy. [114] The classical approximation overlooks the electronic characteristics of molecules and transitions between states, which can only be understood on the quantum level. In contrast, the quantum approximation, while being the most accurate, adds significant complexity by treating light quantum mechanically. In many cases, the classical description of radiation is sufficient since the wavelengths of optical transitions typically exceed the size of the spectroscopically active atom or molecule. For example, the ionization wavelength of the Hydrogen atom can be expressed by

$$\lambda_{ion} = \frac{1}{R_{\infty}} = \frac{4\pi a_0}{\alpha} \quad (3.2)$$

where, a_0 is the Bohr radius and R_{∞} is Rydberg constant. The ratio between the ionization wavelength and the size of Hydrogen atom, represented as its circumference ($2\pi a_0$), will be

$$\frac{\lambda_{ion}}{2\pi a_0} = \frac{4\pi a_0/\alpha}{2\pi a_0} = 2/\alpha \approx 274 \quad (3.3)$$

which clearly demonstrates that, λ_{ion} is ($\log_{10} 274$) ~ 2.5 order magnitude larger than the size of Hydrogen atom, making it possible to neglect the particle (quantum) nature of light and utilize the wave picture.[94] This leads to the adoption of the semi-classical approximation, which is suitable for explaining a variety of spectroscopic features. In this study, we employ this approach, describing the material by its quantum response while considering the propagating radiation classically using Maxwell's equations.

3.2. Photon Field (Maxwell's Equations)

As previously depicted in **Figure 3.1**, electromagnetic radiation spans a spectrum encompassing radio waves, microwaves, infrared light, visible light, ultraviolet rays, X-rays, and gamma rays. Despite their diversity in photon energy (wavelength λ), they share same characteristics described by Maxwell's equations.

Maxwell's **Equations (3.5)-(3.8)** provide a comprehensive mathematical description of electromagnetic phenomena. They also help to understand the behavior of electric, magnetic fields, their interactions with charged particles, and the principles of electromagnetic radiation.[116] They actually show that oscillating electric and magnetic fields can propagate through space in the form of electromagnetic waves with the same speed c , defined as

$$c = (\epsilon_0 \mu_0)^{-1/2} \quad (3.4)$$

where, ϵ_0, μ_0 are the electric permittivity and magnetic permeability in free space, respectively.

The well-known Maxwell's equations and their descriptions are collected in **Table 3.1**. Taking into account that, \mathbf{E}, \mathbf{B} are electric and magnetic field vectors, respectively and \mathbf{H} is the magnetizing field. $(\nabla \cdot), (\nabla \times)$ represent the divergence and curl of the field.

Table 3.1. Maxwell's equations (in differential form) given in free space with no charge density.

Description	Homogenous medium (free space)	
Gauss's theorem for electrostatics	$\nabla \cdot \mathbf{E} = 0$	(3.5)
Gauss's theorem for magnetism (proves no magnetic monopoles)	$\nabla \cdot \mathbf{B} = 0$	(3.6)
Faraday's and Lenz's law of electromagnetic induction	$\nabla \times \mathbf{E} = -\frac{\partial \mathbf{B}}{\partial t}$	(3.7)
Ampere's law for magnetomotive force	$\nabla \times \mathbf{H} = \mu_0 \epsilon_0 \frac{\partial \mathbf{E}}{\partial t}$	(3.8)

The comprehensive derivations and explanations of the equations are omitted and can be found in other sources[116-118], thus, the primary focus is on the main implications of them. Maxwell's equations control the time evolution of electric and magnetic fields, and their solutions show the *transverse nature* of electromagnetic radiation, where the electric and magnetic field are *in phase* and *mutually perpendicular* and to their direction of propagation. In isotropic free space, the four equations combined to two similar equations.

$$\nabla^2 \cdot \mathbf{E} = \epsilon_0 \mu_0 \frac{\partial \mathbf{E}}{\partial t} \quad (3.9)$$

$$\nabla^2 \cdot \mathbf{B} = \epsilon_0 \mu_0 \frac{\partial \mathbf{B}}{\partial t} \quad (3.10)$$

Equations (3.9) and (3.10) are classical wave equations for the waves travelling through free space with speed c . Due to the similarity between the electric and magnetic fields, and instead of two vector fields (\mathbf{E}, \mathbf{B}), their representation can be reduced time-dependent potentials, more precisely to the scalar potential φ and vector potential \mathbf{A} , [94] as follows

$$\mathbf{E} = -\nabla\varphi - \frac{\partial \mathbf{A}}{\partial t} \quad (3.11)$$

$$\mathbf{B} = \nabla \times \mathbf{A} \quad (3.12)$$

and within the Coulomb gauge ($\nabla \cdot \mathbf{A} = 0$), the vector potential can be expressed as

$$\mathbf{A} = A_0 \hat{e} e^{i(\mathbf{k} \cdot \mathbf{r}) - \omega t} \quad (3.13)$$

where, $\mathbf{k} = \omega/c$ is the wave vector, $\omega = 2\pi\nu$ is the angular frequency, \hat{e} is the unit vector, and $\mathbf{r} = (x, y, z)$ is the position vector. A_0 is the amplitude of vector potential, and related to the electric and magnetic amplitudes as

$$A_0 = -\frac{E_0}{\omega} = -c \frac{B_0}{\omega} \quad (3.14)$$

In spectroscopy, one of the most important quantities is the light intensity I , which measure the energy of either emitted or reflected light per unit time per unit area. Owing to the fast change of the electric and magnetic fields with respect the time, so, it is valid to write the energy density in terms of time-averaging over both the electric and magnetic fields. The total average energy density, traveling in non-magnetic material, can be written as

$$\langle U \rangle = \frac{1}{2} \epsilon_0 |E_0|^2 \quad (3.15)$$

and finally the intensity, in vacuum, can be written can as shown in **Equation (3.16)**.

$$I = \frac{1}{2} \epsilon_0 c |E_0|^2 \quad (3.16)$$

3.2.1. Linear and circular polarization of Light

The plane-wave solution of the Maxwell's equation can be rewritten as,

$$\mathbf{E} = \mathbf{E}_0 e^{i(\mathbf{k} \cdot \mathbf{r} - \omega t)} \quad (3.17)$$

where, \mathbf{E}_0 is called the polarization vectors of the electric field, which are complex 3-dimensional vectors. For light propagating along the z-axis (direction of \mathbf{k} vector),

$$\mathbf{E}(\mathbf{z}, t) = (E_x \mathbf{x} + E_y \mathbf{y}) e^{i(kz - \omega t)} \quad (3.18)$$

E_x, E_y are the amplitude along x, y direction. Owing to the linearity of the equation, they can be decomposed into a superposition of sinusoidal functions, with adding a phase angle ϕ , so, it can take the form

$$\mathbf{E}(\mathbf{z}, t) = E_x \mathbf{x} \cos(\mathbf{k} \cdot \mathbf{z} - \omega t) + E_y \mathbf{y} \cos(\mathbf{k} \cdot \mathbf{z} - \omega t + \phi) \quad (3.19)$$

In fact, the relationship between E_x, E_y and ϕ describes the polarization of the light. If $E_y = 0$, that describes a *linearly polarized light*. If $E_x = E_y$ and ϕ has any value but not $\pm n\pi$, that generally produces an *elliptically polarized light*. A special case when if $\phi = \pm\pi/2$ results in *left and right circularly polarized light*, (LCP and RCP light), respectively. From quantum mechanics, that correspond the spin angular momentum of the photons. photon has spin $s = 1$, with two possible spin angular momentum $m_s = \pm 1$, corresponding to the two circularly polarized components (LCP and RCP) of photon, respectively.

3.3. Optical Processes and Experimental Schemes

Light exhibits diverse interactions within an optical medium like solid-state material, as illustrated in **Figure 3.3**. These optical phenomena collectively contribute to a comprehensive understanding of light behavior in optical systems and giving valuable insights into the structural and electronic properties of the system. The subsequent sections briefly explore these processes, elucidating some of the corresponding experimental schemes and their implications on the fundamental characteristics of matter.

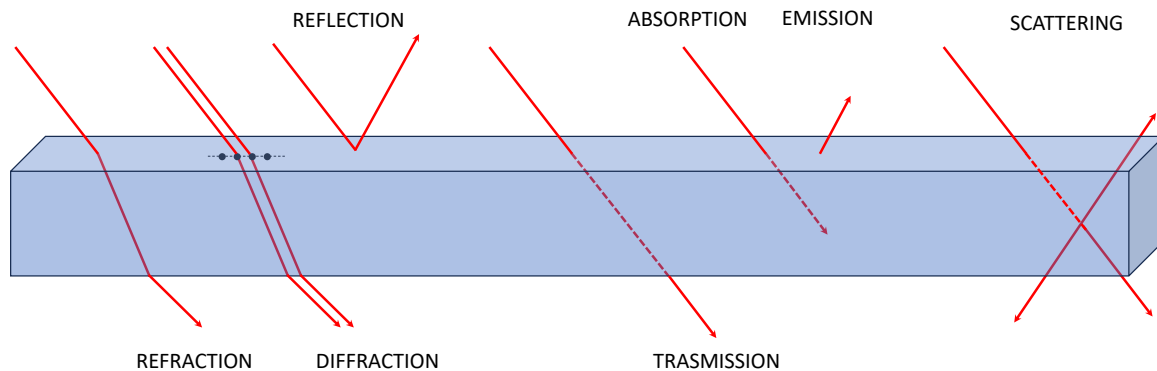


Figure 3.3. The possible optical interactions when a solid material is illuminated with light.

3.3.1. Transmission

When a light is incident to a transparent material, besides light absorption, other portion will be transmitted (**Figure 3.3**). Transmission offers supplementary information to the absorption to investigate for instance band structure in semiconductors. The interrelation between transmission and absorption can be established using the Kramers-Kronig (K-K) relations. It is determined by transmissivity ($T = I_T/I_0$), defined as the ratio of the transmitted (I_T) to incident (I_0) Intensities.[119]

3.3.2. Reflection— band gap in semiconductors

It causes light to bounce off the surface of the material with the same angle of incidence. Similarly, reflectivity spectra provide comparable and supplementary information to absorption measurements, serving as an alternative approach to studying fundamental absorption, for instance direct and indirect band gap of semiconductor. Also, its interrelation with absorption spectra again can be built employing the KK relation, where the reflectivity (R), can be given as the ratio of reflected intensity (I_R) to incident intensity (I_0).[119]

$$R = I_R/I_0 \quad (3.20)$$

There are two types of reflectivity spectra; 1) specular reflection on smooth surfaces, where light reflects at the same angle and 2) diffuse reflection on rough or textured surfaces, where light reflects in various directions due to surface variations. For diffuse reflectivity measurements, an integrating sphere (fully reflective inner surface) is utilized (**Figure 3.4 a**). The light enters the sphere and is transmitted towards the sample. The diffuse reflected light reaches the detector after undergoing multiple reflections on the inner surface of sphere. Diffuse reflectivity spectra are of great importance in solid state phosphors and used to measure the optical band gap of undoped and doped hosts, see **Figure 3.4 b**.

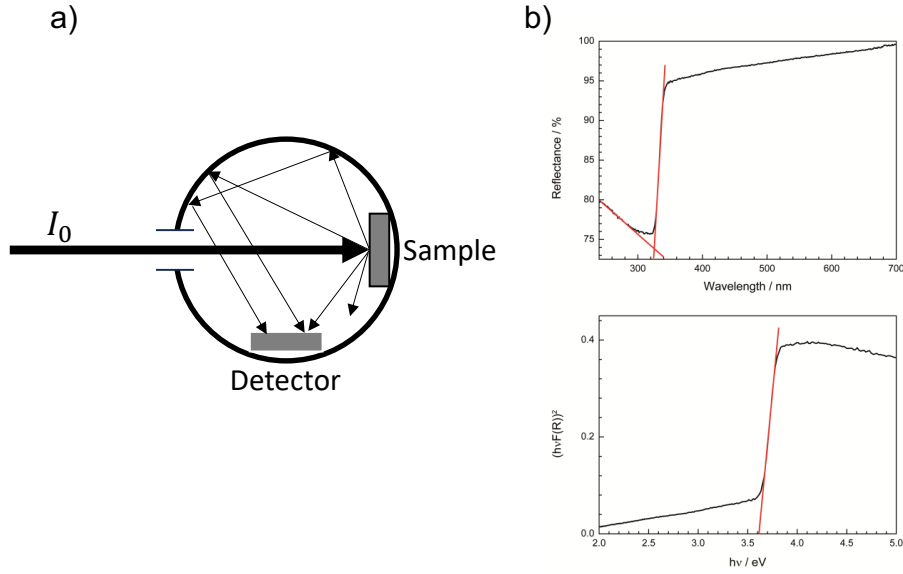


Figure 3.4. a) A schematic presentation of an integrating sphere for measuring diffuse reflectivity spectra. b) Reflectance spectrum and Tauc plot ($n = 1/2$) of $\text{BaLi}_2[\text{Be}_4\text{O}_6]$ (adapted from Ref[120]). The band gap is estimated with both methods and is found in a range from 3.6-3.8 eV. The band gap from UV/vis-reflectance data by drawing two-line tangents to the slope of the reflectance curve. The point of intersection of the tangents is the value of the band gap.

3.3.3. Refraction

It is a phenomenon causing change in direction of light when light passes from one transparent medium to another. This change in direction is due to the difference in the speed of light in the two mediums. It can be quantified by a fundamental property of materials called the refractive index (n) defined as the ratio of the speed of light in a vacuum (c) to the speed of light (with energy ω) in the material (v)

$$n(\omega) = \frac{c}{v} = \sqrt{\frac{\epsilon\mu}{\epsilon_0\mu_0}} \quad (3.21)$$

Clearly, $n(\omega)$ depends on the energy of refracted light leading to famous dispersion of white light when passes through a prism. In spectroscopy, the refractive index affects the propagation of light through materials, influencing spectroscopic techniques and should be including when dealing with absorbed or emitted light. For instance, the intensity of light I related to electric

field in vacuum defined in **Equation (3.16)**, should be modified when light pass through another medium or solvent as

$$I = \frac{1}{8\pi} c n k^2 A_0^2 \quad (3.22)$$

3.3.4. Diffraction and Crystallography

Diffraction is a phenomenon that occurs when waves encounter an obstacle or aperture and undergo bending or spreading out, as show in **Figure 3.3**. This phenomenon is a key tool in determining the atomic structure and symmetry of crystals.

X-ray diffraction has played a crucial role in advancing our understanding of materials and their properties. It has been used to determine the atomic structures of numerous compounds, including complex organic molecules, minerals, proteins, and inorganic solids.[121, 122] When X-rays pass through a crystal, they interact with the electrons surrounding the atoms, causing the X-rays to scatter according the Bragg's law

$$n\lambda = 2d \sin\theta \quad (3.23)$$

where n is an integer representing the order of the diffraction, λ , θ are the wavelength and angle of incidence of the incident X-rays, d is the spacing between the crystal lattice planes. The scattered X-rays interfere constructively and destructively, resulting in a distinct diffraction pattern. The positions and intensities of these spots provide valuable information about the crystal's atomic arrangement. By analyzing the diffraction pattern, comparing the pattern of known crystal structures and mathematical models, information about the arrangement of atoms, the distances between them, and the symmetry of the crystal lattice can be extracted. This knowledge is invaluable for understanding the properties and behavior of crystalline materials.

3.3.5. Absorption, Emission and Luminescence

Generally, absorption refers to the process in which an atom or molecule absorbs energy from incident electromagnetic radiation (photons). When the energy is matching the energy difference between two rotational, vibrational, electronic, or spin energy states, leading to the excitation. This leads to the promotion of system from ground state or lower energy state to a

higher energy excited state. In this discussion we primarily focus will be on electronic transitions.

Emission is the inverse process to absorption. The system spontaneously relaxed from the unstable excited state to its ground state (de-excitation process), emitting photons. This de-excitation process is generally referred to as spontaneous emission, radiative decay or luminescence in solid-state materials. Before the emission, the system stays for a short time, called excited state lifetime, which in conjunction with the emission spectra helps to characterize the nature of transition and the excited state energy levels involved.

Besides the spontaneous emission, the system in the excited state can be triggered to release a photon by an incident photon with the same energy and phase. This process is called the stimulated emission, which amplifies the emission, leading to the production of intense, monochromatic, and coherent beam of light. It is the fundamental processes underlying the operation of lasers.

The absorption and emission processes are characterized by the absorption and emission spectra, which represent the energy of transitions at which the system absorbs or emits most efficiently, i.e., with higher optical coefficients. However, in the absorption spectra, different types of transitions can occur depending on the scanning energy range. These transitions can involve excitations from the ground state to different higher energy levels. In contrast, the emission spectra primarily represent the relaxation process from the lowest excited state back to the ground state. This process follows the Kasha's Rule,[123] which states that in most cases, the emission occurs from the lowest excited state. The emission spectrum provides valuable information about the energy released during the relaxation process and can be used to study the electronic and vibrational properties of the system.

From a microscopic point of view of the transition process from initial state $|\psi_i\rangle$ to a final state $|\psi_j\rangle$ with N and N' are the initial and final state population densities, respectively. The optical transition coefficient $\alpha(\omega)$ of this system can be written as

$$\alpha(\omega) = \sigma_{ij}(\omega)(N - N') \quad (3.24)$$

where $\sigma_{ij}(\omega)$ is the so-called transition cross section and represents the ability of our system to absorb or emit the radiation with energy ω .

On the quantum level, according to Fermi's golden rule, the transition probability σ_{ij} can be given as

$$\sigma_{ij}(\omega) = \frac{\pi A_0^2}{2c^2} |T_{ij}|^2 \delta(\omega - \omega_{ij}) \quad (3.25)$$

where, A_0 is the amplitude of vector potential, as given in **Equation (3.14)**. δ is the delta broadening function while, ω, ω_{ij} are the radiation and transition energies, respectively. T_{ij} is the transition momentum and given by

$$T_{ij} = \langle \psi_j | \hat{T} | \psi_i \rangle, \quad (3.26)$$

The transition moment will be further discussed in next chapters and in the framework of vibronic coupling, due to its importance in the optical spectroscopy. And let's focus now on the how the different spectra are measured.

3.3.5.1. Experimental Absorption, Excitation and Luminescence Spectra

By analyzing the absorption and emission spectroscopy experiments in conjugation with theory, a deeper understanding of the energy levels, transitions, and electronic structure of the material or molecule can be achieved.[114] **Figure 3.5 (a, b, and c)** gives an overview of the optical layout of the famous absorption, excitation, and luminescence spectra detection, respectively. The difference between them lies in the phenomena being observed due to excitation.

Absorption Spectra (Figure 3.5a); when a molecule (or solution) is illuminated with monochromatic light of varying wavelengths, the molecules undergo excitation from the ground state to higher excited states. Different absorbed energies correspond to different energy levels, resulting in the appearance of an absorption band(s) in the optical spectrum. So, absorption spectrum is simply a graphical representation depicting how absorption varies as a function of incident light wavelengths.

In study of the optical properties of photoluminescent solids and ion-doped solid-state materials, the excitation and luminescence spectra are utilized. In contrast to absorption spectra detection, these techniques involve the use of two monochromators (excitation and emission).

Excitation Spectra (Figure 3.5b); show the change of the emission intensity as a function of the excitation wavelengths. The emission monochromator is set to a specific wavelength known for emission from the sample while the excitation monochromatic light is scanned

across the desired excitation range. This range should be broad enough to overlap the sample absorption band(s). (Near-)UV radiation is usually necessary to excite to energy levels above the emission level, typically in the visible or near IR region. The excitation spectrum demonstrates that for effective luminescence to occur in the crystal, the presence of emission levels and upper levels with sufficiently intense absorption is necessary. This explains the variation in luminescence intensity with different excitation modes.

Luminescence spectra (Figure 3.5c); when ions in a crystal that have reached an excited state return to the ground state through radiationless transitions or by emitting radiation. The emission transition manifests as an emission in the crystal, which is observed as a band in the luminescence spectrum. In contrast to excitation spectra, now the excitation wavelength is fixed while the emission wavelength is scanned and recorded. In addition, unlike the absorption or excitation spectra which show different bands corresponding to transitions to different energy levels, the luminescence spectrum exhibits a single narrow emission band. This is because the other broad levels do not emit light. The absorbed energy, causing transitions to these and other levels, is dissipated through fast radiationless transitions until it reaches the lowest emissive level, in accordance with the Kasha's Rule.[123] However, complex luminescence spectra consisting of multiple bands could be detected, for instance, due to presence of several emitting centers or splitting of ground state, which is typical for lanthanides and actinides complexes and materials.[124-126] Finally, the position of the band in the luminescence spectrum is independent of the excitation method and is determined by the spacing between energy levels, although specific bands may appear or be absent depending on the mode of excitation.

In luminescence spectra analysis, the focus is on the spectral composition of the emission, determining the energy level from which radiation occurs. In excitation spectra, one can observe emission resulting from transitions originating from a single emission level. However, the excitation spectrum does not register the luminescence spectrum itself but rather its overall intensity, which depends on the absorption band in which excitation occurs. Therefore, the excitation and absorption spectra will be the same if the sample under investigation follow the Kasha's rule. However, in the former the spectra are determined by the intensity of the emission, not the intensity of the radiation passing through the crystal.

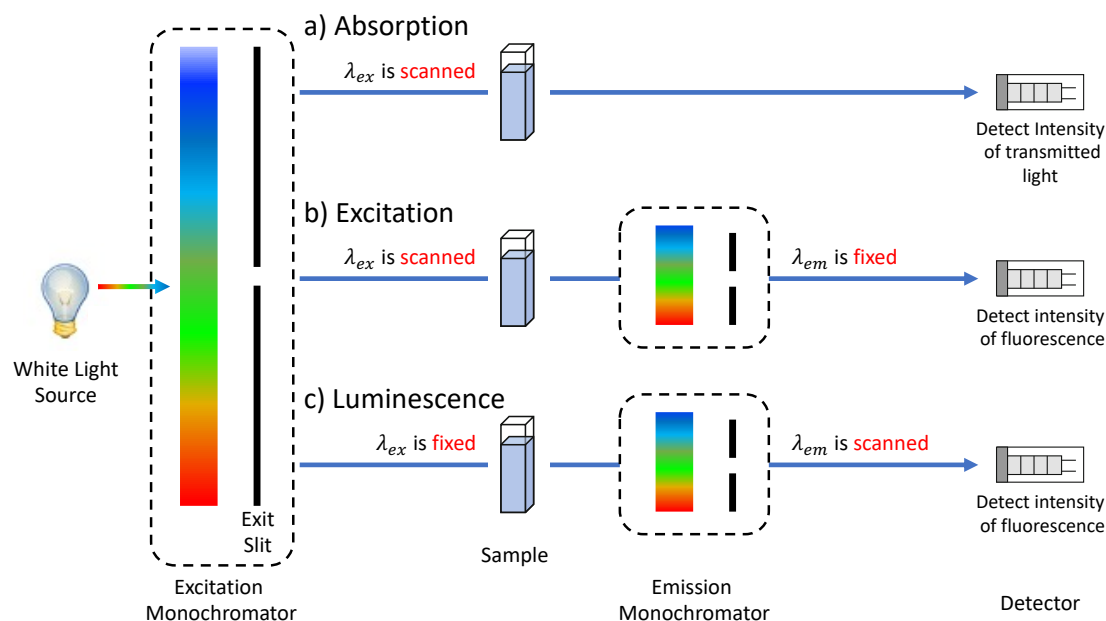


Figure 3.5. A simplified overview of optical layout for experimental measurement of the a) absorption, b) excitation, and c) luminescence spectra.

3.3.6. Scattering and Raman Effect

Also, light can scatter. a common manifestation of scattering is the red color of the sky during sunset, and the blue during the day, both occur because of Rayleigh scattering of the sunlight due to particles in the atmosphere. This type of scattering is an elastic photon process and it is much more intense for higher frequencies.[114] Inelastic photon scattering processes are also possible, known as Raman scattering or emission.

The different Raman emissions are schematically presented in **Figure 3.6**. When light interacts with a sample, various processes occur, including direct specular reflection and elastic scattering (Rayleigh scattering), where light is emitted from the sample at the same energy as the incident light. Raman inelastic scattering involves incident photons inducing a vibrational oscillation specific to the molecule's chemical moiety. In Stokes scattering, energy is absorbed by the molecule, and the emitted photon has a shorter wavelength than the incident photon. If the molecule is initially in a vibrationally excited state, it can de-excite vibrationally, transferring energy to the scattered photon (anti-Stokes Raman scattering). Raman spectroscopy can provide information about vibrational modes and structural changes and environment of molecules and solids.[110, 113, 114, 127-129]

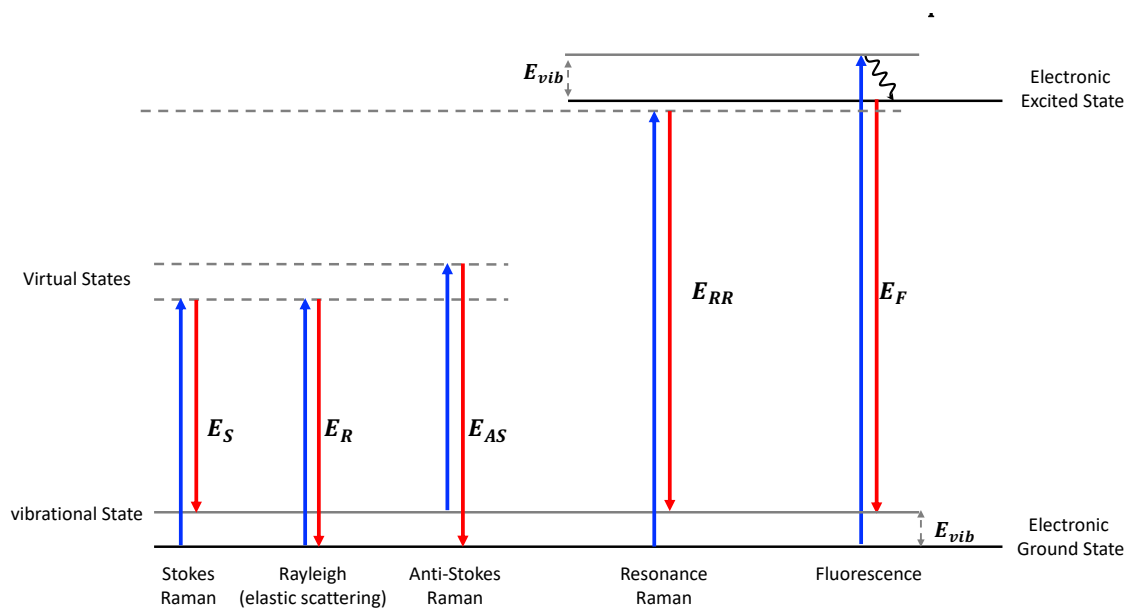


Figure 3.6. Schematic representation of the Raman effect, compared with the fluorescence. Excitation and deexcitation are generally presented by blue and red arrows, respectively. Electron, vibration states are presented by black, gray lines, while virtual states are given in gray dotted lines. E_S, E_R, E_{AS} are the energy of Stokes, Rayleigh scattered, and anti-Stokes photon. E_F, E_{RR} are the energy of fluorescence and resonance Raman emission; E_{vib} , is the energy of molecular vibrational transition.

Finally, resonance Raman (RR) is a special case where the excitation energy is very close to an electronic transition of a molecule. This has the advantage that vibrational transitions associated with the electronic change are substantially enhanced compared to other Raman transitions. The main differences between fluorescence and RR, is the lifetime difference. Fluorescence excited states are longer-lived than the virtual states associated with Raman scattering. In addition, energy of fluorescence emission is generally independent of the energy of the exciting light. In contrast, the light scattering energy increases with the increase in energy of the exciting light. [130]

Raman and infrared absorption spectra are often complementary methods with which to investigate the energy-level structure associated with vibrations. If a vibration (phonon) can cause a change in the dipolar moment of the system, then the vibration is infrared active. On the other hand, if it can cause a change in polarizability, it is Raman active. For molecules with center of inversion (*i*), an infrared-active vibration is Raman inactive, and vice versa, according to the mutual exclusion rule.[128]

3.3.7. Polarization and Chirality

Circular polarization of light has been introduced in **Section 3.2.1**. While isotropic molecules interact with both (LCP/RCP) similarly, chiral molecules are characterized by its differential interaction between left and right circularly polarized (LCP/RCP) light, results in optical activity. In this case, the molecule can differentially absorb or emit, leading to CP absorption ($I_{abs}^{LCP} \neq I_{abs}^{RCP}$) or luminescence ($I_{lum}^{LCP} \neq I_{lum}^{RCP}$) spectroscopies. The optical activity, differential interaction RCP/LCP light, is mainly due to change of the direction/sign of photon angular moment during the excitation or de-excitation transition translated to the absorbed or emit photon. This can be mainly induced by either, spatial chirality (stereochemical asymmetry) in chiral molecules or by spin polarization of the excited states which could be internally induced for example by spin-orbit coupling (SOC).[79, 131, 132] This gives rise to the well-known electronic circular dichroism (ECD) and circularly polarized luminescence (CPL) spectroscopies describing respectively absorption and luminescence processes. A case study of chiral Re complexes, is given **PART III**.

While most optically active substances exhibit inherent chirality, it is possible to externally induce optical activity in certain materials, by applying an external magnetic field. In high spin states $S \geq \frac{1}{2}$, The field will split the degenerate $\pm M_s$ states, which will interact different with CP photons, and leading to differential intensity ($I^{LCP} \neq I^{RCP}$) of the absorption or luminescence spectra, known as magnetic circular dichroism (MCD) and magnetic circularly polarized luminescence (MCPL) spectroscopies, respectively.

To summarize, we have described in this chapter the major light-matter interactions that are probed in the various spectroscopic experiments. In fact, we have seen that light can interact with matter in multiple ways, providing a non-invasive avenue to explore the structure, properties, and dynamics. The effective utilization of various spectroscopic techniques, spanning different electromagnetic field ranges, and their synergistic application enhances our comprehension of the systems under study. The growing complexity of these experimental methods and outcomes necessitates precise interpretation, a demand which can be fulfilled by theoretical and computational studies.[79-81, 83-91] Computational spectroscopy plays a crucial role in providing valuable insights into the electronic structure and properties of chemical systems. This approach helps identify the molecular characteristics responsible for specific spectroscopic properties, creating a more consistent and seamless integration between experimental and computational aspects.

4 Electronic structure of molecules and Ions-doped in Crystals

4.1. Optical Spectroscopy and Quantum Mechanics

Focusing on optical spectroscopy, experimental optical spectra exhibit peaks at various energies, intensities, and shapes. Computational spectroscopy proves instrumental in analyzing these features, providing comprehensive insights into electronic structure, transitions, and the dynamic effects on transitions. In the initial stage, accurate prediction of energy levels involved in the observed transitions becomes imperative for computational spectroscopy. This can be achieved by solving the Schrödinger equation of the system, ensuring an accurate calculation of the transitions present in the spectra.

4.1.1. Schrödinger Equation

Schrödinger equation is milestone of quantum mechanics.[92, 95, 112] Its exact solution gives, in principle, a full description of many-body system including, atoms, molecules, solid-state crystals, ...etc. That allows accurate determination of chemical and physical properties of the system and prediction of its behaviors at different conditions and in presence of external perturbations e.g., light, or magnetic field.

In the canonical formulation of quantum mechanics, and using *Dirac notation*, the system state Ψ_n can be described by a vector $|\Psi_n\rangle$ in the Hilbert space and its time evaluation is governed by time-dependent Schrödinger equation (TD-SE).

$$\hat{H}|\Psi_n\rangle = i\hbar \frac{\partial}{\partial t} |\Psi_n\rangle \quad (4.1)$$

where, $i^2 = -1$, $\hbar (= h/2\pi)$ is the reduced Planck's constant. The state $|\Psi(t, \mathbf{r}, \mathbf{R})\rangle$ is a normalized vector in the Hilbert space on the complex field \mathbb{C} , expressed in terms of time

(t) and spatial coordinates. For arbitrary molecular systems, $\mathbf{R} = \{\mathbf{R}_\alpha, \alpha = 1, \dots, M\}$ for a set of M nuclear coordinates and $\mathbf{r} = \{\mathbf{r}_i, i = 1, \dots, N\}$ for a set of N electronic coordinates. \hat{H} is the Hamiltonian operator with eigenvalues E_n . In stationary state, the wavefunctions take the form

$$|\Psi_n(t, \mathbf{r}, \mathbf{R})\rangle = |\psi_n(\mathbf{r}, \mathbf{R})\rangle e^{-iE_n t/\hbar} \quad (4.2)$$

and states can be described by time-independent Schrödinger equation (TI-SE).

An observable (physical quantity), O is represented with a *linear Hermitian* operator \hat{O} , can be calculated with TI-SE, which generally written as

$$\hat{O} |\psi_n\rangle = O_n |\psi_n\rangle \quad (4.3)$$

and it is an eigenvalue problem. And their eigenvalues are real and eigenfunctions are orthonormal, as shown in relations (4.4) and (4.5), respectively.[92]

$$O = O^* \quad (4.4)$$

$$\delta_{nm} = \begin{cases} 1, & n = m \\ 0, & n \neq m \end{cases} \quad (4.5)$$

Bearing in mind, that characterization of a system properties and spectroscopies, begins with a full description of the electronic structure, energy levels and possible transition under different conditions. The system energy E (summation of ground E_0 and excited $E_{i \geq 1}$ states energies) can be accurately predicted by solving the TI-SE, **Equation (4.6)**, using the “complete” Hamiltonian (\hat{H})

$$\hat{H} |\psi_n(\mathbf{r}, \mathbf{R})\rangle = E_n |\psi_n(\mathbf{r}, \mathbf{R})\rangle \quad (4.6)$$

The complete Hamiltonian (\hat{H}), should contain all interactions in rigorous way, which make it highly complicated. By de facto, those interactions have different relative relevance to be included, from system to other. So, it is reliable to start the (\hat{H}), with the dominating interactions, e.g., electrostatic interactions, and gradually add other interaction as small perturbations (as will be discussed in **Section 4.1.3**).

In addition, characterization of the electronic structure and ground state energies of system has a big impact and helps to determine other properties. That is because the fact that if two operators commute, common eigenstates exist. Consequently, any observable O represented by operator \hat{O} , and if $[\hat{H}, \hat{O}] = 0$, the eigenstates of \hat{H} can be chosen as eigenstates of \hat{O} to determine the eigenvalues of O .

However, analytical solutions of the electronic TI-SE (4.6) is not possible except for very simple systems, like Hydrogen atom. Alternatively, it can be solved either variationally or by perturbation theory, as will be discussed in Sections 4.1.2 and 4.1.3, respectively.

4.1.2. Variational principle

For a given system with time-independent Hamiltonian \hat{H} , and lowest energy eigenvalue E_0 , any given trial normalized well-behaved wavefunction $\tilde{\Phi}(r, R)$ satisfying the appropriate boundary conditions, will be an upper bound to the exact ground state energy of the system (*Variational method*), as follows

$$\hat{H} |\tilde{\varphi}_i(r, R)\rangle = E_i(\tilde{\varphi}_i) |\tilde{\varphi}_i(r, R)\rangle \quad (4.7)$$

$$\left(E_0(|\tilde{\Phi}\rangle) = \frac{\langle \tilde{\Phi} | \hat{H} | \tilde{\Phi} \rangle}{\langle \tilde{\Phi} | \tilde{\Phi} \rangle} \right) \geq \left(E_0(|\Psi\rangle) = \frac{\langle \Psi | \hat{H} | \Psi \rangle}{\langle \Psi | \Psi \rangle} \right) \quad (4.8)$$

and the trial function can be optimized until it has a minimum with respect to the variational coefficient(s) c , as follows

$$\frac{\partial}{\partial c} \langle E \rangle = \frac{\partial}{\partial c} \langle \tilde{\Phi} | \hat{H} | \tilde{\Phi} \rangle = 0 \quad (4.9)$$

However, the accuracy of the predicted energies depends on the quality of trial wavefunction, the lower the energy, the better trial function. The quality of trial function can be improved through linear variational principle, where the trial wavefunction is constructed by linear combination of set of linear independently functions $\{\tilde{\varphi}_n\}$. The variational coefficients $\{c_n\}$ are going to be optimized towards minimum $E_0(|\tilde{\Phi}\rangle)$ with $|\tilde{\Phi}\rangle$ closely approximates the system ground state $|\Psi\rangle$. That can be smoothly done by Lagrange's method of multipliers[92] with the constrain that the eigenfunctions are kept orthonormal.

4.1.3. Perturbation Theory

Perturbation theory (PT) is a very powerful method and provides a procedure to approximate the solutions of SE for \hat{H} of a system which *slightly* differs (perturbed) from a system with known solutions. For a system described by SE as in **Equation (4.6)** which can't be solved exactly, but the exact solutions of unperturbed $\hat{H}^{(0)}$, superscript (0) refers to zero-order or the known solution, and reads

$$\hat{H}^{(0)} |\Psi_n^{(0)}\rangle = E_n^{(0)} |\Psi_n^{(0)}\rangle \quad (4.10)$$

and assuming that \hat{H} is *slightly* perturbed from $\hat{H}^{(0)}$ by perturbation \hat{H}' , so the total \hat{H} can be written as

$$\hat{H} = \hat{H}^{(0)} + \lambda \hat{H}' \quad (4.11)$$

and since the \hat{H} slightly differs from $\hat{H}^{(0)}$, so its eigenfunctions and eigenvalues can be expressed in linear expression of power series in the parameter λ , as follows

$$|\Psi_n\rangle = \sum_{k=0}^{\infty} \lambda^k |\Psi_n^{(k)}\rangle \quad (4.12)$$

$$E_n = \sum_{k=0}^{\infty} \lambda^k E_n^{(k)} \quad (4.13)$$

The perturbed system will reduce to the unperturbed one, in the limit $\lambda \rightarrow 0$. Assuming non-degenerate zero-order WF and coupling of the coefficients of the same power of λ gives the n-order corrections. So, the first- and second-order energy corrections can be found as follows,

$$E_n^{(1)} = \langle \Psi_n^{(0)} | \hat{H}' | \Psi_n^{(0)} \rangle \quad (4.14)$$

$$E_n^{(2)} = \sum_{m \neq n} \frac{|\langle \Psi_m^{(0)} | \hat{H}' | \Psi_n^{(0)} \rangle|^2}{E_n^{(0)} - E_m^{(0)}} \quad (4.15)$$

Now, we can see that, the corrections in the energy depends on the effect of the perturbation operator on the unperturbed WFs. For instance, the first-order energy correction is simply the average of that perturbation $\left(E_n^{(1)} = \int \Psi_n^{(0)*} \hat{H}' \Psi_n^{(0)}\right)$, and the respective the first-order WF corrections, is

$$|\Psi_n^{(1)}\rangle = \sum_{m \neq n} \frac{\langle \Psi_m^{(0)} | \hat{H}' | \Psi_n^{(0)} \rangle}{E_n^{(0)} - E_m^{(0)}} |\Psi_m^{(0)}\rangle \quad (4.16)$$

Again, it may be represented as a linear combination of unperturbed m^{th} electronic states ($m \neq n$), where the coupling coefficient of m^{th} electronic state WF in the correction depend on the energy difference between the m^{th} and n^{th} states. *The smaller the energy difference, the larger the coupling.*

4.2. The Electronic Problem

As discussed previously, the goal is to solve the TI-SE (4.6). For a many-body (polyatomic) system containing a set of interacting N electrons and M nuclei, the total molecular Hamiltonian \hat{H} , of the non-relativistic time-independent Schrödinger equation, can be expressed as in **Equation (4.17)**.

$$\hat{H}(\mathbf{r}, \mathbf{R}) = \hat{T}_e + \hat{U}_{ee} + \hat{T}_n + \hat{U}_{ne} + \hat{U}_{nn} \quad (4.17)$$

where, \hat{T}_e, \hat{T}_n define the electrons and nuclei kinetic energy operators, respectively, \hat{U}_{ne} is the attractive electrostatic nuclei-electrons interaction, and $\hat{U}_{ee}, \hat{U}_{nn}$ define the repulsive interelectron and repulsive internuclear electrostatic interactions, respectively. In the non-relativistic approximation, the spin-orbit and spin-spin interactions are ignored. Generally, it is a safe approximation due their small effect compared to the electrostatics interaction between subatomic particles (electrons and nuclei). However, they play critical role in fine structure of spectra and magnetism for instance in rare-earth transition metal complexes, and they can be added later as perturbations to the Hamiltonian \hat{H} to solve the relativistic \hat{H} in the framework of perturbation theory, taking the solutions of the non-relativistic \hat{H} as the solution of the unpertured system.[92, 114]

4 Electronic Structure of molecules and Ions-doped in Crystals

In more details, these terms of **Equation (4.17)** are expressed respectively, in the *atomic unit* ($\hbar = m_e = 4\pi\epsilon_0 = 1$), as given in **Equation (4.18)**.

$$\hat{H}(\mathbf{r}, \mathbf{R}) = -\sum_{i=1}^N \frac{1}{2} \nabla_i^2 + \sum_{i<j}^N \frac{1}{r_{ij}} - \sum_{\alpha=1}^M \frac{1}{2M_{\alpha}} \nabla_{\alpha}^2 - \sum_{i=1}^N \sum_{\alpha=1}^M \frac{Z_{\alpha}}{r_{i\alpha}} + \sum_{\beta<\alpha}^M \frac{Z_{\alpha}Z_{\beta}}{R_{\alpha\beta}} \quad (4.18)$$

where, (\mathbf{r}, \mathbf{R}) are the electronic and nuclear coordinates, respectively, M_{α} is the atomic mass of nucleus α , and ∇ is the Laplacian operator with respect to the coordinates. $(r_{ij}, r_{i\alpha}, R_{\alpha\beta})$ are position vectors defined as follows ($r_{ij} = |\mathbf{r}_i - \mathbf{r}_j|$, $r_{i\alpha} = |\mathbf{r}_i - \mathbf{R}_{\alpha}|$, and $R_{\alpha\beta} = |\mathbf{R}_{\alpha} - \mathbf{R}_{\beta}|$).

4.3. Adiabatic and Born-Oppenheimer Approximations

Solving the TI-SE for the total molecular non-relativistic Hamiltonian defined in **Equation (4.18)**, can't be done analytically or even numerically unless some approximation is introduced.

One of the most important approximations is the adiabatic approximation, decoupling the nuclear and electronic motions based on the obvious difference in time scale associated with the motion of nuclei compared to the electrons. That is a direct consequence of the significant difference in mass between the electron and a nucleus (M), which in case of Hydrogen atom is 1/1836 (in the order of $\sim 10^{-3}$), and the ratio of average velocities of nuclei and electrons of the same order $\sim 10^{-3}$. The adiabatic approximation, decoupling of the electronic and nuclear motion, can be done under appropriate conditions that, the electrons are instantaneously following the motion of the nuclei, while remaining always in the same stationary state of the electronic Hamiltonian and do not undergo transitions between stationary states. In short, electrons are following the nuclei *adiabatically*. [97]

Within the adiabatic Born-Oppenheimer approximation, electrons moving in fixed nuclei, the term $\hat{T}_n = 0$, and the \hat{U}_{nn} term is constant. Then, the electronic energy (E_{el}) and wavefunction (Ψ), both, *parametrically* depend on the nuclear coordinates (\mathbf{R}), as given in **Equation (4.19)**.

$$\hat{H}_{el}(\mathbf{r}, \mathbf{R})\Psi(\mathbf{r}; \mathbf{R}) = E_{el}(\mathbf{R})\Psi(\mathbf{r}; \mathbf{R}) \quad (4.19)$$

Finally, the total TI-SE of system, including both electrons and nuclei, is solved in two steps,

- 1) solving the electronic problem in a field of fixed-point charges of nuclei and find the electronic energy which parametrically depends on the nuclear coordinate, as depicted in **Equation (4.19)**, then
- 2) using this electronic energy as a potential to solve the nuclear motion, which leads to the construction of potential energy surface (PES).[92, 133]

4.4. Energies levels (Static interaction)

When ion is ‘doped’ in a crystalline structure gives rise to a number of optical bands which are not present in the undoped structure, this center is called an optically active center, and its electronic structure is to a large extent similar to atomic structure of free ion but perturbed by the crystal field of the crystalline environment. This situation is very common for transition metal (TM) and rare-earth (RE) transition metals ions doped in inorganic solids. The valence electrons of TM and RE atoms/ions, especially in the latter, are relatively shielded from the external environments by the outer filled shells. So, their electronic structure and energy levels can be estimated from solution of TI-SE, within the central-field approximation (CFA).

For ion with nuclear charge $+Z$ and N electrons in external crystal-field, the total Hamiltonian, for can be written (in atomic units) as

$$\hat{H} = \hat{H}_0 + \hat{H}_{ee} + \hat{H}_{CF} + \hat{H}_{SOC} \quad (4.20)$$

where, \hat{H}_0 , $\left(\sum_{i=1}^N \left[-\frac{\hbar^2}{2m} \nabla_i^2 - \frac{Z}{r_i}\right]\right)$, represents the central field Hamiltonian, containing the electrostatic field acting on the valence electron due to the nucleus and the inner- and outer-shell electrons). \hat{H}_{ee} , $\left(\frac{1}{2} \sum_{i \neq j=1}^N \frac{1}{r_{ij}}\right)$, is the coulomb interaction among the valence electrons. \hat{H}_{CF} represents the electrostatic interaction of electrons with surrounding ions as point charges and reflects their symmetry distribution. \hat{H}_{SOC} is Hamiltonian of the spin-orbit coupling, which will be ignored for now.

Within the CFA, the total Hamiltonian can be approximated into sum of one-electron operators (\hat{h}_i) , as

$$H = \sum_{i=1}^N \hat{h}_i \quad (4.21)$$

representing an effective total central-field potential on electron i , the approximation is similar to Hartree-Fock approximation, discussed in **Section 5.1.1**. Now, the equation is separatable and can be solved.[134]

4.4.1. Atomic orbitals

First, assuming a free ion/atom, so, $\hat{H}_{CF} = 0$, the eigenvalue of the solution of problem can be given by approximating Ψ as a product of N one-electron wave functions, known as atomic spin orbitals $\{\phi_{k_i}(\mathbf{x}_i)\}$, as follows

$$\Psi(\mathbf{x}_1, \mathbf{x}_2, \dots \mathbf{x}_N) = \prod_{i=1}^N \phi_{k_i}(\mathbf{x}_i) \quad (4.22)$$

where $\mathbf{x}_i = (\mathbf{r}_i, \mathbf{s}_i)$ stands for both space and spin coordinates. $k_i = \{n_i, l_i, m_{li}, m_{si}\}$ donates the set of quantum number completely describes election i . n, l are the principle, orbital angular momentum quantum numbers, respectively while m_l, m_s are the projections of the orbital and spin angular momenta, respectively. The atomic spin orbital ϕ_{k_i} can be presented in polar coordinates, which provides a convenient way to describe the shape and orientation of the orbitals in three-dimensional space, as

$$\phi_{k_i}(r, s) = \frac{1}{r} P_{nl}(r) Y_l^{m_l}(\theta, \phi) \omega_{m_s}(s) \quad (4.23)$$

where, (r, θ, ϕ) are the polar coordinates. $P_{nl}(r)$, $Y_l^{m_l}(\theta, \phi)$ are the radial and angular functions, where the latter is a spherical harmonic where determine the orbital shape described by the azimuthal quantum number (l). That will give rise to the well-known atomic orbitals (AO) s, p, d, f, \dots for $l = 0, 1, 2, 3, \dots$, respectively. $\omega_{m_s}(s)$ is the spin wavefunction and it is an eigenfunction of the \hat{s}^2 and \hat{s}_z spin operators.

However, due to the fermion nature of electrons (the Pauli exclusion principle), requires that the many-electron WF to be antisymmetric with respect the exchange of space and spin coordinated of any two electrons. So, the total wavefunction can be presented as an antisymmetized product of the N occupied spin orbitals (slater determinant).

$$\Psi(\mathbf{x}_1, \dots, \mathbf{x}_N) = (N!)^{-1/2} \begin{vmatrix} \phi_1(\mathbf{x}_1) & \dots & \phi_N(\mathbf{x}_1) \\ \vdots & \ddots & \vdots \\ \phi_i(\mathbf{x}_N) & \dots & \phi_N(\mathbf{x}_N) \end{vmatrix} \quad (4.24)$$

the subscript i identifies a particular choice of the four quantum numbers.[134]

4.4.2. Crystal Field and Coupling Schemes (are Electrons in collective or individual Behavior?)

Now, let's restore the total Hamiltonian, **Equation (4.20)**, where relative strength of the three (H_{ee}, H_{CF}, H_{SOC}) terms leads into different limits,[114]

1) *Weak crystal Field Limit* ($H_{CF} \ll H_{SOC} < H_{ee}$)

Implying, that the crystal field can be treated as a perturbation over the ion energy ^{2S+1}L terms, where L and S are the orbital and spin angular momenta. For example, trivalent rare earth complexes fall in this category, like Eu^{3+} , where valence 4f electrons are highly shielded from CF.

2) *Strong crystal Field Limit* ($H_{SOC} < H_{ee} < H_{CF}$)

Implying, that the crystal field dominate the interaction and splitting of the ^{2S+1}L terms, this usually the situation in TM complexes.

3) *Intermediate crystal Field Limit* ($H_{SOC} < H_{CF} < H_{ee}$)

Implying, that the crystal field is stronger than SOC, and both are less than the valence electron repulsion, so, both of them can be treated as perturbations to the ion energy ^{2S+1}L terms. An example for that is Eu^{2+} complexes. While their ground state is dominated by 4f⁷ highly shield (should follow **limit 1**), their lowest excited states involve excitations to 5d orbitals (should follow **limit 2**), leading to 4f⁶5d¹ configuration which now can be treated within the **intermediate limit 3**. While useful, this is in fact, a rather simplistic approximation of the problem. As it will be discussed later, systems bearing Eu^{2+} ions, need more rigorous treatment.

Furthermore, SOC and valence electron interactions compete each other, leading to two distinct, total angular momentum, coupling schemes:[114]

- 1) ***LS –coupling*** occurs when the electrostatic interaction of valence electrons outweighs the SOC. In this scenario, the orbital momenta of all electrons are summed first to yield the total orbital momentum \mathbf{L} , followed by the combination of their spin momenta to form the total spin momenta \mathbf{S} (*Collective behavior*). Ultimately, these total orbital and spin momenta, \mathbf{L} and \mathbf{S} , are combined to establish the total angular momentum \mathbf{J} for a given configuration

$$\mathbf{L} = \sum_i \hat{\mathbf{l}}_i \quad (4.25)$$

$$\mathbf{S} = \sum_i \hat{\mathbf{s}}_i \quad (4.26)$$

$$\mathbf{J} = \mathbf{L} + \mathbf{S} \quad (4.27)$$

In *LS*-coupling, electrons exhibit a more collective behavior, joining forces to determine total orbital and spin momenta without individual consideration of SO coupling.

- 2) ***JJ –coupling*** arises in the opposite scenario, where the SOC interaction for an individual electron surpasses the interaction between electrons. This is prevalent in heavy atoms due to the proportional increase in SOC energy with the atomic number. In *JJ –coupling*, the orbital and spin momenta of each electron are summed to obtain the total angular momentum j for an individual electron (*Individual behavior*). These individual j momenta are then combined to form the total angular momentum J for the electron configuration

$$\hat{\mathbf{j}}_i = \hat{\mathbf{l}}_i + \hat{\mathbf{s}}_i \quad (4.28)$$

$$\mathbf{J} = \sum_i \hat{\mathbf{j}}_i \quad (4.29)$$

In *JJ –coupling*, the individual properties of electrons, specifically SO coupling, dominate, and electrons exhibit a more individual behavior compared to *LS*-coupling.

Depending on the angular momentum coupling type, distinct sets of quantum numbers are used for describing electronic states. In *LS –coupling*, the four quantum numbers L, M_L, S , and

M_S uniquely describe multielectron states, while in JJ –coupling, the $nljm$ set is employed for characterizing multielectron states.

4.4.3. CF Splitting and CF States

Within the CF effect, the ligands in the vicinity of the ion will affect and split the orbitals, most importantly f and d orbitals, according to the strength and spatial distribution (symmetry) of the ligands around the ion. **Figure 4.1**, give an example of the splitting of 5d orbital, known as $10Dq$, under different local ligand symmetry.

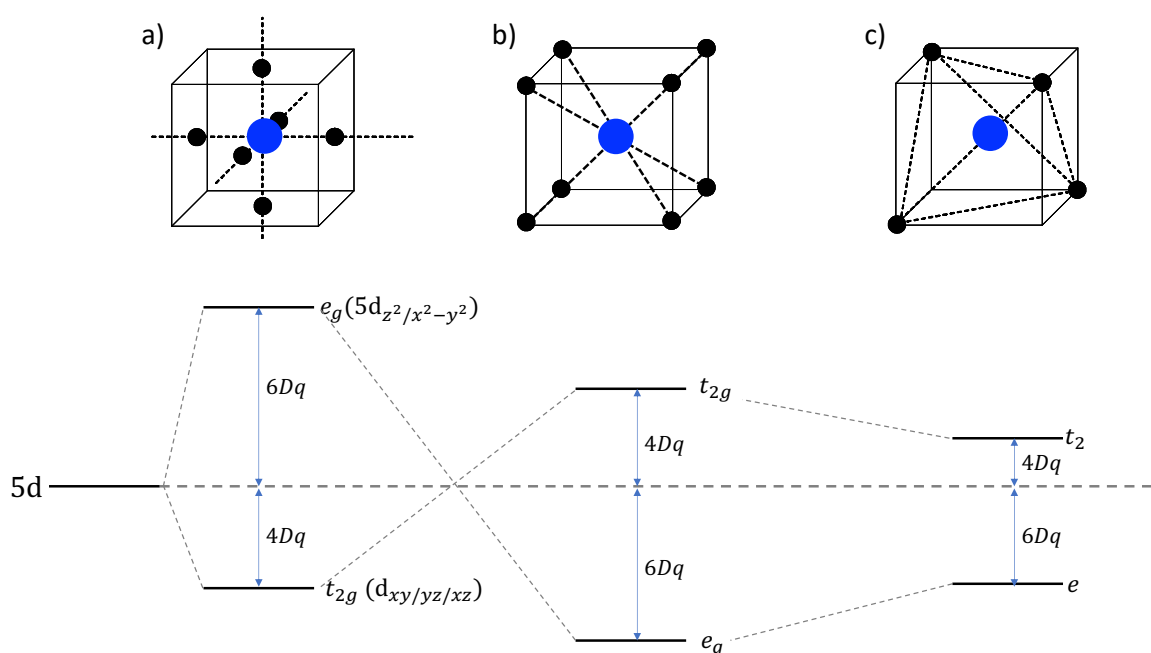


Figure 4.1. The arrangement of ligands (black dots) around a central metal ion (blue dot) and the crystal field splitting of d orbital in different symmetries: a) octahedral, (b) cubic, and c) tetrahedral.

Within the same type of ligand and M-L distances under the three cases (octahedral, cubic, and tetrahedral) gives the following relative splittings,[98, 114]

$$Dq(octahedral) = -\frac{9}{8}Dq(cubic) = -\frac{9}{4}Dq(tetrahedral) \quad (4.30)$$

It is important to emphasize that none of these (atomic or CF) orbitals are observables, in reality, the chemical systems are found in states. For example, for a TM ion with a valence d^1

electron configuration, under cubic field, it transformed into e_g^1 leading to 2E_g and the lowest excited state ($e_g \rightarrow t_{2g}$), leading to ${}^2T_{2g}$. So, we can experimentally detect, the energy difference between these two states through absorption or emission of light matching this difference. While through this simple case, the transformation looks very trivial, the situation will rapidly become complex with more electrons or with multiple open valence shells.[98, 114]

4.4.4. Covalency and chemical bonding (Ligand Field Theory)

Within the CF theory, the surrounding ligands are treated as point charges (ionic picture), ignoring their electronic structure. However, the covalent interactions between the metal center and the ligands are important and should be considered. The nature of these interactions determines the electronic configuration, stability, and properties of the TM and RE complexes.[93, 103, 135]

The ligands can be categorized based on their electron-donating abilities. In the case of TMCs, ligands usually act as Lewis bases, with some serving predominantly as σ –donors (donating electrons to metal orbitals directly) and others as π –donors or π –acceptors (interacting with metal orbitals through the π -system). The σ and π interactions contribute to the overall ligand field around the metal center, as shown in **Figure 4.2**. This effect is commonly referred as covalency, describing the delocalization of electronic density from ligand to metal, and vice versa. This mutual sharing of electron density leads to changes in the electronic structure and, consequently, influences the optical properties of the system. The covalent interaction between the metal and ligands results in different bonding scenarios, impacting the distribution of electrons within the complex. This interplay is fundamental in understanding the intricate electronic configurations and optical behaviors observed in transition metal complexes, particularly those involving the d-block metals mentioned in the provided text.

As shown in **Figure 4.2**, the covalency interaction is contingent upon the overlap integral between the metal center and ligand orbitals. This interplay gives rise to bonding and anti-bonding orbitals, a scenario typically observed in d-containing complexes. When the overlap is zero, the metal orbital assumes a non-bonding character, making the ionic picture apt. This circumstance holds true, especially for 4f electrons, owing to the spatial compactness of these

orbitals and their shielding by outer closed shells, although the covalency effect is more pronounced for larger 5f orbitals.[136, 137]

Within this picture, except for metal centered (MC) electronic transitions between non-bonding orbitals, e.g., ($d \rightarrow d$, $f \rightarrow d$, or $f \rightarrow d$, ..., etc.), all the other transitions can be described as charge transfer (CT) transitions. As illustrated in **Figure 4.2**, CT transition could be metal to ligand CT (MLCT), or ligand to metal CT (LMCT). In addition, there are possibilities for ligand centered (LC) charge transfer where the transition occurred within the same ligand, or it could be from ligand to another ligand charge transfer (LLCT).

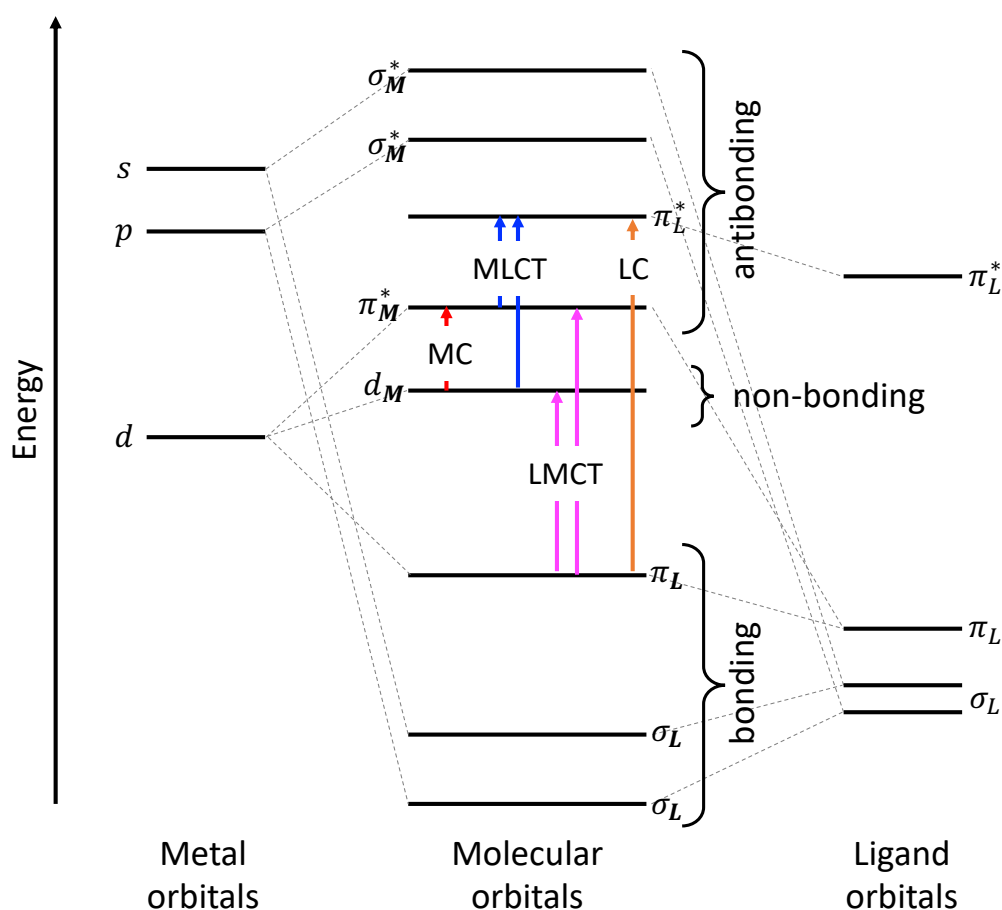


Figure 4.2. A simplified molecular orbital diagram for TM complex, depicting the relative spectroscopic excitation transitions including MC, LC, MLCT, and LMCT. The bonding (σ, π) and antibonding (σ^*, π^*) molecular orbitals are presented with subscripts indicating only the dominating component, (M or L) for metal or ligand, respectively.

4.4.5. Effective Hamiltonian

The accurate description of LF effects, on the electronic structure and transitions in d and f metal complexes, is very crucial to understand and predict electronic, optical and magnetic properties.[103] However, the complete description of the ligand field effect comes with the inherent challenge of representing the complete Hamiltonian for a metal-ligand system, making it impractical to calculate precise energies and projected WFs in the complete space.

One of the most promising approaches for treatment such complex problem is the effective Hamiltonian (EH) approach. The strength of EHs in description of such complex problems lies in their ability to isolate relevant degrees of freedom and use them to construct low-dimensional models, often very easy to solve with minimal computational effort.[138] Let us consider a system described by a Hamiltonian (\hat{H}) acting in the complete Hilbert space \mathcal{H} , while the isolated manifold of M eigenstates of an effective Hamiltonian (\hat{H}_{eff}), which belongs to a smaller \mathcal{H}' Hilbert space. The goal is to construct an effective Hamiltonian such that,

$$\hat{H}_{\text{eff}} |\tilde{\Psi}_I\rangle = E_I |\tilde{\Psi}_I\rangle, |\tilde{\Psi}\rangle \in \mathcal{H}', I = 0, \dots, M \quad (4.31)$$

$$\hat{H} |\Psi_I\rangle = E_I |\Psi_I\rangle, |\Psi\rangle \in \mathcal{H}, I = 0, \dots, \infty \quad (4.32)$$

This is achieved through the recasting of matrix elements in terms of effective parameters. EH theory offers distinct advantages by explicitly deriving model Hamiltonians from more comprehensive ones, ensuring both robust qualitative and quantitative insights into the chemical and physical description of the system. EHs play a pivotal role in rationalizing complicated properties of transition metal complexes, from magneto-structural correlations to the analysis of ligand fields.[138]

In this context, ab initio ligand field theory (AILFT) emerges as a potent tool, the ligand field interactions are described by a group of ligand field parameters (known as Slater-Condon or Racah parameters),[103] which used to construct an EH operator which can retain the original full Hamiltonian but with significantly reduced dimensionality. The EH model is established through a perturbation approach to the metal WFs. That includes the two significant interactions arising from metal interelectronic repulsion and ligand field interaction. The latter considers the influence of the chemical environment on the metal ion, including the SOC interaction. In ORCA, such AILFT EHs can be constructed, for example, utilizing the CASCI/CASSCF Hamiltonians followed by MRPT method like NEVPT2 to introduce dynamic correlation to enhance the quantitative accuracy.[139]

Finally, another pivotal example showing the strength of EHs lies in the description of magnetic structure and properties like zero-field splitting (ZFS) of the relativistic ground or isolated excited states through the spin Hamiltonian (SH) approach, as discussed in **Section 4.4.7**.

4.4.6. Spin-orbit Coupling on the Basis of Quasi Degenerate Perturbation Theory

As has been repeatedly shown spin-orbit coupling (SOC) along with the Zeeman interaction can be introduced in the framework of quasidegenerate perturbation theory (QDPT).[79, 140-145] [146-148] In the QDPT scheme SOC and Zeeman interactions act as perturbation to the non-relativistic Hamiltonian which takes the form:

$$\left\langle \Psi_I^{SM_s} \right| \hat{H}_{BO} + \hat{H}_{SOC} + \hat{H}_Z \left| \Psi_J^{S'M'_s} \right\rangle = \delta_{IJ} \delta_{SS'} \delta_{MM'} E_I^S + \left\langle \Psi_I^{SM_s} \right| \hat{H}_{SOC} + \hat{H}_Z \left| \Psi_J^{S'M'_s} \right\rangle \quad (4.33)$$

where, \hat{H}_{BO} , \hat{H}_Z are the Born-Oppenheimer and Zeeman Hamiltonians. S, M_s are the spin and spin projection of the state $|\Psi^{SM_s}\rangle$.

In this approach, the SOC operator is approximated by the spin-orbit mean field (SOMF) operator[149], which is an effective one-electron operator that contains one- and two-electron SOC integrals and also incorporates the spin-other orbit interaction. Hence, H_{SOC} is given by **Equation (4.34)**.

$$\hat{H}_{SOC} = \sum_i h^{SOC}(x_i) s(i) \quad (4.34)$$

where, $h^{SOC}(x_i)$ is the effective mean-field one-electron spin-orbit operator, (x_i) and $s(i)$ refer to the coordinates and spin-operator of electron i , respectively. By making use of the Wigner-Eckart theorem and the properties of the spin operators, the calculation of the matrix elements of the SOMF operator is given by

$$\langle \Psi_I^{SM} | \hat{H}_{SOC} | \Psi_J^{S'M'} \rangle = \sum_{m=0,\pm 1} (-1)^m \begin{pmatrix} S' & 1 \\ M' & m \end{pmatrix} \begin{pmatrix} S \\ M \end{pmatrix} \underbrace{\langle \Psi_I^{SS} | \hat{H}_{SOC} | \Psi_J^{SS} \rangle}_{Y_{II'}^{SS'}(m)} \quad (4.35)$$

where, m represents the standard vector operator components. $\begin{pmatrix} S' & 1 \\ M' & m \end{pmatrix} \begin{pmatrix} S \\ M \end{pmatrix}$ is a Clebsch-Gordon coefficient that has a single numerical value that is tabulated. It satisfies certain

selection rules and contains all of the M-dependence of the SOC matrix elements. The quantity $Y_{II'}^{SS'}(m)$ is a reduced matrix element. It only depends on the standard components of the two states involved. It has been shown that there are only three non-zero $Y_{II'}^{SS'}(m)$ cases that arise from state pairs that either have the same total spin or differ by one unit[150]:

$$Y_{II'}^{SS'}(-m) = \frac{\sqrt{S(S+1)}}{S} \langle \Psi_{I'}^{SS} | \sum_i z_{-m}(i) \hat{s}_0(i) | \Psi_{I'}^{SS} \rangle \quad (4.36)$$

$$Y_{II'}^{SS+1}(-m) = \sqrt{\frac{2S+3}{2S+1}} \langle \Psi_{I'}^{SS} | \sum_i z_{-m}(i) \hat{s}_{-1}(i) | \Psi_{I'}^{S+1, S+1} \rangle \quad (4.37)$$

$$Y_{II'}^{SS-1}(-m) = \langle \Psi_{I'}^{SS} | \sum_i z_{-m}(i) \hat{s}_{+1}(i) | \Psi_{I'}^{S-1, S-1} \rangle \quad (4.38)$$

Finally, in absence of external magnetic field, the Zeeman Hamiltonian and can be excluded.

4.4.7. Spin Hamiltonian - Zero-Field Splitting for ground and excited multiplets

A full analytical solution of the SH eigenvalue problem for the $S > 1/2$ cases can be found in several textbooks.[151-153] The ZFS, expressed in terms of the \mathbf{D} tensor, is the leading SH parameter for systems with a spin ground state $S > 1/2$. [154] The ZFS describes the lifting of the degeneracy of the $2S + 1$ magnetic sublevels $M_s = S, S - 1, \dots, -S$, which are exactly degenerate at the level of the Born-Oppenheimer (BO) Hamiltonian, in the absence of an external magnetic field. To first order in perturbation theory, the ZFS arises from the direct magnetic dipole spin-spin interaction between unpaired electrons (spin-spin coupling, SSC). To second order, contributions arise from the spin-orbit coupling (SOC) of electronically excited states into the ground state. These effects can be phenomenologically collected in the usual SH:

$$\hat{H}_{ZFS} = \hat{S} \mathbf{D} \hat{S} \quad (4.39)$$

where \hat{S} is the fictitious spin of the considered state. The ZFS parameters are defined in terms of the principal values of the \mathbf{D} tensor, by $D = \frac{3}{2} D_{zz}$ and $E = \frac{1}{2} (D_{xx} - D_{yy})$, in a coordinate system that diagonalizes \mathbf{D} . Typically, ZFS \mathbf{D} tensor in the SH is set to traceless and symmetric

(e.g. the ZFS matrix is diagonal in its eigenframe). Then, **Equation (4.39)** can be rewritten, in which D and E represent the axial and the rhombic components of the ZFS, respectively.

$$H_{ZFS} = D[s_z^2 - S(S+1)/3] + E(S_x^2 - S_y^2) \quad (4.40)$$

The choice of the axis is based on the $0 \leq E/D \leq 1/3$ convention. As shown in **Figure 4.3**, at zero field for a triplet $S = 1$ case the ZFS term in **Equation (4.40)** gives rise to three magnetic sublevels ($M_S = 0, \pm 1$) and eigenvalues (E_j), expressed by **Equations (4.41)**.

$$\begin{aligned} |S, M_S\rangle &= |1, 0\rangle, \quad \frac{1}{\sqrt{2}}\{|1, +1\rangle + |1, -1\rangle\}, \quad \frac{1}{\sqrt{2}}\{|1, +1\rangle - |1, -1\rangle\} \\ E_j &= -\frac{2}{3}D, \quad \frac{1}{3}D + E, \quad \frac{1}{3}D - E \end{aligned} \quad (4.41)$$

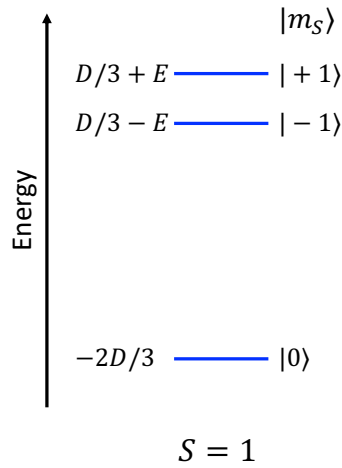


Figure 4.3. The Zero Field Splitting (ZFS) of three magnetic sublevels for spin triplet states, assuming $D > 0$.

4.4.7.1. Calculation of zero field splitting (ZFS)

As discussed above the ZFS parameters can be calculated from first principles.[155] This requires explicit treatment of the SOC, which can be rigorously calculated using the QDPT, on the basis of non-relativistic states. In practice one needs an approximate solution of the BO Hamiltonian of a multireference type, such as CASSCF, MRCI, as discussed further in **Chapter 5**, in the form given in **Equation (4.42)**.

$$|\Psi_I^{SS}\rangle = \sum_{\mu} c_{\mu I} |\Phi_{\mu}^{SS}\rangle \quad (4.42)$$

Here, the upper indices SS stand for a many-particle wavefunction with spin quantum number S and spin projection quantum number $M_S = S$. Since the BO Hamiltonian does not contain any complex valued operator, the $|\Psi_I^{SS}\rangle$ solutions may be chosen to be real-valued. Introduction of SOC requires the lift over of the $(2S + 1)$ degeneracy of the total spin S H_{BO} eigenfunctions. Thus, the basis of the treatment is the $|\Psi_I^{SM}\rangle$ states, in which I covers all the roots calculated in the first step of the procedure and $M = -S, \dots, S$ enumerates all members of a given multiplet. Matrix elements over the $|\Psi_I^{SM}\rangle$ functions are readily generated using the Wigner-Eckart theorem, since all $(2S + 1)$ members of the multiplet share the same spatial part of the wavefunction.[156]

Calculation of ZFS can be effectively calculated based on effective Hamiltonian theory. This yields the entire \mathbf{D} -tensor rather than only the D and E values. This method has been fully implemented in the ORCA suite of programs counting already many successful applications.[157-162]

Within this approach, the effective Hamiltonian, similar to **Equation (4.31)**, reproduces the energy levels of the “exact” Hamiltonian E_I and the wavefunctions $|\Psi_I^{SM}\rangle$ of the considered states projected onto a model space $\tilde{\Psi}_I$, as depicted in **Equation (4.43)**.

$$\hat{H}_{\text{eff}}|\tilde{\Psi}_I^{SM}\rangle = E_I|\tilde{\Psi}_I^{SM}\rangle \quad (4.43)$$

These projected vectors $|\tilde{\Psi}_I^{SM}\rangle$ are then symmetrically orthonormalized resulting in Hermitian effective Hamiltonian, which can be written as

$$\hat{H}_{\text{eff}}|\tilde{\Psi}_K^{SM}\rangle = \sum_K |\tilde{\Psi}_K^{SM}\rangle E_K \langle \tilde{\Psi}_K^{SM}| \quad (4.44)$$

The effective interaction matrix obtained by expanding this Hamiltonian into the basis of determinants belonging to the model space, is compared to the matrix resulted from expanding the model Hamiltonian.

5 Electronic Structure Methods for Ground and Excited States

The milestone of quantum chemistry is solution of Schrödinger equation (SE), but it is exactly solvable only for very simple systems. This chapter briefly introduces the methods employed in this study for computing the electronic structure, the ground and excited states, of multi-electron systems including atoms, molecules, solids. Through these methods the electronic structure and other properties of the chemical system in ground and excited states can be computed, understood in different conditions. [92, 95, 107, 109]

The different approaches can be grouped into two main categories. The wavefunction-based approaches and the density-based particle/hole methods. The entry step into the wavefunction-based approaches is Hartree-Fock (HF) method which lacks correlation energy. Correlation energy can be partially or completely recovered by post HF methods including configuration interaction (CI), couple cluster (CC) and multi-configurational self-consistent-field (MCSCF) methods as well as many-body perturbation theory (MBPT). In contrast, the density-based methods comprise primarily by the density functional theory (DFT), which encompasses various functional variations, and time-dependent DFT (TD-DFT) for computations of excited states.

5.1. Wavefunction Methods

5.1.1. Hartree-Fock (HF) Method

Within the BO approximation introduced in **Section 4.3**, and as discussed earlier in **Section 4.4.1**, the simplest antisymmetrized many-electron wavefunction $|\Psi\rangle$ which can describe the ground state of N -electron system can be written as a single Slater determinant (SD) of a set of

k one-electron spin orbitals $\{\phi_k(\mathbf{x}_j)\}$ with \mathbf{x}_j is electron coordinate [both space and spin; $\mathbf{x}_j = (\mathbf{r}_j, \mathbf{s}_j)$], which takes the form,

$$\Psi(\mathbf{x}_1, \dots, \mathbf{x}_N) = (N!)^{-1/2} |\phi_1(\mathbf{x}_1) \dots \phi_k(\mathbf{x}_N)| \quad (5.1)$$

It is important to remark that, by construction, that SD introduces the effect of exchange correlation between electrons with the same spin however it completely loses other correlations between electrons with opposite spin.[92]

HF approximation is the core approximation in quantum chemistry and its solution provides a good start for higher accurate methods as discussed later. The HF N -electron wavefunction of the system ground state can be write as SD, **Equation (5.1)**, which can be shortened as

$$|\Psi_{HF}\rangle = |\phi_1 \phi_2 \dots \phi_a \phi_b \dots \phi_N\rangle \quad (5.2)$$

In HF method, the total electronic eigenvalue problem in **Equation (4.19)** is approximated into a set of one-electron eigenvalue problems

$$\hat{f} |\phi_a\rangle = \varepsilon_i |\phi_a\rangle \quad (5.3)$$

where, Fock operator \hat{f} is an *effective one-electron* Hamiltonian operator and can be written as

$$\hat{f}(1) = h(1) + v^{HF}(1) \quad (5.4)$$

where, $h(1)$ is *core-Hamiltonian operator* and $v^{HF}(1)$ is an effective one-electron potential operator known as *Hartree-Fock potential*, which approximate the severely problematic two-electron operator r_{12}^{-1} . So, instead of calculating the electron-electron interaction explicitly, it will be approximated as an average potential $v^{HF}(1)$ on electron 1 occupying orbital ϕ_a , arising from clouds of the rest $N - 1$ electrons in the other spin orbitals. The Hartree-Fock potential can be written in terms of coulomb \hat{J} and exchange \hat{K} operators,

$$v^{HF}(1) = \sum_b \hat{J}_b(1) - \hat{K}_b(1) \quad (5.5)$$

That leads to N HF equations of eigenvalue problem as described in **Equation (5.3)**, one for each occupied molecular spin orbital ϕ_a and the eigenvalue ε_a is the orbital energy of electron occupying this spin orbital.

In fact, it is a pseudo-eigenvalue problem (nonlinear), due to the functional dependence of Fock operator $\hat{f}(1)$ on the pseudo-eigenfunction (the solution) $\{\phi_a\}$, through the coulomb and exchange operators. Due to the nonlinearity of HF equations, they shall be solved interactively by *self-consistent-field* (SCF) approach. A trial initial orbital can be used to solve the “pseudo” HF equations providing an improved set of orbitals which can be reintroduced into the calculation as trial orbitals. The process is repeated in SCF cycles until energy variationally converged regarding to some chosen convergence thresholds. [87, 172, 174]

HF solution have three distinct variations: restricted closed-shell HF (RHF), where the spatial components of spin orbitals are identical within each pair of electrons; its open-shell counterpart, ROHF, allowing singly occupied orbitals; and unrestricted HF (UHF), where opposing spin electron pairs are not bound to have the same spatial components.[92, 95]

5.1.2. Correlation Energy

HF ground state wavefunction $|\Psi_{HF}\rangle$ is a good approximation of the many-body electronic wavefunction but not the ‘exact’ wavefunction, due to loss of electron correlation. HF method capture $\sim 99\%$ of the total energy and successfully introduced the correlation of electron exchange between electrons with parallel spins (fermi hole between electron of the same spin). Despite that, HF is a mean field approach where the *instantaneous* electron-electron interaction r_{12}^{-1} is not explicitly considered, and instead it is approximated in average way. This missing part is known as dynamic correlation.[92]

Another deficiency of HF approximation, arise from the fact that the total wavefunction is not necessary well represented by a single slater determinant (single configuration of occupied orbitals) and wavefunction should be extended to include all the excited determinants, this is known as static correlation. This problem will make HF and similar single-determinantal methods to completely fail in systems with (nearly-)degenerate determinants to the ground state determinant.[163]

Several methods, post-HF methods, were introduced to incorporate missing correlation in HF and recover the correlation energy E_{corr} , defined as the difference between the exact energy \mathcal{E}_0 of the non-relativistic Hamiltonian within BO approximation and the corresponding HF limit energy E_0 , obtained with a *complete infinite* basis set,[92]

$$E_{corr} = \mathcal{E}_0 - E_0 \quad (5.6)$$

It is crucial to acknowledge that despite the typically small correlation energy E_{corr} , usually of the order of $\leq 1\%$ of the total energy, but it dominates all intra and intermolecular interactions in the chemical system. So, the evaluation of any computational method to describe chemical or physical properties or interactions is determined by the capability to accurately determinate the correlation energy and to reach the chemical accuracy (≤ 1 kcal/mol error).[86]

Since the original HF method does not take into account electron correlation effects, in order to get the results in better agreement with experiment, a few extensions, the so-called post-HF methods, have been proposed, e.g., Configuration interaction (CI),[164-168] multi configurational self-consistent field (MCSCF) methods,[169, 170] Møller–Plesset Perturbation Theory[171-175], and Coupled Cluster (CC) Theory.[176, 177] Such extensions may improve considerably the quality of calculations, but at the expense of significantly higher demand for computer resources and calculation time.

5.1.3. Configuration Interaction (CI)

Electronic configuration refers to the distribution of electrons within atomic or molecular orbitals of atoms/ions, or molecules, respectively. The electronic configuration can be expressed using a numerical scheme, wherein virtual molecular orbitals (VMOs) are assigned a value of **0**, whereas singly occupied MOs (SOMOs) and doubly occupied MOs (DOMOs) are represented by values of **1** and **2**, respectively. The electronic configuration is based on the Pauli exclusion principle and Hund's rule, which govern how electrons fill orbitals in order to achieve the most stable configuration. Excited configurations can also be constructed, involving occupancy of higher energy orbitals. These excited configurations play a role in understanding electronic transitions, leading to absorption emission processes.

Each configuration can give rise to several configuration state functions (CSFs) for the same total spin S and spatial part but differ in their intermediate couplings. CFS is a symmetry-adapted linear combinations of SDs. CFS captures the different electronic configurations that contribute to the overall wavefunction, considering electron spin and spatial wavefunction combinations and constructed as eigenfunctions of \widehat{S}^2 and \widehat{S}_z operators.[92, 95]

A good start for all post-HF method is HF ground state wavefunction $|\Psi_{HF}\rangle$. In HF calculations on a molecule with N electrons and $2K$ basis functions, obtains a set of $2K$

orthonormal molecular spin orbitals $\{\phi_i\}$ as lowest energy N occupied and $2K - N$ virtual orbitals. The single determinant formed from former orbitals gives $|\Psi_{HF}\rangle$. In addition, $\binom{2K}{N}$ N -tuply excited determinants can be constructed.[92, 95]

To recover the electron correlation, the exact many-body ground state wavefunction $|\Phi\rangle$ can be expressed as a linear combination of all the determinants arising from HF spin orbitals, which refers as configuration Interaction (CI). The total exact WF $|\Phi\rangle$ can be written as follows

$$|\Phi\rangle = c_0|\Psi_{HF}\rangle + \sum_{ar} c_a^r |\Psi_a^r\rangle + \sum_{\substack{a<b \\ r<s}} c_{ab}^{rs} |\Psi_{ab}^{rs}\rangle + \sum_{\substack{a<b<c \\ r<s<t}} c_{abc}^{rst} |\Psi_{abc}^{rst}\rangle + \dots \quad (5.7)$$

where, c_s are the expansion coefficients. a, b, c, \dots and r, s, t, \dots represent the occupied and virtual orbitals, respectively while $|\Psi_a^r\rangle, |\Psi_{ab}^{rs}\rangle, |\Psi_{abc}^{rst}\rangle, \dots$ are the singly, doubly, triply, ... excited determinants, respectively. To achieve the exact $|\Phi\rangle$ of the system, expansion coefficients (c_s) can be interactively optimized in the framework variational principle, as depicted in **Section 4.1.2**.

The CI method includes all excited determinants, known as the full CI (FCI) method. Although FCI represents the exact solution of the many-electron problem, but the computational cost increases exponentially with the number of electrons, making it feasible only for very small systems. That implies truncation of less important excitations. For instance, CIS involves only single excitations from the reference determinant. While CIS approximates excited states, it doesn't affect the ground state energy due to no mixing between the ground state and single excitations $\langle\Psi_{HF}|H|\Psi_a^r\rangle = 0$ (Brillouin's theorem).[92] A refinement in ground state energy accounting for electron correlation is achieved by applying CID (CI with double excitations). The most common implementation of the CI method is CISD method, involves single and double excitations. The CISD method is often used in electronic structure calculations to describe the excited states of molecules. In CISD method, in addition to double excitations mixing, now single excitations can *indirectly* mix with the ground state. That takes place through non-zero coupling of $\langle\Psi_{HF}|H|\Psi_{ab}^{rs}\rangle$ and $\langle\Psi_a^r|H|\Psi_{ab}^{rs}\rangle$. Higher excitations could be also included, for example, CISDT incorporates single, double, and triple excitations.[92, 95]

While the CI method is variational, a lack of size-consistency (extensivity) is a deficiency of truncated CI. The energies of individual subsystems may not sum up to the energy of the composite system, and the quality of the approximation deteriorates rapidly with increasing

molecular size. Thus, complex size-extensive CI methods like ECISDT and ECISDTQ are required to restore size consistency.[178] Nonetheless, CI methods remain computationally demanding, suitable only for small systems in the current scenario.

5.1.4. Multiconfigurational self-consistent field methods (MCSCF)

MCSCF method provide a robust representation of complex electronic structures wherein single electron configuration methods, like RHF/UHF and RKS/UKS-DFT methods, are inadequate and CI methods are not computationally feasible. This arises in server important chemically important system and interactions, for instance, chemical bond formation or cleavage, diradicals, magnetic anisotropy, and transition/rare-earth metal-based systems.[79, 92, 137, 140, 159, 179-183]

In the MCSCF method, the N -electron wavefunction for specific state I with total spin S , can be expressed in CI form as

$$|\Psi_{MCSCF,I}\rangle = \sum_k c_{k,I} |\Psi_k\rangle \quad (5.8)$$

which is represented as a linear combination of a set of CSFs $|\Psi_k\rangle$ (or Slater determinants), each adapted to the total spin S . The expansion coefficients $c_{k,I}$ are determined variationally, as is typical for CI wavefunctions. Now, to get the accurate $|\Psi_{MCSCF,I}\rangle$, both the $|\Psi_k\rangle$ and coefficients (c s) are interactively optimized, within the variational principle, in the frameworks of SCF and CI, respectively.

An important MCSCF approach is the complete active space SCF method (CASSCF), where the linear combination of CSFs includes all that arise from a particular number of electrons in a particular number of orbitals, known as *active space* while the rest MOs (internal DOMOs and external VMOs) are kept frozen, as schematically shown in **Figure 5.1**. [107] Within the active space, all excitations (full CI) are allowed. Unlike HF theory, where orbitals are optimized to minimize the energy of a single Slater determinant, MCSCF/CASSCF goes a step further, allowing the molecular orbitals themselves to adjust during the calculation that minimize the CI energy to achieve more accurate wavefunction description.

In case, the CASSCF CI parameters and active orbitals are optimized for an individual state I , this called state-specific CASSCF (SS-CASSCF). However, in various instances, it becomes advantageous to optimize orbitals not solely for an individual state, but rather for an average

across multiple states leading to state-average CASSCF (SA-CASSCF).[169, 184] Alternatively, the active orbitals can be restricted to build the CI matrix without an SCF optimization step, that is known as CASCI method.

In some cases, CASSCF WF is difficult to converge, or becomes very demanding. One possible solution is to restrict the possible excitation within the active space leading to restricted active space CI (RASCI)[185] or its SCF variant (RASSCF)[186]. In the RASSCF/RASCI, the active space is divided into three subspaces, labelled RAS I, RAS II, and RAS III. Now, the determinants to enter CI are selected as all those which have no more than n holes in RAS I, and no more than m particles in RAS III, where n and m are user-defined. Simultaneously, all excitations (full CI) are allowed in RAS II.

MCSCF methods, usually capture all the static correlation, however missed the dynamic correlation. To restore it, $|\Psi_{MCSCF}\rangle$ are usually used as a reference for multi-reference configuration interaction (MRCI), multi-reference perturbation theories like CASPT2 and NEVPT2,[187] as will be discussed in **Section 5.1.6**.

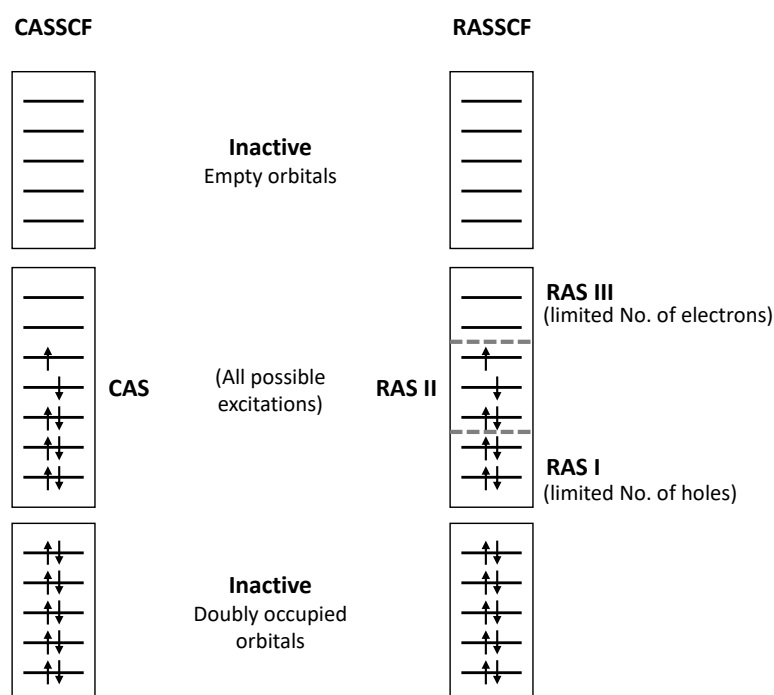


Figure 5.1. Schematic representation of the construction of the orbital space for CASSCF/CASCI (left) and RASSCF/RASCI (right) calculations.

5.1.5. Iterative-Configuration Expansion Configuration Interaction (ICE-CI)

While achieving results close to CI accuracy, requires a substantial expansion of the active space. This expansion comes with a noteworthy computational cost and sometimes is not easily achievable employing previous methods. Recent advancements in approximate methods, such as iterative configuration expansion (ICE-CI)[188, 189] and density matrix renormalization group (DMRG),[190] have proven in efficiently addressing large active spaces at a reasonable cost. These developments are particularly relevant in computations related to the magnetic anisotropy or excitation spectra of multi-metallic centers, especially when dealing with very large active spaces.[115]

ICE-CI, with the capability to manage a few dozen electrons and orbitals, introduces modern tree-based methods for determinant, configuration, or CSF generation. When utilized to formulate the CI problem, ICE-CI establishes a streamlined, efficient, and highly adaptable framework. This framework proves instrumental in resolving complex and incomplete CI problems across diverse chemical spin and symmetry systems.

In essence, when ICE-CI adopts the CSF generation method, its primary role is to produce a succinct wavefunction capturing only the most significant CSFs. The iterative process involves an initial step of selecting a "generator" set, including the HF ground state CSF and the single and double excited CSFs with the strongest interactions with the HF ground state. Subsequently, new single and double excited CSFs are generated based on this "generator" set, and only those with the most substantial interactions are incorporated into the set. This iterative procedure persists until the wavefunction achieves convergence.[188, 189]

5.1.6. Perturbation Theory Methods: MP2, NEVPT2 and QD-NEVPT2

While the main focus of the methods introduced so far was on improving the wavefunction to recover the electron correlation energy, the perturbation methods introduced in this section rely on changing the operator – here the Hamiltonian – acting on the wavefunction to do so. As previously introduced in **Section 4.1.3**, a perturbation operator \hat{V} is added to the ground state (zeroth-order) Hamiltonian $\hat{H}^{(0)}$ as shown in **Equation (5.9)**.

$$\hat{H} = \hat{H}^{(0)} + \lambda \hat{V} \quad (5.9)$$

Here, the parameter λ varies between zero and one. When λ is zero, the resulting Hamiltonian is equivalent to the zeroth-order operator $\hat{H}^{(0)}$, and when it is one, it corresponds to the anticipated correct Hamiltonian \hat{H} . This operator can be incorporated into the TI-SE, Equation (4.6), aiming to recover the missing electron correlation through the added perturbation. Unlike previously described methods, this approach is size-extensive but not variational. Consequently, it does not necessarily yield a higher energy than the exact energy due to its non-variational nature.[191]

One frequently employed technique based on this approach involves the many-body perturbation method known as MPPT (Møller-Plesset Perturbation Theory). In this context, the zeroth-order Hamiltonian, denoted as $\hat{H}^{(0)}$, is all the one-electron Fock operators. The perturbation operator \hat{V} addresses the issue by correcting the electron repulsion. The MP perturbation operator \hat{V} is given by **Equation (5.10)**. [192]

$$\hat{V} = \hat{H} - \hat{H}^{(0)} = \sum_i \sum_{i>j} \frac{1}{r_{ij}} - \sum_i \sum_j \left(J_{ij} - \frac{1}{2} K_{ij} \right) \quad (5.10)$$

The zeroth-order perturbation outcome represents the energy across all non-interacting orbitals. Upon inclusion of the first-order perturbation involving \hat{V} , the HF energy is obtained by definition. The initial correction to the energy concerning electron correlation emerges through second-order perturbation, leading to the MP2 method (Møller-Plesset second-order perturbation).[171, 172] It is feasible to incorporate higher-order perturbations (MP3, MP4, ..., MPn), albeit these are considerably more computationally demanding.[95, 173-175, 192]

In the MP2 approach, the HF ground state single-configurational wavefunction $|\Psi_{HF}\rangle$ serves as the basis. Unlike other perturbation methods based on the same principle of introducing a perturbation operator, which employ a multi-configurational wavefunction. In most instances, this takes the form of a CASSCF wavefunction. Two famous methods that follow this approach are NEVPT2 (N-electron valence state perturbation theory of second order)[193-195] and CASPT2 (complete active space perturbation theory of second order)[196, 197]. Notably, MPn is a single-reference method, relying on a single-configurational wavefunction as a reference for perturbation, while NEVPT2 and CASPT2 are multi-reference methods.

The PT corrections, as elucidated in **Section 4.1.3**, involve an expansion in the inverse powers of the energy splitting between unperturbed levels. However, in cases with small splitting, quasidegenerate states, PT encounters challenges that lead to significant perturbations

and breakdown of the approximation. Quasidegeneracy issues can arise in various scenarios, such as dynamics near avoided crossings, conical intersections, and in spectroscopy, where the mixing of states of different nature markedly influences energies and oscillator strengths. To address these challenges, an extension of the NEVPT2 has been proposed, known as the quasidegenerate (QD) formulation of the NEVPT2 theory, leading to the QD-NEVPT2 method which has demonstrated efficiency in handling such cases.[198]

Finally, both NEVPT2 and its QD variant offer a significant advantage by effectively avoiding problems associated with intruder states. This issue, which can substantially impact methods based on one-electron zero-order Hamiltonians, is nearly absent in both NEVPT2 and QD-NEVPT2 methods. Furthermore, as previously discussed in **Section 5.1.4**, combining PT on top of MCSCF methods, like CASSCF, is justified by addressing total (static and dynamic) electron correlation. MCSCF/CASSCF primarily recovers static correlation linked to nearly degenerate ground state configurations, while perturbation methods focus on dynamic correlation related to electron movement. This combination proves beneficial for capturing both types of correlation, depending on the system and modeling goals.[79, 115, 137, 140, 159, 179-183, 187]

5.1.7. Coupled-Cluster (CC) methods: CCSD, DLPNO-CCSD

In an effort to solve the FCI, which as previously discussed impractical for chemical applications, several approximations have been proposed. Among these approaches, Coupled-Cluster (CC) theory stands out as a method that combines numerous advantages. [199, 200] On one hand, CC method, similar to CI, is an iterative method addressing the electron correlation through inclusion of higher excited determinants. On the other hand, CC methods, unlike CI, are size extensive. In addition, while CI relies on a linear ansatz to improve the WF by accounting for the explicit interaction of one electron with all other electrons, the foundational principle of CC theory relies on an exponential ansatz, where the many-electron interactions are treated through simultaneous electron pair interactions generating what called the “clusters”. The CC wavefunction can be written as,

$$|\Psi_{CC}\rangle = e^{\hat{T}}|\Psi_{HF}\rangle \quad (5.11)$$

where, $|\Psi_{HF}\rangle$ is the HF determinant of the ground state and \hat{T} is the “cluster operator” and can be written as,

$$\hat{T} = \hat{T}_1 + \hat{T}_2 + \hat{T}_3 + \dots \quad (5.12)$$

where \hat{T}_n represents all possible n -fold excitations, expressed as

$$\hat{T}_1 = \sum_{i,a} t_a^i \hat{a}_a^\dagger \hat{a}_i \quad (5.13)$$

$$\hat{T}_2 = \frac{1}{4} \sum_{i,a} t_{ab}^{ij} \hat{a}_a^\dagger \hat{a}_b^\dagger \hat{a}_j \hat{a}_i \quad (5.14)$$

here, i and j refer to occupied while a and b to virtual orbitals. t_a^i , t_{ab}^{ij} are the “cluster amplitudes” which should be determined by solving the CC equations. The $e^{\hat{T}}$ operator can be expanded as a Taylor series as given **Equation (5.15)**, where the repeated application of \hat{T} operator generates the “clusters”. [200]

$$e^{\hat{T}} = 1 + \hat{T} + \frac{\hat{T}^2}{2!} + \frac{\hat{T}^3}{3!} + \dots + \frac{\hat{T}^n}{n!} \quad (5.15)$$

If $n = N$ (all electrons), the CC method converges to the FCI result. In addition, the fast convergence with n , facilitated by the exponential ansatz, allows for truncating the cluster operator at low n , while yielding an accurate approximation to the FCI results. In practical terms, truncation at $n = 2$ defines the CCSD (Coupled Cluster Singles Doubles) method, widely acknowledged as an excellent electronic-structure approach. CCSD(T), augments CCSD by incorporating a non-iterative (perturbative) correction for the triplets (\hat{T}_3) effect, defined the “gold-standard” method in quantum chemistry, which has proven to be an outstanding approximation to FCI, especially for systems which can be well described by a single-determinant WF. [191, 199]

Despite their effectiveness, the computational demand for solving the CCSD equations scales unfavorably. Specifically, it scales with the sixth power (N^6) of molecular size, and for CCSD(T), it scales even with (N^7). Consequently, these methods rigorously apply only to reasonably small molecules. However, advancements in linear-scaling approximations to CCSD(T), through for example DLPNO-CCSD and -CCSD(T) methods. [199] These methods are very practical and promising by recovering 99.99% of the “original” CC energy. DLPNO stands for “domain-based local pair natural orbital”, where the transformation from the MO basis to the DLPNO basis are given in details elsewhere. [201-205] These transformations result

in a confinement of the electron pair correlation to specific domains in space for each pair, significantly enhancing computational efficiency.

Finally, it worth to mention that all discussed CC methods are single-reference methods, starting from HF WF. However, alternative references are possible and occasionally advantageous, for instance, to initiate CC calculations from a multi-configurational WFs, resulting in a multi-reference CC (MR-CC) methods.[199]

5.1.8. Equation of Motion Coupled-Cluster Method (EOM-CC) and STEOM-DLPNO-CCSD Variant

The equation-of-motion Coupled-Cluster (EOM-CC) proves valuable in examining states arising from processes such as excitation, ionization, and electron attachment.[80, 84, 115, 176, 200, 206-212] The EOM-CC approach includes a ground state calculation of a chosen CC level $|\Psi_0\rangle$ and the subsequent calculation of excited states with EOM. The EOM approach obtains excited states by using a linear excitation operator \hat{R}_k as given in **Equation (5.16)**.

$$\hat{H}_N \hat{R}_k |\Psi_0\rangle = \Delta E_k \hat{R}_k |\Psi_0\rangle \quad (5.16)$$

where, \hat{H}_N is the Hamiltonian operator in the normal-order form. $\Delta E_k = E_k - \langle \Phi_0 | \hat{H} | \Phi_0 \rangle$, represents the transition energy connected with the considered process, Φ_0 is a single Slater determinant may be chosen to be the HF reference and E_k is the total energy of the target k -state.

The linear excitation operator (\hat{R}_k) is defined for the excitation energy (EE), ionization potential (IP) and electron affinity (EA), respectively as shown in **Equations (5.17)**

$$\begin{aligned} \hat{R}_k^{EE} &= r_0 + \sum_{i,a} r_a^i \hat{a}_a^\dagger \hat{a}_i + \sum_{i<j, a<b} r_{ab}^{ij} \hat{a}_a^\dagger \hat{a}_i \hat{a}_b^\dagger \hat{a}_j \\ \hat{R}_k^{IP} &= \sum_i r^i \hat{a}_i + \sum_{b,j>i} r_b^{ij} \hat{a}_b^\dagger \hat{a}_j \hat{a}_i \\ \hat{R}_k^{EA} &= \sum_a r_a \hat{a}_a^\dagger + \sum_{j,a>b} r_{ba}^j \hat{a}_b^\dagger \hat{a}_j \hat{a}_a^\dagger \end{aligned} \quad (5.17)$$

with (r) being the excitation operator in respect to a specific virtual orbital (a, b) indicated by its subscript and an occupied orbital (i, j) indicated by the superscript.

In similarity-transformed EOM-DLPNO-CCSD (STEOM-DLPNO-CCSD), the ground state calculation is performed on the DLPNO-CCSD level as described briefly in the previous **Section 5.1.7**. It replaces the Hamiltonian \hat{H} in **Equation (5.16)** with the similarity transformed Hamiltonian $\hat{\bar{H}}$, as follows,

$$\hat{\bar{H}} = e^{-\hat{T}} \hat{H} e^{\hat{T}} \quad (5.18)$$

A second similarity transformation given in **Equation (5.19)** reduces the canonical expansion space of the excited states.[213, 214]

$$G = \{e^{\hat{S}}\}^{-1} \hat{\bar{H}} \{e^{\hat{S}}\} \quad (5.19)$$

\hat{S} is a transformation operator for singles and doubles truncations and is parametrized in terms of IP and EA.

5.2. Density Functional Theory (DFT)

Kohn–Sham density functional theory (KS-DFT) and its time-dependent counterpart (TD-DFT) have gained extensive utility in computational studies, providing precise insights into electronic structure, ground, and excited state properties of both molecules and solid materials[79, 80, 83, 84, 115, 163, 215-218]. It achieves a balanced compromise between accuracy and computational efficiency. At its core, DFT operates on the principle that properties of the N –many-electron system can be expressed as functionals of the ground state electronic density $\rho(\mathbf{r})$, given in **Equation (5.20)**, drastically reducing the complexity from $3N$ –dimensional problem to only 3 spatial coordinate \mathbf{r} .

$$\rho(\mathbf{r}) = N \int \dots \int \psi^*(\mathbf{x}_1, \mathbf{x}_2, \dots, \mathbf{x}_N) \psi(\mathbf{x}_1, \mathbf{x}_2, \dots, \mathbf{x}_N) \delta(\mathbf{r} - \mathbf{x}_1) \delta(\mathbf{r} - \mathbf{x}_2) \dots \delta(\mathbf{r} - \mathbf{x}_N) \quad (5.20)$$

where, \mathbf{x}_j is the j -electron coordinate, donating both space and spin coordinates; $\mathbf{x}_j = (\mathbf{r}_j, \mathbf{s}_j)$.

The efficacy of both DFT and TD-DFT primarily stems from their capacity to accurately describe dynamic correlation within a reasonable computational framework, facilitated by effective exchange-correlation functionals, a challenge for conventional wave function methods. However, DFT does have limitations, particularly in scenarios like (nearly-

)degenerate electronically ground or excited states where multiple configurations are significant (static correlation).[163, 219]

5.2.1. Hohenberg-Kohn Theory

The theory originally developed and formulated by Hohenberg and Kohn, assuming a system of charged spinless fermions with non-degenerate ground state. Similar to previously discussed formulations of WF methods, the DFT total energy can be written as a functional of the electron density as

$$E_{DFT}[\rho(\mathbf{r})] = F[\rho(\mathbf{r})] + \int \rho(\mathbf{r}) V_{ext}(\mathbf{r}) d\mathbf{r} \quad (5.21)$$

where, functional $F[\rho(\mathbf{r})]$ can be defined as follows;

$$\begin{aligned} F[\rho(\mathbf{r})] &= \hat{T}[\rho(\mathbf{r})] + \hat{V}_{ee}[\rho(\mathbf{r})] \\ &= \hat{T}[\rho(\mathbf{r})] + \frac{1}{2} \iint \frac{\rho(\mathbf{r}) \rho(\mathbf{r}')}{|\mathbf{r} - \mathbf{r}'|} d\mathbf{r} d\mathbf{r}' + E_{xc}[\rho(\mathbf{r})] \end{aligned} \quad (5.22)$$

where, \hat{T} and \hat{V}_{ext} are the kinetic energy and the external potential energy which in absence of other external potential is reduced to solely the nuclear-electron attraction term \hat{V}_{ne} . \hat{V}_{ee} is the electron-electron repulsion term which can be written, as shown in **Equation (5.22)**, as sum of Hartree term ($\hat{V}_H[\rho(\mathbf{r})]$) representing the classical Coulomb interaction and the exchange-correlation term ($E_{xc}[\rho(\mathbf{r})]$).

The milestones of the DFT can be summarized in the Hohenberg-Kohn theorems.[220]

Theorem 1 (Uniqueness): The external potential (V_{ext}) is univocally determined by the electronic density $\rho(\mathbf{r})$. Consequently, the electronic density $\rho(\mathbf{r})$ also determines the ground state wavefunction $|\psi\rangle$ and energy E_0 , both obtained by solving TI-SE.

Theorem 2 (Variational Principle): Let $\tilde{\rho}$ be a trail non-negative ground state density normalized to N such that $\int \tilde{\rho}(\mathbf{r}) d\mathbf{r} = N$ and $\int |\nabla \tilde{\rho}^{1/2}(\mathbf{r})|^2 d\mathbf{r} = N$. Variational energy $\tilde{E}_0[\tilde{\rho}]$ can be defined, such that, for $\tilde{\rho} \neq \rho$; always

$\tilde{E}_0[\tilde{\rho}] > E_0[\rho]$, where $E_0[\rho]$ is the exact ground state energy. Consequently, the problem can be Variationally solved by SCF approach.

Theorem 3 (Universality): $F[\rho(\mathbf{r})]$, defined by **Equation (5.22)**, is universal functional in the sense it does not depend explicitly on the external potential V_{ext} in **Equation (5.21)**.

5.2.2. The Kohn-Sham Equations

The Kohn-Sham scheme can be summarized in mapping the interacting many-electron problem into a system of non-interacting electrons moving in effective external potential, with the constrain that both systems have the same ground state (GS) density corresponding to GS WF.

$$\rho(\mathbf{r}) = \sum_i \phi_i^*(\mathbf{r}) \phi_i(\mathbf{r}) = \sum_i |\phi_i(\mathbf{r})|^2 \quad (5.23)$$

That will reduce the many-body problem into a single particle formulation, similar to HF approximation. The density, given in **Equation (5.20)**, is expressed in terms of the resulting orbitals $\{\phi_i(\mathbf{r})\}$, known as Kohn-Sham orbitals. Within the KS theorem,[220-222] the ground state energy can be written as,

$$E[\rho] = T_s[\rho] + E_H[\rho] + E_{ne}[\rho] + E_{xc}[\rho] \quad (5.24)$$

where, T_s is the energy of KS orbitals, given by

$$T_s = \sum_i \langle \phi_i | -\frac{1}{2} \nabla^2 | \phi_i \rangle \quad (5.25)$$

which have been reduced to only the kinetic energy of non-interacting electrons. E_H and E_{ne} represent the classical Coulomb interaction energies for each electron with potential generated by electron density, and nuclei. However, that implies that each electron can interact with all other electrons including itself, since all electrons define the density, leading to the self-interacting error.[223]

Finally, $E_{xc}[\rho]$ is the exchange-correlation term which contains everything else (missing terms and self-interaction error) to make the above expression **(5.24)** exact, and it can be given as,

$$E_{xc}[\rho] = T[\rho] + V_{ee}[\rho] - (T_s[\rho] + E_H[\rho]) \quad (5.26)$$

Now we can see that; **Equation (5.26)** includes the true total kinetic energy T and electron-electron interaction V_{ee} , where the last will recover the missing exchange electron correlation.

While the initial three terms in the **Equation (5.24)** can be precisely determined, the accurate expression for $E_{xc}[\rho]$ remains unknown and can be approximated through various range of functionals classified into LDA, GGA, meta-GGA, hybrid, and double-hybrid functionals. It is convenient that these functionals classes represent an ascending order of accuracy, often referred to as the “Jacob’s ladder of DFT functionals”.[224]

Within each class, a diverse range of functionals aims to achieve total energies that closely agree with experimental results or highly accurate wavefunction energies. Despite their success in delivering excellent energies, there is no guarantee that these functionals will yield good molecular properties. Consequently, extensive literature is dedicated to the statistical evaluation of which functionals perform optimally for specific properties. This ongoing analysis seeks to discern the functional choices that excel in reproducing molecular behaviors and properties.[199]

A first approach to approximate $E_{xc}[\rho]$ is the local density approximation (LDA), as given in **Equation (5.27)**, assuming that the density behaves locally like a homogeneous electron gas of which the exchange-correlation energy ε_{xc} can be determined.[225]

$$E_{xc}[\rho] \approx \int (\rho(r)\varepsilon_{xc} \rho(r))dr \quad (5.27)$$

In response to the substantial error in LDA, both the generalized gradient approximation (GGA) and meta-GGA functional were introduced. While ε_{xc} remains for the electron gas, in GGA the $E_{xc}[\rho]$ depends on both the charge density $\rho(r)$ and its gradient $\nabla\rho(r)$ as shown in **Equation (5.28)**. In contrast, meta-GGA explicitly relies on the semi-local information of the gradient of the density $\nabla^2\rho(r)$ or on the local kinetic energy density τ , as given in **Equation (5.29)**.[95, 225]

$$E_{xc}[\rho] \approx \int (\rho(r)\varepsilon_{xc} (\rho(r), \nabla\rho(r)))dr \quad (5.28)$$

$$E_{xc}[\rho] \approx \int (\rho(r)\epsilon_{xc}(\rho(r), |\nabla\rho(r)|, \nabla^2\rho(r), \tau))dr \quad (5.29)$$

A diverse range of GGA and meta-GGA functionals exists, each distinguished by unique features. Examples include PBE,[226, 227] BLYP,[228, 229], and BP86[228, 230] among GGA functionals, while M06L[231] and TPSS[232] are notable examples within the meta-GGA functionals.

Hybrid functionals mix $E_{xc}[\rho]$ of one of the previously described DFT functionals with exact exchange energy from HF. The variation among hybrid functionals lies in the percentage of HF exchange energy included and the underlying DFT functional. The generic formula is expressed in **Equation (5.30)** with “a” as a constant between 0 and 1.[95, 224, 225]

$$E_{xc}[\rho] \approx (1 - a)E_{xc}^{DFT} + aE_X^{HF} \quad (5.30)$$

Examples include B1LYP and B3LYP, both built on the BLYP GGA functional, incorporates 25% and 20% HF exchange, respectively.[228, 229, 233] PBE0 based on PBE correlation functional with 25% HF exchange.[227, 234, 235].

Finally, double hybrid functionals combine hybrid functionals and MP2. Thus, the $E_{xc}[\rho]$ incorporates and depends on the selected (meta-)GGA functional, exact HF exchange, and perturbation theory in the form of MP2, aiming to address electron correlation. The typical functional form is given in **Equation (5.31)**, where a, b, c are values between 0 and 1.[236]

$$E_{xc}[\rho] \approx (1 - a)E_X^{DFT} + aE_X^{HF} + (1 - b)E_X^{DFT} + aE_X^{MP2} \quad (5.31)$$

In double hybrid functionals, the proportion of exact HF exchange is often more substantial compared to hybrid functionals. This is attributed to the corrective capabilities of MP2, which addresses deficiencies in HF and improves self-interaction errors. Example of double hybrid functionals is B2PLYP[236] functional.

5.3. Time-Dependent DFT (TD-DFT)

A popular approach for computing excited states within the DFT framework is by utilizing TD-DFT.[237] There are multiple TD-DFT approaches which are all typical linear response approaches via perturbation of the ground state density. One of the phrasings that can be used for the TD-DFT problem is Casida's Equation which is a non-Hermitian eigenvalue problem given in **Equation (5.32)**. [238]

$$\begin{pmatrix} A & B \\ B^* & A^* \end{pmatrix} \begin{pmatrix} X \\ Y \end{pmatrix} = \Omega \begin{pmatrix} 1 & 0 \\ 0 & -1 \end{pmatrix} \begin{pmatrix} X \\ Y \end{pmatrix} \quad (5.32)$$

In this context, Ω represents the excitation energy, the vectors X and Y are the occupied-virtual and virtual-occupied blocks of the first-order density response matrix and A and B orbital rotation matrices. A and B are defined in **Equations (5.33)-(5.34)**.

$$\begin{aligned} A_{ia\sigma,jb\eta} = & \delta_{ij}\delta_{ab}\delta_{\sigma\eta}(\varepsilon_{a\sigma} - \varepsilon_{i\eta}) + (a_{\sigma}i_{\sigma}|j_{\eta}b_{\eta}) - c_x\delta_{\sigma\eta}(j_{\sigma}i_{\sigma}|a_{\sigma}b_{\sigma}) \\ & + (a_{\sigma}i_{\sigma}|f_{\sigma\eta}^{xx}|j_{\eta}b_{\eta}) \end{aligned} \quad (5.33)$$

$$B_{ia\sigma,jb\eta} = (a_{\sigma}i_{\sigma}|b_{\eta}j_{\eta}) - c_x\delta_{\sigma\eta}(a_{\sigma}j_{\sigma}|b_{\sigma}i_{\sigma}) + (a_{\sigma}i_{\sigma}|f_{\sigma\eta}^{xx}|j_{\eta}b_{\eta}) \quad (5.34)$$

$(...|...)$ are the two-electron repulsion integrals in the Mulliken notation and $(...|f_{xc}|...)$ is the matrix of the exchange-correlation kernel in the adiabatic approximation of the orbitals with σ and η being spin variables. δ is the Kronecker delta and c_x is a coefficient between zero and one. The third term in **Equation (5.33)** and the second term in **Equation (5.34)** describe the contribution of the HF exchange part of the Kohn-Sham operator. If c_x is 0, this describes the limiting TD-DFT case in which pure DFT functionals are employed (e.g., (meta)-GGA or LDA) and if c_x is 1, it is TD-HF.

6 Theory of Electronic Transitions and Spectroscopies

6.1. Introduction

As previously outlined in **Chapter 3**, spectroscopy serves as a comprehensive investigation into the interactions between light and matter. The light energy interacts with the atomic and molecular system, leading to excitation transitions across the rotational, vibrational, electronic, and magnetic states. Following electronic excitations, relaxations occur, leading to emissions. The exploration of the photophysical properties and optical spectra, covering absorption and emission, emerges as a powerful tool providing valuable insights into electronic and vibrational structure, as well as the excited state dynamics of these chemical system.[79-81, 94]

In alignment with our primary objectives, the pursuit of photoluminescent materials with tailored emission properties necessitates a profound understanding of these processes within the context of light-molecular system interactions. Achieving this requires obtaining accurate solutions for both electronic time-independent and time-dependent Schrödinger equations, demanding the application of approximations and numerical strategies. The central goal of electronic structure theory is to solve the first equation, while chemical dynamics focuses on the second. Both fields have shown substantial evolution in recent decades, introducing various methods with a shared objective. As detailed in the previous **Chapter 5**, methods like DFT/TD-DFT, CC/EOM-CC, MCSCF in conjunction with PT methods like NEVPT2 have proven successful in addressing electronic structure problems of ground and excited states, however it excludes the dynamics effects.[239]

To gain a thorough understanding of dynamics effects on electronic transitions and various optical spectra, it is crucial to accurately determine and explore spectral characteristics such as band position, intensity, shape, and width. Moreover, the consideration of factors such as bands overlap, red/blue shifts resulting from environmental changes, and Stokes/anti-Stokes shifts between absorption and emission bands becomes important. Achieving this requires a comprehensive analysis of electronic and vibrational states involved in transitions, interplay

between them, and the underlying photophysical processes. Computation and analysis of spectral properties in light of selection rules and transition probabilities can provide further insight into transition nature and effect of the environment and dynamics through various coupling mechanisms, including electron- and spin-vibronic couplings, as well as (pseudo-) Jahn-Teller effect.

This chapter provides an overview of radiative and non-radiative processes in molecules and solid-state materials. It delves into the theoretical consideration of molecular motion and its impact on excited states, decay transitions, commonly known as vibronic coupling. Additionally, the chapter explores one of the most famous methods for calculating rates of radiative and non-radiative transitions between vibronic (electronic and vibrational) states. This method, employing the Fermi's Golden Rule within the framework of the path integral formulation, proves to be efficient. Furthermore, its application is extended to the computation and analysis of optical spectra and photophysical properties.

6.2. Radiative vs non-Radiative Processes

While the real scenario is more complex, we aim to present a simplified overview of decay pathways as a foundation to the subsequent sections that delves into the dynamics of excited states and vibronic coupling. In the context of the Jablonski diagram depicted in **Figure 6.1a**, when a molecule encounters photons of light, its electrons undergo promotion from the electronic ground state to higher electronic levels. The ground state of the molecule can exhibit any multiplicity, contingent on its electronic structure (e.g., the number of unpaired electrons, pairing energy, etc.), but it is typically a singlet denoted by S_0 . Upon light absorption, the molecule is elevated exclusively to states with the same ground state multiplicity, adhering to the spin conservation selection rule. In complexes or materials containing heavy atoms/ions that enhance SOC, this selection rule may be relaxed, allowing for the mixing of states with different multiplicities. Starting with S_0 , photons with varying energies result in excitations transitioning to different singlet excited states (S_1 , S_2 , etc.), each with distinct strengths. The strength of the electronic transition depends on other selection rules, the involved eigenstates, and the transition dipole moment between them. Consequently, the absorption spectrum essentially represents the number of absorbed photons (absorbed intensity) as a function of their photon energy.

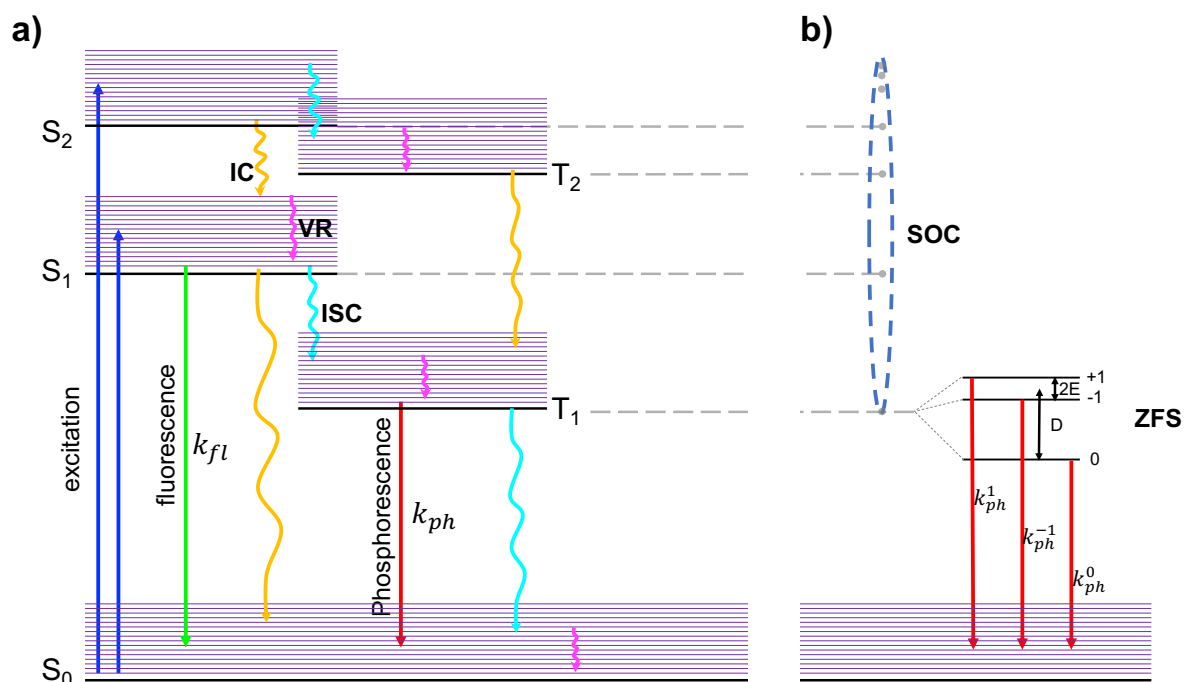


Figure 6.1. a) The Jablonski diagram illustrating fundamental electronic transitions, including radiative processes such as absorption, spin-conserving fluorescence ($\Delta S = 0$), and spin-flip phosphorescence ($\Delta S \neq 0$), are given in blue, green, red arrows, respectively. As well as the nonradiative relaxations like internal conversion (IC), intersystem conversion (ISC), and vibrational (thermal) relaxations (VR), given in orange, cyan, and pink curly arrows. b) Additionally, it depicts the zero-field splitting of the triplet state into three magnetic levels ($M_s = 0, \pm 1$) due to spin-orbit coupling with higher excited states, with the associated D and E parameters of zero-field splitting shown. The decay rate, represented by k , is a general term encompassing various decay processes.

Following excitation, a range of radiative and non-radiative decay processes can occur. Radiative processes encompass fluorescence or phosphorescence, depending on whether light emission involves a transition between two states of the same multiplicity (e.g., from the lowest singlet S_1 to the S_0) or with change of spin (e.g., from the triplet T_1 to the S_0). Typically, emitted light has a lower energy than the absorbed radiation due to luminescence occurring from the lowest energy levels, following Kasha's rule.[123] Additionally, fluorescence or phosphorescence can be differentiated based on their time scales, with the former exhibiting shorter (about $10^{-9} - 10^{-7}$ seconds) and the latter long-lived (about $10^{-4} - 10^{-1}$ seconds) excited states. [240] This time scale is approximate and varies across systems, with

phosphorescence occurring through SOC, especially in systems with strong SOC. In fact, for SOC, multiplicity loses its meaning, and differentiation became less obvious. For the sake of completeness, states with ($S > 1/2$) will experience ZFS due to SOC, as discussed in **Section 4.4.7**. Each of these substates, arising from the SOC-induced splitting, may emit at different rates. **Figure 6.1b** provides a straightforward example illustrating this phenomenon for a triplet excited state.

Non-radiative processes can be more challenging to observe experimentally as they often involve not only the bright or absorbing state defined by the emission energies but also dark states lacking significant oscillator strength but populated from bright states. A transition between electronic states of the same multiplicity is termed internal conversion (IC), e.g., from S_2 to S_1 . Involving states of different multiplicities, such as from S_1 to T_1 , is termed intersystem crossing (ISC).[241] Additionally, there is vibrational relaxation, a rapid non-radiative process involving the transfer to lower vibrational modes within the same electronic states. It is usually a thermal relaxation within the molecule, neighboring molecules, or the solvent. This occurs within a very short time frame ($10^{-14} - 10^{-11}$ seconds).[240] While vibrational relaxation is confined to transitions between vibrational levels, the possibility of IC and ISC arises when vibrational energy levels overlap significantly with electronic energy levels.[94]

The electronic levels of a molecule are defined through PES extending along $3N - 6$ dimensions, where N is the number of atoms in the molecule. The Born-Oppenheimer (BO) approximation neglects the coupling between different PES when discussing electronic excited states. However, in some cases like conical intersection, non-adiabatic couplings between PES, became crucial. Finally, after the excitation and traversing different PESs, the molecule arrives at a different geometrical configuration post-irradiation, it constitutes a photochemical reaction. Conversely, if it returns to its original ground state, it is considered a photophysical process, the term photophysics is used.[242]

Aligning with our main objectives, the quest for photoluminescent material with tailored emission properties, necessitates a deep understanding of processes occurring in molecules post-light excitation. That requires accurate description of dynamics effect on the excited states and the electronic transitions. In the next sections, we will explore the techniques and methods for understanding molecular motion and its effect on the electronic excited states, decay transitions, this generally known as vibronic coupling.

6.3. Vibronic Coupling effect on the optical Spectra

As discussed previously, the complete description of spectral features includes accurate description of the electronic states and transition between them, collectively will give the spectral bands positions and their relative intensities. Furthermore, it is important to describe the shape of the band(s), which is generally controlled by the effect of vibronic coupling on the electronic states and transitions.[79, 80, 243] Vibronic coupling is a rather broad term, which is able to describe several coupling processes. In this section, the effect of vibronic coupling on the absorption and emission shape is explored, again focusing on the main concepts and emphasize factors controlling the band shape.

6.3.1. Adiabatic approximation and Vibronic Coupling

To understand the vibronic coupling, effect of nuclear motion on the electronic structure, and transitions, we have to revisit the adiabatic approximation, introduced in **Section 4.3**. The total Hamiltonian, **Equation (4.17)**, can be divided into 3 components as depicted in **Equation (6.1)**.

$$\hat{H}(\mathbf{r}, \mathbf{R}) = \underbrace{\hat{T}_e + \hat{U}_{ee}}_{\hat{H}_e(\mathbf{r})} + \hat{T}_n + \underbrace{\hat{U}_{ne} + \hat{U}_{nn}}_{\hat{V}(\mathbf{r}, \mathbf{R})} \quad (6.1)$$

At this point, especially in the exploration of molecular vibrations and vibronic coupling, it proves highly advantageous to express the nuclear motions in terms of normal coordinates of nuclei \mathbf{Q} . This facilitates the distinct separation of vibrational nuclear motion from translational and rotational motions. As a consequence, $(3N - 6)$ equations emerge within the framework of Harmonic oscillators, characterized by **Equation (6.2)**.

$$-\frac{1}{2M_\alpha} \frac{\partial^2 \chi_{n_\alpha}}{\partial Q_\alpha^2} + \frac{1}{2} \omega_\alpha^2 Q_\alpha^2 \chi_{n_\alpha} = E_{n_\alpha} \chi_{n_\alpha} \quad (6.2)$$

where, $\chi_{n_\alpha}, E_{n_\alpha}$ are the vibrational eigenfunction and energy of the α -th normal mode. M_α, ω_α represent the reduced mass and frequency of the considered mode, respectively. The normal mode coordinates and the mass-weighted displacement vector $\Delta \mathbf{R}$ from the equilibrium nuclear configuration \mathbf{R}_0 can be correlated and intertransformed through the Hessian matrix (\mathbf{H}). [97, 244]

That simplifies the vibronic coupling in terms of the vibrations (phonons in crystals) of the molecular system. Within the small displacement approximation, the total potential interaction can be expressed as a Taylor series around the equilibrium nuclear configurations $\mathbf{Q}_{\alpha 0}$.

$$\hat{V}(\mathbf{r}, \mathbf{Q}) = V(\mathbf{r}, \mathbf{Q}_{\alpha 0}) + \sum_{\alpha} \left(\frac{\partial V}{\partial Q_{\alpha}} \right)_{Q_{\alpha 0}} Q_{\alpha} + \frac{1}{2} \sum_{\alpha, \beta} \left(\frac{\partial^2 V}{\partial Q_{\alpha} \partial Q_{\beta}} \right)_{Q_{\alpha \beta 0}} Q_{\alpha} Q_{\beta} + \dots \quad (6.3)$$

Equation (6.3) contains the interaction between the electronic structure and nuclear configurations (vibronic coupling), where the first term controls the electron nuclear interaction at fixed nuclear configurations at point $\mathbf{Q}_{\alpha 0}$, usually taken as the ground state. The next terms can be combined together to form the *operator of non-adiabaticity*, represented by vibronic interaction matrix $W_{km}(\mathbf{r}, \mathbf{Q}_{\alpha})$ in terms of small displacement around nuclear configurations at point \mathbf{Q}_{α} , as follows

$$\begin{aligned} W_{km}(\mathbf{r}, \mathbf{Q}) &= \hat{V}(\mathbf{r}, \mathbf{Q}) - V(\mathbf{r}, \mathbf{Q}_{\alpha 0}) \\ &= \sum_{\alpha} \left(\frac{\partial V}{\partial Q_{\alpha}} \right)_{Q_{\alpha 0}} Q_{\alpha} + \frac{1}{2} \sum_{\alpha, \beta} \left(\frac{\partial^2 V}{\partial Q_{\alpha} \partial Q_{\beta}} \right)_{Q_{\alpha \beta 0}} Q_{\alpha} Q_{\beta} + \dots \end{aligned} \quad (6.4)$$

where, the last two summations represent the linear and quadratic vibronic coupling, respectively, which are generally enough with no need to include any other higher order couplings. These terms are responsible for mixing electronic states (k, m) through vibronic coupling.

In the conventional adiabatic Born-Oppenheimer approximation (**Section 4.3**), with a fixed nuclear configuration, $\hat{T}_n(\mathbf{Q})$ and $W(\mathbf{r}, \mathbf{Q})$ are ignored, and $\hat{V}(\mathbf{r}, \mathbf{Q})$ will collapse to only its first term $V(\mathbf{r}, \mathbf{Q}_{\alpha 0})$, which will give the solution of electronic equation as follows:

$$[\hat{H}_e(\mathbf{r}) + V(\mathbf{r}, \mathbf{Q}_{\alpha 0})] \phi_k(\mathbf{r}; \mathbf{Q}_{\alpha 0}) = \varepsilon_k(\mathbf{Q}_{\alpha 0}) \phi_k(\mathbf{r}; \mathbf{Q}_{\alpha 0}) \quad (6.5)$$

That give the set of *electronic* energies $\{\varepsilon_k(\mathbf{Q}_{\alpha 0})\}$ and eigenfunctions $\{|\phi_k(\mathbf{r}; \mathbf{Q}_{\alpha 0})\rangle\}$ at a particular nuclear configuration fixed at point $\mathbf{Q}_{\alpha 0}$. The total wavefunction can be mathematically expanded by the adiabatic electronic basis as given in **Equation (6.6)**.

$$\Psi(\mathbf{r}, \mathbf{Q}_\alpha) = \sum_k \chi_k(\mathbf{Q}_\alpha) \phi_k(\mathbf{r}; \mathbf{Q}_\alpha) \quad (6.6)$$

The expansion coefficients $\{\chi_k(\mathbf{Q}_\alpha)\}$ depend on the nuclear coordinates. The total wavefunction, **Equation (6.6)**, can be used to solve the total TIDE at the nuclear coordinate \mathbf{Q}_α using $\varepsilon_k(\mathbf{Q}_\alpha)$ as potential energy,

$$\hat{T}_n(\mathbf{Q}_\alpha) + \varepsilon_k(\mathbf{Q}_\alpha) + \sum_m W_{km}(\mathbf{r}, \mathbf{Q}_\alpha) \chi_k(\mathbf{Q}_\alpha) = E \Psi(\mathbf{r}, \mathbf{Q}_\alpha) \quad (6.7)$$

Equation (6.7) must be solved for all nuclear configurations $\{\mathbf{Q}_\alpha\}$ where the nuclear wavefunctions are non-vanishing. This results in the vibronic coupling matrix \mathbf{W} . Solving the vibronic coupling problem in such a rigorous way will be complex and very expensive. Other approaches can be utilized to address and approximate the vibronic coupling effect, for example, the path-integral approach which is suitable to treat short-time dynamics of multi-mode vibronic coupling,[245] as will be discussed later in **Section 6.6**.

6.3.2. Frank-Condon approximation, Stokes Shift and Huang-Rhys parameters

Let us further explore the effect of the vibronic coupling on the absorption and emission optical bands. Employing a simple two-level model, we will explore the transition between two electronic energy states ($|\Psi_g\rangle$ and $|\Psi_e\rangle$ for ground and excited states), both characterized by harmonic oscillators along a vibrational normal coordinate Q and with the same frequency $\hbar\omega$ for a selected mode (α), as depicted in **Figure 6.2**. The electronic ground state's PES minimum is at Q_0 (refers to the equilibrium geometry), while the excited state's PES minimum is displaced by (ΔQ) . The vibrational energy levels for both electronic states, denoted as $|v_g\rangle$ and $|v'_e\rangle$ for the ground and excited states, respectively, with vibrational quantum numbers m and n , which can take any integer value $(0, 1, 2, \dots)$. The subscripts (g and e) represent the electronic ground and excited states. For both electronic states, the ground vibrational level possesses a vibrational energy of $(1/2\hbar\omega)$.

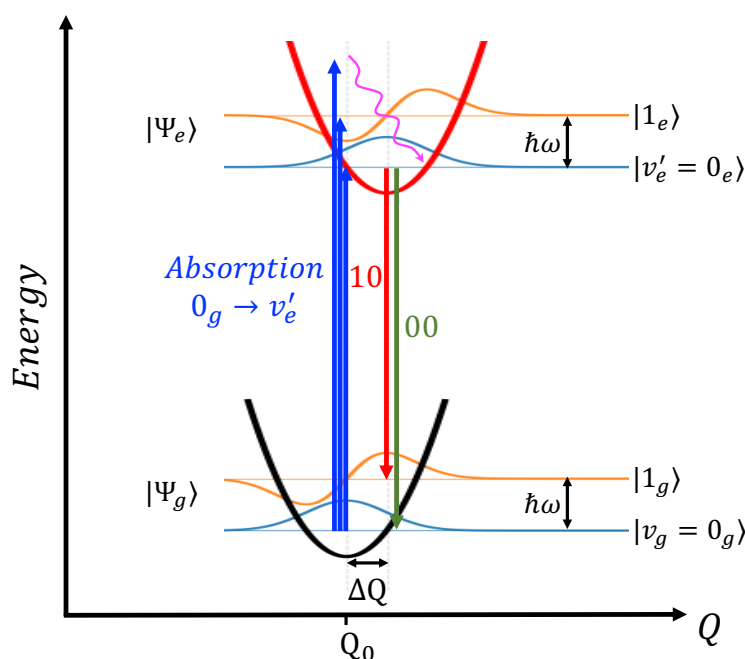


Figure 6.2. A configurational coordinate diagram, along normal coordinates Q of one of the vibrational modes, for transitions between two electronic states; ground state $|\Psi_g\rangle$ and lowest excited state $|\Psi_e\rangle$. Both assumed to be characterized with Harmonic oscillators with the same frequency $\hbar\omega$. Vibrational levels of electronic ground and excited states are presented with $|v_g\rangle$ and $|v'_e\rangle$, respectively where v and v' are the vibrational quantum numbers. The system is assumed at absolute zero temperature (0 K), and the absorption and emission band profiles are constructed based on the $(0_g \rightarrow v'_e)$ and $(v_g \leftarrow 0_e)$, respectively and relative transition probabilities. The minimum of ground state PES is at Q_0 (the equilibrium geometry), while the minimum of the excited state PES is shifted by ΔQ (as discusses in the text). Absorption transitions, reaching different vibrational states, are generally shown with blue arrows. The emission relaxation (00 and 10) representing the $(0_g \leftarrow 0_e)$ and $(1_g \leftarrow 0_e)$, are given in green and red arrow, respectively.

It follows that at absolute temperature (0K), leading to only the lowest (ground) vibrational level is populated in both absorption and emission. The construction of absorption and emission band profiles is based on the $(0_g \rightarrow v'_e)$ and $(0_e \rightarrow v_g)$ series of vibronic transitions, respectively, and depends on the relative electronic transition probabilities. Once again,

following the adiabatic approximation, the vibronic transitions (between the vibrational levels of ground and excited electronic states) occur rapidly enough to maintain the configurational coordinate Q constant, that adhering to the *Frank-Condon (FC) principle*. [114, 246-249] This principle allows us to represent transitions between ground and excited states with vertical arrows as shown in **Figure 6.2**.

Under the FC approximation,

- a) it allows the separation of the electronic and vibrational contributions to the transition,
- b) the electronic wavefunction can be expressed in the static (rigid) picture i.e. at Q_0 ,
- c) because within the optical transition, the light can only interact with valence electrons, so, interaction Hamiltonian can only be restricted to the electronic wavefunctions.

Based on that, the absorption ($0_g \rightarrow v'_e$) and emission ($0_e \rightarrow v_g$) transition cross sections can generally be expressed as shown in **Equation (6.8)**. For the emission, the cross section can be formulated as follows,

$$\sigma_{eg}(0_e \rightarrow v_g) \propto |\langle \Psi_g(Q_0) | \hat{H}_E | \Psi_e(Q_0) \rangle|^2 \sum_v |\langle \chi_v(Q) | \chi_0(Q) \rangle|^2 \quad (6.8)$$

where, \hat{H}_E represents the electronic interaction Hamiltonian between light and electronic states. χ_v and χ_0 are the v^{th} - and 0^{th} -vibrational wavefunctions of ground and excited states, respectively. The term $|\langle \chi_v(Q) | \chi_0(Q) \rangle|^2$ is the Franck-Condon overlap integral. Within the orthonormality of the vibrational wavefunctions under the harmonic oscillator, so,

$$\sum_v |\langle \chi_v(Q) | \chi_0(Q) \rangle|^2 = 1 \quad (6.9)$$

Therefore, within this simple model, the cross section between the electronic states is only dependent on the $|\langle \Psi_g(Q_0) | \hat{H}_E | \Psi_e(Q_0) \rangle|^2$ on the static picture. The dynamic nature of the molecule only influences the band shape without altering the complete transition probability.

Now, let us explore the effect of the Franck-Condon overlap integral and the associated dynamics on band shape. The shape characteristics of the optical band is depicted as an envelope curve over the transitions ($0_g \rightarrow v'_e$) and ($0_e \rightarrow v_g$) for absorption and emission,

respectively, where, the transitions ($0_g \leftrightarrow 0_e$) are referred to as 00 transitions (or zero-phonon lines in solids) occurring without the involvement of vibrational contributions. Consequently, the 00 absorption line aligns with the 00 emission line and both appear at E_{00} ,

$$E_{00} = E_{ad} + \frac{1}{2}\hbar\omega_g - \frac{1}{2}\hbar\omega_e \quad (6.10)$$

where E_{ad} , the adiabatic energy difference between the two electronic states. Again, the model system, $E_{00} = E_{ad}$.

The peak in the absorption band emerges at the energy where the overlap factor is maximized. Due to the shift (ΔQ) between the two PESs, the amplitude probability is maximum between (0_g and $v'_e > 0$) and the absorption peak maximum appears at $E_{00} + (v'_e + \frac{1}{2})\hbar\omega$. Similarly, the maximum emission intensity occurs between ($v_g > 0$ and $v'_e = 0$) at an energy corresponding to $E_{00} - (v_g + \frac{1}{2})\hbar\omega$. Obviously, the emission band occurs at a lower energy than the absorption maximum by $\Delta S = (v_g + v'_e)\hbar\omega$, where v'_e and v_g are the vibrational levels of excited state and ground electronic state with the max. FC overlap in the absorption and emission bands, respectively. This shift (ΔS) is well-known as the *Stokes shift*. This shift is crucial in preventing a significant overlap between the absorption and emission bands; otherwise, the emitted light would be reabsorbed preventing any emission.

To quantify the strength of vibronic coupling (at the FC limit), we discuss the dimensionless Huang-Rhys (HR) parameter (S), which is defined by the following **Equation (6.11)**,

$$S = \sum_{\alpha} s_{\alpha} = \sum_{\alpha} \frac{\lambda_{\alpha}}{\hbar\omega_{\alpha}} \quad (6.11)$$

where, $s_{\alpha}, \lambda_{\alpha}, \omega_{\alpha}$ are the Huang-Rhys factor, the reorganization energy, and the vibrational frequency of the normal mode (α) – FC active mode – involved in the electronic transition. Therefore, the HR parameter serves as a measure of vibronic coupling, at the FC limit, the Stokes shift and the displacement between the ground and excited parabolas ΔQ . In general, sharp or broad optical bands often indicate weak and strong electron-vibronic coupling, respectively. The band shapes discussed so far pertain to spectra obtained at absolute zero temperature, where only the lowest vibrational levels are populated in the departure state. As the temperature rises, higher-energy vibrational levels become populated, concurrently leading to the depopulation of the lowest vibrational level. Upon revisiting **Figure 6.2**, it becomes

apparent that any temperature increase results in a broader emission (absorption) band. This broadening occurs because the excited $v'_e > 0$ ($v_g > 0$) levels become populated, contributing to the emission (absorption) process.

6.3.3. Herzberg-Teller Vibronic Coupling

Within the FC approximation derived using the BO approximation, the electronic transition Hamiltonian (\hat{H}_E), introduced in **Equation (6.8)**, assumes negligible coupling between electronic transition and nuclear motions. However, in reality, the electronic transition exhibits a subtle dependence on the normal coordinates of vibration Q . This dependence originates from the fact that the electronic Hamiltonian \hat{H}_E itself has a functional relationship with the normal coordinates of vibration. This relationship is expressed through a Taylor expansion in nuclear displacements around the equilibrium configuration Q_0 as given in **Equation (6.12)**.

$$\hat{H}_E(Q) = (\hat{H}_E)_0 + \sum_{\alpha} \left(\frac{\partial \hat{H}_E}{\partial Q_{\alpha}} \right)_0 Q_{\alpha} + \frac{1}{2} \sum_{\alpha, \beta} \left(\frac{\partial^2 \hat{H}_E}{\partial Q_{\alpha} \partial Q_{\beta}} \right)_0 Q_{\alpha} Q_{\beta} + \dots \quad (6.12)$$

the subscript zero denotes values at the equilibrium position. The first term represents the electronic transition at the FC limit. The second and higher terms in the expansion serve as perturbations that can mix electronic states. That will lead to improvement of the transition through vibronic coupling, commonly referred to as *intensity borrowing*, as initially proposed by Herzberg and Teller in 1933.[106, 246, 250, 251] In this approach, the amount of borrowed contribution for the α -th vibration is directly proportional to the relevant coupling integral and the displacement Q_{α} . Simultaneously, it is inversely proportional to the energy difference between the two states involved. Hence, this will result in extra broadening in the optical band.

Finally, for a vibrational mode to be HT active and mix two electronic states (Ψ_i, Ψ_j), the following symmetry condition must also be satisfied.

$$\Gamma(\Psi_i) \times \Gamma(Q_{\alpha}) \times \Gamma(\Psi_j) \supset \Gamma_1 \quad (6.13)$$

where Γ is the irreducible representation of states or vibrational mode.

6.3.4. Jahn-Teller and Pseudo Jahn-Teller Effect

Throughout all previous discussions, we consistently assumed non-degenerate electronic states. However, in cases involving highly symmetric molecular structures or optically active centers within a symmetric environment, the electronic states may be degenerate or quasi-degenerate. The Jahn-Teller theorem, formulated by Jahn and Teller in 1937,[252] states that

“All non-linear nuclear configurations are therefore unstable for an orbitally degenerate electronic state”.

While this statement may appear concise, it holds substantial information. Firstly, it is crucial to note that the Jahn-Teller effect (JTE) primarily deals with orbital degeneracy, not spin degeneracy. Spin degeneracy, exemplified by degenerate Kramer’s doubles, can only be influenced or split by magnetic fields, independent of any nuclear motion.[97] Secondly, linear molecular structures require specific consideration, particularly up to quadratic vibronic coupling, which is referred to as the Renner-Teller effect.[253, 254] However, this falls outside the scope of our current study. Finally, as shown in **Figure 6.3a**, the JTE manifests by lowering the potential energy for configurations where the nuclear arrangement exhibits reduced symmetry, lifting the orbital degeneracy and causing the splitting of electronic states. If the Jahn-Teller stabilization energy significantly outweighs the vibrational energy of the JT active mode, the JTE induces a distortion in the molecular structure.[97]

This effect is not exclusive to perfectly degenerate states, see **Figure 6.3(a, b)**, it also emerges in nearly degenerate electronic states, leading to the pseudo Jahn-Teller effect (PJTE).[97, 255] The (P)JTE has profound implications in both chemical and physical implications in the molecular and solid-state materials, for instance in explaining the static distortions in TM complexes and superconductivity in solids.[97]

The (P)JTE, is a vibronic coupling effect which can also be seen as a specific case of conical intersections resulting from a molecule at a high spatial symmetry.[256] For the system at high symmetry not all modes can couple leading to JT distortion. According to the group-theoretical rules, the linear vibronic coupling will be non-zero along some modes (active JT modes), which follows (Γ^*) irreducible presentations (IRs) which belong to the symmetric products of the IRs of the electronic states donated by (Γ).[93, 97] So, the JT active mode should fulfil the following rule,

$$[\Gamma \otimes \Gamma] \supset \Gamma^* \quad (6.14)$$

with another condition, Γ^* can't be a totally symmetric mode Γ_1 because this mode can affect the symmetry.[97] For example in structures under the highly cubic (O_h, T_d) point groups, the two-fold degenerate electronic states (E), and due to $E \otimes E = A_1 \oplus E$, can couple with vibrational mode (e) leading to the famous $E \otimes e$ JT problem.

(P)JTE can also observed in degenerate relativistic states (including the SOC). Although it is well-established that JTE/PJTE is typically suppressed by inclusion of SOC, commonly referred to as the Ham effect.[257, 258] The Ham effect arises from SOC effect, which eliminates degeneracy (SO splitting) through states mixing, which ultimately quenches the JTE. Nevertheless, the recent research studies have shown that in certain electronic configurations, SOC can either suppress or activate the JTE, highlighting the complexity and context-dependent nature of these interactions.[259, 260]

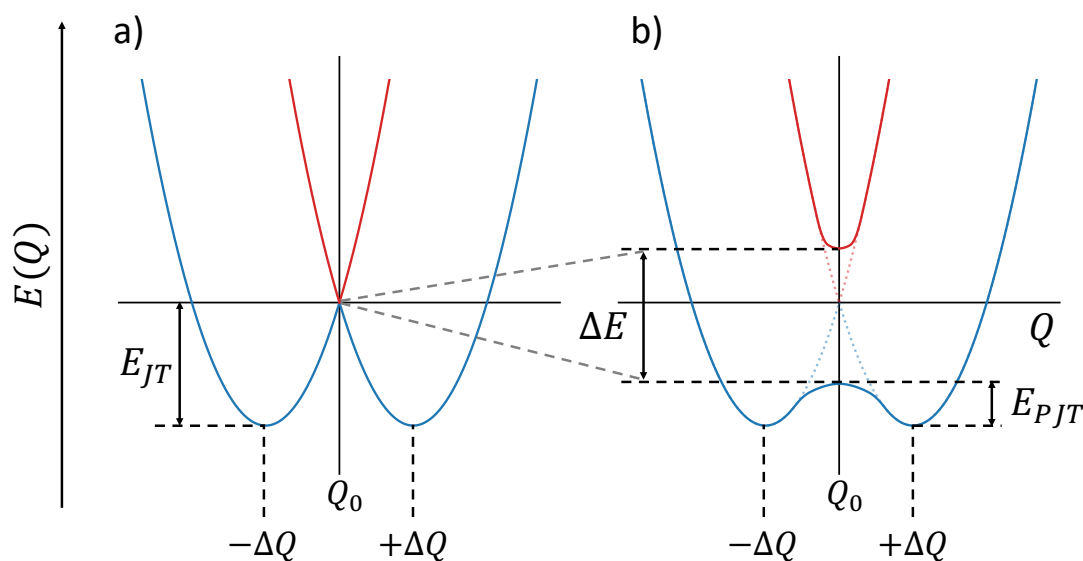


Figure 6.3. Simplified representations of a) JTE and b) PJTE. For a) JTE, there is no PES min. at the point of high symmetry (Q_0) of two-fold degenerate electronic state ($\Delta E = 0$). That results in instability along Q distortion mode, till the system find stability at the in two distorted configurations at $\pm\Delta Q_{min}$. For b) PJTE, at (Q_0) the electronic states are nearly degenerate ($\Delta E \gtrsim 0$). [adapted from Ref.[255]]

6.4. Light Polarization, Natural and Induced Optical Activity

In quantum mechanics, both electrons and photons intrinsically have magnetic angular momentum, known as spin. Photon is integer-spin boson $S = 1$, and the unpolarized light is a superposition of the two allowed spin polarization states $|m_s = \pm 1\rangle$ for left $|LCP\rangle$ and right $|RCP\rangle$ circularly polarized photons, respectively.

Chemical materials are considered optically active if they differentially absorb or emit circularly polarized photons of different handedness, namely left-handed $|LCP\rangle$ and right-handed $|RCP\rangle$ circularly polarized photons ($I^{LCP} \neq I^{RCP}$). [96, 261] The optical activity could be natural or induced.

Natural optical activity is mainly due the molecular chirality (handedness) of the chemical structure. In chiral molecules, the structures are arranged in non-superimposable mirror images known as stereochemical enantiomers where they oppositely interact with CP light in a way leads to optical rotation.[96, 261, 262] Natural optical activity are detected in molecules,[96, 261] clusters, [263] crystals[264]and nanomaterials[265, 266]. In addition, it could be due to the anisotropic environment, for instance anisotropic distribution of solvents, or anisotropic crystal field (CF) in solids. The optical activity is primarily attributed and correlated to the specific distribution of electronic charge within chiral materials. Consequently, such materials exhibit chiroptical spectroscopies, which can investigate the chirality of material at different level and classified according to the propped transitions. In UV/vis region probing transitions of valence electrons leads to electronic circular dichroism (ECD) followed by circularly polarized luminescence (CPL), which respectively provide insights into the CP absorption and emission processes. They are considered complementary and offer a comprehensive understanding of the ground and excited state properties in chiral molecules. Molecular vibrations are also sensitive to the handedness, which is manifested in the vibrational circular dichroism (VCD) or the Raman optical activity (ROA).[96] Finally, CD is also extended x-ray region to investigate the chirality via the core-electron excitations leading to X-ray natural circular dichroism (XNCD).[267]

Although, achiral molecules are optical inactive by nature, the optical activity can be induced by external factor. One of the most famous is by external magnetic field (Faraday effect) which perturbing the electronic structure and magnetic properties of energy levels (Zeeman effect) involved in the optical transition and affect the response to absorb or emits CP

light. That is exhibiting in the magnetic circular dichroism (MCD) and magnetic circularly polarized luminescence (MCPL) spectroscopies for absorption and emission, respectively.

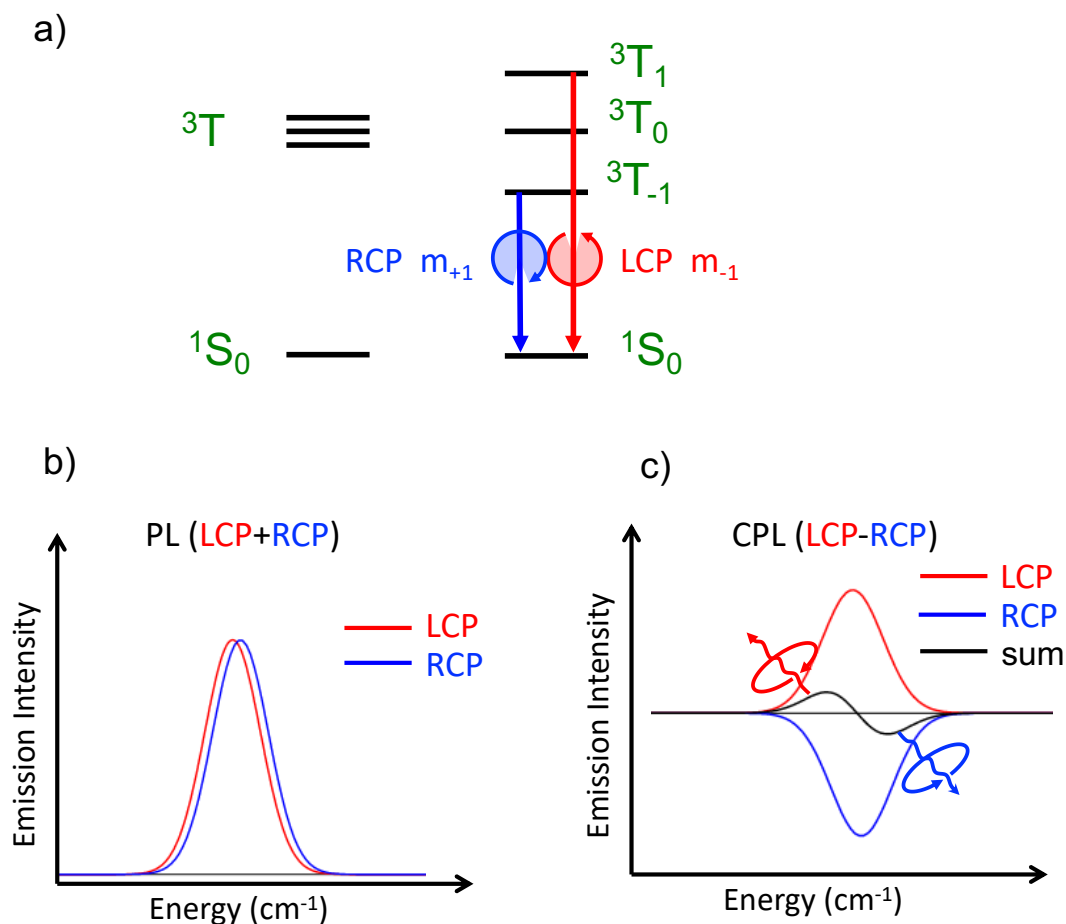


Figure 6.4. a) CPL selection rules for a ground singlet S and an excited triplet T states interacting through SOC. b) The resulted LCP and RCP components of the photoluminescent (PL) spectrum. c) The resulted LCP-RCP circularly polarized photoluminescence (CPL) spectrum together with the LCP and RCP CPL components.

However, for materials with unpaired electrons ($S \geq 1/2$) in the absence of external magnetic field, the degeneracy of spin microstates is lifted leading to states splitting (ZFS). As discussed in **Section 4.4.7**, ZFS takes place due to inter-electron repulsion, exchange effect of the unpaired electrons, spin-orbit, and spin-spin couplings. ZFS causes magnetic anisotropy and can be measured in terms of D, E parameters describing the axial and rhombic anisotropy. ZFS is common in materials with strong SOC, such as materials including heavy TM or RE

atoms, where ZFS range between few to thousands cm^{-1} of energy, directly dependent on the SOC strength. For instance, as show in **Figure 6.4**, for a triplet excited state $2S + 1 = 3$, with magnetic sublevels $|m_s = 0, \pm 1\rangle$, which when relax to the ground singlet state $2S + 1 = 1, |m_s = 0\rangle$ will give CP luminescence. Specifically, the relaxation $|^3T, m_s = \pm 1\rangle \rightarrow |^1S, 0\rangle$ takes place incorporating a change in spin magnetic angular momentum ($\Delta m_s = \pm 1$) which should be compensated, due conservation of angular momentum, by the photon spin angular momentum leading to natural CPL or MCPL where splitting caused by ZFS or external magnetic field, respectively.

6.5. Radiative Transitions and Spectroscopies

6.5.1. Fermi's Golden Rule

Fermi's Golden Rule provides the rate of atomic or molecular electronic transitions (k) take place between a set of stationary initial $|I\rangle$ and final $|F\rangle$ state(s). The Radiative transitions rates can be calculated from the transitions probabilities based of the transition matrix elements in the framework of perturbation theory.[112]

$$k_{i \rightarrow f} = \frac{2\pi}{\hbar} |\langle F | \hat{H} | I \rangle|^2 \delta(E_f) \quad (6.15)$$

where $\langle F | \hat{H} | I \rangle$ is the matrix element of the perturbation operator (\hat{H}) between initial and final states, δ is the density of final states. \hat{H} is the electronic transition operator between the two states which can be induced by external EM field. Alternatively, the full field-matter interaction operator (FFMIO) can be considered by the inclusion of the electromagnetic vector potential in the Hamiltonian for the molecular system.[268] That will be discussed in the next section.

6.5.2. Optical Transition probabilities and oscillator strengths

The general treatment of linear (i.e. one-photon) absorption of light by molecules conventionally starts by considering the electronic Hamiltonian operator of the molecule under the influence of a classical electromagnetic radiation field in the coulomb gauge, i.e.:

$$\hat{H} = \sum_{i=1}^N \left(\frac{1}{2m_e} [\hat{\mathbf{p}}_i^2 + 2e\mathbf{A}(\mathbf{r}_i, t) \cdot \hat{\mathbf{p}}_i] \right) + V(\mathbf{r}_1, \dots, \mathbf{r}_N) \quad (6.16)$$

where $\hat{\mathbf{p}}_i$ is the momentum operator of electron i , V is the total potential for the coulombic interactions between electrons themselves and between electron and the system's nuclei. In the **Equation (6.16)**, higher orders in the vector field \mathbf{A} have been neglected since the weak-field approximation is assumed. The choice of the coulomb gauge facilitates the separation of the total light-matter Hamiltonian in two parts namely, $\hat{H} = \hat{H}^{(0)} + \hat{H}^{(1)}$, where the first term is the isolated electronic Hamiltonian of a system and the second represents the additional term that is due to the presence of the radiation field. The splitting of the Hamiltonian in two parts as shown above makes the utilization of perturbation theory to treat radiative transitions possible.

Calculation of Oscillator Strengths

The combination of the Hamiltonian described above with perturbation theory permits one to describe the probability of one-photo absorption and the subsequent transition of the molecules from the initial (or ground) electronic state Ψ_0 to a final Ψ_n using the so-called oscillator strengths f_{0n} which are dimensionless quantities,

$$f_{0n} = \frac{2m_e}{e^2 E_{0n}} |T_{0n}|^2 \quad (6.17)$$

where E_{0n} is the transition energy and T_{0n} the corresponding transition moment. The different ways to compute oscillator strengths rely on different ways to approximate the transition moments and have their particular strengths and drawbacks[269, 270]

The most straightforward way of computing oscillator strengths relies on a series expansion of the spatial part of the radiation field of the interaction Hamiltonian contained in T_{0n} , i.e. $e^{i\mathbf{k}\cdot\mathbf{r}} = 1 + i\mathbf{k}\cdot\mathbf{r} - 1/2 (\mathbf{k}\cdot\mathbf{r})^2 + \dots$, that eventually results in the *multipole expansion* of T_{0n} as $T_{0n}^{mult} = T_{0n}^{(0)} + T_{0n}^{(1)} + T_{0n}^{(2)} + \dots$, which in principle is infinite. At the infinite limit the corresponding oscillator strength f_{0n}^{mult} , is endowed with the expected properties of f_{0n} , namely the positive definiteness $f_{0n} \geq 0$ and invariance under arbitrary shifts of the coordinate origin with respect to which the various $T_{0n}^{(n)}$ are defined, i.e. $f_{0n}(\mathbf{R}'_O) = f_{0n}(\mathbf{R}_O)$.

In this concept the spectroscopic relevant observable quantities arise by truncation of $|T_{0n}|^2$ up to first order in the wave vector \mathbf{k} which leads to electric dipole, magnetic dipole, electric quadrupole terms,

$$f_{0n} = f_{0n}^{(0)} + f_{0n}^{(1)} + f_{0n}^{(2)} = \frac{2m_e}{e^2 E_{0n}} \left| T_{0n}^{(0)} \right|^2 + \frac{2m_e}{e^2 E_{0n}} \left| T_{0n}^{(1)} \right|^2 \quad (6.18)$$

or

$$\langle f_{0n} \rangle_{\text{iso}} = \langle f_{0n}^{(\mu^2)} \rangle_{\text{iso}} + \langle f_{0n}^{(Q^2)} \rangle_{\text{iso}} + \langle f_{0n}^{(m^2)} \rangle_{\text{iso}} \quad (6.19)$$

where the $\langle \dots \rangle_{\text{iso}}$ stands for classically isotropically averaged quantities for randomly oriented molecules.

The general exact expression for the oscillator strength for a transition from the ground electronic state to an arbitrary one, as given above, still holds even in the presence of the SOC operator,

$$\langle f_{n0} \rangle_{\chi} = \frac{1}{E_{0n}} \sum_{\alpha=x,y} \left| \langle 0 | \sum_{i=1}^N e^{-ikz'_i} \hat{p}'_{i\alpha} | n \rangle \right|^2 \quad (6.20)$$

with the difference being that now the wavefunctions are complex instead of purely real. If we denote the complex conjugate of the ground state wavefunction as $\Psi_0^* = \Psi_0^{\text{Re}} - i\Psi_0^{\text{Im}}$ and the excited state wavefunction as $\Psi_n = \Psi_n^{\text{Re}} + i\Psi_n^{\text{Im}}$. Hence within the multipole expansion formalism the total oscillator strength can be written as:

$$f_{0n} \approx f_{0n}^{(\mu^2)} + f_{0n}^{(Q^2)} + f_{0n}^{(m^2)} \quad (6.21)$$

which in the length representation take the form,

$$f_{0n}^{(\mu^2)} = \frac{2m_e E_{0n}}{3e^2 \hbar^2} \left(\sum_{\alpha} (\text{Re} \mu_{\alpha}^{0n})^2 + \sum_{\alpha} (\text{Im} \mu_{\alpha}^{0n})^2 \right) \quad (6.22)$$

$$f_{0n}^{(Q^2)} = \frac{m_e E_{0n}^3}{20e^2 \hbar^4 c^2} \left[\left(\sum_{\alpha\beta} (\text{Re} Q_{\alpha\beta}^{0n})^2 - \frac{1}{3} \left(\sum_{\alpha} \text{Re} Q_{\alpha\alpha}^{0n} \right)^2 \right) + \left(\sum_{\alpha\beta} (\text{Im} Q_{\alpha\beta}^{0n})^2 - \frac{1}{3} \left(\sum_{\alpha} \text{Im} Q_{\alpha\alpha}^{0n} \right)^2 \right) \right] \quad (6.23)$$

$$f_{0n}^{(m^2)} = \frac{2m_e E_{0n}}{3e^2 \hbar^2} \left(\sum_{\alpha} (\text{Imm}_{\alpha}^{0n})^2 + \sum_{\alpha} (\text{Rem}_{\alpha}^{0n})^2 \right) \quad (6.24)$$

Selection rules for Electronic Transitions

The electronic transitions between energy levels are governed by rigorous constraints, referred to as selection rules. These rules are crucial in determining the probability and intensity of electronic transitions. They can be summarized in two primary selection rules.

a) The Spin Rule ($\Delta S = 0$)

This rule dictates that allowed transitions involve the promotion of electrons without a change in their spin. Ideally, it forbids transitions between states with different total spin, allowing transitions only between states with the same total intrinsic spin ($\Delta S = 0$).

b) The Orbital (Laporte) Rule ($\Delta l = \pm 1$)

This rule is applicable to molecules with a center of symmetry. It forbids transitions within a given set of d or f orbitals if the molecule has a center of symmetry. Hence, transitions within a subshell (like, d→d or f→f), involving a redistribution of electrons within the same set of orbitals, are forbidden.

Despite these selection rules, they can be broken or relaxed through various mechanisms:

a) The spin-orbit coupling

This leads to weak spin-forbidden bands, through mixing with state with different spins.

b) The vibronic coupling

When the molecule's vibrations cause temporary distortions in molecular symmetry, allowing transitions in those moments.

c) Orbital Mixing

Mixing of π -ligand orbitals into f or d orbitals, making transitions no longer purely f→f or d→d.

Finally, besides the localized metal center (MC) transitions, there are charge transfer (CT) Transition, involving a transfer of the electronic density from one center to another. CT could be metal-to-ligand CT (MLCT), or ligand-to-metal CT (MLCT). These transitions are usually

happening at high energy with a large transition dipole moment. It is more extended (delocalized) transition, significantly affecting vibronic and orbital mixing.

6.6. Fermi's Golden Rule and Path Integral

6.6.1. Absorption and luminescence rates and spectra (ABS, PL)

As we shown in **Equation (6.15)**, the absorption or the spontaneous photoluminescence cross section between a set of stationary initial $|I\rangle$ and final $|F\rangle$ state(s) is given by the general expression of the Fermi's golden rule:

$$\sigma_{ABS/PL}(\omega) = \frac{4\pi^2}{c(\omega_{ABS/PL} - \omega_{FI})} |T_{IF}|^2 \delta(E_{FI} \pm \omega_{ABS/PL}) \quad (6.25)$$

where $\omega_{ABS/PL}$ are the excitation and emission photon energies respectively while ω_{FI} are the energies between the initial and final states reached in the absorption or the photoluminescent processes. E_{FI} is the transition energy and δ refers to the line-broadening mechanism arising from the lifetimes of the relevant final states and c is the speed of light. T_{IF} denotes the transition probability which can be accurately calculated, in the framework of FFMIO operator, [268] as previously discussed in **Section 6.5.2**. Within the electric dipole approximation (ED) the respective radiative rates for the absorption and the spontaneous photoluminescence are given by **Equations (6.26)** and **(6.27)**, respectively.

$$k_{ABS}(\omega) = \frac{4\pi^2 \omega_{ABS}}{3} \sum_F |\langle \Psi_I | \hat{\mu} | \Psi_J \rangle|^2 \delta(E_{FI} \pm \omega_{ABS}) \quad (6.26)$$

$$k_{PL}(\omega) = \frac{4\omega_{PL}^3 n^2}{3\hbar c^3} \sum_F |\langle \Psi_I | \hat{\mu} | \Psi_J \rangle|^2 \delta(E_{FI} \pm \omega_{PL}) \quad (6.27)$$

where $\hat{\mu}$ defines the electric dipole operator as $\hat{\mu} = \sum_A Z_A \hat{R}_A - \sum_i \hat{r}_i$, here A sums over nuclei with charges Z_A at positions \hat{R}_A , n is the refractive index, \hbar is the plank constant divided by 2π .

6.6.2. Circularly polarized absorption and luminescence rates and spectra (ECD, CPL) in chiral molecules

As it has been shown many times[268, 271, 272] by defining a laboratory frame in which the \hat{z} -axis defines the direction of the light trajectory, circular polarized light interactions can be generated with the use of the complex vectors $\mathcal{E}_{\pm} = \frac{1}{\sqrt{2}}(\hat{x} \pm i\hat{y})$. In this framework, the FFMIO operator transforms as:

$$T_{IF}^{\pm} = \frac{1}{\sqrt{2}} \sum_{j=1}^N \langle I | e^{-ikr_j} (\mathcal{E} \cdot \hat{p}_x) | F \rangle \pm \langle I | e^{-ikr_j} (\mathcal{E} \cdot \hat{p}_y) | F \rangle \quad (6.28)$$

In both ECD and CPL spectroscopies the measured intensities are related to the difference of absorption or photoluminescence of the left and right polarized transition moments given by:

$$\Delta_{IF}^{L\pm R}(k, \mathcal{E}) = |T_{IF}^{-}|^2 \pm |T_{IF}^{+}|^2 \quad (6.29)$$

which leads to the following expressions for the sum and the difference of the square moduli $|T_{IF}^{\pm}|^2$:

$$\Delta_{IF}^{L+R}(k, \mathcal{E}) = \frac{1}{2} \langle I | \sum_{j=1}^N e^{-ikr_j} (\mathcal{E} \cdot \hat{p}_x) | F \rangle \langle I | \sum_{j=1}^N e^{-ikr_j} (\mathcal{E} \cdot \hat{p}_y) | F \rangle \quad (6.30)$$

$$\Delta_{IF}^{L-R}(k, \mathcal{E}) = -\text{Im}(\langle I | \sum_{j=1}^N e^{-ikr_j} (\mathcal{E} \cdot \hat{p}_x) | F \rangle \langle I | \sum_{j=1}^N e^{-ikr_j} (\mathcal{E} \cdot \hat{p}_y) | F \rangle) \quad (6.31)$$

It has been shown that inclusion of magnetic field and taking into account Zeeman interactions and performing orientational average on expression (6.31) can formulate magnetic circular dichroism (MCD) expressions in the framework of FFMIO operator.[268]

Alternatively, within the ED approximation and upon orientational average, **Equation (6.30)** can be used to generate ABS and PL cross sections presented in **Equations (6.26)** and **(6.27)**. Likewise, **Equation (6.31)** by including ED and magnetic dipole (MD) interactions upon orientational averaging will generate the respective ECD and CPL radiative transition rates:

$$k_{ECD}(\omega) = \frac{16\pi^2 \omega_{ECD}}{3} \sum_F \mathbf{Im}(|\langle \Psi_I | \hat{\mu} | \Psi_F \rangle \langle \Psi_F | \hat{m} | \Psi_I \rangle|) \delta(E_{FI} \pm \omega_{ECD}) \quad (6.32)$$

$$k_{CPL}(\omega) = \frac{16\omega_{CPL}^3 n^2}{3\hbar c^3} \sum_F \mathbf{Im}(|\langle \Psi_I | \hat{\mu} | \Psi_F \rangle \langle \Psi_F | \hat{m} | \Psi_I \rangle|) \delta(E_{FI} \pm \omega_{CPL}) \quad (6.33)$$

As above $\hat{\mu}$ defines electric dipole operator while \hat{m} is the respective magnetic dipole operator $\hat{m} = \frac{1}{2m_e c} \sum_i r_i \times \hat{p}_i$, m_e is the electron mass. In the above expressions $\mathbf{Im}(|\langle \Psi_I | \hat{\mu} | \Psi_F \rangle \langle \Psi_F | \hat{m} | \Psi_I \rangle|)$ represents the rotatory strength (R_{IF}).

Quite commonly the ECD and CPL spectral intensities are represented against normalized absorption and photoluminescent intensities defining, similar expressions for, the dissymmetry factors g_{abs} and g_{lum} :

$$\Delta_{IF}^{L\pm R}(k, \mathcal{E}) = |T_{IF}^-|^2 \pm |T_{IF}^+|^2 \quad (6.34)$$

$$g_{abs}(ECD) = 2 \frac{I_{LCP} - I_{RCP}}{I_{LCP} + I_{RCP}} \sim \frac{4R}{D} \Big|_{GS \text{ Structure}} ; \quad -2 < g_{abs} < 2 \quad (6.35)$$

$$g_{lum}(CPL) = 2 \frac{I_{LCP} - I_{RCP}}{I_{LCP} + I_{RCP}} \sim \frac{4R}{D} \Big|_{ES \text{ Structure}} ; \quad -2 < g_{lum} < 2 \quad (6.36)$$

where $I_{LCP/RCP}$ is the left and right polarized components of the involved absorption or emission process. D and R the square of the transition dipole and the Rotatory strength respectively.[79]

6.6.3. Excited State Dynamics (ESD)

It has been shown that a more direct way to compute linearly and circularly polarized transition rates proceeds through the path integral approach[251, 273-281] in which it is possible to calculate $k_{PL/CPL}^{obs}$ from the Fourier Transform (FT) of the respective correlation function $\chi(t)$

that is computed from the path integral of the multidimensional harmonic oscillator according to:

$$k_{ABS/PL/ECD/CPL}^{obs}(\omega) = 2\alpha \text{Re} \int_0^\infty \chi(t) e^{\pm i\omega t} dt \quad (6.37)$$

with α being a collection of constants while in the exponential TD treatment for ABS and ECD one selects the positive sign and the negative sign for PL and CPL. Hence for linearly polarized transition one-photon rates (ABS, PL) within the ED approximation the correlation function takes the form[273, 274, 282]:

$$\begin{aligned} \chi(t) = e^{\pm i\omega t} & \left[|\mu_e|^2 \rho^{FC}(t) + \sum_k \frac{\partial \mu_e^*}{\partial \bar{Q}_k} \mu_e \rho_k^{HT/FC}(t) + \sum_k \mu_e^* \frac{\partial \mu_e}{\partial \bar{Q}_k} \rho_k^{HT/FC}(t) \right. \\ & \left. + \sum_{kl} \frac{\partial \mu_e^*}{\partial \bar{Q}_k} \frac{\partial \mu_e}{\partial \bar{Q}_l} \rho_k^{HT}(t) \right] \end{aligned} \quad (6.38)$$

while for circularly polarized transition one-photon rates (ECD, CPL) considering electric dipole and magnetic dipole interactions in the expression of the rotatory strengths it takes the form[282]:

$$\begin{aligned} \chi(t) = e^{\pm i\omega t} & \left[\text{Im}[\mu_e m_e^*] \rho^{FC}(t) + \sum_k \text{Im} \left[\mu_e \frac{\partial m_e^*}{\partial \bar{Q}_k} \right] \rho_k^{HT/FC}(t) \right. \\ & \left. + \sum_k \text{Im} \left[\frac{\partial \mu_e}{\partial \bar{Q}_k} m_e^* \right] \rho_k^{HT/FC}(t) + \sum_{kl} \text{Im} \left[\frac{\partial \mu_e}{\partial \bar{Q}_k} \frac{\partial m_e^*}{\partial \bar{Q}_l} \right] \rho_k^{HT}(t) \right] \end{aligned} \quad (6.39)$$

where μ_e and m_e represent the respective transition dipole $\langle \Psi_I | \hat{\mu} | \Psi_F \rangle$ and magnetic dipole $\langle \Psi_F | \hat{m} | \Psi_I \rangle$ moment integrals between initial and final states I, F while:

$$\rho^{FC} = \text{Tr}(e^{-i\hat{H}\tau} e^{-i\hat{H}\tau}) \quad (6.40)$$

$$\rho_k^{HT/FC} = \text{Tr}(\bar{Q}_k e^{-i\hat{H}\tau} e^{-i\hat{H}\tau}) \quad (6.41)$$

$$\rho_{kl}^{HT} = Tr(\bar{Q}_k e^{-i\hat{H}\tau} \bar{Q}_l e^{-i\hat{H}\tau}) \quad (6.42)$$

where, these traces ($\rho^{FC}, \rho_k^{HT/FC}, \rho_{kl}^{HT}$) are evaluated following the approach discussed in Ref[273] within the ESD module as implemented in ORCA.

6.6.4. Thermal Statistical Mechanics

For a long-lived excited state with closely spaced higher excited states, the energy rapidly undergoes thermal redistribution among them. In this scenario, all states contribute to the final emission rate and spectra. This situation is particularly common in phosphorescence, where the inclusion SOC causes non-relativistic states to split into (nearly-)degenerate emissive sublevels, where each may exhibit unique behaviors. For example, in the case of an emissive triplet state, the observed radiative phosphorescence or CPP rates $k_{PL/CPL}^{obs}$ can be determined using **Equations (6.27)** and **(6.33)**, taking into account the Boltzmann population for each state[283] according to **Equation (6.43)**.

$$k_{PL/CPL}^{obs} = \frac{k_1 + k_2 e^{-(\Delta E_{2-1}/k_B T)} + k_3 e^{-(\Delta E_{3-1}/k_B T)}}{1 + e^{-(\Delta E_{2-1}/k_B T)} + e^{-(\Delta E_{3-1}/k_B T)}} \quad (6.43)$$

where k_n are the relaxation rates constant of each magnetic sublevel, ($n = 1 - 3$), and ΔE_{n-1} are the energy difference between the magnetic sublevels and the lowest sublevel. T is the temperature and k_B is the Boltzmann's constant.

6.7. Non-Radiative Transition Rates and Quantum Yields

Apart from linearly and circularly polarized radiative rates, in photoluminescence the involved states can undergo temperature dependent non-radiative relaxation.[284] The luminescence photophysics may be perturbed by non-radiative processes such as internal conversion (IC) and intersystem crossing (ISC). Both unpolarized and circularly polarized radiative rates should take into account excited states that undergo temperature dependent non-radiative relaxation. Within the harmonic approximation and weak coupling limit between the emissive and ground states, non-radiative rates follow the so called weak-coupling limit of “energy gap law” as derived by Englman and Jortner.[284] In the ‘classical’ description the respective potential

energy surfaces PESs show only small displacement, with small Huang Rhys factor ($S \lesssim 1$), from each other and the excited state relaxation process proceeds through the zeroth order vibronic states. Quantum mechanically non-radiative ISC rates between initial $|I\rangle$ and final $|F\rangle$ state(s), can be estimated by,[285, 286]

$$k_{ISC} = \frac{2\pi}{\hbar} \sum_F |\langle \Psi_F | H_{SOC} | \Psi_I \rangle|^2 \delta(E_{FI}) \quad (6.44)$$

Hence, similar to radiative rates $k_{ABS/PL}$, k_{ISC} can be calculated in the framework of ESD through the path integral approach and within the FC/HT approximations. Hence, similarly to radiative phosphorescence, the non-radiative rate of ($T_1 \rightsquigarrow S_0$ ISC) can be calculated employing **Equation (6.44)** considering the Boltzmann populations over sublevels with spin projections $M_S = 0, \pm 1$, as shown in **Equation (6.43)**.

Knowledge of the radiative (k_r) and non-radiative (k_{nr}) rates provides access to the respective relaxation times (τ_r and τ_{nr}) as well as to the PLQY quantity (Φ_{PL}) as given in **Equation (6.45)**.

$$\Phi_{PL} = \frac{k_r}{k_r + k_{nr}} \quad (6.45)$$

6.8. Spin-vibronic/phonon Coupling

Inclusion of spin-vibronic coupling effects, i.e., effect of vibronic coupling on spin-orbit coupled states, in photoluminescent processes requires treatment of the magnetic properties induced within the excited (emissive) multiplet. Here, we assume a triplet ($S = 1$) excited state relaxation.

6.8.1. Spin Hamiltonian

As discussed in **Section 4.4.7**, an excited state spin-Hamiltonian which at zero field and by excluding nuclei interactions consist by only the zero-field splitting (ZFS) term

$$\hat{H}_{S,ZFS} = \hat{S}^T D \hat{S} = \sum_{i,j} D_{ij} \hat{S}_i \hat{S}_j \quad (6.46)$$

Typically, ZFS matrix in the SH is set to traceless and symmetric (e.g. the ZFS matrix is diagonal in its eigenframe) so that

$$\hat{H}_{S,ZFS} = D \left(\hat{S}_z^2 - \frac{S(S+1)}{3} \right) + E(\hat{S}_x^2 - \hat{S}_y^2) \quad (6.47)$$

and within, for instance, an $S = 1$ excited multiplet it takes the matrix form

$$D_{ZFS} = \begin{pmatrix} -1/3D + E & 0 & 0 \\ 0 & -1/3D - E & 0 \\ 0 & 0 & 2/3D \end{pmatrix} \quad (6.48)$$

with $D = 2/3D_z, E = (D_x - D_y)/3$

6.8.2. Spin-vibronic / Spin-Phonon Coupling Effects

Under vibronic coupling conditions the effective Hamiltonian takes the form:

$$\hat{H}_{eff} = \hat{H}_S + \hat{H}_{vib} + \hat{H}_{S-vib} \quad (6.49)$$

where \hat{H}_S corresponds to the static Spin Hamiltonian, including only the zero-field terms at zero-field as defined in **Equation (6.47)** while \hat{H}_{vib} corresponds to the vibrational Hamiltonian which in the Harmonic oscillator approximation takes the form:

$$\hat{H}_{vib} = \hbar\omega \left(n + \frac{1}{2} \right) \quad (6.50)$$

The respective Spin-vibrational Hamiltonian \hat{H}_{S-vib} is defined by restricting to linear terms of the expansion of the Spin-Hamiltonian in a series of normal modes Q_i . Hence by taking into account **Equation (6.47)** for the Spin-Hamiltonian it takes the form:

$$\hat{H}_{S-vib} = \frac{\partial D}{\partial Q_0} Q_i \left(\hat{S}_z^2 - \frac{1}{4} \right) + \frac{\partial E}{\partial Q_0} Q_i (\hat{S}_x^2 - \hat{S}_y^2) \quad (6.51)$$

The basis of the Hamiltonian consists of a set of functions given by products of magnetic sublevels $|S = 1, M_S\rangle, M_S = 1, 0, -1$ and harmonic oscillator wavefunctions $|n\rangle, n$ -the

vibrational number with energies given by **Equation (6.50)**. Assuming weak vibronic coupling limit

$$\hbar\omega \gg \left\langle M_S \left| \hat{S}_z^2 - \frac{1}{4} \right| M'_S \right\rangle \langle 0|Q_i|1' \rangle \quad (6.52)$$

$$\hbar\omega \gg \langle M_S | \hat{S}_x^2 - \hat{S}_y^2 | M'_S \pm 2 \rangle \langle 0|Q_i|1' \rangle \quad (6.53)$$

the basis functions consist of the ground and the first excited state manifolds M_S, M'_S where one vibrational quantum state has been excited $\langle 0|Q_i|1' \rangle$.

In the presence of n coupled vibrational quantum states the effective Hamiltonian \hat{H}_{eff} takes the general form

$$\hat{H}_{eff} = \begin{pmatrix} \hat{H}_S & \hat{H}_{S-vib1} & \hat{H}_{S-vib2} & \hat{H}_{S-vib3} & \dots \\ \hat{H}_{S-vib1}^* & \hat{H}_S + \hbar\omega_1 I & 0 & 0 & 0 \\ \hat{H}_{S-vib2}^* & 0 & \hat{H}_S + \hbar\omega_2 I & 0 & 0 \\ \hat{H}_{S-vib3}^* & 0 & 0 & \hat{H}_S + \hbar\omega_3 I & 0 \\ \vdots & \vdots & \vdots & \vdots & \dots \end{pmatrix} \quad (6.54)$$

This implies that in the concept of spin-vibronic coupling along a photoluminescent process it is possible to determine the static \hat{H}_S ZFS parameters of the emissive excited multiplet by employing the effective Hamiltonian approach at the equilibrium geometry. In a second step by formulating the energy potential (PES) scans for ground and excited relativistically corrected states, along the different contributing normal modes provides access to the various spin-vibronic coupling constants per contributing normal mode.

7 Modelling of Photoluminescent Molecules and solids

Photoluminescent materials commonly manifest in condensed states, such as solutions, powdered forms, and crystalline solids. The different environments can significantly impact the optical properties and must be properly considered when conducting modeling and calculations. This chapter gives an overview on approaches employed to model molecules within solution environments to capture the solvent effects and solids predominantly utilizing the embedded cluster approach.

7.1. Molecular Models for Finite Molecules (Solvent Effect)

Treating of solvents in computational chemistry is an important aspect of accurately modeling molecular systems in diverse environments.[100] Solvents have a considerable influence over the behavior, stability, and properties of molecules, and most importantly electronic and optical response, so precise representation of their effects is crucial to achieve chemical accuracy.[287] In the exploration of optical spectroscopy, the influence of solvents on optical spectra, known as solvatochromism, is of paramount importance.[108, 288-292] This significance is particularly pronounced in decay (emission) processes, where environmental factors not only impact the energy of excited states but also determine the lowest energy (emissive) state. Of special interest, inorganic molecules dominated by charge-transfer (CT) transitions, specifically those involving intramolecular charge transfer from a donor to an acceptor part of the molecule, often linked by conjugated or aromatic bridges, exhibit high sensitivity of CT transitions to the surrounding environment.[79, 293-298]

During the excitation process, changes in charge distribution result in substantial alterations in dipole moments, leading to pronounced modifications in interactions with the environment. Moreover, when hydrogen-bonding sites are involved in CT transitions, the excitation process induces further changes, such as protonation or conformational alterations, in the local environment. Additionally, the solvent effect on the CT excited state can give rise to new

nonradiative deactivation channels, potentially reducing the fluorescence quantum yield and even can cause complete quenching.[288, 292, 299-303]

In light of these considerations, a molecular probe exhibits noticeable solvatochromism when it possesses specific characteristics that render its intermolecular interactions highly sensitive to even minor environmental changes. Key factors in this sensitivity include the nature of excited states, effects on the transition dipole, transition rates, and quantum yields—all of which significantly impact the spectroscopic emission signal in terms of energy and spectral features. [79, 108, 278, 294, 295]

Incorporating solvent effects into computational simulations entails the utilization of several solvation models, with two main approaches: explicit and implicit solvation models. However, each comes with its own advantages and limitations.

7.1.1. Explicit Solvation Models

Explicit solvation models involve the inclusion of solvent molecules within the simulation, so, their interaction with solute molecules is treated quantum mechanically. One common approach is to use DFT and TD-DFT methods to encompass solvent effects on electronic structure and properties of ground and excited states. That will provide a high level of accuracy in capturing solute-solvent interactions, which is valuable for studying systems with specific and intricate solvent effects. However, this method proves to be very computational demanding and limited to few solvation layers.[304]

Other approach, to overcome such limitations, is by employing Quantum Mechanics/Molecular Mechanics (QM/MM) methods. Now, the molecule or active site of the considered studied property is treated at QM methods, and embedded in solvent sphere treated with MM simulations employing explicit solvent molecules intermolecular potentials (force fields).[305-307] However, Conventional force fields assume static charges neglecting polarization effects introduced by solvents. However, an improved treatment can be achieved by using polarizable force fields enabling dynamic adjustment of atomic charges in response to local surroundings and giving more precise representation of solvent-solute interactions.[308] Finally, the electrostatic interactions between the two regions (QM and MM) can be considered at different levels of sophistication, including either mechanical embedding, electrostatic embedding or polarized embedding.

While explicit solvation models, can give more precise and accurate descriptions, they are computationally demanding, particularly for large systems. In addition, defining the correct solvation sphere and achieving sufficient sampling can be challenging, potentially impacting the reliability of the results.[309-311]

7.1.2. Implicit Solvation Models

Implicit solvent models, such as the conductor-like continuum polarization model (C-PCM) [312] and solvation model based on density (SMD)[313], are instrumental by effectively approximate the solvent surroundings without the need to place multiple solvation shells of solvent molecules. Instead, they mimic the effect of a specific solvent on the solute by representing the solvent as a continuous dielectric medium governed by adjustable parameters, including a dielectric constant that dictates the degree of electrostatic screening.[314] Implicit solvation models are particularly advantageous in scenarios where explicit solvent treatment proves computationally demanding.[311]

In C-PCM, the solute is placed within a cavity of roughly molecular shape, and the solvent reaction field is described by apparent polarization charges on the cavity surface. These charges can be either treated as point charges or modelled as spherical Gaussians.[315] In ORCA, when Gaussian charges are considered, the charge positions are determined following a Lebedev quadrature approach. This scheme is known as Gaussian Charge Scheme.[316]

The general procedure of implicit solvation can be summarized as follows; the molecular Hamiltonian of the isolated system is perturbed by the solvent,

$$\hat{H} = \hat{H}^{(0)} + \hat{V} \quad (7.1)$$

where $\hat{H}^{(0)}$ is the Hamiltonian of the isolated molecule, and \hat{V} is the solute-solvent interactions. The SCF procedure leads to the variational minimization of the free energy of the solute G

$$G = \langle \Psi | \hat{H}^{(0)} | \Psi \rangle + \frac{1}{2} \langle \Psi | \hat{V} | \Psi \rangle \quad (7.2)$$

Using the conductor-like boundary condition, the electrostatic potential can be determined by

$$V(\mathbf{r}) + \sum_i^{N_q} V_{q_i}(\mathbf{r}) = 0 \quad (7.3)$$

where V and V_{q_i} are the electrostatic potential due to the solute and the polarization charges, respectively. r is a point on the cavity surface, and N_q is the total number of solvation charges. The vector of polarization charge can then be determined by

$$\mathbf{A}\mathbf{Q} = -\mathbf{V} \quad (7.4)$$

where the vector \mathbf{V} contains the electrostatic potential due to the solute at the position of the charges. The elements of the matrix \mathbf{A} of gaussian charges are

$$A_{ij} = \begin{cases} \frac{\zeta_i \sqrt{2/\pi}}{F_i}, & i = j \\ \frac{\text{erf}(\zeta_{ij} r_{ij})}{r_{ij}}, & i \neq j \end{cases} \quad (7.5)$$

where, ζ_i is the exponent of the Gaussian charge i (within the sphere I), $\zeta_{ij} = \zeta_i \zeta_j / \sqrt{\zeta_i^2 + \zeta_j^2}$, and $r_{ij} = |r_i - r_j|$. The point charges can be designed by Lebedev grid[315] and erf is the gauss error function. The function F_i , is an improved gaussian switching function, measures the contribution of the Gaussian charge i to the solvation energy and given as[317]

$$F_i = \prod_{J, i \notin J}^{\text{atoms}} \left(1 - \frac{1}{2} \{ \text{erf}[\zeta_i (R_J - r_{ij})] + \text{erf}[\zeta_i (R_J + r_{ij})] \} \right) \quad (7.6)$$

where, R_J is the radius of sphere J .

Clearly one of the advantages of implicit solvation models is its simplicity of implementation.[316-318] Furthermore, they are computationally efficient than explicit alternative, rendering them particularly suitable for investigating large systems and when expensive high level computational methods (e.g., CCSD, MRCI) are essential for probing molecular properties. Nevertheless, these models fall short in providing detailed insights into the intricate arrangement and dynamics of individual solvent molecules. Additionally, the accuracy of these models may be sensitive to the choice of parameters, and their generalizability across different types of solutes could pose challenges. Despite these limitations, implicit solvation models continue to hold as valuable tools in computational studies.[311, 319, 320]

7.2. Clusters Models for Solid-State Materials

Inorganic crystalline solid-state materials possess significant potential for diverse industrial and technological applications, including catalysis, LED lighting, sensors, and switches.[17-20, 30-33, 321-323] Modeling these materials involves intricate extended arrangements of cations and anions held together by ionic and covalent bonds, introducing unique characteristics and challenges.[321] Notably, both short-range and long-range electrostatic as well as polarization effects must be considered, with the latter two being particularly intricate in systems featuring covalent bonds with highly polarizable atoms, such as O^{2-} or N^{3-} within the crystal.

Commonly, these materials are studied within the framework of a *supercell periodic approach* employing DFT and TDDFT, addressing ground and excited state properties, respectively.[321] However, this approach is typically limited to lower-level DFT formulations (e.g., GGA), which is insufficient for accurately capturing a wide range of properties. Extending to higher-level DFT functionals (hybrid/double hybrid) or more accurate electronic structure methods (e.g., CCSD(T), MRCI) is challenging due to computational demands. However, periodic calculations employing plane wave function bases continue a suitable method for modeling metals. Metals typically described by “Ions in a sea of electrons” or “Soft Sphere” models,[324] with valence electrons move freely and are highly delocalized throughout the crystal lattice, influenced by the arrangement of nuclei and core electrons.

Alternatively, cluster models, when properly embedded, offer a more practical route for exploring localized ground and excited state properties, leveraging various computational methods with reasonable computational costs. This approach requires careful construction to accurately compute the targeted properties. There are three cluster model approaches: *free clusters*, *hydrogen-saturated clusters*, and *embedded clusters*. Selection depends on the system's geometry, structure, electronic characteristics, intended properties, and computational resources in hand.

7.2.1. Free Cluster Model

The simplest approach involves modeling a finite portion of the bulk solid, typically a repeated unit cell along crystallographic axis. This allows the use of high-level quantum chemistry methods on the finite cluster. However, choosing the appropriate minimum cluster size for specific properties is crucial, and the concept of “*cluster size convergence*” is essential, as

elaborated in the subsequent sections. This model effectively computes local properties such as adsorption, defect formation energies, local excitations, and X-ray spectra. [89, 325] Nonetheless, challenges include issues related to the different structural and chemical environment of outer layer atoms compared to the bulk, and the continuous growth of multipole moments and electrostatic interactions with cluster size increase.[325]

7.2.2. Hydrogen-Saturated Cluster Model

To overcome some challenges encountered in the free cluster model, the hydrogen-saturated cluster approach is employed. This approach involves saturating dangling bonds with hydrogen cations to achieve as neutral and symmetric a total system charge as possible. Although this approach addresses some problems like boundary effects, cumulative total charge, and multiple dipoles. So once again, it still requires careful construction and consideration of cluster size convergence.[89, 141, 325]

7.2.3. Embedded Cluster Approach

The embedded cluster approach, as illustrated in **Figure 7.1**, stands out as a highly promising and extensively adopted methodology, providing comprehensive access to all the electronic structure methods. Throughout the course of this thesis, this approach is predominantly employed for addressing solid-state systems.

Central to this approach is the definition of a finite size atomic cluster, cut from supercell, which is addressed to explicit treatment through quantum methods and referred to as *quantum cluster* (QC). It is crucial that QC is representative and large enough to encapsulate the entire electronic information needed for elucidating the targeted properties. That includes the electronic structure, chemical bonding, and local symmetry features. However, QC is still missing the long-range effects. The long-range interactions are electrostatically approximated by embedding the QC region in *point charges* (PC) region.

The PC region is treated in the framework of classical mechanics (MM), and for addressing the fundamental electrostatic properties of an ideal crystal, the point charges (PCs) must meet specific conditions. In the first place, all atoms in an ideal crystal adhere to a distinct Madelung constant, depending on the crystal symmetry. Consequently, a large number of PCs surrounding QC must be introduced to ensure that all QC atoms approach the correct Madelung constant, with PCs placed on crystal lattice positions to achieve the correct crystal symmetry. Secondly,

an ideal crystal is charge-neutral, prompting the adjustment of PC magnitudes to neutralize any excess charge until the total charge equals zero. Lastly, the charge distribution in an ideal crystal is uniform, necessitating the optimization of PC magnitudes, without violating the previous condition, to align with the charges of respective ions in the QC. The optimization aims to maintain consistent charge at identical lattice positions throughout the model, even within the PC field.

Additionally, the integration of *boundary region* (BR) between the QC and PC regions is introduced, which addressed as *capped-electrostatic core potentials* (c-ECPs). These *ECPs* occupy the lattice positions around the QC and play pivotal role in maintaining the integrity of the QC and preventing the artificial charge flow between the QC and the PCs, ensuring that the QC does not undergo electron leakage and over-delocalization.

In some cases, another small region between the QC and ECP is needed. For instance, in crystalline system with more covalent interactions leading to disruption of bonds on QC surface and surface/interface effects. Also, in case of highly charged QC, which could affect the electronic structure and properties and cause difficulties in SCF convergence of the system energy. So, for more realistic treatment, it would be beneficial to introduce a small layer around QC, which will be treated under cheap level of theory. In most of the cases, it will be treated employing HF method with small basis functions, it is called *Hartree-Fock* (HF) region.

The primary challenge lies in precisely defining and constructing distinct regions within the model. This task is crucial for a comprehensive and accurate representation of the structural and electronic characteristics of the system, enabling precise computation of various electronic, magnetic, optical, and spectroscopic properties. Tackling this challenge requires a systematic approach, involving careful construction of the embedded model and its various constituent regions. In this work, the embedded cluster modelling is strongly related and similar to QM/MM methodology. So, it mainly based and employing the "Ionic-Crystal-QM/MM" approach, as implemented in ORCA computational capabilities for modeling of solids.

The subsequent section provides more details and procedures to construct the electrostatic embedded cluster model used to studying the solid-state Eu^{2+} -doped phosphors and their host.

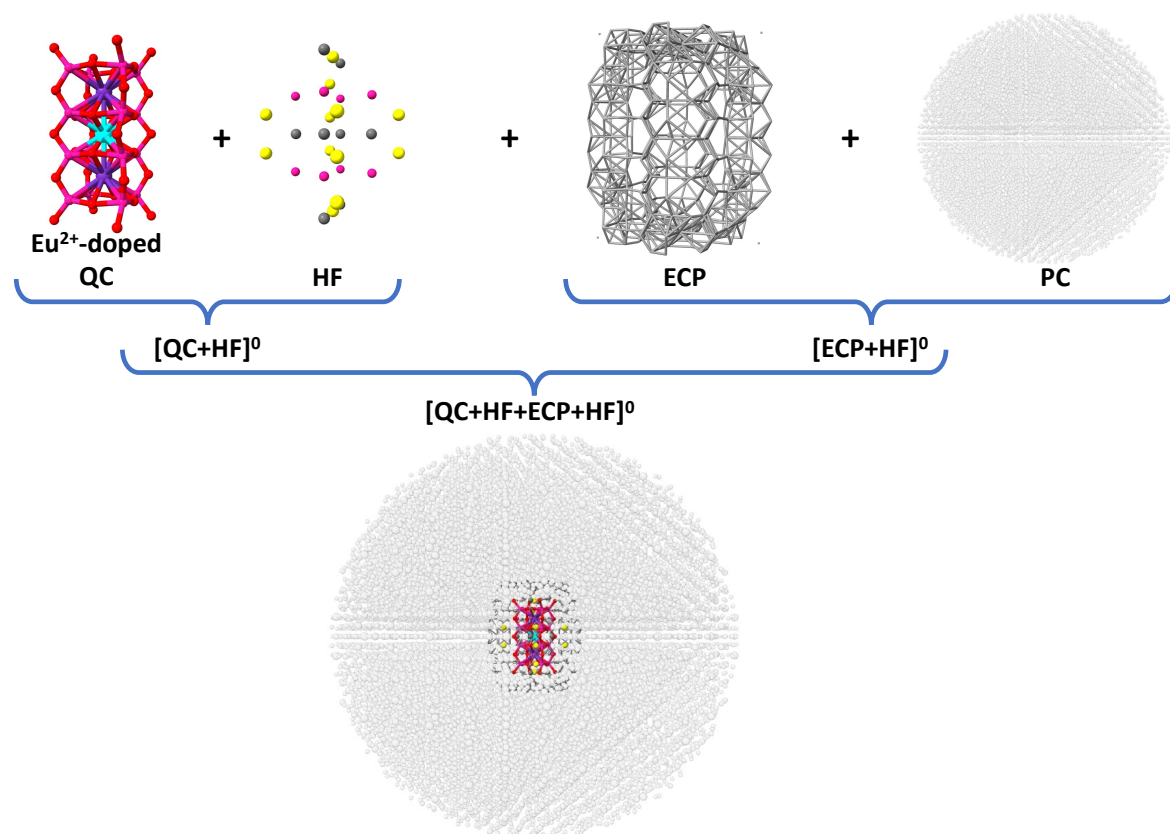


Figure 7.1. Schematic representation of embedded cluster approach, for the trimer cluster of RNLSO:Eu²⁺-doped at Na(1)⁺ center, as well embedding scenario applied to achieve charge neutrality of the clusters. The Eu²⁺ doped RNLSO [EuRb₂Li₁₆O₃₆]⁵²⁻ QC cluster surrounded by a [Na₁₂Li₈Si₈]⁵²⁺ HF layer, giving a neutral [QC + HF]⁰ cluster. The latter is surrounded by BR composed of three layers (314 points) of capped-ECP (ECP) all embedded in 36768 points charges (PC). BOTTOM: The final embedded cluster [QC + HF + ECPs + PC]⁰. For QC and HF regions, atom colors are as follows; Eu (cyan), Rb (purple), Na (yellow), Si (dark gray), Li (pink), O (red). Gray line and spheres representing the cECPs and point charges in BR and PC regions, respectively.

7.3. Protocol to construct an Embedded Cluster Model for Inorganic Solid-state Eu²⁺-doped Phosphors

Through **Part II**, embedded cluster approach[80, 83, 84, 141, 243, 323] will be mainly used to model inorganic solid-state Eu²⁺-doped phosphors in different hosts. The main goal is the calculation of optical band gap and optical (absorption and emission) spectra for the undoped

host and Eu^{2+} -doped structures, respectively. The study includes different types of phosphors including Eu^{2+} -doped phosphors containing a single doping center, which are $\text{Ca}[\text{LiAl}_3\text{N}_4]:\text{Eu}^{2+}$ abbreviated as (CLA),[326] $\text{Sr}[\text{LiAl}_3\text{N}_2\text{O}_2]:\text{Eu}^{2+}$ (SALON),[125] $\text{Sr}[\text{Mg}_3\text{SiN}_4]:\text{Eu}^{2+}$ (SMS),[327] $\text{Ba}[\text{Mg}_3\text{SiN}_4]:\text{Eu}^{2+}$ (BMS)[328] and $\text{SrLi}_2[\text{Be}_4\text{O}_6]:\text{Eu}^{2+}$ (SLBO)[126] phosphors. In addition to phosphors bearing multiple candidate centers for Eu^{2+} doping, which are $\text{Sr}[\text{LiAl}_3\text{N}_4]:\text{Eu}^{2+}$ (SLA), [329] $\text{RbNa}[\text{Li}_3\text{SiO}_4]_2:\text{Eu}^{2+}$ (RNLSO2),[330] $\text{RbNa}_3[\text{Li}_3\text{SiO}_4]_4:\text{Eu}^{2+}$ (RNLSO),[331] $\text{CaBa}[\text{Li}_2\text{Al}_6\text{N}_8]:\text{Eu}^{2+}$ (CBLA2),[124] and $\text{Ca}_3\text{Ba}[\text{LiAl}_3\text{N}_4]_4:\text{Eu}^{2+}$ (CBLA).[243]

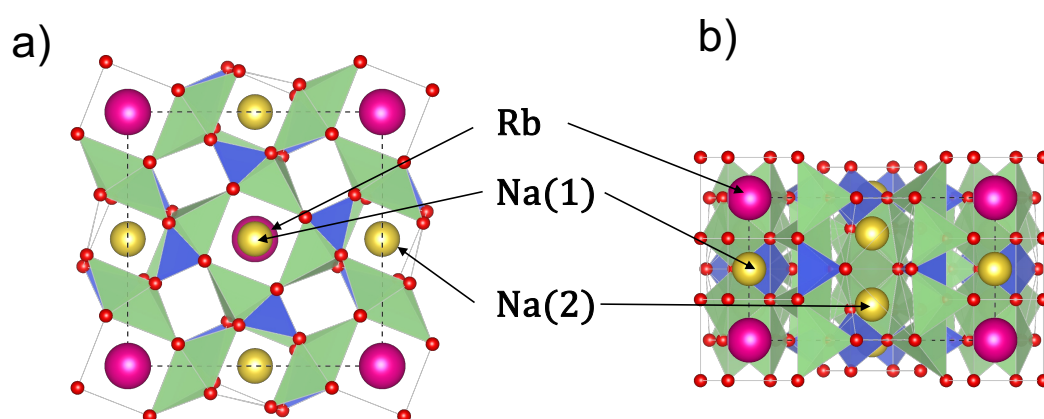


Figure 7.2. a) Top and b) side view of the crystal structure of the RNLSO2 host. The probable cationic doping site Rb, Na1, and Na2 are highlighted. Atom colors: Rb (dark red), Na (yellow), and O (red). $[\text{SiO}_4]$ and $[\text{LiO}_4]$ tetrahedra are filled in blue and green, respectively.

The proper construction of the model and the convergence of size and charge within different regions will be comprehensively discussed using RNLSO phosphor as an illustrative example. RNLSO was selected due to its manifestation of all complexities that could arise during model construction. Firstly, as shown in **Figure 7.2**, RNLSO presents multiple centers for Eu^{2+} doping, involving two Na^+ (Na(1) and Na(2) with different environments) and Rb^+ ions. Additionally, there exists a charge difference between these replaced ions and the Eu^{2+} ion. The model construction protocol outlined in the next discussion is applied in the investigation and calculations of the spectroscopic properties of the host and Eu^{2+} -doped phosphors. However, it is noteworthy that the first issue, pertaining to multiple doping centers,

becomes irrelevant in phosphors with hosts bearing a single doping center as in CLA, SALON, SMS, and BMS phosphors. Similarly, the second issue, concerning charge differences, is not applicable in phosphors with divalent dopant center metal ions (Ca^{2+} , Sr^{2+} , Ba^{2+}), as in CLA, SALON, SMS, BMS, SLA, CBLA, and CBLA2 phosphors.

1. General Remarks

Unless otherwise stated, all crystal structures' coordinates are obtained from the crystallographic data,[124-126, 326-331] refined based on the experimental crystallographic X-ray diffraction. First an “infinitely” large supercell is built by 3D repetition of crystal lattice unit cell along the crystallographic axes, usually $(20 \times 20 \times 20)$. In the chosen scenario and employing the Ionic-Crystal-QM/MM method, the supercell is sliced into four main regions as follows. **Figure 7.1** give a typical illustration of the different regions (QC, HF, ECP, and PC), where the central metal ion (and Eu after doping) is in the center of QC and consequently in the center of the entire model.

Due to the close resemblance in the ionic radii of ($M = \text{Ca}^{2+}$, Sr^{2+} , Ba^{2+} , Na^+ , or Rb^+) with Eu^{2+} ion, as illustrated in **Table 7.1** and further details in **Table 10.1** and **Table 11.1**, and their favorable local environments resulting in $[\text{EuL}_8]$ cuboids (with L being either N, O, or O/N). Eu^{2+} ion can only substitute those ions to form the doped QCs. Notably, Rb^+ and Ca^{2+} ions exhibit an observed difference of +0.36 and -0.19 Å, respectively. As will be discussed further in **Section 11.7**, the larger host cuboid for Rb^+ can accommodate the Eu^{2+} without issues, and later analysis reveals that, in certain cases, doping at Rb^+ is more favorable than at Na^+ in for example in RNLSO2. Conversely, smaller ions like Ca^{2+} , leading to compressed cuboids for Eu accommodation, present challenges, making doping less probable compared to, for example, the Ba^{2+} site in CBLA2.[243]

Furthermore, no other cations substitution (e.g., $M' = \text{Li}^+$, Mg^{2+} , Al^{3+} , or Si^{4+}) due to very small ionic radii results in highly compressed $M'L_4$ tetrahedron or $M'L_6$ octahedron with volume of this polyhedral $\leq 20 \text{ Å}^3$ (in contrast to the 28 - 40 Å^3 range for the ML_8 cuboids). DLPNO-CCSD(T) calculations reveal that such Eu-polyhedra formations lead to structurally unstable configurations compared to the Eu^{2+} -doped cuboids (EuL_8), requiring significant structural relaxation. Similarly, no occupation of interstitial sites on the unsaturated channels is not possible due to sterical reasons.[18, 80, 243]

The low doping limit is considered so that formation of Eu^{2+} -doped phosphors involves the substitution of only one (Ca^{2+} , Sr^{2+} , Ba^{2+} , Na^{+} , or Rb^{+}) cation per undoped QC with Eu^{2+} ion, followed by adopting of the charges and multiplicity, with no multiple doping in the same QC. Consequently, no (Eu^{2+} - Eu^{2+}) interaction is expected. In addition, owing to the strong rigidity of the considered solid-state crystal structures, no further structure relaxation due to Eu^{2+} doping needs to be taken into account.[80, 243]

The formal charges of ions will be initially used to equip the ECP and PC regions and then they are iterative optimized in the framework of the Ionic-Crystal-QMMM embedded cluster protocol in ORCA.[115] The chosen convergence criteria ensure an overall neutral cluster according to the neutrality condition ($q(\text{QC} + \text{HF}) = -q(\text{BR} + \text{PC})$)[141] as well as a uniform charge distribution in all (QC, HF, BR, and PC) regions. In the cases (RNLSO and RNLSO2), when Eu^{2+} is replacing ion with different charge, the charge deficiency within the (QC + HF) will be distrusted over all the charges of (BR + PC) regions.

Table 7.1. Cationic sites (M^{n+}) in the studied hosts, along with their ionic radius (r , in Å), and the difference in ionic radii (Δr , in Å) between ion M^{n+} and Eu^{2+} . All ionic radii are presented for ions in 8-fold cuboid coordination and the ionic radius of $\text{Eu}^{2+} = 1.25$ Å in this coordination.[332]

Cationic Site (M^{n+})	r (Å)	Δr (Å)
Sr^{2+}	1.26	+0.01
Ba^{2+}	1.35	+0.10
Ca^{2+}	1.06	-0.19
Na^{+}	1.18	-0.07
Rb^{+}	1.61	+0.36
Li^{+}	0.90	-0.35
Mg^{2+}	0.86	-0.39
Al^{3+}	0.68	-0.57
Si^{4+}	0.54	-0.71

2. Quantum Cluster (QC) Region

As mentioned above, the system is described by a finite QC which is treated explicitly by quantum chemistry methods. Definition of the complete QC in terms of size, shape, and composition is crucial. Two primary approaches are commonly utilized for defining such QCs: the unit cell approach and the ligand field approach.

The unit cell approach closely aligns with strategies commonly employed in periodic calculations. This method originates from the representation of crystals in unit cells and entails the progressive construction of the model by using building blocks to approximate a complete supercell. An advantage of this approach is that the overall model is either charge-neutral or nearly neutral. However, a drawback of the supercell approach is its potential to disrupt local symmetries and essential chemical bonding.

In contrast, the ligand field approach gives the priority for preserving the coordination environment around a specific center and growing the model around it. This becomes advantageous when properties under consideration are localized around a center of interest, and the local symmetry holds significance. One evident application of this approach is in the study of impurity ions and color centers in crystals, where various spectroscopic properties are explored in relation to the influence of the environment and local symmetry. While the ligand field approach provides valuable chemical insights into the crystal, a notable drawback is the tendency for these clusters to carry a high charge. This challenge can be overcome by employing properly constructed BR (ECP+HF layers). Nevertheless, a careful modeling of both the supercell and ligand field approaches has been shown to yield consistent results for most properties, as discussed in the references [83, 84, 115]. Based on that the ligand field approach will be used through this work.

Recognizing the necessity for a thorough depiction of electronic structure, charge distribution, chemical bonding, and interactions within the QC, it becomes evident that a larger QC generally leads to a more comprehensive representation of the system. Nevertheless, this comes at a higher computational cost and the QC selection requires a balance between accuracy and feasibility. Furthermore, acknowledging the complexity of chemical structures in certain systems, chemical intuition is also very helpful when building the QCs. In such cases, the synergy of computational rigor and chemical insight ensures a nuanced and well-informed determination of the ideal quantum cluster for the study. To identify the optimal QC, minimal QC size effectively representing the system, a systematic approach entails preparing QCs of increasing sizes and monitoring the considered property convergence with the cluster size.[115]

For instance for undoped host RNLSO, quantum clusters (QCs) were constructed by preserving the 8-fold cubic coordination environment around the central alkaline metal ions (Rb^+ , $\text{Na}(1)^+$, and $\text{Na}(2)^+$). Structure expansions containing one, two, three, four, or five central cations per cluster of the host were considered, abbreviated as monomers, dimers, trimers, tetramers, and pentamers clusters. The respective quantum clusters of the host structures are

visualized in **Figure 7.3** and given in details in **Table 7.2**. Eu^{2+} -doped structure will be prepared as mentioned above by replacing the target central metal ion with Eu^{2+} ion.

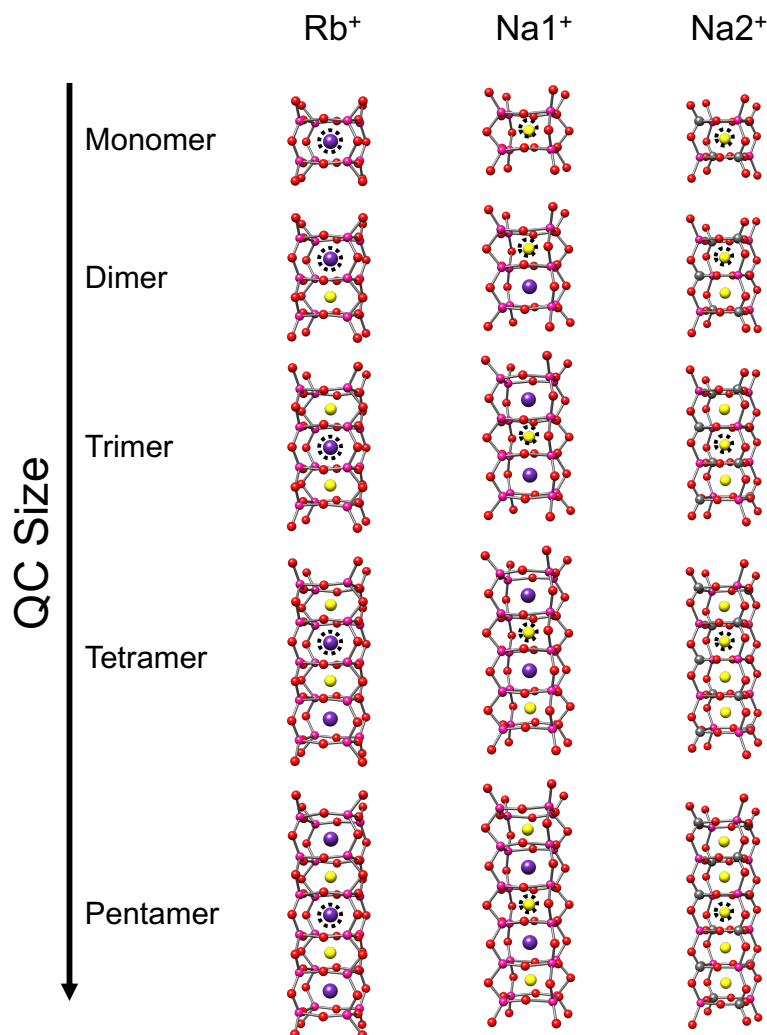


Figure 7.3. All cluster models (QCs) for RNL SO (Rb^+ , Na(1)^+ , Na(2)^+ channels) are given. Different sized models named with respect to number (n) of the central metal ion (Rb^+ , Na^+) in the cluster as (Monomer, Dimer, Trimer, Tetramer, Pentamer for $n=1, 2, 3, 4, 5$, respectively). The Eu^{2+} doping site is indicated with dotted black circle around the ion that will be replaced by Eu^{2+} . Atom colors: Rb (purple), Na (yellow), Si (dark gray), Li (pink), and O (red).

Table 7.2. Description of the employed RNLSO2 undoped and Eu^{2+} -doped clusters at $\text{Na}(1)^+$ center within the embedded cluster approach in terms of the QCs size, the (undoped and Eu^{2+} -doped) QCs composition, HF layers, the number of atoms in the ECP region, the number of points in the PC region. An Eu-doped cluster is constructed by replacing central $\text{Na}(1)^+$ site with Eu^{2+} ion.

Cluster Size	Undoped / Eu^{2+} -doped QCs	HF	n(cECP)	n(PC)
1	$[\text{NaLi}_8\text{O}_{20}]^{31-}/[\text{EuLi}_8\text{O}_{20}]^{30-}$	$[\text{Rb}_2\text{Na}_6\text{Li}_8\text{Si}_4]^{32}$	232	36886
2	$[\text{NaRbLi}_{12}\text{O}_{28}]^{42-}/[\text{EuRbLi}_{12}\text{O}_{28}]^{41-}$	$[\text{RbNaLi}_8\text{Si}_8]^{42}$	254	36864
3	$[\text{NaRb}_2\text{Li}_{16}\text{O}_{36}]^{53-}/[\text{EuRb}_2\text{Li}_{16}\text{O}_{36}]^{52-}$	$[\text{Na}_{12}\text{Li}_8\text{Si}_8]^{52}$	314	36768
4	$[\text{Na}_2\text{Rb}_2\text{Li}_{20}\text{O}_{44}]^{64-}/[\text{EuNaRb}_2\text{Li}_{20}\text{O}_{44}]^{63-}$	$[\text{RbNa}_3\text{Li}_{12}\text{Si}_{12}]^{64}$	342	36740
5	$[\text{Na}_3\text{Rb}_2\text{Li}_{24}\text{O}_{52}]^{75-}/[\text{EuNa}_2\text{Rb}_2\text{Li}_{24}\text{O}_{52}]^{74-}$	$[\text{Rb}_2\text{Na}_{10}\text{Li}_{16}\text{Si}_{12}]^{76}$	396	36650

3. Hatree-Fock (HF) Region

Towards a more accurate description and electronic stability of QC, it would be beneficial to introduce a small region around QC, called Hatree-Fock (HF) region, within the multiscale approaches.[333] This region provides a more realistic electronic environment to QC by annealing the dangling bonds, effectively reducing surface/interface and polarization effects. These issues have been shown to impact optical properties[334, 335] and demand careful treatment and elimination to ensure accurate representation of optical characteristics. In addition, the QC could be highly charged, that is severely affects the electronic structure and consequently computed properties, moreover, that could cause difficulties in SCF convergence of the system energy and wavefunction. So, a carefully selected region around QC, with charge compensating the QC's charge, will be advantageous.

Although the HF region entails additional computational costs, its role, as discussed earlier, does not imply a very complex and accurate treatment. To address this, it will be treated at a more cost-effective level of theory, equipped with a minimal LANL2DZ basis set with the respective HayWadt ECPs.[336-339] The HF layer will be treated at the HF level when employing WF-based methods for the QC. However, it will be treated at the same level when

density DFT methods are employed. (ORCA Manual) Examples of HF layer used in the treatment of RNLSO (for $\text{Na}(1)^+$ doping center) are given in **Table 7.2**.

4. Boundary or Effective Capped Potential (ECP) Region

Electrons of atoms, especially on the surface, in the QC (= QC+HF) are strongly attracted by the positive point charges in the surrounding PC field. For instance, the valence electrons in the $\text{O}^{2-}/\text{N}^{3-} - 2p$ shells can be strongly polarized and will eventually try to occupy their next empty $1s$ orbitals. Whether that is possible, sensitively depends on the basis set employed for the QC. The better the basis set is, the larger is this effect, since more extended basis sets facilitate the flow and delocalization of the QC electrons towards the positive point charges. This effect leads to poor description of electronic structure of QC and consequently large errors in the calculated properties. However, it can be easily avoided by equipping the point charges in a “boundary region” around the quantum cluster by *repulsive capped-effective core potentials* (c-ECPs) which prevent the electrons from flowing into the point charge field. In this work, c-ECPs as included in the SDD framework are employed.[340-343] **Table 7.3** give of the ECPs utilized for various elements.

Table 7.3. The employed types of c-ECPs of class SDD for different elements.

Element	ECP	References
Li, Be	ECP2SDF	[340]
Na, Mg	ECP10SDF	[340]
Al, Si, Ca	ECP10MBW	[341, 342]
Sr, Rb	ECP28MDF	[343]
Ba	ECP46MBW	[341] [341]
O, N	ECP2MWB	[342]

The width of the boundary zone will depend on the form, size, charge of the QC and also on the basis set used for QC (and HF). In ORCA, as implemented in “*ORCA IONIC CRYSTAL QM/MM*” module, the connectivity of atoms within the supercell is examined, enabling the identification of atom layers surrounding the QC. The initial layer comprises atoms directly bonded to the QC atoms, while subsequent layers consist of atoms bonded to the preceding layer, and so on. To determine the minimal needed width of BR, another size convergence is needed. Generally, in Eu^{2+} -doped phosphors and similar system, we have found that 2-3 layers of ECPs is optimal as shown in, **Figure 7.4**. The charges of c-ECPs are determined through the

charge convergence scheme within the QM/MM module, as shown in **Figure 7.5** and discussed in the next section.

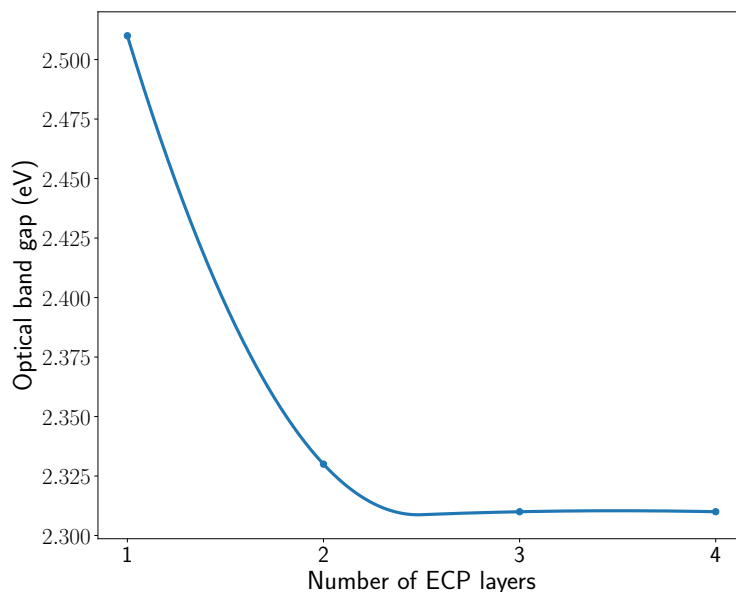


Figure 7.4. Size convergence of the ECP region (number of ECP layer within the ORCA-CRYSTAL-QM/MM module, against the lowest excited state. The calculations were performed on the trimer cluster of RNLSO:Eu²⁺-doped at Na(1)⁺ center, [EuRb₂Li₁₆O₃₆]⁵²⁻ QC and [Na₁₂Li₈Si₈]⁵²⁺ HF layer, employing TD-DFT/PBE0 with def2-TZVP basis. All elements in ECP and PC were capped with the formal charges.

5. Point Charge (PC) Region

As discussed previously, the QC is embedded in an extended PC field to reproduce the long-range electrostatic and polarization effect. Similar to the ECPs, the point charges (PC) positions are taken to coincide with the crystal supercell lattice points. Again, the optimal size of the PC region needs some tests. Obviously, the larger the QC is, the larger PC is needed. Through our investigations in this work, PC region comprising 20,000-50,000 point charges effectively captures the long-range electrostatic effect.

The final charges of both (ECPs and PCs) are determined through the charge convergence scheme within the QM/MM module. Initially, the formal changes of respective ions are utilized for both ECPs and PCs. Formal charges are particularly a good choice for ionic crystals where electrons are strongly localized within the ions. However, the true effective charges in covalent crystals are not easy to be determined due to lack of reliable experiments to determine the effective charges as consequence of the fact that charge is not an observable. Several techniques

have been proposed to estimate the charges of ECPs/PCs with clear discrepancies and inconsistency due to the sensitivity of different charge scheme. For instance, some methods define charges based on the orbitals (e.g., Mulliken[344-347] and Loewdin[348, 349]schemes), the density (e.g., Hirshfeld[350]), or the electrostatic potential (e.g., CHELPG[351-353]). In the considered Eu^{2+} -doped phosphors, CHELPG scheme exhibits the highest stability and the best performance.[115] Finally, the effective charges of ECPs and PCs are determined through iteratively SCF charge convergence processes within the “IONIC CRYSTAL QM/MM” module in ORCA.[354, 355] This is executed while maintaining a homogenous charge distribution within the system and neutralization of the total model charge, expressed as $q(QC + HF) = -q(ECP + PC)$.

Figure 7.5 illustrates an instance of charge convergence utilizing the CHELPG scheme in a selected case of Eu^{2+} -doped trimer QC. The figure demonstrates the smooth convergence of all charges within the ECP and PC regions after a few steps. While the majority of elements displayed only minor deviations from their formal charges, Si^{4+} and Rb^{+} ions exhibited significant changes, account to (-1.4, and -0.4), respectively. This highlights the potential pitfalls associated with relying solely on formal charges in such system and similar systems.

One of the limitations in the current embedding model described so far is, the ions in the point charge field are fixed in space with well-defined charges but they are not polarizable. So, the embedding point charge field cannot respond to electric changes in the QC, caused for instance by local excitations. To address this limitation, the integration of the embedded cluster protocol with polarizable embedding schemes and fast multipole methods is currently undergoing in our laboratory.

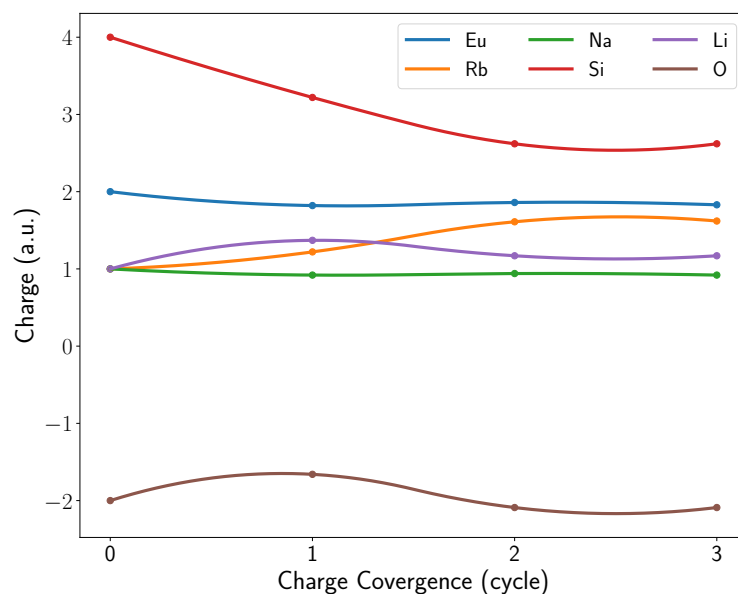


Figure 7.5. Charge convergence of the different elements in the ECP and PC region utilizing the ORCA- CRYSTAL-QM/MM module and CHELPG scheme for charge calculation. The calculations were performed, employing TD-DFT/PBE0 with def2-TZVP basis, on the trimer cluster of RNLSO:Eu²⁺-doped at Na(1)⁺ center, [EuRb₂Li₁₆O₃₆]⁵²⁻ QC, [Na₁₂Li₈Si₈]⁵²⁺ HF layer, 3 ECP layers [Na₁₂Rb₂Li₁₁₆Si₄₀O₁₁₄] and 36768 point charges. Charges of all elements in ECP and PC were initiated with the formal charges (Eu²⁺, Li⁺, Na⁺, Rb⁺, Si⁴⁺, O²⁻). Charge convergence threshold is ($\Delta q \leq 0.01$) with keeping the total system charge $q[\text{QC} + \text{HF} + \text{ECP} + \text{PC}] = 0$.

PART II

Understanding the Electronic Structure and

Photoluminescence in Solids :

Eu²⁺-doped Phosphors as an Example

8 Introduction to PART II

Undoubtedly, the world is currently facing an escalating global power crisis due to the combination of increasing energy demands and limitations posed by conventional power sources. Moreover, urgent imperatives to curb carbon emissions and promote sustainability are adding to the challenge. So, there is a pressing necessity to develop efficient and cost-effective methods for power consumption and to embrace renewable energy sources.[356, 357] Among the potential solutions, phosphor-converged light-emitting diodes (pc-LEDs) emerge as a promising option. These advanced light sources utilize multiple phosphor layers to achieve higher light emission efficiency. Through the process of photon down-conversion, high-energy photons are converted into multiple low-energy ones resulting in reduced energy waste accompanied with improved luminous efficiency.[120, 357] Furthermore, pc-LEDs demonstrate exceptional durability and extended lifespans compared to traditional lighting technologies, thereby contributing to decreased material consumption and energy demand. Their eco-friendly attributes and efficiency position them as a compelling alternative to conventional lighting, playing a significant role in energy conservation and facilitating the transition to a sustainable and electrified future.[15, 18-20, 32, 120, 329, 331, 357-363]

Of particular interest among the different luminescent phosphor materials are the lanthanides activated solid-state phosphor materials. These materials possess unique and tunable emission properties that are in high demand across a broad spectrum of applications. Moreover, they serve as fundamental building blocks for various solid-state devices, including energy-efficient phosphor-converged white LEDs (pc-WLEDs), solid-state lasers, liquid crystal displays, solar cells, and near-infrared detection technologies.[17-20, 30-52]

For pc-WLEDs applications, Eu^{2+} stands out among the various activators due to its remarkable *intensively emissive* and *host-tunable* $4f^65d^1 \rightarrow 4f^7$ electronic transition. In particular, the Eu^{2+} -activated nitride, oxynitride, and oxide UCr_4C_4 host-based phosphors exhibit exceptional luminescence properties. These phosphors exhibit host-tunable narrow-

band emissions in terms of spectral emission color and bandwidth, offering a wide range of colors spanning from near infrared (NIR) to blue lights. Additionally, they demonstrate high thermal stability and remarkable luminescence efficiency.[20, 30, 125, 126, 327-329, 360, 364-382]

The progress in the field of UCr_4C_4 narrow-band emission phosphors has been remarkably improved since PHILIPS filed the patent (US 9,546,319) in 2013.[383] Subsequently in 2014, Schnick's group have make breakthroughs with the development of the $\text{Sr}[\text{LiAl}_3\text{N}_4]:\text{Eu}^{2+}$ (SLA)[329] nitride red phosphor. That has paved the way for research on nitride narrow-band emission phosphors as next-generation for pc-LEDs.[18, 20] This also led to the subsequent development of other notable red-emitting phosphors like $\text{Sr}[\text{Mg}_3\text{SiN}_4]:\text{Eu}^{2+}$ (SMS)[327], $\text{Ca}[\text{LiAl}_3\text{N}_4]:\text{Eu}^{2+}$ (CLA)[326], $\text{Sr}[\text{Mg}_2\text{Al}_2\text{N}_4]:\text{Eu}^{2+}$ (SMA),[384] and $\text{CaBa}[\text{Li}_2\text{Al}_6\text{N}_8]:\text{Eu}^{2+}$ (CBLA)[124]. In addition, Huppertz's group successfully synthesized oxynitride phosphors, such as $\text{Sr}[\text{Al}_2\text{Li}_2\text{O}_2\text{N}_2]:\text{Eu}^{2+}$ (SALON)[125], which opened up possibilities for blue-shifted emission through the reduction of the crystal field effect and further color tuning. In 2018, OSRAM Opto Semiconductors, based on a patent (WO 2018/029299), presented a series of alkali lithosilicate oxide phosphors for green and cyan phosphors.[385] These phosphors with narrow-band emission offer a wide range of color tunability, albeit at the expense of increased structural complexity. Moreover, Xia's group also made significant contributions to the development of alkali lithosilicate phosphors and their potential applications.[38, 331, 359-362, 386] Despite the advantages and unique properties of Eu^{2+} -doped phosphors for pc-WLEDs, there are remaining challenges in understanding and controlling the tuning mechanisms for these materials.

The importance of Eu^{2+} -based pc-LEDs as next-generation lighting sources for illumination purposes has motivated research to improve the quality of white light. As a result, there is a drive to develop novel, highly efficient, cost-effective, and environmentally friendly phosphor materials with specific emission characteristics.[15, 16, 18-20, 38, 357, 386] However, successful design of innovative materials featuring pc-LED phosphors requires a high degree of tunability of the emission band color, width, Stokes shift, and thermal stability.[16, 18, 20, 126, 377-379, 387-389] This necessitates exploring various strategies, including host lattice selection, crystal structure engineering, dopant concentration, co-doping, and excitation source control.[20, 30, 126, 326-329, 360, 365-371, 390, 391] Nevertheless, most of these strategies have relied on chemical intuition and trial-and-error methods, which can be time-intensive and not necessarily successful. Therefore, there is a pressing need for reliable chemical and

structural engineering strategies for designing innovative Eu^{2+} -doped inorganic solid-states phosphors tailored for desired applications. These strategies are driven and guided by a comprehensive understanding of the electronic structure, luminescence mechanism within the activator (Eu^{2+}) ion and the influence of both chemical and structural properties on both static and dynamic limits.[80, 243]

Theory investigation plays a crucial role in unraveling the theory-structure-property relationships that can guide the search and design of new materials. Additionally, data-driven computation through artificial intelligence (AI) can accelerate the search for the next generation of phosphors for emerging applications.[15, 76]

Although significant advancements have been made in the understanding of luminescence, Eu^{2+} -based luminescent materials remain challenging to study due to the intricate electron configurations and complexity of their excited states. The complexities inherent in such Eu^{2+} -doped materials, are multi-faceted, involving:[74, 80, 243]

1. Complexities related to the host and Eu doping environments

- Crystal field (CF) effect and the symmetry variations within the Eu^{2+} doping environment, across different hosts, results in diverse CF strengths, splittings and orbital stabilizations in both the valence d and f orbital manifolds.
- Eu-Ligand covalency, especially in the 5d orbitals, exhibits high sensitivity to the local ligand structure concerning symmetry, Eu-Ligand bond distances, and the type of ligands.
- In some hosts, there are multiple candidates for Eu doping, emphasizing the crucial need for a precise estimation of relative doping probabilities among different doping sites to fully comprehend luminescence characteristics.
- In addition, the existence of multiple candidates for Eu doping can lead to overlapping emission bands if they emit at close energies and have relative doping probabilities.
- There is a possibility for the Eu ion to occupy interstitial spaces within the host lattice.
- In some hosts, Eu^{2+} may replace metal ions with lower or higher ionic charges, resulting in charge deficiency or excessiveness within the host lattice, for instance (Li^+ , Na^+ , K^+ , or Cs^+) ions in alkali lithosilicate hosts.[385]
- At high doping concentrations, there is a higher possibility of multiple Eu ions doping closer sites. This proximity enables them to influence and undergo energy exchange with each other, influencing luminescence efficiency.

- The host optical band gap energy especially if it is relatively small or comparable to the emission energy, results in reduction of luminescence efficiency through non-radiative emission processes. This effect becomes more pronounced with increasing temperature, leading to a reduction in the thermal stability of Eu-doped phosphors.

2. Complexities of properly describing the electronic structure properties of the ground and emissive excited state manifolds

- The dense and complex excited states manifold arises from both ($4f^7 \rightarrow 4f^7$) and ($4f^7 \rightarrow 4f^6 5d$) excitations.
- Significant electron correlation effects (electrons in highly compacted 4f-orbital are severely correlated).
- Interconfigurational $4f^7 \rightarrow 4f^6 5d$ transition, breaks the favorable half-filled high-spin ($4f^7$) electron configuration resulting in radial correlation between 4f, 5d and 5f manifolds.[392]
- Strong spin-orbit coupling (SOC) effects in high-spin open-shell ground and excited states.

3. Complexities of properly describing the dynamic properties of the excited emissive state manifold

- The vibronic and phonon couplings within the local Eu^{2+} doped and lattice environments, respectively and their impacts on the electronic energy of ground and the excited states.
- The vibronic effect on SOC (spin-vibronic coupling), transitions strength (Herzberg-Teller coupling).
- Possibility of symmetry lowering by (pseudo-)Jahn-Teller (PJT) effects which lead to (quasi-)degeneracy breaking of the emissive excited states, and consequently strong vibronic coupling,
- The interplay between different couplings and ligand field effects and the strength of the Eu-Ligand covalency especially in the 5d-based emissive excited states.
- Finally, the non-radiative relaxation processes.

all these factors influence both the ground and excited states electronic and magnetic structures and finally dictate the relaxation and the photoluminescence characteristics. That leads to different, and sometimes contradictory, analyses explanations of the experimental spectra and results.[74]

Theoretical calculations, including density functional theory (DFT) and wavefunction theory (WFT) methods, in conjugation with excited states dynamics (ESD) computational protocols, offer accurate results and a promising avenue for further and exploration and descriptions through. Moreover, the recent improvement in modern high-level electronic theory methods accompanied with significant growth in computational power can now be utilized to provide an accurate description of the electronic structure and transitions within these materials. This computational progress allows for precise reproduction of experimental values and spectra while providing valuable insights into the origin and characteristics of various phenomena, including band emissions, Stokes shifts, non-radiative relaxation, and energy transfer rates.[80, 82, 242, 243, 273, 274]

As a result, the scientific and technological significance of these materials has prompted intense research efforts, making it essential to develop computational tools, protocols, and electronic-structural descriptors. These offer promising solutions to understand and predict the luminescence behavior of Eu-doped phosphors more effectively, which can facilitate the discovery and design of tailor-made luminescent materials to meet the evolving demands of modern society.[80, 243]

8.1. Objectives and Overview of the forthcoming chapters

The main objective of this part is to systematically develop a computational protocol that enables a comprehensive exploration and understanding of the electronic structure, states, and the optical transitions in Eu²⁺-doped phosphors. This includes investigating the vibronic coupling effects and their impact on the luminescent characteristics of the considered systems. Furthermore, the objective is extended to identify the principal structural, chemical, and electronic descriptors govern the emission spectral features and broadening mechanism. Finally, the study also gives perspectives about the promising future tuning methods towards phosphors with desired luminescence properties for solid-state applications. To achieve that through the study the most cutting-edge techniques, discussed through **Chapters 5-7**, were systematically and progressively utilized. The investigations employ the high-level electronic structure methods, spectroscopic analysis, and excited-state dynamics. Particularly, NTO analysis based on DFT/TD-DFT, DLPNO-CCSD-based local energy decomposition (LED) analysis, CASSCF/NEVPT2 excitation energies, SOC analysis, and vibronic/spin-vibronic coupling analysis through excited state dynamics (ESD) methods have emerged as indispensable tools in the study and prediction of luminescence properties.

In **Chapter 9**, the electronic structure of Eu^{2+} ion is introduced and explored, both in its free form and within a highly symmetric model structure resembling Eu^{2+} -doped phosphors. The analysis reveals the intricate nature of electronic structure properties, emphasizing the sensitivity of 4f5d-based excited states to local ligand structures and the ligand field effect.[74] Furthermore, it highlights the electronic-structural instability in highly symmetric structures, results in symmetry breaking through (P)JTE. The significance of the local environment over SOC is also emphasized, showcasing how the interplay of all various couplings shapes the electronic and magnetic structures, influencing relaxation and photoluminescence characteristics. This sets the stage for a systematic exploration of luminescence in Eu^{2+} -doped phosphors in the upcoming chapters.

In **Chapter 10**, a computational protocol is developed on a set of representative examples of UCr_4C_4 -based nitride, oxo-nitride, and oxide Eu^{2+} -doped phosphors, all featuring a single Eu doping center. The protocol is based on TD-DFT method and operates in conjunction with ESD approach to consider vibronic coupling on both FC and HT limits. The protocol exhibits high predictive accuracy for the optical properties and the experimental absorption and emission spectral features of Eu^{2+} -doped phosphors. Electronic descriptors are identified, revealing a robust correlation with the energy position and bandwidth of experimental emission bands, which can be directly utilized without the need for elaborate calculations. These descriptors can be leveraged for a systematic design of novel phosphor materials with tailored photoluminescence properties.[80]

Subsequently, in **Chapter 11**, the efficacy and generality of the previously proposed protocol and descriptors are affirmed through expanding the investigated chemical systems, encompassing a new set of UCr_4C_4 -based phosphors bearing multiple candidate centers for Eu^{2+} doping. The DLPNO-CCSD method is employed to predict relative doping probabilities among different centers. The doping sites are further examined through LED analysis decomposing the DLPNO-CCSD doping energies into distinct chemical interactions (e.g., ionic and covalent). Finally, this validation demonstrates the versatility and generality of the developed protocol and the defined descriptors to accurately predict luminescence characteristics for Eu^{2+} -doped phosphors of any arbitrary complexity.[243]

The results of **Chapters (10,11)** highlight the crucial role of the $\text{Eu}(5d)\text{-Ligand}(2p)$ covalency of the 4f5d-based emissive states on the broadening of the emission spectra. Furthermore, the study elucidates the implications arising from MLCT transitions intersecting

with the localized $4f^6 5d^1 \rightarrow 4f^7$ main relaxations on the broadening and thermal stability of emission in such phosphors.[80, 243]

These insights and the defined descriptors provide valuable guidelines for the design and development of highly efficient phosphors with tailored properties. Building on this foundation and intertwining experimental observations and theoretical investigation, **Chapter 12** presents a detailed example of the *in silico* designed Eu^{2+} -doped phosphor $\text{Ca}_3\text{Ba}[\text{LiAl}_3\text{N}_4]_4:\text{Eu}^{2+}$ (CBLA) with unprecedented narrow-band red emission.[243]

Finally in **Chapter 13**, we delve into the emission process and its dependence on spin-orbit (SOC) and spin-vibronic (SVC) couplings, revealing the broadening mechanism in Eu^{2+} -doped narrow-band emitting phosphors. This investigation focuses on the correlation between crystal structure variations and luminescence, utilizing experimental luminescence spectra at both room and cryogenic temperatures for enhanced resolution. Employing a computational strategy that integrates multiconfigurational WF-based methods like SA-CASSCF/NEVPT2 considering SOC, we analyze electronic structure, transitions, and magnetic properties. The study concentrates on a set of Eu^{2+} -doped phosphor systems to establish principles governing relaxation and broadening mechanisms. The results underscore the significance of magnetic structure and dynamics of both ground and excited states, as well as vibronic transitions, in accurately predicting relaxation times and understanding the fine-tuning of emission spectra.

In summary, by addressing these challenges, our research aims to contribute valuable insights to the field of lanthanides-activated materials, specifically focusing on Eu^{2+} -doped phosphors, and advance the understanding of their luminescent behavior. The insights gained in this study, aim to contribute to the engineering of innovative Eu^{2+} -doped materials with fine-tunable luminescence properties for applications in lighting, displays, and sensing.

9 Electronic Structure of Free Eu^{2+} Ion and Doped in Perfect Cubic Ligand Field

Europium (Eu) is a lanthanide element with unique electronic properties, and its divalent state, Eu^{2+} , draws special attention owing to its intriguing luminescence properties observed in many Eu^{2+} -doped materials. It is important at the beginning to have a clear picture of the electronic, magnetic, and spectroscopic properties of Eu^{2+} ion, and examine the impacts of introduction of the ligand coordination environment. Hence, this chapter focuses on exploring the impact of an “ideal” cubic ligand coordination field to the Eu^{2+} ion. This establishes a reference point for real-world cases studied in the subsequent chapters. In addition, the chapter will shed light on some of the complexities associated with the study of these materials, as introduced in the previous chapter.

9.1. Free Eu^{2+} Ion

The divalent Europium ion (Eu^{2+}) possesses $[\text{Xe}]4f^7$, or $4f^7$ for short, electronic configuration. The half-filled 4f shell is spatially compacted and well-shielded from the environment by the closed $5s^2$ and $5p^6$ outer shells.[393] The seven electrons in f shell are significantly correlated, [74] and can be arranged in many different ways given by the binomial coefficient $\binom{14}{7}$ leading to 3432 degenerate atomic microstates (including 8 octet ($S = 7/2$), 288 sextet ($S = 5/2$), 1568 quartet ($S = 3/2$) and 1568 doublet ($S = 1/2$) microstates), where S represents the total spin quantum number. This degeneracy is partly or totally lifted due to several perturbations including interelectronic repulsion, spin-orbit coupling, and Zeeman effect, in addition to the ligand field effect of surrounding, upon the ion doping.

The introduction of the interelectronic repulsion results in the $4f^7$ configuration characterized by $119\ ^{2S+1}L$ terms, where L is the total orbital angular momentum quantum numbers.[394] Free Eu^{2+} ion in the ground state, the $4f^7$ electronic configuration gives rise to the stable ground 8S term. Additionally, Eu^{2+} ion exhibits a very dense excited states manifold

due to several possible excitation transitions. Within the 1-electron picture, firstly the parity-forbidden intraconfigurational spin-flip $4f^7 \rightarrow 4f^7$ transitions. The other excitation pathway is to excite electron to the empty 5d orbitals via spin-conserving interconfigurational $4f^7 \rightarrow 4f^6 5d^1$ single electron excitations. The latter is of great importance where its decay process $4f^6 5d^1 \rightarrow 4f^7$ will energetically be the lowest pathway and dominate the luminescence in Eu^{2+} -doped materials. That is a clear consequence of a higher impact of ligand field effects on the 5d orbitals compared to the 4f orbitals, as elaborated in subsequent sections.

Furthermore, the energy levels in Eu^{2+} are strongly influenced by spin-orbit coupling (SOC). All that sums up results in a very complex electronic and magnetic structure of Eu^{2+} -doped materials. Multiconfigurational wavefunction methods have proved to be very adequate and powerful to study such systems.[74] So, for precise description of the electronic structure of the free Eu^{2+} ion, a CASSCF calculations in conjugation with NEVPT2 are employed.

9.1.1. Calculations details

The electronic structure (ground and excited states manifolds) of the Eu^{2+} ion was computed using the state-average complete active space self-consistent field (SA-CASSCF) [169, 184] method, in combination with second-order N-electron valence state perturbation theory (NEVPT2).[193, 395] The quasi-restricted (QRO)[396] based on DFT/PBE0[227, 234, 235] Kohn Sham (KS) orbitals used as initial orbitals. The complete active space CAS(7,19) is selected, encompassing the complete Eu 4f, 5d and 5f shells. The SA-CASSCF CI was optimized by averaging over 36 octet and 35 sextet states, employing the ICE-CI solver.[188, 189] The energetics and properties of spin states were computed by introduction of spin-orbit coupling (SOC) in the framework of quasidegenerate perturbation theory (QDPT). [140, 149] Furthermore, zero-field splitting (ZFS) parameters ($D, E/D$) for the states were computed employing the spin Hamiltonian formulation, as depicted in **Section 4.4.7**.

For accurate computations, the segmented all-electron relativistically re-contracted (SARC) scheme[397-400] was employed, utilizing the (SARC-DKH-TZVPP) basis set for Eu element. To account for scalar relativistic effects, second-order Douglas-Kroll-Hess relativistic corrections (DKH2)[401, 402] were consistently applied throughout the calculations, employing the finite nucleus model.[403]

Active space selection

It is well-known that the crucial step of a CASSCF calculation is the selection of the appropriate and representative active space, which is not always straightforward and requires an understanding of the system and properties being investigated. The emission in Eu^{2+} -doped materials, where we are focusing on, is mainly characterized by interconfigurational ($4f^7 \rightarrow 4f^65d^1$) excitation/relaxation transitions, so an active space CAS(7,12) looks by-de-facto resealable for this problem. Other orbitals could be included, e.g., Eu 6s and 6p or/and Ligand (L) 2p orbitals in doped structures, where the latter give rise to MLCT or LMCT. However, those transitions appear in general in the higher edge of the absorption spectra, which out of scope of this study focusing of the Eu^{2+} -doped materials emission. So, for the sake of computational effort, those orbitals and corresponding transition will be ignored.

However, as shown in **Figure 9.1**, 4f shell is significantly spatially compact, and interconfigurational transition to a more diffuse (5d) orbital occurs with a break of many f-f pairs.[392] All result in large radial dynamical correlation effects which can be solved by the inclusion of 5f shell, which has a strong overlap with 5d orbitals. The presence of a more diffuse f shell will give additional flexibility to the 4f electrons and correctly recover this correlation effects giving accurate NEVPT2 corrections, this is well-known as double shell effect.[392, 404] So, the CASSCF active space is extended, CAS(7,19), including 7 electrons in (4f, 5d, and 5f) shells' orbitals.

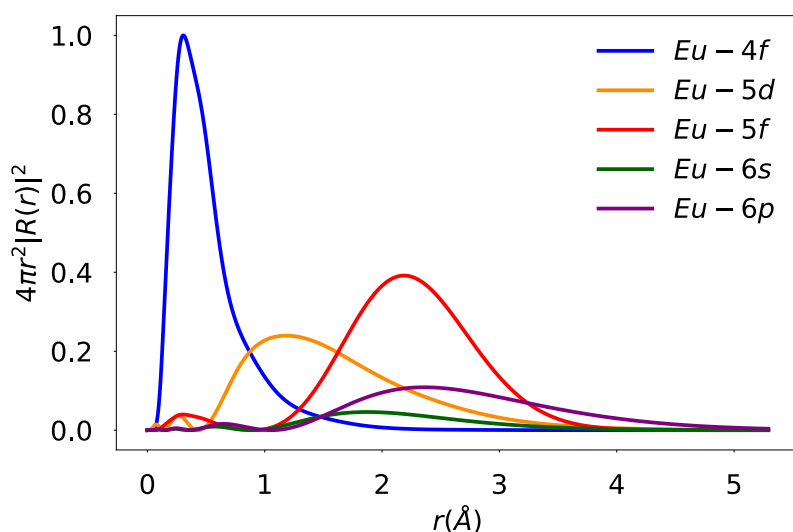


Figure 9.1. Calculated radial wavefunction ($4\pi r^2 |R(r)|^2$) as a function of atomic distance (in Å) for 4f, 5d, 5f, 6s, and 6p shells in Eu^{2+} .

9.1.2. Electronic structure of Eu^{2+} ion

Figure 9.2 shows the computed non-relativistic lowest 36 octet and 35 sextet states and corresponding relativistic energy levels employing SA-CASSCF(7,19) calculations, with inclusion of the dynamical correlation perturbatively computed by NEVPT2 method. Then, the results are compared with experimental energy levels adapted from NIST database and Ref [405]. First, Eu^{2+} suffers a significant dynamical correlation, for instance, 16365, and 6045 cm^{-1} NEVPT2 corrections for the lowest octet and sextet non-relativistic states, respectively. That leads to accurate computation of relativistic energy levels at CASSCF/NEVPT2/SOC level compared to experimentally detected energy levels [405] with MAE of 2360 cm^{-1} (0.29 eV).

SA-CASSCF/NEVPT2 results show that free Eu^{2+} has a ($^8S_{7/2}$) ground term, with the excited multiplet due to the spin-flip ($2S + 1 = 6$) parity-forbidden f-f transition with lowest sextet term is 6P (at 30368 cm^{-1} , 3.8 eV) and higher terms are also detected $^6(I, P, D, F, P, S)$. As well, spin-conserving ($2S + 1 = 8$) single electron interconfigurational excitation $4f^7 \rightarrow 4f^65d^1$ with the electronic configuration ($4f^65d^1$) giving rise $^{2S+1=8}\{^7F \otimes ^2D\}$ multiplets excited states with the lowest octet term 8H (33682 cm^{-1} , 4.2 eV) followed by $^8(D, P, F, G)$ higher terms.

Inclusion of SOC, ground term is weakly split to 4 Kramer's doublets (KDs), with $M_s = \pm 7/2, \pm 5/2, \pm 3/2, \pm 1/2$. The weak splitting of ground state, almost degenerate, with ZFS $D = 0.0045 \text{ cm}^{-1}$ and $E/D = 0.0001$, is due to

- no orbital angular momentum within in the S ground term with ($L = 0$).
- no SOC with higher octet $4f^65d^1$ -based states owing to vanishing $\langle f|h_{\text{soc}}|d \rangle$ coupling.

The energy splitting is attributed to SOC coupling with excited spin-flip sextet ($4f^7$)-based terms, however that coupling is very weak due to large energy gap.

In contrast, SOC exerts a more pronounced influence on the excited states, inducing a strong mixing among them. In fact, the absence of isolated excited SOC multiplet and the continuous nature of the SOC levels lead to a failure of the spin-Hamiltonian approach as effective Hamiltonian, thereby yielding unreliable results.

The energy gap between the ground KDs and low-lying excited KDs is $\sim 29700 \text{ cm}^{-1}$. These transitions occur at relatively high energy, corresponding to ultraviolet (UV) excitation and emission.

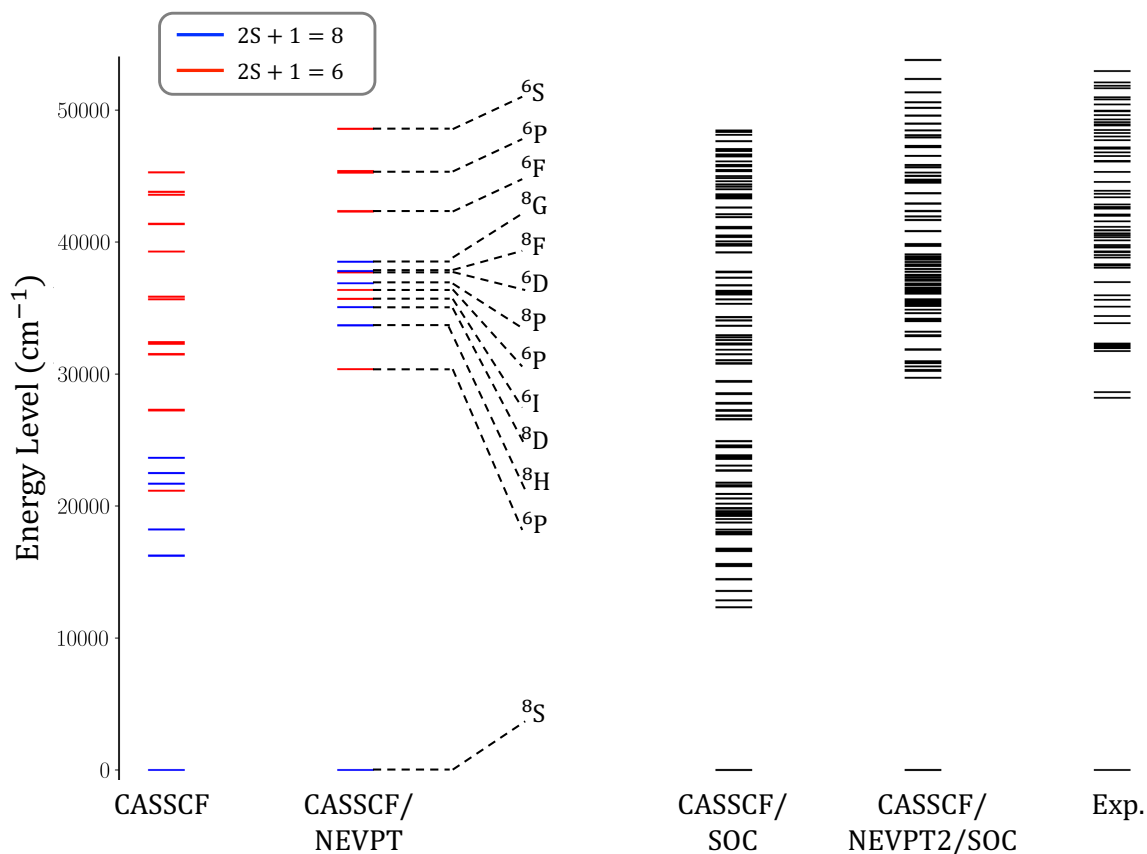


Figure 9.2. Non-relativistic and relativistic energy levels of free Eu^{2+} ion calculated employing $(^836 \mid ^635)\text{-SA-CASSCF}(7,19)/\text{NEVPT2}$ and experiments (adapted from Ref [405]). For all the lowest energy level is normalized to zero for better comparison.

9.2. Eu^{2+} in cubic (inverted O_h) ligand field

In the preceding section, the electronic structure of free Eu^{2+} ion has been investigated, unraveling its fundamental properties. However, when Eu ion, as impurity, is incorporated in solid-state materials, the surrounding environment exerts a significant influence on the electronic and optical properties. To initiate our exploration, we will focus on a simplified model structure featuring Eu within a highly symmetric field, specifically a perfect cubic ligand field, as shown **Figure 9.4b**. Although Eu^{2+} ions are typically encountered in more complex and distorted environments within Eu^{2+} -doped phosphors, this straightforward scenario serves as a foundational starting point and a valuable reference for delving into more intricate cases.

9.2.1. Calculations details

Preliminary SA-CASSCF(7,19)/NEVPT2 calculations conducted on $\text{O}_h\text{-}[\text{Eu}(\text{NH}_3)_8]^{2+}$ model structure, shown in **Figure 9.3**, employing the same methodology for free Eu^{2+} ion (refer to **Section 9.1.1**). The relativistically re-contracted def2-TZVP basis sets for DKH of the Ahlrichs group[406, 407], specifically utilizing the DKH-def2-TZVP basis set, were used for all main group element atoms except Eu. The Hessian was calculated at DFT level of theory employing PBE0[227, 234, 235] functional. A potential energy surface (PES) scan along a vibrational mode, selected based on the symmetry rules, was performed utilizing SA-CASSCF(7,19)/NEVPT2 both with and without the inclusion of the SOC.[140, 149]

9.2.2. Electronic structure of Eu^{2+} in cubic (inverted O_h) ligand field

As discussed above, Eu^{2+} ion has a ground term $^8\text{S}_{7/2}(4\text{f}^7)$ with lowest excited terms are the sextet $^6\text{P}(4\text{f}^7)$ and the octet $^8\text{H}(4\text{f}^65\text{d}^1)$. Upon Eu doping in the crystalline host, the latter is get strongly stabilized, and became the emitting state, by strong interaction of 5d orbitals with the lattice.

As illustrated in **Figure 9.3**, the degeneracy of the 4f and 5d orbitals are lift in the coordinated $[\text{EuN}_8]$ prefect cubic structure. The centrosymmetric cubic symmetry will follow the notation of the regular O_h point group but with inverted splitting of the orbitals (inverted O_h symmetry). It also could be regarded as composed of two tetrahedra. The 5d orbitals split into lower e_g ($5\text{d}_{z^2/x^2-y^2}$) and higher energy t_{2g} ($5\text{d}_{xy/xz/yz}$) molecular orbitals (MOs), with crystal field splitting ($\Delta_{\text{cubic}} = 2\Delta_{T_d} = -8/9 \Delta_{\text{O}_h}$), where Δ is the $10Dq$.[408] Similarly, albeit with a weaker impact resulting from the shielding effect of the outer closed shells, the 4f orbitals split into t_{1u} ($4\text{f}_{z^3/xz^2/yz^2}$), t_{1u} ($4\text{f}_{z(x^2-y^2)/x(x^2-3y^2)/y(y^2-3x^2)}$) and a_{2u} (4f_{xyz}) MOs. In fact, the investigated model structure revealed an unexpected splitting of the 4f orbitals adheres to the regular O_h orbital ordering ($a_{2u} < t_{1u} < t_{1u}$), rather than the inverted O_h . This deviation from the anticipated behavior is attributed to the relatively weak LF strength imposed by NH_3 ligand in the model structure. However, a contrasting scenario emerges in Eu^{2+} -doped phosphors featuring stronger ligand fields with oxide (O^{2-}) or nitride (N^{3-}) ligands. In these environments, the a_{2u} MO, associated with the 4f_{xyz} orbital and characterized by loops that directly point towards the ligands, experiences stronger destabilization compared to the

respective t_{1u} and t_{2u} 4f-based MOs. This interaction effectively restores the inverted orbital splitting order ($a_{2u} > t_{1u} > t_{2u}$).

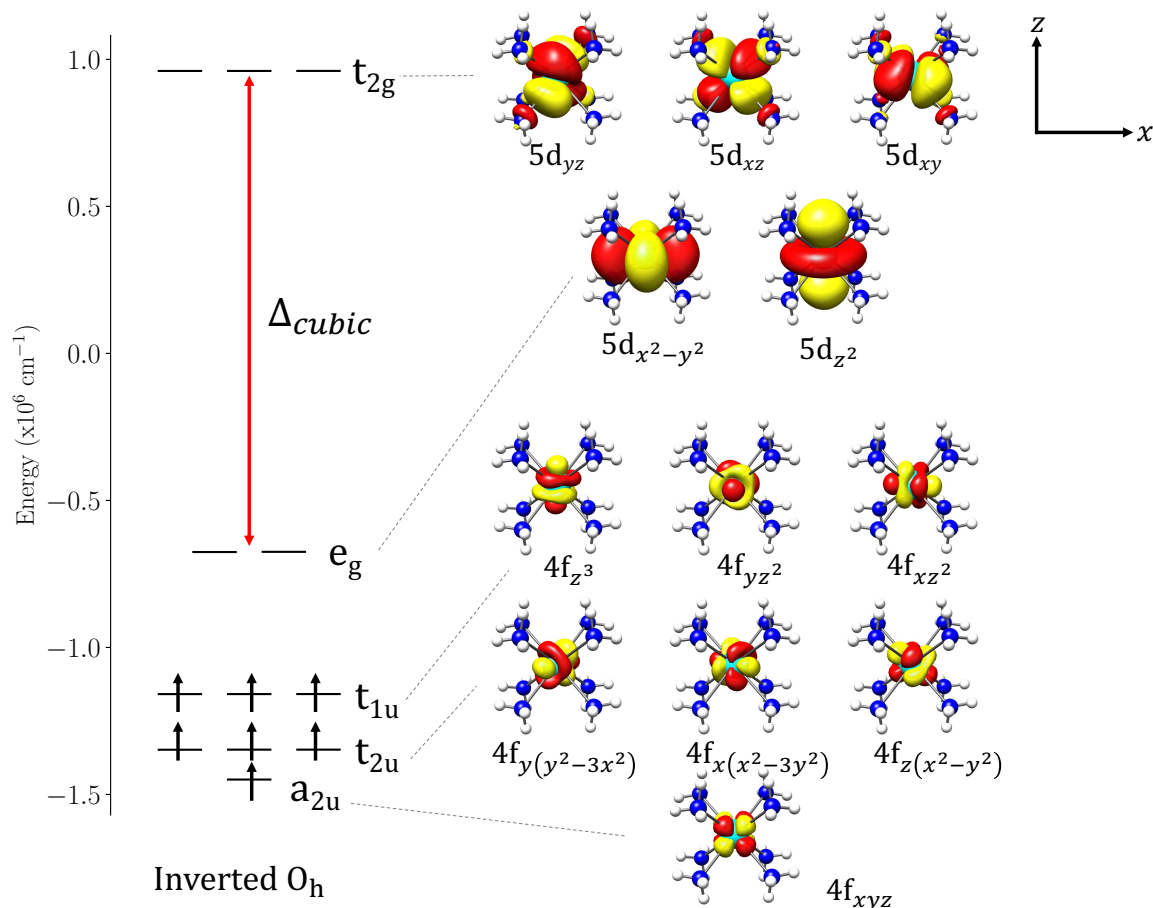


Figure 9.3. The CASSCF(7,19) optimized active orbitals and their energies calculated in $[\text{Eu}(\text{NH}_3)_8]^{2+}$ model structure. The figure shows the orbital splitting of 4f, 5d orbitals under ideal cubic (inverted O_h) symmetry. The 5f orbitals are omitted.

On the ligand field limit, as shown in **Figure 9.4** and **Figure 9.5** (at $Q = 0$), the ground $^8S_{7/2}(4f^7)$ term transformed as $^8A_{1u}$ state with the $(a_{2u}^1 t_{1u}^3 t_{2u}^3)$ electronic configuration. The lowest excited atomic term $^8H(4f^6 5d^1)$ is transformed and split into $^8(T_{2g}, E_g, 2T_{1g})$ states. These states arise from the excitation $4f^7 \rightarrow 4f^6 5d^1$, precisely $(a_{2u} t_{1u} t_{2u})^7 \rightarrow (a_{2u} t_{1u} t_{2u})^6 (e_g t_{2g})^1$ which encompassing the three electronic excited configurations $(a_{2u}^1 t_{1u}^3 t_{2u}^2 e_g^1, a_{2u}^1 t_{1u}^2 t_{2u}^3 e_g^1, t_{1u}^3 t_{2u}^3 e_g^1)$. Within the studied model system, the lowest excited

9 Electronic Structure of Free Eu^{2+} Ion and Doped in Perfect Cubic Ligand Field

state is ${}^8T_{2g}$ arises from the first excited configuration due to stabilization of t_{1u} MO over the others, while other states ${}^8(E_g, 2T_{1g})$ are higher in energy. However, as discussed in the previous section, in some other cases, the order could be reversed leads to stabilization of a_{2u} MO and 8E_g as lowest excited state arises from the latest electronic excited configuration.

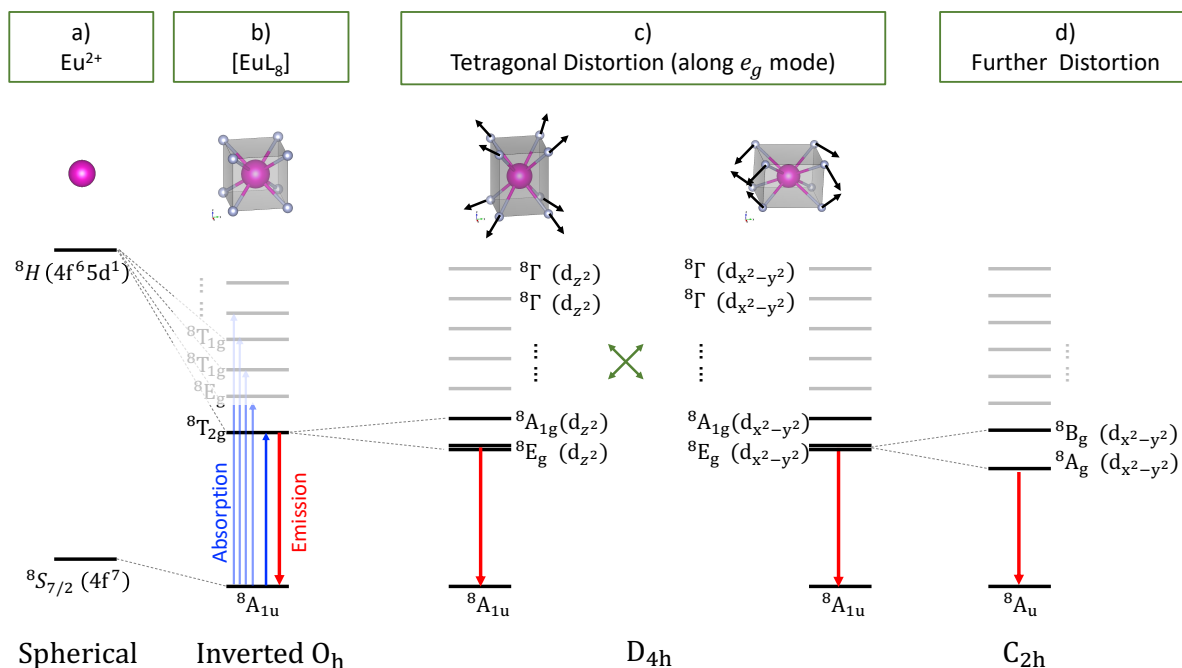


Figure 9.4. A simplified description of the electronic structure and transitions within the Eu^{2+} ion free and doped in various LF symmetries. a) The ground and lowest excited atomic terms of free Eu^{2+} ion in spherical symmetry. b) The transformation and splitting of these terms into energy states under the cubic field (inverted O_h). c) Additional splitting of these states due to vibronic coupling or (P)JTE along the tetragonal distortion (e_g vibrational mode) leading to D_{4h} point group is schematically illustrated. Different distortion pathways are explored, showcasing varied orbital orderings and the dominance of distinct 5d orbitals in the lowest excited states. d) Continuing with further distortion to an arbitrary lower-symmetric point group (e.g., C_{2h}). In this scenario, the lowest excited state (E_g in D_{4h}) is split into two excited states both dominated by the same type of 5d orbital. Only one pathway is presented, dominated by $(d_{x^2-y^2})$, while acknowledging that the alternative pathway, where lowest excited states are dominated by (d_{z^2}) , is also possible but omitted for sake of clarity. Blue and red arrows denote the corresponding optical processes of absorption and emission, respectively. Within this representation, SOC is generally neglected for simplification purposes.

Finally, the orbital degeneracy of the ground and excited states could be subsequently lifted by geometrically distortion of the ligand network. In addition, the spin degeneracy of these states also is lifted by SOC leaving only Kramer's doublets (KDs). In fact, in the studied Eu^{2+} -doped phosphors within the scope of this work, Eu is doped in distorted ligand structure, introducing a lower level of symmetry around it (for example, see **Table 10.1** and **Table 11.1**). This distortion may originate intrinsically from the host crystal structure or be induced upon Eu doping, potentially by the (pseudo-) Jahn-Teller effect (JTE or PJTE). As discussed in the next section, this effect becomes particularly evident where the degeneracy of excited states induces PJT distortion. This leads to the tetragonal distortion of the perfect cube of studied model structure and, consequently, further splitting of the excited states.

Based on the nature of the distortion, variations in the order and strength of splitting within the 5d and 4f orbitals may occur. Particularly distinct distortion pathways, as highlighted in **Figure 9.4**, can result in the predominant domination by either ($5d_{z^2}$) or ($5d_{x^2-y^2}$) orbital in the lowest excited (emissive) state. This distinction holds a significant influence on the luminescence characteristics of Eu^{2+} -doped phosphors[80], as elaborated in the next chapters.

The exploration of (P)JTE can pivotally help to understand and unravel the intricate interplay between the local environment and the electronic behavior of Eu^{2+} ions within these materials and its implications for the optical properties. A preliminary investigation into the electronic structure of Eu^{2+} in a cubic ligand field and the consequential impact of distortion by PJTE is conducted on an $[\text{EuN}_8\text{H}_{24}]^{2+}$ model structure in the upcoming section.

9.3. PJTE in Eu^{2+} in prefect cubic Ligand Field

Within the $[\text{EuN}_8\text{H}_{24}]^{2+}$ model structure under a cubic crystal field (O_h), the electronic ground and excited states suffer from PJTE. First, the lowest excited states could be twofold (E_g) or threefold (T_{1g}, T_{2g}) degenerate. According to the group-theoretical rules, the vibronic coupling will be non-zero along some normal modes (active JT modes), which can be determined from the symmetric products of the states donated by $[\Gamma \otimes \Gamma]$:[93, 97]

$$\begin{aligned} [E_g \otimes E_g] &= A_{1g} \oplus E_g \\ [T_{2g} \otimes T_{2g}] &= [T_{1g} \otimes T_{1g}] = A_{1g} \oplus E_g \oplus T_{2g} \end{aligned}$$

and excluding the totally symmetric (A_{1g}) term as it can't alter the symmetry. So, E_g state can couple e_g mode leading to the well-known $E_g - e_g$ pJT problem. While both (T_{1g}, T_{2g}) states

behave similarly leading to $T_{2g} - (e_g \oplus t_{2g})$ pJT problem. So, there are five even-parity active JT modes; two (E_g type) for tetragonal distortion and three (T_{2g} type) for trigonal distortions. However, due to the weaker coupling and the complexity of $T_{2g} - t_{2g}$ case compared to $T_{2g} - e_g$, so as a first approximation the $T_{2g} - t_{2g}$ coupling will be skipped from the investigation and we focused only on the tetragonal distortions.

Figure 9.5a illustrates the PES scan, employing SA-CASSCF(7,19)/NEVPT2 level of theory, along tetragonal distortion (e_g mode) on the model system. PJTE splitting is clearly detected in both ground and lowest excited states with stabilization energies of $E_{JT}^g \sim 2000$ and $E_{JT}^e \sim 600 \text{ cm}^{-1}$. The coupling leads to symmetry lowering from O_h ($Q = 0$) to D_{4h} at $|\Delta Q_{JT}^g| = 6$ and $|\Delta Q_{JT}^e| = 4$ for ground and lowest excited states, respectively.

Although the ground state at the high symmetry point (A_{1u}) is non-degenerate, it exhibits pronounced e_g - PJTE, indicating its instability. That could be attributed to the indirect influence of the excited states on ground state through CI mixing. Splitting of both 4f and 5d orbitals also observed along PES scan, as shown in **Figure A. 1**. That is also consistent with our previous observation of the overlap between 4f and 5d orbitals (refer to **Figure 9.1**) and the bonding and vibronic coupling analyses on the lanthanides ions (Ln) which showed that they can't be simply treated as $(4f^n)$ instead behave like $(4f^n 5d^0)$. [136]

The octet states $^8\Gamma$ are eightfold spin degenerate. After inclusion of SOC, within the octahedral double group (O' point group), $^8\Gamma$ split into 3 components ($\Gamma_6 \oplus \Gamma_7 \oplus \Gamma_8$) on the Bethe's notation or ($E'_2 \oplus E'_3 \oplus G'$) on Mullikan's notations, where the first two are spin-doublet while the latest is spin-quadruplet degenerate. Again, the PJT active modes can be determined from the antisymmetric product of the states donated by $\{\Gamma \otimes \Gamma\}$; [93, 97]

$$\begin{aligned}\{\Gamma_6 \otimes \Gamma_6\} &= \{\Gamma_7 \otimes \Gamma_7\} = A_1 \oplus E \\ \{\Gamma_8 \otimes \Gamma_8\} &= A_1 \oplus E \oplus T_2\end{aligned}$$

applying the same approximation as previously discussed, excluding A_1, T_2 terms, the problem can be effectively reduced into $(\Gamma_6 \oplus \Gamma_7 \oplus \Gamma_8) - e$ PJT problem. As shown in **Figure 9.5 b**, the relativistic four ground KDs show the same stabilization energy as non-relativistic ground state with negligible splitting between 4 KDs, signifying a negligible SOC effect in the ground state. However, SOC excited states exhibit a different and more complex behavior. First, the lowest excited $4f^6 5d^1$ multiplet splits (for the lowest 4 KDs) by about ~ 200 (at $|\Delta Q| = 0$) – 1000 (at $|\Delta Q| = 4 - 6$) cm^{-1} . The spin-quadruplet degenerate excited state (Γ_8), which

initially encompasses two degenerate KDs, undergoes a split into two KDs (Γ_6 and Γ_7) by PJT effect. Conversely, the spin-doublet degenerate excited state (Γ_6 and Γ_7) and as KDs can't undergo splitting by JT/PJT effect however each experiences stabilization towards the lower symmetric structure. Focusing on the lowest excited SOC state (Γ_8), split by PJT into 2 KDs, where the lowest excited KDs demonstrate a pronounced stabilization $E_{JT}^{e'} \sim 900 \text{ cm}^{-1}$ compared to $\sim 600 \text{ cm}^{-1}$ for the original non-relativistic lowest excited state.

It is well-established that JTE/PJTE is typically suppressed by inclusion of SOC, a phenomenon explained and referred to as the Ham effect[257, 258]. In practice, SOC effectively removes the degeneracy of the states. However, Γ_8 state, under O' symmetry, retains the degeneracy and the SOC not only fails to suppress but also activates PJT effect. A similar behavior has been observed in spin-quadruplet degenerate states in 4d and 5d transition metal compounds.[259, 260]

In addition as seen in **Figure 9.5**, on the non-relativistic limit the energy gaps between the ground and lowest excited (emissive) states are ~ 22500 (at $|\Delta Q| = 0$) and ~ 24000 (at $|\Delta Q| = 4 - 6$) cm^{-1} , so, the local environment effect due to the structural transformation change the emissive transition energy by $\sim 1500 \text{ cm}^{-1}$. On the relativistic limit, the energy gaps between the ground and lowest excited (emissive) KDs are (~ 21400 (at $|\Delta Q| = 0$) – 22500 (at $|\Delta Q| = 4 - 6$) cm^{-1} , so, inclusion of both structural effect and SOC, change the emissive transition energy by $\sim 1100 \text{ cm}^{-1}$. We can see that local environmental effect (including crystal and ligand effects, symmetry changes, and later vibronic coupling) dominates the emission band energy to higher limit exceeding the SOC effect. So, at a first approximation, the SOC effect is obscured by the band broadening mechanism and may be overlooked on the broader scale. Nevertheless, SOC can influence the fine electronic and magnetic structure of both the ground and emissive multiplets, and its effect should be considered when studying the fine-tuning effects in narrow band emissions.

Finally, it is important to keep in mind that the structure can undergo further splitting due to the lower symmetry experienced in real-life phosphors, as elucidated in **Figure 9.4c-d**, **Table 10.1**, and **Table 11.1**. Furthermore, the bonding and covalency between the Eu^{2+} and ligands is also equally crucial, exerting a significant influence on the electronic states, transitions, and optical properties, as we have shown in our work [80, 243] and further discussed in next chapters.

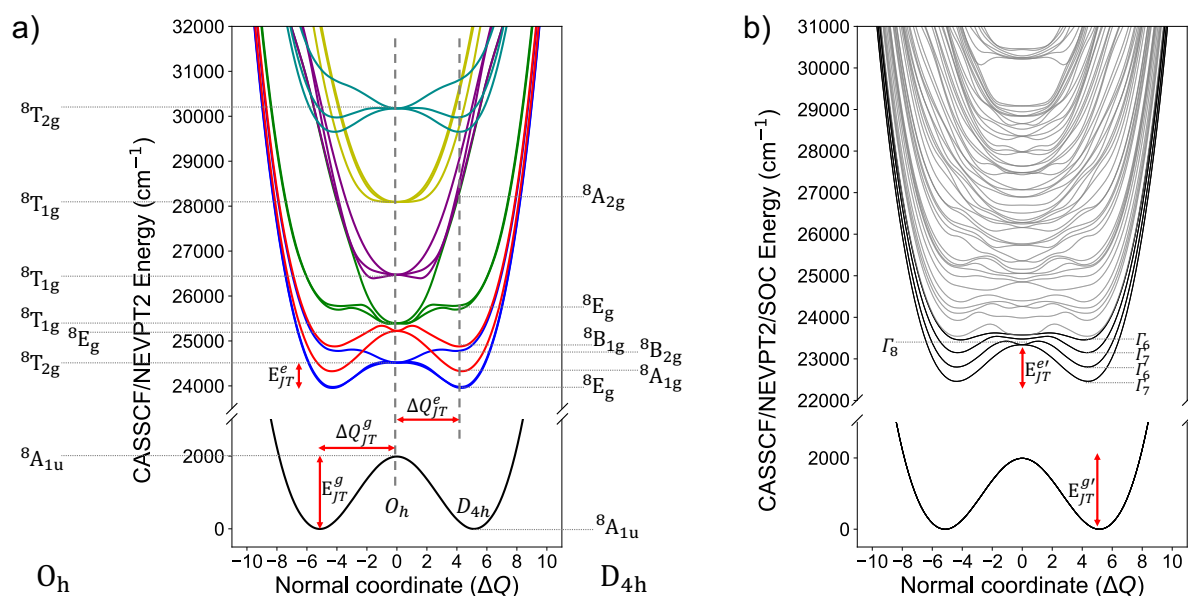


Figure 9.5. a) PES of non-relativistic ground and excited states calculated using CASSCF(7,19)/NEVPT2 and scanned along e_g mode. The states at higher symmetry (O_h , at $\Delta Q = 0$) and at lower symmetry (D_{4h} , at $\Delta Q = 4 - 6$) are also given. b) Corresponding PES scan of relativistic states with the inclusion of SOC. E_{JT}^g, E_{JT}^e are the pJT stabilization energies of ground and lowest excited states on the non-relativistic limit, respectively. While $E_{JT}'^g, E_{JT}'^e$ are the stabilization energies of ground KDs and lowest excited KDs on the relativistic limit, respectively.

9.4. A qualitative analysis of Absorption and emission processes in Eu^{2+} -doped phosphors

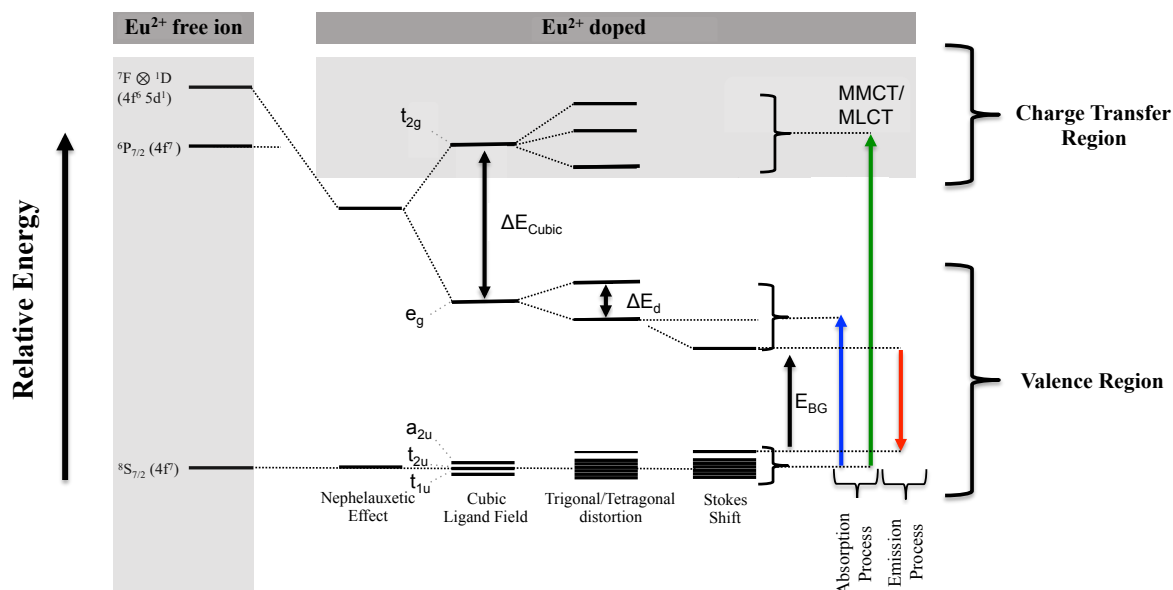
Critical to the functionality and application of pc-LEDs is the optical characteristics of the employed phosphor. When selecting phosphors, various criteria must be met, encompassing factors such as the emission band position (color) and width, a compatible excitation spectrum, thermal stability, and quantum efficiency.[19, 20, 76]

Considering the electronic structure investigations in the previous sections, a qualitative representation of the optical processes (absorption and emission) in Eu^{2+} -doped phosphors can be given. As shown in **Scheme 9.1**, the energy gap and excitations between ground and excited terms are very high in energy spanning most of the UV range. However, in crystal host the separation between the ground 4f-based and excited 4f5d-based energy levels, can be reduced

to approach the near UV and visible wavelength range. This adjustment is facilitated by nephelauxetic effects and ligand field splitting (LFS). In these phosphors, the $4f^7 \rightarrow 4f^6 5d^1$ transitions define their excitation and emission characteristics. However, these transitions are host-tunable i.e. significantly influenced by the crystal structure and local domains of the host material. The intensity, peak position, and width of these spectroscopic transitions are collectively modulated by the host, with mainly the 5d orbitals, representing the excited state, being particularly vulnerable to factors such as host structure, coordination site symmetry, anion polarizability, and the covalency with the anionic framework.

In summary, when Eu^{2+} is doped in 8-fold coordinated host environments $[\text{EuL}_8]$, under the 1-electron picture, action of interelectronic repulsion will stabilize the $2S+1=8$ excited state multiplets of the $4f^6 5d^1$ shell above the $2S+1=8$ $4f^7 5d^0$ ground state multiplets. It follows that the cubic ligand field splitting (LFS) will lift the degeneracy of the 4f and 5d orbitals in an inverted octahedral order with LFS in 5d manifold, refers to Δ_{cubic} . Further distortions towards tetragonal/trigonal ligand fields will further lift the remaining orbital degeneracies and consequently the ground and excited states degeneracy. The type of distortion, local symmetries and LFS are collectively quantifying the 5d splitting characteristics which dominate the electronic and optical properties. For instance, compression of the $[\text{EuL}_8]$ cuboid and short Eu-L bond lengths in the coordination environment results in a large LFS, leading to a significant stabilization of the lowest d level, causing an emission redshift. In addition, the lowest $5d_{z^2}/5d_{x^2-y^2}$ dominating the emissive state can have consequences on the emission characteristics.[80]

It follows that, quantities like the LFS (ΔE_{cubic} , ΔE_d), band gap energies, E_{BG} and Stokes shifts (ΔS) are important quantities of the absorption and emission processes which determine the energy position and the bandwidth of the different spectral features. In addition, the energy difference between the valence $\text{Eu } 4f \rightarrow \text{Eu } 5d_{z^2/x^2-y^2}$ and the metal to metal charge transfer $\text{Eu } 4f \rightarrow \text{Eu } 5d_{xz/yz/xy}$ (MMCT) excitations or the metal to ligand charge transfer $\text{Eu } 4f \rightarrow \text{L } 3p_{x/y/z}$ (MLCT) can be thought as a measure of the Eu^{2+} doped phosphors thermal stability. [80, 371] These CT excited states are high in energy and significantly overlap with the host electronic manifold. As the temperature increases, the population of these states is enhanced. These states have a high probability to relax through non-radiative pathways causing a significant reduction in the emission quantum yield.



Scheme 9.1. Schematic representation of the absorption and emission processes in Eu^{2+} doped phosphors together with the most important energy quantities that dominate the energy position and the bandwidth of the spectral features.

9.5. Conclusions

In this chapter, the electronic structure and transitions of Eu^{2+} ion free and doped in simple model structure mimicking the Eu^{2+} -doped phosphors have been studied. The complexities in describing the electronic structure properties of the ground and emissive excited states were analyzed in detail. It was shown that the density of states involves various excitations, with the intra- and inter-configurational $4f^7 \rightarrow 4f^7$ and $4f^7 \rightarrow 4f^6 5d^1$ transitions that are affected by electron correlation effects, and spin-orbit coupling. In particular, the $4f5d$ -based excited states shown to be in addition sensitive to the ligand field effects of the local ligand structures.

It was in particular highlighted that Eu^{2+} -doped highly symmetric structures show the electronic-structural instabilities leading to symmetry breaking through JTE or PJTE. This introduces, at a basic level, dynamical interactions (vibronic effects) that impact electronic and optical properties, influencing energy levels and transition strengths. In conclusion, the influence of the local environment seems to be more substantial than SOC effects, both in static and dynamic limits. The presence of CT transitions is noted to enhance non-radiative relaxation, thereby affecting the emission efficiency. The interplay between various couplings, coupled with non-radiative relaxation processes, collectively shapes the electronic and magnetic structures of ground and excited states, governing relaxations, and

photoluminescence characteristics. In the following chapters, these effects and interactions will be analyzed in a thorough and systematic way aiming to ultimately unravel the structural-electronic-optical properties correlations governing the luminescence in Eu^{2+} -doped phosphors.

10 Luminescence in Eu^{2+} -doped Phosphors for pc-WLEDs – Design the Computational Protocol and Define the Electronic Descriptors

The results of this chapter have been published in J. Am. Chem. Soc., 2022, 144 (18), 8038–8053. DOI: 10.1021/jacs.2c00218

10.1. Introduction

In this chapter, a systematic multimethod computational protocol is presented that is able to predict the experimental absorption and emission spectral shapes of solid-state Eu^{2+} -doped phosphors for pc-WLEDs applications. The protocol is based on TD-DFT and operates in conjunction with an Excited State Dynamics (ESD) approach in the framework of embedded cluster approach. It contains a thorough electronic structure analysis of the computed spectral features that is performed on the basis of the symmetry and Natural Transition Orbitals (NTOs) analysis. For this purpose, a study set was carefully selected and comprised representative examples of nitride, oxynitride, and oxide UCr_4C_4 -type phosphors, known for their promising luminescence features and high tunability provided by the host structure. The study included the red-emitting $\text{Ca}[\text{LiAl}_3\text{N}_4]:\text{Eu}^{2+}$, [326] $\text{Sr}[\text{LiAl}_3\text{N}_4]:\text{Eu}^{2+}$, [329] $\text{Sr}[\text{LiAl}_3\text{N}_2\text{O}_2]:\text{Eu}^{2+}$, [125] $\text{Sr}[\text{Mg}_3\text{SiN}_4]\text{Eu}^{2+}$, [327] $\text{Ba}[\text{Mg}_3\text{SiN}_4]\text{Eu}^{2+}$, [409] and blue-emitting $\text{SrLi}_2[\text{Be}_4\text{O}_6]:\text{Eu}^{2+}$ [126] phosphors.

The agreement between theory and experiment of both absorption and emission spectra is very good, thus allowing for a quantitative analysis of the observed and computed spectral features. It is demonstrated that across the set of studied Eu^{2+} doped phosphors, the energy distribution and the band shape of the emission spectrum is related to the nature of the 4f-5d transitions that are probed in the absorption process. Given the nearly non-bonding nature of the 4f-orbitals, the critical factor lies in the covalency of the 5d acceptor orbitals. These orbitals become populated in the electronically excited state, ultimately leading to emission. The

stronger the anti-bonding interaction between the Eu²⁺ (5d) and the (N³/O²⁻) ligands in the excited state is, the larger the excited state distortion and the less rigid the relaxation will be. Consequently, the corresponding emission will get broader due to the vibronic progression that is induced by the structural distortion and dynamics. In addition, the energy separation of the absorption bands that are dominated by states with valence 4f-5d and metal to ligand charge transfer (MLCT) character, defines a measure for the thermal quenching of the studied Eu²⁺-doped phosphors. The higher the energy separation between the 4f-5d and the MLCT excitations is, the more thermally stable the respective phosphors will be. That is because the thermal quenching of the emission through non-radiative relaxation processes by host based MLCT states is avoided.

In a next step of the analysis, simple descriptors are identified that show a strong correlation with the energy position and bandwidth of the experimental emission bands without the need for elaborate calculations. In fact, a simple linear relationship is found between the 5d covalency (the degree of covalent dilution of the 5d acceptor orbital) obtained from ground-state DFT calculations with the width of the emission band. The same simple DFT calculations lead to a linear relation between the computed optical band gap energy and the maximum of the emission energy of the studied phosphors.

Overall, we believe that this study and the established correlations between the electronic and optical properties serve as an important reference for designing new Eu²⁺-doped phosphors with desired photoluminescence properties.

10.2. Study Set – Geometric Structure

In the first step, we define a representative study set. It should be emphasized that owing to the vast number of available Eu²⁺-doped phosphors, a representative group should be carefully chosen to form our study set, which constructs the basis for developing a robust computational protocol. In the next chapter, the protocol is extended to include more complicated systems.

The chosen study set of the pc-LED phosphors is presented in **Figure 10.1** together with the major structural characteristics of the different coordination environments around the doped Eu²⁺ centers. It consists of six well-known Eu²⁺-doped phosphors. Namely, the oxoberyllate phosphor SrLi₂[Be₄O₆]:Eu²⁺ abbreviated as (SLBO)[126], oxonitridolithoaluminate Sr[Li₂Al₂O₂N₂]:Eu²⁺ (SALON)[358], nitridomagnesosilicate M[Mg₃SiN₄]:Eu²⁺ (M = Sr (SMS) [327], Ba (BMS)[328]), and nitridolithoaluminate M[LiAl₃N₄]:Eu²⁺ (M = Sr

(SLA)[329], Ca (CLA) [326]) phosphors. They were selected for the study based on the following criteria:

- 1) All phosphors' hosts adopt the UCr_4C_4 crystal structure, which has demonstrated to be highly suitable for phosphors exhibiting narrow-band emission.[383, 410]
- 2) They encompass diverse host classes and ligand field environments, represented by oxide, oxynitride, nitride inorganic host.
- 3) They exhibit emissions covering a broad range of wavelengths from red to blue of the optical spectrum.
- 4) They contain single candidate doping center available for the Eu^{2+} activator ion, namely $\text{Ca}^{2+}/\text{Sr}^{2+}/\text{Ba}^{2+}$ ions. (except for SLA with two Sr^{2+} doing centers, as elaborated below)

As shown in **Figure 10.1** and **Table 10.1**, the selected nitride phosphors contain an ordered distribution of edge- and corner-sharing $(\text{Si}/\text{Mg})\text{N}_4$ or $(\text{Al}/\text{Li})\text{N}_4$ tetrahedral building units which are forming *vierer* ring channels. The host M^{2+} ions ($\text{M} = \text{Ba}, \text{Sr}, \text{Ca}$) as well as the doped Eu^{2+} ions are placed at the center of those *vierer* ring channels, and they are 8-fold coordinated by nitride N^{3-} ions. In all the cases the symmetry is lower than cubic (inverted O_h), as a result cuboid-like polyhedra Eu/ML_8 are formed (for simplicity these polyhedra will be referred to as cuboids). In particular, the nitridomagnesosilicate phosphors $\text{M}[\text{Mg}_3\text{SiN}_4]:\text{Eu}^{2+}$ ($\text{M} = \text{Sr}$ (SMS), Ba (BMS)) crystallize in an ordered variant of the UCr_4C_4 structure type. SMS crystallizes in a tetragonal crystal structure with space group $I4_1/a$, isotypic to $\text{Na}[\text{Li}_3\text{SiO}_4]$ with the local symmetry of the Eu/SrN_8 coordination polyhedra being distorted cubic (approximated by S_4). On the contrary, BMS is a distorted variant of the UCr_4C_4 structure type as it crystallizes in triclinic space group $P\bar{1}$, however its local symmetry of the Eu/SrN_8 is less distorted and can be approximately by cubic symmetry (inverted O_h).

Similarly, the nitridolithoaluminate phosphors $\text{M}[\text{LiAl}_3\text{N}_4]:\text{Eu}^{2+}$ ($\text{M} = \text{Sr}$ (SLA), Ca (CLA)) are also tetragonally distorted variants of the UCr_4C_4 structure type crystallizing in triclinic $P\bar{1}$ and tetragonal $I4_1/a$ space groups, respectively. In all selected phosphors, there is a single candidate center ($\text{Ca}^{2+}/\text{Sr}^{2+}/\text{Ba}^{2+}$) for the Eu^{2+} doping, except for SLA, there are in principle two doping candidate sites ($\text{Sr}1^{2+}/\text{Sr}2^{2+}$) with two different cationic compositions of the first coordination shell ($[\text{LiAl}_7]^{22}/[\text{Li}_3\text{Al}_5]^{18}$, respectively), however, the two sites have very similar local geometric structure in term of Eu-N bond distances, symmetries, and cuboid volumes (**Table 10.1**). As in the case of SMS, the $(\text{Eu}/\text{Sr}1\text{N}_8, \text{Eu}/\text{Sr}2\text{N}_8)$ and Eu/CaN_8 centers in SLA and CLA, respectively are tetragonally distorted – they can be approximated by S_4 symmetry. Along the BMS, SMS, SLA and CLA sequence the crystal field strength, as well as the Eu/MN_8

cuboids compression is increasing.[18] This is reflected to the decrease of the Eu-M (M=Ba, Sr, Ca) (from 3.45 Å to 3.21 Å) and Eu-N (from 2.90 Å to 2.75 Å) bond lengths as well as the Eu/MN₈ cuboids volume (from 39.5 to 31.9 Å³), respectively across the sequence.

The oxonitridolithoaluminate phosphor Sr[Li₂Al₂O₂N₂]:Eu²⁺ (SALON) is also an ordered variant of UCr₄C₄ structure type that crystallizes in the tetragonal space group *P4₂/m*. Two kinds of tetrahedra ([AlON₃]⁸⁻ and [LiO₃N]⁸⁻) are forming a condensed network of tetrahedra leading to three different types of channels along the [001] direction. The channel hosting the Sr²⁺ or the doped Eu²⁺ cations form Eu/SrN₄O₄ in *C_{2h}* symmetric cuboids with Sr-N: 2.76 Å, Sr-O: 2.66 Å and Eu-Sr: 3.21 Å bond lengths.

Finally, the oxoberyllate phosphor SrLi₂[Be₄O₆]:Eu²⁺ (SLBO) crystallizes in space group *P4/ncc* and contains edge and corner sharing BeO₄ tetrahedra which are forming two kinds of *vierer* ring channels along the [001] direction. The channel hosting the Sr²⁺ or the doped Eu²⁺ ions form Eu/SrO₈ (in *C₄* symmetry) sequences of truncated bipyramidal cuboids in which the individual Eu/SrO₈ cuboids are rotated by 45° with respect to each other. The Eu-O bond lengths range between 2.6 and 2.8 Å while the Eu-Sr bond lengths are quite elongated (4.5 Å). This is due to the fact that the rotated pairs of the Eu/SrO₈ cuboids do not share common faces, as in all the other selected phosphors. To show that our new method can be applied on phosphors comprising the entire visible spectrum, and having a structure that is not related to the UCr₄C₄ type, a blue phosphor was additionally selected with SLBO, in contrast to all the above presented nitride and oxo-nitride red phosphors. All these structural characteristics and their influence on the emission properties of the study set of the chosen phosphors will be thoroughly investigated below.

Phosphor	SrLi ₂ [Be ₄ O ₆]: Eu ²⁺ SLBO	Sr[Al ₂ Li ₂ O ₂ N ₂]: Eu ²⁺ SALON	Ba[Mg ₃ SiN ₄]: Eu ²⁺ BMS	Sr[Mg ₃ SiN ₄]: Eu ²⁺ SMS	Sr[LiAl ₃ N ₄]: Eu ²⁺ SLA	Ca[LiAl ₃ N ₄]: Eu ²⁺ CLA
a) Structure Space group	tetragonal <i>P4 / ncc</i>	tetragonal <i>P4₂ / m</i>	triclinic <i>P</i> $\bar{1}$	tetragonal <i>I</i> 4 _{1/a}	triclinic <i>P</i> $\bar{1}$	tetragonal <i>I</i> 4 _{1/a}
b) Host Structure						
c) No. of crys. sites	1	1	1	1	2	1
d) Cuboid side view						
e) Cuboid top view						
f) Avg. bond distance	Eu-Sr 4.50 Å Eu-O ₁ 2.60 Å Eu-O ₂ 2.80 Å	Eu-Sr 3.20 Å Eu-N 2.76 Å Eu-O 2.66 Å	Eu-Ba 3.45 Å Eu-N 2.90 Å	Eu-Sr 3.38 Å Eu-N 2.86 Å	Eu-Sr 3.30 Å Eu-N 2.80 Å	Eu-Ca 3.21 Å Eu-N 2.75 Å
g) Eu ²⁺ local Symmetry	Truncated Bipyramidal (C ₄)	Cubic (C _{2h})	Cubic (inverted O _h)	Distorted Cubic ~(S ₄)	Distorted Cubic (S ₄)	Distorted Cubic (S ₄)
Ligand	Oxide	Oxo-nitride	Nitride			
Phosphor type	Blue Phosphor	Red Phosphors				

Figure 10.1. Atomic structures of red SMS, SLA, CLA, BMS, SALON and blue SLBO phosphors. a) and b) Graphical representation of phosphor host crystal structures together with their crystallographic space groups. c) The number of crystallographic sites for Eu^{2+} , d and e) side and top view of cuboids containing the two adjacent EuL_8 and ML_8 cuboids ($M = \text{Ca, Sr, Ba, L} = \text{N, O}$). f) Most important bond lengths Eu-M and Eu-L . g) Local symmetry around the Eu/ML_8 centers. Atom colors: Ca (light green), Sr (green), Ba (deep green), Eu (cyan), Si (gray), Mg (orange), Al (yellowish pink), Li (pink), N (blue), O (red).

Table 10.1. Structural and geometrical information of selected phosphors including the host crystal space group, doping site(s) (M^{2+}), their ionic radius r and in parentheses (Δr), all in Å. Δr is the difference in ionic radii between replaced ion M^{2+} and Eu^{2+} , where, the ionic radius of $\text{Eu}^{2+} = 1.25$ Å at cuboid 8-fold coordination.[332] Ligand (L) in cuboid ML_8 , (L = N or O), average M/Eu-L bond distances, local symmetry (Γ) of EuL_8 cuboid, volume (V) of the cuboid, and the first coordination shell cationic compositions are given.

Phosphor	Host Crystal Space	Doping Site (M^{2+})	r (Δr) (Å)	L	Avg. M/Eu-L (Å)	Γ^a	V (Å ³)	First shell cations
$\text{SrLi}_2[\text{Be}_4\text{O}_6]:\text{Eu}^{2+}$ SLBO	$P4/ncc$	Sr^{2+}	1.26 (+0.01)	O1 O2	2.60 2.80	C_4	28.81	$[\text{Li}_4\text{Be}_4]^{12+}$
$\text{Sr}[\text{Al}_2\text{Li}_2\text{O}_2\text{N}_2]:\text{Eu}^{2+}$ SALON	$P4_2/m$	Sr^{2+}	1.26 (+0.01)	N O	2.76 2.66	C_{2h}	30.41	$[\text{Li}_4\text{Al}_4]^{16+}$
$\text{Ba}[\text{Mg}_3\text{SiN}_4]:\text{Eu}^{2+}$ BMS	$P\bar{1}$	Ba^{2+}	1.35 (+0.10)	N	2.90	O_h	39.54	$[\text{Si}_2\text{Mg}_6]^{20+}$
$\text{Sr}[\text{Mg}_3\text{SiN}_4]:\text{Eu}^{2+}$ SMS	$I4_1/a$	Sr^{2+}	1.26 (+0.01)	N	2.86	$C_2 \sim S_4$	37.0	$[\text{Si}_2\text{Mg}_6]^{20+}$
$\text{Sr}[\text{LiAl}_3\text{N}_4]:\text{Eu}^{2+}$ SLA	$P\bar{1}$	Sr^{12+}	1.26 (+0.01)	N	2.80	$C_2 \sim S_4$	34.04	$[\text{LiAl}_7]^{22+}$
		Sr^{22+}		N	2.80	$C_{2h} \sim S_4$	34.28	$[\text{Li}_3\text{Al}_5]^{18+}$
$\text{Ca}[\text{LiAl}_3\text{N}_4]:\text{Eu}^{2+}$ CLA	$I4_1/a$	Ca^{2+}	1.06 (-0.19)	N	2.75	S_4	31.88	$[\text{Li}_2\text{Al}_6]^{20+}$

^{a)} in some cases, the local symmetry of EuL_8 cuboid is slightly deviated from a higher symmetric point group. Initially, the true point group is provided, followed by the approximated point group.

10.3. Experimental Spectra

The experimental absorption and emission spectra of the chosen study set of the Eu^{2+} doped phosphors are presented in **Figure 10.2**. All the absorption spectra are quite broad in the visible energy region 16000-25000 cm^{-1} . The nitride phosphors CLA, SLA and SMS show a broad absorption band with increasing band maximum position observed at 21280 cm^{-1} , 21460 cm^{-1}

and 22730 cm^{-1} , respectively. In accordance, the oxynitride SALON and oxide SLBO phosphors show absorption spectra with band maxima at 22220 cm^{-1} and 23100 cm^{-1} , respectively. Interestingly, the band maxima increase in the sequence CLA, SLA, SALON ~ SMS, SLBO. As it will be discussed in the electronic structure section this blue shift in the absorption maxima along the above sequence is associated with the subsequent decrease of the crystal field strength of the coordination environment around the Eu. On the contrary, BMS seems to deviate for this trend showing a red shift in the absorption spectrum in which the band maximum position is located at 21310 cm^{-1} .

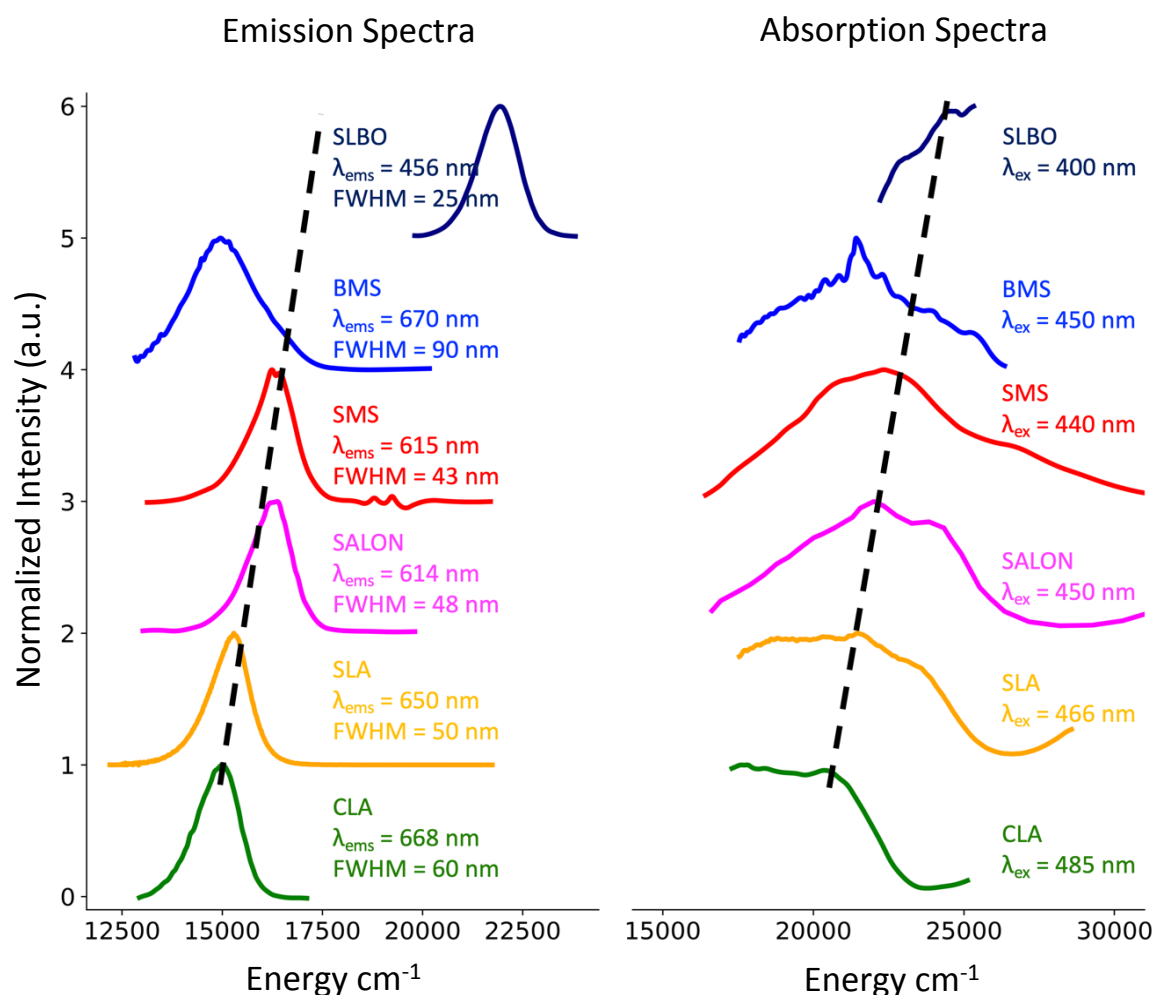


Figure 10.2. Experimental absorption (right) and emission (left) spectra of the selected phosphors (CLA: green, SLA: orange, SALON: pink, SMS: red, BMS: blue, SLBO: dark blue)

In all the cases, with excitation in the energy region 20600-25000 cm⁻¹ (or wavelength region 400-485 nm), a single band emission band is observed in the energy region 12500 to 22500 cm⁻¹ with full width half maximum (FWHM) that ranges between 1220 and 1990 cm⁻¹ (25 and 90 nm). In particular, CLA, SLA, SALON, SMS, SLBO show a narrow band emission with bandwidths ranging between 60 nm (1330 cm⁻¹) in CLA dropping down to 25 nm (1220 cm⁻¹) in SLBO. While SLA, SMS, and SALON exhibits FWHM of (50, 43, 48 nm) ~ (1180, 1140, 1220 cm⁻¹), respectively. In accordance with the absorption spectra the band maximum of the emission band is increasing along the sequence CLA (14970 cm⁻¹), SLA (15385 cm⁻¹), SALON (16287 cm⁻¹) ~ SMS (16260 cm⁻¹), SLBO (21930 cm⁻¹). All are emitting in the red region, while the latest emitting quite deeply into the blue visible light frequency range (450-490 nm).

In the case of the absorption spectrum of BMS, the respective emission spectrum declines from the above trend showing a band maximum located at 14925 cm⁻¹, with a noticeably broad bandwidth (FWHM=90 nm or 1990 cm⁻¹). In following sections, the intensity mechanism dominating the observed trends will be thoroughly investigated.

10.4. Computational Protocol and calculations details

The computational protocol that is employed in this study aims to investigate the optical properties of both the host and Eu²⁺-doped structures. The protocol can be summarized in the following steps:

Step 1: Construction of Cluster Model System

In an effort to determine the minimum representative quantum cluster model in the framework of the embedded cluster approach, we follow the procedure discussed in **Section 7.3**. For this purpose, a set of growing size cluster model systems for both Eu²⁺-doped and undoped host structures were constructed. The selection of an appropriate cluster size was based on size convergence, where experimental absorption spectra and the optical band gap were used as references for the doped and undoped structures.

Step 2: Optical spectra Calculations

Computation and analysis of absorption and emission spectra. The time-dependent DFT (TD-DFT) in conjugation with excited state dynamics (ESD) methods, coupled with the chosen DFT

functional, was employed for this purpose. The analysis was facilitated and became more informative by employing the Natural Transition Orbital (NTO) analysis.

Step 4: Determining Electronic Descriptors

Based on the obtained results and analyses, a set of electronic descriptors is defined. These descriptors play a crucial role in accurately and efficiently predicting the emission properties of Eu²⁺-doped phosphors, in terms of luminescence color, bandwidth, stokes shift and thermal stabilities. Structural and crystal field parameters effects are also considered.

Step 5: Validation and Extension

In the subsequent chapter (**Chapter 12**), the computational protocol is extended, and the identified descriptors are validated. This validation involved testing a group of Eu²⁺-doped phosphors with more complex structural and emission properties.

All calculations were performed employing the ORCA 5.0 suite of programs.[411, 412] Unless otherwise stated, crystal structures' coordinates were obtained from the crystallographic data,[124, 126, 326-331, 358] refined based on the experimental crystallographic X-ray diffraction. All the clusters were constructed on the basis of the embedded cluster approach.

In all calculations, the def2-TZVP basis set of the Ahlrichs group[406, 407] were used for all main group element atoms while for Eu the segmented all-electron relativistically re-contracted (SARC) scheme[397-400] was employed. The calculations were accelerated by employing the resolution of identity approximation (RI)[413] for the Coulomb integrals, while the exchange terms were efficiently computed using the 'chain-of-spheres' (COSX)[414, 415] approximation by utilizing the SARC/J coulomb fitting and def2-TZVP/C correlation auxiliary basis sets, respectively. Second-order Douglas-Kroll-Hess relativistic corrections (DKH2)[401, 402] were used throughout to account for scalar relativistic effects, employing the finite nucleus model.[403] The Hartree-Fock (HF) layers used in the embedding cluster calculations were equipped with a minimal LANL2DZ basis set with the respective HayWadt ECPs.[336-339]

The optical band gap of the host structures were calculated by the similarity transformed equation of motion domain-based local pair natural orbital coupled cluster singles and doubles (STEOM-DLPNO-CCSD)[416-419] as well as TD-DFT[237] levels of theory employing PBE0 functional[227, 234, 235].

Absorption spectra were computed at the TD-DFT/PBE0 employing Tamm-Dancoff approximation (TDA)[420] accompanied by the Natural Transition Orbital (NTOs) analysis for the computed bands. Photoluminescence spectra were computed using TD-DFT/TDA/PBE0 employing the excited state dynamics (ESD) path integral protocol[273-275] in which vibronic coupling is included within the Frank-Condon and Herzberg–Teller coupling schemes. In this framework, the ground state hessian was calculated at DFT/PBE0 level while the excited state geometry and hessian obtained by approximating excited state PES through vertical gradient (VGFC) model as discussed in ESD module.[273] A constant Gaussian broadening was used for all presented absorption and emission spectra which amounts to a FWHM of 1500 cm⁻¹ and 500 cm⁻¹, respectively. For better visual agreement with the experimental absorption spectra a second Gaussian broadening with FWHM of 3000 cm⁻¹ was used in some of the computed absorption spectra.

10.5. Embedding Cluster Approach

10.5.1. Construction of the cluster models

Representative model structures for the calculations of the spectroscopic properties of the host and Eu²⁺ doped phosphors were constructed on the basis of the embedded cluster approach, as depicted in details **Section 7.3**. In the chosen scenario,[83, 84, 141, 333, 421] the embedded cluster model consists of four regions (see **Figure 7.1**) : QC, HF, ECP, PC, as depicted in **Table 10.2**. All regions are extracted from the respective crystallographic supercells.

In a first step, various quantum clusters (QCs) were constructed by preserving the 8-fold cubic coordination environment around the central alkaline earth metal ions (Ca²⁺, Sr²⁺, Ba²⁺). Structure expansions containing one, two, three or four central cations of the host phosphors were considered, abbreviated as monomers, dimers, and trimers. For SLA, due to the presence of two adjacent candidate (Sr1²⁺/Sr2²⁺) for the Eu doping, the dimer and tetramers clusters are constructed. The respective quantum clusters of the host structures of SMS, BMS, SLA, CLA, SALON and SLBO phosphors are visualized in **Figure 10.3**.

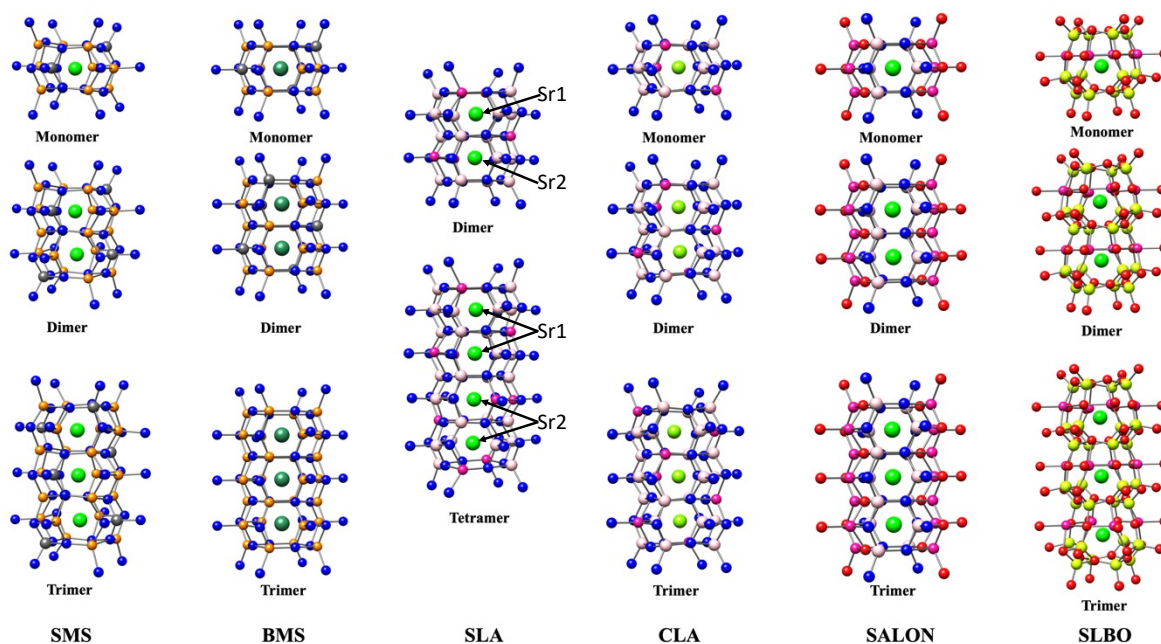


Figure 10.3. Graphical representation of (monomer, dimer, trimer, or tetramer) undoped clusters of SMS, BMS, CLA, SALON, SLBO used for band gap calculations. The respective doped clusters were constructed by replacing one of the central cations M ($\text{M} = \text{Ca}^{2+}$, Sr^{2+} , Ba^{2+}), with Eu^{2+} . Atom color-coding: Ca (light green), Sr (green), Ba (deep green), Si (gray), Mg (orange), Al (yellowish pink), Li (pink), N (blue), O (red).

As discussed and attributed in **Section 7.3**, the low doping limit is considered so that formation of Eu^{2+} doped phosphors involves the substitution one (Ca^{2+} , Sr^{2+} , Ba^{2+}) cation per cluster.[332] due to the similarity of their ionic radii, as shown in **Table 10.1**. In addition, no (Eu^{2+} - Eu^{2+}) interaction is expected, as well, no other cations substitution (e.g., Li^+ , Mg^{2+} , Al^{3+} , or Si^{4+}) or occupation of interstitial sites on the unsaturated channels is not possible due to steric reasons.[18, 80] Hence the corresponding candidate structures for the respective Eu^{2+} doped phosphors are straightforward constructed from the host model structures of **Figure 10.3** by replacing one Sr^{2+} , Ca^{2+} or Ba^{2+} cations with Eu^{2+} . Owing to the strong rigidity of the considered solid-state crystal structures, no further structure relaxation due to Eu^{2+} doping needs to be taken into account.

Table 10.2. Detailed description of the employed clusters within the embedded cluster approach in terms of the QC and HF layers compositions, the number of atoms in the ECP region, the number of point charges in the PC region and the converged CHELPG charges in ECP and PC.

Phosphor	QC	HF	n(cECP)	n(PC)	CHELPG Charges
$\text{SrLi}_2[\text{Be}_4\text{O}_6]:\text{Eu}^{2+}$ SLBO	$[\text{EuLi}_4\text{Be}_{12}\text{O}_{32}]^{34-}$	$[\text{Li}_4\text{Be}_{15}]^{34}$	327	43016	Sr : +2.10
	$[\text{EuSrLi}_8\text{Be}_{20}\text{O}_{52}]^{52-}$	$[\text{Sr}_2\text{Li}_6\text{Be}_{21}]^{52}$	443	42867	Li : +0.96
	$[\text{EuSr}_2\text{Li}_{12}\text{Be}_{28}\text{O}_{72}]^{70-}$	$[\text{Sr}_2\text{Li}_{10}\text{Be}_{28}]^{70}$	559	42718	Be : +1.31
					O : -1.94
$\text{Sr}[\text{Al}_2\text{Li}_2\text{O}_2\text{N}_2]:\text{Eu}^{2+}$ SALON	$[\text{EuLi}_6\text{Al}_6\text{O}_{12}\text{N}_{12}]^{34-}$	$[\text{Sr}_2\text{Li}_6\text{Al}_8]^{34}$	186	39486	Sr : +1.64
	$[\text{EuSrLi}_{10}\text{Al}_{10}\text{O}_{18}\text{N}_{18}]^{46-}$	$[\text{Sr}_2\text{Li}_9\text{Al}_{11}]^{46}$	222	39429	Li : +1.16
	$[\text{EuSr}_2\text{Li}_{14}\text{Al}_{14}\text{O}_{24}\text{N}_{24}]^{58-}$	$[\text{Sr}_2\text{Li}_{12}\text{Al}_{14}]^{58}$	258	39372	Al : +2.74
					O : -1.78
$\text{Ba}[\text{Mg}_3\text{SiN}_4]:\text{Eu}^{2+}$ BMS	$[\text{EuMg}_9\text{Si}_3\text{N}_{24}]^{40-}$	$[\text{Ba}_2\text{Mg}_{12}\text{Si}_3]^{40}$	186	34464	Sr : +2.20
	$[\text{EuBaMg}_{15}\text{Si}_5\text{N}_{36}]^{54-}$	$[\text{Ba}_2\text{Mg}_{17}\text{Si}_4]^{54}$	222	34407	Mg : +2.26
	$[\text{EuBa}_2\text{Mg}_{21}\text{Si}_7\text{N}_{48}]^{68-}$	$[\text{Ba}_2\text{Mg}_{22}\text{Si}_5]^{68}$	460	34148	Si : +3.42
					N : -2.74
$\text{Sr}[\text{Mg}_3\text{SiN}_4]:\text{Eu}^{2+}$ SMS	$[\text{EuMg}_9\text{Si}_3\text{N}_{24}]^{40-}$	$[\text{Sr}_2\text{Mg}_{12}\text{Si}_3]^{40}$	57	42130	Sr : +2.07
	$[\text{EuSrMg}_{15}\text{Si}_5\text{N}_{36}]^{54-}$	$[\text{Sr}_2\text{Mg}_{17}\text{Si}_4]^{54}$	72	42093	Mg : +2.03
	$[\text{EuSr}_2\text{Mg}_{21}\text{Si}_7\text{N}_{48}]^{68-}$	$[\text{Sr}_2\text{Mg}_{22}\text{Si}_5]^{68}$	267	41878	Si : +3.66
					N : -2.81
$\text{Sr}[\text{LiAl}_3\text{N}_4]:\text{Eu}^{2+}$ SLA	$[\text{EuSrLi}_5\text{Al}_{15}\text{N}_{36}]^{54-}$	$[\text{Sr}_2\text{Li}_5\text{Al}_{15}]^{54}$	218	42600	Sr : +2.02
	$[\text{EuSr}_3\text{Li}_{10}\text{Al}_{26}\text{N}_{60}]^{84-}$	$[\text{Sr}_2\text{Li}_8\text{Al}_{24}]^{84}$	294	42482	Li : +0.94
					Al : +2.93
$\text{Ca}[\text{LiAl}_3\text{N}_4]:\text{Eu}^{2+}$ CLA	$[\text{EuLi}_3\text{Al}_9\text{N}_{24}]^{40-}$	$[\text{Ca}_2\text{Li}_3\text{Al}_{11}]^{40}$	186	46838	Sr : +2.02
	$[\text{EuCaLi}_5\text{Al}_{15}\text{N}_{36}]^{54-}$	$[\text{Ca}_2\text{Li}_8\text{Al}_{14}]^{54}$	222	46781	Li : +1.36
	$[\text{EuCa}_2\text{Li}_7\text{Al}_{21}\text{N}_{48}]^{68-}$	$[\text{Ca}_2\text{Li}_7\text{Al}_{19}]^{68}$	258	46724	Al : +2.73
					N : -2.80

As is shown in **Table 10.2**, all these clusters are highly negatively charged hence, they are equipped with HF layer. The (QC+HF) clusters are embedded in an external PC field, consisting of about 35000 to 45000 charges, to account for the long-range coulombic forces. In order to avoid electron leakage and overdelocalization from the (QC+HF) to the PC region, ECP region of 2–3 layers is introduced between (QC+HF) and PC regions, where, the corresponding crystallographic positions are substituted by repulsive capped effective core potentials (cECPs) as included in the SDD framework. The employed types of cECPs for all

elements are given in **Table 7.3**. The charges equipped the ECP and PC regions were optimized in the framework of the Ionic-Crystal-QMMM embedded cluster protocol in ORCA employing the CHELPG[351, 352] scheme for calculating the charges of ions. The chosen convergence criteria ensure an overall neutral cluster according to the neutrality condition ($q(\text{QC} + \text{HF}) = -q(\text{BR} + \text{PC})$)[141] as well as a uniform charge distribution in all (QC, HF, BR, and PC) regions. The final optimized charges are given in **Table 10.2**.

It should be noted that within the employed embedding scheme, the positions and magnitudes of the point charges are kept fixed while no additional corrections for the long range electrostatics are taken into account.[84, 422] This scheme has been proven successful in treating a variety of chemical problems in the field of semiconductors, insulators as well as molecular crystals.[83, 84, 140, 142, 421, 423-428] Note that while this scheme can be applied to a broad range of systems, metallic systems or materials for which the electronic structure is strongly delocalized cannot be treated.

10.5.2. Cluster size convergence

In a next step, we perform cluster size convergence of the candidate clusters presented in **Figure 10.3** and **Table 10.2** with respect to the optical band gap (E_g) energies of the host phosphor structures and the absorption and emission spectral shapes of the Eu²⁺ doped phosphors. For these purpose we choose to present the cases of (SMS)[327] and (CLA)[326]. As seen in **Figure 10.4 a** and **c**, the computed optical band gap energies at the PBE0 TD-DFT and STEOM-DLPNO-CCSD levels of theory in both cases are converged for the trimeric structures ($\{[\text{EuSr}_2\text{Mg}_{21}\text{Si}_7\text{N}_{48}]^{68-} + [\text{Sr}_2\text{Mg}_{22}\text{Si}_5]^{68+}\}^0$ and $\{[\text{EuCa}_2\text{Li}_7\text{Al}_{21}\text{N}_{48}]^{68-} + [\text{Ca}_2\text{Li}_7\text{Al}_{19}]^{68+}\}^0$). However, only when the STEOM-DLPNO-CCSD method is employed, the computed band gap energies of the SMS and CLA host trimer structures are matching the experimental values with errors that are below 0.05 eV, while the respective PBE0 TD-DFT results deviate more than 0.5 eV from the experimental values. Nevertheless, this is still an acceptable deviation showing that PBE0 TD-DFT is a valid method to describe the absorption and emission spectra of these systems. In fact, as shown in **Figure 10.4 b** and **d**, the shape of the PBE0 TD-DFT computed absorption and emission spectra of the Eu²⁺ doped dimer and trimer structures has converged while both type of spectra show nice agreement with the experiment. It should be emphasized that at the converged cluster sizes (e.g. trimer structures) placing the Eu²⁺ at the center or the edge cuboids does not alter the computed quantities. Hence

based of the above results in the case of SMS, BMS, CLA, and SLBO the dimer Eu^{2+} doped structures have been chosen to study the absorption and fluorescence spectra of the study set of the Eu^{2+} doped phosphors. In the case of SLA, both dimer and tetramer clusters showed similar results, so again the dimer Eu^{2+} doped structure used, where in the dimer cluster only on site (either Sr1^{2+} or Sr2^{2+}) is Eu doped, and the final spectra will be sum of the partial spectra of the two sites. Finally, in the case of SALON trimer clusters were used, as it shows better agreement with the experiment as shown later.

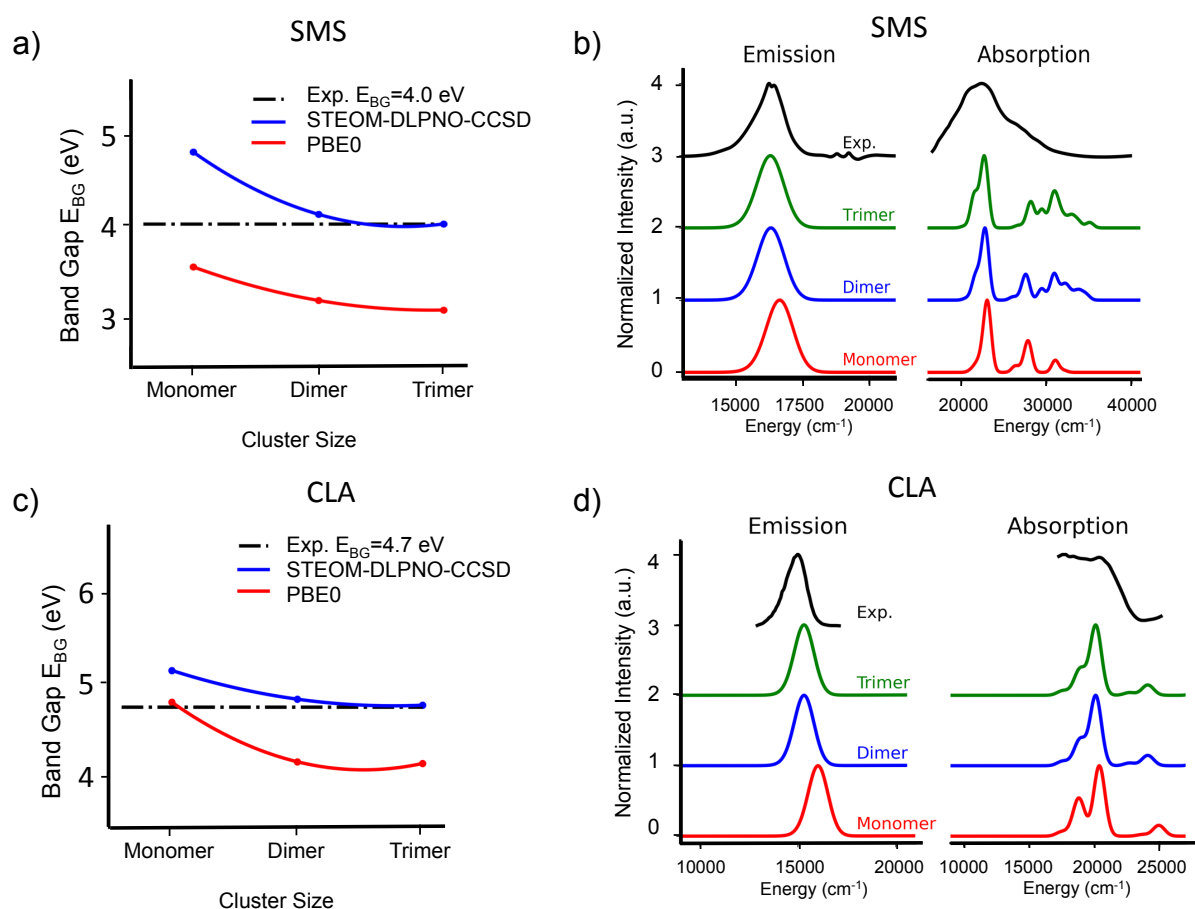


Figure 10.4. Cluster size convergence of SMS and CLA phosphors with respect to optical band gap energies and (a, c) absorption and fluorescence spectra (b, d). The band gap energies are computed at the PBE0 TD-DFT and STEOM-DLPNO-CCSD level of theory while the absorption and fluorescence spectra at the PBE0 TD-DFT level in the framework of ESD approach.

10.6. Absorption and Emission Processes: A Qualitative Electronic Structure Analysis

Let us now discuss the most important factors that influence the absorption and emission processes in Eu^{2+} -doped phosphors in which Eu^{2+} is doped in 8-fold coordinate host environments. For this purpose, we will undertake an electronic structure analysis based on the monomer (dimer, trimer etc.) structures presented in **Figure 10.3**.

The electronic structure of the free Eu^{2+} ion and its behavior when doped in ideal cubic crystal field (inverted O_h), has been previously discussed **Chapter 9**. Additionally, **Section 9.4** introduced a qualitative analysis of absorption and emission processes in Eu^{2+} -doped phosphors, which was summarized in **Scheme 9.1**. The phosphors investigated here, with Eu local symmetry lower than the ideal cubic, can be viewed as distorted structures from the ideal case. Notably, quantities such as ligand field splittings (LFS) ($\Delta E_{\text{cubic}}, \Delta E_d$), band gap energies, E_{BG} and Stokes shifts (ΔS) emerged as crucial factors influencing absorption and emission processes, determining the energy position and bandwidth of different spectral features. Furthermore, the presence of MLCT states, which significantly overlap with the host electronic manifold, increases the probability of relaxation through non-radiative pathways, leading to a substantial reduction in the emission quantum yield and thermal stability.[80, 371]

Focusing now on the Eu^{2+} doped nitride phosphors (SMS, BMS, SLA and CLA), while in BMS, the Eu^{2+} is coordinated in an 8-fold N^{3-} network in an approximate cubic symmetry, in SMS, SLA and CLA a tetragonal distortion occurs around the Eu^{2+} center which reduces the symmetry of the EuN_8 building block from cubic (inverted O_h) to D_{4h} . In reality, due to additional distortions in the host frame the center of inversion is lost reducing further the symmetry of EuN_8 , which can be approximated to S_4 . The molecular orbital (MO) energy splitting of the ground state configurations of BMS, SMS, SLA and CLA, in cubic and S_4 symmetries, together with the most important single electron excitations arising from these ground state electron configurations within the 1-electron picture is visualized in **Figure 10.5**. In SMS, SLA and CLA the S_4 symmetric 8A ground state obtains the $1e^1 1a^1 1b^1 2e^1 2a^1 3b^0 2a^0 3e^0 4b^0$ electron configuration. It follows that valence $\text{Eu } 4f \rightarrow \text{Eu } 5d_{z^2/x^2-y^2}$ single electron excitations or electron decays $\text{Eu } 5d_{z^2/x^2-y^2} \rightarrow \text{Eu } 4f$ will give rise to $2S+1=8$ and $2S+1=6$ multiplets of A and E symmetries along the absorption and emission processes, respectively. BMS, on the contrary, obtains $^8A_{1u}$ ground state. As illustrated in **Figure 10.5**, under cubic symmetry the Si-2s and N-2p orbitals in the SiN_4 cuboid

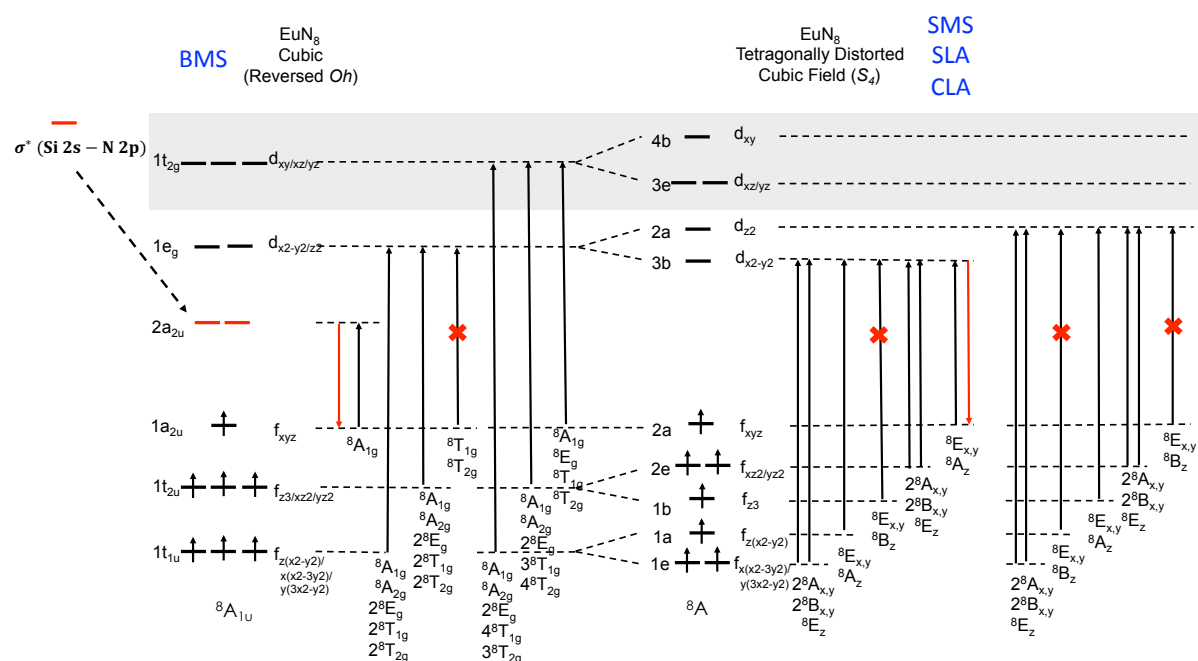


Figure 10.5. Qualitative molecular orbital diagram of the monomeric of nitride doped Eu^{2+} phosphors adopted for cubic (reversed O_h) EuN_8 centers (BMS) and for EuN_8 centers (SMS, SLA and CLA) of in S_4 symmetry. Black arrows indicate absorption processes. Red arrows indicate emission processes and red crosses indicate dipole forbidden transitions.

Similar to Eu^{2+} doped nitride phosphors SMS and SLA, oxo-nitride SALON and oxide SLBO phosphors show distorted cubic geometries in which the EuO_4N_4 and EuO_8 building units show C_{2h} and C_4 symmetries around the Eu^{2+} centers. As illustrated in **Figure 10.6**, under these local symmetries SALON has an $^8\text{A}_u$ ground state with $1a_u^1 1b_u^1 2b_u^1 2a_u^1 3b_u^1 4b_u^1 3a_u^1 4a_u^0 5a_u^0 6a_u^0 5b_u^0 6b_u^0$ electron configuration while SLBO has an ^8A ground state with $1e^2 1b^1 1a^1 2e^2 2b^1 3b^0 2a^0 3e^0 4b^0$ electron configuration. In both cases, valence $\text{Eu } 4f \rightarrow \text{Eu } 5d_{z^2/x^2-y^2}$ single electron excitations or electron decays $\text{Eu } 5d_{z^2/x^2-y^2} \rightarrow \text{Eu } 4f$ will give

rise to $2S+1=8$ and $2S+1=6$ multiplets of (A_g, B_g for SALON and A, B, E for SLBO) symmetries along the absorption and emission processes, respectively.

Ultimately, as depicted in **Figure 10.1**, the emission energy is contingent upon the strength of the ligand field strength and 4f-5d splitting, where both decrease along nitride, oxynitride, and oxide phosphors sequence. However, the Eu-L bond distance also plays a role, introducing another contributing factor in the final determination of the emission energy.

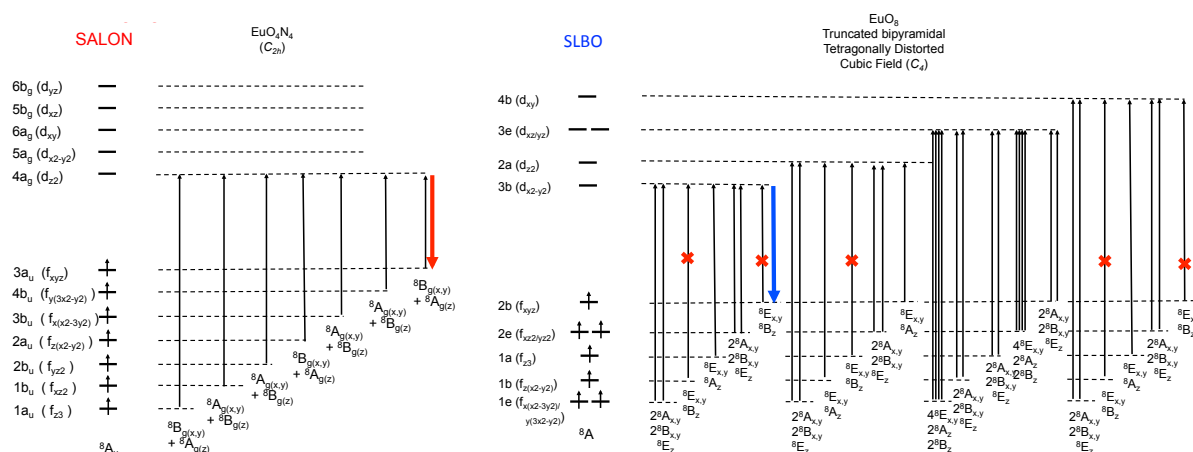


Figure 10.6. Qualitative molecular orbital diagram of the monomeric oxonitride and oxide doped Eu^{2+} phosphors adopted for cubic (C_{2h}) EuO_4N_4 centers (SALON) and for tetrahedrally distorted (C_4) EuO_8 centers (SLBO). Black arrows indicate absorption processes. Red and blue arrows indicate (red and blue color, respectively) emission processes and red crosses indicate dipole forbidden transitions.

10.7. A theoretical protocol for understanding the absorption and luminescence spectra in Eu^{2+} -doped phosphors

All the above qualitative observations will be used in the next section in order to develop a theoretical protocol that is able to

- 1) predict the absorption and fluorescence spectra band shapes,
- 2) provide insight on the nature of the dominating spectral features, and
- 3) predict the thermal stability of the different phosphors.

As discussed in the computational **Section 10.4**, the absorption and fluorescence spectra are computed at the TD-DFT/PBE0 level of theory in conjugation with the ESD approach to account for the vibronic coupling. Analysis of the electronic transitions and impact on the spectral features is performed on the basis of natural transition orbitals (NTOs).

10.7.1. Nitride phosphors

Starting with the nitride Eu^{2+} -doped phosphors including SMS, BMS, SLA and CLA. Respectively, **Figures 4.7-10** illustrate their computed versus experiment absorption and fluorescence spectra as well as the NTO analysis of the relevant absorption/fluorescence bands. Generally, for all the studied cases, the agreement between theory and experiment is very good allowing a quantitative analysis of the spectral features.

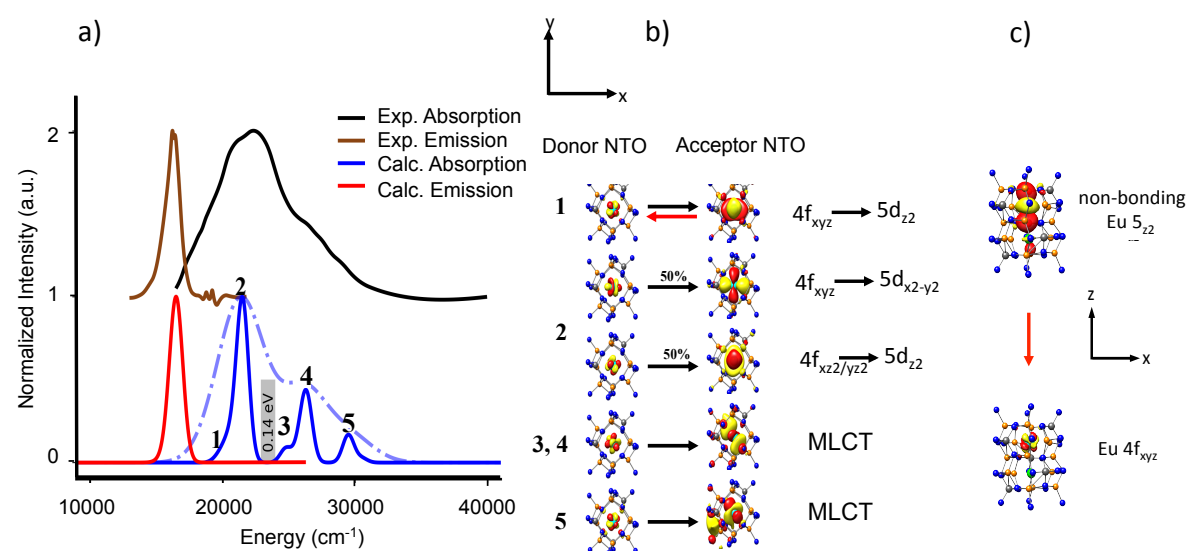


Figure 10.7. a) SMS experimental (black), calculated TD-DFT/PBE0 absorption (blue, light blue) spectra and experimental (brown), TD-DFT/PBE0/ESD calculated (red) emission spectra. b) NTO analysis of the relevant bands in absorption spectra and c) the 1st transition responsible for emission upon relaxation.

First, as seen in **Figure 10.7**, for SMS four bands dominate the absorption spectrum. The first two bands (1,2), according to the NTO analysis, involve $\text{Eu } 4f_{xyz} \rightarrow \text{Eu } 5d_{z^2}$ and ($\text{Eu } 4f_{xyz} \rightarrow \text{Eu } 5d_{x^2-y^2} / \text{Eu } 4f_{xz^2/yz^2} \rightarrow \text{Eu } 5d_{x^2-y^2}$) single electron excitations,

respectively. The shoulder (band 3) and bands (4,5) are dominated by MLCT type of excitations. Band 1 shows that the emission process involves electron decay from a non-bonding Eu 5d_{z²} orbital to an isolated Eu 4f_{xyz} orbital. Since there is no significant distortion in the excited state relative to the electronic ground state, there can also be no vibronic progression thus leading to narrow band emission. Consequently, the rigid nature of this transition causes narrow band emission. The energy separation between the valence bands (1,2) and the MLCT bands (3,4,5) is ~1150 cm⁻¹ (0.14 eV). Such a small energy separation indicates that thermal quenching of the emission through non-radiative relaxation processes is possible explaining the poor thermal stability of SMS. In fact, the computed emission spectra from bands 3 and 4 lead to negligible intensity emission lines.

Let us now discuss the case of the narrow band phosphors SLA and CLA. These phosphors have shown somewhat larger emission bandwidths (FWHM(SLA) = 50 nm~1180 cm⁻¹ and FWHM(CLA) = 60 nm~1330cm⁻¹) with respect to the SMS (FWHM(SMS) = 43 nm~1140cm⁻¹). The computed versus experiment absorption and fluorescence spectra are visualized in **Figure 10.8** and **Figure 10.9**. Once again, the agreement between theory and experiment is satisfactory allowing a quantitative analysis of the experimentally observed spectral features. In the case of SLA presented in **Figure 10.8**, there are two different Eu doping candidate sites, with similar local geometric and electronic structure, however exact local symmetry around Sr2 is more order than Sr1 resulting in some transition restriction for Eu at Sr2. Generally, they exhibit similar absorption spectra while the emission spectra were dominated by emission of Eu doping Sr1 site resulting in the narrow bandwidth. The computed absorption spectra are the sum of partial absorption spectra for Eu doping the two sites, and both show similar NTO analysis. The computed spectra are dominated by three bands, which according to the NTO analysis are characterized by Eu 4f_{xyz} → Eu 5d_{x²-y²} - N 2p (band 1), Eu 4f_{xyz} → Eu 5d_{x²-y²} (band 2), and metal to ligand charge transfer (MLCT, band 3) single electron excitation contributions. As band 1 indicates, the emission process (for Eu doping Sr1) involves an electron decay from a practically anti-bonding Eu 5d_{x²-y²} - N 2p molecular orbital to an isolated Eu 4f_{xyz} orbital. This introduces little vibronic interaction with the environment, which is associated to the 2% N 2p character of the acceptor NTO orbital that dominates absorption band 1. Once again, the rigid nature of this transition causes narrow band emission however due to the anti-bonding character of the acceptor NTO orbital participating in the emission process the SLA emission spectra are broader than those of SMS. On the contrary, the higher thermal stability of SLA phosphor in comparison to SMS is associated to the large energy

separation between the valence and MLCT bands in the absorption spectrum, which amounts to 0.35 eV in SLA in comparison to 0.14 eV in SMS. This is also in agreement with experimental observation from direct nitrogen 1s2p RXES measurements.[371]

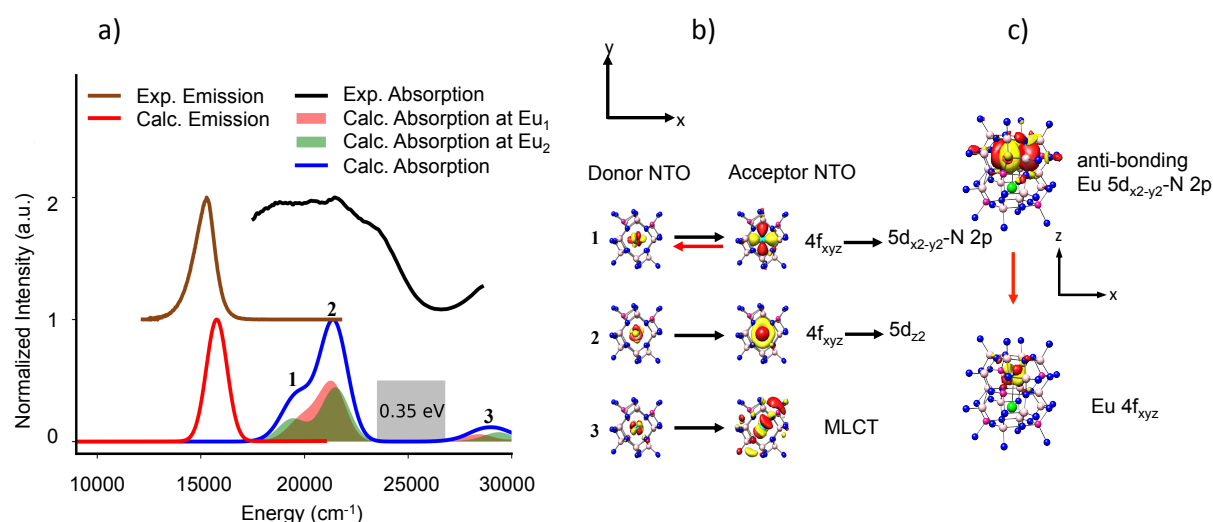


Figure 10.8. a) SLA experimental (black), calculated TDDFT/PBE0 absorption (blue) spectra and experimental (brown), TDDFT/PBE0/ESD calculated (red) emission spectra. The calculated absorption spectrum is the sum of partial absorption spectra of Eu(1,2) doping at two sites (Sr1 and Sr2). For the emission, the spectrum was dominated by emission spectra at Sr1. b) NTO analysis of the relevant bands in absorption spectra and c) the 1st transition responsible for emission upon relaxation, for Eu doping Sr1 site.

In the case of CLA, the computed absorption spectrum presented in **Figure 10.9** shows five bands which according to the NTO analysis are characterized by Eu $4f_{xyz} \rightarrow$ Eu $5d_{x^2-y^2} -$ N 2p (band 1), Eu $4f_{xz^2/yz^2} \rightarrow$ Eu $5d_{x^2-y^2} -$ N 2p (band 2), Eu $4f_{xz^2/yz^2} \rightarrow$ Eu $5d_{z^2}$ (band 3), and metal to ligand charge transfer (MLCT, shoulder band 4 and bands 5) single electron excitation contributions. As in the case of SLA, band 1 indicates that the emission process involves an electron decay from a practically anti-bonding Eu $5d_{x^2-y^2} -$ N 2p molecular orbital to an isolated Eu $4f_{xyz}$ orbital which again introduce little vibronic interaction with the environment.

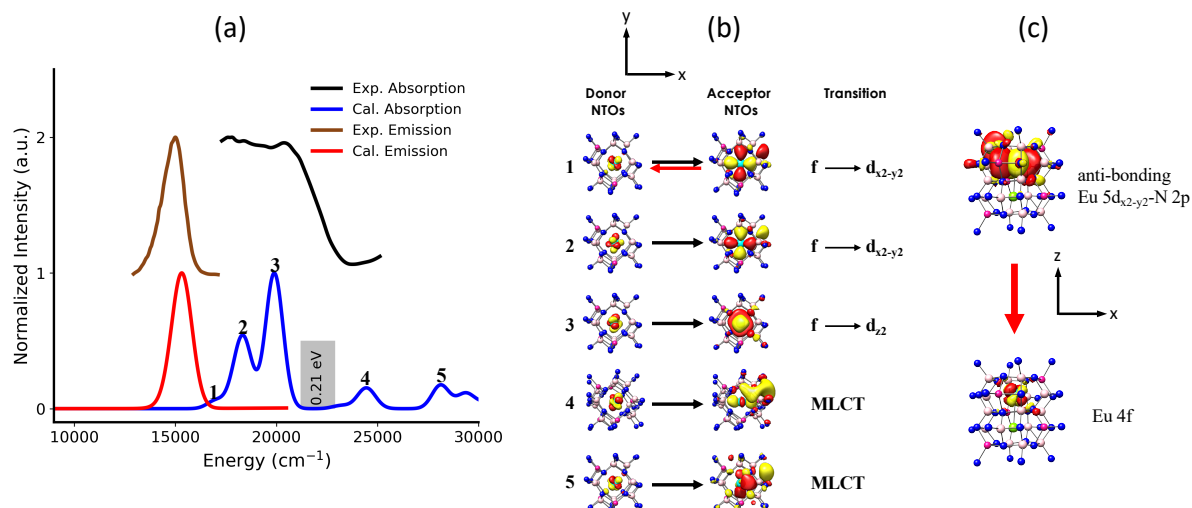


Figure 10.9. a) CLA experimental (black), calculated TD-DFT/PBE0 absorption (blue) spectra and experimental (brown), TD-DFT/PBE0/ESD calculated (red) emission spectra. b) NTO analysis of the relevant bands in absorption spectra and c) the 1st transition responsible for emission upon relaxation.

In comparison to SLA, the N 2p contribution to the NTO donor orbital dominating band 1 increases from 2% to 4%. Such increase in the NTO orbital anti-bonding character is associated to the higher degree of compression of the EuN_8 cuboid and consequently the further increase of the crystal field strength in CLA in comparison to SLA. As a result, a narrow band emission is observed with larger bandwidth with respect to both SLA and SMS. The energy separation between valence band (3) and MLCT (5) band is $\sim 1700 \text{ cm}^{-1}$ (0.21 eV) indicating an intermediate thermal stability between SLA and SMS.

In the case of BMS the situation changes rapidly. As it has been discussed in the previous **Section 10.6** and shown in **Figure 10.5**, the ligand based anti-bonding $\sigma^*(\text{Si-2s}, \text{N-2p})$ MO is stabilized below the Eu-5d MOs. This situation is reflected to both the absorption and emission spectra. The computed absorption spectrum presented in **Figure 10.10** indicates that five bands dominate the broad unresolved experimental spectral feature in the energy range 18000 and 26000 cm^{-1} . According to the NTO analysis, all these bands have significant metal to ligand charge transfer character (MLCT). In particular, bands 1 and 2 in contrast to all other nitride phosphors has pure MLCT character dominated by $\text{Eu } 4f_{xyz} \rightarrow \sigma^*(\text{N } 2p - \text{Si } 2s)$ single electron excitation. Band 3 has mixed valence $\text{Eu } 4f_{z^3} \rightarrow \text{Eu } 5d_{x^2-y^2} - \text{N } 2p$ and MLCT

characters while bands 4 and 5 have solely MLCT single electron excitation characters. Hence the emission process from band 1 results in a red shifted emission spectrum in contrast to what is expected by the crystal field strength due to structural expansion of the EuN_8 cuboid (39.54 \AA^3) and longer Eu-N bond distance 2.9 \AA (**Figure 10.1** and **Table 10.1**). This is also reflected to the experimental and computed Stokes shifts presented in **Table 10.3**. While the Stokes shifts in the case of SMS, SLA and CLA range between $500 - 1000 \text{ cm}^{-1}$, in the case of BMS they are larger than 2500 cm^{-1} . The bandwidth of the computed emission spectrum in accordance with the experimental one and is also increased ($\text{FWHM}(\text{BMS}) = 90 \text{ nm} \sim 1990 \text{ cm}^{-1}$) in comparison to the observed and computed bandwidths in SMS, SLA and CLA. This is due to the non-rigid nature of the transition, in which vibrations within the host ligand framework participate and apparently dominate the band broadening mechanism. This is also supported by the computed fluorescence rates and relaxations times presented in **Table A. 2**. As seen at the Frank-Condon approximation and upon applying Herzberg–Teller corrections in the case of BMS the computed fluorescence rates are > 3 orders of magnitude smaller while the respective relaxation times are about 5 orders of magnitude larger in comparison to the other phosphors reflecting a different relaxation pathway. Nevertheless, these relaxation times at the fluorescence time frame are very small and cannot be safely used to define rigidity.

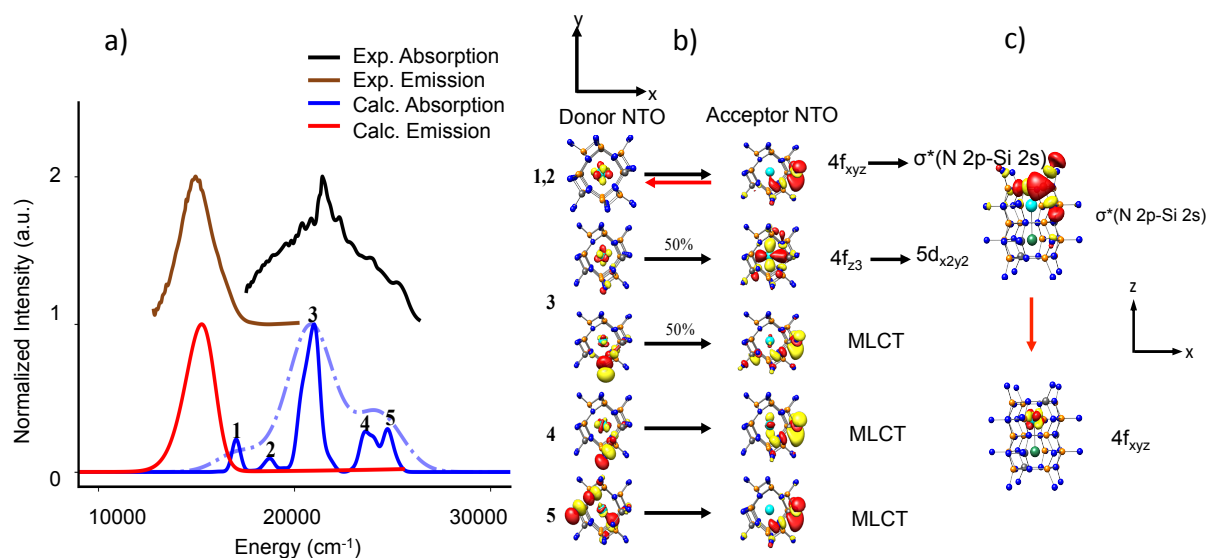


Figure 10.10. a) BMS experimental (black), calculated TD-DFT/PBE0 absorption (blue, light blue) spectra and experimental (brown), TD-DFT/PBE0/ESD calculated (red) emission spectra. b) NTO analysis of the relevant bands in absorption spectra and c) the 1st transition responsible for emission upon relaxation.

It should be noted that one of the most commonly used quantities to define rigidity and thermal quenching is the Debye temperature.[429, 430] The Debye temperature although it is a proxy of rigidity is not always predictive of thermal quenching.[431, 432] A more valid quantity is the Huang–Rhys factor S which is a measure of the strength of the electron-phonon coupling in the emission process.[364, 433, 434] In fact along the study set the computed Huang–Rhys factors presented in **Table A. 1** follow the trend of the energy separation of the MLCT band. In particular, small Huang–Rhys factors that are indicative of structural rigidity of excited (emissive) state compared to ground state and are associated with large MLCT band separation reflecting a higher thermally stable phosphor.

To conclude this part, we have developed in this section a computational protocol that is able to relate the emission bandwidth of the nitride phosphors to the nature of the single electron decay that dominates the emission process from the first excited state that is reached in the absorption spectrum. In the next section, we will apply this protocol to characteristic examples from the oxonitride and the oxide families of phosphors, namely SALON and SLBO.

10.7.2. Oxynitride and oxide phosphors

In the case of SALON, the computed versus experimental absorption and fluorescence spectra are visualized in **Figure 10.11**. As seen, the agreement between theory and experiment is once again very good, thus allowing a quantitative analysis of the experimentally observed spectral features. The absorption spectrum is consisting of five bands which according to NTO analysis all involve valence Eu 4f \rightarrow Eu 5d single electron excitations, namely Eu 4f_{xyz} \rightarrow Eu 5d_{z²} (band 1), Eu 4f_{z³} \rightarrow Eu 5d_{z²} (band 2), Eu 4f_{xyz} \rightarrow Eu 5d_{x²-y²} – N/O 2p (band 3, band 4), and Eu 4f_{xz²/yz²} \rightarrow Eu 5d_{xy/xz/yz} – N/O 2p (band 5) single electron excitation contributions. Similar to SMS the emission process involves an electron decay from a non-bonding Eu 5d_{z²} orbital to an isolated Eu 4f_{xyz} orbital, with practically negligible vibronic interaction with the lattice environment. Again, the rigid nature of the transition is the reason of the observed narrow bandwidth emission (FWHM = 46 nm /1220 cm⁻¹). As described above, band 5 has significant MLCT character. Hence, in SALON, excluding Band 4 due to its very weak intensity compared to other bands, the energy separation between the valence bands (1,2,3) and the MLCT band (5) (~10000 cm⁻¹, ~1.0 eV) is associated with an observed high thermal stability.

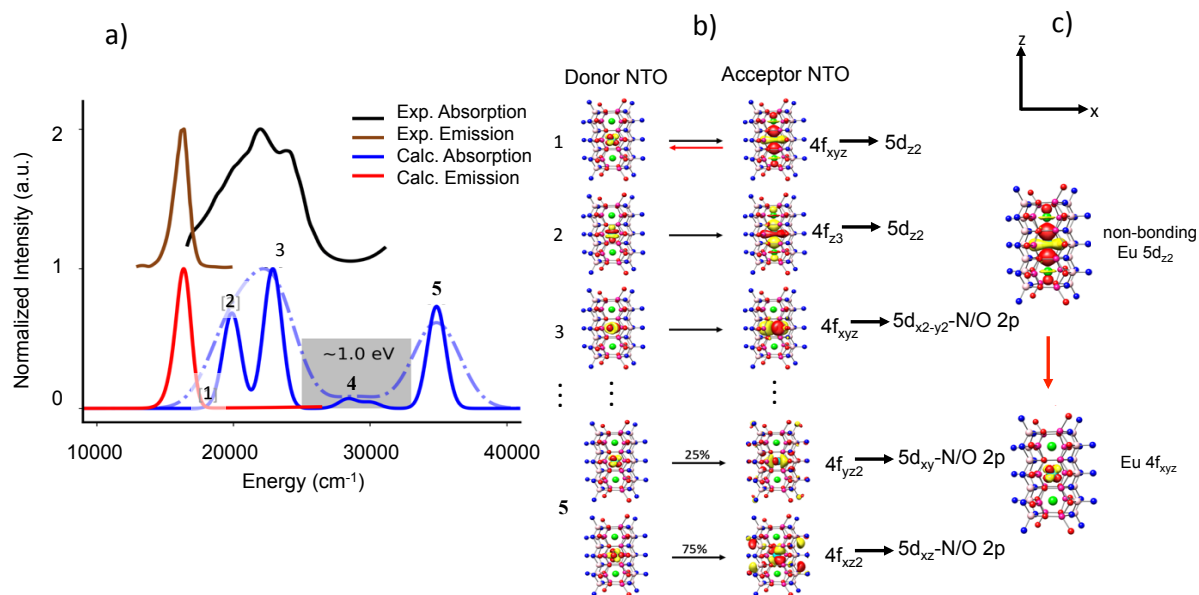


Figure 10.11. a) SALON experimental (black), calculated TD-DFT/PBE0 absorption (blue, light blue) spectra and experimental (brown), TD-DFT/PBE0/ESD calculated (red) emission spectra. b) NTO analysis of the relevant bands in absorption spectra and c) the 1st transition responsible for emission upon relaxation.

As a final example we discuss the case of blue emitting SLBO. The computed versus experimental absorption and fluorescence spectra are visualized in **Figure 10.12**. According to NTO analysis, the absorption spectral features are dominated by the valence Eu $4f_{xyz} \rightarrow$ Eu $5d_{x^2-y^2}$ (band 1) and Eu $4f_{xz^2}/yz^2 \rightarrow$ Eu $5d_{x^2-y^2}$ (band 2) single electron excitations. Under C_4 truncated square bipyramidal coordination environment of the EuO_8 building units the manifold of the f orbitals remains compact. This results in a blue shift of all the absorption bands in comparison to all other phosphors which adopt distorted cubic EuN_8 or EuN_4O_4 building units. In addition, in such coordination environment around the Eu^{2+} center the Eu $5d_{x^2-y^2}$ MO remains essentially non-bonded. Once again, the rigid nature of the Eu $5d_{x^2-y^2} \rightarrow 4f_{xyz}$ transition is the reason of the observed narrow bandwidth emission ($\text{FWHM} = 25 \text{ nm}/1220 \text{ cm}^{-1}$). This also results in the smallest experimental and calculated Stokes shift (**Table 10.3**) across the series validating the blue shift in the observed emission spectrum. Likewise, to SLA and SALON, SLBO shows high thermal stability which is consistent with the absence of MLCT absorption bands in the region $25000\text{--}30000 \text{ cm}^{-1}$. One can conclude that as long as valence and MLCT bands are separated by more than 0.3 eV a thermally stable phosphor should be expected.

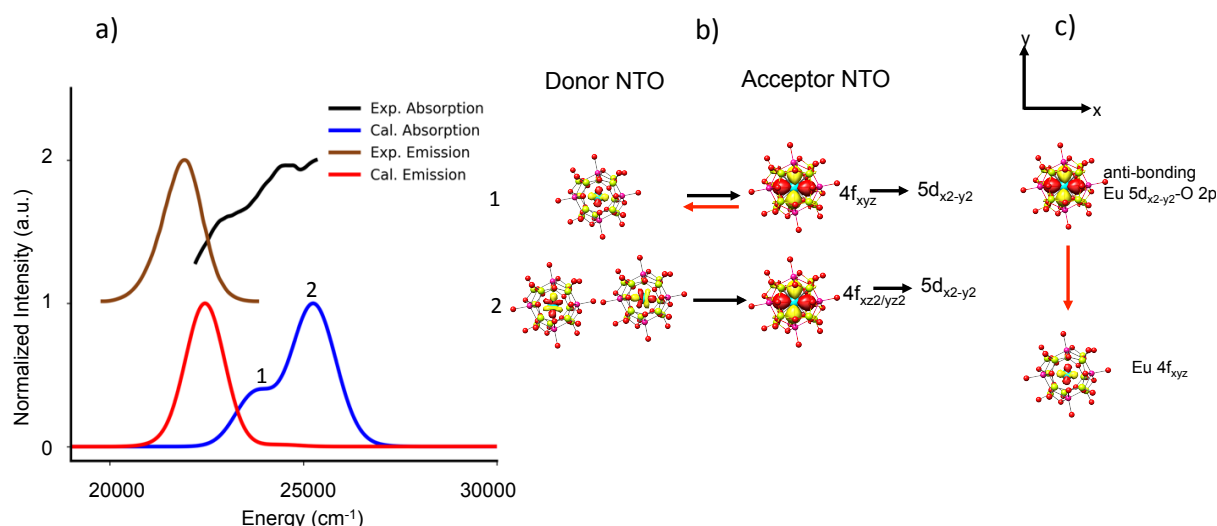


Figure 10.12. a) SLBO experimental (black), calculated TD-DFT/PBE0 absorption (blue, light blue) spectra and experimental (brown), TD-DFT/PBE0/ESD calculated (red) emission spectra. b) NTO analysis of the relevant bands in absorption spectra and c) the 1st transition responsible for emission upon relaxation.

Table 10.3. Experimental and computed emission bandwidth (FWHM) and stokes shift (ΔS) as well as computed Huang–Rhys factor (S) for the study set (BMS, SMS, CLA, SLA, SALON and SLBO) phosphors.

Phosphor	Experimental		Calculated		
	FWHM (cm ⁻¹) [nm]	ΔS (cm ⁻¹)	FWHM (cm ⁻¹)	ΔS (cm ⁻¹)	S
Ba[Mg ₃ SiN ₄]:Eu ²⁺ BMS	1990 [90]	3500	2015	2810	0.360
Sr[Mg ₃ SiN ₄]:Eu ²⁺ SMS	1140 [43]	750	1150	950	0.084
Ca[LiAl ₃ N ₄]:Eu ²⁺ CLA	1330 [60]	1000	1340	847	0.035
Sr[LiAl ₃ N ₄]:Eu ²⁺ SLA	1180 [50]	800	1140	840	0.010
Sr[Al ₂ Li ₂ O ₂ N ₂]:Eu ²⁺ SALON	1220 [46]	1100	1220	1150	0.029
SrLi ₂ [Be ₄ O ₆]:Eu ²⁺ SLBO	1210 [25]	980	1220	750	0.012

10.8. Definition of geometrical versus covalency descriptors

Up to this point of analysis, we have described a computational protocol that provides actual computation of the absorption and emission spectra of a study set of phosphors accompanied by a thorough electronic structure analysis of all the observed spectral features. The protocol has high predictive ability and is able to explain the energy position and the bandwidth of all the experimentally observed absorption and emission bands. Hence it serves as a powerful analytical tool in the design and synthesis of new phosphors for analyzing or even predicting the spectroscopic response of known or newly synthesized candidate phosphors. In the same direction it is also desirable to define descriptors, which could aid the experimental synthesis of candidate phosphors without the need of employing such elaborate calculations in each and every design idea that arrives on the synthesis table. In this sense a successful definition of descriptors may play a pre-screening role across a massive selection of candidate phosphors towards only those that fulfill the design criteria.

In the **Appendix A.1**, a number of commonly employed descriptors are discussed. It is demonstrated that the energy distribution as well as the intensity mechanism of the absorption and emission process in phosphors goes beyond the geometrical characteristics of the first and second coordination spheres. In contrast, experimental optical band gaps have been employed in order to find linear relationships between absorption and emission energy maxima defining emission color descriptors in a large set of phosphors.[364, 435] However, for a given material the band gap energies are closely related to the type of the employed experimental spectroscopic measurement, the experimental conditions, as well as the experimental resolution. Hence typically for a given material the experimental band gap energy variations range between 0.5 to 1 eV and can reach up to 2-3 eV (e.g. in inorganic semiconductors).[84] These variations might not always be systematic rendering the definition of experimental band gap energies within a narrow energy window for every candidate-studied system a difficult task. In an alternative scenario the calculated band gap energies can be used, provided that the employed methodology is carefully calibrated.

It was shown above that the computed PBE0/TD-DFT band gap energies of the SMS and CLA host structures are deviating from experiment and reference DLPNO-STEOM-CCSD calculations by about 0.5-0.8 eV while the computed PBE0/TD-DFT absorption spectra are in very good agreement with respect to the experimental absorption spectral for all the studied phosphors. Hence in a subsequent step we investigate the relation of the computed PBE0/TD-

DFT absorption energy maximum of band 1 (corresponding to the band gap energy) with respect to the experimental emission maximum across the study set of the phosphors (**Figure 10.13a**). An excellent linear relation is observed, thus defining a direct emission color descriptor across the study set of the phosphors. The advantage of using computed over experimentally determined optical band gaps is the resolution of the computed band 1 which allows the better definition of the linear relation. At the PBE0/def2-TZVP TD-DFT level the resulting linear relation reads:

$$\begin{aligned} \text{Experimental Emission Max}(\text{cm}^{-1}) \\ = 0.9334 * \text{Calculated Absorption Band 1 Max}(\text{cm}^{-1}) \\ - 419.04(\text{cm}^{-1}) \end{aligned} \quad (10.1)$$

In the previous **Section 10.7**, it was shown that the bandwidth of the emission band is directly related to the rigidity of the dominating emission process single electron decay. In particular, the non-bonding or the anti-bonding character of the acceptor Eu 5d MO reached by the absorption process and dominate the respective emission process seems to play a crucial role in the intensity mechanism of the narrow band phosphors. As a measure of this rigidity, we define the coefficient α^2 of the Eu 5d based MO. Of course, these MO coefficients are not a direct measure of “rigidity”. However, they are a helpful description in this context as they measure the degree of involvement of the Eu center in a covalent bond with its ligands. If there is a degree of covalency in this bond, this also means that there will be a structural distortion upon population or depopulation of the relevant bonding or antibonding orbitals. This is giving rise to a structural distortion relative to the ground state, which results in the possibility of a vibronic progression that will in turn broaden the emission band. Thus, as the Eu 4f based MOs remain essentially non-bonding, the critical quantity is the covalency of the 5d-MO that gets populated in the electronically excited state.

Similar covalency measures have been correlated to a number of spectroscopic properties like metal and ligand hyperfine couplings and zero field splittings in electron paramagnetic resonance (EPR), ligand K-edges in X-ray absorption spectroscopy and ligand to metal charge transfer (LMCT) intensities.[150, 436, 437] In **Figure 10.13 b**, the linear relation between the experimental emission bandwidth and the Eu 5d coefficient α^2 of the acceptor NTO participating in the emission process is visualized. As is seen the non-bonded acceptor NTO in

SMS, SLA and SLBO obtain α^2 values that are about ~ 1 . The increased anti-bonding character of the acceptor NTO in SALON and CLA reduces the α^2 to values that range between 0.8-0.9 while they drop to values below 0.6 in the case of BMS in which the acceptor NTO is a ligand based orbital. As a result, a linear relationship can be identified between the experimental emission bandwidth (in cm^{-1} units) and the computed Eu 5d α^2 which at the PBE0/def2-TZVP TD-DFT level reads:

$$\text{Experimental Emission FWHM}(\text{cm}^{-1}) = -2530.7 * \text{Eu 5d } \alpha^2 + 3638.4(\text{cm}^{-1}) \quad (10.2)$$

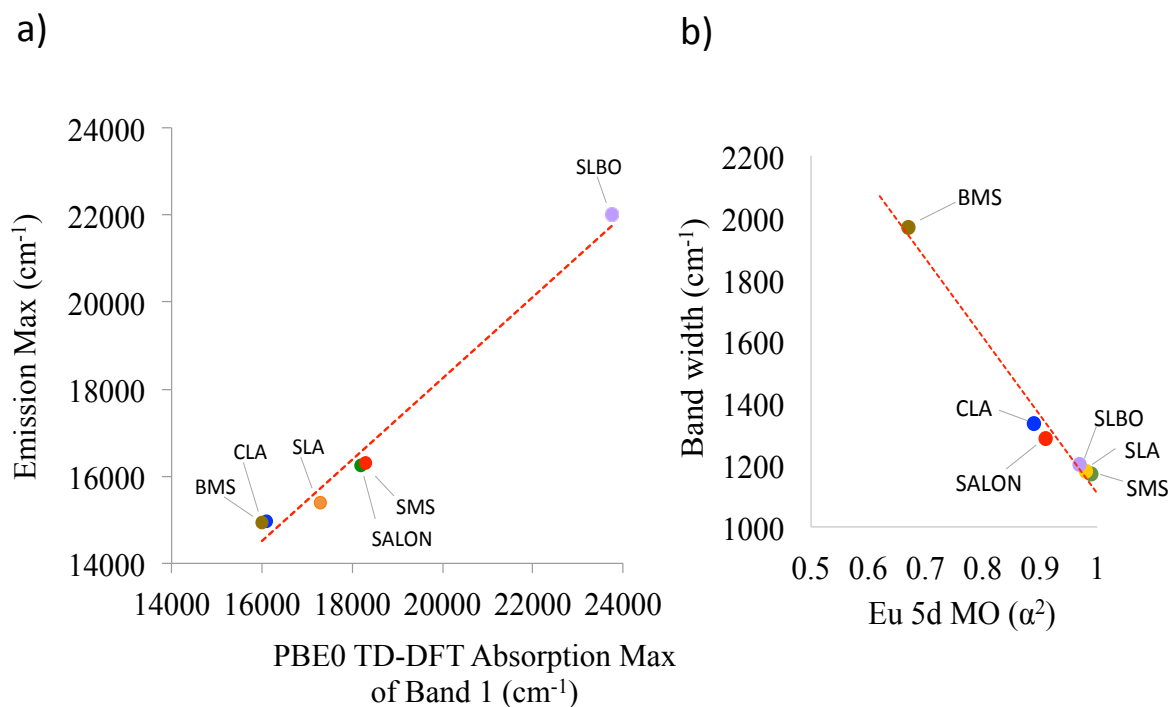


Figure 10.13. a) Experimental emission Max (cm^{-1}) as a function of PBE0 TD-DFT computed absorption Max (cm^{-1}) of Band 1. b) Experimental emission bandwidth (cm^{-1}) as a function of the covalency coefficient α^2 of the acceptor Eu 5d MO in the emission process for SMS (green cycle), BMS (brown cycle), SLA (orange cycle), CLA (blue cycle), SALON (red cycle) and SLBO (purple cycle). The red dotted line displays a linear regression.

Hence, according to the discussion above for a candidate Eu²⁺ phosphor one only needs to perform a conventional TD-DFT calculation in order to estimate the energy position of the 1st absorption band as well as the Eu 5d a^2 coefficient from an accompanied NTO analysis on this band. This will provide a robust prediction of the expected color and bandwidth of the emission spectrum of the candidate Eu²⁺ phosphor.

10.9. Summary and Conclusions

In this Chapter, a computational protocol was developed for the first time, that is able to predict the energy position, the shape and the bandwidth of the absorption and emission spectra of Eu²⁺ doped phosphors. For this purpose, a study set of well-known Eu²⁺ doped nitride, oxonitride and oxide phosphors was chosen, namely Sr[Mg₃SiN₄]:Eu²⁺ (SMS), Ba[Mg₃SiN₄]:Eu²⁺ (BMS), Ca[LiAl₃N₄]:Eu²⁺ (CLA), Sr[LiAl₃N₄]:Eu²⁺ (SLA), Sr[Al₂Li₂O₂N₂]:Eu²⁺ (SALON) and SrLi₂[Be₄O₆]:Eu²⁺ (SLBO). This set of phosphors contains a broad variety of energy shifts of the absorption and emission spectral features as well as the emission bandwidths. The construction of cluster models was performed in the framework of the embedded cluster approach. The size of the designed cluster models converged rapidly with respect to the band gap of the host ligand families computed at the STEOM-DLPNO-CC and TD-DFT levels of theories as well as the absorption spectra shapes computed at the TD-DFT level of theory.

Prior to the spectra computations a detailed geometrical and electronic structure analysis was performed which helped to identify those factors which influence the intensities and the energy distribution of the absorption and emission spectra in terms of

- 1) crystal field strengths,
- 2) the coordination environment around the Eu centers,
- 3) the Stokes shift variations and
- 4) the nature of the single electron excitations or electron decays dominating the absorption and emission processes.

In a next step, the shapes of the absorption and the fluorescence spectra of the family of the chosen Eu²⁺ doped phosphors were computed at the TD-DFT level in the framework of the excited state dynamics (ESD) approach. The excellent agreement between theory and experiment allowed a quantitative electronic structure analysis in the framework of natural transition orbitals analysis. It was shown that the energy position and the bandwidth of the emission band are influenced by the rigidity of the electron decay processes dominating the

emission spectral feature. In particular the non-bonding character of the acceptor Eu 5d NTO is responsible for the narrow band emission and the small Stoke shifts of the emission bands in SMS and SLBO. On the contrary as the anti-bonding character of the acceptor Eu 5d NTO increases (the cases of SLA, CLA and SALON) the bandwidth as well as the Stokes shift of the emission band increases. In BMS the ligand based anti-bonding $\sigma^*(\text{Si-2s, N-2p})$ MO is stabilized below the Eu-5d MOs. As a result, the rigidity of the electron decay dominating the emission process is altered, leading to an increase in both the emission bandwidth and the Stokes shift. The effect is strong and is able to overcome the expectations from the crystal field strength. As a result, a red shift broad emission spectrum is observed. It should be mentioned that such broadening effects owning the low-lying MLCT transitions are also referred to as “trapped exciton emission” or “anomalous emission” and have been observed in other phosphor materials.[438] As a measure of the thermal stability of the studied Eu²⁺ doped phosphors the energy separation between the valence and MLCT absorption bands was defined. In principle an energy separation that are above 0.3 eV point to thermally stable Eu²⁺ doped phosphors as in the case of SLA, SALON and SLBO. The above-presented protocol was found to perform equally well in all the studied phosphors. Hence, in a final step of the analysis it was employed to identify a uniform set of descriptors that are able to estimate both the energy position and the bandwidth of the emission bands of newly designed Eu²⁺-doped candidate materials. It was found that the energy position of the 1st computed band relates linearly with the energy position of the experimental emission band. While analysis of the nature of the one electron excitation dominating this band revealed that the covalency coefficient Eu 5d a^2 relates also linearly with the bandwidth of the emission band. We foresee that it will be possible in the future to employ these descriptors for pre-screening large datasets of Eu²⁺-doped phosphor candidates for application in LEDs.

However, the question arises: are the proposed protocol and descriptors universally applicable to other types of Eu²⁺-doped phosphors? This is the focal point of investigation and validation in the upcoming chapter.

11 Luminescence in Narrow-band Eu^{2+} -doped Phosphors bearing Multiple Candidate Eu^{2+} doping centers – Extending and Validation of the Proposed Protocol and Descriptors

The results of this chapter have been published in Phys. Chem. Chem. Phys., 2024, 26(7), 6277-6291. DOI: 10.1039/D3CP06039J

11.1. Introduction

In **Chapter 10**, a comprehensive computational protocol has been introduced, which is carefully designed to predict the absorption and emission spectral shapes of Eu^{2+} -doped phosphors, with a focus on nitride/oxy-nitride/oxide UCr_4C_4 -based phosphors containing a single Eu doping center. This protocol, based on the embedded cluster approach and operated in the framework of TD-DFT in conjugation with ESD approach, provided valuable insights into the photoluminescence behavior of these phosphors. Descriptors linking band gap energy and covalency of excited state orbitals to the color and linewidth of the emission band were extracted, demonstrating the protocol's efficacy.

Building upon this foundation, the objective of this chapter is to extend the applicability of our computational protocol to a considerably progressing class of Eu^{2+} -doped phosphors, which encompasses materials bearing multiple candidate Eu doping centers. In doing so, a set of UCr_4C_4 -based narrow-band Eu^{2+} -doped phosphors is selected, including the nitridolithoaluminate $\text{CaBa}[\text{Li}_2\text{Al}_6\text{N}_8]:\text{Eu}^{2+}$ (CBLA2), the alkali lithosilicates $\text{RbNa}_3[\text{Li}_3\text{SiO}_4]_4:\text{Eu}^{2+}$ (RNLSO) and $\text{RbNa}[\text{Li}_3\text{SiO}_4]_2:\text{Eu}^{2+}$ (RNLSO2). This extension of our computational protocol represents a crucial step towards a more comprehensive and systematic understanding of luminescent phosphor materials. The aim is to show and prove the generality of the proposed protocol and descriptors for Eu^{2+} -doped phosphors. The investigation of these

complex phosphor systems is promising for enhancing tunability and pave the way for achieving desirable photoluminescence properties for various applications.

Across the study set the most probable center for Eu²⁺ doping is identified at the couple cluster (CC) level of theory, employing the domain local pair natural orbitals couple cluster singles and doubles with perturbative triples (DLPNO-CCSD(T)) method, in conjunction with local energy decomposition analysis (LED).

Prior to the spectra computation, a set of DFT functionals consisting of various DFT families is evaluated for their ability to predict the band gap energies of

- 1) the undoped host structures against available experimental data and excited state CC computations employing the similarity transform DLPNO-CCSD (STEOM-DLPNO-CCSD) level of theory.
- 2) the Eu²⁺-doped structures against CASSCF/NEVPT2 method, accounting for spin-orbital coupling (SOC) effect.

This due to the critical role of the lowest excitation band of the Eu²⁺-doped phosphors in determining emission band characteristics,[80] as elucidated in the preceding chapter. Notably, neglecting SOC is a valid approximation when analyzing emission band characteristics within the scope of coarse structure. However, as it was discussed in **Chapter 9** and will be further investigated in **Chapter 13**, SOC plays a pivotal role in understanding the mechanisms governing emission intensity in such phosphors and in fine tuning the emission band broadening. Hence, overall hybrid functionals show the best performance in computing the band gaps in both steps. In particular, PBE0 shows the best agreement between theory and experiment, then it is chosen for the production calculations.

This chapter demonstrates that the extended computational protocol has proven its effectiveness in predicting the optical properties of Eu²⁺-doped phosphors, demonstrating excellent agreement with experimental data. Additionally, the previously established descriptors, which accurately forecast the color and bandwidth of Eu²⁺-doped phosphors, generally hold to find broad applicability in phosphor materials of apparently almost arbitrary complexity. Moreover, it represents a significant advancement toward a more comprehensive understanding and design of luminescent materials.

Indeed, the inclusion of multiple candidate Eu doping centers in the study set further enhances the protocol's applicability, opening up new avenues for systematic exploration of photoluminescence properties in a broader range of phosphor materials. By elucidating the

intricate relationships between electronic structure, emission behavior, and spectral properties, this research contributes to the progress of luminescent materials science and its diverse technological applications. These findings are of paramount importance as they offer new opportunities to control tunability and achieve tailored photoluminescence properties, inspiring the design of novel phosphor materials with unique optical characteristics.

11.2. Study set of Phosphors and Geometrical Properties

Three well-known Eu²⁺-doped UC₄C₄-based phosphors are selected to consist the study set on the basis of the following criteria.

- 1) They are emitting in the wide range between infrared, red, cyan and blue range of the optical spectrum,
- 2) They contain multiple candidate doping centers available for the Eu²⁺ activator ion in a variation of coordination environments and
- 3) They show a variation of emission signals containing a single or multiple bands that show up at various energies and intensities.

In particular, the study set consists of the red and near-infrared emitting Eu²⁺-doped nitridolithoaluminate phosphor CaBa[LiAl₃N₄]₂:Eu²⁺, abbreviated as (CBLA2:Eu²⁺)[124] and is completed by the blue and cyan emitting Eu²⁺-doped alkali lithosilicate phosphors RbNa₃[Li₃SiO₄]₄:Eu²⁺ (RNLSO:Eu²⁺)[331] and RbNa[Li₃SiO₄]₂:Eu²⁺ (RNLSO2:Eu²⁺)[330]. The molecular structures are visualized in **Figure 11.1**. RNLSO adopts the tetragonal (*I4/m*) space group while CBLA2 and RNLSO2 crystalize in the monoclinic (*C2/m*) space group. All host crystal structures adopt a rigid UC₄C₄ structure type with highly condensed tetrahedra networks built by vertex- and edge-sharing tetrahedra. Namely, (Al/Li)N₄ nitride tetrahedra in CBLA2 and (Si/Li)O₄ oxide tetrahedra in both RNLSO and RNLSO2. The tetrahedra network forms *vierer*-ring channels, which could be empty or filled with cations ((Ca²⁺/ Ba²⁺) or (Na⁺/ Rb⁺)). These cations form nitride (Ca²⁺/ Ba²⁺)N₈ or oxide (Na⁺/ Rb⁺)O₈ cuboids, respectively. In RNLSO2 and CBLA2, the occupied channel has only one type of cation, hence along the principle symmetry rotation axis cuboid sequences are formed with (Rb⁺--- Rb⁺--- Rb⁺, Na⁺--- Na⁺--- Na⁺), (Ba²⁺--- Ba²⁺--- Ba²⁺ and Ca²⁺--- Ca²⁺--- Ca²⁺) central cations building units, respectively. In contrast, in the case of RNLSO, Na¹⁺ and Rb⁺ are alternating in the same channel forming cuboid sequences with Na¹⁺--- Rb⁺--- Na¹⁺ (or equivalently Rb⁺--- Na¹⁺--- Rb⁺) central cation building units as well as Na²⁺--- Na²⁺--- Na²⁺ ones. In CBLA2, two

different double chains can be distinguished, one composed solely of AlN_4 tetrahedra and one composed of one *einer* single chain of AlN_4 tetrahedra and one *einer* single chain of LiN_4 tetrahedra.

In **Figure 11.1**, the probable cation sites for Eu^{2+} doping are highlighted. The selection of the doping sites are based on 1) the similarity of their ionic radii (r) with Eu^{2+} [332] and 2) their suitability for Eu^{2+} doping in a host environment that minimizes the steric effects[18, 80]. In fact, as seen in **Table 11.1**, Eu^{2+} doping at Ca^{2+} and Na^+ is expected to form strained EuL_8 (L is $\text{N}^{3-}/\text{O}^{2-}$) cuboids with $\Delta r_{\text{Ca}^{2+}-\text{Eu}^{2+}} = -0.19 \text{ \AA}$ and $\Delta r_{\text{Na}^+-\text{Eu}^{2+}} = -0.07 \text{ \AA}$ and EuL_8 cuboid volume that varies between 29.5 \AA^3 and 30.1 \AA^3 . On the contrary, Eu^{2+} doping at Ba^{2+} and Rb^+ is expected to form rather relaxed EuL_8 cuboids with $\Delta r_{\text{Ba}^{2+}-\text{Eu}^{2+}} = 0.10 \text{ \AA}$ and $\Delta r_{\text{Rb}^+-\text{Eu}^{2+}} = 0.36 \text{ \AA}$ and EuL_8 cuboid volume that varies between 37.6 \AA^3 and 40.5 \AA^3 . In particular, the Eu^{2+} -doped CBLA2 phosphor has two candidate doping centers at Ca^{2+} and Ba^{2+} positions. RNLSO phosphor has three candidate doping centers at Na^+ , Na^{2+} and Rb^+ positions. RNLSO2 phosphor has three candidate doping centers at Na^+ , Na^{2+} and Rb^+ positions. Finally, RNLSO2 phosphor has two candidate doping centers at Na^+ , and Rb^+ positions.

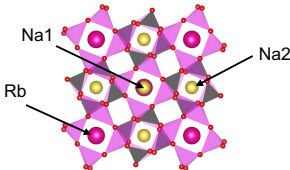
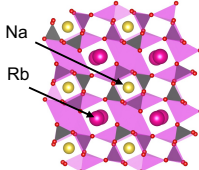
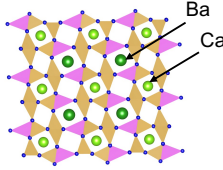
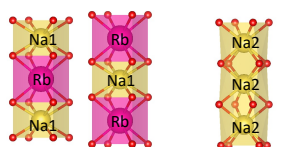
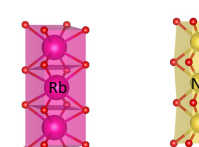
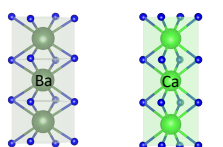
Phosphor's Host	a) Oxide RbNa ₃ [Li ₃ SiO ₄] ₄ RNLSO		b) Oxide RbNa[Li ₃ SiO ₄] ₂ RNLSO2		c) Nitride CaBa [LiAl ₃ N ₄] ₂ CBLA2																																	
Crystal system	Tetragonal		Monoclinic		Monoclinic																																	
Space group	(I4/m)		(C2/m)		(C2/m)																																	
Crystal Structure																																						
Doping centers																																						
Bond length	<table><tr><td>Rb-Na1</td><td>3.20 Å</td></tr></table> <table><tr><td>Rb-O</td><td>3.00 Å</td></tr><tr><td>Na1-O</td><td>2.70 Å</td></tr></table> <table><tr><td>Na2-Na2</td><td>3.15 Å</td></tr><tr><td>Na2-O1</td><td>2.45 Å</td></tr><tr><td>Na2-O2</td><td>2.75 Å</td></tr></table>		Rb-Na1	3.20 Å	Rb-O	3.00 Å	Na1-O	2.70 Å	Na2-Na2	3.15 Å	Na2-O1	2.45 Å	Na2-O2	2.75 Å	<table><tr><td>Rb-Rb</td><td>3.20 Å</td></tr><tr><td>Rb-O</td><td>3.00 Å</td></tr></table> <table><tr><td>Na-Na</td><td>3.20 Å</td></tr><tr><td>Na-O</td><td>2.55 Å</td></tr></table>		Rb-Rb	3.20 Å	Rb-O	3.00 Å	Na-Na	3.20 Å	Na-O	2.55 Å	<table><tr><td>Ba-Ba</td><td>3.31 Å</td></tr><tr><td>Ba-N1</td><td>2.83 Å</td></tr><tr><td>Ba-N2</td><td>2.96 Å</td></tr></table> <table><tr><td>Ca-Ca</td><td>3.30 Å</td></tr><tr><td>Ca-N1</td><td>2.65 Å</td></tr><tr><td>Ca-N1</td><td>2.73 Å</td></tr></table>		Ba-Ba	3.31 Å	Ba-N1	2.83 Å	Ba-N2	2.96 Å	Ca-Ca	3.30 Å	Ca-N1	2.65 Å	Ca-N1	2.73 Å
Rb-Na1	3.20 Å																																					
Rb-O	3.00 Å																																					
Na1-O	2.70 Å																																					
Na2-Na2	3.15 Å																																					
Na2-O1	2.45 Å																																					
Na2-O2	2.75 Å																																					
Rb-Rb	3.20 Å																																					
Rb-O	3.00 Å																																					
Na-Na	3.20 Å																																					
Na-O	2.55 Å																																					
Ba-Ba	3.31 Å																																					
Ba-N1	2.83 Å																																					
Ba-N2	2.96 Å																																					
Ca-Ca	3.30 Å																																					
Ca-N1	2.65 Å																																					
Ca-N1	2.73 Å																																					
Local Symmetry	Elongated (Rb) Compressed (Na) C _{2h}		Elongated Compressed C _{2h}		Elongated Compressed D _{4h}																																	

Figure 11.1. The crystal structure and the space group of the studied phosphors' hosts: RNLSO, RNLSO2, and CBLA2. The probable cationic doping site for each structure, together with the most important bond lengths, and symmetry labels around the probable sites are also provided. Atom colors: Rb (dark red), Na (yellow), Ca (light green), Ba (deep green), Si (dark gray), Al (yellowish pink), Li (pink), N (blue), O (red).

Table 11.1. Structural and geometrical information of selected phosphors including the host crystal space group, cuboid ML_8 , ($\text{L} = \text{N}$ or O) at the different candidate doping centers for CBLA2 ($\text{M}=\text{Ba}^{2+}$ or Ca^{2+}), RNLSO ($\text{M}=\text{Rb}^+$, Na^{1+} or Na^{2+}) and RNLSO2 ($\text{M}=\text{Rb}^+$ or Na^+) in terms of ($\text{M}^{\text{m}+}$) ion ionic radius r and in parentheses (Δr), all in Å. Δr is the difference in ionic radii between replaced ion $\text{M}^{\text{m}+}$ and Eu^{2+} , where, the ionic radius of $\text{Eu}^{2+} = 1.25$ Å at cuboid 8-fold coordination.[332] In addition to average M/Eu-L bond distances and the first coordination shell cationic compositions.

Phosphor	Host Crystal Space	Doping Site ($\text{M}^{\text{m}+}$)	$r[332]$ (Δr) (Å)	L	(Avg.) M/Eu-L bond distance (Å)	Volume of ML_8 cuboid (Å ³)	First shell cations
CaBa[Li ₂ Al ₆ O ₈]:Eu ²⁺ CBLA2	<i>C2/m</i>	Ba ²⁺	1.35 (+0.10)	N	2.90	37.60	[Li ₄ Al ₄] ¹⁶⁺
		Ca ²⁺	1.06 (-0.19)	N	2.70	29.50	[Al ₈] ²⁴⁺
RbNa ₃ [Li ₃ SiO ₄] ₄ :Eu ²⁺ RNLSO	<i>I4/m</i>	Rb ⁺	1.61 (+0.36)	O	3.00	40.00	[Li ₈] ⁸⁺
		Na ¹⁺	1.18 (-0.07)	O	2.70	30.17	[Li ₈] ⁸⁺
		Na ²⁺	1.18 (-0.07)	O	2.60	30.61	[Li ₄ Si ₄] ²⁰⁺
RbNa[Li ₃ SiO ₄] ₂ :Eu ²⁺ RNLSO2	<i>C2/m</i>	Rb ⁺	1.61 (+0.36)	O	3.00	40.50	[Li ₄ Si ₄] ²⁰⁺
		Na ⁺	1.18 (-0.07)	O	2.60	29.45	[Li ₈] ⁸⁺

As shown in **Figure 11.1**, CBLA2 is isotypic to RNLSO2, hence Eu^{2+} doping at Ca^{2+} and Ba^{2+} centers form compressed and elongated EuN_8 cuboids of C_{2h} symmetry with average bond

distances of (Ca/Eu)-N 2.65-2.75 Å and (Eu/Ca)-Ca 3.30 Å while, (Eu/Ba)-N 2.83-2.96 Å and (Eu/Ba)-Ba is 3.31 Å. These cuboids deviate by only 1-2% from ‘ideal’ D_{4h} symmetry. In the case of RNLSO Eu²⁺ doping at Na1⁺ or Rb⁺ centers form compressed and elongated EuO₈ cuboids of C_{2h} symmetry respectively with average bond distance of (Na1/Eu)-O ~ 2.71 Å, (Rb/Eu)-O ~ 3.01 Å. In contrast, Eu²⁺ doping at Na2⁺ centers forms compressed cuboids of D_{2d} symmetry with (Na2/Eu)-O 2.45-2.75 Å. Similarly, in the case of RNLSO2 Eu²⁺ doping at Na1⁺ or Rb⁺ centers form compressed and elongated EuO₈ cuboids of C_{2h} symmetry respectively with average bond distance of (Na/Eu)-O 2.55 Å and (Rb/Eu)-O 3.00 Å. In this system, Rb⁺ ions are not perfectly aligned in straight lines, reducing the possible inter cubic Eu²⁺ - Rb⁺ interactions.

11.3. Experimental Results

The experimental absorption and emission spectra of the nitride (CBLA2)[124] and oxide (RNLSO and RNLSO2)[330, 331] Eu²⁺-doped phosphors are shown in **Figure 11.2**. The absorption spectra show broad bands and shift towards higher energies in the sequence CBLA2 (15000-25000 cm⁻¹) to RNLSO2 (22000-40000 cm⁻¹), and RNLSO (24000-40000 cm⁻¹). Upon applying a laser excitation all studied cases show a main emission narrow band that shifts also towards higher energies in the same sequence.

In particular, CBLA2:Eu²⁺ upon excitation with a 444 nm laser, exhibits an intense, narrow red emission band at 639-636 nm (15650–15723 cm⁻¹) with FWHM 48-57 nm (~1095-1266 cm⁻¹) and a weak broad infrared (IR) emission band at 790 nm (12660 cm⁻¹) and FWHM ~89 nm (~1430 cm⁻¹). The intensity of the later band improves with increase of the Eu²⁺ doping concentration. The two bands have been assigned to emission from Eu²⁺-doped centers at Ba²⁺ and Ca²⁺ positions, respectively.[124] On the contrary, RNLSO:Eu²⁺ upon excitation with a 400 nm laser exhibits a unique narrow blue emission band at 471 nm (21230 cm⁻¹) with FWHM 22.5 nm (~1015 cm⁻¹).[331] In the case of RNLSO2 two bands show up when a variety of excitation lasers in the 400 nm region is employed.[330] A high intensity narrow green emission band at 523 nm (19120 cm⁻¹) with FWHM 40 nm (~1465 cm⁻¹) shows up. A second weaker intensity cyan emission band shows up at higher energies (472 nm, 21185 cm⁻¹). These bands have been ascribed to Eu²⁺-doped centers at Na⁺ and Rb⁺ positions, respectively, while

it has been shown that their relative intensity varies with the Eu^{2+} doping concentration at the Na^+ and Rb^+ positions.[331, 439]

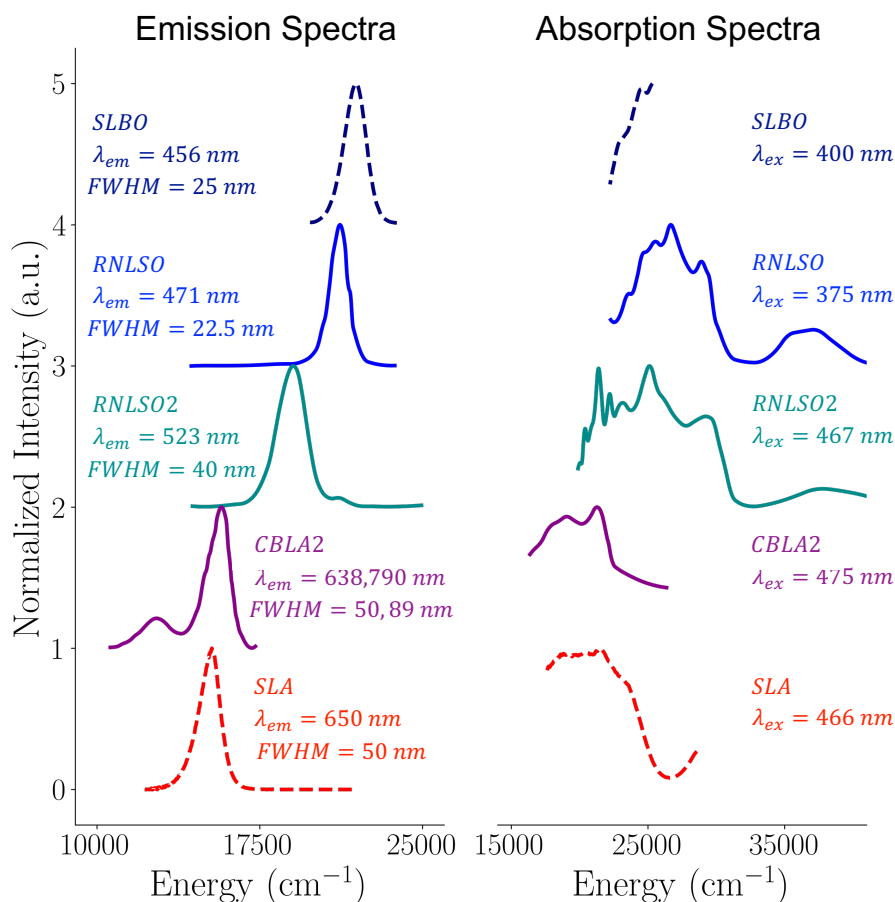


Figure 11.2. Experimental emission (left) absorption (right) spectra of Eu^{2+} -doped phosphors with multiple doping centers (RNLSO in solid blue, RNLSO2 in solid dark-cyan and CBLA in solid dark-magenta) compared with previously studied very well-known phosphors (nitride SLA phosphor in dotted red, and oxide SLBO phosphor in dotted navy-blue).

As seen in **Figure 11.2**, the study set of phosphors lies between the absorption and emission characteristics of two well-known narrow band phosphors, namely the red emitting nitride $\text{SLA}:\text{Eu}^{2+}$ [329] and the blue emitting oxide $\text{SLBO}:\text{Eu}^{2+}$ [126] phosphors. While $\text{SLBO}:\text{Eu}^{2+}$ contains a single doping site for Eu doping, in $\text{SLA}:\text{Eu}^{2+}$ there are in principle two doping candidate sites. The two sites have similar local geometric structure but they are not identical. Hence while at room temperature within the experimental resolution the two sites provide

similar absorption spectra and emission spectra[80] it has been recently shown that at low temperature they provide unique emission bands signatures in the vibrationally resolved emission spectrum.[440] These phosphors define the lower and upper boundaries of a range of Eu²⁺doped phosphors in which the crystal field strength as well as the Eu/ML₈ cuboid compression is increasing.[80] It should be noted that the actual bottom boundary in the Eu²⁺-doped phosphors is defined by the narrow band red emitting Ca[LiAl₃N₄]:Eu²⁺ (CLA: Eu²⁺) phosphor.[326] As seen the CBLA2: Eu²⁺ emission spectrum is blue shifted by +300 cm⁻¹ with respect to the SLA:Eu²⁺ one, showing similar bandwidth range, FWHM~50 nm (1090 cm⁻¹). Likewise, the RNLSO:Eu²⁺ emission spectrum is red shifted by 700 cm⁻¹ with respect to the SLBO:Eu²⁺ one, showing again a similar bandwidth range in the ultranarrow band regime, FWHM~22-25 nm (1010-1220 cm⁻¹). RNLSO2 lies in between the above described cases indicating that complex phosphors with multiple candidate doping centers might still show linear property characteristics like the single doping center phosphors.

To conclude this part, while RNLSO:Eu²⁺ show unique blue emission band. RNLSO2:Eu²⁺ show a predominant cyan emission band and a higher energy and weaker intensity blue emission bands that are tunable by the excitation laser (compare experimental single and multiple peaks emission bands of spectra shown in **Figure 11.10** and **Figure 11.11**, respectively). The isotypic to RNLSO2:Eu²⁺, CBLA2:Eu²⁺ show besides the main red emission band a broad IR band. In principle the presence of a second or multiple bands besides the main emission band is undesirable in the novel phosphors design efforts as they may reduce effectively their brightness, performance and efficiency. While in the case of RNLSO2:Eu²⁺ the higher energy, second weaker intensity blue emission band is tunable by the choice of the laser excitation energy, [330] the IR band in CBLA2:Eu²⁺ can only be suppressed at low Eu²⁺ doping concentrations. [124] This emphasizes the urgent need for advancing the information content of the emission intensity mechanism in these materials. The next sections are dedicated to a non-standard routine computational strategy towards designing phosphors with desired photoluminescence properties.

11.4. Electronic Structure Analysis. Insights into the Emission mechanism of multiple doping centers

The electronic structure principles that determine the emission properties of Eu^{2+} -doped phosphors have been previously discussed in detail in **Section 9.4**. Here, we will briefly recapitulate them and expand the discussion to cover multiple doping centers.

As shown in **Scheme 9.1**, The free Eu^{2+} ion has a very stable octet ground state with a half-filled f-shell (GS) $^8\text{S}_{7/2} (4\text{f}^7 5\text{d}^0)$. Upon excitation, an electron is excited to the empty 5d orbitals via spin-conserving one-electron excitations $^8\text{S}_{7/2} (4\text{f}^7) \rightarrow ^7\text{F} \otimes ^2\text{D} (4\text{f}^6 5\text{d}^1)$. While these transitions are located at somewhat high energies, (e.g. the atomic spectroscopic ^8H term ($4\text{f}^6 5\text{d}^1$) is located at about 4.2 eV), they are both parity and spin allowed. Hence, these are intense transitions that are highly tunable by the environment given the strong interaction of the outer 5d-orbital shell with the ligand framework.[80]

When Eu^{2+} is doped in 8-fold coordinated host environments, in accord with Hund's rule the interelectronic repulsion stabilizes the highest multiplicity ($2S+1=8$) excited state multiplets of the $4\text{f}^6 5\text{d}^1$ configuration over the $2S+1=8$ $4\text{f}^7 5\text{d}^0$ ground state multiplets. In addition, the cubic ligand field splitting will lift the degeneracy of the 4f and 5d orbitals in an inverted octahedral order ($\Delta_{\text{cubic}} = -8/9\Delta_{\text{Oh}}$) leading to a ground state electron configuration ($\text{t}_{2\text{u}}^3 \text{t}_{1\text{u}}^3 \text{a}_{2\text{u}}^1 \text{e}_{\text{g}}^0 \text{t}_{2\text{g}}^0$) of the ($4\text{f}^7 5\text{d}^0$) shells. Further distortions towards tetragonal/trigonal ligand fields will lift any remaining orbital degeneracies and consequently the ground and excited state degeneracies. As has been explored in detail here[80] and in preceding chapter, quantities like the ligand field splitting, band gap energies and Stokes shifts are important quantities of the absorption and emission processes as they can be employed to determine the energy position and the bandwidth of the different spectral features.

Within the 1-electron picture these quantities can be collectively represented by the ligand field splitting ΔE_{LF} and the f-d energy separation ΔE_{fd} and Stokes shift ΔE_{S} . As shown in detail, in **Figure 11.3** and **Figure 11.4**, across the study set a collection of $\text{Eu}(\text{N/O})_8$ cuboids may form at the various doping positions. All the cuboids are distorted from the ideal cubic symmetry which significantly affects the nature of the involved absorption and emission processes.

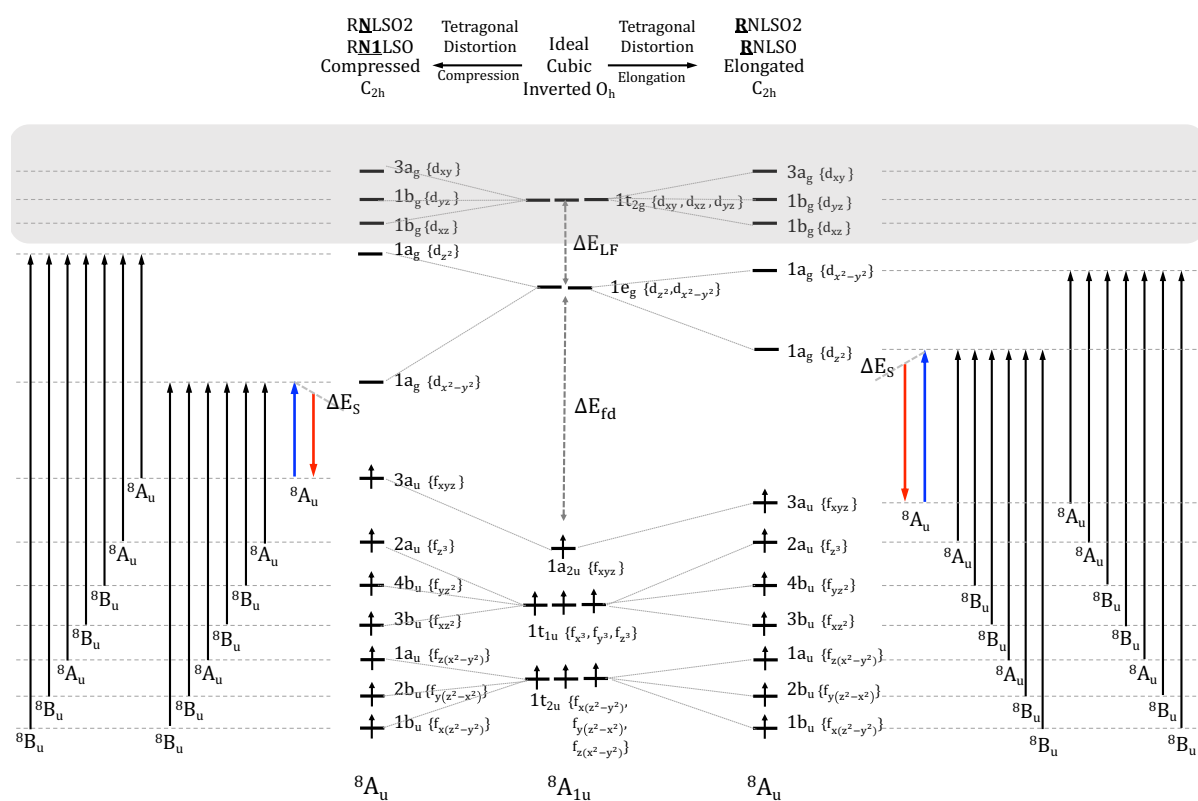
In the case of CBLA, doping at Ba^{2+} center forms a tetragonally elongated ($\text{D}_{4\text{h}}$) EuN_8 cuboid. This leads to absorption and emission processes consisting from the z-polarized dipole allowed $\text{Eu } 4\text{f}_{z^3} \leftrightarrow \text{Eu } 5\text{d}_{z^2}$ electron transitions and decays. In contrast, doping at Ca^{2+} center

leads to a strongly tetragonally compressed (D_{4h}) EuN_8 cuboid (**Table 11.1**). As shown in **Table A. 3**, in comparison to the tetragonally elongated cuboids the ΔE_{LF} is increased while the ΔE_{fd} is decreased rather strongly leading to red-shifted absorption and emission processes consisting from the dipole forbidden $\text{Eu } 4f_{xyz} \leftrightarrow \text{Eu } 5d_{x^2-y^2}$ electron transitions and decays. This is not surprising as in fact the color of the phosphors is associated by the predominant $\text{Eu} - 4f \leftrightarrow \text{Eu} - 5d$ transition.[80]

A similar picture is observed in the case of $\text{RNLSO}:\text{Eu}^{2+}$ and $\text{RNLSO}_2:\text{Eu}^{2+}$ when Eu^{2+} is doped at Rb^+ and $\text{Na}^{1+}/\text{Na}^+$ positions. In particular, doping at Rb^+ positions forms tetragonally elongated (C_{2h}) EuO_8 cuboids. This leads to absorption and emission processes consisting from the z-polarized dipole allowed $\text{Eu } 4f_{z^3} \leftrightarrow \text{Eu } 5d_{z^2}$ electron transitions and decays. In contrast, doping at $\text{Na}^{1+}/\text{Na}^+$ positions leads to tetragonally compressed (C_{2h}) EuO_8 cuboids. Once again in comparison to the elongated EuO_8 cuboids the ΔE_{LF} is increased while the ΔE_{fd} is decreased, as shown in **Table A. 3**, leading to red-shifted absorption and emission processes consisting from dipole allowed $\text{Eu } 4f_{xyz} \leftrightarrow \text{Eu } 5d_{x^2-y^2}$ electron transitions and decays. In the case of $\text{RNLSO}:\text{Eu}^{2+}$ when Eu^{2+} is doped at Na^{2+} position a tetragonally compressed (D_{2d}) EuO_8 cuboid is formed. In comparison to the tetragonally compressed (C_{2h}) EuO_8 cuboids when Eu^{2+} doping occurs at the Na^{1+} positions the ΔE_{LF} and ΔE_{fd} are further increased and decreased, respectively, as shown in **Table A. 3**.

As a result, further red-shifted absorption and emission processes are observed which consist however of dipole forbidden $\text{Eu } 4f_{xyz} \leftrightarrow \text{Eu } 5d_{x^2-y^2}$ electron transitions and decays (**Figure 11.3**).

Qualitatively, the above analysis suggests that the blue-shifted main intensity band as well as the red-shifted low intensity band of $\text{CBLA}:\text{Eu}^{2+}$ originates from Eu^{2+} doping at Ba^{2+} and Ca^{2+} position, respectively. Similarly, in the case of $\text{RNLSO}:\text{Eu}^{2+}$ and $\text{RNLSO}_2:\text{Eu}^{2+}$ emissions are expected to increase in energy in the sequence of the Na^{2+} , Na^{1+} and Rb^+ doping positions. Among them the Na^{2+} positions are the least probable as they are associated with dipole forbidden transitions (**Figure 11.4**).



169

environments a) D_{4h} for CBLA: Eu^{2+} and b) C_{2h} for RNLSO: Eu^{2+} and RNLSO2: Eu^{2+} . The involved electronic transitions consisting the absorption and emission processes are adopted with the 1-electron picture. Blue and red arrows indicate the most important absorption and relevant emission processes, respectively. Dotted arrows indicate dipole forbidden transitions. ΔE_{LF} , ΔE_{fd} and ΔE_{S} , represent the ligand field splitting of Eu 5d, the energy separation between barycenters of Eu 4f-5d manifolds, and the expected Stocks shift, respectively.

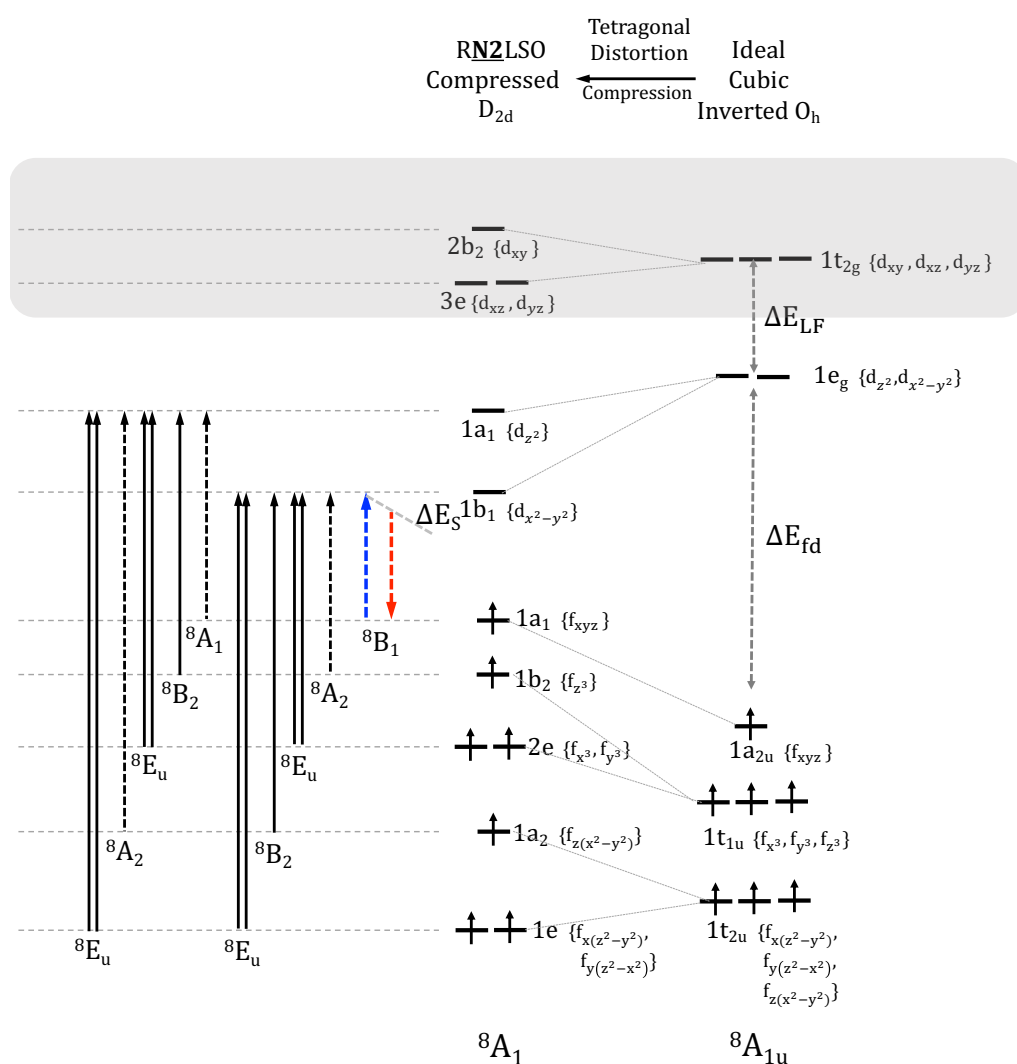


Figure 11.4. Molecular orbital diagram of the case of RNLSO: Eu^{2+} in which the Eu^{2+} -doped at the Na^{2+} positions form D_{2d} tetragonally compressed EuO_8 cuboids. The involved electronic transitions consisting the absorption and emission processes are adopted with the 1-electron picture. Solid and blue arrows indicate the most important absorption processes. Red arrows indicate the relevant emission processes. Dotted arrows indicate dipole forbidden transitions.

11.5. Computational Details

Since this research is an extension to the computational protocol that is previously introduced in **Chapter 10, Sections 10.4-10.5**. So, in this work, for the new class of Eu²⁺-doped phosphors, we will use the same computational methods, procedure. So, the most important points are only highlighted.

- All calculations were performed employing the ORCA 5.0 suite of programs.[354, 355, 411, 412] Crystal structures' coordinates of new hosts (CBLA2, RNLSO2, RNLSO) were taken from the crystallographic data,[124, 330, 331] refined based on the experimental crystallographic X-ray diffraction.
- The optical band gap of the host structures were calculated utilizing STEOM-DLPNO-CCSD[416, 417] as well as TD-DFT[237] methods. In the latter, a collection of DFT functionals were chosen, belonging to the GGA: PBE,[226] hybrid: PBE0,[227, 234, 235] range separated hybrid: CAM-B3LYP,[441] double hybrid: B2PLYP,[236] and range separated double hybrid: ω B2PLYP[442] families.
- TD-DFT, employing the same mentioned functionals were employed to compute the band gap energies of the Eu²⁺-doped structures.
- As we will see later, PBE0 functional give best result for calculation band gap of both host and doped structures. The Eu²⁺ doping energies at different candidate sites were computed at DFT/PBE0 and DLPNO-CCSD(T) levels of theory.[201, 205, 443] DLPNO-CCSD(T) doping energies were decomposed into a chemically meaningful energies on the basis of local energy decomposition (LED) approach[149, 414] starting from quasi-restricted (QRO)[396] Kohn Sham (KS) orbitals.
- TD-DFT, employing the same motioned functionals, as well as complete active space (SA-CASSCF) [169, 184] method in conjunction with second order N-electron valence state perturbation theory (NEVPT2) [193, 395] including spin-orbit coupling (SOC) were employed to compute the band gap energies of the Eu²⁺-doped structures.
- Preliminary calculations for estimating the multi-root nature of the Eu²⁺-doped phosphors emission process and the effect of the SOC and spin state energetics of the emission bands were performed employing the SA-CASSCF(7,19)/NEVPT2/SOC. As discussed in next **Section 11.6** the SOC interactions do not significantly influence the emission band energy positions, hence they were excluded from the production calculations.

- As discussed in **Section 11.6**, based on these results the TD-DFT/PBE0 was chosen for the production calculations of optical properties. At different Eu^{2+} doping sites, absorption and emission spectra were computed at the TD-DFT/PBE0 and TD-DFT/PBE0/ESD, respectively, with the same setup as discussed in **Section 10.4**.

11.5.1. Construction of the Cluster Models

All cluster models were constructed on the basis of the embedded cluster approach, [83, 84, 141, 421], as discussed in **Section 10.4**, illustrated in **Figure 7.1** and following the general protocol presented in **Section 7.3**. The series of the chosen cluster models consist of sequences of cuboid structures ranging from monomers to pentamers. Further information about the employed cluster models is provided in **Figure 11.5** and **Table A. 4**.

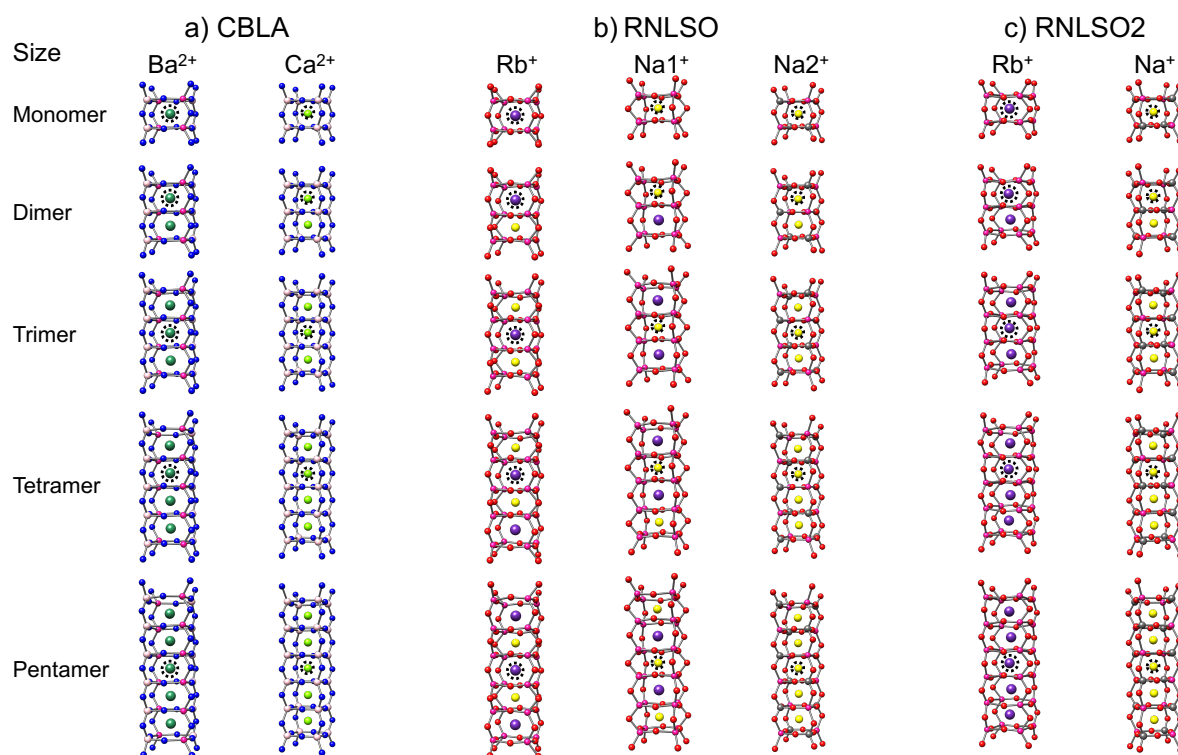


Figure 11.5. All cluster models (QCs) for a) CBLA (Ca^{2+} and Ba^{2+} channels), b) RNLSO (Rb^+ , Na^{1+} , Na^{2+} channels), c) RNLSO2 (Rb^+ , Na^+). Different sized models named with respect to number (n) of the central metal ion (Ca^{2+} , Ba^{2+} , Rb^+ , Na^+) in the cluster as (Monomer, Dimer, Trimer, Tetramer, Pentamer for $n=1, 2, 3, 4, 5$, respectively). The Eu^{2+} doping site is indicated with dotted black circle around the ion that will be replaced by Eu^{2+} . Atom colors: Eu (cyan), Rb (purple), Na (yellow), Ca (light green), Ba (deep green), Si (dark gray), Al (yellowish pink), Li (pink), N (blue), O (red).

11.6. Computational considerations.

As is discussed in detail in **Appendix A.2** (*cluster size convergence – choice of the computational protocol*), initially the cluster size convergence was evaluated on the basis of the band gap energies of the host structures. For this purpose, the band gaps (E_g) energies were computed at the STEOM-DLPNO-CCSD and TD-DFT levels of theory. In particular for the later, a selection of density functionals was chosen from the GGA, hybrid, range separated hybrid, double hybrid and range separated double hybrid families, respectively. The lowest excitation energies, for all employed functionals, were converged at the trimer cluster size. In the case of the CBLA2 clusters the lowest excitation energy (optical E_g) is observed for the clusters containing Ba^{2+} centers while in the case of RNLSO and RNLSO2 clusters the lowest excitation energy (optical E_g) is observed for the clusters containing Na^+ centers. As has been observed previously[80, 84] the STEOM-DLPNO-CCSD shows the best performance in computed experimental band gaps. In fact, the mean absolute errors (MAE) in the case of RNLSO and RNLSO2 drop below 0.03 eV in comparison to the available experimental data. In contrast in the case of TD-DFT calculations employing different functionals the computed MAE values decrease in the sequence PBE, PBE0, CAM-B3LYP, B2PLYP and ω B2PLYP (MAE=4.6, 3.1, 2.4, 3.0, and 1.9 eV, respectively). This general failure of TD-DFT to computed the band gap energies of these systems is not surprising[444] as in fact they reflect non-rigid $\text{O}^{2-} - 2p \rightarrow \text{Na}^+ - 3s$ (for RNLSO and RNLSO2) and $\text{N}^{3-} - 2p \rightarrow \text{Ba}^{2+} - 5d$ (for CBLA2) ligand to metal charge transfer (LMCT) transitions. For RNLSO (at central Na^{1+} which give the lowest excitation energy among other sites), this is collectively shown in **Figure 11.6**.

In a next step we compute the first excitation energies of the Eu^{2+} -doped phosphors at the various doping centers at the TD-DFT and the SA-CASSCF(7,19)/NEVPT2 levels of theory employing the monomer clusters. In these calculations the active space is expanded to include besides the 4f5d shells the 5f-shell owing to its overlap with the 5d as discussed in **Section 9.1.1**. The results are presented in **Table A. 6**. In sharp contrast, with the band gap energy computations on the undoped phosphors, in particular the hybrid functionals (PBE0, CAM-B3LYP) show noticeable smaller deviations when compared against the SA-CASSCF(7,19)/NEVPT2 computed values, MAE \sim 500-700 cm^{-1} (0.06-0.09 eV). This is due to the different nature of the probed transition. In the case of the undoped phosphors the transitions that dominate the band gap energies are of LMCT character while in the case of the Eu^{2+} -doped ones they have a rigid $4f \rightarrow 5d$ character.

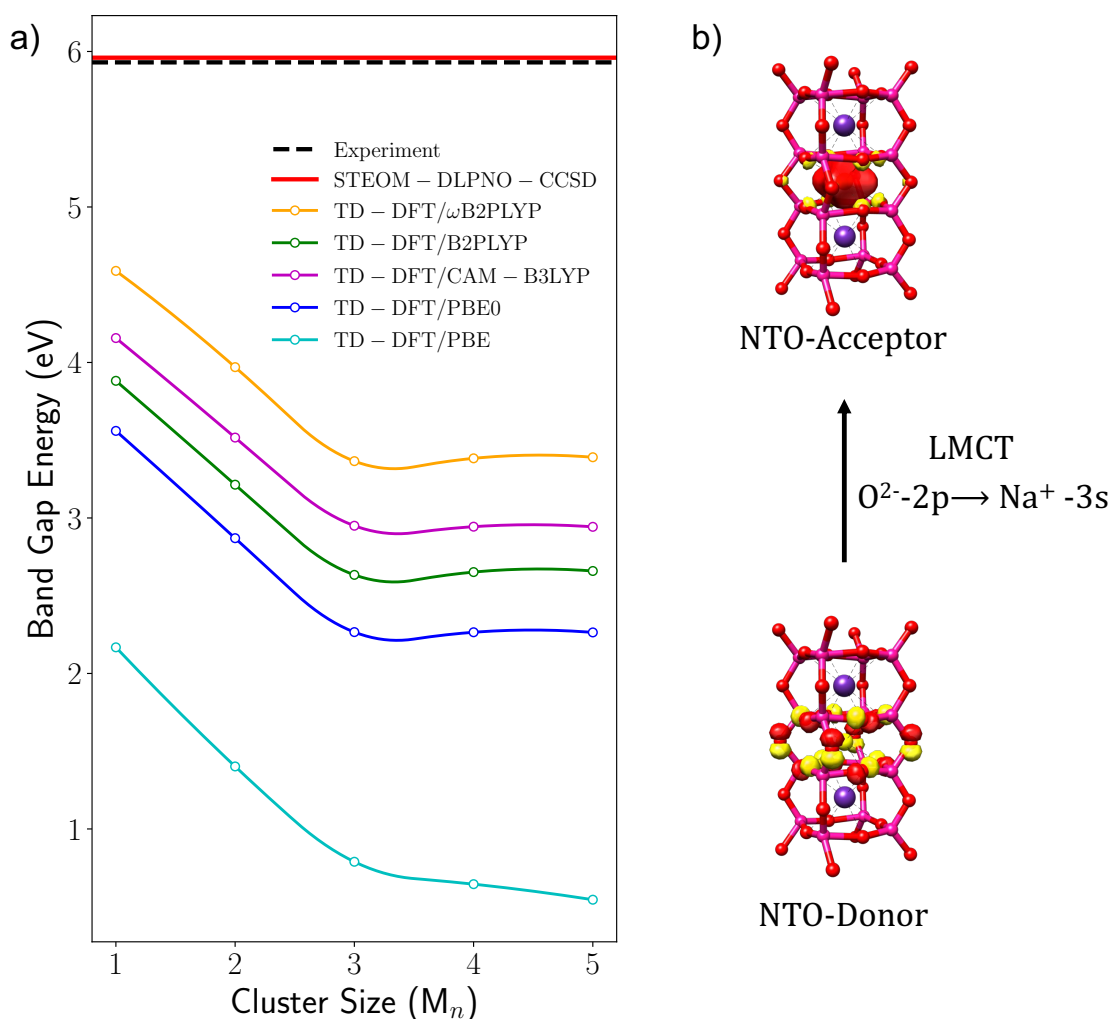


Figure 11.6. a) Experimental (black) and calculated optical band gap, E_g (eV) with TD-DFT/PBE (cyan), PBE0 (blue), CAM-B3LYP (pink), B2PLYP (green) and ω B2PLYP (orange) at different size of undoped QC clusters (1: monomer, 2: dimer, 3: trimer, 4: tetramer, 5: pentamer) and with STEOM-DLPNO-CCSD (red) only at the trimer cluster for RNLSO. b) The nature of the first excitation in RNLSO at central Na^{1+} based on NTO analysis. Note: for STEOM-DLPNO-CCSD, monomer, dimer, and trimer clusters exhibit nearly identical E_g values (refer to **Figure A. 4b**), while larger clusters (tetramer, pentamer), present challenges in computation due to resource limitations.

In a following step, based on its performance the PBE0 hybrid functional is employed to compute the absorption spectra of the study set of the Eu^{2+} -doped phosphors in the sequence monomer to pentamer clusters shown in **Figure 11.5**. The results are presented in **Figure A. 5** showing once again that in all studied cases the TD-DFT/PBE0 computed spectra converge for the trimer cluster size. Provided that the spectra are shifted by $\sim 500 - 700 \text{ cm}^{-1}$, the computed spectra are also in satisfactory visual agreement to experiment in terms of the number and the relative intensities of the computed bands.

In an effort to investigate the influence of spin-orbit coupling SOC effects in the emissive states of $4f^6 5d^1$ excited configuration, preliminary results on the CBLA2 cuboids (**Figure A. 6**) showed that at the relativistic limit the $4f^6 5d^1$ multiplet splits by about $\sim 600\text{-}1100 \text{ cm}^{-1}$ which is consistent with the atomic Eu^{2+} SOC constant (1200 cm^{-1} calculated employing ab initio ligand field theory[137, 139, 182, 183] ($4f^6 5d^1$)). It is also consistent with the previous results on $[\text{EuN}_8\text{H}_{24}]^{2+}$ model structure, where it was obvious that for $4f^6 5d^1$ excited states the local environmental effect dominates the SOC effects, as discussed in **Section 9.3**. While this state splitting can influence the magnetic nature of the emissive multiplet and fine tune the narrow band width has only limited impact to the emissive band energy position. Hence for the time being SOC effects were excluded from the production calculations.

Collectively, on the basis of the above results and in an effort to stay consistent with our previous study on narrow band Eu^{2+} -doped phosphors,[80] in the following sections the trimer structures are chosen for the production calculations and analysis of the absorption and emission processes employing the TD-DFT/PBE0 computational protocol in conjunction with the excited state dynamics (ESD).

11.7. Finding the most doping probable site for Eu^{2+} (Doping Descriptor)

Prior entering the spectra computation and analysis sections, the major question that arises is how probable to Eu^{2+} doping is each of the Ca^{2+} , Ba^{2+} , Na^+ / Na1^+ / Na2^+ and Rb^+ host positions in the study set of CBLA and RNSLO and RNSLO2 phosphors. To answer this question, we employ DFT/PBE0 as well as DLPNO-CCSD(T) followed by a local energy decomposition analysis (LED) levels of theory.

In this concept the doping energy $\Delta E_{\text{Doping}}^{\text{CCSD(T)}}$ is computed according to **Equation (11.1)**

$$\begin{aligned}
 \Delta E_{\text{Doping}}^{\text{CCSD(T)}} &= \Delta E_{\text{Doped-str.}}^{\text{CCSD(T)}} - \delta \Delta E_{\text{Host}}^{\text{CCSD(T)}} \\
 &= \left[E_{\text{Doped-Str.}}^{\text{CCSD(T)}} - E_{\text{Ligand}}^{\text{CCSD(T)}} - E_{\text{free-Eu}^{2+}}^{\text{CCSD(T)}} \right] \\
 &\quad - \delta \left[E_{\text{Host}}^{\text{CCSD(T)}} - E_{\text{Ligand}}^{\text{CCSD(T)}} - E_{\text{free-M}^{m+}}^{\text{CCSD(T)}} \right]
 \end{aligned} \tag{11.1}$$

where $\Delta E_{\text{Doped-str.}}^{\text{CCSD(T)}}$, $\Delta E_{\text{Host}}^{\text{CCSD(T)}}$ are total interaction in doped and host (undoped) structures, respectively. They are expressed in terms of the following energy quantities;

- 1) the energy of embedded Eu^{2+} -doped structure ($E_{\text{Doped-Str.}}^{\text{CCSD(T)}}$),
- 2) the energy of the embedded host structure ($E_{\text{Host}}^{\text{CCSD(T)}}$),
- 3) the energy of the embedded host structure without the M^{m+} ion ($E_{\text{Ligand}}^{\text{CCSD(T)}}$),
- 4) the energy of the free Eu^{2+} ($E_{\text{free-Eu}^{2+}}^{\text{CCSD(T)}}$), and
- 5) the energy of the free M^{m+} ions ($E_{\text{free-M}^{m+}}^{\text{CCSD(T)}}$). δ , is a coefficient introduced to compensate charge change during Eu^{2+} doping and equals ($\text{charge}_{\text{Eu}^{2+}} - \text{charge}_{\text{M}^{m+}} + 1$), giving $\delta = 1$ for $\text{Ca}^{2+}/\text{Ba}^{2+}$ and 2 for $\text{Na}^{+}/\text{Rb}^{+}$.

The results for the different doping centers in CBLA and RNSLO and RNSLO2 are provided in **Table 11.2**. Focusing on the DLPNO-CCSD(T) results in the case of CBLA Eu^{2+} doping at Ba^{2+} centers provides more stable structures with respect to Eu^{2+} doping at Ca^{2+} centers by 3 eV. In RNLISO, Eu^{2+} doping at (Rb^{+} , Na^{1+}) centers provide similar DLPNO-CCSD(T) doping energies (-1.66, -1.32 eV) while Eu^{2+} doping at Na^{2+} provides rather less stable structures (-0.88 eV). Similarly, in RNLISO2 Eu^{2+} doping at Rb^{+} centers provides more stable structures with respect to Eu^{2+} doping at Na^{+} centers by ~ 2.5 eV. The DFT computed doping energies show qualitatively similar trends to DLPNO-CCSD(T). Not surprisingly the DFT results are however somewhat unbalanced as for example they predict a positive doping energy position for the Ca^{2+} doping sites in CBLA and a rather overstabilization of the Rb^{+} doping positions with respect to the Na^{+} ones in RNLISO and RNLISO2. Similar imbalances have been observed in the case of RNSLO2.[330] Hence the DLPNO-CCSD(T) results are chosen for further analysis.

Table 11.2. Eu^{2+} doping energies for RNLSO, RNLSO2 and CBLA at the different candidate doping centers of trimers clusters computed at DFT(PBE0) and DLPNO-CCSD(T) methods.

Phosphor	Doping site	Doping Energy (eV)	
		PBE0	DLPNO-CCSD(T)
CaBa[Li ₂ Al ₆ O ₈]:Eu ²⁺	Ba ²⁺	-1.62	-3.67
CBLA	Ca ²⁺	1.65	-0.67
RbNa ₃ [Li ₃ SiO ₄] ₄ :Eu ²⁺	Na1 ⁺	-2.55	-1.32
	Na2 ⁺	-2.09	-0.88
	Rb ⁺	-4.42	-1.66
RNLSO			
RbNa[Li ₃ SiO ₄] ₂ :Eu ²⁺	Na ⁺	-2.14	-0.87
RNLSO2	Rb ⁺	-4.51	-3.34

11.7.1. Understanding the Eu^{2+} doping in the framework of DLPNO-CCSD(T)/LED analysis

Entering the LED analysis, the DLPNO-CCSD(T) computed doping energies are decomposed into a set of chemically and physically meaningful inter- and intra-fragment contributions between the Eu^{2+} doped center and the host cuboid environment. This analysis is used below in an afford to shed light on

- 1) the type of interactions encountered by Eu^{2+} per doping site and
- 2) the favorable doping scheme that is followed by each phosphor in the study set.

As is presented with black bars in **Figure 11.7**, in the framework of LED, the doping energy ($\Delta E_{\text{Doping}}^{\text{CCSD}(T)}$), for all studied systems at different probable Eu^{2+} doping centers, are calculated as the difference in binding energy (ΔE_{int}) between Eu^{2+} -doped structure and host, taking into account charge compensation coefficient (δ) as following **Equation (11.1)**. (ΔE_{int}) in each structure is decomposed in reference DFT/PBE0 contributions ($\Delta E_{\text{int}}^{\text{REF}}$) and correlation contributions ($\Delta E_{\text{int}}^{\text{C}}$) and reads as follows in **Equation (11.2)**

$$\Delta E_{int} = \Delta E_{int}^{REF} + \Delta E_{int}^C \quad (11.2)$$

ΔE_{int}^{REF} is the sum of three contributions, namely the electronic preparation, the electrostatic and the exchange interactions, as shown in **relation (11.3)**, based on KS orbitals and QROs for host and doped structures, respectively.

$$\Delta E_{int}^{REF} = \Delta E_{El-prep.}^{REF(PBE0)} + \Delta E_{Elstat.}^{REF(PBE0)} + \Delta E_{Exch.}^{REF(PBE0)} \quad (11.3)$$

ΔE_{int}^C is the sum of, DLPNO-CCSD(T) correlations, divided in dispersion and non-dispersion contributions, and triples correction in the interaction as shown in **relation (11.4)**.

$$\Delta E_{int}^C = \Delta E_{disp}^{C-CCSD} + \Delta E_{non-disp}^{C-CCSD} + \Delta E_{int}^{C-(T)} \quad (11.4)$$

In principle ΔE_{int}^{REF} is associated with the stable formation of the Eu^{2+} -doped phosphor and it is sensitive to the interactions with the first and second coordination spheres of the host cuboid structures. Hence repulsive or positive ΔE_{int}^{REF} interactions translate to an unrelaxed EuL_8 formations while negative or attractive ΔE_{int}^{REF} interactions translate to a rather relaxed and thus stable EuL_8 cuboid formation. Similarly, to ΔE_{int}^{REF} , ΔE_{int}^C is sensitive to the formation of the bonding character around the EuL_8 cuboids.

Taking everything together, ΔE_{int}^{REF} is positive in the least probable site for each system (+1.8, +0.9, +1.1 eV) for (CBLA: Eu^{2+} at Ca^{2+} , RNLSO2: Eu^{2+} at Na^+ , and RNLSO: Eu^{2+} at Na^{2+} , respectively) indicating its instability for Eu^{2+} doping due to significant compression in EuL_8 cuboid, shorter Eu-L ligand and strong repulsion with the second shell of cations, as shown in **Table 11.1**. On the contrary, the most probable site for each system exhibits a strong and negative ΔE_{int}^{REF} of (-2.3, -3.0, -1.4 eV) for (CBLA2: Eu^{2+} at Ba^{2+} , RNLSO2: Eu^{2+} at Rb^+ , and RNLSO: Eu^{2+} at Rb^+ , respectively). While, RNLSO: Eu^{2+} at Na^{1+} , show negligible difference between doped and host structures.

The dispersion corrections follow the difference in the ionic radii between the substituted cations and Eu^{2+} (**Table 11.1**). They are hence repulsive in the most probable and more relaxed EuL_8 cuboids of (CBLA2: Eu^{2+} at Ba^{2+} , RNLSO2: Eu^{2+} at Rb^+ , and RNLSO: Eu^{2+} at Rb^+ , respectively). Similarly, as expected, stronger non-dispersion corrections are observed in the more covalent nitride (CBLA2) with respect to the oxide (RNLSO and RNLSO2) phosphors.

Compressed versus elongated EuL_8 cuboids show also larger non-dispersion interactions that are associated with stronger Eu-N/O covalent interactions and bond lengths in accord to **Table 11.1**. Finally, the most stable EuL_8 cuboids show also the smallest triples corrections across the study set that are inverted proportional to the doping energy.

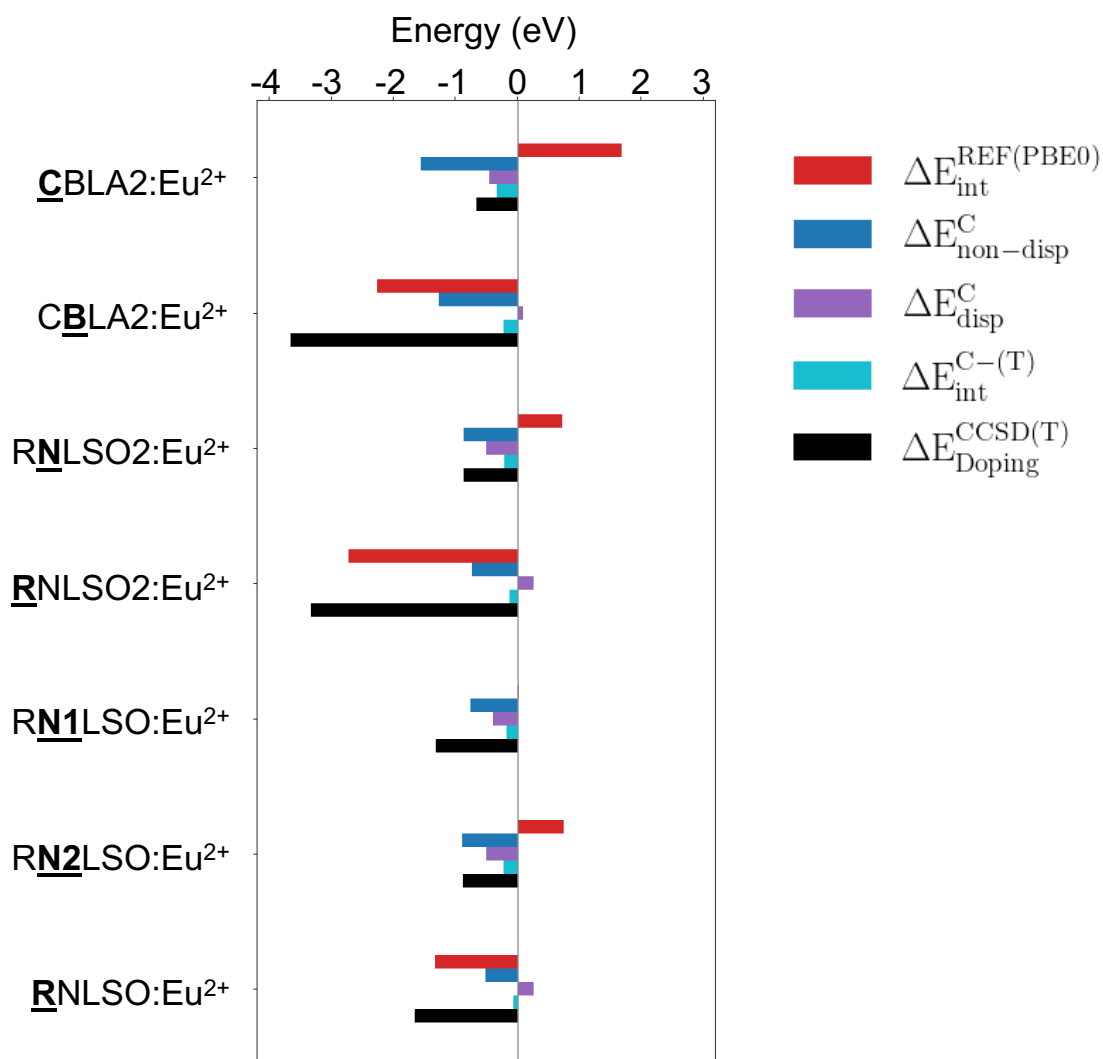


Figure 11.7. LED analysis of DLPNO-CCSD(T) doping energies (black bars) for all the studied systems at probable site for Eu^{2+} doping, which is decomposed into its contributions as $\Delta E_{\text{int}}^{\text{REF}}$, $\Delta E_{\text{non-disp}}^{\text{C}}$, $\Delta E_{\text{disp}}^{\text{C}}$, and $\Delta E_{\text{int}}^{\text{C-(T)}}$ in red, blue, purple, and cyan bars respectively. The doping site of host is bolded and underlined.

11.8. Absorption and Emission Spectra

In a further step the absorption and emission spectra are computed employing the ESD/TD-DFT PBE0 protocol in conjunction with NTO analysis of the most important absorption bands. This analysis is provided in **Figures 5.8-5.11**. In each system, the total absorption or emission spectrum is presented as a sum of all different Eu^{2+} doping sites, by taking into account the probability of these different sites for Eu^{2+} doping.

In the case of CBLA2 (**Figure 11.8**), the main emission band arises from absorption band 3. The emission process involves an Eu^{2+} center doped at the Ba^{2+} site and takes place from a $\text{Eu } 5d_{z^2}$ based molecular orbital MO with covalency factor $a^2 = 0.94$. In contrast the lower energy and weak intensity emission band arises from absorption band 1. The emission process involves an Eu^{2+} center doped at the Ca^{2+} site involving a $\text{Eu } 5d_{x^2-y^2}$ based molecular orbital MO with covalency factor $a^2 = 0.87$. Absorption band 2 arises from an Eu^{2+} center doped at the Ca^{2+} site and involves an $\text{Eu } 4f_{y(3x^2-y^2)} \rightarrow \text{Eu } 5d_{x^2-y^2}$ electron excitation showing no pronounced emission intensity. Likewise, the high energy absorption band 4 arises from an Eu^{2+} center doped at the Ba^{2+} site and involves an $\text{Eu } 4f_{xyz} \rightarrow \text{Eu } 5d_{x^2-y^2}$ electron excitation showing negligible emission intensity.

In the case of RNLSO (**Figure 11.9**), the main absorption band located at 20000 and 30000 cm^{-1} spectrum window contains contributions from Eu^{2+} center doped at both Na^{2+} (band 1, 2), Na^{1+} (band 3) and Rb^{+} (band 4) centers. Similarly, the high energy absorption band located at 32000 and 43000 cm^{-1} spectrum window contains mixed contributions from Eu^{2+} centers doped at both Rb^{+} (band 5), Na^{1+} (band 6) and Na^{2+} (band 7) centers. Analysis shows that the main emission band arises from an Eu^{2+} center doped at the Na^{1+} site and takes place from the non-bonding $\text{Eu } 5d_{x^2-y^2}$ based MO with a^2 of 0.95 reached by absorption band 3. On the contrary, the lower energy and weak intensity emission band arises from an Eu^{2+} center doped at the Na^{2+} site involving a $\text{Eu } 5d_{x^2-y^2}$ based molecular orbital MO with covalency factor $a^2 = 0.87$ reached by absorption band 1. Interestingly, although Rb^{+} site showed the highest probability for Eu^{2+} doping, it has no contribution in the emission process because its lowest excited state lies beyond the employed experimental laser, band 4. Hence the relevant states reached by the absorption process are not populated.

In the case of RNLSO2 (**Figure 11.10**), the main absorption band located at 18000 and 32000 cm^{-1} spectrum window contains contributions from Eu^{2+} center doped at both Na^{+} (bands

1, 3), and Rb⁺ (bands 2, 4) centers. The high energy shoulder located at 37000 cm⁻¹ arises from Eu²⁺ centers doped at Na⁺ (band 5) centers. Analysis shows that the main emission band 1* arises from an Eu²⁺ centers doped at the Na⁺ sites and takes place from the non-bonding Eu 5d_{x²-y²} based MO with a^2 of 0.92 leading to broader emission than in the case of RNLSO. A weak blue shifted emission band 2* arises from an Eu²⁺ centers doped at the Rb⁺ sites reached by absorption band 2 and takes place from the non-bonding Eu 5d_{z²} based MO with $a^2 = 0.97$. In accord with the experiment, as shown in **Figure 11.11**, by bringing the absorption laser in resonance with absorption band 2 corresponding to Eu²⁺ centers doped at the Rb⁺ sites it is possible to tune the emission intensities of band 1* and band 2*.

Finally, all studied phosphors exhibit a high thermal stability due to high host optical band gaps (4.94, 5.96, 5.82 eV for CBLA2, RNLSO2, and RNLSO, respectively calculated with STEOM-DLPNO-CCSD level of theory), as well as the absence of MLCT transitions along all the absorption spectra, that in agreement with the experimental results.[124, 330, 331]

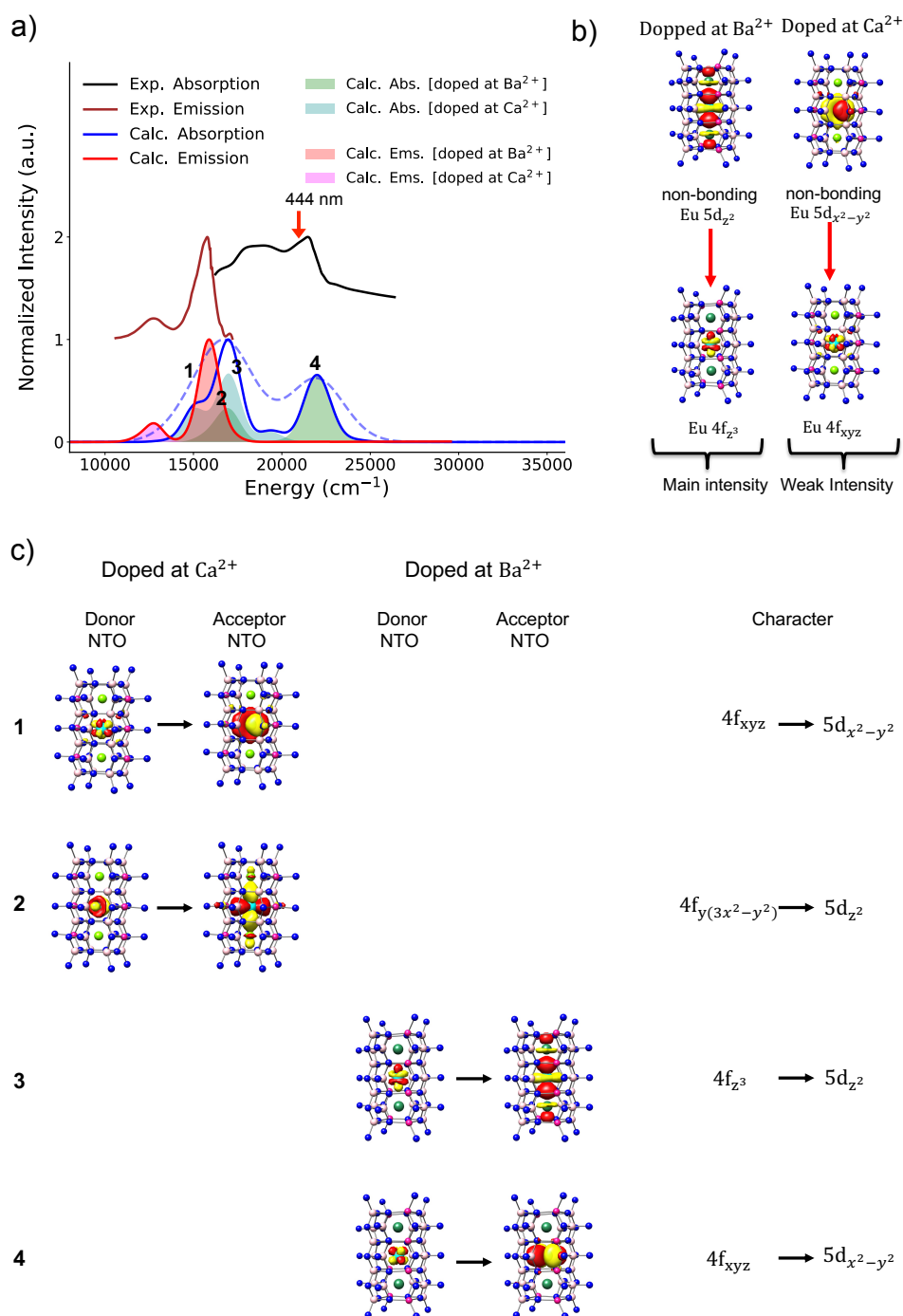


Figure 11.8. a) CBLA2 experimental (black), calculated TD-DFT/PBE0 absorption (blue; solid and dashed lines plotted with gaussian broadening 1500, 3000 cm^{-1} , respectively) spectra and experimental (brown), ESD/TD-DFT/PBE0 calculated (red) emission spectra. Filled colored bands indicate individual contributions of the different Eu^{2+} -doped centers. b) The 1st transition responsible for emission upon relaxation for all the candidate Eu^{2+} -doped centers and c) NTO analysis of the relevant bands in absorption spectra. The red arrow indicates laser energy in emission experiment.

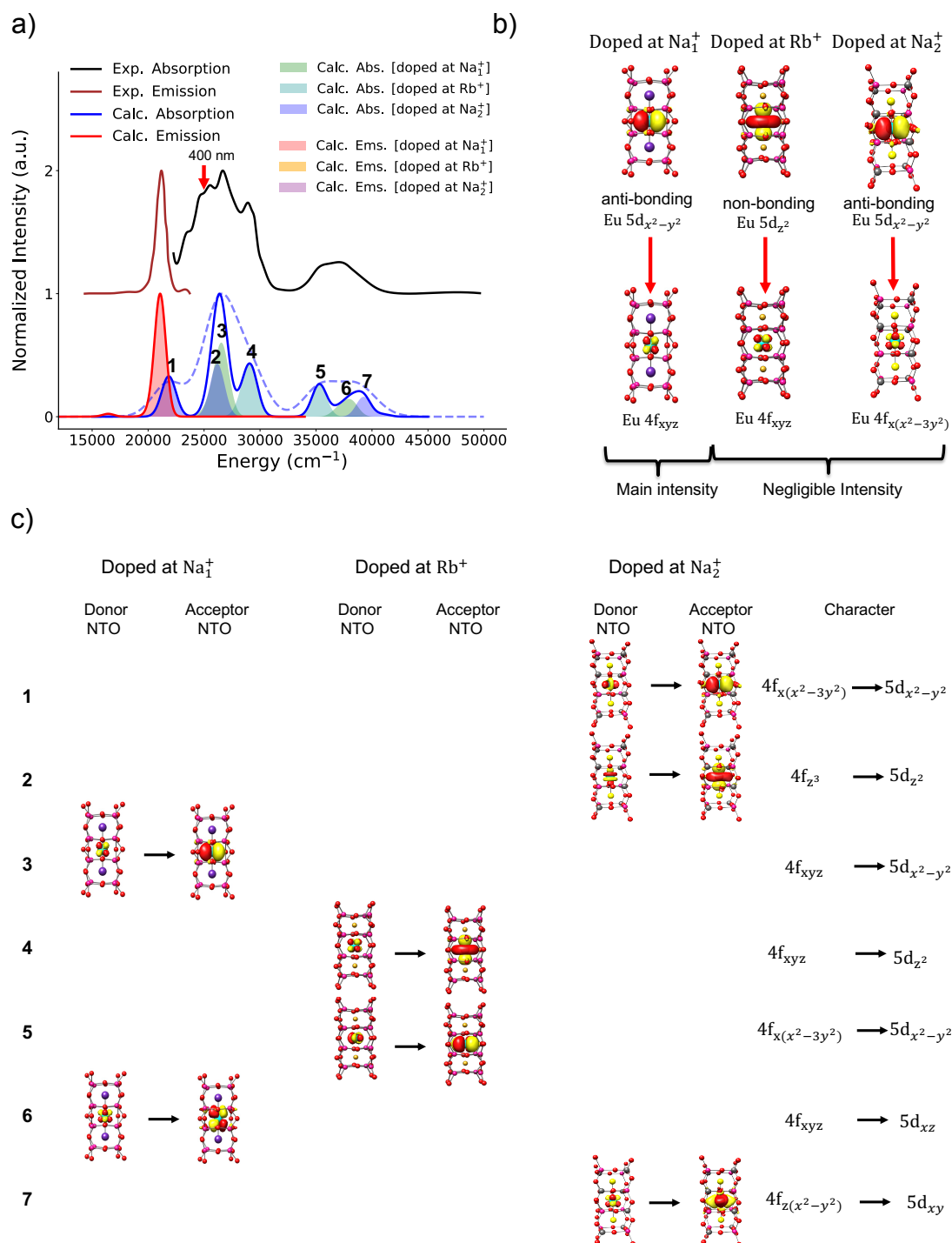


Figure 11.9. a) RNLSO experimental (black), calculated TD-DFT/PBE0 absorption (blue, light blue) spectra and experimental (brown), ESD/TD-DFT/PBE0 calculated (red) emission spectra. Colored bands indicate individual contributions of the different Eu^{2+} -doped centers. b) The 1st transition responsible for emission upon relaxation for all the candidate Eu^{2+} -doped centers and c) NTO analysis of the relevant bands in absorption spectra. The red arrow indicates laser energy in emission experiment.

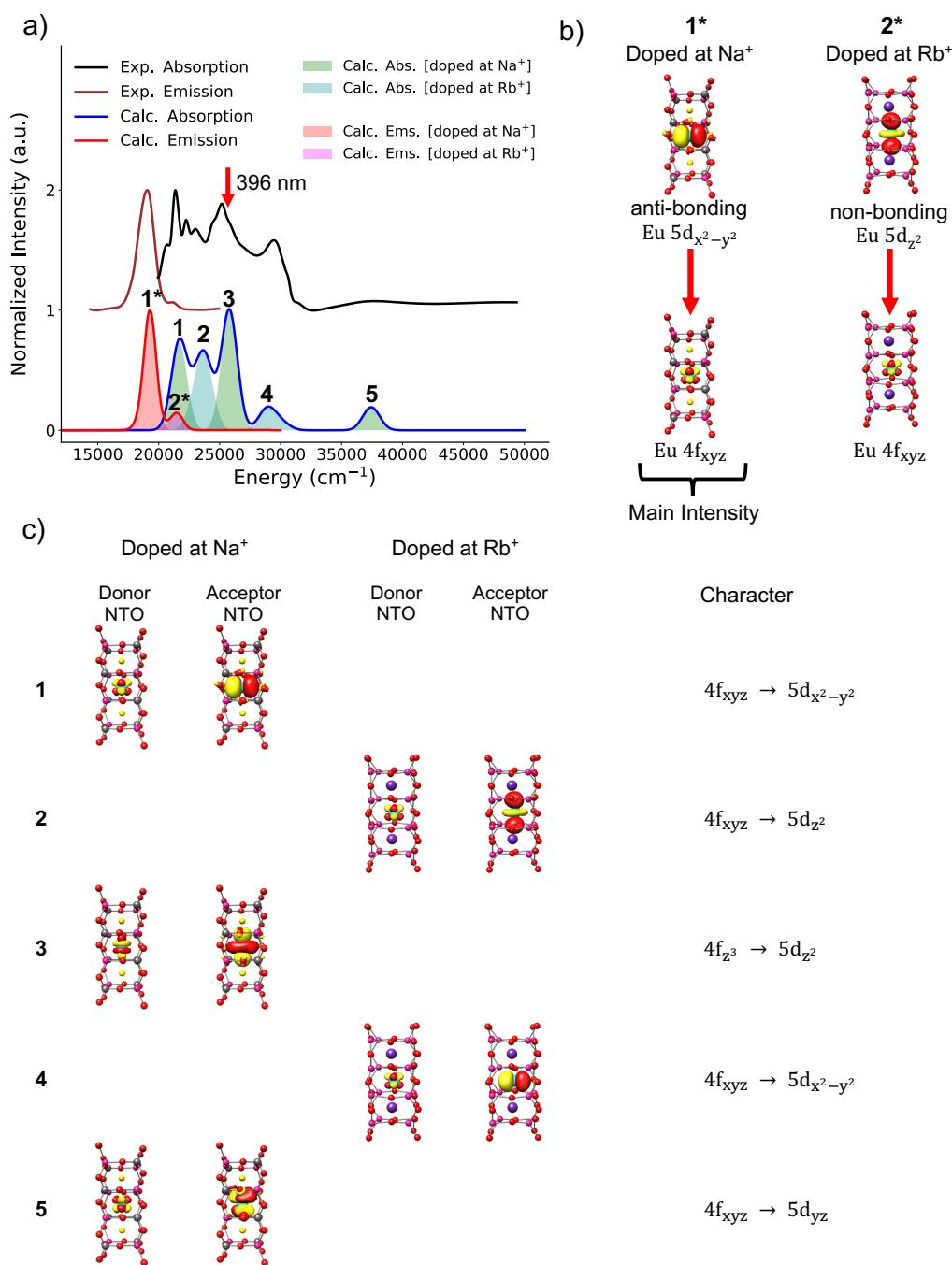


Figure 11.10. a) RNLSO2 experimental (black), calculated TD-DFT/PBE0 absorption (blue, light blue) spectra and experimental (brown), ESD/TD-DFT/PBE0 calculated (red) emission spectra. Colored bands indicate individual contributions of the different Eu^{2+} -doped centers. b) The 1st transition responsible for emission upon relaxation for all the candidate Eu^{2+} -doped centers and c) NTO analysis of the relevant bands in absorption spectra. The red arrow indicates laser energy (396 nm) in emission experiment.

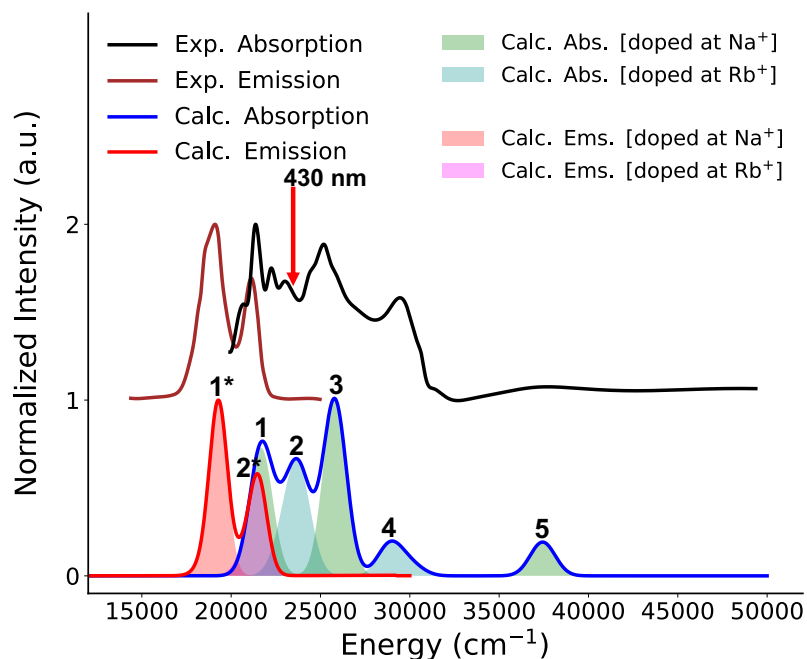


Figure 11.11. RNLSO2 experimental (black), calculated TD-DFT/PBE0 absorption (blue) spectra and experimental (brown), ESD/TD-DFT/PBE0 calculated (red) emission spectra. The emission spectrum is computed on the basis of a 430 nm laser that provides intensity enhancement to emission band 2* that originates from Eu^{2+} -doped at Rb^+ centers.

11.9. Validity of the Proposed Computational Protocol and Defined Descriptors Predicting Luminescence Properties of Solid-state Eu^{2+} -doped Phosphors

In the previous Chapter, **Section 10.8**, general descriptors have been defined that are able to predict the emission color and bandwidth of Eu^{2+} -doped phosphors bearing a single candidate center for Eu^{2+} doping.[80] These descriptors are based on the electronic characteristic of the first excited state dominating the emission process. In particular, the emission band properties can be predicted from the energy position of the first excited state ($4f^65d^1$) and the covalency cofactor a^2 of the Eu 5d based MO. At the TD-DFT PBE0/def2-TZVP level of theory the corresponding linear relations read:

$$\begin{aligned} \text{Expected Emission Band Max}(\text{cm}^{-1}) \\ = 0.9334 * E_1(\text{cm}^{-1}) - 419.04(\text{cm}^{-1}) \end{aligned} \quad (11.5)$$

$$\begin{aligned} \text{Expected Emission Band FWHM}(\text{cm}^{-1}) \\ = -2530.7 * \text{Eu 5d } a^2 + 3638.4(\text{cm}^{-1}) \end{aligned} \quad (11.6)$$

where, E_1 is the energy position of the 1st absorption band, while the Eu 5d a^2 coefficient is degree of covalency in Eu(5d) – L(2p) bond. As previously[80] described, Eu 5d a^2 coefficient is directly extracted from involved acceptor NTO consisting the absorption band.

In a last step of our analysis, we test the applicability of the above descriptors by considering in addition the study set of Eu^{2+} -doped phosphors bearing multiple candidate centers for Eu^{2+} doping. As seen in **Table 11.3** and visually in **Figure A. 14**, in all the cases the employed relations are able to predict the energy position, the shape and the bandwidth of the absorption and emission spectra showing excellent agreement between theory and experiment. In fact, for the study set of Eu^{2+} -doped phosphors containing one or multiple doping centers the predicted emission energy positions, the respective bandwidth and Stokes shifts show mean absolute errors (MAE) with respect to experiment that vary in the range 0.01, 0.04 and 0.16, respectively.

Table 11.3. Experimental versus predicted maximum emission energy positions and bandwidths according to the descriptors relations (1) and (2) for a given computed maximum absorption band maximum and the respective covalency factor ($5d \alpha^2$) and calculated Stokes Shift ΔS for previously studied (BMS, SMS, CLA, SALON, SLBO): Eu^{2+} and (RNLSO, RNLSO2, CBLA2): Eu^{2+} -doped phosphors at emitting centers.

Phosphor	Doping site	Experimental Emission Band			Calculated First Absorption band		Predicted Emission Band		
		Energy	Width	ΔS	Energy	$\text{Eu}^{2+} 5d \alpha^2$	Energy	Width	ΔS
		(cm^{-1})	(cm^{-1})	(cm^{-1})	(cm^{-1})		(cm^{-1})	(cm^{-1})	(cm^{-1})
Ba[Mg ₃ SiN ₄]: Eu^{2+} BMS	Ba ²⁺	14920	2015	3500	16000	0.64	14925	1950	2810
Sr[Mg ₃ SiN ₄]: Eu^{2+} SMS	Sr ²⁺	16250	1150	750	18200	0.97	16260	1150	950
Ca[LiAl ₃ N ₄]: Eu^{2+} CLA	Ca ²⁺	14980	1340	1000	16150	0.84	14970	1350	847
Sr[LiAl ₃ N ₄]: Eu^{2+} SLA	Sr ²⁺	15380	1180	800	17200	0.96	15384	1160	840
Sr[Al ₂ Li ₂ O ₂ N ₂]: Eu^{2+} SALON	Sr ²⁺	16300	1220	1100	18100	0.90	16286	1220	1150
<i>Continued in the next page</i>									

11 Luminescence in Eu^{2+} -doped phosphors for WLEDs: Validation of the Proposed Protocol

Phosphor	Doping site	Experimental Emission Band			Calculated First Absorption band		Predicted Emission Band		
		Energy	Width	ΔS	Energy	$\text{Eu}^{2+} 5d$	Energy	Width	ΔS
		(cm^{-1})	(cm^{-1})	(cm^{-1})	(cm^{-1})	α^2	(cm^{-1})	(cm^{-1})	(cm^{-1})
$\text{SrLi}_2[\text{Be}_4\text{O}_6]:\text{Eu}^{2+}$ SLBO	Sr^{2+}	22000	1220	980	23800	0.95	21929	1170	750
$\text{RbNa}_3[\text{Li}_3\text{SiO}_4]_4:\text{Eu}^{2+}$ RNLSO	Na^{1+}	21231	1015	--	23087	0.95	21968	1234	1120
$\text{RbNa}[\text{Li}_3\text{SiO}_4]_2:\text{Eu}^{2+}$ RNLSO2	Na^{+}	19121	1465	--	20030	0.92	19367	1496	670
$\text{CaBa}[\text{LiAl}_3\text{N}_4]_2:\text{Eu}^{2+}$ CBLA2	Ba^{2+}	15674	1191	--	17100	0.94	15484	1259	1570
	Ca^{2+}	12658	1450	--	14400	0.87	12970	1436	1310
MAE(%)							0.01	0.04	0.16

11.10. Summary and Conclusions

A previously designed computational protocol for the color and the bandwidth prediction of narrow band phosphors was extended to Eu^{2+} -doped phosphors containing multiple probable centers for Eu^{2+} doping. Namely, the narrow-band phosphors (Ca/Ba) nitridolithoaluminate $\text{CaBa}[\text{Li}_2\text{Al}_6\text{N}_8]:\text{Eu}^{2+}$ (CBLA2)[124], alkali (Na/Rb) lithosilicate $\text{RbNa}_3[\text{Li}_3\text{SiO}_4]_4:\text{Eu}^{2+}$ (RNLSO)[331] and $\text{RbNa}[\text{Li}_3\text{SiO}_4]_2:\text{Eu}^{2+}$ (RNLSO2)[330] phosphors.

Following a thorough electronic structure analysis, converged embedded cluster structures were constructed for the variety of the Eu^{2+} -doped positions (Ca^{2+} , Ba^{2+} , Na^+ or Rb^+) across the study set of phosphors. In this context a representative set of density functionals belonging to the GGA, hybrid, range separated hybrid, double hybrid and range separated double hybrid density functional families was evaluated for its ability to compute the band gap energies of the undoped and Eu^{2+} -doped phosphor structures. The DFT computed band gap energies were evaluated against experimental as well as STEOM- DLPNO-CCSD and CASSCF/NEVPT2 computed reference values, for the undoped and Eu^{2+} -doped phosphors, respectively. In both cases the hybrid functionals PBE0 and CAM-B3LYP, gave the best performance. Hence for consistency with our previous study the PBE0 functional was chosen for the production calculations.

The Eu^{2+} doping energies at the different sites of the host structures were calculated at the DLPNO-CCSD(T) level as the difference between the interaction energies between the Eu^{2+} -doped and host (undoped) structures. These calculations predicted that in the case of CBLA2, and RNLSO and RNLSO2 Eu^{2+} -doped phosphors, the most probable positions for doping are the Ba^{2+} and Rb^+ centers, respectively, followed by Ca^{2+} and Na^+ ones. In contrast, similar calculations performed at the DFT/PBE0 level showed rather unbalanced results. In a further step the nature of the DLPNO-CCSD(T) computed Eu^{2+} doping energies was analyzed on the basis of the LED scheme. It was demonstrated that the Eu^{2+} doping energy depends on the difference between the ionic radii of the Eu^{2+} and the substituted cation M^{m+} as $\Delta r_{\text{M}^{m+}-\text{Eu}^{2+}}$, and the type (compressed/elongated) of the formulated EuL_8 cuboids and much less to the strength of the Eu-O/N covalent interactions and the second coordination sphere of the EuL_8 cuboids. In particular it was shown that the most probable doping centers are those enabling the formation of elongated EuL_8 cuboids.

The absorption and luminescence spectra of the chosen study set of phosphors were computed, on the basis of the defined doping and symmetry selection rules, showing very good agreement with the experimental results. Once again it was shown that the suppression of the Eu-O/N covalent interactions, as well as the steric effects imposed by the second coordination sphere is the origin of the desired narrow band emission across the most probable centers for Eu²⁺doping. In accord to experiment in the case of the CBLA2 and RNSLO2 phosphors it was demonstrated that the emission spectrum from particular absorption bands across the different probable Eu²⁺ doping centers provides tunability towards desired photoluminescence properties.

In a final step the previously defined descriptor relations for the color and the emission bandwidth of the Eu²⁺-doped phosphors were validated on the employed study set. The mean absolute errors with respect to experiment found to range between 0.01 and 0.04 for the color and bandwidth, respectively. This indicates that these descriptors are generalizable to Eu²⁺-doped phosphors of arbitrary complexity. Hence, they could potentially be used to evaluate sets of novel Eu²⁺-doped phosphors in order to provide genuine predictions of their properties. In fact, that will be addressed in the next chapter, where our investigation reveals the potential for systematic enhancement of the emission properties of the CBLA2 phosphor towards a hypothetical CBLA phosphor, demonstrating unprecedented narrow band red emission characteristics.

Finally, we believe that the results presented herein are important in the design of novel narrow band phosphors with tunable emission properties and further improve quality and energy efficiency of LEDs.

12 Eu²⁺-doped Phosphors Engineered – Prediction of an Unprecedented Narrow-band Red-Emitting Eu²⁺-doped Phosphor (CBLA)

The results of this chapter have been published in Phys. Chem. Chem. Phys., 2024, 26(7), 6277-6291. DOI: 10.1039/D3CP06039J

12.1. Introduction

Building upon the insights and findings through the preceding chapters, it becomes evident that theoretical investigations can effectively help and guide the synthesis efforts, leading to the refinement of existing Eu²⁺-doped phosphors and the proposal of innovative phosphors with tailored optical properties for technological and industrial applications. A notable example examined earlier is the CBLA2 phosphor, which exhibits significant narrow band emission in the red region however, a notable drawback lies in its diminished emission in the infrared (IR) region. This chapter advances our exploration, revealing the potential for a systematic enhancement of the emission properties of the CBLA2 phosphor, towards a hypothetical CBLA phosphor, demonstrating unprecedented narrow band red emission characteristics.

12.2. Collaborative Exploration: Bridging Experimental Insights with Theoretical Perspectives Towards Promising Eu²⁺-doped Phosphors

This section aims to highlight the importance of a fruitful collaborative interplay between the experimental and theoretical domains. Following particularly insightful discussions with our experimental collaborators from professor's Schnick group, we developed strategies for tuning emission band spectral features in Eu²⁺-doped Phosphors, by navigating through experimental findings, theoretical frameworks, and analytical interpretations. This synergistic effort has

culminated in the in-silico identification of highly promising candidate, specifically red-emitting narrow-band Eu-doped phosphor referred to as CBLA. The ensuing exploration captures the convergence of hands-on experimentation and theoretical understanding, guiding us towards innovative solutions in the realm of luminescent materials. As of the current state of research, ongoing efforts persist in the synthesis of the proposed phosphor, CBLA, to either validate or challenge our theoretical postulations.

12.2.1. Insights into the emission intensity mechanism of CLA:Eu²⁺, SLA:Eu²⁺, and CBLA2:Eu²⁺ Phosphors

As previously discussed in **Sections 10.2** and **10.7**, the red-emitting CLA:Eu²⁺ and SLA:Eu²⁺ phosphors share the same chemical formula for their host, M[LiAl₃N₄], where M is Ca and Sr, respectively. Despite the common chemical composition, these phosphors exhibit distinct crystal structures, with CLA crystallizing in the tetragonal (*I*4₁/*a*) space group while SLA crystallizes in the triclinic (*P* $\bar{1}$) space group. Both structures feature a highly rigid network of [Al/LiN₄] tetrahedra, facilitating weak vibronic coupling through the rigid 4f⁶5d_{x²-y²} → 4f⁷ relaxation. However, SLA demonstrates superior chemical and luminescent properties.

A closer examination reveals that, the crystal structure of CLA is more symmetric, and the slightly smaller Ca ions result in a compressed and symmetric [EuN₈]²²⁻ cuboids with (*S*₄) local symmetry compared to SLA, in which larger cuboids with (*C*₂ and *C*_{2h}) symmetries accommodate Eu²⁺ doping at Sr1 and Sr2 sites. This leads to stronger ligand field and covalency interactions in CLA 4f and, most importantly, 5d orbitals, resulting in a red-shifted and broadened emission band (Exp. FWHM 1340 cm⁻¹). The broader band is due to stronger vibronic coupling induced by larger covalency in Eu 5d_{x²-y²} excited orbital with the nitride ligands,[80] compared to narrower emission band in SLA (Exp. FWHM 1180 cm⁻¹).

While the situation is complicate, the need for additional space in the Eu cuboid cavity is apparent. This space is critical for enhancing doping, as discussed in **Section 11.7**. Additionally, cuboid expansion can reduce the Eu-L interaction (covalency), vibronic coupling, and ultimately narrowing the bandwidth. However, this expansion also causes a blue shift in the emission energy, explaining the challenge in finding red phosphors with sharp emission bands.

One potential step toward narrower phosphor emission band involves synthesizing a Ba variant of the series, Ba[LiAl₃N₄] (BLA), although such a host has not yet been successfully synthesized. Schnick's group was able to successfully synthesize the mixed CaBa[LiAl₃N₄]₂

(CBLA2) phosphor host, featuring multiple Eu doping centers (Ca/Ba), which crystalized in the monoclinic $C2/m$ space group.

Now, we can see that CBLA2:Eu²⁺ exhibits a remarkably narrow and intense red emission band (Exp. FWHM 1095-1266 cm⁻¹, whereas our calculation based on the electronic descriptors gives 1190 cm⁻¹) which is as narrow as that of SLA (Exp. FWHM 1180 cm⁻¹) and blue-shifted by +300 cm⁻¹ with respect to SLA. Again, the luminescence mechanism involves a highly rigid relaxation process with a non-bonding Eu 5d_{z²} – Ba 5d_{z²} MO. Clearly, the presence of Eu between the two Ba ions induces the stabilization of Eu 5d_{z²} over 5d_{x²-y²} which will be advantageous and more likely to give narrow-band emission, as discussed in **Chapter 10**. However, a lower-energy and weaker-intensity broad infrared (IR) emission band from Eu²⁺ doped at the Ca²⁺ site (Exp. FWHM 1430 cm⁻¹) is aligned with antibonding 5d_{x²-y²} excited orbital and poses challenges due to strong compression within the Eu cuboid, limiting its potential as a red-emitting phosphor.

These observations collectively underscore the existing challenges. The question arises: how can we address these issues?

One potential approach involves eliminating the Ca²⁺ site, resulting in BLA:Eu²⁺. Or alternatively, instead of eliminating of the emission of Eu doped CBLA (at Ca site), it can be improved through [CaN₈] cuboid expansion. However, as shown that single-cationic channels featuring solely Ca in both CLA and CBLA2 lead to compressed [CaN₈] cuboids. So, the [CaN₈] cuboids expansion could be achieved through sandwiching that cuboids with larger [CaN₈] with a larger [SrN₈] or further larger [BaN₈] cuboids leading to alternating Ba²⁺--Ca²⁺-Ba²⁺ channels. Within such channel, besides doping at Ba site, Eu doing Ca sites can again induce stabilization of advantageous non-bonding Eu 5d_{z²} excited orbital through constructive overlap with Ba 5d_{z²} orbitals on the two sides. That may be achieved through careful structural engineering. Indeed, this behavior have been detected however in oxide phosphors, when we explore the RNLSO2:Eu²⁺ and RNLSO:Eu²⁺.

12.2.2. Insights into the emission intensity mechanism of RNLSO:Eu²⁺, RNLSO2:Eu²⁺, and CBLA2:Eu²⁺ phosphor

The electronic structure and emission of RNLSO2:Eu²⁺, RNLSO:Eu²⁺, and CBLA2:Eu²⁺ phosphors have been discussed in the preceding **chapter 11**, however, some key points and some structural-electronic-emission properties correlation are we recalled and highlighted.

RNLSO2 and RNLSO sharing common chemical formula $M[\text{Li}_3\text{SiO}_4]_2$ with $M = \text{RbNa}$ and $\text{Rb}_{0.5}\text{Na}_{1.5}$, respectively where, they crystallized in monoclinic ($C2/m$ like CBLA2) and tetrahedral ($I4/m$) space groups, respectively. They show significant differences in the emission properties of Eu^{2+} centers doped at different sites.

Recalling (refer to **Figure 11.1** and **Figure 11.10**), in RNLSO2, like CBLA2, doping at larger cuboid of Rb^+ is more probable than in Na^+ center and it exhibits overlapping emission bands arising from Eu^{2+} doping at both sites, with the emission primarily stemming from the Na^+ site. In contrast (refer to **Figure 11.9**), in RNLSO, with three probable doping centers, arranged in their doping probabilities as $\text{Na}(2)^+$, $\text{Na}(1)^+$, and Rb^+ sites, and showed a single narrow emission band originating from the $\text{Na}1^+$ site, where the Eu^{2+} is compressed oxide cuboid and sandwiched between two massive Rb^+ ions.

The emission in RNLSO2 at Na^+ is broader compared to RNLSO at $\text{Na}1^+$ due to the nature of the non-bonding $\text{Eu } 5d_{x^2-y^2}$ based MO. Additionally, a weak blue-shifted emission band is observed in RNLSO2, originating from Eu^{2+} centers doped at the Rb^+ sites. So, the transformation from RNLSO2 to RNLSO lead to improvement of the luminescence in the oxide domain, provide a valuable strategy to model new phosphor to word optimization of the CBLA2 properties to achieve desired luminescent properties.

In fact, in contrast to CBLA2 in the case of RNLSO2 (**Figure A. 8 a-b**) the main emission band 1* arises from an Eu^{2+} centers doped at the Na^+ sites (in relation to Ca^{2+} sites in CBLA2) and takes place from the non-bonding $\text{Eu } 5d_{x^2-y^2}$ based MO with a^2 of 0.92. A weak blue shifted emission band 2* arises from an Eu^{2+} centers doped at the Rb^+ sites (in relation to Ba^{2+} sites in CBLA2) reached by absorption band 2 and takes place from the non-bonding $\text{Eu } 5d_{z^2}$ based MO with $a^2 = 0.97$. As shown in **Figure 11.11** and in accord to experiment the intensity of this second band can be tuned by the excitation laser. In the case of RNLSO (**Figure A. 8 c-d**) the main emission band arises from an Eu^{2+} center doped at the $\text{Na}(1)^+$ site and takes place again from the non-bonding $\text{Eu } 5d_{x^2-y^2}$ based MO with a^2 of 0.95.

It should be emphasized that the emission bands arising from Eu^{2+} centers doped at Ca^{2+} , Na^+ and $\text{Na}(1)^+$ sites in the case of CBLA2, RNLSO2 and RNLSO have the following characteristics 1) involve compressed EuN_8 and EuO_8 cuboids, 2) take place from non-bonding $\text{Eu } 5d_{x^2-y^2}$ based MO and 3) the RNLSO band is blue shifted ($\text{FWHM}=1015 \text{ cm}^{-1}$, 22.5 nm) with respect to the RNLSO2 ($\text{FWHM}= 1465 \text{ cm}^{-1}$, 40 nm) band by 2100 cm^{-1} with narrower bandwidth by 450 cm^{-1} respectively. Hence there is a clear relation between the geometric

characteristics around the Eu²⁺ centers and their emission properties in these systems. This is in accord with the descriptor relations discussed in **Sections (10.8, 5.9)**, **Figure A. 14**, and **Table A. 8**.

Up to this point of analysis it has been shown that owing to the very rigid nature of the emissive states in both Eu²⁺-doped phosphors bearing one or multiple doping centers the TDDFT/PBE0 computed spectra provide satisfactory agreement to the experimentally observed absorption and emission spectral features allowing for a quantitative analysis. However, for the identification of the probable Eu²⁺-doping centers at the ground state and a comprehensive qualitative and quantitative description that connects the strength of electrostatic and covalent interactions between the Eu²⁺ and the coordination environment provided by the phosphor host structure, the sensitivity provided by DLPNO-CCSD(T) computed energies and their respective LED analysis is required. These two successful approaches will be employed below towards an in-silico investigation of new Eu²⁺ doped phosphor with tailored photoluminescence properties.

12.3. Designing a CBLA:Eu²⁺-doped phosphor with potentially improved emission properties.

12.3.1. The impact of the host environment to the emission properties of the Eu²⁺-doped phosphors.

In a next step we investigate the effect of the host environments to the electronic structure, chemical bonding and consequently emission properties of the studied phosphors. The results are summarized in **Figure 12.1**.

As shown in **Figure 12.1a**, in the case of RNLSO the Na1⁺ sites form host cuboids (Na1⁺O₈) that are tetragonally compressed with respect to the (Na⁺O₈) cuboids in RNLSO₂, owing to the formation of the Rb⁺--- Na1⁺--- Rb⁺ cuboid sequence. As discussed in the previous sections, these sites dominate the emission bands in the respective Eu²⁺-doped phosphors. In particular, Na1⁺ centers have higher probability for Eu²⁺ doping with respect to the Na⁺ sites in RNLSO₂ while they result in emission bands that are blue shifted and narrower. LED analysis confirms that Eu²⁺ doping at the Na⁺ sites in RNLSO₂ results in repulsive ionic interactions with the [O₈Li₄Si₄Na₂]⁶⁺ host environment that is only partially compensated by attractive covalent interactions leading to an overall low probability for Eu²⁺ doping at these centers. In contrast,

Eu²⁺ doping at the Rb⁺--- Na¹⁺--- Rb⁺ tetragonally compressed cuboid sequence in RNLSO shows almost neutral ionic interaction (+0.02 eV) with the [O₈Li₈Rb₂]⁶⁻ host coordination environment and slightly reduced covalent interactions. This is also reflected to the EuO₈ cuboids volumes and Eu-O bond distances (29.3 Å³, 2.6 Å in RNLSO2 and 30.2 Å³, 2.7 Å in RNLSO). Overall, the analysis confirms the improvement in the doping probability at the Na¹⁺ centers of RNLSO with respect to the Na⁺ centers in RNLSO2. While the EuO₈ cuboid expansion and the covalency reduction along this direction are also consistent with the blue shifted and narrower bandwidth emission signal in RNLSO in comparison to RLNSO2 for these doped centers. We would like to emphasize that while within the LED framework the covalent interactions are probed in the ground state it has been shown than owing to the fact that the open Eu²⁺ 4f⁸ shell is only marginally involved in the bonding[136] hence, important covalent interactions with the host environment in the Eu²⁺ 5d and 6s shells probing indirectly the bonding characteristics of the excited emissive states of the 4f⁷5d¹ shell.

Na⁺ and Rb⁺ sites in RNLSO2, resemble the characteristics of the Ca²⁺ and Ba²⁺ sites in CBLA2. As shown in **Figure A. 7**, Eu²⁺ doping at the respective Rb⁺ and Ba²⁺ sites in RNLSO2 and CBLA2 leads in favorable doping situations. This is reflected to both the ionic and covalent interactions between the Eu²⁺ site and host environment. Owing to the negatively charged host environments, [O₈Li₈Na₂]⁶⁻ and [N₈Al₄Li₄Ba₂]⁴⁻ the Eu²⁺ site - host environment ionic interactions are attractive (2.7 and 2.3 eV) while the EuO₈ and EuN₈ cuboid expansions (Eu-O ~ 3.00 Å and 40.5 Å³ cuboid volume and Eu-N ~ 2.93 Å and 37.6 Å³ cuboid volume, respectively) lead to weaker covalent interactions, hence to a weaker vibronic coupling in these sites, that is also reflected in the reduction of the emission bandwidths in comparison to the emission spectra originating from the respective Eu²⁺-doped Na⁺ and Ca²⁺ sites.

Likewise to the Rb⁺ and Ba²⁺ sites, Eu²⁺ doping at Na⁺ and Ca²⁺ in RNLSO2 and CBLA2 phosphors not only result in compressed EuO₈ and EuN₈ cuboids with similar principle emission characteristics with respect to the non-bonding Eu 5d_{x²-y²} MO character of the emissive state, but also in terms of their probabilities for Eu²⁺ doping **Figure 12.1**, and **Table A. 7**. As shown in **Figure 12.1 a** and **b**, both the Na⁺ sites in RNLSO2 and the Ca²⁺ sites in CBLA2 are less favorable for Eu²⁺ doping showing significant repulsive ionic (+1.7 eV) interactions owing to the positive [N₈Al₈Ca₂]⁴⁺ coordination environment opposing the rather covalent Eu²⁺-host interactions (-2.4 eV). Hence as in the case of RNLSO2, at the Eu²⁺-doped Na⁺ sites, in the case of CBLA2 the overall doping probability, for the Eu²⁺-doped Ca²⁺ sites is significantly reduced.

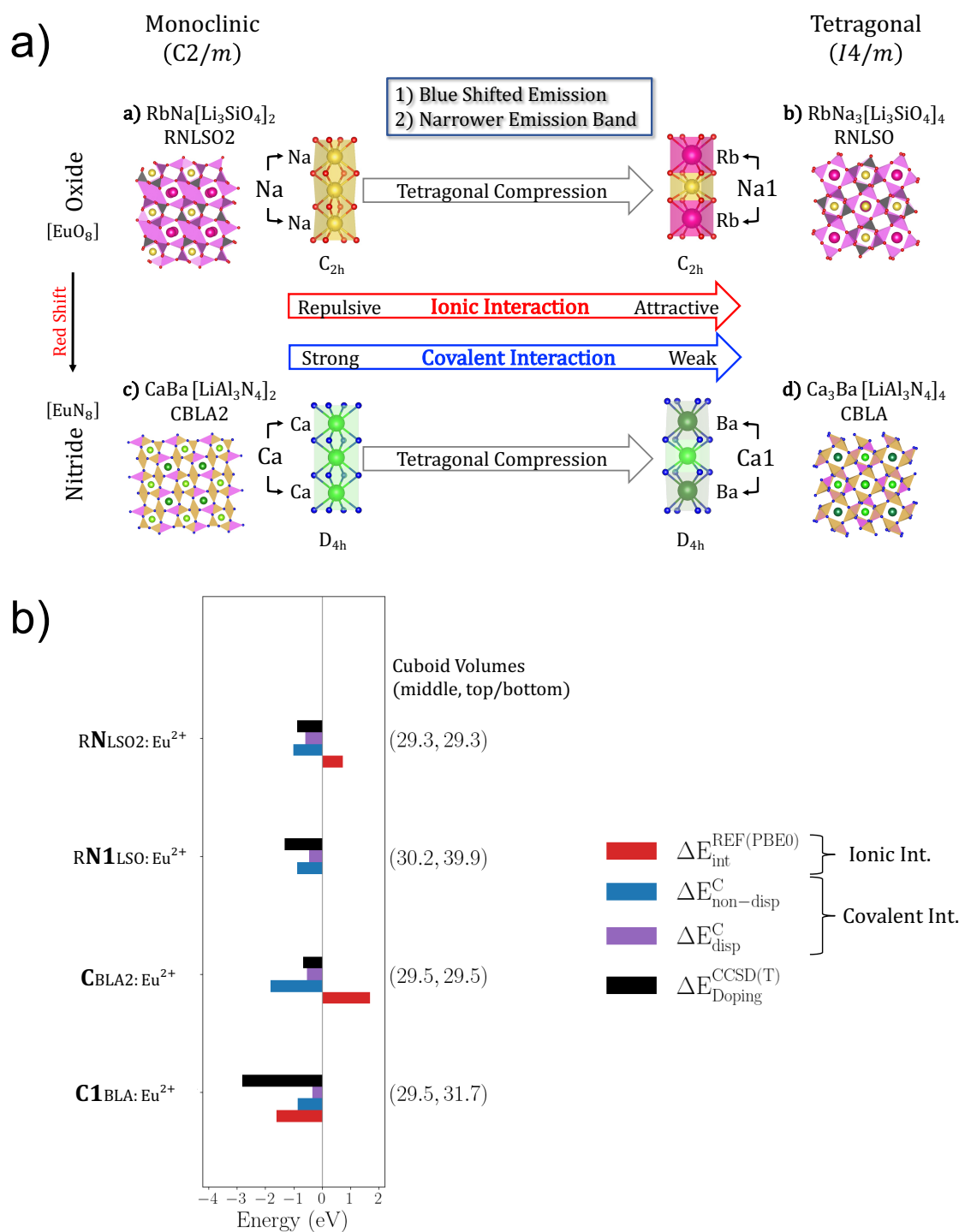


Figure 12.1. a) The impact of the tetragonal cuboid compression of the Na⁺ and Ca²⁺ Eu²⁺-doping centers in RNLSO2 and CBLA2 towards RNLSO and the isotypic CBLA phosphors. b) Analysis of the DLPNO-CCSD(T) computed probability for Eu²⁺-doping in these phosphors on the basis ionic and covalent Eu²⁺-host interactions in the framework of LED.

These results confirm the experimental and computational observations that at the RNLSO₂:Eu²⁺ phosphor the emission band characteristics can be improved by either tuning the excitation laser to higher energies to basically probe the emission originating from Eu²⁺-doped Rb⁺ over Na⁺ sites. Alternatively one may resort to the RNLSO:Eu²⁺ phosphor to benefit by the improved doping probability of the Eu²⁺-doped Na¹⁺ sites towards a unique, narrow band blue shifted emission band in comparison to the Eu²⁺-doped Na¹⁺ sites of RNLSO₂:Eu²⁺. In contrast in the case of CBLA₂:Eu²⁺ phosphor the only possibility to reduce the emission intensity losses into the IR is to in principle reduced the Eu²⁺ doping concentration to suppress the emission from the low probability for Eu²⁺ doping at Ca²⁺ centers at the cost of reducing the total light intensity and brightness of the phosphor. Hence at this point the question arises whether it is possible to alter the unfavorable emission characteristics of the CBLA₂:Eu²⁺ phosphor by generating the hypothetical CBLA:Eu²⁺-doped phosphor that is isotypic to the RNLSO:Eu²⁺ phosphor. The structural characteristics of the hypothetical CBLA:Eu²⁺-doped phosphor are provided in the supporting information (**Appendix A.3** and **Figure A. 12**).

As shown in **Figure 12.1 a** and **b** likewise to the Na¹⁺ centers of RNLSO, the Ca^{1²⁺} centers in CBLA form tetragonally compressed (Ca²⁺N₈) cuboids owing to the formation of the asymmetric Ba²⁺--- Ca^{1²⁺}--- Ba²⁺ cuboid sequence. In contrast to the Eu²⁺-doped Ca²⁺ sites in CBLA₂:Eu²⁺ Eu²⁺ doping at Ca^{1²⁺} centers becomes favorable owing to 1) the attractive ionic interactions between Eu²⁺ and [N₈Al₈Ba₂]⁴⁺ host environment and the reduced covalent interactions leading to an improved probability for Eu²⁺ doping at these sites. The Eu²⁺N₈ expansion (Eu-N, volume) and the suppression of the Eu host covalent interactions could in fact lead to a blue shifted narrow band emission signal in comparison to the Ca²⁺ Eu²⁺-doped positions. However as in fact shown in **Table A. 7** and **Figure A. 7**, in CBLA:Eu²⁺ the doping probability of both the Ca^{1²⁺}, Ca^{2²⁺} and Ba²⁺ in comparison to the respective Ca²⁺ and Ba²⁺ Eu²⁺-doped centers in CBLA₂:Eu²⁺, improves. The degree, this could actually lead to a candidate phosphor with improved emission properties will be investigated below.

12.3.2. Vibronic Coupling Effect along the tetragonal distortion pathway

Seeking further validation for the structural factors that could lead to a hypothetical candidate CBLA:Eu²⁺ phosphor with optimum emission properties, we analyze the vibronic coupling effect on the known CBLA₂, RNLSO and RNLSO₂ phosphors. At this point as shown schematically at **Figure 9.4**, it is useful to recall that in ‘ideal’ cubic symmetry (inverted O_h)

EuL₈ (L=O, N) cuboid the emissive ⁸T_{2g} is subject to pseudo Jahn Teller (PEJT) effect towards tetragonally distorted cuboids (elongated or compressed along the 4-fold symmetry axis) leading to D_{4h} symmetry through coupling with the e_g vibrational modes. In practice, for example in the presence of more than one cuboid, the situation is more complex as coupling with the respective t_{2g} is enabled, leading to a series of (T_{2g}⊗(e_g + t_{2g})) PEJT along the tetragonal distortion pathway.

As discussed in **Section 11.2**, in the case of CBLA2 Eu doping at Ba²⁺ centers results in tetragonally elongated EuN₈ cuboids with volume 37.5 Å³ surrounded by tetragonally elongated BaN₈ cuboids of the same volume while doping at Ca²⁺ centers results in tetragonally compressed EuN₈ cuboids with volume 29.5 Å³ surrounded by tetragonally compressed CaN₈ cuboids of the same volume. Along the list of vibrational modes that influence the emission bands in CBLA2 according to their computed Huang-Rhys factors (S)[274, 275], the e_g group of vibrational modes, illustrated in **Figure A. 9** and **Figure A. 10a**, shows the most significant contributions. Not surprisingly these group of modes represents the tetragonal distortion pathway of EuN₈, BaN₈ and CaN₈ cuboids. The DLPNO-CCSD(T) potential energy surfaces PES were computed as well as the respective emission spectra along the tetragonal distortion pathway at both Ba²⁺ and Ca²⁺ doping centers. The results are summarized in **Figure 12.2** and **Figure A. 10**.

As seen in **Figure A. 10**, at the Ba doping centers both the EuN₈ cuboids at the doped Ba²⁺ center and the BaN₈ cuboids of the undoped centers maintain practically similar cuboid volumes along the tetragonal distortion pathway (~37Å³ at Q=0, ~33 Å³, at Q=6). In contrast at the Ca doping centers the EuN₈ cuboid compress further (from 29.5 Å³ to 28.85 Å³) while the CaN₈ ones expand (from 30.5 Å³ at Q=0 to 37.3 Å³ at Q=6). A similar trend is observed in the computed emission spectra shown in both **Figure A. 10** and **Figure 12.2**. In fact, along the compression pathway the emission arising from Eu²⁺-doped Ba²⁺ centers remains unaffected in terms of energy position and absolute intensity the respective emission band arising from Eu²⁺-doped Ca²⁺ centers becomes blue-shifted with increasing intensity. Along the tetragonal distortion pathway at normal mode value Q=3 it actually overtakes the total intensity while at Q=6 dominates the emission signal providing a unique red emission band at ~14300 cm⁻¹. It becomes evident that structural modifications that could stabilize the Eu²⁺-doped centers around the Q=6 magnitude of the axial compression pathway would potentially lead to an unprecedented narrow band red-emitting phosphor.

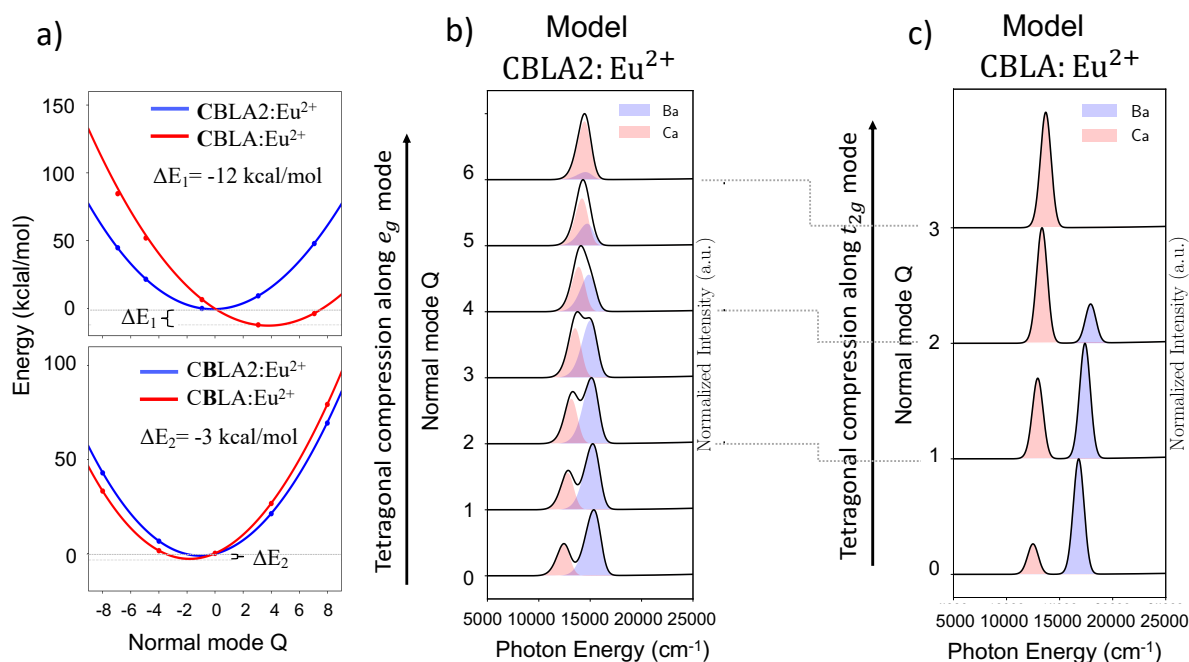


Figure 12.2. a) DLPNO CCSD(T) PES of the CBLA2:Eu²⁺ and CBLA:Eu²⁺ model structures at both the Ca²⁺ and Ba²⁺ doping centers, along the respective e_g and t_{2g} tetragonally distorted pathways. b) The normalized ESD/TDDFT/PBE0 computed emission spectra of the CBLA2:Eu²⁺ model along the e_g tetragonal distortion pathway. c) The normalized ESD/TDDFT/PBE0 computed emission spectra of the CBLA:Eu²⁺ model structure along the respective t_{2g} tetragonal distortion pathway. The relevant energies follow the CBLA2:Eu²⁺ $\xrightarrow[-2\text{Ba}]{-2\text{Ca}}$ CBLA:Eu²⁺ and CBLA2:Eu²⁺ $\xrightarrow[+2\text{Ca}]{-2\text{Ba}}$ CBLA:Eu²⁺ and transformations at the Ca²⁺ and Ba²⁺ doping centers, respectively.

Hence in a next step at the trimer model CBLA2:Eu² structures containing Ca²⁺ doping centers we exchange the Ca²⁺ undoped centers with Ba²⁺ in order to better accommodate the MN₈ (M=Ca²⁺, Ba²⁺) expansion along the EuN₈ compression pathway. Likewise, at the trimer structures that contain Ba²⁺ doping centers we exchange the bulky Ba²⁺ centers with the smaller Ca²⁺ centers in an effort to minimize any remaining geometric strain at the CaN₈ cuboids along the EuN₈ compression pathway. In this way the host cuboid asymmetric sequences Ba²⁺---Ca²⁺---Ba²⁺ and Ca²⁺---Ba²⁺---Ca²⁺ that are actually present in CBLA are formed. This is shown in **Figure A. 11**. As expected, this structural modification creates an asymmetry at the doped Ca²⁺ and Ba²⁺ sites in both the doped EuN₈ cuboids (35.8 Å³ at Ca²⁺ site, 43.7 Å³ at Ba²⁺ site) and undoped BaN₈ cuboids (33.2 Å³ at Ca²⁺ site) and CaN₈ cuboids (32.4 Å³ at Ba²⁺

site) at the formal CBLA2:Eu²⁺ equilibrium structure (Q~0). This is reducing further the local cuboid symmetries from D_{4h} to C_{2h}. This activates a combination of e_g and t_{2g} modes that lead the tetragonal distortion. Allowing the system to relax along the tetragonally compression pathway we compute once again the relevant CBLA:Eu²⁺ model PES.

In order to be able to compare the energetics between the CBLA2:Eu²⁺ and CBLA:Eu²⁺ PESs, the CBLA:Eu²⁺ is constructed on the basis of the CBLA2:Eu²⁺ $\xrightarrow[-2Ba]{-2Ca}$ CBLA:Eu²⁺ and CBLA2:Eu²⁺ $\xrightarrow[-2Ca]{-2Ba}$ CBLA:Eu²⁺ and transformations at the Ca²⁺ and Ba²⁺ doping centers, respectively. As seen in **Figure 12.2a** at the Ca²⁺, Eu²⁺-doped site the CBLA:Eu²⁺ PES in comparison to the CBLA2:Eu²⁺ PES stabilizes at Q=3 at about 12 kcal/mole indicating that along the tetragonal distortion pathway the transformation of CBLA2:Eu²⁺ to CBLA:Eu²⁺ is energetically feasible. In contrast, no significant stabilization is observed of the CBLA:Eu²⁺ over the CBLA2:Eu²⁺ at the Eu²⁺-doped Ba²⁺ centers. The relevant computed emission spectra are provided at **Figure 12.3a** and **Figure A. 11**. Interestingly, the intensity overtake at the Eu²⁺-doped Ca²⁺ centers happens already at Q=2, in comparison to model CBLA2:Eu²⁺ (Q=4) and at Q=3 the emission is dominated by the Eu²⁺-doped Ca²⁺ centers showing a red emission band at 14700 cm⁻¹. The respective emission band corresponding to the Eu²⁺-doped Ba²⁺ centers is shifted to higher energies and loses practically its intensity at Q=3.

12.3.3. CBLA an ‘ideal’ hypothetical host for a red Eu-doped phosphor with extraordinary emission properties

In the previous section the structural modifications that are necessary to transform CBLA2:Eu²⁺ phosphor to a unique narrow band red emitting phosphor were discussed in detail. This in principle requires the presence of a hypothetical host with 1) containing an asymmetric sequence of cuboids around the Ca and Ba doping centers. For example, sequences of cuboids with Ba²⁺---Ca²⁺---Ba²⁺ and Ca²⁺---Ba²⁺---Ca²⁺ building units and 2) formation of EuN₈ cuboids so that the Eu 4f_{xyz} ↔ Eu 5d_{x²-y²} electron decay represent dipole allowed processes.

Looking into the structural characteristics of the isotypic CBLA2, RNLSO2 and RNLSO we demonstrated in the previous sections that formation of the Ca₃Ba[LiAl₃N₄]₄:Eu²⁺, CBLA host structure that is isotypic to RNLSO adopting the tetragonal (*I4/m*) space group fulfils the above structural requirements (**Figure A. 12**). Hence in a last step of our analysis the optical absorption and emission characteristics for the hypothetical CBLA:Eu²⁺ phosphor are

discussed. In fact, as is seen in **Figure A. 13a** in the hypothetical Ca²⁺ and Ba²⁺ are alternating in the same channel forming cuboid sequences with Ca1²⁺--- Ba²⁺--- Ca1²⁺ (or equivalently Ba²⁺--- Ca1²⁺--- Ba²⁺) with elongated and compressed central cation BaN₈ and Ca1N₈ cuboids as well as Ca2²⁺--- Ca2²⁺--- Ca2²⁺ ones with elongated Ca2N₈ cuboids. As shown in **Table A. 7**, all these doping positions are in principle available for Eu doping. As expected, the computed absorption spectrum shows distinct energy separation (~ 0.5 eV) between local (4f-5d) and metal to ligand charge transfer (MLCT) bands resulting in a potentially thermally stable Eu doped phosphor. According to the NTO analysis at the Eu²⁺-doped Ca1²⁺ centers emission from the C_{2h} symmetric compressed EuN₈ cuboid is dominated by Eu 4f_{xyz} \leftrightarrow Eu 5d_{x²-y²} electron decays, while at Ba and Ca2 doped centers, emission from C_{2h} symmetric elongated EuN₈ cuboid emission is dominated by Eu 4f_{xyz} \leftrightarrow Eu 5d_{z²} electron decays.

As seen in **Figure 12.3** and according to the expectations from the descriptors relations (**Figure A. 14** and **Table A. 8**) the computed emission spectrum is characterized by a unique narrow red band with FWHM 1170 cm⁻¹ (56 nm) at 14800 cm⁻¹ originating by the Eu²⁺ -doped Ca1²⁺ centers. In this concept, CBLA:Eu²⁺ can be seen as a candidate derivative of CBLA2:Eu²⁺ with considerably improved photoluminescence properties. However, all the above require confirmation from the actual synthesis of CBLA:Eu²⁺ phosphors. We believe that the present study serves as an example of how systematic computational chemistry can be used to aid the synthetic efforts towards novel phosphor materials.

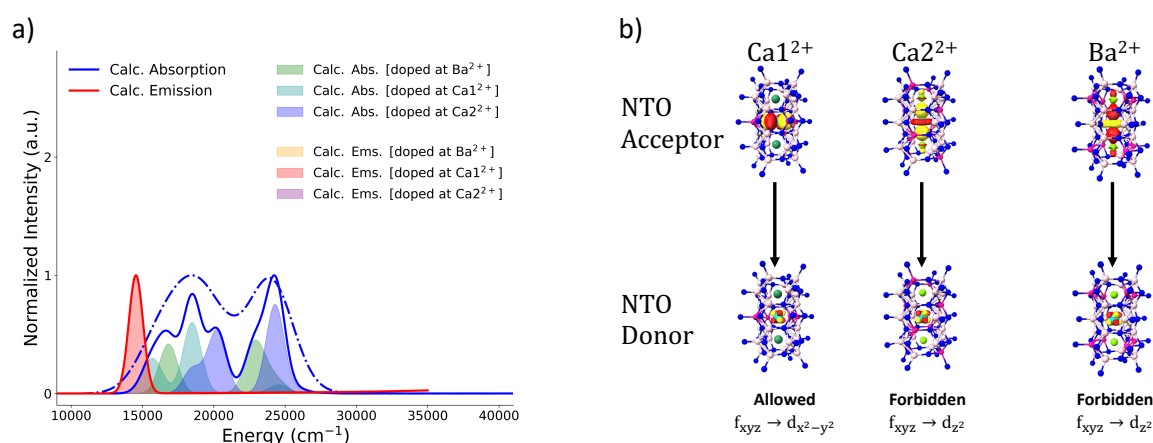


Figure 12.3. a) CBLA, calculated TD-DFT/PBE0 absorption (blue; solid and dashed lines plotted with gaussian broadening 1500, 3000 cm⁻¹, respectively) spectra and ESD/TD-DFT/PBE0 calculated (red) emission spectra. Filled colored bands indicate individual contributions of the different Eu²⁺-doped centers. b) The 1st transition responsible for emission upon relaxation for all the candidate Eu²⁺-doped centers (Ca(1)²⁺, Ca(2)²⁺, and Ba²⁺).

12.4. Conclusions

In conclusion, till this point we have showcased the effectiveness of the proposed protocol in accurately predicting the emission properties of Eu²⁺-doped phosphors. The insights gained underscore the significant role of theoretical investigations in guiding and enhancing synthesis efforts. This not only refines existing Eu²⁺-doped phosphors but also paves the way for the development of innovative phosphors with tailored optical properties for diverse technological and industrial applications. A prime illustration, is the CBLA2 phosphor, featuring noteworthy narrow band emission in the red region. However, a notable limitation is its emission in the infrared (IR) region. This chapter served as an advancement in our exploration, unveiling the potential for a systematic enhancement of the emission properties of the CBLA2:Eu²⁺ phosphor. Through in-silico synthesis, a novel CBLA:Eu²⁺ phosphor was proposed, showcasing unprecedented narrow band red emission characteristics.

Finally, achieving precise control over the characteristics of the emission band requires a more profound comprehension and manipulation of the underlying parameters governing the emission process. Consequently, the forthcoming chapter seeks to enhance our understanding of emission band behavior and deeper insight into the mechanisms governing emission intensity, alongside investigating the quantum efficiency of narrow-band phosphors. This endeavor involves an extension of the established computational protocol to incorporate multiplet effects, including spin-orbit and spin-vibronic couplings. In parallel, the defined electronic descriptors can be expanded in an effort to possibly identify new materials that can serve as narrow band phosphors with tailored properties.

13 Broadening Mechanism of Luminescence in Narrow-band Eu^{2+} -doped Phosphors

13.1. Introduction

In continuation of our investigation into Eu^{2+} -doped phosphors, this chapter focuses on elucidating the principles governing the band broadening mechanism in Eu^{2+} -doped narrow band phosphors. Specifically, our objectives are to explore the correlations between crystal structure variations in different hosts and luminescence, comprehend the relaxation mechanisms driving the broadening of luminescence spectra, and investigate the interplay among electronic, magnetic, and vibrational states influencing spectral profiles.

As illustrated through the last three chapters that, it is possible with careful setup intertwining DFT/TD-DFT based methods with ESD approach to successfully reproduce the room temperature (RT) luminescence spectra of Eu^{2+} doped narrow band phosphors and provide a satisfactory electronic structure analysis of the predominant transitions. For instance, this protocol was able to unravel the significance of the $\text{Eu}(5d)\text{-L}(2p)$ covalency of the $4f5d$ -based emissive states, and the mechanism this is influencing the broadening of the emission. It was also able to probe the implications that arise from MLCT crossing the localized $4f^65d^1 \rightarrow 4f^7$ main relaxations on the broadening and thermal stability of emission in such phosphors.[80] However, the complete picture of the predominant factors that impact the luminescence spectra leading to narrow emission bands are still elusive requiring further and accurate investigations from both experimental and theoretical perspectives.

Hence as a next step we expand our investigation efforts to involve experimental luminescence spectra at both room (300K) and low (6K) temperatures, providing an opportunity to explore spectroscopic and electronic structure descriptors influencing luminescence mechanisms on both the static and dynamic limits. In fact, low temperature (cryogenic) luminescence spectra are more informative and provide advantages for discerning

the intrinsic properties of luminescent materials. They allow for isolation of specific features, and gaining insights into radiative decay, transitions, and lifetimes. These spectra are characterized by sharper peaks due to reduced thermal energy, minimize thermal quenching, enhance resolution, and boost sensitivity in spectroscopic analysis.

It should be emphasized that comprehensive understanding of the luminescence, requires to expand our analysis beyond the so far described DFT-based computational protocol. In fact, problems of such complexity require to employ multiconfigurational wavefunction (MC WF)-based methods. These methods have been proven instrumental in enabling the study of excited states with diverse nature, probing ligand field, charge transfer states and excel in accurately capturing the impact of both static and dynamic correlation. In addition, enhanced by state-of-the-art relativistic Hamiltonians and spin-orbit coupling treatments, this approach delivers reliable descriptions magnetic structure of states and interactions between an optically active center and the host. This approach has demonstrated its accuracy and efficacy in interpreting electronic and magnetic structure and remarkable quantitative agreement with experimental absorption, and luminescence spectra of transition metal [79, 85, 87, 136, 137, 140, 146, 182, 445, 446] and rare-earth transition metal ions[79, 85, 87, 136, 137, 140, 146, 182, 445, 446] and rare-earth transition metal ions.[74, 136, 137, 446-448]

In this study, we focus on set of Eu^{2+} -doped phosphors cases (SLA, CBLA2, SMS, SALON, and SLBO), characterized by specific ligand environments and crystalline matrices and correlation with emission band characteristics. By analyzing the impact of covalency, spin-orbit coupling, and vibronic couplings across these diverse systems, we aim to establish overarching principles governing the relaxation and broadening mechanism and selection rule of the luminescence in Eu^{2+} -doped phosphors. To achieve that with high accuracy, the electronic structure, transitions (excitations and deexcitations) are studied and calculated with MC WF-based methods. In particular, the state average complete active space self-consistent field in conjunction with N-electron valence second-order perturbation theory (SA-CASSCF/NEVPT2) is employed, taking into account relativistic effect by spin-orbit coupling (SOC). The properties of magnetic (SOC) states and their spin-vibronic coupling with the environment are studied by zero-field splitting (ZFS) with corresponding parameter ($D, E/D$) of ground and emitting-excited states employing effective spin Hamiltonian approach. Luminescence spectra are calculated at different temperature by the excited state dynamics (ESD) path integral protocol[273-275] to account for vibronic couplings at Frank-Condon (FC) and Herzberg–Teller (HT) limits.

The employed computational strategy towards understanding the broadening mechanism, is schematically represented in **Figure 13.1 (a-c)**. It will be shown that the above computational approach is able to unequivocally interpret all the experimental features and unravel the complex intensity mechanism of the photoluminescence in Eu^{2+} -doped narrow band phosphors.

It will be shown that the magnetic structure, especially, of the ground state is very crucial as is impacted by the Eu-L covalency interactions. In addition, we will draw special attention to the significance of HT coupling and vibronic transitions to accurately calculate and understand the emission spectra, and relaxation times.

The insights gained in this study, aim to contribute to the engineering of innovative Eu^{2+} -doped materials with fine-tunable luminescence properties for applications in lighting, displays, and sensing.

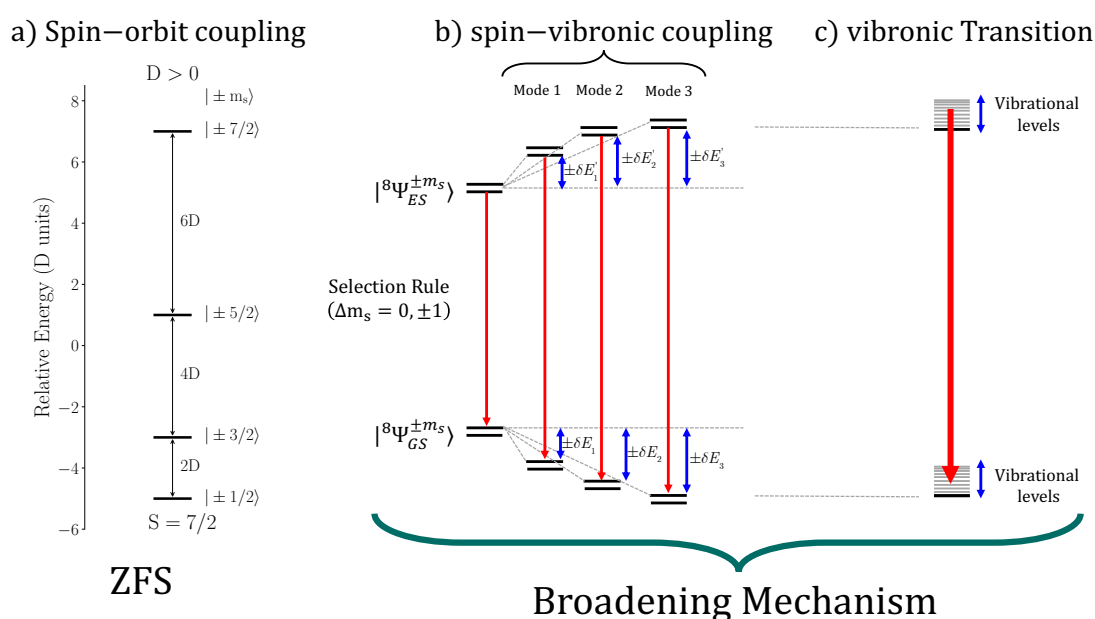


Figure 13.1. Schematic representation of the most important interaction/couplings controlling the broadening mechanism in solid-state phosphors. a) ZFS and anisotropy of the states controlled by SOC, relative energy (in units of D) of ZFS of octet multiplet ($S = 7/2$) state for ($D > 0$ axial and $|E/D| = 0$ rhombic ZFS), the order is reversed in case ($D < 0$). b) of the effect of spin-vibronic coupling in perturbing the GS and ES relativistic state through mixing with higher state through SOC and its effect on the emission broadening mechanism c) the fine vibronic transitions between the relativistic SOC state.

13.2. Study Set

A set of Eu^{2+} -doped phosphors were selected for the study, where they encompass a diverse range of symmetries, lattice structures, and bonding environments, each contributing to their unique luminescent properties. The set includes the NIR and red-emitting $\text{CaBa}[\text{Li}_2\text{Al}_6\text{O}_8]_2:\text{Eu}^{2+}$ (CBLA2)[124], the red-emitting $\text{Sr}[\text{LiAl}_3\text{N}_4]:\text{Eu}^{2+}$ (SLA)[329], $\text{Sr}[\text{Mg}_3\text{SiN}_4]:\text{Eu}^{2+}$ (SMS)[449], $\text{Sr}[\text{Al}_2\text{Li}_2\text{O}_2\text{N}_2]:\text{Eu}^{2+}$ (SALON)[125], and the blue-emitting $\text{SrLi}_2[\text{Be}_4\text{O}_6]:\text{Eu}^{2+}$ (SLBO)[126] phosphors. The structural and geometrical properties of the selected phosphors' hosts and Eu^{2+} doped cuboids have been discussed previous, refer to **Sections (10.2 and 11.2)**, **Figure 10.1**, **Figure 11.1**, **Table 10.1** and **Table 11.1**.

While for SMS, SALON, and SLBO, they have only single candidate for Eu doping (Sr^{2+}), SLA and CBLA2 have two metal centers for the Eu doping. So, for simplicity through this chapter, S1LA and S2LA refer to SLA doped at Sr^{1+} and Sr^{2+} centers, respectively. Similarly, **CBLA2** and **CBLA2** refer to CBLA2 doped at the Ca^{2+} and Ba^{2+} centers, where the doping center is bolded.

13.3. Experimental Spectra

The experimental emission spectra of the studied (SLA, CBLA2, SMS, SALON, and SLBO): Eu^{2+} -doped phosphors recorded at room (300K) and cryogenic (6K) temperatures are provided in **Figure 13.2** and important features of the spectra are summarized in **Table 13.1**.

The investigation of emission spectra at room temperature (RT) has been covered in earlier chapters (**Sections 10.3 and 11.3**). However, the emission spectra at lower temperatures reveal intriguing feature changes. These spectra offer valuable insights into the luminescent behavior and properties of these phosphors, contributing to a better understanding of the underlying broadening mechanism. Consequently, they are given more focus and emphasizing changes in the luminescence due to decrease in temperature.

Generally, the luminescence spectra are blue-shifted with the reduction in ligand field strength (LFS), corresponding to the expansion of the $[\text{EuL}_8]$ cuboid or the transition from nitride ($\text{L}=\text{N}^{3-}$), oxynitride ($\text{N}^{3-}/\text{O}^{2-}$) to oxide (O^{2-}) ligands in the 1st coordination ligands. The 6K emission spectra exhibit no significant shift in emission band max. energy ($E_{\text{max}}^{\text{ems}}$) in comparison to the 300K spectra. However, the emission band becomes narrower with

temperature-dependent broadening reduction $\Delta\delta$ ($= \text{FWHM}_{300\text{K}} - \text{FWHM}_{6\text{K}}$) ranging between ~ 410 - 932 cm^{-1} .

At 6K, the spectra are more structured and vibronically resolved in SLA and CBLA2 phosphors accompanied with large $\Delta\delta$. For SLA, while it has two doping sites but exhibits only one peak at both low and high temperature. SLBO also exhibits some resolution with a clear splitting of the emission band at low temperature but with small $\Delta\delta$. In SMS and SALON, no vibronic progression is detected at 6K again with small $\Delta\delta$.

In SLA and CBLA2 the reduction of the bandwidth ($\Delta\delta$) occurs from both low- and high-energy bandsides (stokes and anti-stokes bandsides) with ($\Delta\delta \sim 680, 860$ and 630 cm^{-1}) for SLA and CBLA2 at Ba^{2+} and Ca^{2+} doping sites, respectively. In SMS, SALON, and SLBO, ($\Delta\delta$) occurs mainly on the anti-stokes bandside, with ($\Delta\delta \sim 240, 410$ and 400 cm^{-1}), respectively.

Overall, temperature-dependent broadening is clearly and consistently observed across the different studied phosphors. Low temperatures reveal variations in observed spectroscopic features, prompting a thorough investigation of the origin of these divergent observations in the subsequent sections.

13.3.1. What defines the narrow band broadening in narrow band phosphors?

The emission band is defined by its energy position, intensity, and bandwidth. Conventionally, the bandwidth of optical bands is conventionally determined on the basis of the magnitude of full width at half maximum (FWHM). Hence FWHM is used as a ‘ruler’ that in a first approximation can categorize the different optical bands (or respective emitter) as broad or narrow (phosphor). However, in the case of the narrow band phosphors this ruler loses sensitivity. For example, in the case of Eu^{2+} -doped phosphors SLBO and SALON, on the wavelength scale FWHM amounts to 25 and 48 nm at 300K and 17 and 31 nm at 6K. That is consistent with their assignment as “ultra-narrow” blue- and “narrow” red-emitting phosphors, respectively. However, on the wavenumber energy scale the two phosphors have same FWHM 1220 cm^{-1} at 300K. In contrast, at low temperature (6K) the order of the FWHM values is reversed, with respect to nm scale, amounting to 810 cm^{-1} and 820 cm^{-1} for SALON and SLBO, respectively.

Furthermore, this study reveals that categorizing the emission process of Eu^{2+} -doped phosphors as ultranarrow, narrow, or broad, as commonly done in literature, [125, 126, 329] is a more complex task than initially perceived. In fact, the luminescence in Eu^{2+} -doped phosphors is very complex and challenging to study. Some of the complexities have been summarized in the introduction **Chapter 8**. Through this study, we will show that while some phosphors exhibit very similar bandwidths, they can follow distinct relaxation pathways influenced by various factors. In fact, the oversimplification in these and similar phosphors systems can be misleading and may result in incorrect or contradictory explanations.[74, 440, 450]

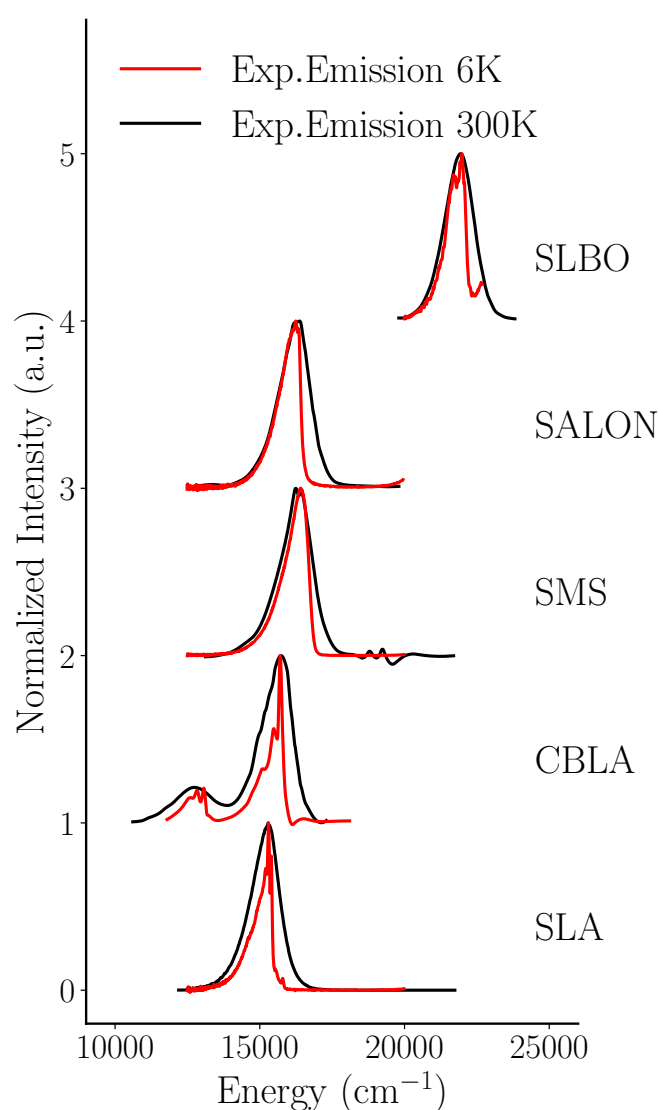


Figure 13.2. Experimental Emission spectra at 6K (red) and 300K (black) of the studied (SLA, CBLA2, SMS, SALON, SLBO): Eu^{2+} -doped phosphors.

Table 13.1. Experimental emission spectra band max. energy ($E_{\text{max}}^{\text{ems}}$), color, bandwidth (FWHM) at 6K and 300K, and temperature-dependent broadening $\Delta\delta$ ($= \text{FWHM}_{300\text{K}} - \text{FWHM}_{6\text{K}}$) for the studied (SLA, CBLA2, SMS, SALON, SLBO): Eu^{2+} -doped phosphors. The exp. excitation laser used for the emission measurement is also given. All energies are given in both cm^{-1} and nm, where the latter are given in square paratheses.

Phosphor	Excitation laser (cm ⁻¹) [nm]	Experimental Emission Band				
		Color	E _{max} ^{ems}	FWHM _{300K}	FWHM _{6K}	Δδ
			(cm ⁻¹) [nm]			
Sr[LiAl ₃ N ₄]:Eu ²⁺ SLA[329]	22727 [440]	red	15385 [650]	1180 [50]	500 [23]	680
CaBa[LiAl ₃ O ₄] ₂ :Eu ²⁺ CBLA2[124]	22523 [444]	red	15674 [638]	1230 [50]	370 [15]	860
		NIR	12658 [790]	1430 [89]	800 [50]	630
Sr[Mg ₃ SiN ₄]:Eu ²⁺ SMS[449]	22222 [450]	red	16250 [615]	1140 [43]	900 [34]	240
Sr[Al ₂ Li ₂ O ₂ N ₂]:Eu ²⁺ SALON[125]	22222 [450]	red	16260 [614]	1220 [48]	810 [31]	410
SrLi ₂ [Be ₄ O ₆]:Eu ²⁺ SLBO[126]	25000 [400]	blue	21978 [455]	1200 [25]	820 [17]	400

13.4. Theory

13.4.1. Zero-Field Splitting (ZFS) and Effective Spin Hamiltonian

As have been discussed in **Sections 4.4.5-4.4.7**, owing to the strong SOC by Eu^{2+} , the ground and excited states, with spin S , split into Kramer's doublets (KDs) with spin projection quantum numbers (M_S) taking values $-S, S + 1, \dots, S$. As shown in **Section 4.4.7**, SOC can be treated in the framework of quasidegenerate perturbation theory (QDPT).[140, 149] And the relativistic state ($|\Psi_J^{M_S}\rangle$), the SOC-corrected wavefunction, can be represented by

$$|\Psi_J^{M_S}\rangle = |\Phi_J^{S,M_S}\rangle + \sum_{K \neq J} \sum_{S'} \sum_{M'_S} |\Phi_K^{S',M'_S}\rangle \frac{\langle \Phi_K^{S',M'_S} | H_{SOC} | \Phi_J^{S,M_S} \rangle}{E_K - E_J} \quad (13.1)$$

where, $|\Phi_J^{S,M_S}\rangle$ and $|\Phi_K^{S',M'_S}\rangle$ are the non-relativistic states separated with energies E_J and E_K , respectively. H_{SOC} is spin-orbit coupling Hamiltonian which depends on the electronic configurations and symmetry of, and inversely to the energy difference between coupled states.

In the absence of an external magnetic field, the magnetic energy levels of both the ground and the lowest excited states undergo a splitting by both effects of the SOC and the surrounding environment, this is known as zero-field splitting (ZFS). For Eu^{2+} , the octet ($S = 7/2$) ground $^8S_{7/2}$ state and lowest excited (emitting) state of the excited $^8\{^7F \otimes ^1D\}$ multiplet, each of these states split into eight relativistically corrected SO-states, each grouped in 4 KDs, with $M_S = \pm 7/2, \pm 5/2, \pm 3/2, \pm 1/2$.

The energy description of the ground and lowest excited states can be described with effective spin-Hamiltonian (SH) formulation at zero field (ZFS), excluding nuclear interaction, as depicted in **Equations (4.39)-(4.41)** and within an ($S = 7/2$) excited multiplet, ZFS matrix takes the form

$$\hat{H}_{S,ZFS} = \begin{pmatrix} & |+\frac{7}{2}\rangle & |+\frac{5}{2}\rangle & |+\frac{3}{2}\rangle & |+\frac{1}{2}\rangle & |-\frac{1}{2}\rangle & |-\frac{3}{2}\rangle & |-\frac{5}{2}\rangle & |-\frac{7}{2}\rangle \\ \langle+\frac{7}{2}| & 7D & 0 & \sqrt{7}\sqrt{3}E & 0 & 0 & 0 & 0 & 0 \\ \langle+\frac{5}{2}| & 0 & D & 0 & 3\sqrt{5}E & 0 & 0 & 0 & 0 \\ \langle+\frac{3}{2}| & \sqrt{7}\sqrt{3}E & 0 & -3D & 0 & 2\sqrt{15}E & 0 & 0 & 0 \\ \langle+\frac{1}{2}| & 0 & 3\sqrt{5}E & 0 & -5D & 0 & 2\sqrt{15}E & 0 & 0 \\ \langle-\frac{1}{2}| & 0 & 0 & 2\sqrt{15}E & 0 & -5D & 0 & 3\sqrt{5}E & 0 \\ \langle-\frac{3}{2}| & 0 & 0 & 0 & 2\sqrt{15}E & 0 & -3D & 0 & \sqrt{7}\sqrt{3}E \\ \langle-\frac{5}{2}| & 0 & 0 & 0 & 0 & 3\sqrt{5}E & 0 & D & 0 \\ \langle-\frac{7}{2}| & 0 & 0 & 0 & 0 & 0 & \sqrt{7}\sqrt{3}E & 0 & 7D \end{pmatrix} \quad (13.2)$$

with $D = 2/3D_z$, $E = (D_x - D_y)/3$ and finally leading to SH ($S = 7/2$) as in **Equation (13.2)**. In case of axial, or near axial conditions where $E \sim 0$, the 4 Kramers doublets are splitted by $7D$, D , $-3D$, $-5D$, energy units, as shown in **Figure 13.1a**. The ZFS (D and E/D) parameters are usually used to describe the magnetic structure of the relativistic states. The ZF splitting arises due to interactions within the electrons' environment, primarily stemming from SOC and the asymmetry of the local environment.

13.4.2. Theory of photoluminescence relaxation times

The transition rate of spontaneous luminescence between a set of relativistically corrected initial (excited) $|\Psi_I\rangle$ and final (ground) $|\Psi_J\rangle$ state(s) is given by the general expression of the Fermi's golden rule:

$$k_{PL}(\omega) = \frac{4\omega_{PL}^3 n^2}{3\hbar c^3} \sum_J B_J(T)/Z \sum_I |\langle\Psi_I|\hat{\mu}|\Psi_J\rangle|^2 \delta(E_{IJ} \pm \omega_{PL}) \quad (13.3)$$

where $\hat{\mu}$ defines the electric dipole operator as $\hat{\mu} = \sum_A Z_A \hat{R}_A - \sum_i \hat{r}_i$, here A sums over nuclei with charges Z_A at positions \hat{R}_A , i over the electrons, n is the refractive index, \hbar is the reduced Planck constant. $B_J(T)$, Z are the Boltzmann population of the excited states at temperature T , and partition function.

Under the adiabatic approximation, the electronic and vibrational wavefunction can be split,

$$k_{PL}(\omega) = \frac{4\omega_{PL}^3 n^2}{3\hbar c^3} \sum_J B_J(T)/Z \sum_I |\mu_{IJ}^{e,R}|^2 \langle \chi_I | \chi_J \rangle^2 \delta(E_{ij} \pm \omega_{PL}) \quad (13.4)$$

where, χ_I is the vibrational WF and $\langle \chi_I | \chi_J \rangle^2$ is the Frank-Condon (FC) coupling factor between PESs of states I, J and δ is the correlation function. $\mu_{IJ}^{e,R}$ is the electronic transition between the relativistic states and can be written as,

$$\begin{aligned} \mu_{IJ}^{e,R} = & \sum_K \sum_{S'} \sum_{M'_S} \frac{\langle \Phi_I^{S,M_S} | H_{IK}^{SOC} | \Phi_K^{S',M'_S} \rangle \langle \Phi_K^{S',M'_S} | \mu^{e,N} | \Phi_J^{S,M_S} \rangle}{E_K - E_I} \\ & + \sum_K \sum_{S'} \sum_{M'_S} \frac{\langle \Phi_I^{S,M_S} | \mu^{e,N} | \Phi_K^{S',M'_S} \rangle \langle \Phi_K^{S',M'_S} | H_{KJ}^{SOC} | \Phi_J^{S,M_S} \rangle}{E_K - E_J} \end{aligned} \quad (13.5)$$

where, in the first and second terms the ground state I and excited state J are SOC-perturbed, respectively. $\mu^{e,N}$, is the electronic transition between the non-relativistic states given by Φ . Due to the large energy gap between the ground I and excited states $\{K\}$, the first term can be safely dropped, and the equation can be simplified as follows

$$\mu_{IJ}^{e,R} = \sum_K \mu_{IK}^{e,N} H_{KJ}^{SOC} \quad (13.6)$$

where K runs for all the excited states including J and

$$\mu_{Ik}^e = \sum_{S'} \sum_{M'_S} \langle \Phi_I^{S,M_S} | \mu | \Phi_K^{S',M'_S} \rangle \quad (13.7)$$

$$H_{kJ}^{SOC} = \sum_{S'} \sum_{M'_S} \frac{\langle \Phi_K^{S',M'_S} | H_{KJ}^{SOC} | \Phi_J^{S,M_S} \rangle}{\Delta E_{KJ}} \quad (13.8)$$

13 Broadening Mechanism of Luminescence in Narrow-band Eu^{2+} -doped phosphors

Inclusion of vibronic coupling, assuming that electronic transition dipole μ_{IJ}^e vary slowly with respect to the nuclear motion, so the transition dipole can be expanded as Taylor's series around the equilibrium geometry ($Q = 0$) is given by

$$\mu(Q) = \mu(Q=0) + \sum_{\alpha} \left. \frac{\partial \mu}{\partial Q_{\alpha}} \right|_{Q_{\alpha}=0} Q_{\alpha} + \frac{1}{2} \sum_{\alpha, \beta} \left. \frac{\partial^2 \mu}{\partial Q_{\alpha} \partial Q_{\beta}} \right|_{Q_{\alpha, \beta}=0} Q_{\alpha} Q_{\beta} + \dots \quad (13.9)$$

where, Q represents the vibrational normal mode coordinates and α is the vibrational normal modes, for $3N - 6$ modes. Equivalently it can be given by

$$\mu_{IJ}^e(Q) = \mu_0 e^{\xi Q} \quad (13.10)$$

where, μ_0 is the transition probability before vibronic coupling (FC), ξ is the vibronic coupling $\frac{\partial(\sum_k \mu_{Ik}^e H_{kJ}^{SOC})}{\partial Q_{\alpha}}$. Up to second order the different contributing terms can be represented by the matrix presented in **Scheme 13.1**.

	μ_{Ik}^e	$\mu_{Ik}^e / \partial Q_{\alpha}$	$\mu_{Ik}^e / \partial^2 Q_{\alpha}$
H_{kj}^{SOC}	FC (0 th order HT x 0 th order SVC)	1 st order HT	2 nd order HT
$H_{kj}^{SOC} / \partial Q_{\alpha}$	1 st order SVC	(1 st order HT x 1 st order SVC)	
$H_{kj}^{SOC} / \partial^2 Q_{\alpha}$	2 nd order SVC		

Scheme 13.1. Schematic representation different vibronic coupling, growing from 0th (in red), 1st (linear, in green), to 2nd (quadratic, in blue) order Herzberg-Teller coupling (HT) and spin-vibronic coupling (SVC) on columns and rows, respectively. The 0th order of vibronic coupling (both HT and SVC) give the Frank-Condon coupling (FC) limit.

Excluding the higher ($2^{\text{nd}}, \dots$) order terms due to their difficulty to calculate,

$$\mu_{IJ}^e(Q) = \sum_k \mu_{Ik}^e H_{kJ}^{\text{SOC}}(0) + \sum_{\alpha} \frac{\partial(\sum_k \mu_{Ik}^e H_{kJ}^{\text{SOC}})}{\partial Q_{\alpha}} \bigg|_0 Q_{\alpha} \quad (13.11)$$

where, the first term represents the FC limit. The second terms give the linear vibronic coupling of SOC and electronic transition dipole. That can be pictorially shown as in **Scheme 13.1**.

From **Equation (13.11)**,

- at the FC limit ($\xi = 0$), the relaxation rate k_{PL} (also time $\tau_{PL} = 1/k_{PL}$) and total electronic transition between I, J states is in linear relation with the nonrelativistic transition dipole between ground I state to the excited states manifold $\{K\}$ as μ_{Ik}^e and their SOC coupling H_{kJ}^{SOC} .
- While at the HT limit ($\xi \neq 0$), the relaxation rate k_{PL} will grow exponentially with increasing the vibronic coupling. The vibronic coupling will play critical rule and dominate the relaxation processes, emission band broadening as we see in the main text.

13.5. Computational Details

All calculations were performed employing the ORCA 5.0 suite of programs.[354, 355, 411, 412] Crystal structures' coordinates were taken from the crystallographic data,[124-126, 329-331, 449] refined based on the experimental crystallographic X-ray diffraction. refined based on the experimental crystallographic X-ray diffraction. All the clusters were constructed on the basis of the embedded cluster approach, as discussed in **Section 7.3**. While, as shown in **Chapters 10** and **11**, cluster size has been converged in some cases to dimer and in some other cases to trimer cluster, so, for sake of consistency, trimer clusters are employed for all the studied phosphors. In each cluster, the Eu will replace the central metal ion in the center (Ca/Sr/Ba). For phosphors featuring multiple Eu^{2+} doping centers, they are treated in separated clusters, where only the studied center is replaced with Eu ion. All the other cluster preparation details have been done and discussed previously in **Sections 10.5** and **11.5**.

In all calculations, the relativistically re-contracted def2-TZVP basis set of the Ahlrichs group[406, 407] were used for all main group element atoms while for Sr, Ba and Eu the segmented all-electron relativistically re-contracted (SARC) scheme[397-400] was employed.

was employed. The calculations were accelerated by employing the resolution of identity approximation (RI)[413] for the Coulomb integrals, while the exchange terms were efficiently computed using the ‘chain-of-spheres’ (COSX)[414, 415] approximation by utilizing the SARC/J coulomb fitting and def2-TZVP/C correlation auxiliary basis sets, respectively. Second-order Douglas-Kroll-Hess relativistic corrections (DKH2)[401, 402] were used throughout to account for scalar relativistic effects, employing the finite nucleus model.[403]

SA-CASSCF[169, 184, 193, 395] method in conjunction with NEVPT2[193, 395] was employed to compute the electronic structure (ground and excited states manifolds) of the Eu^{2+} -doped structures. The selected active space was expanded to include Eu 4f, 5d and 5f shells. In fact, inclusion of 5f shell is essential, as the inter-shell $4f \rightarrow 5d$ transitions introduce large radial dynamical correlation effects which can be accurately treated by NEVPT2 in conjunction with an expanded CAS(7,19), as discussed in **Section 9.1.1**.

The energetics and properties of spin states are computed by introduction of SOC in the framework of QDPT. [140, 149] As discussed in **Section 13.4**, the ground and lowest excited states are studied in terms of the ZFS parameters ($D, E/D$) in the framework of the spin Hamiltonian formulation.

Luminescence spectra at different temperatures (6 and 300K) were computed using SA-CASSCF(7,19)/NEVPT2/SOC in conjunction with the ESD path integral protocol[273-275] includes Duschinsky mixing and vibronic coupling including the zero-order Frank-Condon (FC) and first-order Herzberg–Teller (HT) coupling schemes. Huang-Rhys (HR) parameter (S) and derivative of the electronic Hamiltonian ($\xi = \partial H / \partial Q$) along normal mode Q , are used as descriptors for the vibronic coupling on FC and HT coupling limits, respectively.

In the relativistic limit, the ground and excited (emissive) states consist of four Kramers doublets (KDs) each. Hence, the final emission spectra are computed as the sum of all 64 transitions between 4 excited KDs to the 4 ground KDs, considering the thermal population of the excited KDs according to Boltzmann distribution at specific temperature.

Unless otherwise mentioned, the spectra convolution was initially performed employing a constant Gaussian broadening using a 10 cm^{-1} linewidth in an effort to collect as much as possible information about the emission profile and vibronic interactions. Unless otherwise stated, a second Gaussian broadening using a 250 cm^{-1} linewidth was applied for a better visual agreement with the experimental spectra.

13.6. Analysis of the Electronic and Magnetic Structure of Ground and Excited Emissive States

13.6.1. Non-Relativistic Limit

To investigate the electronic structure of the Eu^{2+} -doped phosphors under study, SA-CASSCF(7,19) calculations were conducted averaging over 36 octet and 35 sextet states. This can be simply expressed as $\text{SA}(^836,^635)\text{-CASSCF}(7,19)$. Then, NEVPT2 method will be applied to incorporate dynamic correlation effects. While for free Eu^{2+} ion, both 4f and 5f are degenerate and the lowest excited states are sextet ($4f^7$) excited states (refer to **Figure 9.3**), Eu^{2+} doping in crystal structure induces splitting in both 4f and 5d orbitals by ligand field effect (LFE). Details about symmetries and Eu-L bond length of $[\text{EuL}_8]$ cuboids are given in **Table 13.2**, **Table 10.1**, and **Table 11.1**.

The splitting and configurations of SA-CASSCF optimized active orbitals are given in **Figure A. 15** and **Table A. 9**. The calculated non-relativistic states across the studied phosphors are presented in **Figure 13.3**. Generally, for all the cases, the octet ground state is well isolated from all the excited states. While the excited states manifold is dense, it can be categorized into two regions with respect to the lowest excited sextet states. The lower region, contains the lowest 14 ($4f^65d^1$) excited states, representing single electron excitations from all the seven 4f to lowest two $5d_{z^2/x^2-y^2}$, originated from e_g orbital splitting, see **Figure 13.4 b**. While the upper region contains overlapping between octet states arises from the 21 ($4f^65d^1$) excited states, arising from all $4f \rightarrow 5d_{xy/xz/yz}$ single excitations, and the 35 sextet ($4f^7$) excited states. The splitting between the octet manifold between the two regions follow, the splitting of 5d orbitals. The total splitting of sextet excited manifold is very similar for most of the cases, with two extreme cases CBLA2 and SLBO, in terms of the energy gap between the lowest sextet and the ground state ($\sim 23000 \text{ cm}^{-1}$) and the total splitting of the manifold (22000 cm^{-1}), such similarity reflect the weak impact and less sensitivity of the 4f orbitals and its corresponding states to the crystal field effect (CFE). For SLBO and CBLA2, the energy gaps with the ground state are ~ 28000 and 16000 cm^{-1} , respectively while the total splittings of the sextet manifold are ~ 12000 and 30000 cm^{-1} . That again reflects the weakest CFE on 4f orbitals by the pure oxide ligand in the former, and the strongest CFE by very compressed nitride local structure in the latter, as clearly shown in the splitting of 4f orbitals **Figure A. 15**. In SLBO, the weak CFE also, in addition to higher symmetric local cuboid of C_4 , results in degeneracy in 4f orbitals.

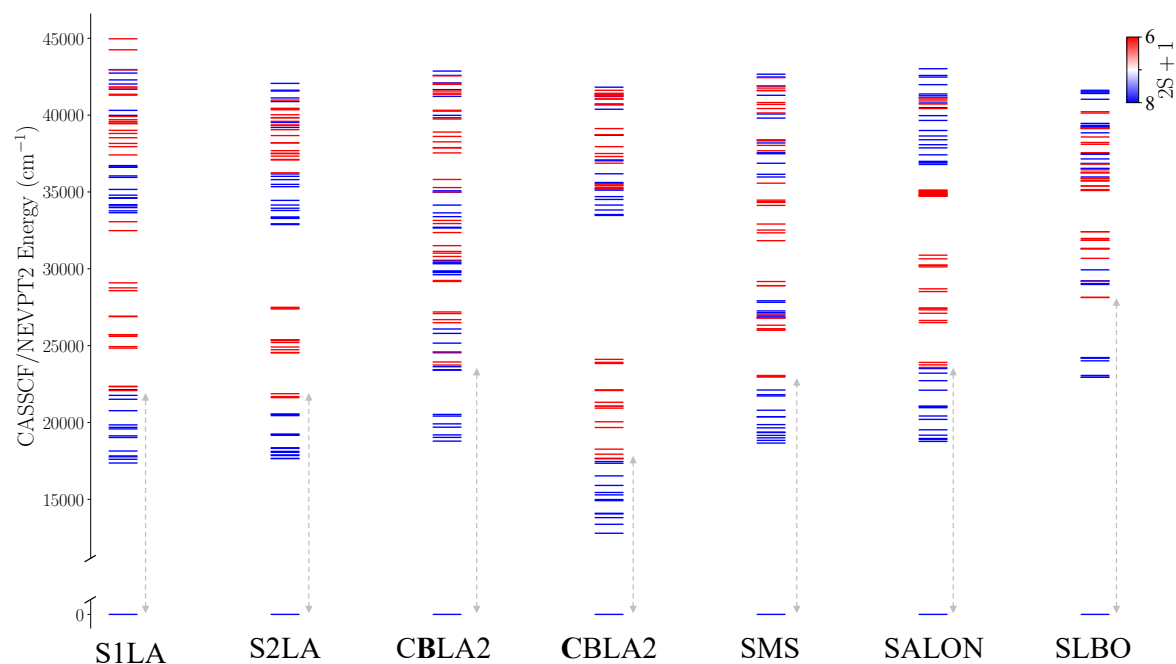


Figure 13.3. The energies (in cm^{-1}) of the non-relativistic states across the studied phosphors, calculated employing SA($836,635$)-CASCF(7,19)/NEVPT2. The energy gap between the ground and lowest sextet state is visually illustrated by dashed gray arrows.

Now let us focus on the lowest excited states, which dominate the emission process. As has been previously discussed,[80] the (emitting) excited state in Eu^{2+} doped phosphors comprises $(4f^6 5d_{z^2}^1)$ – or $(4f^6 5d_{x^2-y^2/xy}^1)$ – based molecular orbital. The splitting is controlled by both the host phosphor first (Eu in L_8 cube) and second (Eu in L_4 square planar) coordination spheres around the Eu^{2+} ion, where the latter have lower impact due to longer distance from the Eu ion. In principle lower the symmetry of Eu environment from ideal cubic (inverted O_h) symmetry lift the degeneracy of the e_g orbitals, as illustrated in **Figure 13.4**. In fact, for all the studied system, the $d_{x^2-y^2}$ and d_{xy} share the same irreducible representations within the Eu local environment point group, so they can mix. Lowering of symmetry owing to the synergic action of 1st and 2nd coordination spheres may stabilize either $5d_{x^2-y^2/xy}$ or $5d_{z^2}$ to dominate the lowest excited state, as have been introduced in **Section 9.2.2** and summarized in **Figure 13.4**. While, for all studied cases, the lowest 5d orbital are clearly split, in SMS, the lowest 5d orbitals are very close in energy, while the lowest one is dominated by $5d_{z^2}$. As well as, in the case of S2LA, the two orbitals remain practically quasi-degenerate, both showing mixed

$(4f^6 5d_{z^2/x^2-y^2/xy}^1)$, characters, as summarize in **Figure 13.4** or in more details in **Table A. 9**.

For all cases, the 5d orbitals have some contributions from ligand ($L - 2p$) orbitals, where L is either N^{3-} or O^{2-} , denoted as the Eu-L covalent interaction or the covalency, while the 4f are purely non-bonding.[136, 137]

Across the study set the GS and ES generally transform as $^8A_u/A$ in centrosymmetric/non-centrosymmetric point groups, respectively. In SLBO, the lowest ES is doubly degenerate E due to degenerate 4f orbitals. Overall, the emission band origin across the study set follows the electron decay patterns shown in **Table 13.2**.

Table 13.2. Local cuboid symmetries (Γ), predominant emission transition, and the dominating 4f orbital during the emission, on the non-relativistic limit, across the study set of phosphors and different doping sites.

Phosphors	Doping site	Γ	Emission process	4f
Centrosymmetric Structures				
SALON	Sr^{2+}	C_{2h}	$^8A_u(4f^6 5d_{z^2}^1) \rightarrow ^8A_u(4f^7)$	$4f_{xyz}$
CBLA2	Ba^{2+}			
S2LA ¹⁾	Sr^{2+}	C_{2h}	$^8A_u(4f^6 5d_{z^2/x^2-y^2/xy}^1) \rightarrow ^8A_u(4f^7)$	$4f_{xyz}$
CBLA2	Sr^{2+}	D_{4h}	$^8A_u(4f^6 5d_{x^2-y^2/xy}^1) \rightarrow ^8A_u(4f^7)$	$4f_{xyz}$
Non centrosymmetric Structures				
SMS	Sr^{2+}	C_2	$^8A(4f^6 5d_{z^2}^1) \rightarrow ^8A(4f^7)$	$4f_{xyz}$
S1LA	Sr^{2+}	C_s		
SLBO ²⁾	Sr^{2+}	C_4	$^8E(4f^6 5d_{x^2-y^2/xy}^1) \rightarrow ^8A(4f^7)$	$4f_{xyz/z(x^2-y^2)}$

1) while local environment $[\text{EuN}_8]$ cuboid transforms as C_{2h} , it lowers fast to C_s after including neighboring cuboids.

2) the excited state is subject to $((A \oplus E) \otimes (e \oplus a))$ pseudo Jahn Teller effect (PJT).

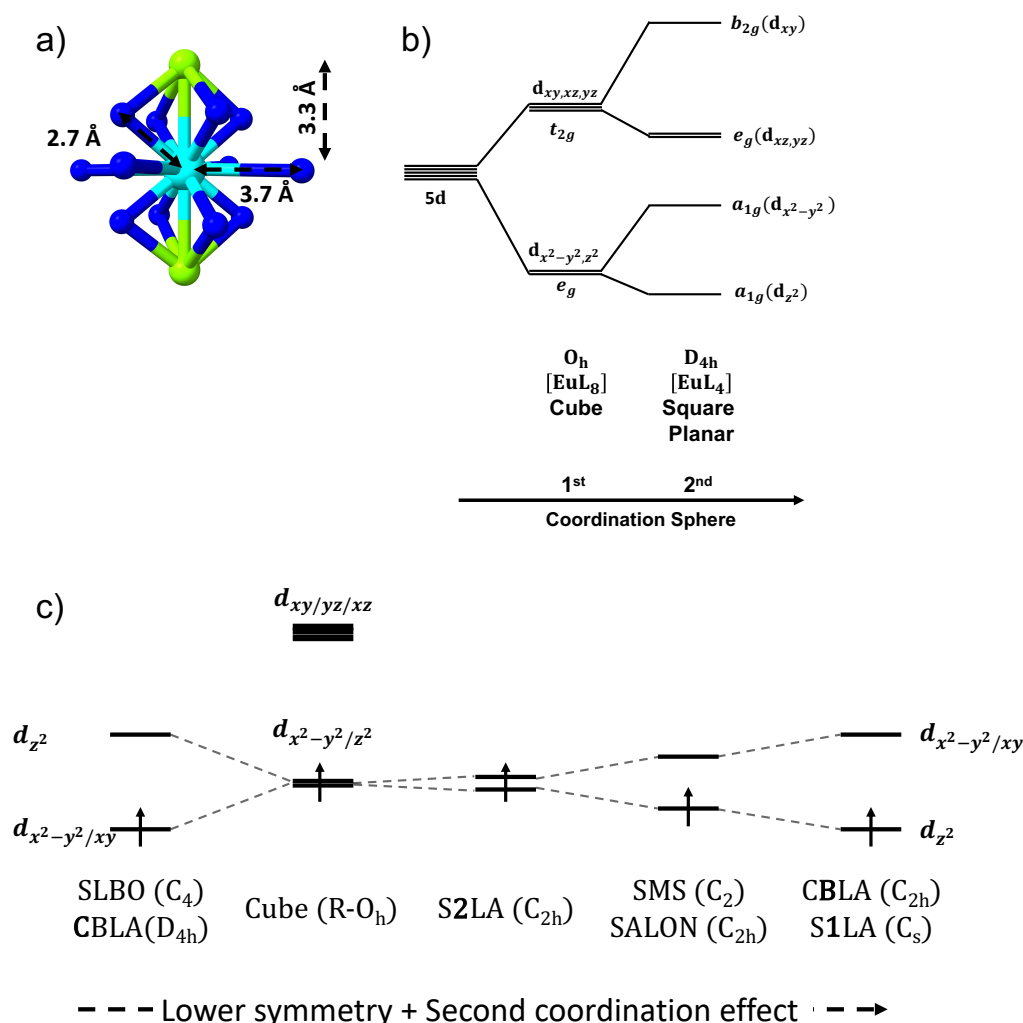


Figure 13.4. a) Ligand environment of Eu in the studied phosphors, bond distances are given for CBLA2 phosphors doped at Ca site. The environment is overlapped N₈ cube (in the 1st coordination) and N₄ square planar (in the 2nd coordination sphere). Atom colors: Eu (cyan), Ca (green), and N (blue). b) Splitting of d orbitals by reversed O_h 1st coordination L₈ cube and then successive splitting by D_{4h} 2nd coordination square planar L₄. c) Observed splitting of the lowest 5d orbitals (e_g in ideal cubic field) across the different systems.

13.6.2. Relativistic Limit

In the non-relativistic limit, the electronic and luminescent aspects appear relatively straightforward. However, once moving to the relativistic limit, the complexity of the problem escalates rapidly. In the former scenario, the emissive electronic relaxation can generally be described as a one-electron $5d \rightarrow 4f$ decay. Specifically, this involves the transition from the lowest 5d orbital to the highest 4f orbital, considering the splitting of these orbitals due to the

combined effects of the crystal and ligand field. In that context, the dominating influence on the 5d orbitals is primarily due to the static environmental effect or its dynamic component, which manifests in vibronic coupling. As a result, a significant emphasis has been placed on examining the characteristics of the 5d orbitals, with particular focus on the lowest one due to its pivotal role in the luminescent behavior.

However, on the relativistic limit, the complete 4f orbital is curial and dominate the magnetic structure of both the ground and excited states. First, they are much closer to the heavy Eu nucleus leading to much relativistic and SOC effects. Second, owing to the shielding of 4f orbitals and the consequent weak environmental effect, they are weakly split with $\sim 4000 \text{ cm}^{-1}$ for all studied phosphors, (again with two extremes ~ 2000 and $\sim 8000 \text{ cm}^{-1}$ for SLBO and CBLA2), compared to $\sim 40000 \text{ cm}^{-1}$ total splitting in 5d orbitals, as show in **Figure A. 15**.

The calculated relativistic states across the studied phosphors are presented in **Figure 13.5**. Generally, for all the cases, all the states are split into KDs. While, the ground KDs are well isolated from the excited KDs, the excited state manifold is very dense characterized by one or two continuous bands.

Again, focusing on the octet ground (GS) and lowest excited (ES) states. At the relativistic limit, both parent non-relativistic octet, acceptor GS and donor ES are splitting into 4 KDs, with M_s components $M_s = \pm 7/2, \pm 5/2, \pm 3/2, \pm 1/2$. For GS, they mix only weakly with higher excited states but exhibit strong mixing in ES. SOC strength $\left(= \sqrt{\text{Re}(\text{SOC})^2 + \text{Im}(\text{SOC})^2} \right)$, between the emissive excited state $^8|\Psi_1\rangle$ with all the higher $^{2S+1}|\Psi_J\rangle$ states can be estimated by the following relation.

$$\text{SOC} = \sum_{S=7/2,5/2} \sum_{M_s=S-1,S,S+1} \sum_J \frac{\langle ^{2S+1}\Psi_J^{M_s} | H_{\text{SOC}} | ^8\Psi_1^{M_s} \rangle}{E_J - E_1} \quad (13.12)$$

where $S = 7/2, 5/2$ and M_s can take $S, S \pm 1$, (according to $\Delta M_s = 0, \pm 1$ selection rule[271]). The energy splitting of the M_s is subject to ground and excited states zero field splitting ZFS, quantified by $(D, E/D)$ parameters. Further details are provided in **Section 13.4**.

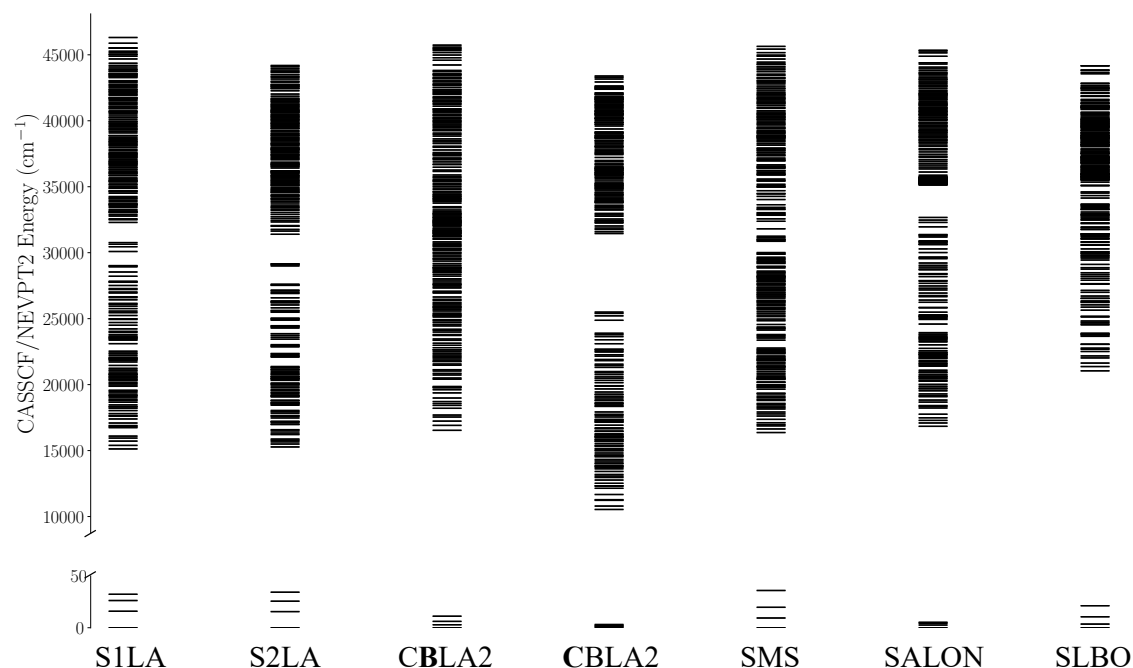


Figure 13.5. The energies (in cm^{-1}) of the relativistic states across the studied phosphors, calculated employing SA(⁸36,⁶35)-CASSCF(7,19)/NEVPT2/SOC.

13.6.2.1. Ground State magnetic structure and ZFS

As a result, the ZFS in GS $^8|\Psi_0\rangle(4f^7)$, is weak ($|D| < 3 \text{ cm}^{-1}$) and occurs only due to SOC interactions with excited spin-flip sextet states $^6|\Psi_f\rangle(4f^7)$, while no coupling with excited octet $^8|\Psi_f\rangle(4f^65d^1)$ states, owing to vanishing of $\langle f|h_{\text{soc}}|d\rangle = 0$ coupling. The coupling between octet ground and octet excited state can be possible through covalent interactions however, 4f orbital are mainly non-bonding. However, as previously discussed in **Section 9.3**, complete description of the ground state of Eu^{2+} is like $(4f^n5d^0)$. [136] Hence in this concept the 5d covalent interactions are probing indirectly the bonding characteristics of the ground state.

The ZFS values of ground state across the studied phosphors are given in **Table 13.3**, and non-relativistic and relativistic energy levels are shown in **Figure 13.3**, and **Figure 13.5**, respectively.

Table 13.3. Calculated ZFS ($D, E/D$) parameters of ground state multiplet, across the studied set of Eu^{2+} -doped phosphors (SLA, CBLA2, SMS, SALON, SLBO): Eu^{2+} , and their various doping sites (M^{2+}).

Phosphor	M^{2+}	ZFS_{GS}	
		D	E/D
		(cm ⁻¹)	
S1LA	Sr1 ²⁺	-2.66	0.07
S2LA	Sr2 ²⁺	-2.68	0.16
CBLA2	Ba ²⁺	+0.86	0.18
CBLA2	Ca ²⁺	+0.21	0.32
SMS	Sr ²⁺	+2.79	0.17
SALON	Sr ²⁺	-0.43	0.04
SLBO	Sr ²⁺	+1.78	0.00

The magnetic anisotropy of GS is quantified by ZFS (D, E). In fact, its explanation is not straightforward and need more investigations, however, it is mainly dominated by

- The energy gap between GS and higher sextet manifold. (the smaller the gap, the stronger SOC, and the larger the $|D|$ value and the smaller E/D)
- The symmetry around the Eu local environment. (The lower the symmetry, the less restriction on SOC between the states)
- The degree of covalency within the total active space. (the higher covalency, the smaller $|D|$, and the larger E/D)

The value and sign of D is a measure of the splitting and the direction of stabilization of M_S KDs, respectively, as shown in **Figure 13.1**.

We can see that some phosphors show ground state with axial anisotropy, $E/D \sim 0$ (S1LA, SALON, SLBO). E/D value can be taken as good indicator of mixing with higher sextet manifold. This mixing contaminates the ground state with sextet character, which will slow down the relaxation transition from lowest excited state, dominated by octet non-relativistic

states. Later (see, **Figure 13.7**), we will see that the relaxation rate has a strong dependence on the anisotropy of ground state.

13.6.2.2. Excited (emissive) state magnetic structure

SOC mixing in emitting ES $^8 |\Psi_1\rangle(4f^6 5d^1)$, is in contrast to GS, strong and occurs due to mixing with excited spin-conserving octet states $^8 |\Psi_J\rangle(4f^6 5d^1)$ which are in energy proximity to it ($< 1000 \text{ cm}^{-1}$). As shown in **Figure A. 16**, in all cases in principle all 7 non-relativistic states (representing the 7 $4f_{m_l} \rightarrow 5d$ transitions, $m_l = -3, \dots, 3$) are required for converging the SOC effects in the emissive state. In this concept, the excited state ZFS in the emissive multiplet becomes practically undefined. The 4 KDs consisting the emissive multiplet are almost equally spacing, separated by $200\text{-}300 \text{ cm}^{-1}$. Hence emission occurs practically from an isolated emissive KD due to thermal depopulation of higher KDs, approaching zero at 6K. One may conclude that in practice for a given phosphor the emission process will depend on the nature of the isolated excited emissive KD and the GS magnetic structure.

The magnetic structure of the excited emissive “multiplet“, depends on three main parameters in descending order in terms of their impact as follows.

- The degeneracy in the parent emissive non-relativistic state.
- The dependence of the SOC effects to the type of Eu^{2+} 5d orbital dominating the excited state.
- The covalency of the Eu^{2+} 5d MO which competes the SOC interactions. In following, the covalency ($\text{Eu } 5d \text{ } a^2$) is directly extracted from involved CASSCF active orbitals.

For the study set of phosphors these factors are summarized in **Figure 13.6**. First, $(5d_{x^2-y^2/xy})$ -based ES leads to stronger SOC, For instance (SLBO, ~ 500 times and SLA2 ~ 50 times) stronger than the other cases with cases with $(5d_{z^2})$ -based ES. This is because, the former has a strong orbital angular coupling between $\langle 5d_{xy} | l_z | 5d_{x^2-y^2} \rangle$, which is missing in the latter, for example compare S1LA and S2LA (SLA doped at Sr1 and Sr2 sites with very similar covalency in 5d orbital). In addition, $(5d_{x^2-y^2/xy})$ - based ES, show approximate linear dependence between SOC magnitude and the covalency of 5d orbitals. In contrast, phosphors with $(5d_{z^2})$ - based ES, show similar ES SOC effects amounting to $100\text{-}200 \text{ cm}^{-1}$ and in practice no dependence to $\text{Eu}^{2+} - 5d_{z^2}$ covalency.

Finally, across the study set, SLBO shows the largest SOC interactions, extraordinary compared to rest cases, in its lowest excited state. That is owing to the degeneracy of the emissive excited states adopting electron configurations $^8\text{E}(\text{b}^1\text{a}^1\text{e}^2\text{b}^1\text{e}^1\text{b}^1)$. In contrast, CBLA2, with $(5\text{d}_{x^2-y^2/xy})$ -based emissive state shows the smaller SOC interactions in line with the phosphors bearing a (5d_{z^2}) -based excited state. This is associated with the compressed nitride cuboid structure leading to significant covalent between the 5d orbitals and the nitride ligands, suppressing the SOC effect.

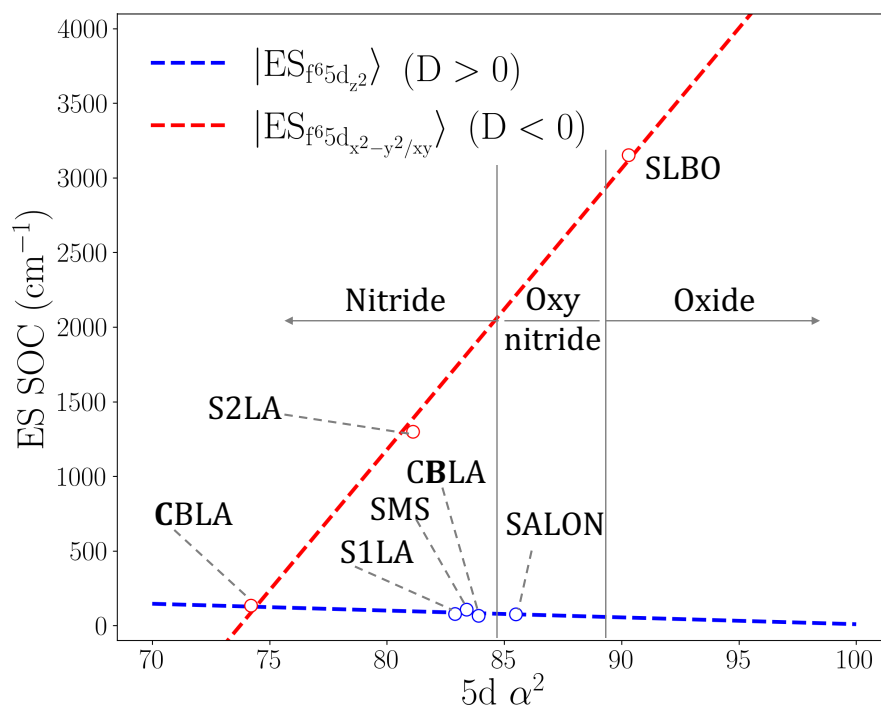


Figure 13.6. SOC of the emitting (lowest excited) state against the covalency of the 5d manifold. Covalency was calculated as total mixing of $L - 2p$ orbitals in $5\text{d}_{x^2-y^2/xy}$ or 5d_{z^2} orbitals of SA-CASSCF optimized active space while SOC is computed on the basis of the SOC reduced matrix elements following **Equation (13.12)**.

13.7. Emission mechanism at the Static Limit. The role of the ground and excited state magnetic structures.

At the static limit the different scenarios of the emission process from in principle an isolated excited KD to all possible GS KDs is depicted in **Scheme 13.2**.

Consistent with the discussions in **Subsection 13.6.2.1**, across all studied cases, the GS KDs exhibit weak splitting ($\Delta E < 50 \text{ cm}^{-1}$), where it can follow either an axial $D > 0$ or $D < 0$ splitting pattern (e.g. $M_s = \pm 1/2, \pm 3/2, \pm 5/2, \pm 7/2$, for $D > 0$, and vice versa). Large $|D|$ and axial $E/D = 0$ GS ZFS is of paramount importance as this leads to GS KDs with pure M_s component, restricting the number of possible relaxation pathways and thus resulting in fast and narrow band emission in this static limit.

In contrast, at the lowest excited emissive state ES the magnetic structure, splitting, and relaxation, can be classified into 2 main cases as dictated in **Scheme 13.2(a,b)** and **(c,d)**, the lowest, isolated ES KD is dominated by $M_s \pm 1/2$ or $\pm 7/2$ components, respectively.

In this context the emissive processes can be categorized according to the GS ZFS character:

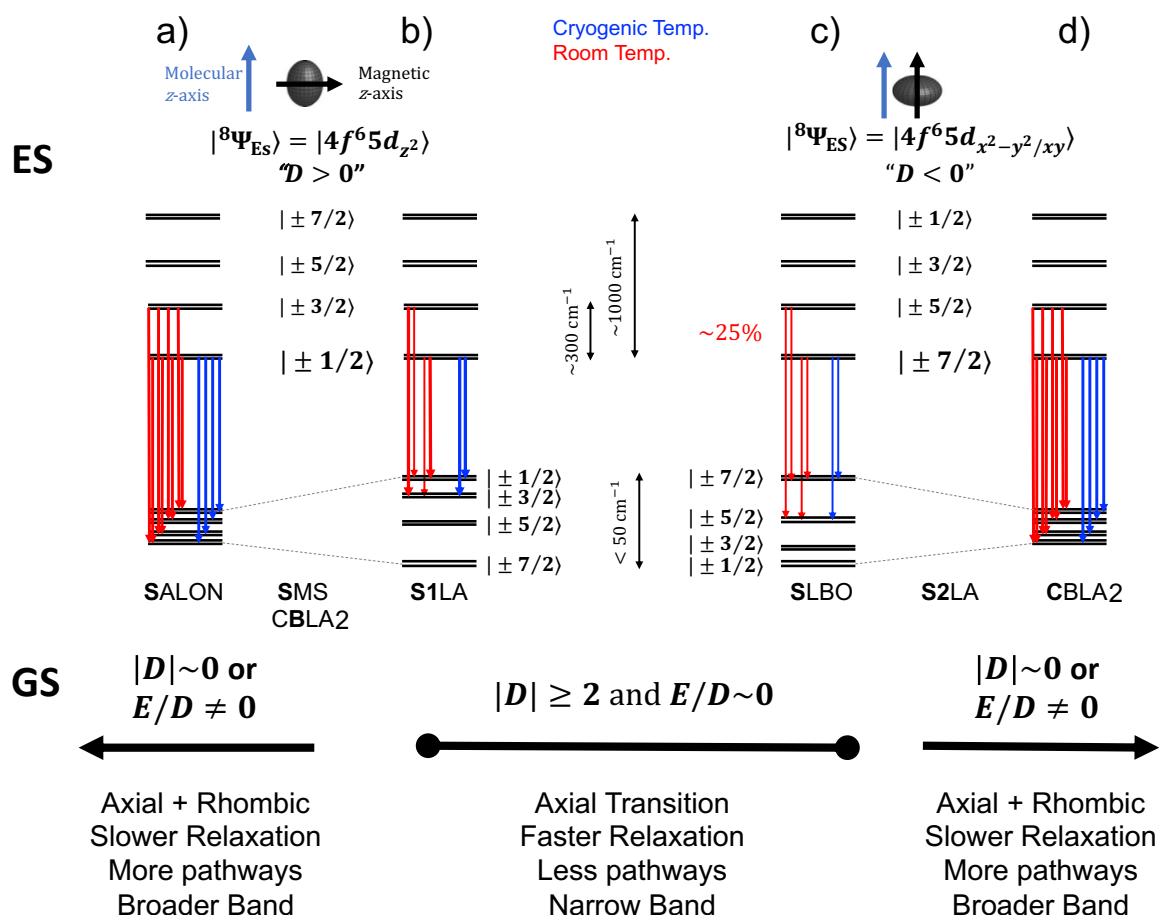
1) GS with axial ZFS ($|D| \geq 2, E \sim 0$) (**Scheme 13.2(b,c)**)

- The GS KDs are magnetically pure, leading to axial fast relaxation from the lowest KDs dominated by $\pm 1/2$ or $\pm 7/2$ for $(4f^6 5d_{z^2})^-$ and $(4f^6 5d_{x^2-y^2/xy})^-$ -based ES, respectively, leading to a domination of the ($\Delta M_s = 0$) relaxations.
- This restricts the number of the available relaxations pathways hence leading to emission bands with effectively reduced linewidths.

2) GS with rhombic ZFS ($|D| \sim 0$ or $E/D \neq 0$) (**Scheme 13.2(a,d)**)

- In this case, the GS KDs are mixed, enabling relaxation to all the GS KDs from dominating M_s components in the lowest excited KDs, on the basis of the $\Delta M_s = 0, \pm 1$ selection rule.
- As a result, in principle all the GS KDs become accessible and more relaxations pathways become available, leading to slower relaxation and larger emission bands with broader linewidths in comparison to the axial cases.

At elevated temperatures (e.g. RT) higher ES KDs may become thermally populated, which could in principle contribute emission intensity as well as increase the emission band broadening.



Scheme 13.2. The two possible relaxation patterns, first, the predominant faster axial ($\Delta Ms = 0$) relaxations pattern in both b) and c) the GS follow an axial magnetic structure ($|D| \geq 2, E/D = 0$). Additionally, in b) the lowest ES KDs is dominated by $\pm 1/2$ due to $(4f^6 5d_{z^2})$ -based ES (" $D > 0$ ") while in c) it is dominated by $\pm 7/2$ due to $(4f^6 5d_{x^2-y^2/xy})$ -based ES (" $D < 0$ "). Second, both axial and rhombic ($\Delta Ms = 0, \pm 1$) relaxations occur in a) and d) while the ES magnetic structure is not changed but the GS magnetic structure is more degenerate with mixed Ms states due to either smaller $|D|$, larger E/D or both. Note that, (" $D > 0$ ") means behaves like this situation, where it was not possible to give definite values due to failure of SH, for ES ZFS calculation. Blue and red arrows indicate low and room temperature emission pathways, where at low cryogenic temperature only lowest excited KDs can contribute and with increase in temperature, higher excited KDs are thermally populated and contribute. Thick arrows involve emission process involving KDs with $\Delta Ms = 0, \pm 1$ while thin arrows indicate emission processes that involve only KDs with $\Delta Ms = 0$.

13.8. Emission mechanism at dynamic limit

In this section the vibronic coupling effects to the emission process are considered (A detailed analysis is provided in **Sections 13.4.2** and **6.3**). The different relaxation pathways from the emissive excited KDs (ES) to the ground KDs within the Franck-Condon (FC) and Herzberg-Teller (HT) limits are provided in **Scheme 13.3**.

In the dynamic limit the nuclear relaxation can in principle affect 2 main factors that constitute the emission process, the involved electronic and vibrational transitions:

- **Dynamic effects on the electronic transitions**

As shown in **Scheme 13.3a**, in a first approximation, the emission spectra arise predominately from electronic relaxation of the lowest excited to all ground KDs $|I; KD'_1\rangle \rightarrow |F; KD_{1,2,3,4}\rangle$ at the respective energy differences (adiabatic energy) E_{ad} . SOC and HT can simultaneously mix the emissive $|I; KD'_1\rangle$ and higher excited KDs $|K; KD'_{2,3,4,\dots}\rangle$. These effects are less pronounced in the GS KDs manifold, due to large energy gap. Hence in the ideal case of only one coupled vibrational state this would lead to a unique and narrow emission band broadened only by the strength of the electronic state mixing (SOC and HT).

- **Dynamic effects on the vibrational transitions**

In a second step we considered in addition relaxation on the involved vibrational states. The following possible scenarios exist:

1) Frank-Condon limit (FC) and Huang-Rhys parameter ($S = 0$)

In this case, there is no displacement between the emissive and ground states, (this displacement is quantified by the magnitude of the Hugaan-Rhys (S) parameter). Hence $S = 0$ indicates parallel PESs, and due to the orthogonality of harmonic vibrational states (**Scheme 13.3a**) at low temperatures (e.g. 6K) only $\Delta v_{fi} = 0$ relaxation is allowed. So only one line is expected at energy E_{00} owing to the vibrationally allowed $0_i \rightarrow 0_f$ relaxation. In addition, the $1_i = 1_f$ transitions located also at $E_{11} = E_{00}$ energies could potentially contribute intensity at higher temperatures. Here, $0_i, 1_i$

represent the ground and first excited vibrational energy level, of the initial electronic state I , and so on for $0_f, 1_f$ of the final electronic state F .

2) Frank-Condon limit (FC) and $S > 0$

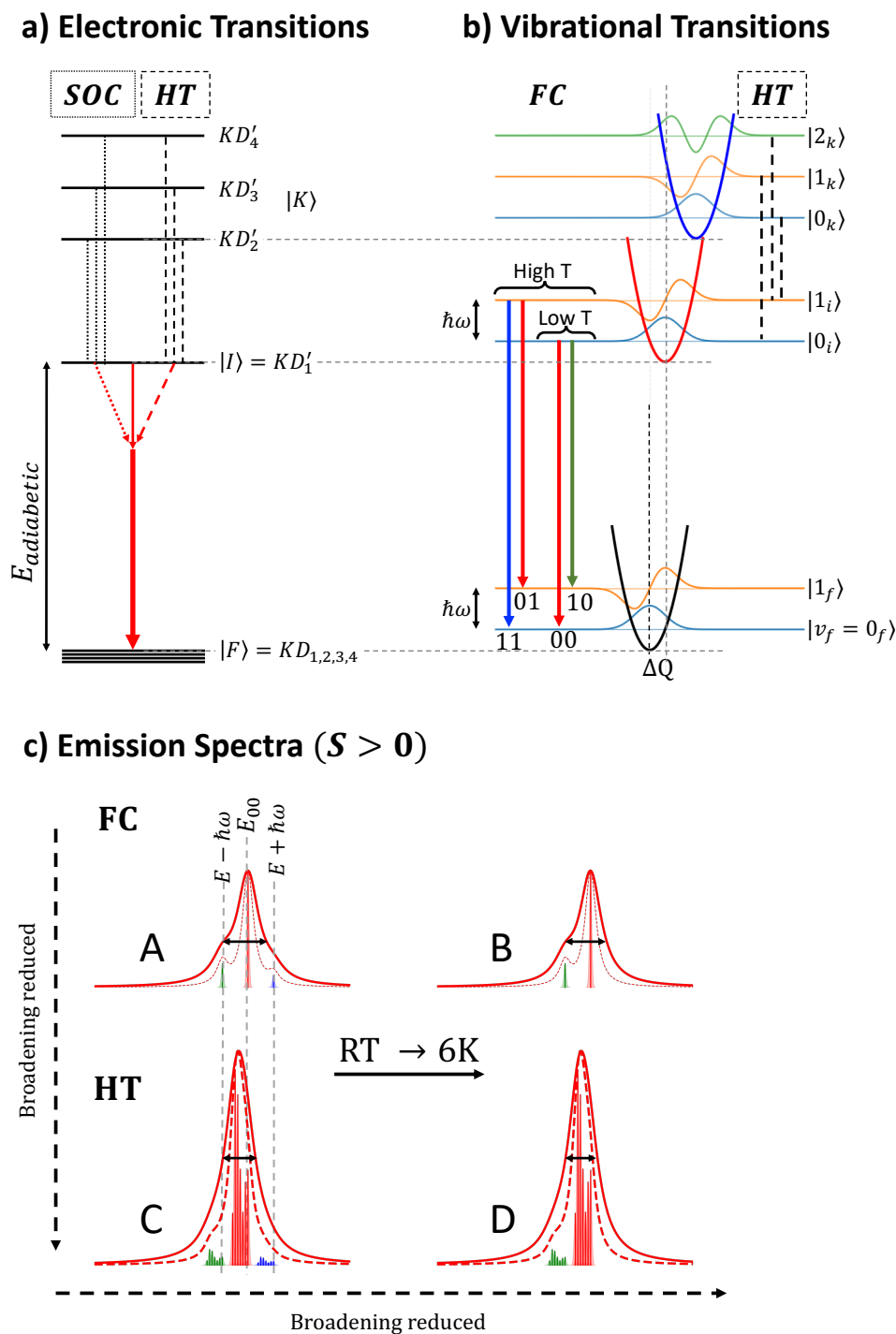
Typically owing to relaxation along coupled vibrational modes, the emissive ES following the excitation process is shifted with respect to the GS as dictated by the non-zero HR factors ($S > 0$). During the relaxation ES could preserve or change the system (GS) symmetry which occurs mainly along totally and non-totally symmetric modes, respectively. Due to the ES PES displacement the orthogonality rules relaxed, consequently, besides the main $\Delta v_{fi} = 0$ bands, weaker intensity bands ($\Delta v_{fi} = \pm 1$) at $E \pm \hbar\omega$ will show up (**Scheme 13.3(b,c)**). It should be noted that the ($\Delta v_{fi} = +1$) band will disappear at low temperature due thermal depopulation of 1_f state.

3) Herzberg-Teller coupling (HT) and $S > 0$

Considering further HT coupling effects, the emissive excited state $|I; KD'_1\rangle$ can mix with higher excited KDs $|K; KD'_{2,3,4,\dots}\rangle$ along a set HT active mode. As shown in **Equations (13.9)-(13.11)** and **Scheme 13.1**, these nuclear motions will drastically affect the transition dipole moment ($\partial\mu/\partial Q$). Hence in principle both the transition rate and intensity will be improved through such intensity borrowing mechanism (**Scheme 13.3(a,b)**). In fact, all ($\Delta v_{fi} = \pm 1$) lines of HT active modes can contribute intensities which are distributed along the vibrational frequencies domain, leading to exponential improve of the emission rate/intensity (compared to FC), with red-shift in emission max. Similar to FC, temperature reduction leads to suppression of the higher energy band.

In the previous discussion, only one vibrational mode was considered, however, several modes can contribute. The Huang-Rhys factor (S) is computed by the following **Equation (13.13)**, where, $s_\alpha, \lambda_\alpha, \omega_\alpha$ are the Huang-Rhys factor, the reorganization energy, and the vibrational energy of the normal mode (α) involved in the electronic transition.

$$S = \sum_{\alpha} s_{\alpha} = \sum_{\alpha} \frac{\lambda_{\alpha}}{\hbar\omega_{\alpha}} \quad (13.13)$$



Scheme 13.3. The most important factors influencing the emission process: a) The electronic transitions from the emissive to the ground KDs $|I; KD'_1\rangle \rightarrow |F; KD_{1,2,3,4}\rangle$ are impacted by SOC and HT vibronic effects within the emissive $|I; KD'_1\rangle$ and higher excited KDs $|K; KD'_{2,3,4,\dots}\rangle$. b) The vibrational transitions at FC and HT limits, give rise to $|I, v_i = 0\rangle \rightarrow |F, v_f = 0, 1, \dots\rangle$ and emission processes $|I, v_i = 0, 1\rangle \rightarrow |F, v_f = 0, 1, \dots\rangle$ at low and high temperatures, respectively. c) Summary of the emission band intensities assuming a typical FC coupling condition (Huang-Rhys parameter $S > 0$) and considering the various scenarios, of FC and HT coupling limits relevant to RT and cryogenic temperatures. The overall intensity profile convoluted using Lorentzian with linewidth of (250 and 500 cm^{-1} given with dashed and solid lines, respectively).

13.9. Relation of magnetic structure with the dynamic nature of the emissive process

Now, let us discuss the correlation between the magnetic structure of ground and emissive states with dynamic nature of the emission process, assuming the following example, where

- 1) the emissive and ground states are almost parallel ($S > 0$, but small),
- 2) the GS has axial ZFS (e.g. $D < 0$), and
- 3) the isolated emissive ES KD'_1 consist of $Ms = \pm 7/2$.

At low temperature, the primary emission process will involve the $|KD'_1, 0_i\rangle \rightarrow |KD_1, 0_f\rangle$ transition where KDs (KD'_1 and KD_1) contribute with their $Ms = \pm 7/2$ components giving rise to both main $0_i \rightarrow 0_f$ and satellite $0_i \rightarrow 1_f$ emission bands **Scheme 13.3(c)–B**.

As shown in **Scheme 13.3(c)–D**, HT coupling with excited state KDs, KD_k with $Ms = \pm 7/2$ components will in principle tend to maintain the axial symmetry of the system giving rise to matrix elements $\langle KD'_1, 0_i | \partial H / \partial Q | KD_k, 0_k \rangle$ that couple with the totally symmetric modes 0_i and 0_k , hence increasing the intensity of the $0_i \rightarrow 0_f$ band. In contrast, coupling with excited and ground state KDs, with $Ms \pm 1$ will in principle introduce rhombicity in the system enabling coupling in addition with non-symmetric modes giving rise to both $0_i \rightarrow 0_f$ and $0_i \rightarrow 1_f$ bands.

Hence, at the limit of state coupling with axial ZFS, following the selection rule $\langle \Gamma_{I;KD'_1} | \Gamma_{\text{vib}} | \Gamma_{F;KD_1} \rangle$, $\Gamma_{I;KD'_1} = \Gamma_{F;KD_1}$, the intensity of the $0_i \rightarrow 0_f$ will grow much faster than the intensity of the $0_i \rightarrow 1_f$ further reducing the bandwidth of the final emission band.

At higher temperatures, in addition, weaker intensity band due to $1_i \rightarrow 0_f$ transition will also appear at higher energy, increasing the broadening of the band at both FC and HT limits, **Scheme 13.3(c)–A and C**, respectively.

In this concept, it is useful to discuss the relation of the emission intensity and relaxation times at both the FC limit and HT limits. **Table 13.4** shows all the emission characteristics across the studied phosphors, employing the employing ESD approach based on CASSCF/NEVPT2/SOC method. These characteristics include the S parameters and HT vibronic couplings $\left(\xi = \left\| \left(\frac{\partial H}{\partial Q} \right)_{Q_0} \right\| \right)$, and the relaxation times at different 6 and 300K calculated at both FC and FC+HT limits.

Table 13.4. The calculated total Huang-Rhys parameter (S) representing the FC vibronic coupling, total norm of first order derivative per mode $\xi = (\|(\partial H/\partial Q)_{Q_0}\|)$ representing the strength of the HT vibronic coupling, and the calculated relaxation times τ (μs) at RT and 6K at both the FC and FC+HT limits are given, across the studied set of Eu^{2+} -doped phosphors (SLA, CBLA2, SMS, SALON, SLBO): Eu^{2+} , and their various doping sites (M^{2+}). They were calculate employing ESD approach based on CASSCF/NEVPT2/SOC method.

Phosphor	M^{2+}	$S^{\text{a)}}$	$\xi^{\text{a)}}$	τ (300K)		τ (6K)	
				FC	FC+HT	FC	FC+HT
				(μs)			
S1LA	Sr1 ²⁺	0.74	8.96	4.8	0.01	4.9	0.02
S2LA	Sr2 ²⁺	0.91	4.16	11.0	0.06	11.0	0.08
CBLA2	Ba ²⁺	1.60	7.22	3.7	0.33	3.7	0.43
CBLA2	Ca ²⁺	1.44	1.31	14.0	2.60	15.0	2.70
SMS	Sr ²⁺	1.24	4.30	6.7	0.03	6.6	0.05
SALON	Sr ²⁺	1.10	0.30	4.0	2.20	3.9	2.60
SLBO ^{b)}	Sr ²⁺	0.98	113	2.6	1.40×10^{-5}	2.2	2.20×10^{-5}

^{a)} No change in S or ξ are found at different temperatures.

^{b)} SLBO shows extraordinary vibronic coupling on the HT limit, due to PJTE, as show later.

In this concept, it is useful to discuss the relation of the emission intensity and relaxation at the FC limit and HT limits, whereas more details are given in **Sections 13.4.2**.

As shown in **Scheme 13.3**, and discussed in **Equations (13.9)-(13.11)** at the FC limit, the emission relaxation time is directly proportional to square of the transition dipole between the SO-coupled states. Consequently, as previous discussed in **Subsection 13.6.2.1**, it depends on the anisotropy of ground and excited SO-states. Particularly for the ground states, where its rhombicity (E/D) implies the introduction of sextet character to the ground states results in slowing down the relaxation rate.

Figure 13.7(a) shows an approximate linear dependence between the relaxation time (τ), at FC limit, and the rhombicity E/D of the ground state across the studied phosphors, especially, for phosphors characterized with axial relaxation (smaller E/D). To provide a comprehensive overview, **Figure 13.7(a)** also presents a heatmaps of the transition dipole μ between excited and ground M_s states. These heatmaps are plotted for the μ between the 4 lowest excited KDs, weighted by their Boltzmann thermal population according at 300K with respect to their energies, and four ground KDs. We can see a significant diagonal contribution in the respective GS and ES KDs heatmaps, as E/D approaching 0, which restricting the transition to ($\Delta M_s = 0$) pathway, and vice versa. The same behavior is detected for both phosphor with emissive state is dominated by $(4f^6 5d_{x^2-y^2/xy})$, as in SLBO, or by $(4f^6 5d_{z^2})$ as in SALON and S1LA.

The situation changes as the GS rhombicity increases ($E/D > 0.15$). In these cases, the model is too simplistic to describe the relaxation behavior of phosphors with medium to high GS rhombicity indicating that a more complete model that incorporates in addition excited state mixing effects needs to be taken into account.

In this direction inclusion of higher order vibronic coupling (HT), will *exponentially* reduce the relaxation time with increase of vibronic coupling ($\partial H/\partial Q$), (as depicted in **Scheme 13.1** and **Equations (13.9)-(13.11)**). Hence significant HT coupling contributions in phosphors with in principle axial relaxation, will tend to reduce the emission band broadening if HT couple with, leading to significantly improvement of the main 00 band relative to the side bands and vice versa for the system following less axial (rhombic) relaxation broadening, as shown in **Figure 13.8**.

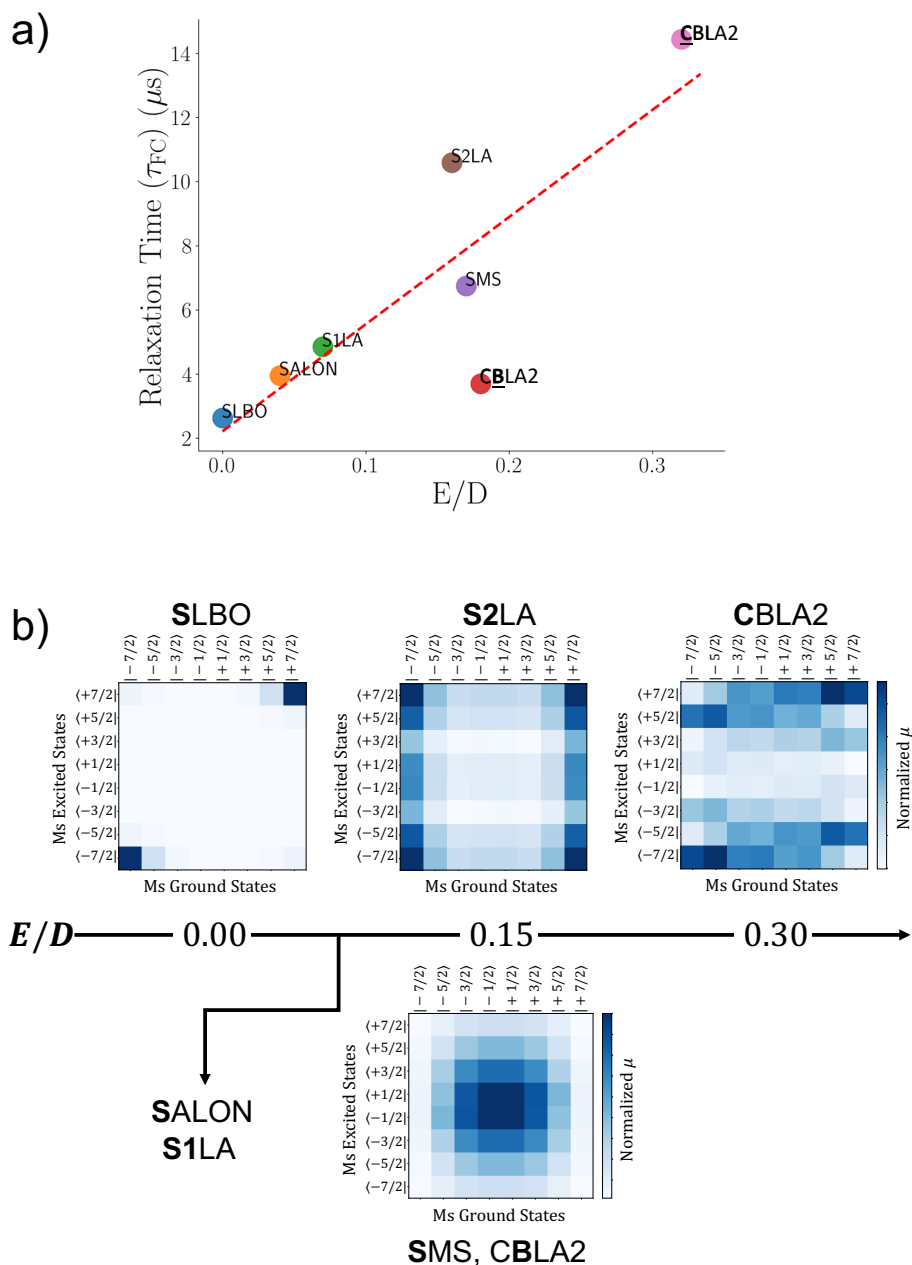


Figure 13.7. a) The dependence of the relaxation time τ (μs) at 300K, within the Frank-Condon approximation, to the rhombicity E/D of the ground state across the study set of phosphors. b) Heatmaps of transition dipole between excited and ground M_s states (between 4 lowest excited KDs and 4 ground KDs). Significant diagonal contributions in the respective GS and ES KDs heatmaps indicate $E/D \sim 0$ and vice versa. Also in b) for phosphors (in top; SLBO, S2LA, and CBLA2) and (in bottom; SALON, S1LA, SMS and CBLA2), the ES is based on $(4f^6 5d_{x^2-y^2/xy})$ and $(4f^6 5d_{z^2})$ electronic configuration. For (SALON, S1LA, SMS and CBLA2) phosphor, they show very similar heat maps while little difference in E/D , so, only one heatmap is given.

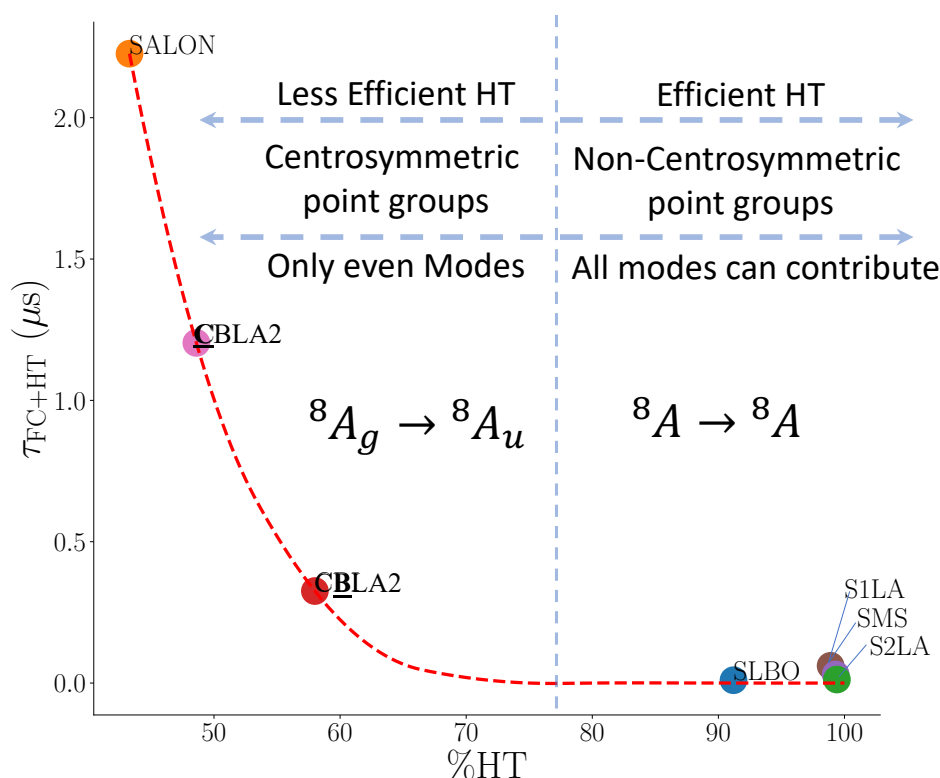


Figure 13.8. The change of total (Frank-Condon + Herzberg-Teller) Relaxation times (μs) at different phosphors with % HT coupling.

In practice (vibronic)-perturbation/mixing of the emitting states with higher excited states, $\left(\xi = \left\| \left(\frac{\partial H}{\partial Q} \right)_{Q_0} \right\| \right)$ will improve the transition dipole intensities and impact the intensities between main (00) and sides (01, 10) bands emission pathways. As seen in **Figure 13.8**, phosphors with centrosymmetric local environment of Eu, show weaker 1st order vibronic coupling (HT) and vice versa. In fact under centrosymmetric symmetry transition dipole matrix transforms as

$$\left\langle A_u \left| \frac{\partial \mu(\Gamma_u)}{\partial Q_\alpha(\Gamma^*)} \right| A_g \right\rangle \neq 0 \quad \text{if } \Gamma^* \subset \Gamma_g \quad (1)$$

This implies that the linear vibronic coupling of the electronic transition is nonzero only for even modes, which effectively reduces the number of the contributing modes and the efficiency of HT.

To conclude this part in the previous sections we have identified the crucial factors that correlate the magnetic structure with the dynamic vibronic coupling in Eu^{2+} doped phosphors. In practice among the studied cases those obtaining low temperature emission from an isolated excited KD to a GS manifold with axial ZFS that shows small Huang Rhys factors S with the emissive ES (at the FC limit), but possible strong HT couplings, are expected to result in the narrowest possible emission bands.

13.10. Luminescence Spectra

In this section, the computed room and low temperature emission spectra across the studied set of phosphors are discussed in the context of all the above factors. We will try to focus directly on the main factors and how that affect the spectral feature, while most of the comparison and details have been give earlier.

All spectra were computed at FC and HT coupling limit and at RT and 6K, and the spectra are the sum all contributions arising from the 4 lowest excited KDs ($|\Psi_{8,9..14,15}\rangle$) weighted with their Boltzmann thermal population (according their energies and the considered temperature) to all the ground 4 KDs ($|\Psi_{0,1...,6,7}\rangle$).

All the emission spectra across the studied phosphors were calculated employing the employing ESD approach based on CASSCF/NEVPT2/SOC method. For all the cases, the correlation function is calculated using a gaussian lineshape with small linewidth of 10 cm^{-1} , to capture all the vibronic features. And then it is recalculated with larger linewidth 250 cm^{-1} for better match with the experimental spectra. Only for phosphors featuring multiple centers for Eu^{2+} doping, specifically, SLBO and CBLA, the better match with experiments at 6K was achieved with 50 cm^{-1} . In addition, for those phosphors, the final calculated spectra are given by summing the partial spectra of Eu^{2+} doping the different centers.

The most important experimental and calculated emission characteristics are given in **Table 13.1** and **Table 13.4**, respectively.

13.10.1. Luminescence Spectra in $\text{SLA}:\text{Eu}^{2+}$

The experimental versus computed spectra of Eu^{2+} -doped SLA at 300 and 6K are given in **Figure 13.9**. The spectra for each site separately are given in **Figure A. 17**.

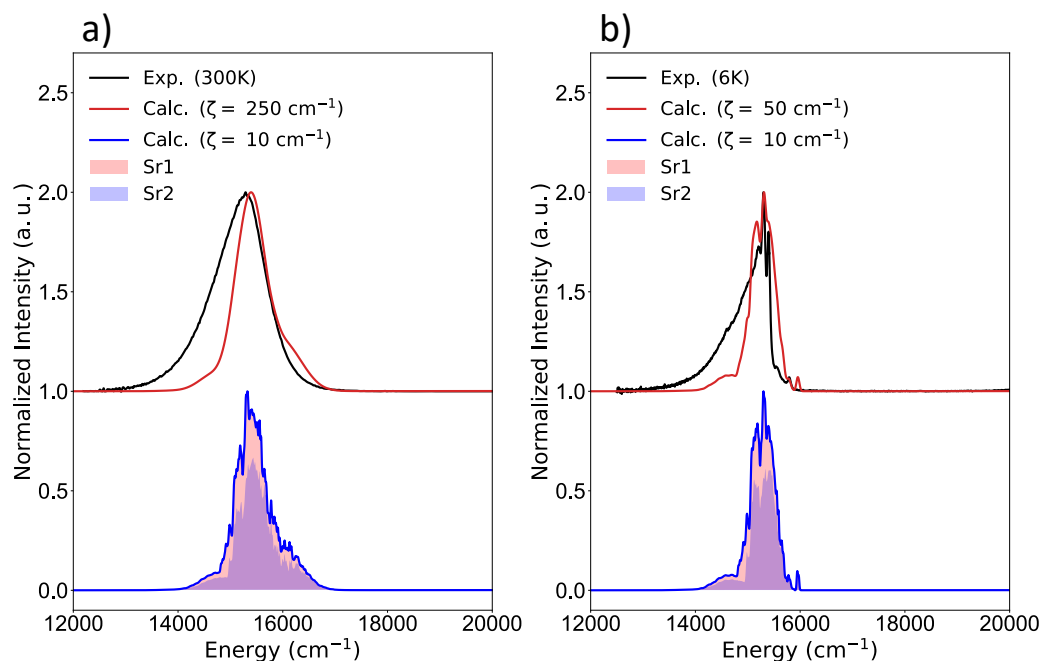


Figure 13.9. Experimental (black) and calculated (Frank-Condon + Herzberg-Teller) luminescence spectra for $\text{SLA}:\text{Eu}^{2+}$ using gaussian broadening with 10 (blue) and ζ (red) cm^{-1} linewidth at 300K (left panel, with $\zeta = 250 \text{ cm}^{-1}$) and 6K (right panel, with $\zeta = 50 \text{ cm}^{-1}$). The calculated spectra are the sum of the contributions from the two doping sites, Sr1 and Sr2 in red and blue fills, respectively.

While SLA is featuring two Eu^{2+} doping centers (Sr1 and Sr2), it exhibits a very unique emission spectra with a single emission at both 300 and 6K with a narrow band emission on both temperatures. FWHM_{RT} magnitudes of 1180 cm^{-1} , while at 6K the spectra became highly structured providing in principle very narrow emission bands with $\text{FWHM}_{6\text{K}}$ decreases effetely to 500 cm^{-1} .

At the static limit, S1LA exhibit $(4f^65d_{z^2})$ -based ES compared to a mixed $(4f^65d_{z^2/x^2-y^2})$ -based ES in S2LA. Additionally, both display similar weak $5d(\text{Eu}) - 2p(\text{N})$ covalency on both sites ($\alpha^2 \sim 83$) (**Figure 13.6**).

While their electronic structures are generally similar, notable distinctions emerge in their magnetic structures, influencing relaxation and emission characteristics. S1LA exhibits more (fast) axial relaxation dominated by $(\pm 1/2 \rightarrow \pm 1/2)$ due to axial GS ZFS ($D = -2.7 \text{ cm}^{-1}, E/D = 0.07$), see **Table 13.3**. In contrast, S2LA exhibit GS ZFS ($D = -2.7 \text{ cm}^{-1}, E/D = 0.16$) which leads to both axial and rhombic pathways. In particular, in the case of S2LA the available relaxation pathways are somewhat restricted ($\Delta M_s = 0, \pm 1$), consisting of $(+7/2 \rightarrow +7/2 \text{ and } -7/2 \rightarrow -7/2)$, followed by $(+7/2 \rightarrow +5/2 \text{ and } -7/2 \rightarrow -5/2)$, as shown in **Figure 13.7**. Hence at the static limit, the available relaxation pathways more in S2LA compared to S1LA, with slower relaxation due to higher rhombicity in the ground state. This would in principle render the S2LA bandwidth broader than S1LA, which is only partially true. Hence, we need to further consider the impact of the nuclear motion relaxation.

At the dynamic limit, first within the FC limit, both show the weakest HR parameter ($S = 0.74$ and 0.91 for S1LA and S2LA, respectively), as shown in **Table 13.4**, ensuring *semi* parallel GS and ES PESs. By recalling from **Section 13.8**, that smaller S leads to:

- Exclusive domination of coupling by totally symmetric (Γ_s) over non-totally symmetric (Γ_a) modes.
- (Γ_s) is accompanied with ($\Delta M_s = 0$) mixing (i.e, mixing KDs with the same symmetry, mixing emissive KDs with higher excited KDs with same $|\pm M_s\rangle$), while (Γ_a) allows ($\Delta M_s = \pm 1$) introducing rhombicity to the emissive KDs.
- In this framework, 00 band dominate the intensity over (01 and 10) side bands (due to orthogonality rules of vibrational WFs) on both FC and HT limits.

That is again consistent with the degree of the HT vibronic coupling (ξ) and its impact on the emission spectra. Stronger HT in S1LA (9.0) followed by 4.2 for S2LA (**Table 13.4**).

Overall, to conclude in SLA the low HR values leads to $\Delta M_s = 0$ emission processes that are also dominated by symmetric modes (Γ_s) giving rise to the main 00 band. Large HT contributions further suppress bands 10 (at 6K) and both 10 and 01 (at 300K) band(s) with respect to the main 00 band. That leads to a similar axial emission characteristic, while at Sr2 site emits with lower intensity and slightly broader band. In addition, the emission calculation shows that they will emit with very close band maximum, SLA2 emits at slightly higher energy with $\sim 300 \text{ cm}^{-1}$. This results in a very narrow (FWHM 500 cm^{-1}) and vibrational resolved emission band (**Figure 13.9**) and short relaxation times (τ) (**Table 13.4**).

As we can see that temperature increase leads thermal activation of more vibrational modes which results in reduction of the relaxation time (0.01 and 0.06 μs for S1LA and S2LA, respectively) at 300K compared to (0.02 and 0.08 μs) at 6K. However, that also leads to more broadening in the emission band, as seen in **Figure 13.9**.

While our calculated spectra generally agree satisfactorily with experimental data, we observe limitations on the lower energy side of the emission band maximum. Specifically, our calculations could not fully capture all the features in that region. This difficulty is commonly encountered due to the dominant influence of phonon coupling by the extended crystal structure. Addressing this challenge often requires the use of a more extensive model structure.

In conclusion, the case of SLA: Eu^{2+} stands out as a noteworthy example, demonstrating the effectiveness of a combination characterized by the domination of axial relaxation ($E/D \rightarrow 0$), small S , and large ξ in producing *narrow-band* Eu^{2+} -doped phosphors. In the subsequent two cases, we will explore how deviations from this particular combination can result in broader emission profiles.

13.10.2. Luminescence Spectra in SALON: Eu^{2+} and SMS: Eu^{2+}

The experimental versus computed spectra of Eu^{2+} -doped SALON and SMS are provided in **Figure 13.10** and **Figure 13.11**, respectively.

They both exhibited a $(4f^65d_{z^2})$ - based ES, exhibit similar ES covalency ($\alpha^2 \sim 86, 84\%$, respectively, as shown in **Figure 13.6**). In fact, while the ZFS parameters of SMS ($D = -2.8 \text{ cm}^{-1}$, $E/D = 0.17$) and SALON ($D = -0.4 \text{ cm}^{-1}$, $E/D = 0.04$) look different, they will behave similarly.

For SALON, the negligible E/D which indicate axial GS however it is accompanied with very small D leading to degenerate ground states. For SMS, it exhibits a very similar GS ZFS to S2LA, but with different ES structure. So, for both (SALON and SMS), that leads to axial ($\pm 1/2 \rightarrow \pm 1/2$) emission pathways, followed by ($\pm 1/2 \rightarrow \pm 3/2$ and $\pm 3/2 \rightarrow \pm 1/2$), as shown in **Figure 13.7**.

They both show intermediate HR parameter ($S = 1.10$ and 1.24) indicating more shifted ES PES compared to GS, and consequently (01, 10) side bands should slightly improve compared with main 00 band (compared with SLA: Eu^{2+} case).

Also, we can see the difference in S is also reflected in the relaxation time on FC limit, where SALON with less shifted PESs, relax faster ($4.0 \mu\text{s}$) compared to SMS ($6.7 \mu\text{s}$).

However, on HT limit, the situation is completely different, again, the high symmetry in SALON, effectively reduces the contributing vibrations to only even Γ_s modes resulting in the weakest HT coupling (0.3), with little reduction of relaxation time ($2.2 \mu\text{s}$). So, both FC and HT peaks contribute and overlap to unresolved spectra, with the dominance of FC ($\sim 70\%$) leading to an increased broadening of the emission band at varying temperatures. This impact is evident in the FWHM values of the RT and 6K spectra (1220 cm^{-1} and 840 cm^{-1}).

On the other hand, in SMS, HT coupling involving both $(\Gamma_s + \Gamma_a)$ modes, resulting in ($\sim 100\%$ HT) with significant reduction in the relaxation time ($0.03 \mu\text{s}$). However, that comes at the expense of the broadening due simultaneous growth of sides and main bands. Once again, these are reflected to the FWHM values of the RT and 6K spectra (1140 cm^{-1} and 900 cm^{-1}).

In contrast to SLA with smaller S , in SMS, both $(\Gamma_s \text{ and } \Gamma_a)$ modes contribute (axial + rhombic HT couplings) giving rise, besides the main 00 band, to 01 and 10 bands. This leads to vibrationally unresolved emission band and broader with respect to SLA.

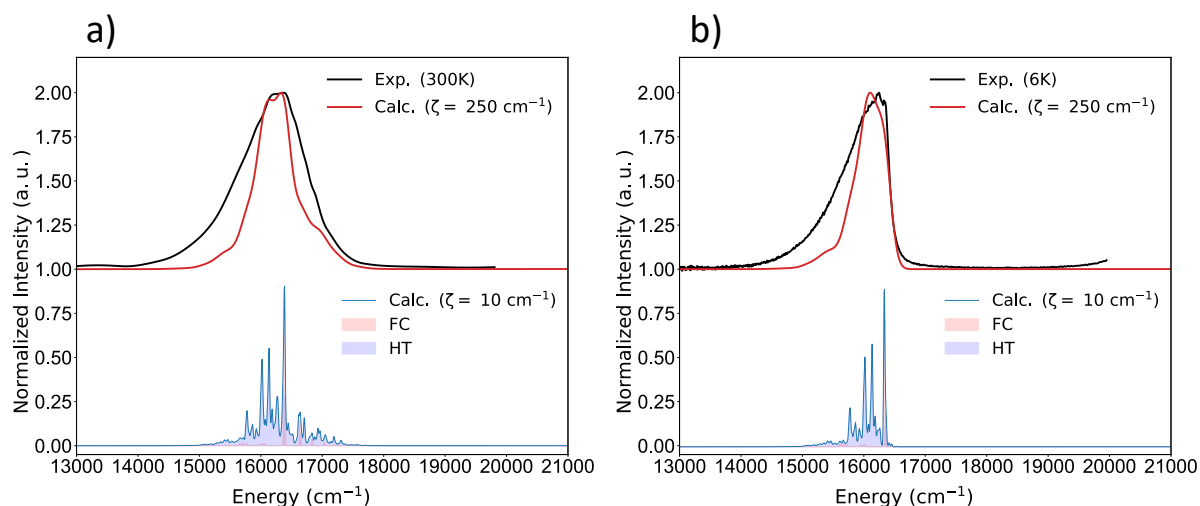


Figure 13.10. Experimental (black) and calculated (Frank-Condon + Herzberg-Teller) luminescence spectra for SALON:Eu²⁺ using gaussian broadening with 10 (blue) and 250 (red) cm^{-1} linewidth at 300K (left panel) and 6K (right panel). The contributions of FC and HT are given in red and blue fill, respectively.

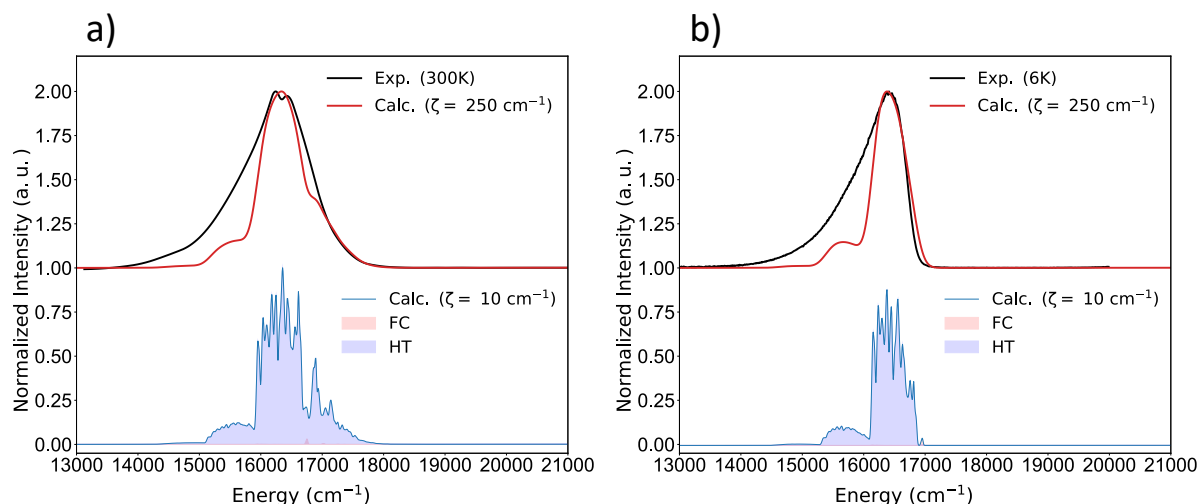


Figure 13.11. Experimental (black) and calculated (Frank-Condon + Herzberg-Teller) luminescence spectra for SALON: Eu^{2+} using gaussian broadening with 10 (blue) and 250 (red) cm^{-1} linewidth at 300K (left panel) and 6K (right panel). The contributions of FC and HT are given in red and blue fill, respectively.

13.10.3. Luminescence Spectra in SLBO: Eu^{2+}

The experimental versus computed spectra of Eu^{2+} -doped SLBO are shown **Figure 13.12**. SLBO exhibits weak HR parameter ($S = 0.9$) which is consistent with the suppressed covalency of the $(4f^6 5d_{x^2-y^2/xy})$ -based ES ($\alpha^2 > 92\%$) aligned with the pure Eu-oxide cuboid. It also shows *perfect* axial ZFS GS ($D = +1.8 \text{ cm}^{-1}$, $E/D = 0.001$), all results in pure axial relaxation with predominant ($\Delta Ms = 0$; $\pm 7/2 \rightarrow \pm 7/2$) emission pathways between the ES and KDs that also show the fastest relaxation times across the study set on FC limit, (2.6 and 2.2 μs at 300 and 6K, respectively). However, it shows extraordinary HT vibronic coupling (113) due to the doubly degeneracy of its emissive state (**Table 13.2**) which is suffering a dynamic PJTE.

PJTE can only occurs through non-totally symmetric vibrational mode (Γ_a), which can change of symmetry of the structure, which will activate $\Delta Ms = \pm 1$. That will lead to exponential decrease of the relaxation time (1.40×10^{-5} and $2.2 \times 10^{-5} \mu\text{s}$ at 300 and 6K, respectively). Additionally, it also leads to growth of (01,10) side bands simultaneously with the main 00 band. So, at room temperature, the spectra are very broad (FWHM 1210 cm^{-1}) and

not resolved. The spectra became also broad at 6K (FWHM 800 cm^{-1}), and the main band of the spectrum very clearly splits due to PJTE to emissive state.

To further corroborate these observation, the dominating HT active mode was scanned employing CASSCF/NEVPT2/SOC method along the e mode, revealing PJTE stabilization ($250, 230\text{ cm}^{-1}$ in the ground and lowest excited KDs), as shown in **Figure 13.13**, aligning with the observed splitting in the main band ($\sim 300\text{ cm}^{-1}$).

In principle the different nature of the emissive ES enables a large pattern of contributing vibrations and extraordinary HT vibronic coupling with respect to other phosphors. However, the larger rigidity of the structure leads overall to normal “not extraordinary” FWHM values of the RT and 6K spectra among the study set (1210 cm^{-1} and 800 cm^{-1}).

While the unique nature of the emissive ES in SLBO allows for a diverse array of contributing vibrations and remarkable HT vibronic coupling compared to other phosphors, the overall structural rigidity leads to FWHM values of (1210 cm^{-1} and 800 cm^{-1}) at the RT and 6K spectra within the standard range for Eu^{2+} -doped phosphors, lacking any extraordinary broadening.

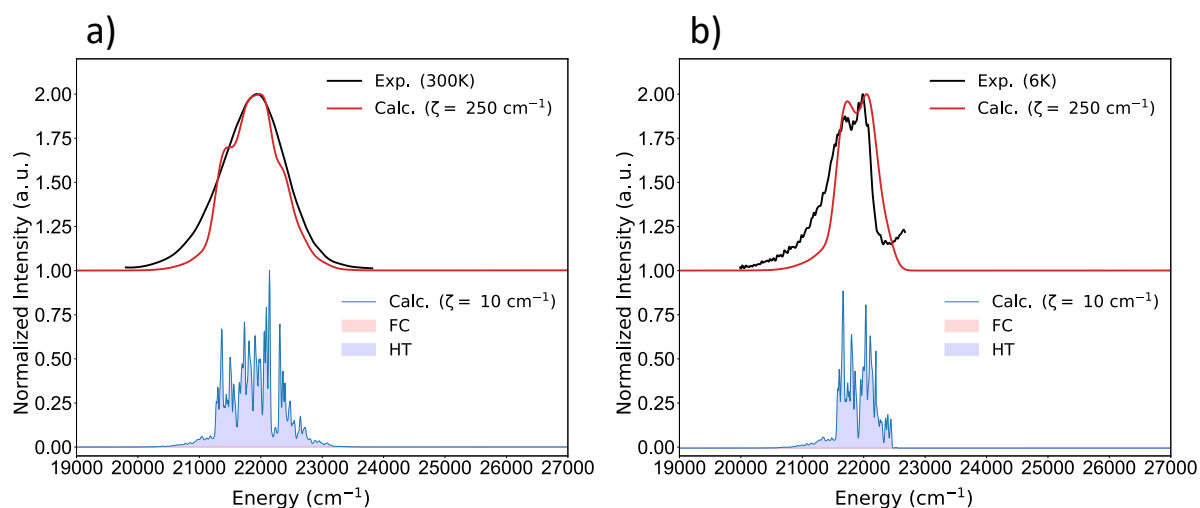


Figure 13.12. Experimental (black) and calculated (Frank-Condon + Herzberg-Teller) luminescence spectra for SLBO: Eu^{2+} using gaussian broadening with 10 (blue) and 250 (red) cm^{-1} linewidth at 300K (left panel) and 6K (right panel). The contributions of FC and HT are given in red and blue fill, respectively.

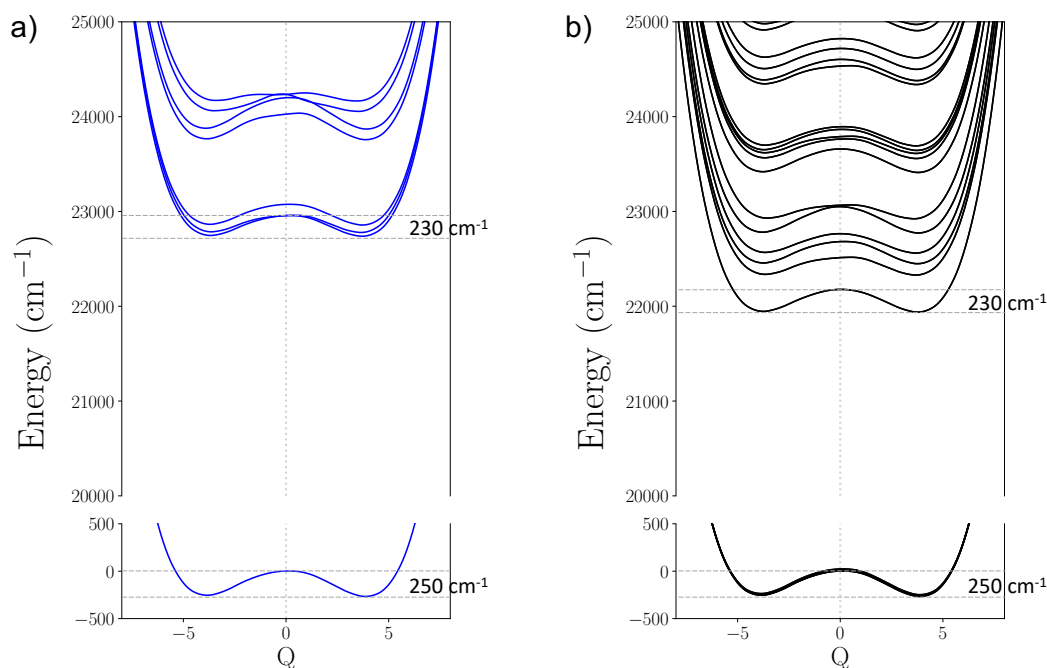


Figure 13.13. SA-CASSC(7,19)/NEVPT2 PES scan along PJTE (/ HT) active (e) mode a) without SOC for the ground and lowest 7 excited non-relativistic states, b) including SOC for the corresponding relativistic states. In addition, PJTE stabilization energy are given.

13.10.4. Luminescence Spectra in CBLA2:Eu²⁺

The experimental versus computed spectra of Eu^{2+} -doped CBLA at 300 and 6K are given in **Figure 13.14**. The spectra for each site separately are given in **Figure A. 18**.

In fact, CBLA (Eu^{2+} doping at Ba site), is similar to SALON, where Eu in C_{2h} local symmetry with $(4f^65d_{z^2})$ -based ES, but with a higher GS ZFS ($D = +0.9 \text{ cm}^{-1}$, $E/D = 0.18$), in accord with slightly higher covalency due nitride cuboid.

However, it exhibits the larger $S = 1.6$ and the centrosymmetric nature of the local symmetry leads to equal contributions from FC (40%) and HT (60%), where we can see large improvement of the axial relaxation ($\pm 1/2 \rightarrow \pm 1/2$) manifested in large improvement of the highly resolved main band through HT coupling with Γ_s and reduction of relaxation time (4 to $0.33 \mu\text{s}$). This is clearly reflected by large change in the FWHM values of the RT and 6K spectra (1300 cm^{-1} and 370 cm^{-1}).

Eu doping at Ca site, with again large $S = 1.4$ in accord with the highest covalency of the $(4f^65d_{x^2-y^2/xy})$ -based ES ($\alpha^2 < 75\%$) and very rhombic GS ZFS ($D = +0.2 \text{ cm}^{-1}$, $E/$

$D = 0.32$),. All leads to a clear rhombic relaxation pathway, and weaker coupling mostly with Γ_a modes, leading noisy weak peak in the IR region. Due its weaker intensity is very difficult to give accurate FWHM, but approximately, it is with the RT and 6K spectra change from 1430 cm^{-1} to 800 cm^{-1} .

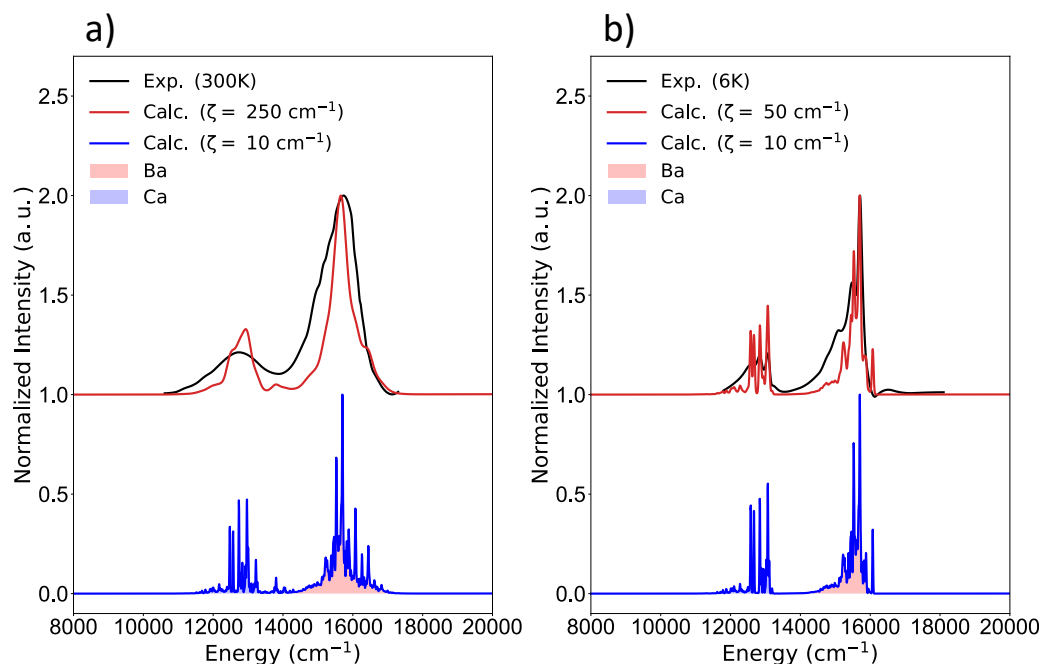


Figure 13.14. Experimental (black) and calculated (Frank-Condon + Herzberg-Teller) luminescence spectra for CBLA2:Eu^{2+} using gaussian broadening with 10 (blue) and ζ (red) cm^{-1} linewidth at 300K (left panel, with $\zeta = 250 \text{ cm}^{-1}$) and 6K (right panel, with $\zeta = 50 \text{ cm}^{-1}$). The calculated spectra are the sum of the contributions from the two doping sites, Ba and Ca in red and blue fills, respectively.

13.11. Conclusions and Requirements for a narrow Eu-doped band phosphor

In this study we have presented a systematic investigation of all the crucial factors that contribute intensity and constitute the emission bands in a representative studied set of Eu²⁺-narrow band phosphors. It was shown in particular that:

1) Suppression of Structural Relaxation

This also allows to suppress requirements for structural relaxation of the ES with respect to GS leading to small HR S factors at the FC limit. In particular the choice of phosphor host needs to maintain lower symmetry on the formed cuboid EuL₈ to ensure,

- No degeneracy in GS or ES which can induce (P)JTE.
- Smaller S , and weakly displaced ES PES with respect to GS.
- Strong HT (accompanied with smaller S) coupling, that will reduce the relaxation time, lead to intense emission, and reduce non-radiative relaxations. (strong HT means both strength of coupling per mode and number of active HT modes)
- Improving over the active HT modes.

2) The GS needs to obtain an axial magnetic structure

This allows to maintain a very rigid structure with an axial magnetic structure $E/D \sim 0$ on the GS and emissive ES that only give rise to $\Delta M_s = 0$ emission pathways between the ES and KDs.

3) Strong SOC is required in the ES multiplet so that it can lead to an isolated emitting magnetic sublevel (or KD). Strong SOC interactions lead to strong HT interactions so that minimum nuclear motion at the excited state results in large values of transition rates and intensities. This also brings the emission relaxation time to the exponential decay regime. Leading to intense emission spectra with fast relaxation times on the main band, suppressing the sides bands

In summary, this study contributes close insights into the intrinsic electronic and magnetic properties of Eu²⁺-doped phosphors, guiding the design of tailored narrow-band phosphors for towards applications.

14 Concluding Remarks of PART II

Towards Design and Tune of Solid-state Eu^{2+} -doped phosphors Materials

This comprehensive study delved into the intricate realm of Eu^{2+} -doped narrow band phosphors, aiming to unravel the complexities of their electronic, structural, and optical properties. Across four meticulously examined chapters, our investigation unfolded a multifaceted narrative that spans from foundational electronic structure considerations to the practical implications for designing tailored phosphors with finely tuned optical characteristics.

In the introductory **Chapter 9**, we explored the nature of the electronic structure and transitions of Eu^{2+} ions in a model structure reflecting Eu^{2+} -doped phosphors. The landscape of excited states proved to be intricate, shaped by various excitations, electron correlation effects, and spin-orbit couplings. Particularly, the sensitivity of 4f5d-based states to local ligand structures was highlighted. The study sheds light on the electronic-structural instability in highly symmetric structures, revealing the dynamical interactions (vibronic effects) that impact electronic and optical properties. We emphasize that the local environment's influence surpasses that of spin-orbit coupling, impacting both static and dynamic limits. This, in fact, set the stage for a thorough study of luminescence mechanisms in subsequent chapters.

Chapters 10 and 11 introduced a groundbreaking computational protocol designed to predict the energy position, shape, and bandwidth of absorption and emission spectra in Eu^{2+} -doped phosphors. Utilizing a set of well-known phosphors, the protocol exhibits remarkable accuracy in reproducing the available experimental data. The study highlighted the importance of crystal field strengths, coordination environments, and the nature of electron excitations in shaping absorption and emission spectra. The protocol's versatility was demonstrated across various phosphors, laying the foundation for identifying descriptors capable of estimating emission bands in newly designed materials. The question of universal applicability becomes a focal point for the ensuing investigations.

In **Chapter 12**, we built upon the insights gained in previous chapters, recognizing the instrumental role of theoretical investigations in guiding synthesis efforts. The study focuses on enhancing the emission properties of CBLA2 phosphor, showcasing the potential for systematic refinement towards a hypothetical CBLA phosphor with unprecedented narrow band red emission characteristics. This chapter underscores the synergy between theoretical insights and practical applications, providing a roadmap for advancing phosphors with enhanced optical characteristics.

The concluding **Chapter (13)** summarized the cumulative knowledge gained, presenting a set of requirements for designing narrow-band Eu^{2+} -doped phosphors. Suppression of structural relaxation, maintenance of axial magnetic structure, and strong spin-orbit coupling emerge as crucial parameters. The study provides close insights into the intrinsic electronic and magnetic properties, offering guidance for the development of tailored narrow-band phosphors.

Collectively, these chapters paint a nuanced picture of Eu^{2+} -doped narrow band phosphors, showcasing the potential for theoretical investigations to inform and shape the synthesis of innovative materials. From unraveling electronic complexities to predicting emission spectra and refining practical applications, each chapter contributes to a holistic understanding of these materials. As we peer into the future, the identified descriptors and requirements stand poised to drive advancements, enabling the design of Eu^{2+} -doped phosphors with finely tuned luminescence properties for diverse technological applications. This comprehensive exploration paves the way for a new era of tailored phosphors, offering unprecedented control over optical characteristics and opening avenues for innovation in lighting, displays, and sensing technologies.

PART III

Towards Design and Control of Circularly Polarized (CP) Photoluminescent Materials with Long-lived Excited States

15 Introduction to PART III

This part is dedicated to the exploration of one of the most intriguing classes of photoluminescent materials: circularly polarized (CP) photoluminescent materials. These materials exhibit not only ordinary photoluminescence but also distinct interactions with different polarization states of light, known as optical activity. This unique feature broadens the scope for the studying light-matter interactions and the investigations of correlations between electronic and optical properties. Moreover, it opens up avenues for applications across diverse domains.[53]

The development of materials exhibiting circularly polarized luminescence (CPL) has garnered significant interest in recent years due to their promising applications in 3D optical displays,[54-59] optical sensors,[56, 60, 61] photoelectric devices,[62-67] disease detection,[451] asymmetric synthetic photochemistry,[68] anti-counterfeiting,[69-71] cryptography, [72, 73] and the promotion of plant growth.[452] An ideal CPL material is characterized by multi-color emission, a high photoluminescence quantum yield (Φ), and a large luminescence dissymmetry factor (g_{lum}).[77] However, achieving an enlargement of both g_{lum} and Φ often comes at the expense of one another. This underscores the importance of identifying high-quality materials with significant g_{lum} values for advancements in this field.[78]

Furthermore, unraveling the CPL activity in transition metal complexes presents a unique set of challenges[57], primarily influenced by the properties of excited multiplet states[453]. This demands a thorough investigation and comprehension of CPL mechanisms, specifically their correlation with both structural and electronic properties, where computational studies are necessary to delve deeper into these intricate relationships.[53, 79, 251, 273, 275, 280, 281, 454-470]

In **PART I**, we described the theory of circularly polarized (CP) light interactions and explored computational methods for calculating spectra and properties, as discussed in

Sections (6.4-6.6). On these bases, the current part focus on the practical applications of these theories and methods. Specifically, we aim at establishing a comprehensive computational protocol designed for the systematic investigation and elucidation of circularly polarized absorption (ECD) and luminescence (CPL) properties, especially, unraveling CPL relaxation mechanisms and uncovering some of the governing selection rules.

The following **Chapter 16**, presents a computational protocol for predicting the optical properties of chiral Re(I) complexes. The protocol utilizes TD-DFT calculations in conjunction with the ESD approach to analyze ABS, PL, ECD, and CPL spectroscopies. It consists of a set of chiral Re(I) family of complexes [*fac*-ReX(CO)₃L], where X is either Cl or I and L is N-heterocyclic carbene extended with π -conjugated [5]-helicenic unit. The NTOs and TheoDORE analyses aid in identifying the nature of transitions dominating the emission processes. The study reveals that different charge transfer (CT) pathways lead to varying magnetic structures of the excited (emissive) states. In addition, the strong SOC induced by the heavy Re elements in these complexes, enables emission from the long-lived triplet state. We will see that, the interplay between the spatial chirality and spin polarization of the triplet excited (emissive) states has implications on the CPL spectra and properties of the complexes. Depending on the electronic, magnetic structures of the excited states and the coupling between these two effects, one can observe either improved or reduced CPL intensity. In addition, these characteristics significantly impact the photoluminescent properties, including spectral bands, spin-vibronic coupling, relaxation times, and quantum yields. Finally, the study emphasizes the crucial role of spin-vibronic coupling in controlling the observed photophysics of Re(I) complexes in this class.

In conclusion, the proposed protocol holds the potential for studying the optical properties of chiral transition metal (TM) and rare earth (RE) complexes and materials. Furthermore, this study not only contributes to the understanding of circularly polarized luminescence (CPL) mechanisms but also provides valuable insights into the design and fine-tuning of high-performance CPL materials with improved optical properties.

16 Theoretical Spectroscopy of Circularly Polarized Absorption and Photoluminescence in Chiral Transition Metal Complexes. Chiral Re(I) complexes as Case Study

The results of this chapter have been published in J. Chem. Phys. **2023**, 159 (8), 084102.
DOI: 10.1063/5.0153742

16.1. Introduction

The design of new chiral transition metal complexes, in which chirality is imposed by a chiral ligand environment, is crucial for the development of challenging applications in catalysis, molecular recognition and photovoltaics.[54-67, 471-477] Over the last decades, there is an increasing interest in the synthesis of photochemically active chiral transition metal (TM) complexes with relatively long-lived excited states due to their role in several important applications in photocatalysis,[478] optical switches[479] and organic light emitting diodes (OLED).[459, 469, 480, 481] In this direction a large number of 2nd and 3rd row transition metal compounds with chiral character, either intrinsic to the metal or brought by the ligands, have been synthesized focusing on asymmetric catalysis, non-racemic mixtures or chiroptical devices.[482-494] In contrast, first row transition metal complexes find applications in visible light induced asymmetric photoredox reactivity,[495, 496] near IR chiro-optical properties[497, 498] or structural probes.[499-501] Synthesis of chiral rhenium(I) complexes for the enantioselective functionalization of organic compounds started in the 90's[502] and has been developed intensively this past decade within the context of anion sensing or chirality-driven reactivity, ferroelectricity, luminescence and stereochemistry[503-505] or as candidates for probing parity violation.[506] Among them, very interesting Re(I) complexes featuring helicene-bipyridine and -N-heterocyclic carbenes (NHC) have been synthesized and characterized by highly resolved circularly polarized optical spectra.[507, 508]

Besides conventional UV/Vis absorption (ABS) and photoluminescence (PL) spectroscopies, circularly polarized absorption/electronic circular dichroism (CD or ECD) as well as circularly polarized luminescence (CPL) spectroscopies are extensively employed to investigate the electronic, optical, photoluminescent, structural and stereochemical properties of a wide variety of chemical systems in their ground and excited states,[57, 65, 67, 456, 458, 508-514] finding applications in chiral sensing, bio-imaging or optical information processing.[472, 479, 503]

In this direction computational chemistry plays a pivotal role in modeling and interpreting experimental ECD and CPL spectra[489, 496, 508, 509, 515] in an effort to deliver valuable information about the various chemical and optical contributions to the chiroptical properties[516-518] and about their correlation not only with nuclear arrangement but also with nuclear motion. Deciphering CPL activity in transition metal complexes is especially challenging[57] because of being driven by excited multiplet state properties.[453] A number of recent methodological developments in the field have focused in providing the correct band shape in optical and photoluminescent spectra[251, 273, 275, 280, 281, 454, 455], treating ECD spectra beyond the dipole approximation[268, 519] and computing the intensities of CPL spectra.[53, 456-462] This has provided access to an increasing number of computational studies on organic chiral chemical systems, delivering valuable structure to electronic and optical properties correlations.[53, 280, 460, 461, 463-469, 520]

The interpretation of chiro-optical photoluminescent spectra in coordination chemistry needs a proper theoretical protocol able to treat on a same footing a variety of excited state characters, namely metal-centered, metal to ligand, ligand to ligand, intra-ligand charge transfer, and ligand-centered (MC, MLCT, LLCT, ILCT, LC) at various multiplicities. A rigorous theoretical protocol needs to include ground and excited state dynamical properties, spin-orbit coupling, vibronic coupling, and spin-vibronic coupling effects.[79, 241] Apart from these effects which control the photoluminescence properties and the radiative emissive processes the occurrence of non-radiative processes may perturb the luminescence mechanisms. This has been shown to be the case for instance in the photoluminescence spectra of late transition metal chiral molecules bearing Re[79, 521], Os[521, 522], Ru[297]. Hence, non-radiative relaxation times as well as the photoluminescent quantum yield (PLQY) become relevant quantities in the photoluminescent spectroscopy implying additional computational challenges. As a result, studies which aim an understanding over the intensity mechanism of

photoluminescent spectra are rather scarce[80, 523-529] while even fewer have involved chiral chemical systems.[132, 241, 530]

Problems of such electronic complexity, found in the fields of excited state dynamics (ESD) and inter-system crossings ISC[241, 524, 531, 532], single molecular magnetism[140, 254, 533, 534] and resonance X-ray emission spectroscopies,[253, 535-537] are more adequately treated at the level of single- and multireference wavefunction based theories. It is however only very recently that such methods have been employed successfully to predict photoluminescence spectral properties of medium size and model chemical systems.[207, 273, 275, 298, 461, 538] For ‘real’ world applications an alternative is offered by the time-dependent density functional theory (TD-DFT) which is commonly employed to compute photophysical properties like PL[80, 215, 539, 540] and CPL[456, 465, 541] spectra in classes of chemical systems ranging from molecular systems to solid state catalysts. However, without a systematic supervision and calibration of the above protocols against parameters with understood origin and known error bars, it is impossible to arrive to protocols of general and ‘black-box’ style applicability.[86] This might have dramatic consequences on machine learning (ML) techniques, an actively growing field of applications, employed to simulate photophysical properties of materials[541-544]. This is illustrated by examples of such carefully calibrated TD-DFT protocols against wavefunction based methods, allowing for instance the interpretation of the spectroscopic response in Vanadia based catalysts[322, 545] or the identification of general descriptors that offer a robust prediction of the color and the bandwidth of narrow band photoluminescent Eu^{2+} doped phosphors,[80, 243] as discussed in details and shown in **PART II**.

In this work a relevant computational protocol is developed that is able to predict the photochemical and photophysical properties and the intensity mechanism of both PL and CPL spectra of a set of recently synthesized chiral Re(I) complexes [*fac*- $\text{ReX}(\text{CO})_3\text{L}$][508] where X stands for Cl or I and L is either N-heterocyclic carbene (NHC) or NHC extended with π -conjugated [5]-helicenic unit. The study is mainly based on an efficient implementation for computing absorption and emission transition rates[273, 275] in the framework of Excited State Dynamics (ESD). In the present work this protocol was extended to be able to treat in addition circularly polarized transition rates providing access to bandshape calculations of ECD and CPL spectra. Employing carefully calibrated TD-DFT calculations in conjunction with the ESD approach, we were able to successfully treat in addition to absorption (ABS) and photoluminescence (PL), circularly polarized absorption (ECD) and photoluminescence (CPL)

spectroscopies as well as radiative and non-radiative relaxation times and PLQY values on the entire study set. The performance of various DFT/TD-DFT protocols and functionals in computing ABS and ECD spectra was evaluated with respect to the state-of-art similarity transformed equation of motion domain-local pair natural orbital based coupled cluster (STEOM-DLPNO-CCSD)[416, 417].

The agreement between theoretical and experimental spectra, including absorption (ABS, ECD) and emission (PL, CPL), is excellent, which is validating a quantitative interpretation of the spectral features on the basis of Natural Transition Orbitals (NTOs) and TheoDORE analyses. It is demonstrated that across the set of studied Re(I) diastereomers, the emission process in the case of NHC diastereomers is MLCT in nature and is dominated by the easy-axis anisotropy of the emissive excited multiplet. On the contrary, in the cases of the helicenic, NHC extended with π -conjugated [5]-helicenic unit, diastereomers the emission process is ILCT in nature and is dominated by the respective easy-plane anisotropy of the emissive excited multiplet. This affects remarkably the photoluminescent properties of the molecules in terms of PL and CPL spectral band shapes, spin-vibronic coupling, relaxation times, as well as the respective quantum yields. Spin-vibronic coupling effects are investigated at the level of the state-average complete active space self-consistent field method (SA-CASSCF)[169, 184] in conjunction with N-electron valence 2nd order perturbation theory (NEVPT2)[193, 395] and its quasi-degenerate variant (QD-NEVPT2)[198]. It is in fact demonstrated that a spin-vibronic coupling mechanism controls the observed photophysics of this class of Re(I) complexes.

In summary, this research work, along with the proposed protocol, enables the exploration of optical properties in chiral transition metal complexes in general. Moreover, it can contribute to the design of high-performance CPL materials, thereby enhancing their overall optical properties.

16.2. Theoretical considerations

The theoretical basis of this study has been discussed in detail in **Chapter 6** in **PART I**, specifically, **Sections (6.4-6.7)**.

It has been shown that a direct way to compute unpolarized as well as, circularly polarized transition rates is by employing the Fermi's Golden rule which can be efficiently solved through the path integral approach.[251, 273, 275-281] That results in a unified formulation of ABS, PL, ECD and CPL spectroscopies. In particular, it has been shown recently this

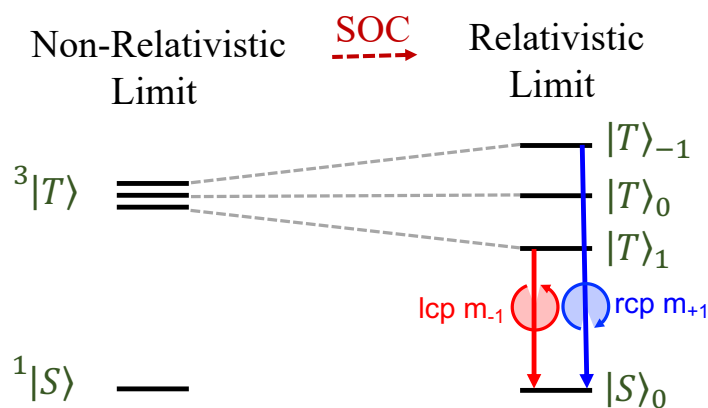
formulation can be very efficiently implemented for absorption and emission radiative and non-radiative transition rates including spin-orbit coupling and vibronic coupling effects.[79, 273, 275]

For CP spectra, the ECD and CPL spectral intensities are represented normalized against the total absorption and photoluminescent intensities defining, similar expressions for, the respective dissymmetry factors g_{abs} and g_{lum} :

$$g_{\text{abs}}(\text{ECD}) \text{ or } g_{\text{lum}}(\text{CPL}) = 2 \frac{I_{\text{LCP}} - I_{\text{RCP}}}{I_{\text{LCP}} + I_{\text{RCP}}} \sim \frac{4R}{D}, -2 < g_{\text{abs}} \text{ or } g_{\text{lum}} < 2 \quad (16.1)$$

where $I_{\text{LCP/RCP}}$ are respectively the left and right polarized components of the involved absorption or emission process. D and R are the square of the transition electric dipole and the rotatory strength, respectively.

It should be noted that the selection rules of CPL are in close resemblance to the MCD C-terms.[271, 546] In fact, as is shown in **Scheme 16.1**, for a ground singlet and an excited triplet state in the presence of SOC the CPL intensity proceeds through the $M_S = \pm 1$ components of the parent non-relativistic excited triplet $^3|T\rangle$ state and the $M_S = 0$ component of the singlet $^1|S\rangle$ ground state.



Scheme 16.1. Schematic representation of the fundamental aspects of the CPL intensity mechanism.

Finally, the calculation of spin-vibronic coupling and non-radiative rates (through ISC from triplet excited state to ground states), follow the theoretical considerations discussed in Sections 6.8 and 6.7, respectively.

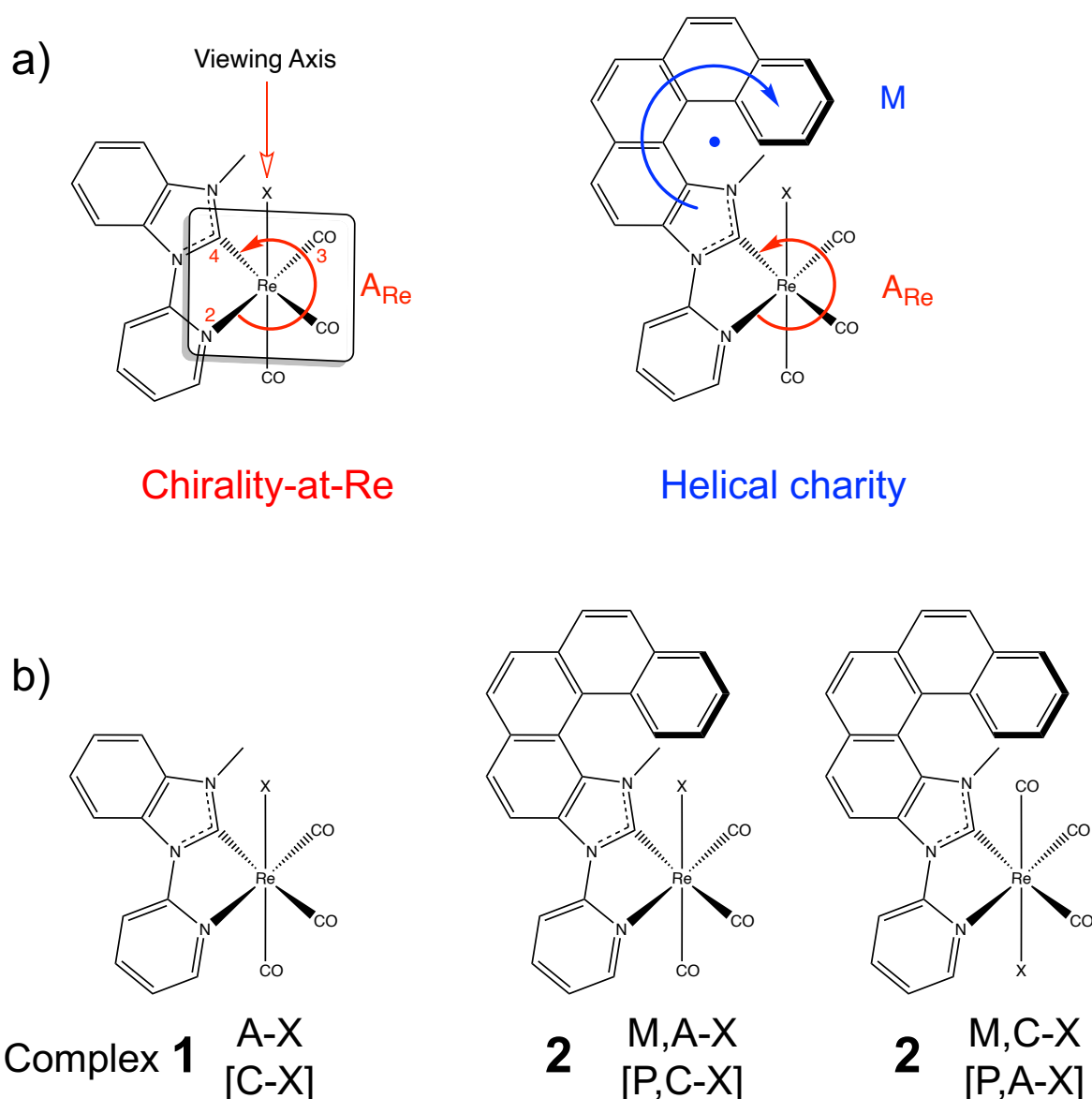
16.3. Choice of the Study Set – Geometric Structure

The chosen study set consists of two subsets of enantiopure chiral-at-Re^I neutral complexes of the chemical form [*fac*-Re^IX(CO)₃L], where L is an N-heterocyclic carbene (NHC) ligand and halogen X is either Cl or I. First, L is 1-(2-pyridyl)-4-methyl-benzimidazole defining first subset of complexes of type **1**. In the second subset, L is a Helicenic-N-heterocyclic carbene (Helicenic-NHC) chelating ligand, in particular 1-(2-pyridyl)-2[5]-Helicenic-4-methyl-imidazole, defining complexes of type **2**. The schematic representation of complexes **1** and **2** are depicted in **Scheme 16.2**. Complexes **2** exhibit significant and intriguing chiroptical and photophysical properties, as discussed in details in next section, and are promising for potential applications over their parent structures lacking the respective helicenic unit (complexes **1**).^[508] That makes the chosen set very appropriate to study correlations between structural, electronic and (chiro-) optical properties in this class of transition metal complexes.

In both complexes of type **1** and **2**, Re(I) [5d⁶] is coordinated in a *pseudo*-octahedral coordination environment defined by a halogen X ligand (Cl or I) occupying the axial position. Three *fac*-oriented carbonyl (CO) groups, one is occupying the second axial position and the other two are coordinated equatorially in the same plane of the bidentate chelating (:C[^]N) NHC ligand. This geometrical orientation forms a chiral center-at-Re abbreviated as A- and C- for left- and right-handed isomers, according to Cahn-Ingold-Prelog (CIP) rules for ligand ordering,^[547, 548] as depicted in **Scheme 16.2a**. As a result, the parent model complexes **1** can be found in the following forms, which are abbreviated as **1** A-Cl / C-Cl and **1** A-I / C-I for Cl- and I-substituted enantiomer pairs, respectively.

In contrast, upon substitution of the ligand (L) with the naturally-bent [5]-helicenic chain, a second ligand-based chirality shows up, namely helical chirality abbreviated as M- and P- for left- and right-handed helical configurations, as depicted in **Scheme 16.2a**. The helicenic model complexes of type **2**, are found in two diastereomeric forms where each form has two enantiomeric pairs. In the first diastereomeric isomer, the halogen and the helical chain are parallel aligned, sterically affecting each other. These enantiomeric pairs are abbreviated as **2** M,A-Cl / P,C-Cl and **2** M,A-I / P,C-I pairs for Cl- and I-substituted enantiomer pairs,

respectively. In a similar fashion in the second diastereomeric isomer, the halogen and the helical chain are anti-parallel aligned with no steric interaction between them to form enantiomeric pairs that are abbreviated as **2** M,C-Cl / P,A-Cl and **2** M,C-I / P,A-I for Cl- and I-substituted enantiomer pairs, respectively. The DFT optimized molecular structures of the diastereomers of complexes types **1** and **2** are provided in **Figure 16.1**.



Scheme 16.2. Schematic representation of $[fac-ReX(CO)_3L]$ molecular structures of the stereoisomer pairs with center (Re) chirality (complexes of type **1**) and both center (Re) and helical chirality (complexes of type **2**). L = 1-(2-pyridyl)-4-methyl-benzimidazole, for **1** and L = 1-(2-pyridyl)-2[4]-helicenic-4-methyl-imidazole for **2**, while X = Cl or I.

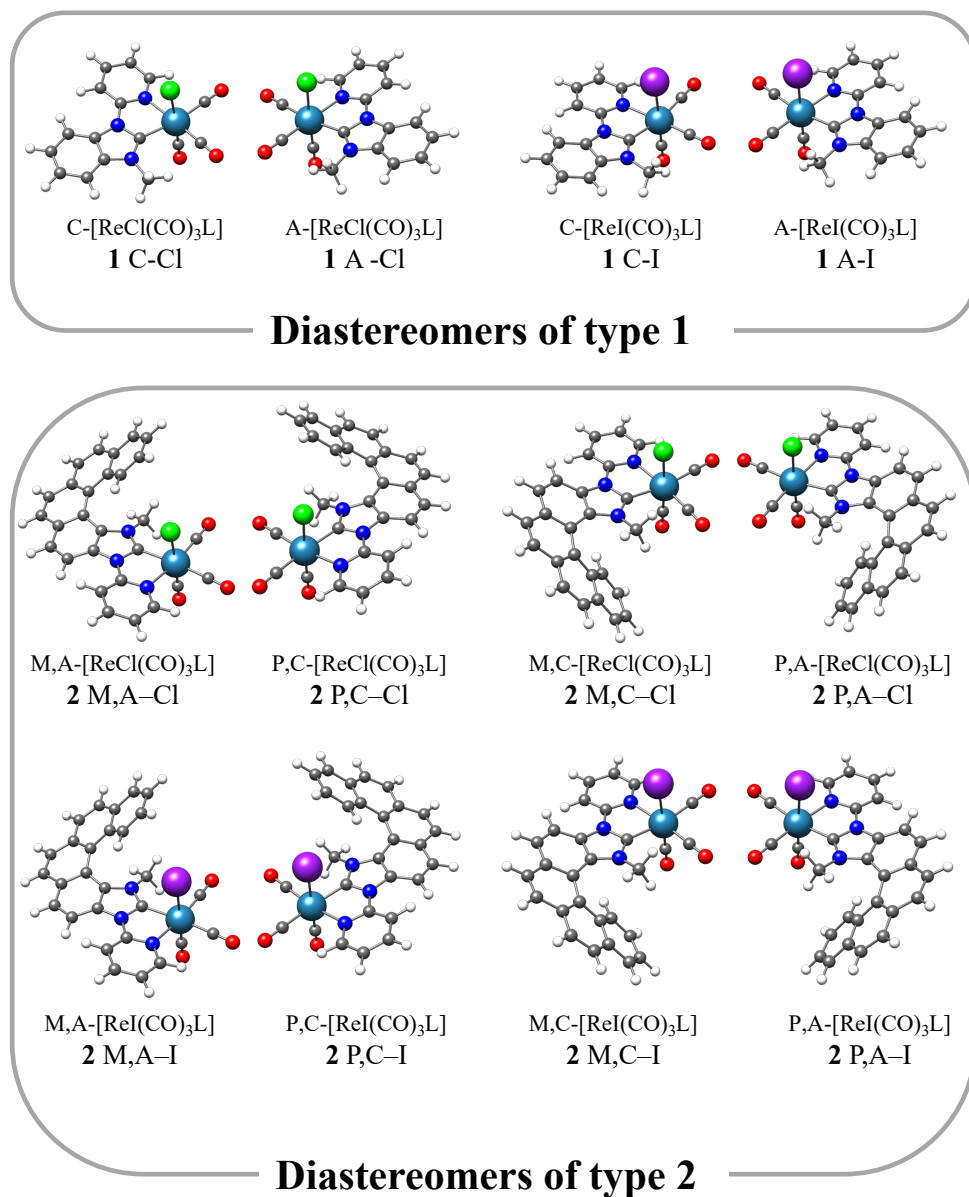


Figure 16.1. A 3D representation of the DFT-optimized molecular structures of the different diastereomer pairs of complexes **1** and **2** forming the study set.

16.4. Experimental (Chiro-) Optical Properties and Photophysics

The experimental ABS, ECD, phosphorescence and CPL spectra of the enantiomeric pairs of complexes **1** and **2**, are collectively presented in **Figure 16.2**. These spectra have been recently recorded at ambient temperature in CH₂Cl₂, and further experimental details and sample preparation have been reported elsewhere.[508]

Both complexes exhibit broad absorption bands ($\geq 25\,000\text{ cm}^{-1}$) with mirror-image ECD spectra of each enantiomeric pair. The absorption spectra recorded between 250 and 500 nm ($40\,000$ and $20\,000\text{ cm}^{-1}$) show two weak intensity bands located at $25\,000\text{ cm}^{-1}$ and two higher intensity and strongly overlapping absorption bands [3,4] located at $\sim 32\,000$, $35\,000\text{ cm}^{-1}$. An even higher intensity absorption/ECD band [5] is located at the high energy region of the spectrum $> 40\,000\text{ cm}^{-1}$. All these bands have been qualitatively assigned as CT bands namely MLCT/XLCT (bands [1,2] of complex of type **1**), ILCT/MLCT (bands [1,2] of complex of type **2**), and MLCT/XLCT/ILCT (bands [3-5] of complexes of type **1** and **2**).[508] The chloride and iodide substituted complexes present similar spectral features with increase of halogen-to-ligand CT (XLCT) contributions and higher intensity in the iodide compounds.

The experimental emission spectra of diastereomers **1** and **2** recorded at 295K are presented in **Figure 16.2**, (panels a-f). In particular the NHC diastereomers of type **1** (panels a and b) exhibit broad and unresolved phosphorescence spectra located at $19\,570\text{ cm}^{-1}$. On the contrary, both the Cl- and I- helicenic diastereomers (panels c-f) exhibit vibrationally resolved and structured emission spectra, that are slightly red shifted, showing the highest intensity band at $\sim 19\,250\text{ cm}^{-1}$ followed by a lower intensity band at $18\,100\text{ cm}^{-1}$ and a shoulder at $16\,500\text{ cm}^{-1}$. As shown in **Table 16.1**, the measured phosphorescence lifetimes range from a few tens of μs in the iodide helicenic diastereomers to a few hundred in the chloride ones at room temperature and increase to a few thousands at 77K. The non-helicenic diastereomers are characterized by short phosphorescence lifetimes of a few μs at 77K to 100 ns at room temperature.

The measured CPL spectra are provided in **Figure 16.2**. The Cl or I-helicenic M,C and P,A enantiomers (panels d and f) in which the halogen and the helicenic ligands are oriented antiparallel, show the largest intensities in the CPL spectra. On the contrary, the spectra intensity drops rapidly in Cl-helicenic or even disappears in I-helicenic M,A and P,C enantiomers (panels c and e) in which the halogen and the helicenic ligands are oriented

antiparallel. The CPL activity drops drastically in Complex **1** enantiomers with no signal in the iodide enantiomers (panels **a** and **b**).

The challenge of the present theoretical study is to decipher and rationalize the photophysics of this class of chiral molecules and to determine (chiro-)optical properties directly comparable to the experimental data. For this purpose, the electronic structure data obtained by various methods of quantum chemistry have been calibrated and combined to treat rigorously and quantitatively the various spectroscopies investigated here. The next section is dedicated to the developed computational strategy.

Table 16.1. Experimental excited states lifetimes (adapted from Ref [508]) at room (295K) and low (77K) temperatures of complexes **1** and **2**.

Complex	$t_{\text{phosp.}} (\mu\text{s})$	$t_{\text{phosp.}} (\mu\text{s})$
	77K	295K
1 A-Cl	4.7	0.1
1 C-Cl	4.7	0.1
1 A-I	5.2	0.1
1 C-I	5.2	0.1
2 M,A-Cl	6200	710
2 P,C-Cl	5900	680
2 M,C-Cl	5400	410
2 P,A-Cl	6100	480
2 M,A-I	7700	50
2 P,C-I	7600	60
2 M,C-I	6600	44
2 P,A-I	6500	43

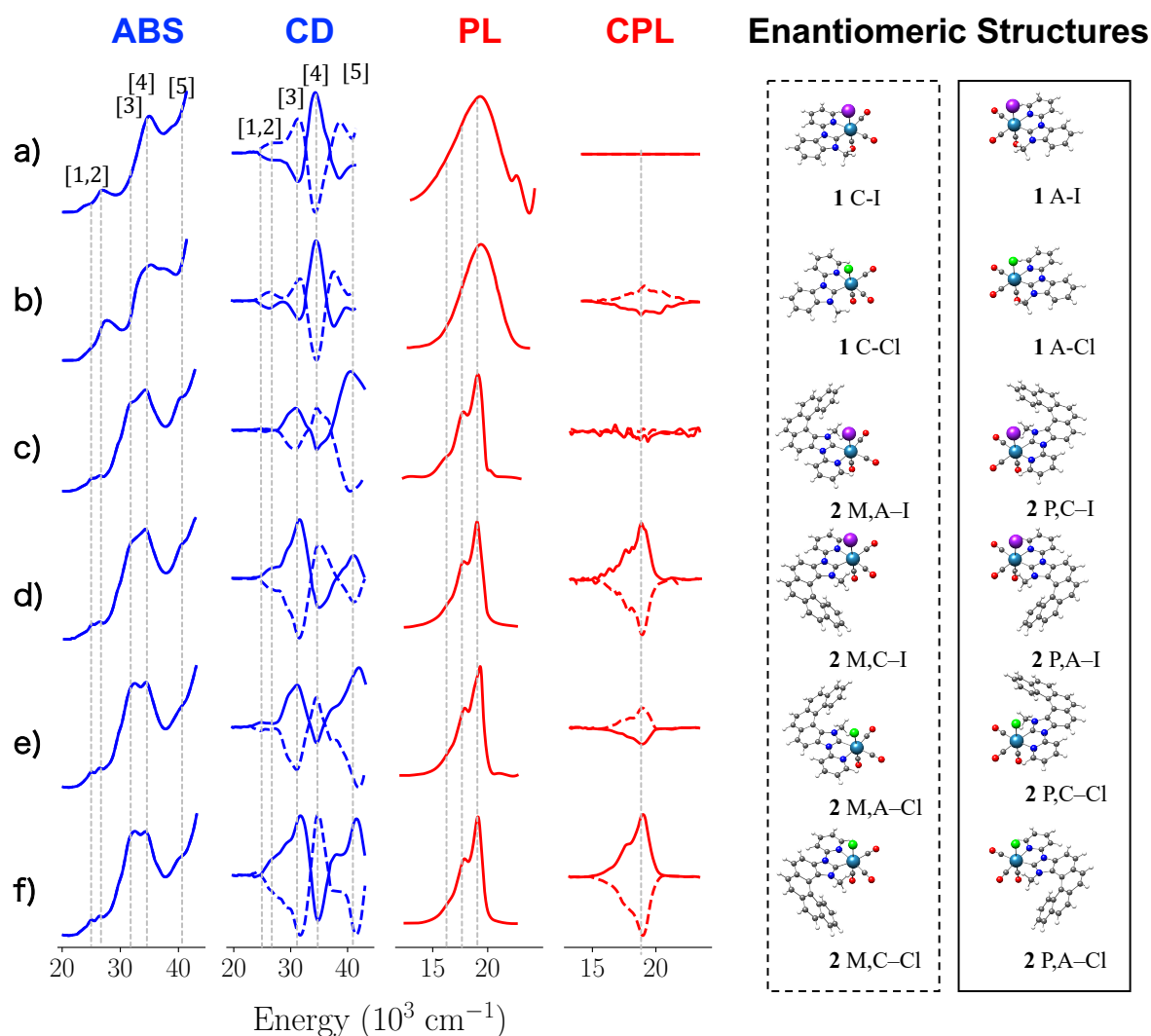


Figure 16.2. Experimental spectra (ABS, CD, PL, CPL) of the study set of the enantiomeric left and right handed structures shown with dotted and solid lines, respectively (adapted from Ref [508]). Namely a) NHC I-structures complex **1** (C-/A-I), b) NHC Cl-structures complex **1** (C-/A-Cl), c) I-helicenic structures complex **2** (M,A-/P,C-I), d) I-helicenic structures complex **2** (M,C-/P,A-I), e) Cl-helicenic structures complex **2** (M,A-/P,C-Cl), e) Cl-helicenic structures complex **2** (M,C-/P,A-Cl). As absorption and phosphorescence spectra of both enantiomeric structure pairs are identical, only the spectrum corresponding to the left (A) handed structures is presented. All spectra were normalized with respect to the highest intensity spectrum of **2** P,A-Cl. Grey dot lines indicate the most pronounced spectral features across the different spectra.

16.5. Computational Strategy

All calculations were performed with ORCA 5.0 suite of programs.[354, 549, 550] Ground and excited states geometry optimization and frequencies over the crystallographic coordinates, taken from the experimental crystallographic X-ray diffraction data,[508] were computed at the DFT level employing the PBE0[227, 235] functional with the Grimme's dispersion correction.[551, 552] The excited state optimizations were performed at the TD-DFT level of theory using the ground state restricted KS determinant as reference. In all calculations, the def2-TZVP triple ζ quality basis sets of the Ahlrichs group [406, 407, 553] were employed in conjunction with the def2-TZVP/J Coulomb fitting basis for the resolution of identity.[554, 555] To account for solvent effects, as introduced in **Section 7.1.2**, on the transitions, all calculations are utilizing the linear response conductor-like polarizable continuum model (LR-C-PCM)[308, 556] as implemented in ORCA[316], with CH₂CL₂ solvent to be consistent with the experimental reference data.

All spectra were computed on the optimized structures. Preliminary ABS and CD spectra were computed employing the STEOM-DLPNO-CCSD[418, 419, 557] and full TD-DFT[237] levels of theory employing a collection of DFT functionals belonging to the generalized gradient approximation (GGA): BP86,[228, 230] PBE,[226] hybrid: PBE0,[227, 234, 235] BHLYP,[558] B3LYP,[228, 229, 233, 559] hybrid meta-GGA: M06,[231] range separated hybrid: CAM-B3LYP[441], wB97,[560] and double hybrid: B2PLYP[236] families. The STEOM-DLPNO-CCSD spectra were computed employing tight criteria for the selection of the PNO pairs (TightPNO, TCutPNO 10^{-7} , and TCutPairs 10^{-5}). As it will be shown below based on its performance in computing the experimental ABS and ECD spectra as well as against the STEOM-DLPNO-CCSD computed ABS and ECD spectra, TD-DFT(PBE0) was chosen to compute all the production ABS, ECD and Photoluminescence spectra. The different transitions are characterized on the basis of both natural transition orbitals (NTOs) and TheoDORÉ[561] analyses.

Photoluminescence (phosphorescence) spectra and circularly polarized photoluminescence (CPL) spectra as well as individual radiative and non-radiative (ISC) relaxation rates for each triplet state sublevel were computed at the TD-DFT(PBE0)/SOC level of theory by employing the excited state dynamics (ESD) path integral protocol[273, 275] which includes Duschinsky mixing vibronic coupling in the framework of Frank-Condon and Herzberg–Teller coupling schemes. The photoluminescence radiative, non-radiative rates and quantum yield were

computed at the experimental temperatures (77K and 295K). In these calculations the energy differences between the involved states at the respective ground and excited optimized geometries were computed at the DLPNO-CCSD(T)[416, 417] level of theory.

Spin-vibronic constants analysis and excited state zero-field splitting calculations (ZFS) were performed constructing the PES of the involved vibrational normal mode on the basis of state-average complete active space (SA-CASSCF) method [169, 184] in conjunction with second order N-electron valence state perturbation theory (NEVPT2) [193, 395] and its quasi-degenerate (QD-NEVPT2)[198] variant by using the strongly contracted (SC) NEVPT2 algorithm to account for the dynamic correlation. Scalar relativistic effects were computed in the framework of the second-order Douglas-Kroll-Hess correction (DKH2)[401, 402] employing the finite nucleus model.[403] In all these calculations the segmented all-electron relativistically recontacted DKH-def2-TZVP basis set was employed for all main elements while for Re and I the respective relativistically recontacted SARC-DKH-TZVP basis set[397-400] was employed. The calculations were accelerated by employing the resolution of identity approximation (RI)[413] for the Coulomb integrals, while the exchange terms were efficiently computed using the ‘chain-of-spheres’ (COSX)[414, 415] approximation by utilizing the SARC/J coulomb fitting and def2-TZVP/C correlation auxiliary basis sets, respectively. A constant Gaussian broadening was used for all presented absorption and ECD spectra which amounts to a linewidth of 1500 cm⁻¹. For better visual agreement with the experimental absorption spectra a second Gaussian broadening with linewidth of 3000 cm⁻¹ was used in some of the computed spectra. Similarly, a constant Gaussian broadening line width was used for all presented emission spectra with inhomogeneous line width of 10 cm⁻¹ at 77 and 295K experimental temperatures.

As a comparison measure of the shape of two different spectra, the mean absolute error of the calculated areas $MAE_{area_{1,2}}$ is used, which is defined according to the relation: $MAE_{area_{1,2}} = \% \frac{|area_1 - area_2|}{area_1}$. The vibrational modes to enter the PES spin-vibronic analysis were selected based on the Huang-Rhys factors (S) in the T₁/S₀ phosphorescence calculations or from the analysis of preliminary Resonance Raman (RR) calculations.

16.6. Absorption and Emission processes. A qualitative electronic structure analysis

The analysis first begins with discussing the most important factors that influence the absorption and emission processes of chiral Re(I) enantiomeric pair structures **1** and **2**. As shown in **Figure 16.1**, in both complexes the Re(I) center is imposed in a pseudo-octahedral (O_h) coordination environment, surrounded by one halogen (X, either Cl or I), three carbonyl (CO) groups arranged in a *facial* configuration [*fac*-Re(CO)₃], and a chelating bidentate (:C[^]N) N-heterocyclic carbene (NHC) ligand (L).

Under approximately C_{3v} symmetry around the Re(I) complexes **1** and **2** obtain a low-spin d^6 singlet ground state $S_0(^1A_1)$. It follows that valence single electron excitations or electron decays will give rise to CT type of transitions (MLCT, XLCT, LLCT and ILCT) of $2S + 1 = 1$ and $2S + 1 = 3$ multiplets of A_2 and E symmetries along the absorption and emission processes, respectively.

In particular, as seen in **Figure 16.3a**, the enantiomeric pairs **1** C-/A-Cl and **1** C-/A-I have valence electron configuration:

$$(\text{Re} - d_{xy} - \pi_{CO}^*)^2 (\text{Re} - d_{yz} - \pi_{CO}^* - p_{Cl/I}^*)^2 (\text{Re} - d_{xz} - \pi_{CO}^* - p_{Cl/I}^*)^2 (\pi_{Pyridine}^*)^0 (\pi_{Imadazol-Pyridine}^*)^0$$

the lowest excitations $(\text{Re} - d_{yz/xz} - \pi_{CO}^* - p_{Cl/I}^*)^2 \rightarrow (\pi_{Pyridine}^*)^0$ give rise to a pair of E-symmetric $^1,3\text{MLCT}/^1,3\text{XLCT}$ transitions which dominate the emission process. Similarly, $(\text{Re} - d_{xy/x^2-y^2} - \pi_{CO}^*)^2 \rightarrow (\pi_{Pyridine}^*)^0$, $(\text{Re} - d_{xz/yz} - p_{Cl/I}^*)^2 \rightarrow (\pi_{Pyridine}^*)^0$, and $(\pi_{Imadazol-Pyridine}^*)^2 \rightarrow (\pi_{Pyridine}^*)^0$ excitations give rise to E-symmetric $^1,3\text{MLCT}$, $^1,3\text{XLCT}$ and A_2 -symmetric $^1,3\text{LLCT}$ type of transitions, respectively, which will consist the high energy region of the absorption spectrum. In comparison to chloride complexes, the iodide complexes show a slight stabilization of Re-based orbitals, owing to the stronger-covalency Re-X interactions which increase the XLCT character in the respective $^1,3\text{MLCT}/\text{XLCT}$ transitions.

In Complexes **2**, extending the L ligand with helicenic chain introduces a set of $(\pi - \pi^*)_{\text{Helicene}}$ orbitals on the chain, which are located around the valence orbitals. This gives rise to a set $^1,3\text{ILCT}$ type of transitions which are able to mix with other CT transitions. As shown in **Figure 16.3b**, the amount of mixing and the character of the resulted transition

depends of the X halogen type. In particular, complexes **2** (with X=Cl), have valence electron configuration:

$$(\pi_{Helicene})^2 (Re - d_{yz} - \pi_{CO}^* - p_{Cl}^*)^2 (Re - d_{xz} - \pi_{CO}^* - p_{Cl}^*)^2 (\pi_{Pyridine-Helicene}^*)^0 (\pi_{Helicene}^*)^0$$

while in the iodide derivative the increase of the Re-I covalency stabilizes the Re-based $d_{yz/xz} - \pi_{CO}^* - p_I^*$ below the $\pi_{Helicene}$ orbital, and leads to valence electron configuration:

$$(Re - d_{yz} - \pi_{CO}^* - p_I^*)^2 (Re - d_{xz} - \pi_{CO}^* - p_I^*)^2 (\pi_{Helicene})^2 (\pi_{Pyridine-Helicene}^*)^0 (\pi_{Helicene}^*)^0.$$

Likewise to complexes **1** diastereomers, $(d_{yz/xz} - \pi_{CO}^* - p_{Cl/I}^*)^2 \rightarrow (\pi_{Helicene}^*)^0$ excitations give rise to a pair of E-symmetric ${}^{1,3}MLCT/{}^{1,3}XLCT$ transitions while $(\pi_{Helicene})^2 \rightarrow (\pi_{Helicene}^*)^0$ to an A_2 -symmetric ${}^{1,3}ILCT$ type of transitions. This set of transitions dominate the emission and first bands of absorption process, while the high energy part of the absorption spectrum consists once again of a set of 3MLCT , ${}^{1,3}LLCT$ and ${}^{1,3}XLCT$ transitions.

It should be noted that while MLCT and XLCT transitions can be both z – or xy – polarized transitions, LLCT and ILCT transitions are in principle $\pi \rightarrow \pi^*$ z –polarized transitions. In practice, under C_{3v} symmetry the A_2 -symmetric $\pi \rightarrow \pi^*$ transitions, involving orbital symmetries a_1 and a_2 ($a_1 \rightarrow a_2$), are electric dipole forbidden but magnetic dipole allowed. In a first approximation this is expected to influence both the ECD, CPL intensities as well as the g_{abs} and g_{lum} values.

In principle, the transitions consisting the absorption and emission processes will be a linear combination of the parent MLCT, XLCT, LLCT and ILCT transitions represented as:

$${}^{3,1}CT = \alpha {}^{3,1}MLCT_{n=1,2...} + \beta {}^{3,1}XLCT + \gamma {}^{3,1}LLCT + \delta {}^{3,1}ILCT \quad (16.2)$$

where, $\alpha, \beta, \gamma, \delta$ define the mixing coefficients. Further mixing of the different singlet and triplet ${}^{1,3}CT$ transitions is provided through SOC leading to state manifolds consisting magnetic sublevels with $M_S = 0, \pm 1$. Finally, vibronic coupling may add a dynamic band shape character to the absorption and emission processes while spin-vibronic coupling might influence the excited state magnetic properties and hence the nature of the intensity mechanism and the relaxation times of the observed phosphorescence and the circularly polarized phosphorescence spectra of diastereomers **1** and **2**. In the following all the above aspects will be studied thoroughly.

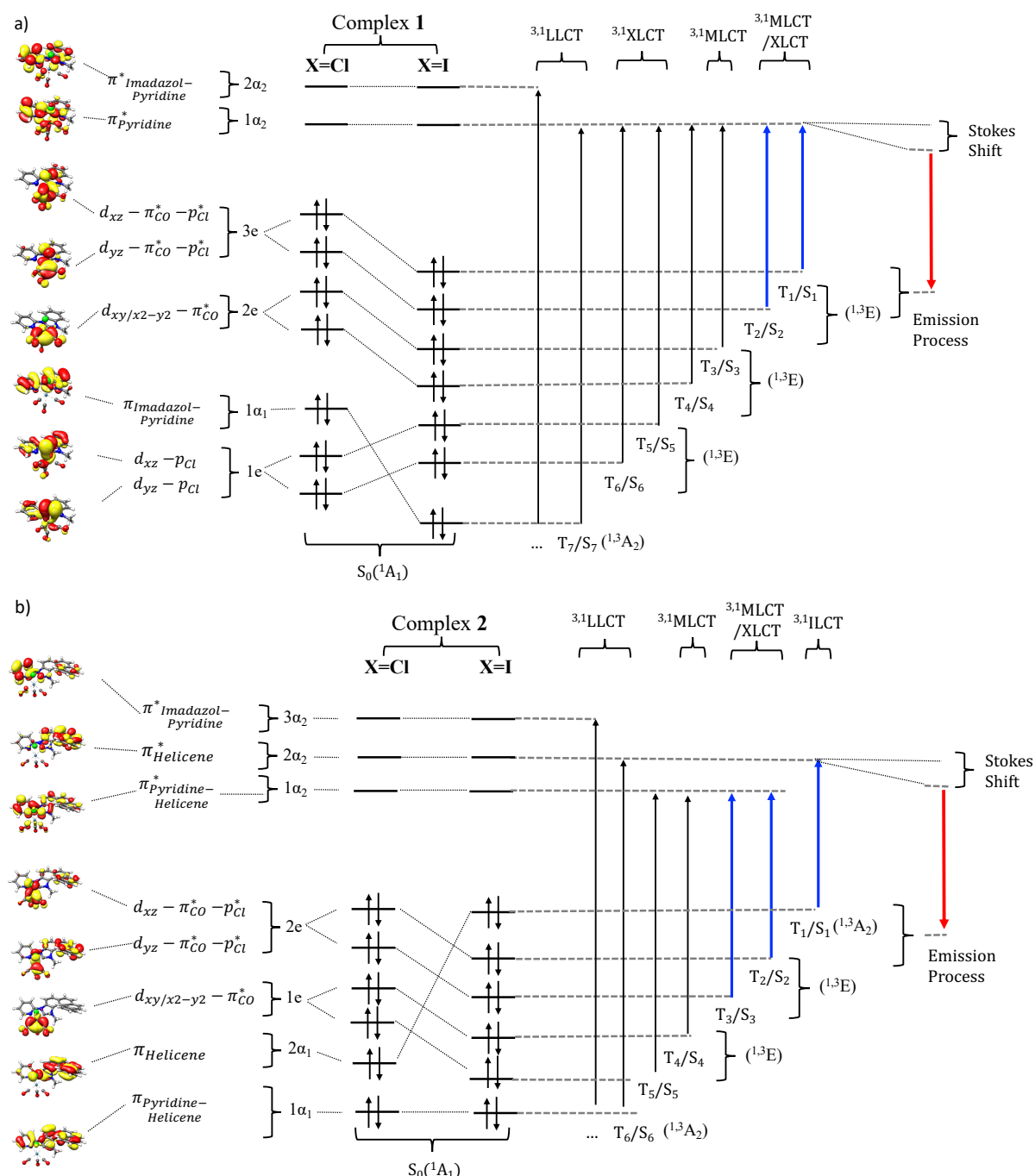


Figure 16.3. a) and b) PBE0/def2-TZVP MO diagrams of the Cl derivatives of complexes type **1** and **2**, respectively, adapted in an ‘ideal’ C_{3v} symmetry around the Re centers. In both complexes the different type of single electron excitations, depicted within the 1-electron picture, are giving rise to E-symmetric MLCT and/or XLCT, as well as A_2 symmetric LLCT types of transitions. In the case of complexes type **2**, $(\pi_{\text{Helicene}})^2 \rightarrow (\pi^*_{\text{Helicene}})^0$ excitations with the Helicenic ligand give in addition rise to A_2 symmetric ILCT types of transitions. Additionally, the relaxation of the lowest excited state leads to emission, visually represented as a red line, with energy red-shifted from the corresponding excitation energy by Stokes shift.

16.6.1. Insights into the nature of the Emissive Excited State

In a first step, the geometrical structures of ground and first singlet and triplet states were optimized, followed by frequency calculation, both computed at the DFT/TD-DFT (PBE0) level in CH₂Cl₂ solvent, as discussed in **Section 16.5**. Most relevant structural parameters are given in **Table B. 1**. The results show a good agreement between calculated and available experimental structural values extracted from X-ray diffraction data.[508]

Based on the above qualitative analysis (**Section 16.6**), one may conclude that in the non-Helicenic diastereomers of type **1**, the MLCT/XLCT transitions will dominate the emission process. While in the Helicenic diastereomers of type **2**, the emission process will be dominated by a mixture of MLCT/XLCT and $\pi - \pi^*$ ILCT (within the Helicenic ligand) transitions. In fact, that could be preliminary confirmed through analysis and comparison of the IR spectra and bonding structure changes between ground and the lowest excited states in complexes **1** and **2**.

In practice, MLCT transitions, involving CT from $\text{Re}_{5d_{yz/xz}} - \text{CO}\pi^*$ occupied MO, will weaken the (Re \rightarrow CO) π -backdonation. Consequently, this reduces the population of π_{CO}^* MOs, and results in shorter and stronger C-O bond. Such a structural change can be detected by blue shift in the IR peaks corresponding to CO symmetric and non-symmetric stretching vibrations. These peaks are very sensitive to C-O bond length and utilized in several studies,[562, 563] to discern the nature of the excited state, specifically distinguishing the MLCT from other type of CT away from Re center leaving the IR peaks unchanged. This is indeed observed in the computed IR spectra of complexes **1** and **2**.

Figure 16.4(a and b), present the IR spectra for the non-relativistic lowest singlet excited ($2S+1=1$, S_1) and triplet excited ($2S+1=3$, T_1) states, respectively compared with the respective spectra of the ground state S_0 . We focus on the spectral region around 2000 cm⁻¹ in which the symmetric and asymmetric CO stretching vibrations are prominent.[295]

When comparing the CO vibration peaks of complexes **1** and **2** to the ‘ideal’ [*O*_h-Re(I)(CO)₆]⁺ model complex,[564] we observe similarities in both complexes (**1** and **2**), where their peaks are generally appearing at lower energies compared to the reference peaks. This indicates a weakening of the CO bond strength due to the coordination of halogen and NHC ligands in both complexes (**1** and **2**) with respect to the reference structure.

Owing to the electronic excitations (as seen in the lowest singlet and triplet excited states compared to ground state), the asymmetric CO stretching vibrations in complexes of type **1** is shifted to higher energies with respect to complexes of type **2**, indicating a clear MLCT excited states in complexes **1**. This is also consistent with the fact that in complexes **2** the lowest absorption and emission processes contain, or are dominated by, ILCT excitations within the Helicene unit in addition to MLCT/XLCT contributions. Finally, that also indicates that vibronic coupling (interplay between electronic and vibrational structure) should play a significant role in the emission processes, especially in complexes **1**, and should be carefully taken into account.

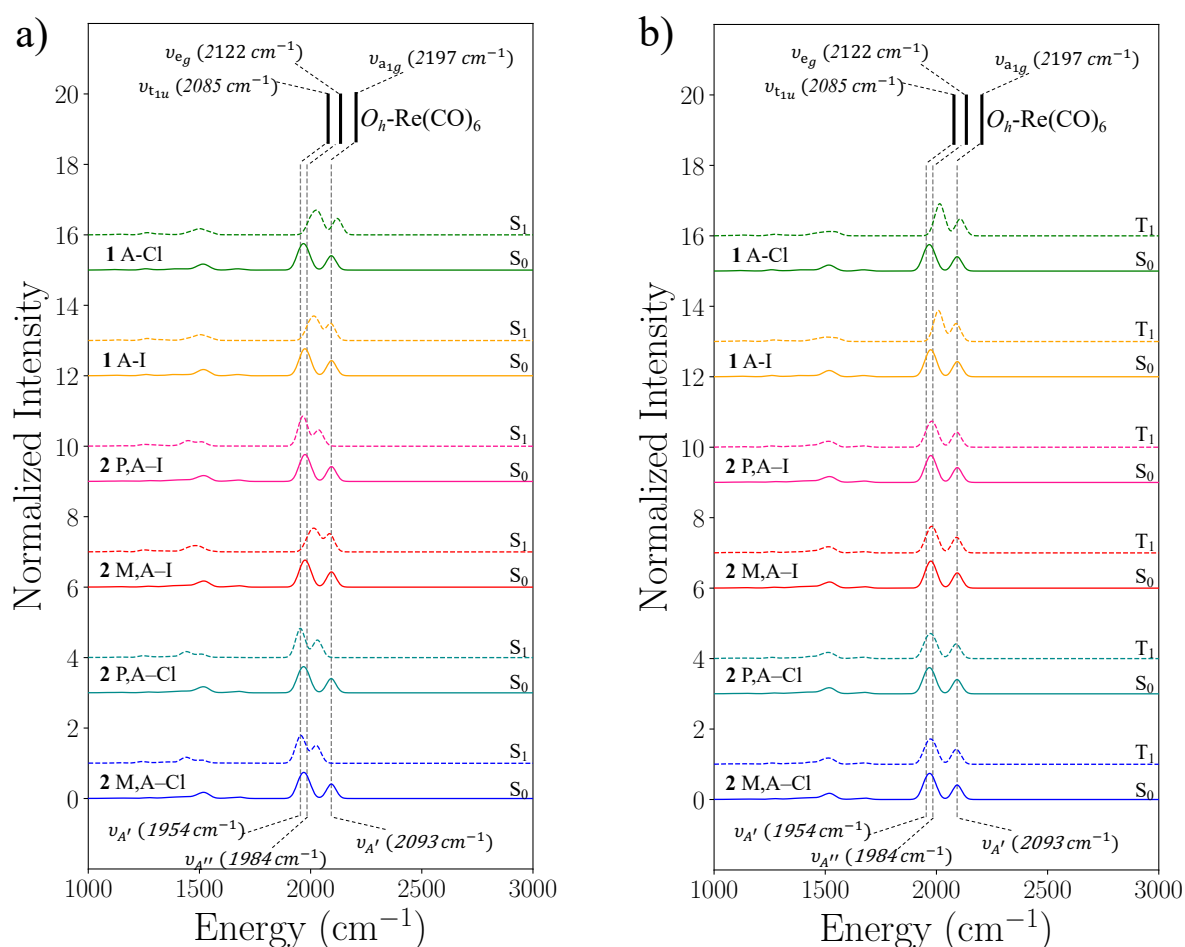


Figure 16.4. IR spectra of a) optimized ground and first singlet states geometries, b) optimized ground and first triplet states geometries, of all studied complexes (**1** and **2**). For sake of comparison, the symmetric and asymmetric CO vibrations of bond in the ground state of the reference $O_h\text{-[Re(CO)}_6\text{)]}^+$ complex are depicted at the top (taken from Ref.[564]). In addition, for both complexes (**1** and **2**), the CO vibrations of the ground states are similar and given in bottom.

16.7. Absorption and ECD spectra

16.7.1. Calibration of the TD-DFT protocol

Prior entering the spectra computation section and analysis we evaluate the performance of various TD-DFT functionals in computing the Absorption and ECD spectra of the diastereomers **1** and **2**. As a matter of fact, the choice of the “best” DFT functional with the desired level of accuracy is not trivial and depends on the specific system and the targeted property. In a first step, the ABS and ECD spectra of complex **1** A-Cl are computed employing the STEOM-DLPNO-CCSD[416-419] and full TD-DFT[237] levels of theory employing a collection of DFT functionals belonging to the GGA: BP86,[228, 230] PBE,[226] hybrid: PBE0,[227, 234, 235] BHLYP,[558] B3LYP,[228, 229, 233, 559] hybrid meta-GGA: M06,[231] range separated hybrid: CAM-B3LYP[441], wB97,[560] and double hybrid: B2PLYP[236] families. The computed non-relativistic and relativistic ABS and ECD spectra of complex **1** A-Cl compared with the respective experimental spectra are collectively provided in **Figure B. 1** and **Figure 16.5**, respectively.

As seen in **Figure 16.5**, the MAE errors with respect to experiment drop below 10% when employing STEOM-DLPNO-CCSD + SOC to compute the ABS and ECD spectra of **1** A-Cl, respectively. This is not surprising as in fact STEOM-DLPNO-CCSD level of theory has been successfully used to evaluate the performance of TD-DFT protocols in computing band gap energies of organic and inorganic semiconductors[84] and inorganic phosphor materials.[80] At the TD-DFT + SOC level functionals containing no Hartree Fock (HF) exchange e.g. the GGA BP86 and PBE and those with small HF exchange (e.g. in range separated hybrid wB97, 10%HF) or large HF exchange (e.g. in hybrid BHLYP, 50%HF) show avg. MAEs $\geq 25\%$. Such behavior can be attributed to the fact that none of the above functionals is able to provide a balance description of the diverse nature of the involved CT transitions (MLCT, XLCT, ILCT).

In contrast, the situation improves when hybrid functionals with moderate HF exchange, such as M06, PBE0, and B3LYP (with 27%, 25% and 20%HF, respectively) are employed. They in fact perform satisfactorily showing MAE values of (18, 14, and 22)%, respectively. Interestingly the range separated hybrid (CAM-B3LYP) performs worst in comparison to its hybrid variant (MAE=26%).

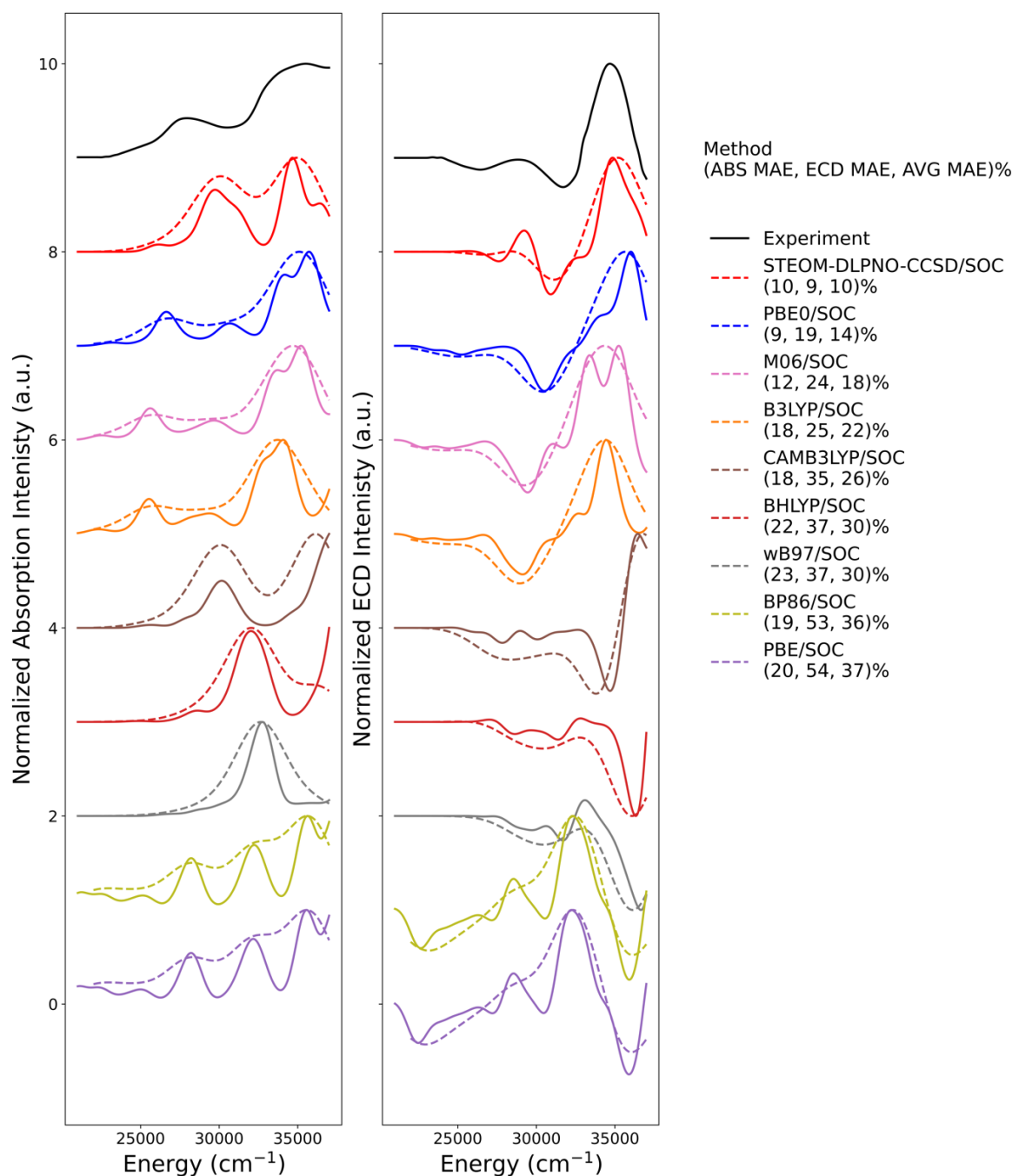


Figure 16.5. Experimental (black) vs. calculated relativistic STEOM-DLPNO-CCSD (red), relativistic TD-DFT/BP86 (olive), PBE (purple), BHLYP (pale red), PBE0 (blue), B3LYP (orange), M06 (pink), CAMB3LYP (brown), wB97 (gray) ABS (left side) and ECD (right side) spectra of complex **1** A-Cl. Solid lines indicate constant Gaussian broadening of 1500 cm⁻¹ while dotted lines indicate constant Gaussian broadening of 3000 cm⁻¹. Given in parenthesis are the %MAE errors with respect to experiment, for (ABS, ECD and their average).

In a next step, we select the bottom and upper limits of the above “best” performing functionals namely the PBE0 and B3LYP and we compare their performance across all complexes in the study set in the framework of ABS and ECD TD-DFT + SOC computations. These results are collectively presented in **Figures B.2-4** and **Table B. 2**. Once again PBE0/TD-DFT + SOC shows the smallest errors in comparison to the experimental Absorption and ECD spectra. These errors amount to about 12% and 19% respectively. The respective errors employing the B3LYP/TD-DFT methods are ranked a bit higher, amounting in average to ~19% and ~33% for the Absorption and ECD spectra respectively.

Based on the above results while all the TD-DFT computed absorption and ECD spectra across the study set exhibit satisfactory agreement with experiment, PBE0/TD-DFT + SOC method shows the smallest MAE errors across the study set, hence it is chosen for all the production Absorption, ECD, PL and CPL calculations.

16.7.2. Non-Relativistic Absorption and ECD spectra

16.7.2.1. Parent Non-Helicenic Complexes (Complexes 1 A/C-Cl/I)

The experimental versus PBE0/TD-DFT calculated Absorption and ECD spectra of **1 A-Cl** and **1 A-I** are provided in **Figure 16.6 (a and b)**. For clarity, only the spectra of the left-handed (A-) enantiomers are discussed. The complementary spectra of the right-handed (C-) models are in **Figure B. 5**. In principle, the absorption spectra can be divided into three main regions. The first region extends between 24000-26000 cm⁻¹ and includes the weak intensity bands 1-3. NTO analysis shows that bands 1, 2 have mixed MLCT/XLCT characters consisting of $Re - d_{yz/xz} - Cl/I - p_{x/y}^* \rightarrow \pi_{Pyridine}^*$ single electron excitations. As expected, the XLCT character of the excitation increases from Cl to I. On the contrary, band 3 is basically a pure MLCT transition consisting of $Re - d_{xy} \rightarrow \pi_{Pyridine}^*$ single electron excitation. The second region extends between 32000-40000 cm⁻¹ and includes bands 4-6. According to the NTO analysis, these bands have mainly XLCT character ($Cl/I - p_{x/y}^* \rightarrow \pi_{Pyridine}^*$) containing small contributions from MLCT ($Re - d_{yz/xz} - Cl/I - p_{x/y}^* \rightarrow \pi_{Pyridine}^*$) and LLCT ($\pi_{Pyridine} \rightarrow \pi_{Pyridine}^*$ and $\pi_{Imidazole} \rightarrow \pi_{Pyridine}^*$) characters. Finally, the high energy region > 40000 cm⁻¹ consisting of bands 7-8 are mainly XLCT character ($Cl/I - p_{x/y}^* \rightarrow \pi_{Pyridine/Imidazole}^*$). These results are also consistent with the TheoDORE analysis presented in **Table B. 3** and **Table B. 4**. Looking into the respective ECD spectra, bands 1-3 show weak ECD intensities

due to fact that they consist of mainly MLCT characters with pronounced experimental $g_{\text{abs}} \sim 0.003$ (**Figure B. 11a**). Moving at higher energies (bands 4-6) where the respective ECD intensities increase along with the XLCT and LLCT characters in these transitions increase. This is also reflected to the experimental g_{abs} values that are now smaller ($g_{\text{abs}} \sim 0.002$, **Figure B. 11a**). At higher energy regions, bands 7 and 8 in the case of **1 A-Cl** the ECD intensity drops while in the case of **1 A-I** maintains its high intensity in comparison to bands 4-6. This indicates a more complex ECD intensity mechanism in this bands as they combine a multitude of XLCT, LLCT types of excitations. At these energies the experimental g_{abs} values drop below 0.001, as shown in **Figure B. 11a**.

16.7.2.2. Helicenic complexes of X-Helicenic parallel (2 M,A / P,C-Cl / I) and anti-parallel (2 M,C / P,A-Cl / I) aligned

The experimental versus PBE0/TD-DFT calculated Absorption and ECD spectra of **2 M,A-Cl** and **2 P,A-Cl** are provided in **Figure 16.7 (a and b)**, respectively while for the respective **2 M,A-I** and **2 P,A-I** the same information are provided in **Figure 16.8 (a and b)**, respectively. Once again, the complementary spectra of the right-handed (C-) models are given in **Figure B. 6** and **Figure B. 7**. In all these cases there are 3 weak intensity bands around 25000 and 27000 cm^{-1} . According to the NTO analysis, these bands are assigned as MLCT/XLCT transitions consisting of $Re - d_{yz/xz} - Cl/I - p_{x/y}^* \rightarrow \pi_{\text{Pyridine}}^*$ single electron excitations while band 3 has an ILCT character consisting of $\pi_{\text{Helicene}} \rightarrow \pi_{\text{Helicene}}^*$ single electron excitation. This is in contrast to the diastereomer complexes **1** in which the first bands are all MLCT/XLCT in nature. At energies between 30000 and 40000 cm^{-1} bands 4-6 consist from a mixture of MLCT/XLCT and ILCT transitions while $> 40000 \text{ cm}^{-1}$ band 7 and 8 consist from a mixture of XLCT and ILCT transitions. Once again, these results are consistent with the TheoDORE analysis presented in **Table B. 5** and **Table B. 6**.

As in the case of diastereomers **1** the ECD intensities increase at higher energies bands (4-7). In all bands there is in principle a pronounce mixing between MLCT/XLCT and ILCT transitions. This together with a more pronounced symmetry reduction around the Re(I) center to C_s , renders all the transitions both electric dipole and magnetic dipole allowed. This is reflected in the experimental and calculated g_{abs} values (**Figure B. 11b**) that vary only between $g_{\text{abs}} \sim 0.002$ and 0.001 across the experimentally observed and computed bands.

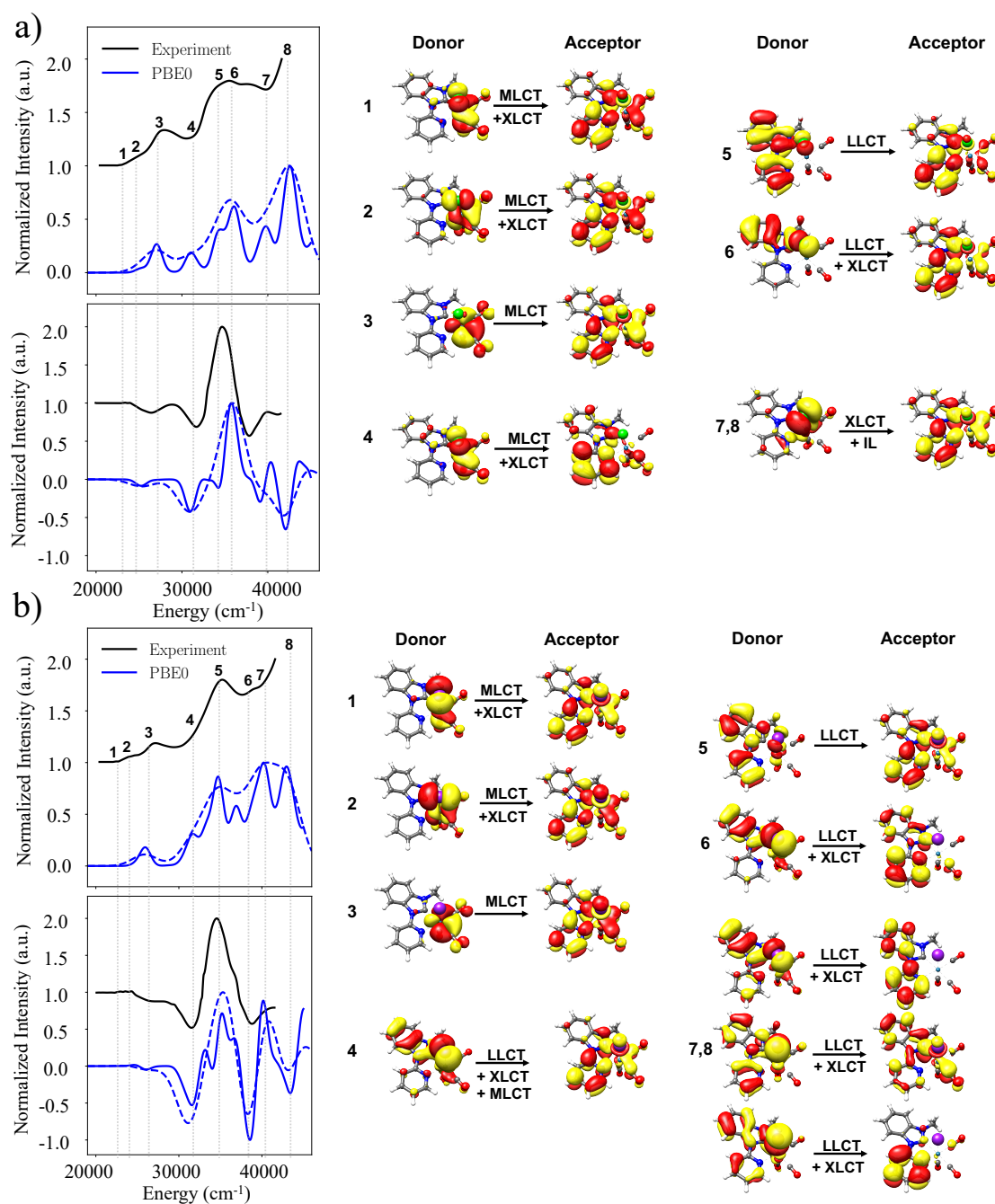


Figure 16.6. Experimental (black) and PBE0/TD-DFT (blue) absorption and ECD spectra of non-helical enantiomers a) **1 A-Cl** and b) **1 A-I**. The nature of the most important bands 1-8 is discussed in the framework of NTO analysis. Solid lines indicate constant Gaussian broadening of 1500 cm⁻¹ while dotted lines indicate constant Gaussian broadening of 3000 cm⁻¹.

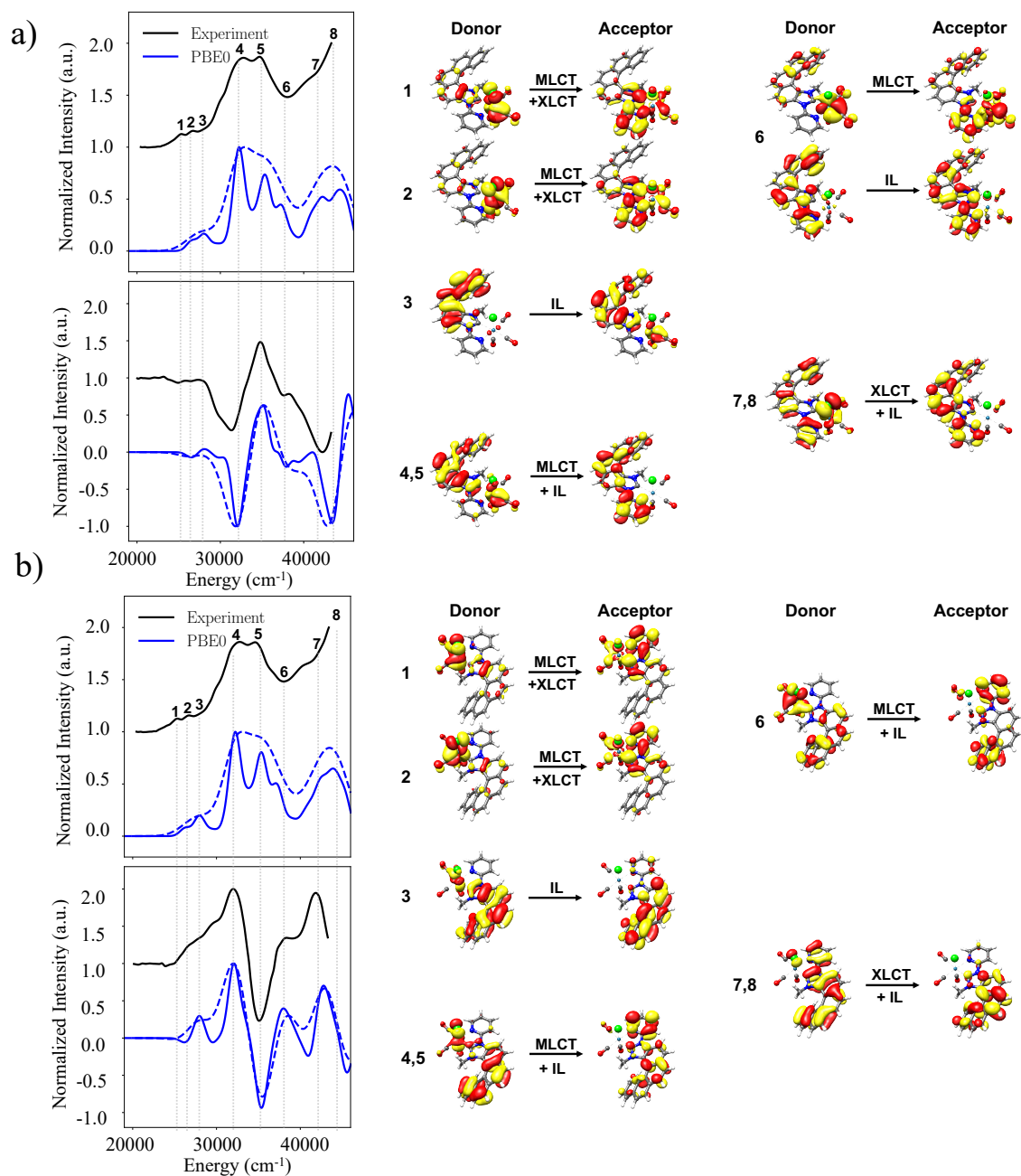


Figure 16.7. Experimental (black) and PBE0/TD-DFT (blue) absorption and ECD spectra of helicenic enantiomers a) **2** M,A-Cl and b) **2** P,A-Cl. The nature of the most important bands 1-8 is discussed in the framework of NTO analysis. Solid lines indicate constant Gaussian broadening of 1500 cm⁻¹ while dotted lines indicate constant Gaussian broadening of 3000 cm⁻¹.

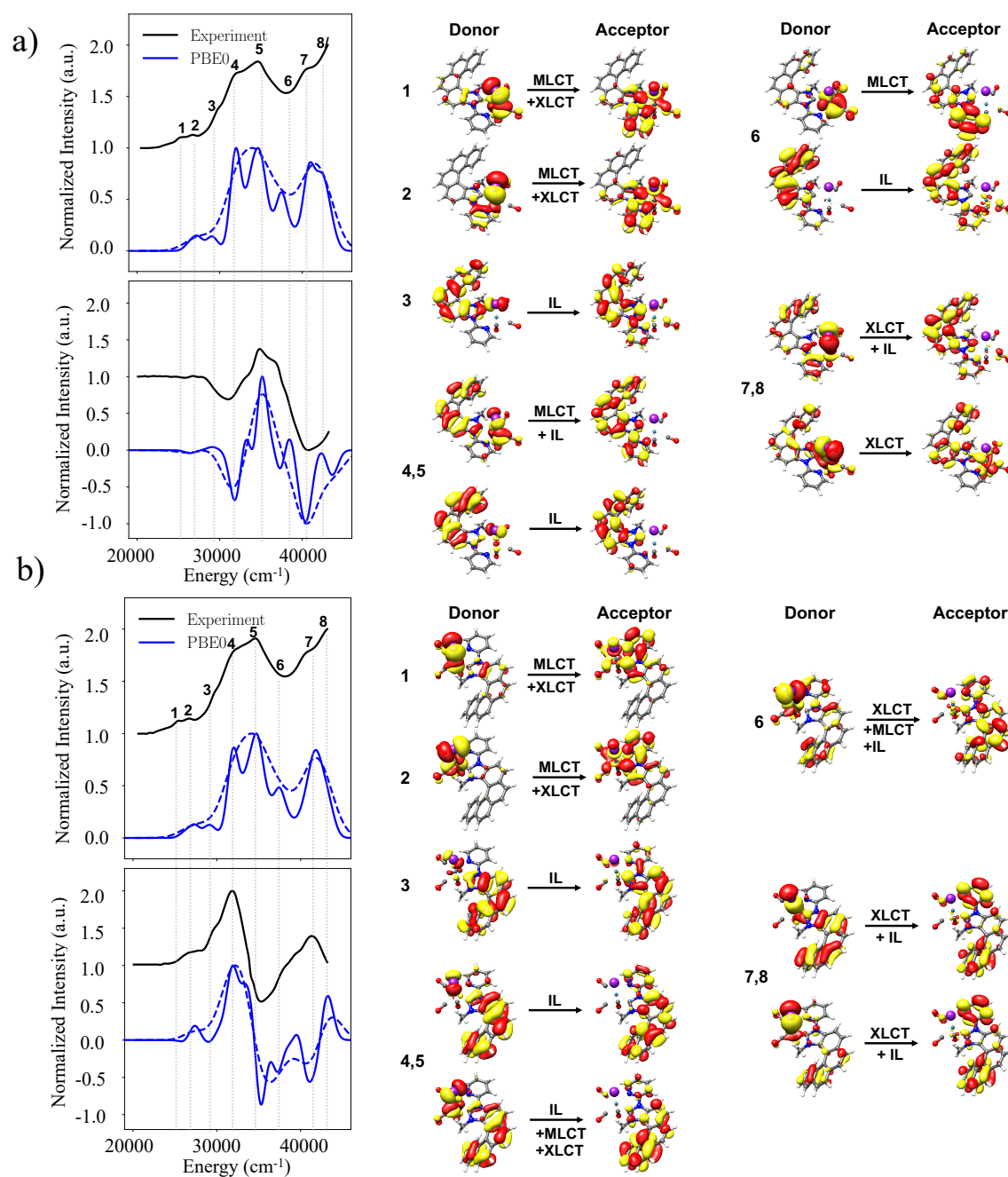


Figure 16.8. Experimental (black) and PBE0/TD-DFT (blue) absorption and ECD spectra of helicene enantiomer a) **2 M,A-I** and b) **2 P,A-I**. The nature of the most important bands 1-8 is discussed in the framework of NTO analysis. Solid lines indicate constant Gaussian broadening of 1500 cm⁻¹ while dotted lines indicate constant Gaussian broadening of 3000 cm⁻¹.

16.7.3. Relativistically corrected Absorption, ECD and g_{abs} spectra

In a next step we turn on the SOC interactions. The relevant relativistically corrected Absorption and ECD spectra are presented in **Figure 16.9** for the non-Helicenic enantiomers **1** A-Cl and **1** A-I and the respective Helicenic enantiomers, **2** M,A-Cl and **2** M,A-I. These cases are chosen as representative examples. While the spectra, of all the studied complexes, of the **1** A/C-Cl/I, **2** M,A/P,C/M,C/P,A-Cl, and **2** M,A/P,C/M,C/P,A-I enantiomers are presented in **Figure B. 8**, **Figure B. 9** and **Figure B. 10**, respectively.

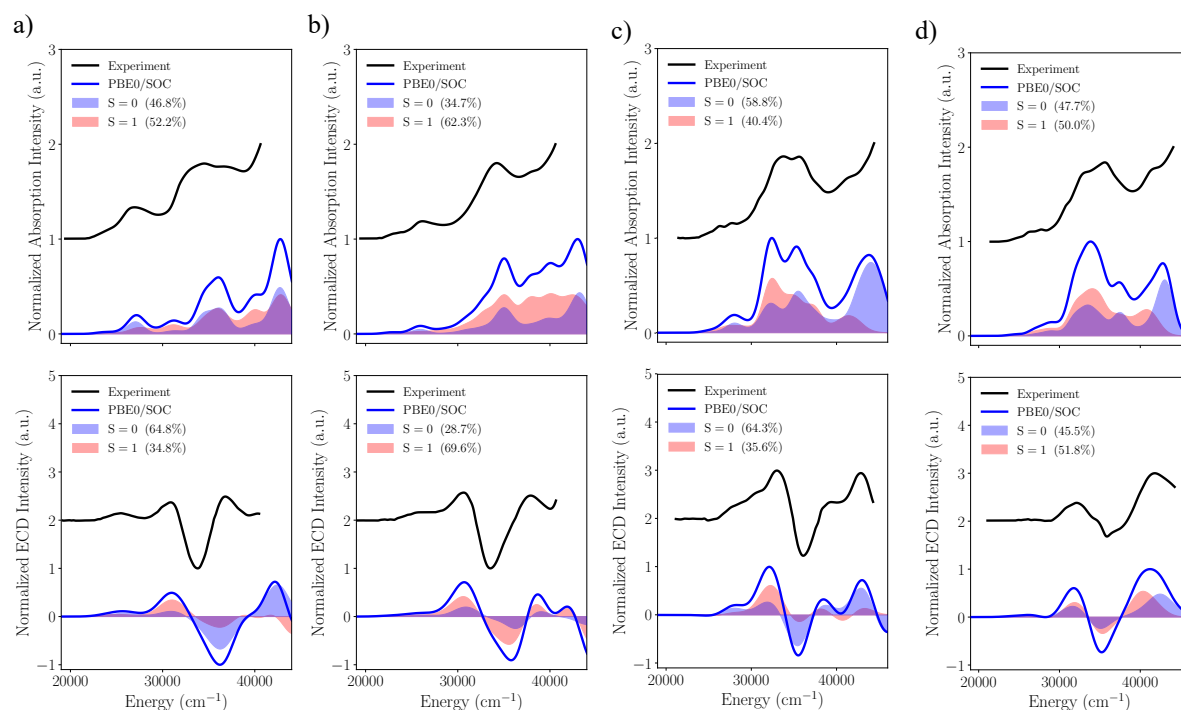


Figure 16.9. Experimental (black) and PBE0/TD-DFT + SOC (blue) absorption and ECD spectra of non-helicenic enantiomers a) **1** A-Cl and b) **1** A-I and of helicenic enantiomers, c) **2** M,A-Cl and d) **2** M,A-I. The spectra are analyzed in terms of contributing parent non-relativistic singlet (light red) and triplet (light blue). Solid lines indicate constant Gaussian broadening of 1500 cm^{-1} .

As seen in **Figure 16.9**, the analysis of the spectral features in terms of parent non-relativistic singlet (light blue) and triplet (light red) states reveals that all spectral features consist of a significant amount of parent not-relativistic triplet states which ranges between

~40-60%. Analysis of the individual contributions presented in **Tables B.7-B.10** reveals that the low-lying excitation problem in both **1** and **2** diastereomers involves 6-states which at the non-relativistic limit consists of the ground the excited states singlets S_0 , S_1 and S_2 as well as the respective excited state Triplets T_1 , T_2 and T_3 . Interestingly while in both **1** and **2** diastereomers states S_1 - S_2 and T_2 - T_3 are all MLCT/XLCT with contributions from LLCT in the case of **1** or ILCT in the case of **2**, the character of the T_1 state differs significantly. It is again an MLCT/XLCT character in the case of **1** diastereomers but it is a pure ILCT in the case of **2** diastereomers. At the relativistic limit, the lowest SOC states $|\Psi_{0-9}\rangle$ consist of magnetic sublevels $M_S = 0, \pm 1$ with contributions from the various non-relativistic states as shown in **Tables B.7-B.10**.

To sum up, in all cases the PBE0/TD-DFT computed ABS and ECD spectra are in very good agreement with experiment. This allowed a thorough analysis of the computed bands in terms of the NTO and the TheoDORE analyses for complexes **1** and **2**, respectively. The TheoDORE analyses of the lowest excited states across the studied set are provided in **Figure 16.10**.

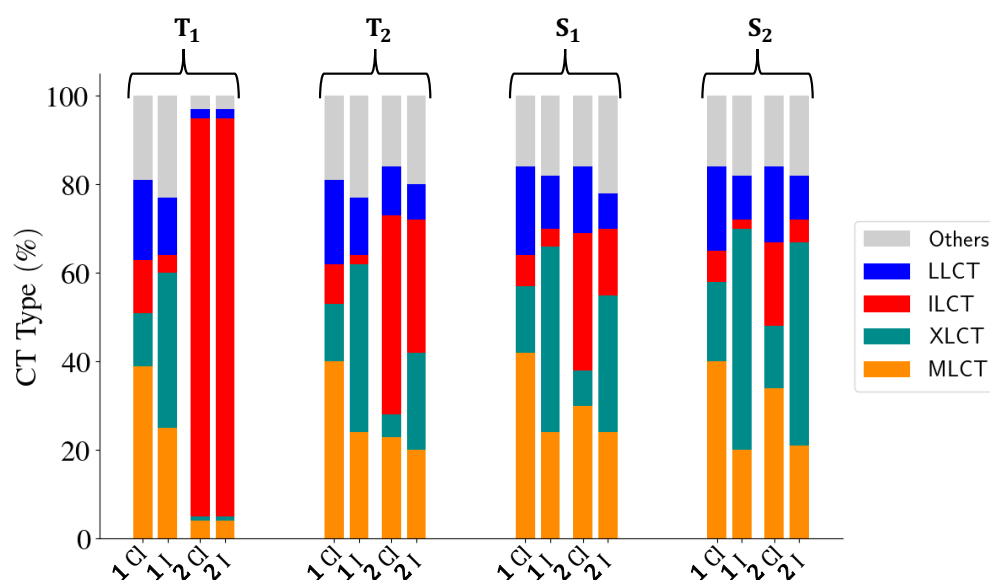


Figure 16.10. TheoDORE Analysis of lowest excited states ($T_{1,2}$ and $S_{1,2}$) of $X=\text{Cl}$ or I for Complex **1**, **2**.

The low-lying excited states, that may contribute to the emission process, are assigned to MLCT/XLCT transitions in complexes **1**, while non-negligible contributions of ILCT characters occur in complexes **2**, especially in T₁ which appears to be purely ILCT whatever the axial ligand is, Cl or I (**Figure 16.10**). The high energy regions (T₂, S₁, S₂) contain major contributions of XLCT, LLCT and ILCT transitions, the XLCT character being more pronounced in both iodide complexes **1** and **2**.

16.8. Phosphorescence Spectra and Excited State lifetimes

The emission spectroscopies, excited state kinetics and photophysics mechanisms of **1** and **2** diastereomers, are presented in the following sections. They are based on the calibrated PBE0/TD-DFT+SOC computational protocol discussed above.

16.8.1. Non-helicenic NHC diastereomers

Let us now turn into the computation of the phosphorescence spectra of the non-helicenic diastereomers **1** A-Cl and **1** A-I. The Experimental versus PBE0/TD-DFT+SOC spectra together with the most important magnetic sublevel contributions are presented in **Figure 16.11** (**a** and **b**). Deconvolution of the relevant magnetic sublevels in terms of M_s contributions and the associated relaxation rates are given in **Table 16.2** and **Table B.11**. The complementary spectra of the C- enantiomers are presented in **Figure B.12**.

The agreement to experiment is very good which allows for further analysis. Both the experimental and computed phosphorescence spectra are broad and structureless. This is reflected to the Huang-Rhys computed factors (S) which gives a measure of the strength of the electron-phonon coupling in the emission process.[274] In fact, as seen in **Figure B.16** the computed S values are about 4. These large values are associated with vibrational disorders around the emitting Re(I) center owing to asymmetric CO stretching vibration as well as symmetric and asymmetric stretching vibrations within the pyridyl ligand which extend over the entire range of the vibrational spectrum within 200-2000 cm⁻¹.

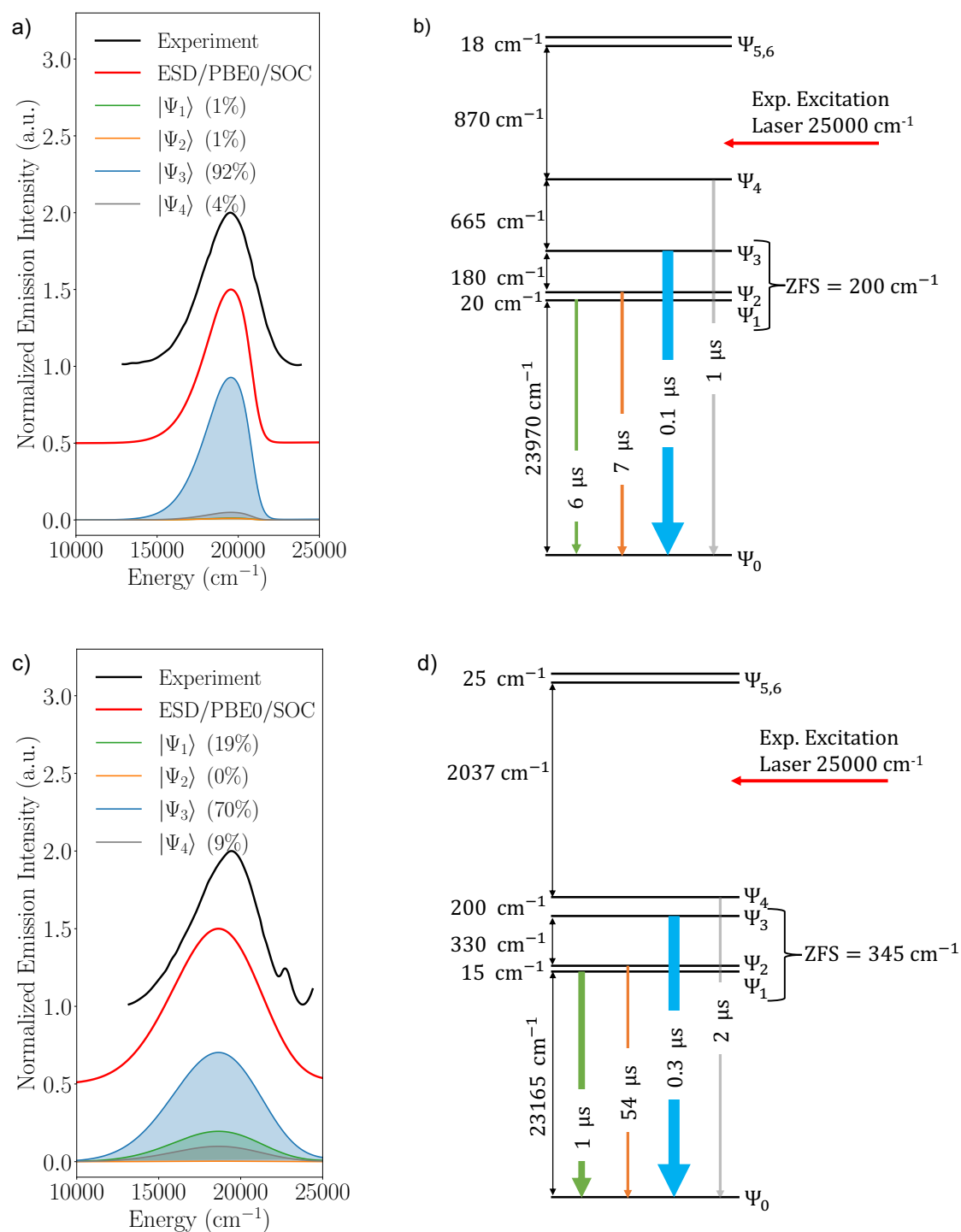


Figure 16.11. Experimental versus PBE0/TD-DFT/SOC calculated phosphorescence spectra of NHC **1** A-Cl (a) and **1** A-I (c) enantiomers together with the most important magnetic sublevel contributions and associated computed relaxation times from the relevant magnetic sublevels (b) and (d). Red arrows indicate the experimental energy of the laser excitation.

Table 16.2. Deconvolution of the of the relevant magnetic sublevels to the emission process in terms of M_S contributions for diastereomers **1** A-Cl/I together with the respective room and low temperature total ($t_{295/77K}$) and partial ($t_{295/77K}^n$) relaxation times in (μs). Partial relaxation times of a given state n , are calculated as $1/(k_r^n + k_{nr}^n)$, where k_r^n, k_{nr}^n are the Boltzmann averaged radiative and non-radiative rate constants. At RT non-radiative relaxation is in addition taken into account.

Complex	SOC State $ \Psi_n\rangle$	SOC State Composition	Energy (cm^{-1})	$^*t_{295K}^n$ (μs)	t_{295K} (μs)	$^*t_{77K}^n$ (μs)	t_{77K} (μs)
1 A-Cl	$ \Psi_0\rangle$	99% $S_0(0)$	0				
	$ \Psi_1\rangle$	72% $T_1(\pm 1)$ + 18% $T_2(\pm 1)$	24123	6		19	
	$ \Psi_2\rangle$	74% $T_1(\pm 1)$ + 18% $T_2(\pm 1)$	24143	7	0.07	31	3.2
	$ \Psi_3\rangle$	10% $S_2(0)$ + 87% $T_1(0)$	24326	0.1		4	
	$ \Psi_4\rangle$	26% $S_1(0)$ + 63% $T_2(0)$	24990	1		--	
1 A-I	$ \Psi_0\rangle$	99% $S_0(0)$	0				
	$ \Psi_1\rangle$	58% $T_1(\pm 1)$ + 34% $T_2(\pm 1)$	23324	1		5	
	$ \Psi_2\rangle$	58% $T_1(\pm 1)$ + 36% $T_2(\pm 1)$	23336	54	0.19	344	4.4
	$ \Psi_3\rangle$	15% $S_2(0)$ + 77% $T_1(0)$	23676	0.3		198	
	$ \Psi_4\rangle$	33% $S_1(0)$ + 59% $T_2(0)$	23887	2		--	
2 MA-Cl	$ \Psi_0\rangle$	99% $S_0(0)$	0				
	$ \Psi_1\rangle$	73% $T_1(0)$ + 26% $T_1(\pm 1)$	18853	3×10^3		28×10^3	
	$ \Psi_2\rangle$	6% $T_1(0)$ + 92% $T_1(\pm 1)$	18853	21×10^3	701	202×10^3	6626
	$ \Psi_3\rangle$	20% $T_1(0)$ + 78% $T_1(\pm 1)$	18853	1×10^3		9×10^3	
2 PA-Cl	$ \Psi_0\rangle$	99% $S_0(0)$	0				
	$ \Psi_1\rangle$	26% $T_1(0)$ + 72% $T_1(\pm 1)$	18881	14×10^3		345×10^3	
	$ \Psi_2\rangle$	73% $T_1(0)$ + 26% $T_1(\pm 1)$	18881	34×10^3	433	850×10^3	5427
	$ \Psi_3\rangle$	98% $T_1(\pm 1)$	18881	0.5×10^3		6×10^3	

Deconvolution of the spectrum reveals that the emission process involves magnetic sublevels $|\Psi_{1-4}\rangle$. Although, $|\Psi_4\rangle$ is close in energy to the emitting states ($\Delta E_{4,1} = 865,545 \text{ cm}^{-1}$), at 295K in the case of Cl and I it only slightly contributes to the emission by about 4% and 9%, respectively. In a first approximation, one would think that $|\Psi_{1-3}\rangle$ are the magnetic sublevel components of the non-relativistic T_1 state. However as shown in **Table 16.2**, there is a pronounced mixing between non-relativistic $T_1 \leftrightarrow T_2$, $T_1 \leftrightarrow S_2$ and $T_2 \leftrightarrow S_1$ states.

In particular $|\Psi_{1-2}\rangle$ states consist of contributions of the $M_S = \pm 1$ components of the T_1 and T_2 non-relativistic triplet states while $|\Psi_3\rangle$ state consists of contributions of the $M_S = 0$ components of T_1 and S_2 non-relativistic triplet and singlet states. This later mixing causes a pronounced energy splitting within the magnetic sublevel components leading to about axial excited state zero-field splitting parameters which in the case of **1 A-Cl** amounts to $|D| \sim 200 \text{ cm}^{-1}$ and $|E/D| \sim 0.09$ while in the case of **1 A-I** amounts to $|D| \sim 345 \text{ cm}^{-1}$ and $|E/D| \sim 0.04$. The z-magnetic axis (D_{zz}) shows -21° deviations from the z- molecular axis that orients along the Re-X bond (**Figure B.22a**).

Such z- magnetic axis (or easy axis) anisotropy is responsible for the fast relaxation of the observed emission spectra which amounts to about $4\mu\text{s}$ at 77K and just $0.1\mu\text{s}$ at room temperature (RT). In fact, the analysis shows that the emission spectra are in principle dominated (> 90 and 70% , for Cl and I, respectively) by $|\Psi_3\rangle \rightarrow |\Psi_0\rangle$ emission process which provides the fastest relaxation pathway proceeding through the $M_S = 0$ components of the parent non-relativistic ground S_0 and T_1 and S_2 excited states. However, at low temperature (77K) the relaxation from $|\Psi_{1-2}\rangle$ is improved at the expense of $|\Psi_3\rangle$, which suffers from an exponential reduction in population. This effect is once again more pronounced in the case of the I-structure in comparison to Cl one, due to the larger ZFS magnitude. The computation of the total relaxation times involving both radiative and non-radiative processes are given in **Table B.11**. At RT the contributions of non-radiative processes are in fact not negligible. As shown in **Table 16.3**, the computed relaxation times agree well with both the RT and low temperature experiments.

Table 16.3. Experimental and Calculated (FC+HT) excited states relaxation rates and lifetimes at room (295K) and low (77K) temperatures. See also **Table B.11** for further information.

Complex	$t_{\text{phosp.}} (\mu\text{s})$		$t_{\text{phosp.}} (\mu\text{s})$	
	77K		295K	
	Exp.	PBE0/SOC	Exp.	PBE0/SOC
1 A-Cl	4.7	3.6	0.1	0.07
1 C-Cl	4.7	3.2	0.1	0.07
1 A-I	5.2	4.4	0.1	0.19
1 C-I	5.2	4.4	0.1	0.18
2 M,A-Cl	6200	6626	710	701
2 P,C-Cl	5900	6212	680	720
2 M,C-Cl	5400	5374	410	425
2 P,A-Cl	6100	5427	480	433
2 M,A-I	7700	8395	50	49
2 P,C-I	7600	8741	60	53
2 M,C-I	6600	6500	44	44
2 P,A-I	6500	6010	43	45

16.8.2. Helicenic diastereomers

In a next step we discuss the phosphorescence spectra of the helicenic diastereomers **2** P,A-Cl/I and **2** M,A-Cl/I. The Experimental versus ESD/TD-DFT/PBE0+SOC spectra together with the most important magnetic sublevel contributions and relaxation times are presented in **Figure 16.12 (a-d)** for the Cl-substituted diastereomers and in **Figure B.13** for the respective I-substituted ones. Deconvolution of the relevant magnetic sublevels in terms of M_S contributions and the associated relaxation rates are given in **Table 16.2** and **Table B.11**. The complementary spectra of the C- enantiomers are presented in **Figures B.14** and **B.15**.

Once again, in all the cases the agreement to experiment is very good allowing for further analysis. In contrast to diastereomers of type **1**, type **2** diastereomers are characterized by vibrationally resolved experimental and computed phosphorescence spectra. As shown in **Figure B.16**, the computed Huang-Rhys factors are now smaller ($S \sim 1.5$) with respect to diastereomers of type **1**. This indicates a rather local vibronic coupling located in the 1200-1700 cm^{-1} energy range. The involved vibrational modes consist mainly of symmetric and asymmetric conjugated C=C bond stretching vibration modes within the helicenic ligands correlated to the important contribution of $\pi \leftarrow \pi^*$ ILCT electronic transitions.

Deconvolution of the spectra reveals that in all the cases the emission process involves an isolated multiplet consisting of magnetic $|\Psi_{1-3}\rangle$ states that are nearly degenerate. As is shown in **Table 16.2** and **Table B.11** the relativistic $|\Psi_{1-3}\rangle$ states are solely composed by the $M_S = 0, \pm 1$ magnetic sublevels of the parent non-relativistic T_1 state owing to the low-lying ILCT transition within the helicenic ligand. In all the cases this results in a small and rhombic excited state ZFS ($|D| \sim 1 \text{ cm}^{-1}$ and $|E/D| \sim 0.31$). Hence in contrast to diastereomers of complexes **1** which show a pronounced easy axis anisotropy in the Re-CO building unit, diastereomers of complexes **2** show an easy plane anisotropy in the helicenic ligand (**Figure B.22**). In the case of the enantiomers **2** P,A-Cl and **2** P,A-I (**Figure 16.12(c and d)**, **Figure B.13b** and **Table B.11**), in which the halogen and the helicenic ligand are oriented anti-parallel, the emission spectra are dominated by $|\Psi_3\rangle \rightarrow |\Psi_0\rangle$ and $|\Psi_{1,2}\rangle \rightarrow |\Psi_0\rangle$ emission processes, respectively, which proceed mainly through $M_S = \pm 1$ components of the parent non-relativistic excited T_1 state to the $M_S = 0$ component of the S_0 ground state.

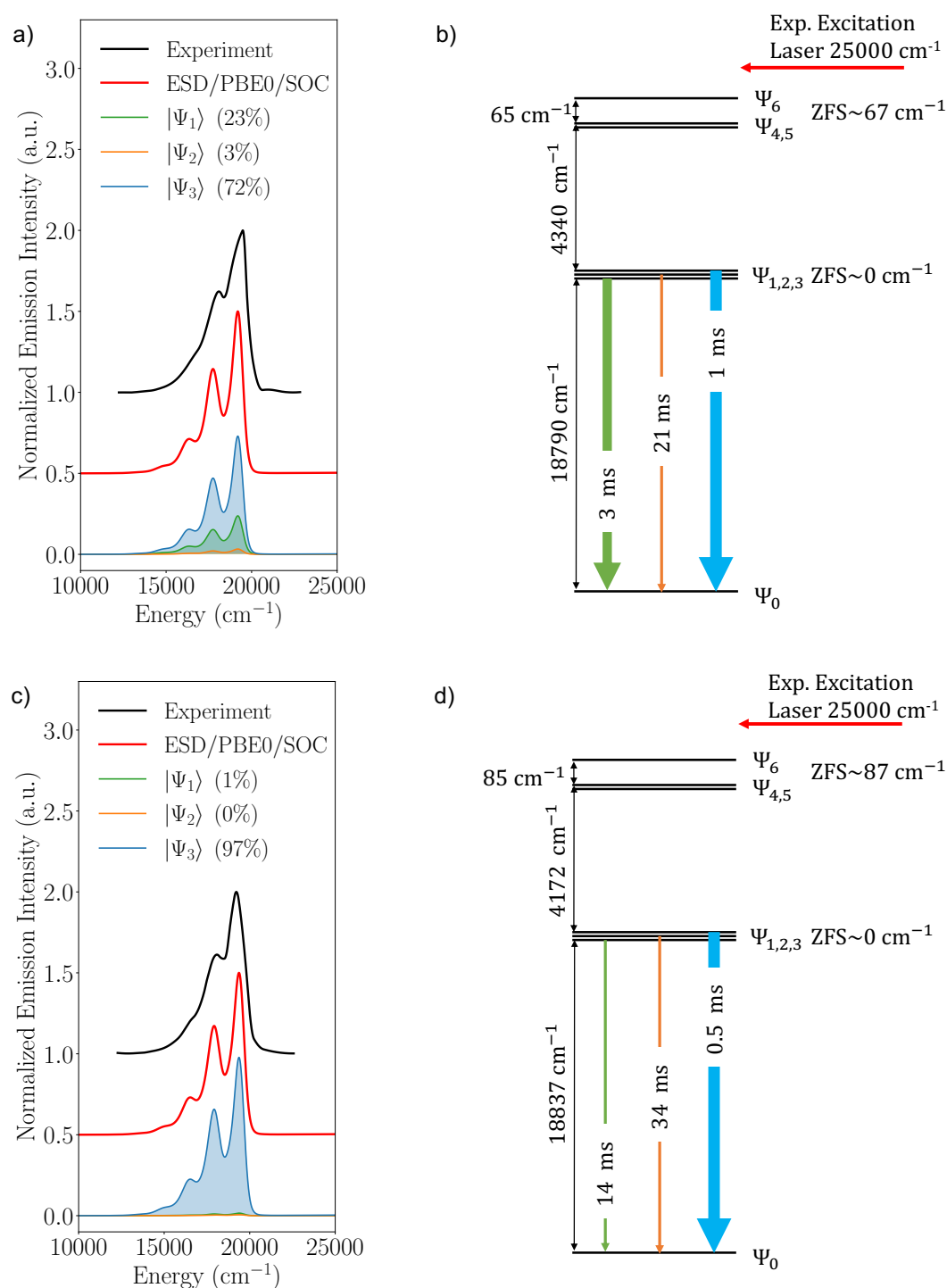


Figure 16.12. a) Experimental versus PBE0/TD-DFT/SOC calculated phosphorescence spectra of helicenic 2 M,A-Cl (a) and 2 P,A-Cl (c) enantiomers together with the most important magnetic sublevel contributions. b) and d) Computed relaxation times from the relevant magnetic sublevels. Red arrows indicate the experimental energy of the laser excitation.

This is in sharp contrast to diastereomers of type **1** in which the easy axis anisotropy results in emission processes which proceed directly via, the fastest in easy axis domain, the $M_S = 0$ components of the involved parent non-relativistic excited and ground states. Such ‘indirect’ emission process is reflected to the relaxation times presented in **Table 16.2**. In fact, the experimental and computed relaxation times of diastereomers of type **2** are ~ 3 orders of magnitude slower in comparison to diastereomers of type **1**.

The more steric environment imposed by the parallel in comparison to the anti-parallel alignment of the halogen vs helicenic ligands in these diastereomers, has also a noticeable effect in the relaxation times. In fact in the case of enantiomers **2 M,A-Cl** and **2 M,A-I** (**Figure 16.12(a and b)**, **Figure B.13a** and **Table B.11**) in which the halogen and the helicenic ligand are oriented parallel (**Figure B.22b**) the relaxation times are even slower than the respective **2 P,A-Cl** and **2 P,A-I** enantiomers. Once again as shown in **Figure 16.12b**, the excited states multiplet $|\Psi_{1,2,3}\rangle$ shows pronounced easy-plane anisotropy. Hence the emission spectra involve $|\Psi_{1,2,3}\rangle \rightarrow |\Psi_0\rangle$ emission processes which mainly proceed through the $M_S = \pm 1$ component of the parent non-relativistic excited T_1 state and the $M_S = 0$ component of the S_0 ground state. However, the parallel alignment of the halogen and the helicenic ligand provides a steric effect to the magnetization axis rotation (**Figure B.22c**) leading to even slower relaxation times. This effect is clearly more pronounced in the case of the iodide halogen ligand.

As in the case of diastereomers of type **1** at RT (295K) the experimental relaxation times decrease by one and two orders of magnitude with respect to the ones observed at 77K for Cl-substituted and I-substituted helicenic complexes, respectively. The relaxation times computed on the basis of radiative and non-radiative relaxation rates are presented in **Table 16.2**, **Table 16.3** and **Table B.11**. Again, the agreement with the experimental data is very good. In the case of the I-substituted helicenic diastereomers the non-radiative rates compared to respective Cl-substituted ones and are on average higher by a factor of ~ 10 -15. As a result, the I-substituted helicenic photoluminescence quantum yield (PLQY) Φ_{PL} values are about one order of magnitude lower with respect to the Cl-substituted ones. As it will be discussed in detail in **Section 16.10**, this indicates a more pronounced mixing between the vibrational states of the ground and excited state multiplets $|\Psi_{0-3}\rangle$ and has a direct influence on the spin-vibronic coupling mechanism that controls the photophysics.

16.9. Circularly polarized luminescence (CPL) spectra and CPL intensity mechanism

In an effort to further understand the principles of the photoluminescence intensity mechanism of the chemical systems under study we discuss in this section the respective circularly polarized luminescence spectra of diastereomers **1** and **2**. As it was shown in the above section, in the case of diastereomers **1** the emission process proceeds through the $M_S = 0$ components of the involved parent non-relativistic ground and excited states. This leads in principle to negligible intensity CPL spectra, as shown in **Figure 16.2**. On the contrary, significant intensity variations are observed within the enantiomeric pairs of diastereomers **2**. This is not surprising as in fact the intensity of the CPL spectra is directly associated to the composition of the $M_S = \pm 1$ components of the involved parent non-relativistic ground and excited states (**Scheme 16.1**). The experimental versus PBE0/TD-DFT/SOC calculated CPL spectra of diastereomers **2** are visualized in **Figure 16.13**. Once again in all the studied cases the agreement between experimental and theoretical spectra is very good allowing for further quantitative analysis.

Let us recapitulate at this point the principal selection rules of the CPL spectroscopy. According to the transition rate of **Equation (6.33)**, the CPL intensity is at first associated to the product $\sum_{i=x,y,z} (\mu_{IF}^{Re})_i * (m_{IF}^{Im})_i * \cos\theta$ between the x,y and z components of the electric and magnetic transition dipole moments between the initial emitting state I and final state F , where θ is the angle between the respective transition dipole vectors. This implies that involved non-orthogonal electric and magnetic transition dipole moments are maximized for an angle $\theta = 0^\circ$ or when the respective transition dipole vectors are colinear. Second, SOC interactions within and along the involved initial emitting states I are also influencing the CPL intensity while third, spin-vibronic coupling provides additional CPL intensity mechanism modulations. In a first step we employ the first two CPL selection rules (transition dipole properties and SOC state interactions) in an effort to develop visual selection rules that are able to explain the CPL signs and intensities in complexes **1** and **2**. In fact, this way of analyzing transition dipole properties has been proven instrumental in understanding the principles of the intensity mechanism in the core electron and valence MLCT transitions in X-ray spectroscopy[565] and UV/Vis spectra[437] as well as to predict the sign of the MCD C-terms in magnetic circular dichroism spectroscopy.[271, 566]

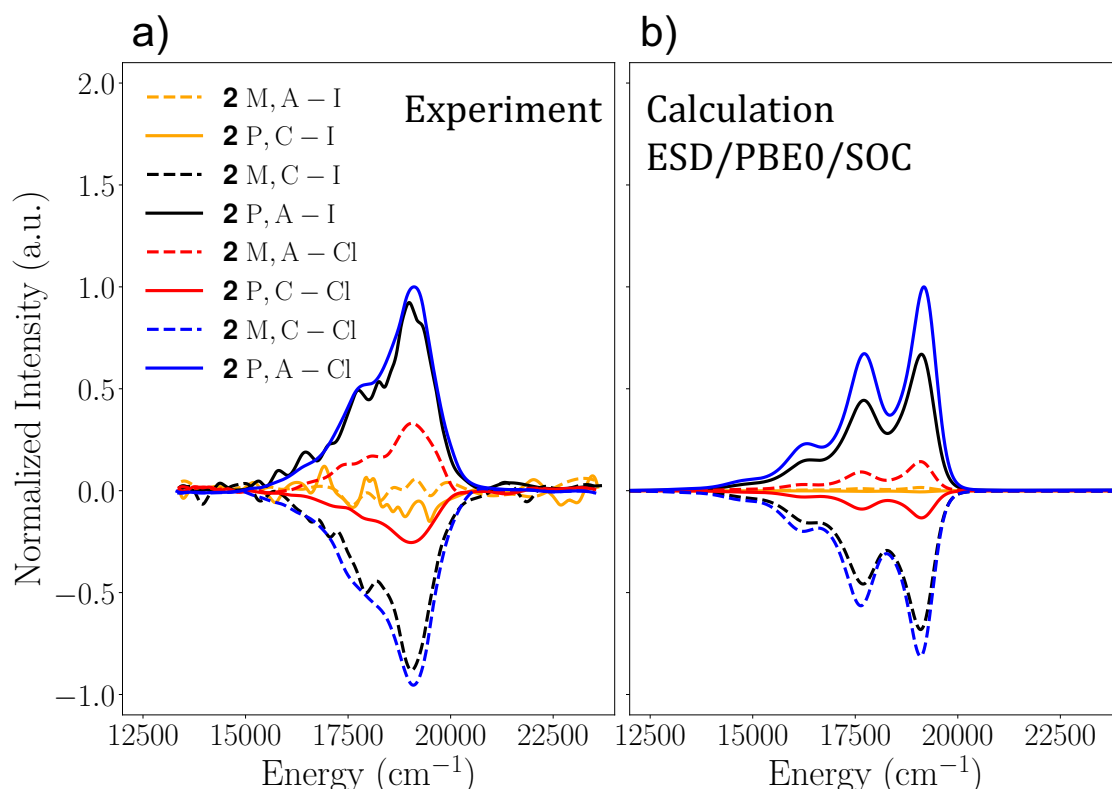


Figure 16.13. a) Experimental versus b) PBE0/TD-DFT/SOC Calculated CPL spectra of enantiomeric pairs **2** M,A-Cl (dotted red line) and **2** P,C-Cl (solid red line), **2** M, C-Cl (dotted blue line) and **2** P,A-Cl (solid blue line), **2** M,A-I (dotted orange line) and **2** P,C-I (solid orange line) and **2** M, C-I (dotted black line) and **2** P,A-I (solid black line).

We first discuss complexes **1** which showed negligible CPL intensities (**Figure 16.2**). As discussed in the electronic structure **Section 16.6**, the emitting state in these complexes is E-symmetric 3E (T_1, T_2) which give rise to x, y polarized electric and magnetic dipole allowed $|\pi^*\rangle \rightarrow |d_{yz/xz} - p_{y,x}\rangle$ electron decays with pronounced MLCT/XLCT characters. SOC can mix between the corresponding excited triplet and singlet non-relativistic states 3E (T_1, T_2) and 1E (S_1, S_2) though rotation along the molecular/magnetic z axis (**Figure B.22a**). For the pair of emitting 3E (T_1, T_2) states this is graphically illustrated in **Figure 16.14**.

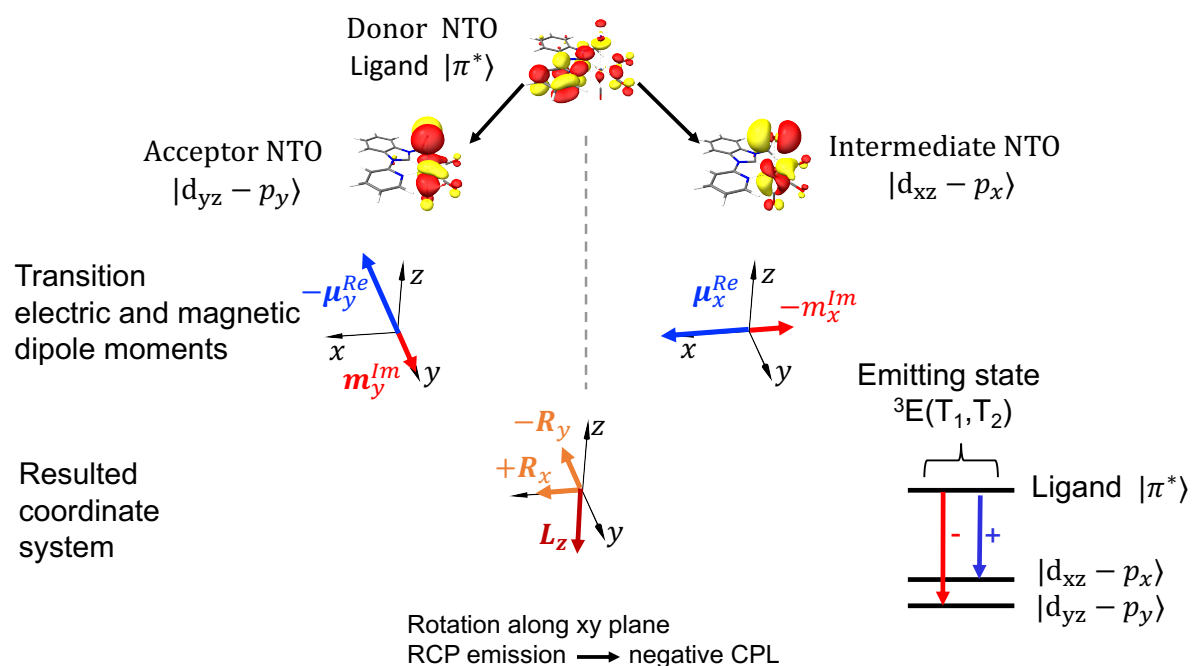


Figure 16.14. Graphical prediction of the CPL sign for the $|\pi^*\rangle \rightarrow |d_{yz} - p_y\rangle$ emission which characterizes complexes **1** emission process via MLCT/XLCT transitions- electron decays.

The electric and magnetic transition dipole moments of these non-relativistic states oppose each other lowering the intensity of the respective rotatory strengths. At the non-relativistic limit, assuming that SOC acts perturbatively to the $|\pi^*\rangle \rightarrow |d_{yz} - p_y\rangle$ emission process, the resulted rotatory strengths and the reduced spin-orbit vector form a left-handed system. It follows that for positive $\Delta E_{T_2-T_1}$ this will lead to emission of right-handed photons, thereby resulting in a negative CPL intensity. In contrast, the CPL signal of the $|\pi^*\rangle \rightarrow |d_{xz} - p_x\rangle$ emission has a positive sign. It should be noted that this process is analogous to the ‘J-K’ coupling mechanism in MCD.[271] It becomes evident that the emitting state degeneracy cancels out the respective CPL signals leading to none or negligible CPL intensity ($I_{LCP-RCP} \sim 0$) for complexes of type **1**. The situation is more pronounced in iodide complexes due to the higher magnitude of XLCT admixture ($1 - p_{xy}$) and SOC interaction in the emission process. At the relativistic limit it was shown in **Table 16.2** that $|\Psi_3\rangle \rightarrow |\Psi_0\rangle$ emission process provides the fastest relaxation pathway proceeding through the $M_S = 0$ components of the parent non-relativistic ground S_0 and T_1 and S_2 excited states, thus creating in principle unpolarized photons.

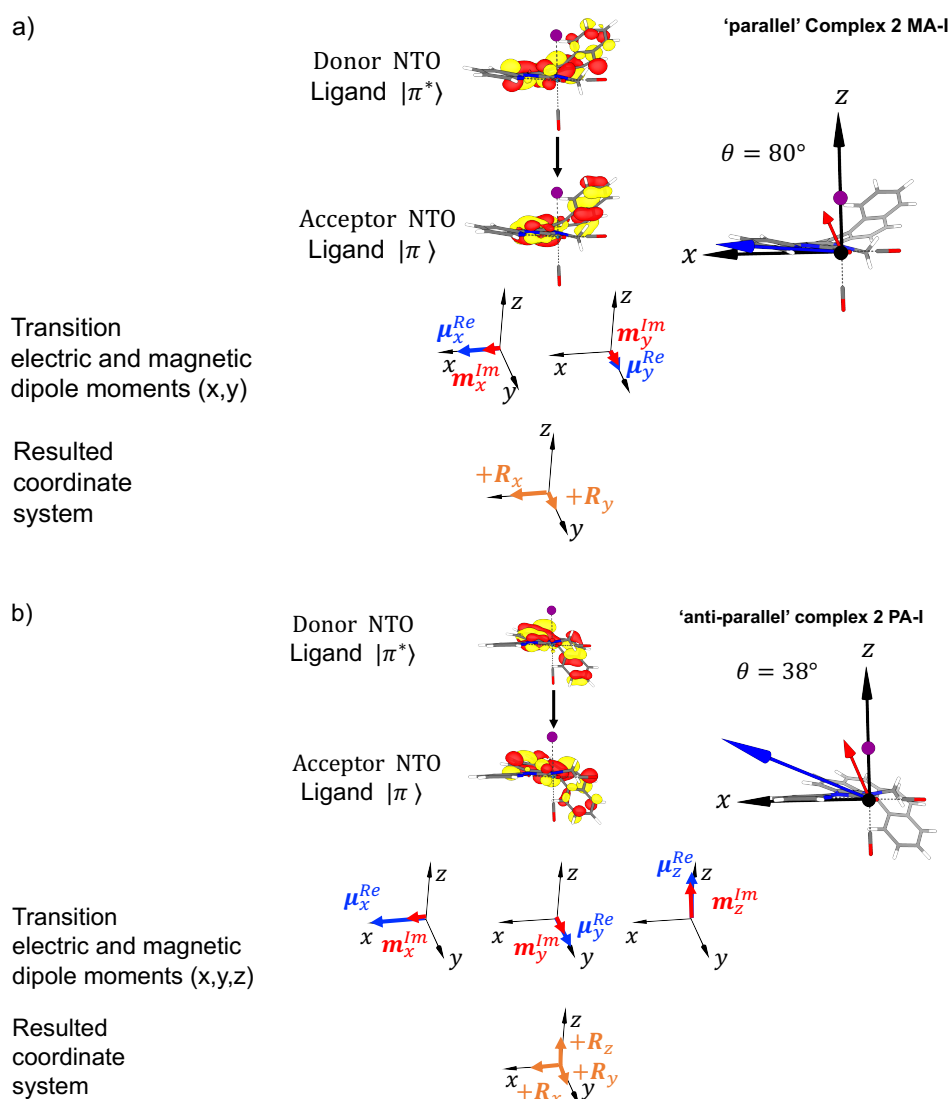


Figure 16.15. Graphical representation of interaction between transition electric μ and magnetic m dipole moments along the $|\pi^*\rangle \rightarrow |\pi\rangle$ ILCT emission process for a) ‘parallel’ complex **2 M,A-I** and b) ‘anti parallel’ complex **2 P,A-I**.

As shown in **Figure 16.15a**, in the case of parallel alignment of the halogen and the helicenic ligand in complexes **2 M,A/P,C-I/Cl**, the $\pi^* \rightarrow \pi$ ILCT emission process involves mainly x and z polarized electric and magnetic dipole electron decays. Hence the respective dipole vectors are nearly orthogonal $\theta \sim 80/60^\circ$, resulting in a negligible and weak intensity set of rotatory strengths in the xy plane for I/Cl, respectively. As it was briefly discussed in **Section 16.8** and also shown in **Table B.11**, in the case of parallel aligned halogen/helicenic **2 M,A-I** and **2 P,C-I**, the helicenic ring C=C stretching vibrations are sterically blocked becoming more rigid. As discussed in the previous section the z -axis of the magnetic axis frame of the emissive

triplet state is defined along the D_{zz} axis component of the respective zero field splitting tensor. Likewise to complexes of type **1**, in the case of complexes of type **2** with parallel alignment of the halogen and the helicenic ligand the D_{zz} axis is aligned about 21° with respect to the molecular z-axis of the ground state molecular geometry (**Figure B.22(a,b)**). This implies that the rotation of the induced magnetic moment is also sterically blocked and mainly restricted around the molecular z-axis.

At the relativistic limit, the involved emitting $|\Psi_{1,2}\rangle \rightarrow |\Psi_0\rangle$ states, consist of similar contributions of the $M_S = \pm 1$ components ($\sim 42\%$) of the parent non-relativistic T_1 excited state while the respective $M_S = 0$ contributions are (17%). Although these states actually dominate the intensity of the respective PL spectra (**Table 16.2**), as shown in **Table B.12** they provide negligible magnetic transition moments, due to the magnetic blocking, and consequently negligible CPL intensities. Hence, $|\Psi_3\rangle \rightarrow |\Psi_0\rangle$ becomes consequently the only available transition for CPL intensity along the z-molecular axis. In fact, $|\Psi_3\rangle$ consists of 82% $M_S = 0$ contributions of the parent non-relativistic T_1 excited state and leads to orthogonal electric and magnetic transition vectors ($\theta \sim 80^\circ$). As a result, the differential CPL spectra have negligible intensity ($|g_{lum}| \sim 3 - 4 \times 10^{-3}$) (**Table B.12**).

Substitution of the axial ligand ($X = I$) by a less bulky halide (Cl) induces a small increase of the CPL intensity in **2 M,A-Cl** and **2 P,C-Cl** as compared to **2 M,A-I** and **2 P,C-I**. Indeed, in this case the CPL- dominating emitting $|\Psi_{1,2}\rangle \rightarrow |\Psi_0\rangle$ states are characterized by slightly equal $M_S = 0$ and ± 1 component contributions of the parent non-relativistic T_1 excited state, (**Table B.11**). This is all reflected to the larger $|R| \sim 1.5 \times 10^{-41}$ values and the smaller angle between electric and magnetic transition vectors ($\theta \sim 60^\circ$). This also results to slightly higher CPL intensity ($|g_{lum}| \sim 5.7 \times 10^{-2}$), in comparison to the iodide case (**Table B.12**).

In contrast, in the case of the sterically-free anti-parallel aligned halogen/Helicenic **2 P,A-Cl/I** and **2 M,C-Cl/I** enantiomeric pairs, the rotation of the induced magnetic moment is practically free (**Figure B.22c**). As shown in **Figure 16.15b** in the case of **2 P,A-I** enantiomer the $\pi^* \rightarrow \pi$ ILCT emission process involves practically x,y,z polarized electric and magnetic dipole electron decays as the angle of the respective dipole vectors is $\theta \sim 38^\circ$. At the relativistic limit, the leading emission process $|\Psi_3\rangle \rightarrow |\Psi_0\rangle$ involves predominately $M_S = \pm 1$ components from the parent non-relativistic T_1 states resulting to emitted CP photons that give rise to CPL intensities with $|g_{lum}| \sim 13 \times 10^{-2}$, which are ~ 3 times higher in comparison to the respective ‘parallel’ variants (**Table B.12**). Once again, substitution of the iodide by a less bulky halide

leads to a slight increase in CPL intensity ($|g_{lum}| \sim 15 \times 10^{-2}$) in lines with the decrease of the $M_s = 0$ contributions on the $|\Psi_3\rangle \rightarrow |\Psi_0\rangle$ emission process.

Up to this point of analysis we have developed a calibrated TD-DFT protocol that takes into account the necessary excited state dynamics in order to predict the photoluminescence properties (phosphorescence and CPL spectra, radiative and non-radiative relaxation times and quantum yields) of the studied Re(I) chiral complexes. All the above presented analysis demonstrated that the involved emission processes in the non-helicenic and the helicenic Re(I) diastereomers **1** and **2** proceed via two fundamentally different multi-state intensity mechanisms controlled by i) the electronic nature of the emitting excited state multiplet; ii) the induced magnetic anisotropy of this emitting multiplet. Seeking further validation of these important findings we will undergo in the next section a spin-vibronic coupling analysis on the basis of CASSCF/QD-NEVPT2 potential energy surface (PES) scans along the involved normal vibrational modes.

16.10. Spin-vibronic Coupling

16.10.1. SA-CASSCF/QD-NEVPT2 Potential Energy Surfaces Scans

The theoretical principles of the spin-vibronic coupling interactions are discussed in the theory in **Section 6.8**. Before entering the discussion dedicated to the spin-vibronic interactions a careful selection of the relevant normal vibrational modes that need to enter into the analysis has to be performed. In general, it is a common practice to select the modes on the basis of the computed Huang-Rhys factors (S) which, as discussed above in **Section 16.8** and also in **Section 6.3.2**, defines a measure of the strength of the electron–phonon coupling in the emission process.[274] An alternative approach arises by considering that relaxed fluorescence and consequently phosphorescence share the same origins with RR spectroscopy. The relevant analysis is provided in **Figures B.16** and **B.17**, respectively. The analysis showed that in the cases of diastereomers **1** the symmetric and asymmetric CO stretching vibrations (modes 1-3) as well as the pyridyl ring stretching (mode 4) are selected to enter the spin-vibronic analysis. These observations are consistent with the MLCT character of the emissive state for these systems. Likewise, in the case of diastereomers **2** only the helicenic ring stretching vibrations (modes 5,6) are selected to enter the spin-vibronic analysis. Once again this is consistent with the ILCT character of the emissive state of these systems.

The calculation of the state-average SA-CASSCF PES scans, along the selected vibrational modes, involves CAS(8,8) and CAS(10,11) active spaces (**Figures B.18 and B.19**), for the diastereomers **1** and **2**, respectively. The PES scans are constructed for the set of the low lying excited singlets ($|S_{1-3}\rangle$) and triplets ($|T_{1-3}\rangle$) besides the ground state singlet $|S_0\rangle$ at the non-relativistic limit followed by SOC corrections ($|\Psi_{0-12}\rangle$). As seen in **Figure B.20**, unless SA-CASSCF/QD-NEVPT2 is employed, the correct state splitting and a proper treatment of the state avoiding crossings are not correctly reproduced at the SA-CASSCF and SA-CASSCF/NEVPT2 levels of theory. Hence the multi-state SA-CASSCF/QD-NEVPT2 protocol was employed for the production calculations.

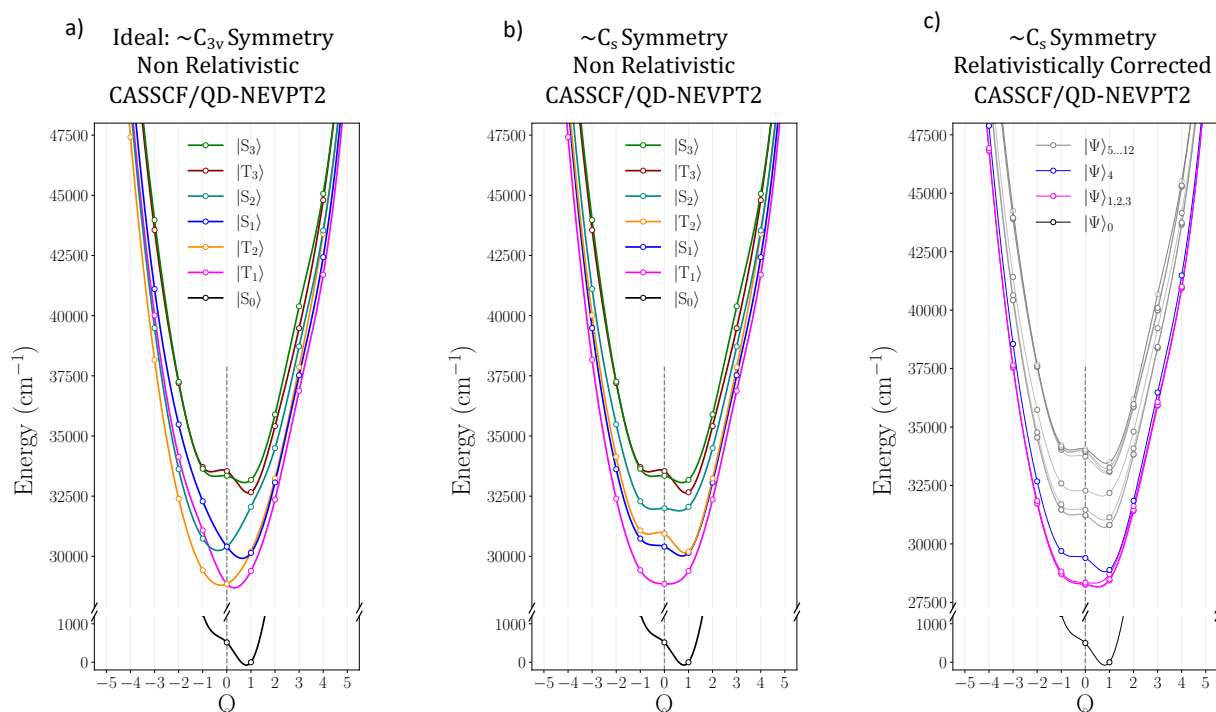


Figure 16.16. (8,8) SA-CASSCF/QD-NEVPT2 PES scan along a chosen mode representing one of the asymmetric stretching CO vibrations for 1 A-Cl a) for an ‘ideal’ C_{3v} symmetry around Re(I) in the non-relativistic limit. b) for the ‘actual’ C_s symmetry around Re(I) in the non-relativistic limit and c) for the ‘actual’ C_s symmetry around Re(I) including relativistic SOC corrections.

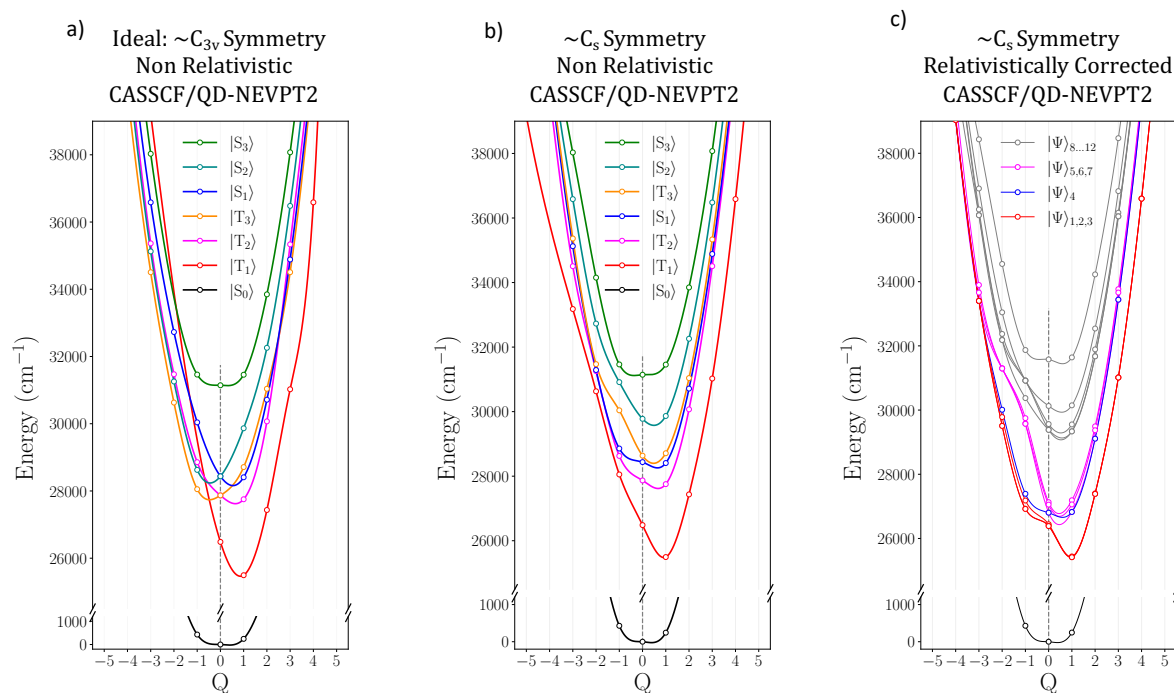


Figure 16.17. (11,8) SA-CASSCF/QD-NEVPT2 PES scan along a chosen mode representing asymmetric stretching helicenic vibrations for 2 M,A-Cl a) for an ‘ideal’ C_{3v} symmetry around Re(I) in the non-relativistic limit. b) for the ‘actual’ C_s symmetry around Re(I) in the non-relativistic limit and c) for the ‘actual’ C_s symmetry around Re(I) including relativistic SOC corrections.

Representative PES scans for **1** A-Cl and **2** M,A-Cl are provided in **Figure 16.16** and **Figure 16.17** along the asymmetric stretching CO vibration and the helicenic ring stretching vibrations, respectively. In a first approximation we assume ‘ideal’ C_{3v} symmetry around the Re(I) centers (**Figure 16.16a** and **Figure 16.17a**). In accordance with the excitation diagram presented in **Figure 16.3** in the case of **1** A-Cl at the equilibrium Q_0 point a number of E-symmetric MLCT, MLCT/XLCT transitions are observed owing to a sequence of $(A + E) \times \varepsilon$ Jahn Teller problems which are stabilized at $Q_{1,-1}$ minimum geometries. On the contrary in the case of **2** M,A-Cl besides the respective E-symmetric MLCT, MLCT/XLCT transitions the A_2 -symmetric ILCT transition forming state $|T_1\rangle$, is stabilized at Q_1 minimum geometry. This later state is separated by more than 2000 cm^{-1} with respect to the higher lying singlet and triplet MLCT, MLCT/XLCT states. By further considering the C_s symmetry reduction around the Re(I) center (**Figure 16.16b** and **Figure 16.17b**) as well as the SOC mixing between singlet and triplet states, one observes the final PES scans of the involved multiplets $|\Psi_{0-12}\rangle$ (**Figure 16.16c** and **Figure 16.17c**).

Table 16.4. SA-CASSCF/QD-NEVPT2 computed axial and rhombic excited state multiplet ZFS parameters (D (cm^{-1}) and E/D) at equilibrium and minimum energy geometries together with the respective axial and rhombic spin-vibronic coupling constants ξ_D (cm^{-1}) and ξ_E along a selected set of vibrational normal modes **1 A-Cl** and **2 M,A-Cl** enantiomers.

Complex	CAS (m,n)	Mode [†]	ZFS Parameters				Spin-Vibronic Coupling Parameters	
			Q _{eq.}		Q _{min.}		Axial coupling ξ _D	Rhombic Coupling ξ _E
			D	E/D	D	E/D		
1 A-Cl	(8,8)	1	-83.14	0.07	-248.29	0.10	-83.99	-7.56
		2	-85.14	0.01	-350.15	0.05	-121.83	-9.75
		3	-85.14	0.04	-319.15	0.08	-119.83	-9.59
		4	-86.75	0.08	-84.59	0.20	-119.04	-8.33
Total/Average			-84.72	0.05	-250.25	0.09	-110.63	-7.74
2 M,A-Cl	(10,11)	5	-5.54	0.27	-3.86	0.30	-20.05	-2.41
		6	-5.53	0.25	-4.40	0.23	-20.58	-2.12
Total/Average			-5.53	0.25	-4.13	0.25	-20.27	-2.23

[†]The vibrational normal modes are visualized in **Figures B.16** and **B.17**.

As is shown in **Table 16.4**, in the case of **1** A-Cl the ZFS splitting parameters derived for the excited state multiplet $|\Psi_{1-3}\rangle$ (**Figure 16.16c**) show an axial ZFS and negative D value ($D \sim -85 \text{ cm}^{-1}$, $E/D \sim 0.05$) as well as axial and negative spin-vibronic coupling parameters ($\xi_D \sim -110 \text{ cm}^{-1}$, $\xi_E \sim -8 \text{ cm}^{-1}$). On the contrary, in the case of **2** M,A-Cl the ZFS parameters ($D \sim -5 \text{ cm}^{-1}$, $E/D \sim 0.25$) as well as the spin-vibronic coupling constants ($\xi_D \sim -20 \text{ cm}^{-1}$, $\xi_E \sim -2 \text{ cm}^{-1}$) derived from the isolated multiplet $|\Psi_{1-3}\rangle$ (**Figure 16.17c**) are of much lower magnitude containing significant axial and rhombic components. These results validate the TD-DFT observations reflecting the major MLCT and ILCT character of the $|\Psi_{1-3}\rangle$ multiplet in diastereomers **1** and **2**, respectively. As shown in **Table B.13**, while in the case of diastereomers **1** the magnitude of D increases in the sequence Cl, I, the spin-vibronic coupling constants indicate similar excited state relaxation patterns. In contrast, in the case of diastereomers **2** there is no significant change in the magnitude of D in the sequence Cl, I. This is not the case on the spin-vibronic coupling constants as in fact the ILCT excited state multiplet relax more in the Cl- than in the I- diastereomers. In fact, as seen in **Table B.13** and **Figure B.21** for the case of **2** M,A-I the spin-vibronic constants are negligible reflecting an almost parallel alignment of the ground $|\Psi_0\rangle$ and the excited state $|\Psi_{1-3}\rangle$ PESs. It should be noted that this is also in accord with the experimental and computed quantum yields which reflect resemblance between ground and excited state vibrational modes with pronounced non-radiative relaxation rates (**Table B.11**)

16.11. Summary and Conclusions

In this work a computational protocol was developed that is able to predict photoluminescent properties of chiral transition metal complexes. For this purpose, a study set of previously synthesized chiral Re(I) halide complexes of the type $[fac-ReX(CO)_3L]$ [508] was chosen (X being Cl or I and L being a N-heterocyclic (NHC) or helicenic-NHC ligands respectively). This set of chiral diastereomers contains a broad variety of ABS, ECD, Phosphorescence and CPL spectroscopic properties.

A detailed geometrical and electronic structure analysis was performed in order to identify the factors controlling the character of the excited states which contribute to the absorption and emission processes in terms of MLCT/XLCT and LLCT transitions/decays in the NHC diastereomers and of ILCT transitions in the helicenic diastereomers.

Calibration of various TD-DFT protocols was performed against experimental data as well as STEOM-DLPNO-CCSD reference method results, regarding their ability to compute the ABS and ECD spectra of selected diastereomers from the study set. Based on these results the PBE0/TD-DFT protocol was chosen for the production calculations.

The shapes of the absorption and the phosphorescence spectra of the whole set of enantiomers associated to the chosen chiral Re(I) molecules were computed at the PBE0/TD-DFT level in the framework of the excited state dynamics (ESD) approach of the ORCA computational package. In particular, besides absorption and emission transition rates for generating ABS and PL spectra, ESD was extended to be able to treat circularly polarized radiative, as well as non-radiative transition rates, providing access to the computation of ECD, CPL spectra and photoluminescent quantum yield (PLQY) values. The very good agreement between theory and experiment allowed a quantitative electronic structure analysis of all the observed bands. In particular this was performed in the framework of natural transition orbitals (NTO) and TheoDORE analysis of all the observed parent non-relativistic and the relativistically corrected spectral features. It was demonstrated that the excited state multiplet that leads the emission process in the NHC diastereomers is of MLCT/XLCT character while in the helicenic diastereomers is mainly ILCT.

In view of the good agreement between experimental and computed phosphorescence spectra a further detailed analysis is provided. It was revealed that the emissive multiplet in NHC diastereomers has axial anisotropy with large and negative ZFS parameters, while in helicenic diastereomers it is isolated and has easy-plane anisotropy with small ZFS parameters.

This was found to have a pronounced effect on the emission spectra resolutions and on both the radiative and non-radiative relaxations times. The NHC diastereomer emission process provides the fastest relaxation pathway proceeding through the $M_S = 0$ components of the parent non-relativistic ground S_0 and T_1 and S_2 excited states. In contrast, in the helicenic diastereomers the emission process proceeds mainly through $M_S = 0, \pm 1$ components of the parent non-relativistic excited T_1 state and the $M_S = 0$ component of the S_0 ground state. The later contributions found to be sensitive to steric effects which in a sense block the free-rotation of the induced magnetization on the easy-plane. Such steric effects have a direct and significant effect on the phosphorescence relaxation times of the helicenic diastereomers possessing parallel vs. antiparallel aligned halogen and helicenic ligand. They are also responsible for the intensity variations observed on the CPL spectra of the helicenic diastereomers.

Seeking further validation of this multistate photoluminescent intensity mechanisms in a last step we performed a spin-vibronic analysis at the SA-CASSCF/QD-NEVPT2 level of theory. Selection of the relevant vibrational modes was performed on the basis of Huang-Rhys factor analysis and RR computed spectra. The analysis confirmed the TD-DFT observation revealing strong spin-vibronic coupling effects in the NHC diastereomers and much weaker effects in case of the helicenic diastereomers. In particular in the I-substituted helicenic diastereomers the spin vibronic-coupling is practically negligible. These observations are also consistent with the photoluminescence quantum yields and the relaxation rates.

We believe that the presented results are of paramount importance in the field of the photoluminescent chiral transition metal complexes. Research in our laboratories is ongoing, for further exploring the abilities of the established protocol in investigating the photoluminescent properties of novel chiral transition metal chemical systems. The fundamental understanding of the parameters that govern chiroptical properties in coordination chemistry compounds is essential to a rational design of new chiral transition metal emitter

17 General Conclusion: A Journey through Photoluminescence Complexity

In the pursuit of unraveling the photophysical properties of photoluminescent inorganic solid-state and organometallic materials, this thesis embarked on a comprehensive journey spanning computational protocols, fundamental principles, and thorough electronic structure investigation of specific luminescent systems. The overarching motivation was to overcome challenges inherent in understanding f-block and d-block element-containing materials, fostering a deeper comprehension of their electronic, structural, and optical intricacies. Through a systematic approach, this research aimed to contribute not only to fundamental knowledge but also to the practical design of materials with tailored luminescent properties, promising advancements in diverse fields.

The initial segment laid the groundwork, elucidating the fundamental principles of computational chemistry and spectroscopy. This established the significance of these tools in analyzing the optical properties of transition and rare transition metal ions in both molecular complexes and solid-state materials. By establishing correlations between optical features and structural/electronic characteristics, this foundation became a valuable guide for designing new materials with targeted properties.

Transitioning into the heart of the study, the focus shifted to Eu^{2+} -doped phosphors. The objectives were clear: develop a computational protocol to explore electronic structures, states, and optical transitions, and unravel the impact of vibronic coupling effects. The findings, intricately woven across multiple chapters, demonstrated the versatility of the computational protocol. From accurately predicting optical properties and emission features to systematically enhancing the emission properties of specific phosphors, the research exemplified the power of theoretical insights in guiding practical applications.

The exploration did not stop at computational predictions; it extended to establishing requirements for designing narrow-band Eu^{2+} -doped phosphors. Suppression of structural relaxation, maintenance of axial magnetic structure, and strong spin-orbit coupling emerged as pivotal parameters. The study provided close insights into the intrinsic electronic and magnetic properties of these phosphors, offering guidelines for their tailored design. The journey, encapsulated in these chapters, was a testament to the synergy between theoretical understanding and practical applications.

Venturing further into the realm of chiral Re(I) complexes, the research unfolded a groundbreaking computational protocol. This protocol, designed to predict the optical properties of chiral complexes, harnessed TD-DFT calculations and an ESD approach. Through a meticulous analysis of diastereomers within the $[\text{fac-ReX}(\text{CO})_3\text{L}]$ family, the study uncovered distinctive emission characteristics influenced by spin-vibronic coupling. This chapter not only expanded the horizons of computational chemistry but also delved into the chiroptical intricacies of transition metal complexes.

In conclusion, this thesis transcends the confines of academic exploration. It is a testament to the transformative potential of computational insights in guiding the design and understanding of luminescent materials. From foundational principles to specific luminescent systems, each chapter contributes to a holistic narrative, offering valuable guidelines for future research and applications. The implications extend beyond theoretical advancements, promising innovations in energy-efficient lighting technologies, luminescent probes for biological imaging, and novel materials for quantum information processing. As we stand at the intersection of fundamental science and practical innovation, this research serves as a beacon, illuminating the path toward a future where tailored luminescent materials shape technological landscapes and societal advancement.

Appendixes

A. Additional Information to PART II

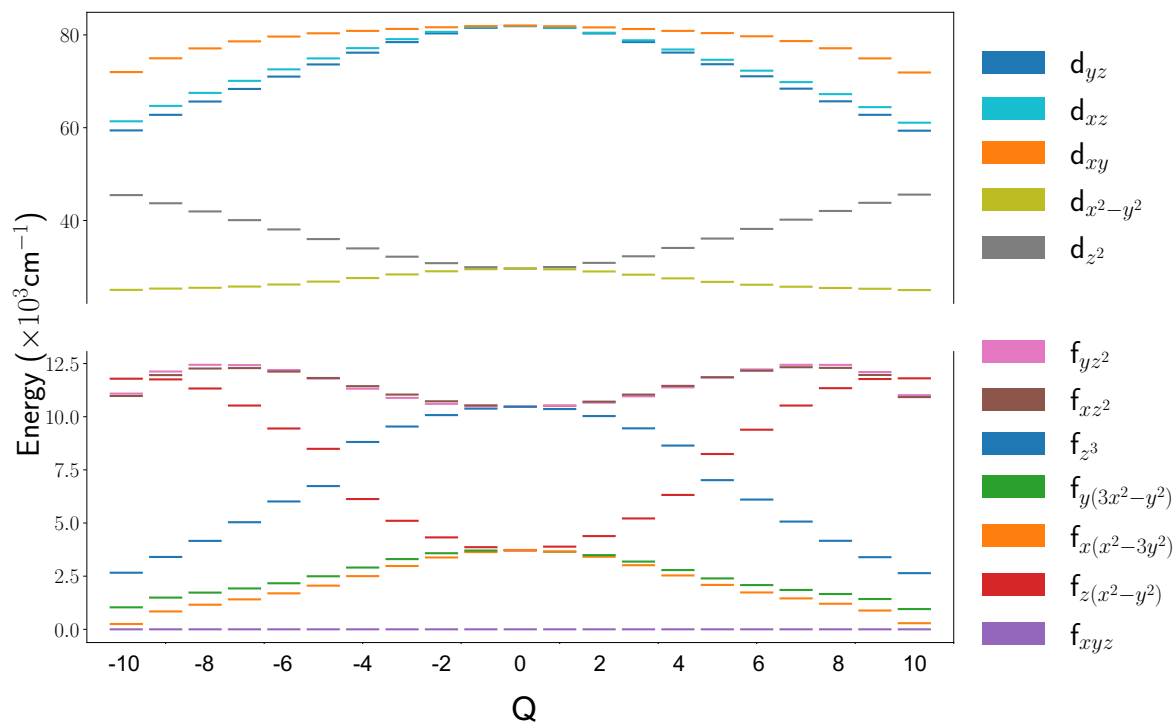


Figure A. 1. The change of orbital energy of CASSCF(7,19) optimized active orbitals with PES scanned along e_g mode, calculated on $[\text{Eu}(\text{NH}_3)_8]^{2+}$ model structure. The 5f active orbitals are omitted.

Table A. 1. The computed $\text{FWHM}_{300\text{K}}$, reorganization energy and Huang–Rhys factor S for BMS, SMS, CLA, SLA, SALON and SLBO phosphors.

Phosphor	Doping site	$\text{FWHM}_{300\text{K}}$ (cm^{-1})	Reorganization energy (cm^{-1})	S
Ba[Mg ₃ SiN ₄]:Eu ²⁺ (BMS)	Ba ²⁺	2015	300.44	0.360
Sr[Mg ₃ SiN ₄]:Eu ²⁺ (SMS)	Sr ²⁺	1150	70.29	0.084
Ca[LiAl ₃ N ₄]:Eu ²⁺ (CLA)	Ca ²⁺	1340	28.40	0.035
Sr[LiAl ₃ N ₄]:Eu ²⁺ (SLA)	Sr ¹²⁺	1140	7.85	0.010
Sr[Al ₂ Li ₂ O ₂ N ₂]:Eu ²⁺ (SALON)	Sr ²⁺	1220	23.72	0.029
SrLi ₂ [Be ₄ O ₆]:Eu ²⁺ (SLBO)	Sr ²⁺	1220	8.58	0.012

Table A. 2. The calculated luminescence rates, R_{flu} (s^{-1}) and relaxation times τ_{flu} (s) for the study set of the Eu²⁺ doped phosphors within Franck Condon (FC) and with and without Herzberg Teller (HT) corrections, for BMS, SMS, CLA, SLA, SALON and SLBO phosphors.

Phosphor	Doping site	FC		FC/HT	
		R_{flu} (s^{-1})	τ_{flu} (s)	R_{flu} (s^{-1})	τ_{flu} (s)
Ba[Mg ₃ SiN ₄]:Eu ²⁺ BMS	Ba ²⁺	1.5x10 ⁴	6.7 x10 ⁻⁵	1.5x10 ⁵	1.9 x10 ⁻⁶
Sr[Mg ₃ SiN ₄]:Eu ²⁺ SMS	Sr ²⁺	1.4x10 ⁵	7.1 x10 ⁻⁶	1.4x10 ⁹	1.1 x10 ⁻¹⁰
Ca[LiAl ₃ N ₄]:Eu ²⁺ CLA	Ca ²⁺	6.9x10 ⁴	1.5 x10 ⁻⁵	6.9x10 ¹⁰	3.3 x10 ⁻¹¹
Sr[LiAl ₃ N ₄]:Eu ²⁺ SLA	Sr ¹²⁺	1.3x10 ⁵	7.7 x10 ⁻⁶	1.3x10 ⁹	1.4 x10 ⁻¹⁰
Sr[Al ₂ Li ₂ O ₂ N ₂]:Eu ²⁺ SALON	Sr ²⁺	1.4x10 ³	7.1 x10 ⁻⁴	1.4x10 ⁸	2.2 x10 ⁻⁹
SrLi ₂ [Be ₄ O ₆]:Eu ²⁺ SLBO	Sr ²⁺	1.3x10 ⁴	7.7 x10 ⁻⁵	1.3x10 ⁸	1.6 x10 ⁻⁹

A.1. Descriptors in phosphors

Experimental optical band gaps as well as the energy splitting of the f-orbitals define two widely used descriptors. In fact, as it was shown in **Scheme 9.1**, optical band gaps can be used to predict the energy position of the emission band and define the color of the phosphor. Recently, experimental band gaps have been used as descriptors in the framework of machine learning techniques¹⁻² Similarly, a quantitative descriptor refers to the energy splitting between the two highest Eu f-based MOs. It has been shown that an energy separation by more than 0.1 eV is necessary to achieve emission with narrow bandwidth.[365] This is based on the idea that large energy splitting in these MOs will prevent multiple overlapping relaxation transitions giving homogenous emission with narrow band. Unfortunately, none of the above descriptors is able to properly probe the chemical environment around the doped Eu²⁺ across the phosphors. Hence such descriptors cannot capture the case of anomalous emission of BMS or the Stokes shift variation across the different phosphors of the study set. It was shown (**Section 10.8**) that the energy position and bandwidth of the emission spectrum in phosphors is directly related to the metal-ligand covalency around the Eu²⁺ centers. In the following we will develop descriptors that are based on the metal-ligand chemical environment of these systems.

First, the relation of the coordination environment around the Eu²⁺ centers with the experimental emission maximum across the set of the chosen phosphors is investigated. The results are shown in **Figure A. 2**. As is shown, a linear relation between the average bond length Eu-L, L=N, O is obtained for the series SMS, CLA, SLA and SALON. As illustrated in **Figure 10.1** this behavior reflects the fact that a decrease of the crystal field strength is associated with a blue shift in the emission maximum. However, such a relation is still not sensitive enough to predict the red shift of BMS as well as the blue shift of SLBO. Computation of the respective Eu-L, L=N, O average force constants across the series shows the exact same behavior (**Figure A. 2 b**) which might be expected based on Badger's rule.[567] By contrast, some degree of linear relation involving the entire study set of the phosphors is observed between the average bond length Eu-M, M=Sr, Ca, Ba of the Eu center and the host ligand counter ion (**Figure A. 2 c**). However, none of these descriptors is entirely satisfactory.

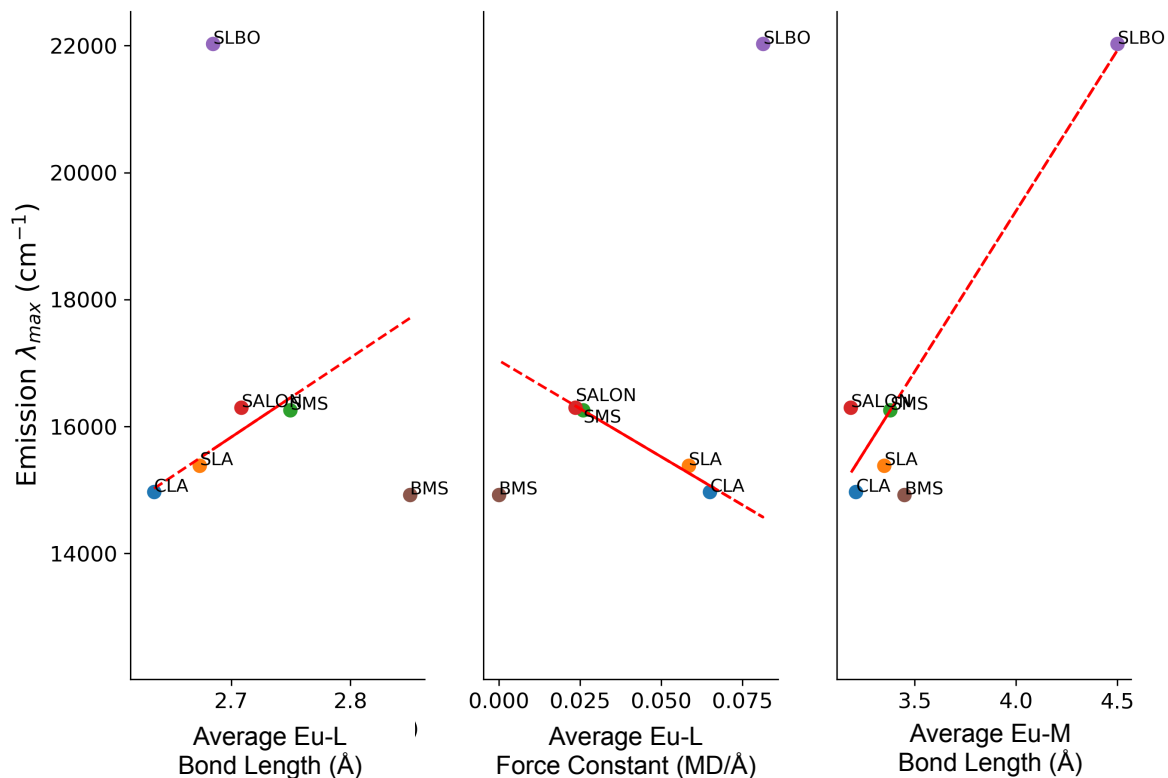


Figure A. 2. Experimental emission band energy at max. intensity, λ_{\max} (cm⁻¹) as a function of a) the average bond length Eu – L (Å), b) the average force constant Eu – L (MD/Å) and c) the average bond length Eu – M (Å) in SMS (green cycle), BMS (brown cycle), SLA (orange cycle), CLA (blue cycle), SALON (red cycle) and SLBO (purple cycle). Red dot is a linear regression.

Table A. 3. The DFT(PBE0) ligand field splitting (ΔE_{LF}) of Eu 5d orbital and the energy separation between barycenters of 4f-5d manifolds (ΔE_{fd}), of CBLA2, RNLSO, and RNLSO2 phosphors at their different candidate doping centers (M). For CBLA2 (M=Ba²⁺ or Ca²⁺), RNLSO (M=Rb⁺, Na1⁺ or Na2⁺) and RNLSO2 (M=Rb⁺ or Na⁺).

Phosphor	Doping site	ΔE_{fd} (eV)	ΔE_{LF} (eV)
CaBa[LiAl ₃ N ₄] ₂ :Eu ²⁺	Ba ²⁺	3.08	2.17
CBLA2	Ca ²⁺	1.06	4.63
RbNa ₃ [Li ₃ SiO ₄] ₄ :Eu ²⁺	Rb ⁺	4.16	1.60
	Na1 ⁺	2.94	3.06
	Na2 ⁺	2.42	3.60
RNLSO			
RbNa[Li ₃ SiO ₄] ₂ :Eu ²⁺	Rb ⁺	3.03	2.02
RNLSO2	Na ⁺	2.38	3.68

A. Additional Information to PART II

Table A. 4. Description of the employed (RNLSO, RNLSO2, CBLA2) Eu^{2+} -doped clusters within the embedded cluster approach in terms of the doping site (M), QCs size (N), the QCs composition, HF layers, the number of atoms in the ECP region, the number of points in the PC region and the converged CHELPG charges of ECPs and PCs. An Eu-doped cluster is constructed by replacing one doping site, ($\text{Na}^+/\text{Rb}^+/\text{Ca}^{2+}/\text{Ba}^{2+}$) cation.

Phosphor	Doping site	Cluster Size	QC	HF	n(cECP)	n(PC)	CHELPG Charges
$\text{RbNa}_3[\text{Li}_3\text{SiO}_4]_4\text{Eu}^{2+}$ RNLSO	Na^{1+}	1	$[\text{EuLi}_8\text{O}_{20}]^{30-}$	$[\text{Rb}_2\text{Na}_6\text{Li}_8\text{Si}_4]^{32}$	232	36886	Rb:1.62, Na:0.92, Si: 2.62, Li: 1.17, O: -2.09
		2	$[\text{EuRbLi}_{12}\text{O}_{28}]^{41-}$	$[\text{RbNaLi}_8\text{Si}_8]^{42}$	254	36864	
		3	$[\text{EuRb}_2\text{Li}_{16}\text{O}_{36}]^{52-}$	$[\text{Na}_{12}\text{Li}_8\text{Si}_8]^{52}$	314	36768	
		4	$[\text{EuRb}_2\text{NaLi}_{20}\text{O}_{44}]^{63-}$	$[\text{RbNa}_3\text{Li}_{12}\text{Si}_{12}]^{64}$	342	36740	
		5	$[\text{EuRb}_2\text{Na}_2\text{Li}_{24}\text{O}_{52}]^{74-}$	$[\text{Rb}_2\text{Na}_{10}\text{Li}_{16}\text{Si}_{12}]^{76}$	396	36650	
	Na^{2+}	1	$[\text{EuLi}_4\text{Si}_4\text{O}_{20}]^{18-}$	$[\text{Rb}_3\text{Na}_5\text{Li}_{12}]^{20}$	200	36918	Rb:1.55, Na:1.04, Si: 2.78, Li: 1.20, O: -2.06
		2	$[\text{EuNaLi}_6\text{Si}_6\text{O}_{28}]^{23-}$	$[\text{Rb}_2\text{Na}_6\text{Li}_{16}]^{24}$	230	36932	
		3	$[\text{EuNa}_2\text{Li}_8\text{Si}_8\text{O}_{36}]^{28-}$	$[\text{Rb}_4\text{Na}_6\text{Li}_{20}]^{30}$	274	36808	
		4	$[\text{EuNa}_3\text{Li}_{10}\text{Si}_{10}\text{O}_{44}]^{33-}$	$[\text{Rb}_2\text{Na}_8\text{Li}_{24}]^{34}$	310	36816	
		5	$[\text{EuNa}_4\text{Li}_{12}\text{Si}_{12}\text{O}_{52}]^{38-}$	$[\text{Rb}_5\text{Na}_7\text{Li}_{28}]^{40}$	348	36698	
	Rb^{+}	1	$[\text{EuLi}_8\text{O}_{20}]^{30-}$	$[\text{Na}_{10}\text{Li}_4\text{Si}_4]^{30}$	230	36878	Rb:1.53, Na:0.99, Si: 2.66, Li: 1.13, O: -2.00
		2	$[\text{EuNaLi}_{12}\text{O}_{28}]^{41-}$	$[\text{RbNaLi}_8\text{Si}_8]^{42}$	254	36864	
		3	$[\text{EuNa}_2\text{Li}_{16}\text{O}_{36}]^{52-}$	$[\text{Rb}_2\text{Na}_8\text{Li}_{12}\text{Si}_8]^{54}$	314	36756	
		4	$[\text{EuRbNa}_2\text{Li}_{20}\text{O}_{44}]^{63-}$	$[\text{RbNa}_3\text{Li}_{12}\text{Si}_{12}]^{64}$	342	36740	
		5	$[\text{EuRb}_2\text{Na}_2\text{Li}_{24}\text{O}_{52}]^{74-}$	$[\text{Na}_{16}\text{Li}_{12}\text{Si}_{12}]^{76}$	396	36638	
$\text{RbNa}[\text{Li}_3\text{SiO}_4]_2\text{Eu}^{2+}$ RNLSO2	Na^{+}	1	$[\text{EuLi}_4\text{Si}_4\text{O}_{20}]^{18-}$	$[\text{Rb}_4\text{Na}_2\text{Li}_{12}]^{18}$	192	36428	Rb:1.47, Na:0.90, Si: 2.74, Li: 1.13, O: -2.21
		2	$[\text{EuNaLi}_6\text{Si}_6\text{O}_{28}]^{23-}$	$[\text{Rb}_6\text{Na}_2\text{Li}_{16}]^{24}$	230	36454	
		3	$[\text{EuNa}_2\text{Li}_8\text{Si}_8\text{O}_{36}]^{28-}$	$[\text{Rb}_8\text{Na}_2\text{Li}_{20}]^{30}$	274	36308	
		4	$[\text{EuNa}_3\text{Li}_{10}\text{Si}_{10}\text{O}_{44}]^{33-}$	$[\text{Rb}_8\text{Na}_2\text{Li}_{24}]^{34}$	310	36338	
		5	$[\text{EuNa}_4\text{Li}_{12}\text{Si}_{12}\text{O}_{52}]^{38-}$	$[\text{Rb}_8\text{Na}_2\text{Li}_{28}]^{38}$	346	36202	
	Rb^{+}	1	$[\text{EuLi}_8\text{O}_{20}]^{30-}$	$[\text{Rb}_2\text{Na}_8\text{Li}_6\text{Si}_4]^{32}$	232	36318	Rb:1.56, Na:1.00, Si: 2.81, Li: 1.18, O: -2.17
		2	$[\text{EuRbLi}_{12}\text{O}_{28}]^{41-}$	$[\text{Rb}_2\text{Na}_2\text{Li}_6\text{Si}_8]^{42}$	260	36402	
		3	$[\text{EuRb}_2\text{Li}_{16}\text{O}_{36}]^{52-}$	$[\text{Rb}_2\text{Na}_{12}\text{Li}_8\text{Si}_8]^{54}$	314	36200	
		4	$[\text{EuRb}_3\text{Li}_{20}\text{O}_{44}]^{63-}$	$[\text{Rb}_2\text{Na}_2\text{Li}_{12}\text{Si}_{12}]^{64}$	342	36284	
		5	$[\text{EuRb}_4\text{Li}_{24}\text{O}_{52}]^{74-}$	$[\text{Rb}_2\text{Na}_4\text{Li}_{14}\text{Si}_{14}]^{76}$	384	36100	
	Ba^{2+}	1	$[\text{EuLi}_4\text{Al}_4\text{N}_{20}]^{42-}$	$[\text{Ca}_8\text{Ba}_2\text{Al}_8]^{44}$	224	35228	Ba:1.87, Ca:1.63, Al: 1.93, Li: 0.88, N: -2.36
		2	$[\text{EuBaLi}_6\text{Al}_6\text{N}_{28}]^{56-}$	$[\text{Ca}_2\text{Ba}_2\text{Al}_{16}]^{56}$	256	35086	
		3	$[\text{EuBa}_2\text{Li}_8\text{Al}_8\text{N}_{36}]^{70-}$	$[\text{Ca}_4\text{Ba}_2\text{Al}_{20}]^{72}$	298	35120	
		4	$[\text{EuBa}_3\text{Li}_{10}\text{Al}_{10}\text{N}_{44}]^{84-}$	$[\text{Ca}_4\text{Ba}_2\text{Al}_{24}]^{84}$	344	34962	
		5	$[\text{EuBa}_4\text{Li}_{12}\text{Al}_{12}\text{N}_{52}]^{98-}$	$[\text{Ca}_6\text{Ba}_2\text{Al}_{28}]^{100}$	386	34996	
$\text{CaBa}[\text{LiAl}_3\text{N}_4]_2$ CBLA2	Ca^{2+}	1	$[\text{EuAl}_8\text{N}_{20}]^{34-}$	$[\text{Ca}_2\text{Ba}_4\text{Li}_6\text{Al}_6]^{36}$	192	35264	Ba:1.77, Ca:1.63, Al: 1.93, Li: 0.93, N: -2.27
		2	$[\text{EuCaAl}_{12}\text{N}_{28}]^{44-}$	$[\text{Ca}_2\text{Ba}_4\text{Li}_8\text{Al}_8]^{44}$	234	35096	
		3	$[\text{EuCa}_2\text{Al}_{16}\text{N}_{36}]^{54-}$	$[\text{Ca}_2\text{Ba}_8\text{Li}_4\text{Al}_{10}]^{54}$	272	35150	
		4	$[\text{EuCa}_3\text{Al}_{20}\text{N}_{44}]^{64-}$	$[\text{Ca}_2\text{Ba}_{12}\text{Li}_{12}\text{Al}_8]^{64}$	314	34978	
		5	$[\text{EuCa}_4\text{Al}_{24}\text{N}_{52}]^{74-}$	$[\text{Ca}_2\text{Ba}_8\text{Li}_{14}\text{Al}_{14}]^{76}$	346	35038	

A.2. Cluster Size Convergence – Choice of the Computational Protocol

Initially, it is essential to identify the minimum cluster size that encapsulates all relevant electronic structure information and the most efficient computational protocol (DFT functional) in both the host and doped materials. For, each probable doping center, the optical band gap of the host structures were calculated by the similarity transformed equation of motion domain-based local pair natural orbital coupled cluster singles and doubles (STEOM-DLPNO-CCSD)[416, 417] as well as TD-DFT[237] methods. In the latter, a collection of DFT functionals were chosen, belonging to the GGA: PBE,[226] hybrid: PBE0,[227, 234, 235] range separated hybrid: CAM-B3LYP,[441] double hybrid: B2PLYP,[236] and range separated double hybrid: ω B2PLYP[442] families. Similarly, TD-DFT and CASSCF(7,19)/NEVPT2 methods were employed to compute the band gap energies of the Eu^{2+} -doped structures.

As a first step the cluster size convergence is evaluated on the basis of the optical band gap (E_g) energies of the host structures. As has been described previously, [84] the optical band gap is defined as the lowest optically allowed electronic excitation energy.

As seen in **Figure A. 3**, the lowest excitation energies in the host, for all employed functionals, were converged at the trimer cluster size. In the case of the CBLA clusters the lowest excitation energy (optical E_g) is observed for the clusters containing Ba^{2+} centers while in the case of RNLSO and RNLSO2 clusters the lowest excitation energy (optical E_g) is observed for the clusters containing Na^+ centers.

As shown in **Figure A. 3** and **Figure A. 4**, and **Table A. 5**, in comparison to the available experimental data[330, 376] the computed values show significant underestimations and non-systematic deviations ranging between $\sim 15500\text{-}37500\text{ cm}^{-1}$ (1.9-4.6 eV). In contrast, as has been observed previously[80, 84] the situation changes rapidly when STEOM-DLPNO-CCSD is employed to compute the band gap energies (**Figure A. 4**). In the case of RNLSO and RNLSO2 the MAE errors drop below 0.03 eV in comparison to the available experimental data. Hence in a next step STEOM-DLPNO-CCSD is employed to evaluate the performance of the various DFT functionals.

Table A. 5 shows that in comparison to the STEOM-DLPNO-CCSD computed values MAE decreases in the sequence PBE, PBE0, CAM-B3LYP, B2PLYP and ω B2PLYP (MAE=4.6, 3.1, 2.4, 3.0, and 1.9 eV, respectively). This general failure of TD-DFT to computed the E_g energies

of these systems is not surprising[444] as in fact they reflect non-rigid $O^{2-} - 2p \rightarrow Na^+ - 3s$ (for RNLSO and RNLSO2) and $N^{3-} - 2p \rightarrow Ba^{2+} - 5d$ (for CBLA2) ligand to metal charge transfer (LMCT) transitions. This is shown in **Figure 11.6** for RNLSO as a collective representative example, where experimental optical band gap can be reproduced only on STEOM-DLPNO-CCSD level of theory on the trimer cluster.

In a next step, the first excitation energies of the Eu^{2+} -doped phosphors were computed at the various doping centers at the TD-DFT and the CASSCF(7,19)/NEVPT2 levels of theory employing the monomer clusters. The results are presented in **Table A. 6**. By comparing the various TD-DFT computed energies against the CASSCF/NEVPT2 values, which are taken as a reference, the situation with respect to the undoped phosphors is changing drastically. GGA and double hybrid functionals outperform showing MAE values which range between ~ 5000 - 7000 cm^{-1} (0.62-0.87 eV) from the reference CASSCF/NEVPT2 values. In contrast, the hybrid functionals (PBE0, CAM-B3LYP) show noticeable smaller deviations when compared against the EOM-CCSD computed values, MAE ~ 500 - 700 cm^{-1} (0.06-0.09 eV). This is due to the different nature of the probed transition. In the case of the undoped phosphors the transitions that dominates the band gap energies are of LMCT character while in the case of the Eu^{2+} -doped ones they have a rigid $4f \rightarrow 5d$ character. This implies that hybrid functionals (PBE0 or CAM-B3LYP) are indeed good candidates for targeting the absorption and photoluminescence properties of the study set of Eu^{2+} -doped phosphors.

In a last step based on its performance the PBE0 hybrid functional is employed to compute the absorption spectra of the study set of the Eu^{2+} -doped phosphors in the sequence monomer to pentamer clusters. The results are presented in **Figure A. 5** showing once again that in all studied cases the TD-DFT/PBE0 computed spectra converge for the trimer cluster size. Provided that the spectra are shifted by $\sim 500 - 700\text{ cm}^{-1}$, the computed spectra are also in satisfactory visual agreement to experiment in terms of the number and the relative intensities of the computed bands.

Based of the above results and in an effort to stay consistent with our previous study on narrow band Eu^{2+} -doped phosphors,[80] in the following sections the trimer structures are chosen for the production calculations and analysis of the absorption and emission processes employing the TD-DFT/PBE0 computational protocol in conjunction with the excited state dynamics (ESD).

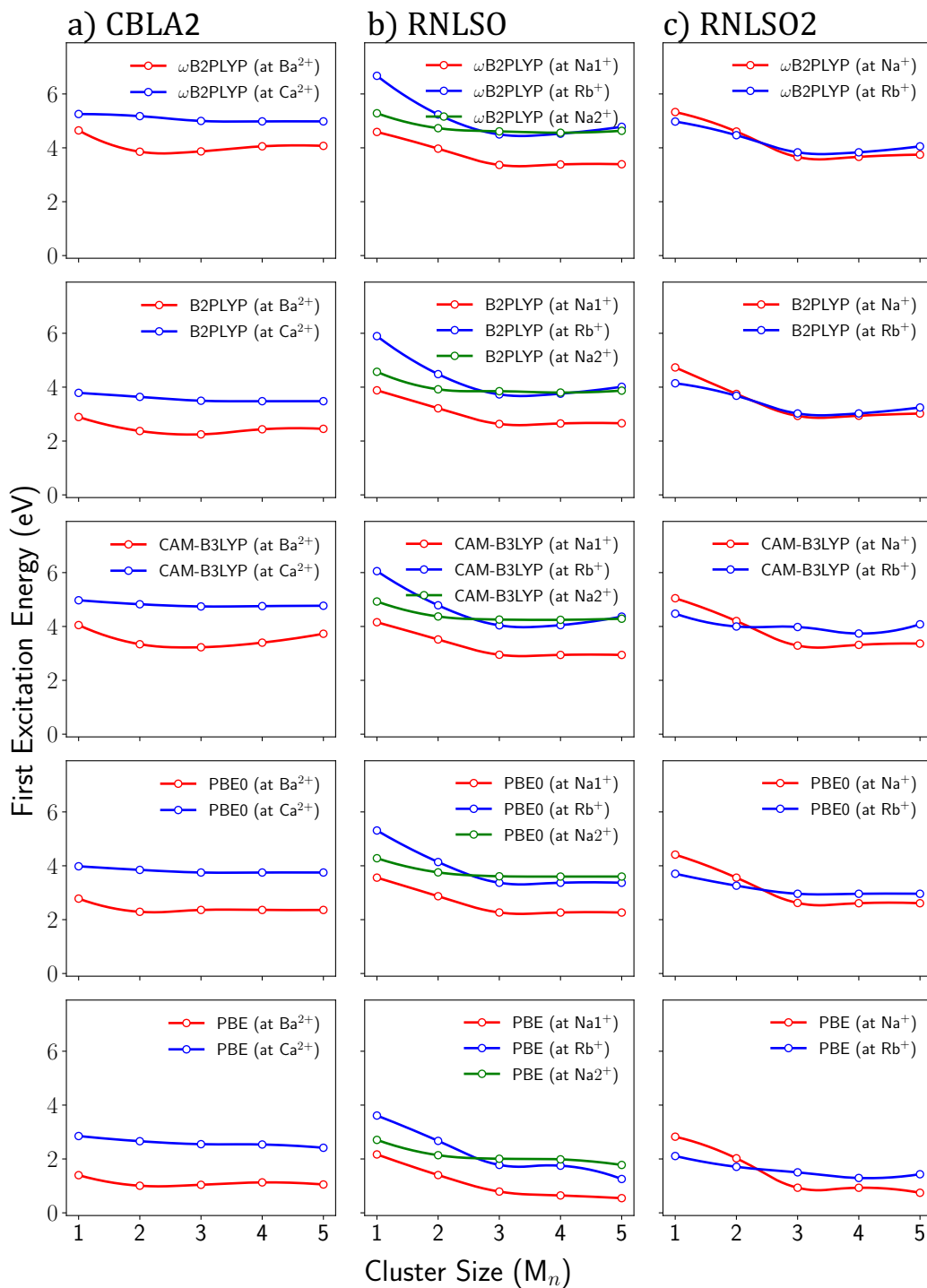


Figure A. 3. TD-DFT computed first excitation energies (eV) of the hosts for the variety undoped QC sizes (n = 1: monomers, 2: dimers, 3: trimers, 4: tetramers, 5: pentamers) across the employed study set of phosphors, a) CBLA2 (at Ba^{2+} site in red and at Ca^{2+} site blue), b) RNLSO (at Na^{1+} site in red, at Rb^{+} site in blue, and at Na^{2+} site in green), c) RNLSO2 (at Na^{+} site in red and at Rb^{+} site in blue). The following DFT functionals were employed, ω B2PLYP (1st row), B2PLYP (2nd row) CAM-B3LYP (3rd row), PBE0 (4th row) and PBE (5th row).

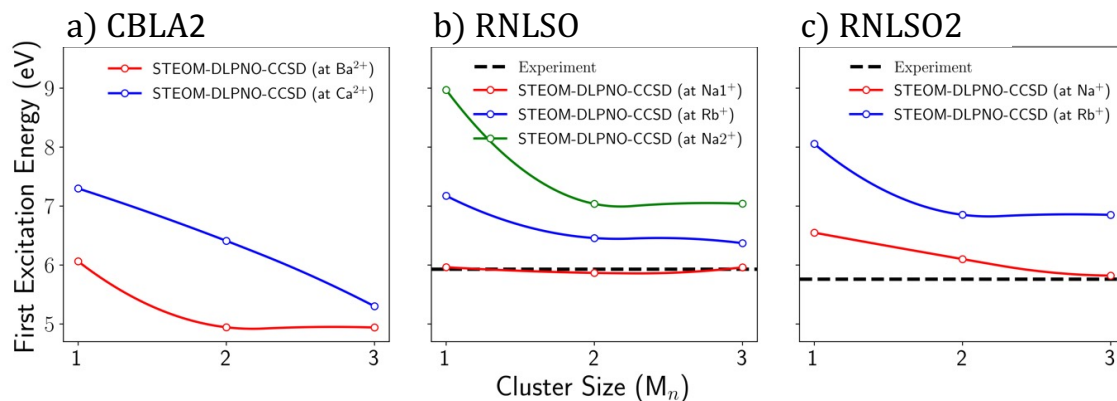


Figure A. 4. STEOM-DLPNO-CCSD computed first excitation energies (eV) of the hosts, for the variety undoped QC sizes ($n = 1$: monomers, 2: dimers, 3: trimers), across the employed study set of phosphors, a) CBLA2 (at Ba^{2+} site in red and at Ca^{2+} site blue), b) RNLSO (at Na^+ site in red, at Rb^+ site in blue, and at $Na2^+$ site in green), c) RNLSO2 (at Na^+ site in red and at Rb^+ site in blue). In the case of RNLSO, RNLSO2 black dotted lines represent the available experimental optical band gap energies[330, 376].

Note: STEOM-DLPNO-CCSD computations for larger clusters (tetramers and pentamers) present challenges due to resource limitations, where calculations became very expensive in terms of memory and time. In addition, it is clear that in all cases the size convergence has been reached at trimer clusters. Only for CBLA2 at Ca^{2+} site, the size convergence is not reached, however, the optical band gap for CBLA2 was estimated based converged first excitation energies of CBLA2 at Ba^{2+} site which is lower in energy with respect energies at Ca^{2+} sites.

Table A. 5. Calculated band gaps of trimer clusters of CBLA2, RNLSO, and RNLSO2 phosphors' hosts using TD-DFT/ PBE, PBE0, CAM-B3LYP, B2PLYP and ω B2PLYP as well as using STEOM-DLPNO-CCSD. The calculated optical band gap (E_g) energy is chosen as the lowest first excitation energies across different metal centers per host (**Figure A. 3** and **Figure A. 4**) and compared with available measured experimental E_g . All values are in cm^{-1} , and also in eV in parentheses.

Phosphor's Host	Central cation	Calc. optical band gap in cm ⁻¹ (eV)						Exp. band gap cm ⁻¹ (eV)
		TD-DFT					STEOM-DLPNO-CCSD	
		PBE	PBE0	CAM-B3LYP	B2PLYP	ωB2PLYP		
CaBa[LiAl ₃ N ₄] ₂ CBLA2	Ba ²⁺	8388 (1.04)	19035 (2.36)	26052 (3.23)	18147 (2.25)	31214 (3.87)	39844 (4.94)	--
RbNa ₃ [Li ₃ SiO ₄] ₄ RNLSO	Na ¹⁺	6372 (0.79)	18309 (2.27)	23793 (2.95)	21212 (2.63)	12582 (1.56)	48071 (5.96)	47829 (5.93)
RbNa[Li ₃ SiO ₄] ₂ RNLSO2	Na ⁺	7501 (0.93)	21132 (2.62)	26536 (3.29)	23632 (2.93)	29520 (3.66)	46941 (5.82)	46458 (5.76)
*MAE		37289 (4.62)	25218 (3.13)	19249 (2.39)	23712 (2.94)	15405 (1.91)	241 (0.03)	

*MAE are calculated with respect to the experiment, except for CBLA2, due to lack of experimental E_g , STEOM-DLPNO-CCSD is taken as a reference.

Table A. 6. The first excitation energies (in cm^{-1}) calculated using TD-DFT employing various functionals (PBE, PBE0, CAM-B3LYP, B2PLYP, and ω B2PLYP) as well as CASSCF(7,19)/NEVPT2 for the smallest Eu^{2+} -doped embedded clusters (monomers, $n=1$). All the probable doping site was tested $\text{Ba}^{2+}/\text{Ca}^{2+}$ and $\text{Na}^{+}/\text{Rb}^{+}$ for CBLA2 and both RNLSO and RNLSO2, respectively. The energy shift (in cm^{-1}) of the TD/DFT computed first excited state energy from the respective CASSCF-NEVPT2 energy is shown in parentheses. In the last two rows, the mean absolute errors MAE and the mean absolute deviations MAE(%) of the computed first excited state are presented taking the computed CASSCF/NEVPT2 energies as reference.

Phosphor	Doping site	1 st Excitation Energy (cm^{-1})					CASSCF/ NEVPT2
		PBE	PBE0	CAM-B3LYP	B2PLYP	ω B2PLYP	
$\text{CaBa}[\text{LiAl}_3\text{N}_4]_2:\text{Eu}^{2+}$ CBLA2	Ba^{2+}	12406 (8773)	21601 (-422)	21764 (-585)	14537 (6642)	16118 (5061)	21179
	Ca^{2+}	3807 (8561)	12170 (198)	11998 (370)	5142 (7226)	7343 (5025)	12368
$\text{RbNa}_3[\text{Li}_3\text{SiO}_4]_4:\text{Eu}^{2+}$ RNLSO	Na^{1+}	16402 (5880)	22104 (178)	22072 (210)	16664 (5618)	17687 (4595)	22282
	Na^{2+}	13052 (6886)	20876 (-938)	19192 (746)	12669 (7269)	14853 (5085)	19938
	Rb^{+}	24621 (4248)	29242 (-373)	28481 (388)	23181 (5688)	23657 (5212)	28869
$\text{RbNa}[\text{Li}_3\text{SiO}_4]_2:\text{Eu}^{2+}$ RNLSO2	Na^{+}	12680 (7023)	20586 (-883)	18895 (808)	12431 (7272)	14656 (5047)	19703
	Rb^{+}	12803 (10039)	22237 (605)	21294 (1548)	15181 (7661)	16521 (6321)	22842
MAE		7344.3	513.7	665.0	6768.0	5192.3	--
MAE (%)		34.9	2.4	3.2	32.2	24.7	--

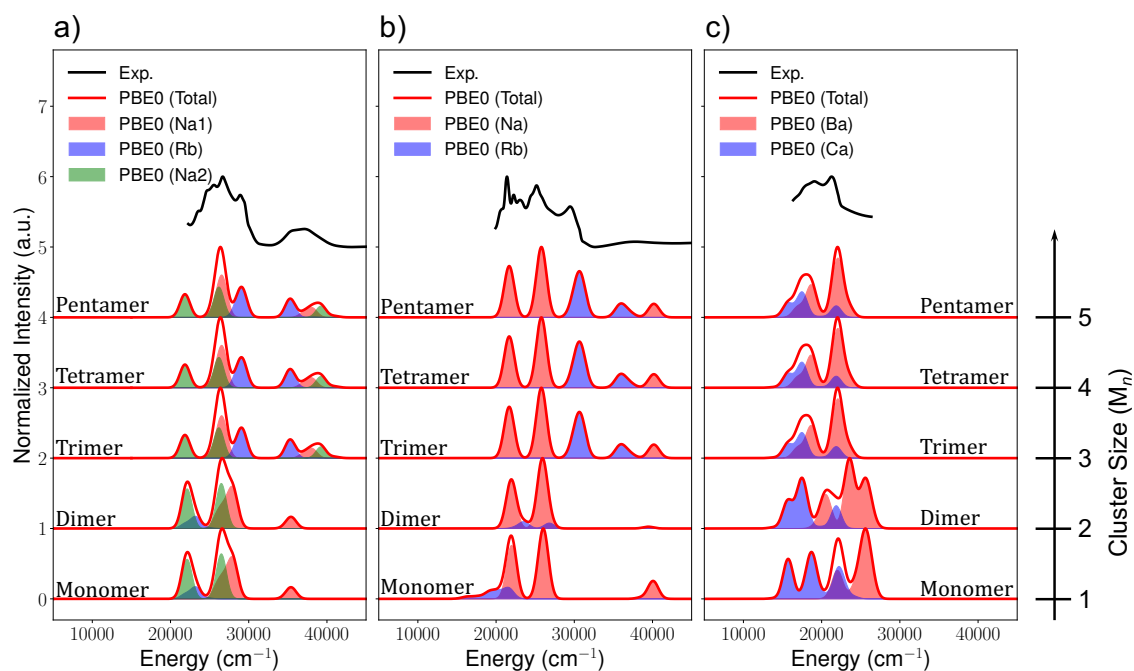


Figure A. 5. Experimental (in black) and TD-DFT PBE0 calculated (in red) absorption spectra at different size doped QC (monomers, dimers, trimers, tetramers, and pentamers) for a) RNLSO (Na1 site in pale red, Rb site in pale blue, and Na2 site in pale green fill), b) RNLSO2 (Na site in pale red and Rb site in pale blue fill) and c) CBLA2 (Ba site in pale red and Ca site in pale blue fill). A shift between 500-700 cm⁻¹ is applied to spectra for agreement to the experimental spectra.

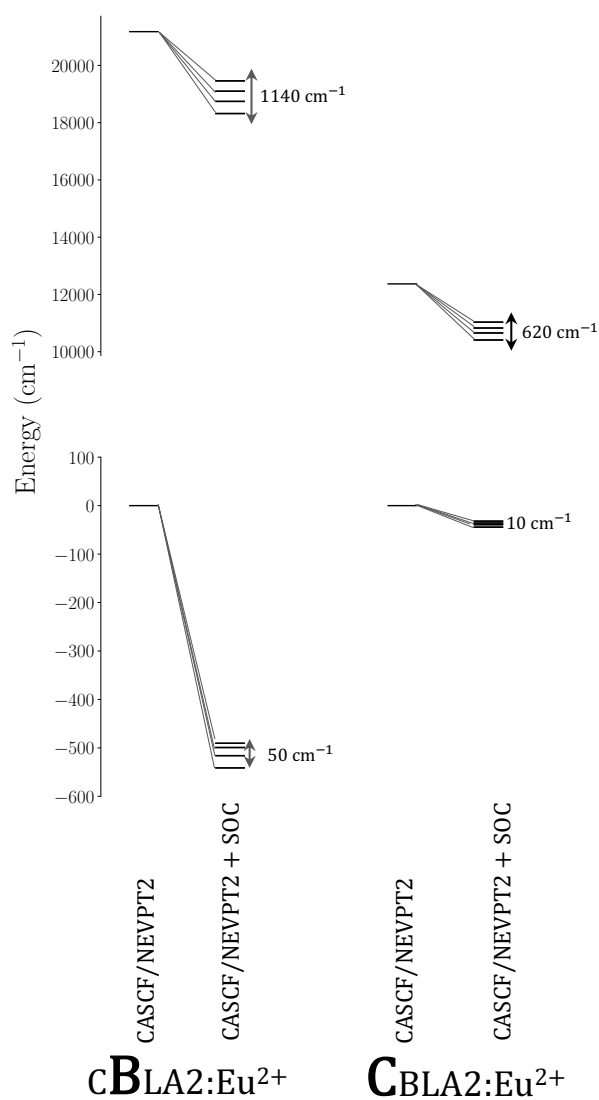


Figure A. 6. SA-CASSCF(7,19)/NEVPT2 non-relativistic ground and lowest (emitting) excited state and their relaxation and splitting due SOC of the monomer structure of CBLA2:Eu^{2+} doped at Ba^{2+} and Ca^{2+} sites, respectively.

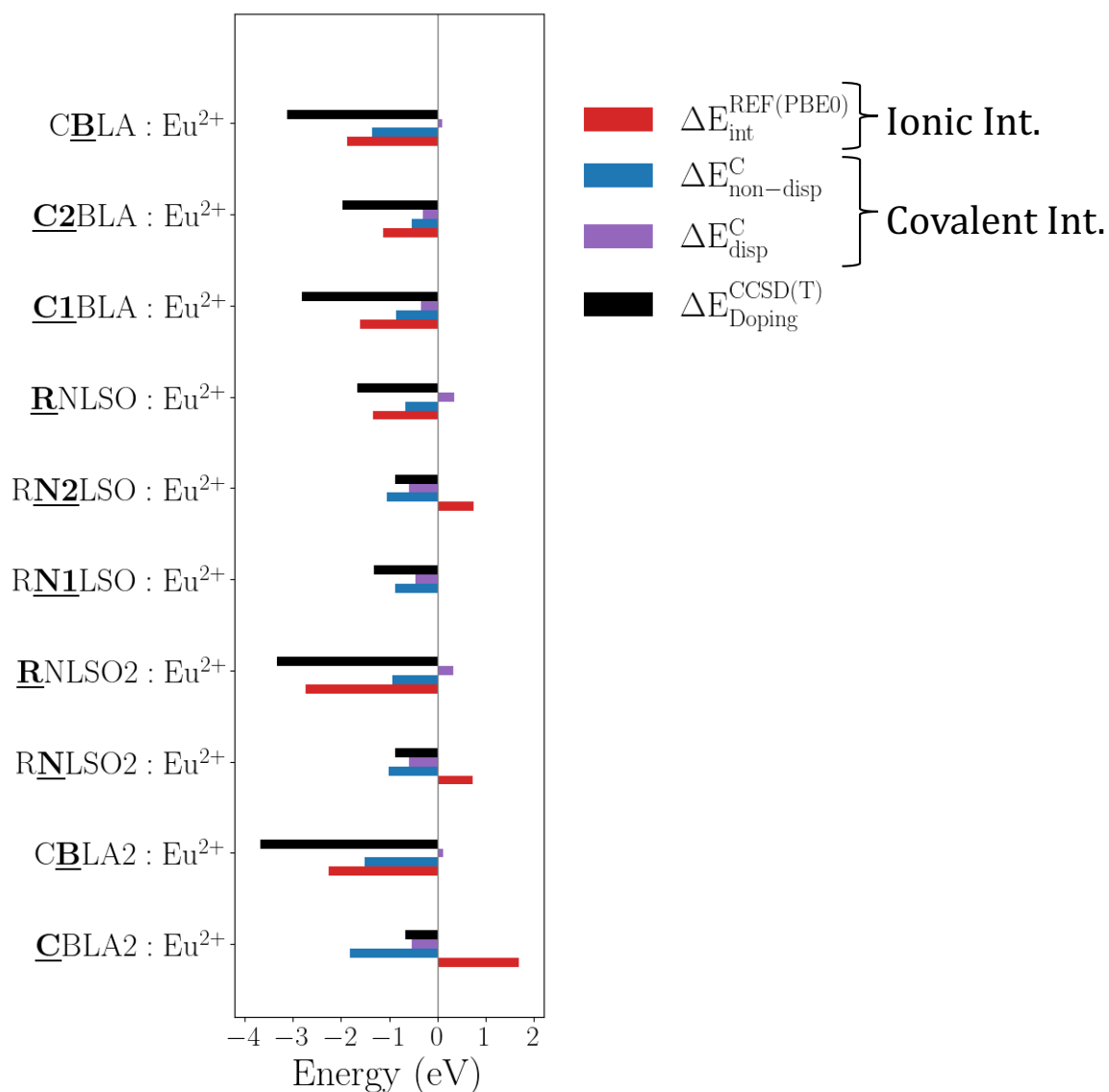


Figure A. 7. Local energy decomposition (LED) analysis of DLPNO-CCSD(T) doping energies (black bars) for for all the studied systems (CBLA2, RNLSO2, RNLSO and proposed CBLA) at the all probable sites for Eu^{2+} doping in terms of ionic ($\Delta E_{\text{int}}^{\text{REF}}$) and covalent ($\Delta E_{\text{non-disp}}^{\text{C}}$ and $\Delta E_{\text{disp}}^{\text{C}}$) interactions, shown in in red, blue, and purple bars, respectively.

A. Additional Information to PART II

Table A. 7. Eu^{2+} doping energies (eV) for CBLA2, CBLA, RNLSO, and RNLSO2, at the different candidate doping centers of trimers clusters computed at DFT(PBE0) and DLPNO-CCSD(T) methods.

Phosphor	Doping site	Doping Energy (eV)	
		PBE0	DLPNO-CCSD(T)
$\text{CaBa}[\text{LiAl}_3\text{O}_4]_2:\text{Eu}^{2+}$ CBLA2	Ba^{2+}	-1.62	-3.67
	Ca^{2+}	1.65	-0.67
$\text{Ca}_3\text{Ba}[\text{LiAl}_3\text{O}_4]_4:\text{Eu}^{2+}$ CBLA	Ba^{2+}	-2.93	-3.12
	$\text{Ca}(1)^{2+}$	0.63	-2.81
	$\text{Ca}(2)^{2+}$	1.33	-1.97
$\text{RbNa}_3[\text{Li}_3\text{SiO}_4]_4:\text{Eu}^{2+}$ RNLSO	$\text{Na}(1)^+$	-2.55	-1.32
	$\text{Na}(2)^+$	-2.09	-0.88
	Rb^+	-4.42	-1.66
$\text{RbNa}[\text{Li}_3\text{SiO}_4]_2:\text{Eu}^{2+}$ RNLSO2	Na^+	-2.14	-0.87
	Rb^+	-4.51	-3.34

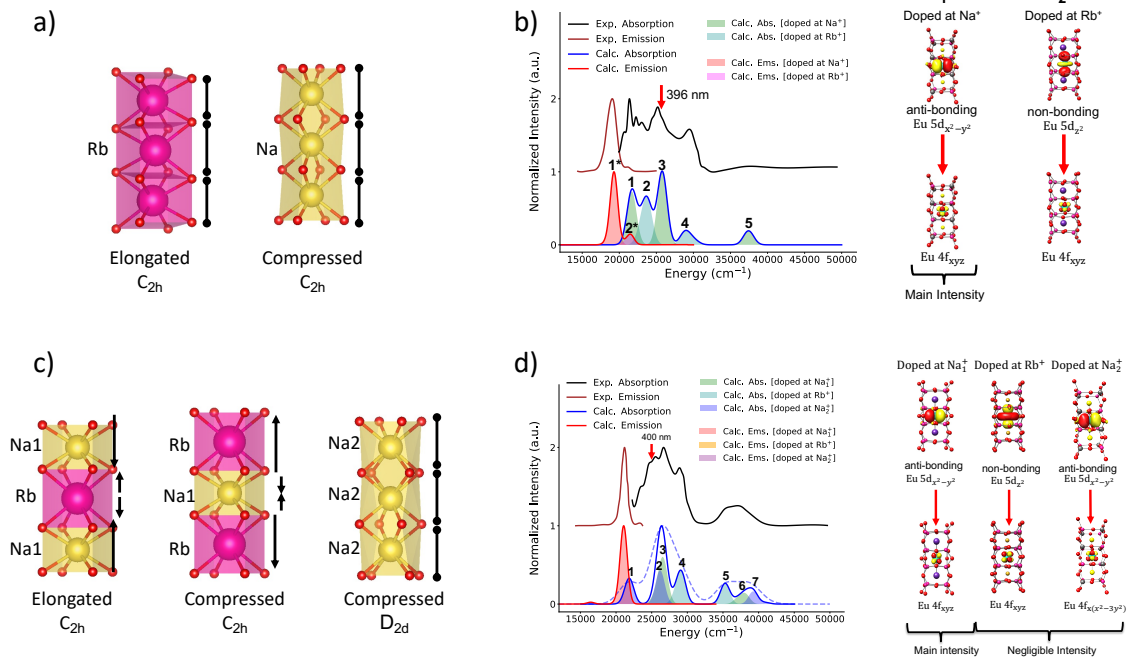


Figure A. 8. a, c) Trimer cuboids and b,d) experimental and ESD/TD-DFT/PBE0 calculation absorption and emission spectra alongside NTO analysis of the lowest excited states at probable doping sites for RNLSO2:Eu²⁺ and RNLSO:Eu²⁺, respectively.

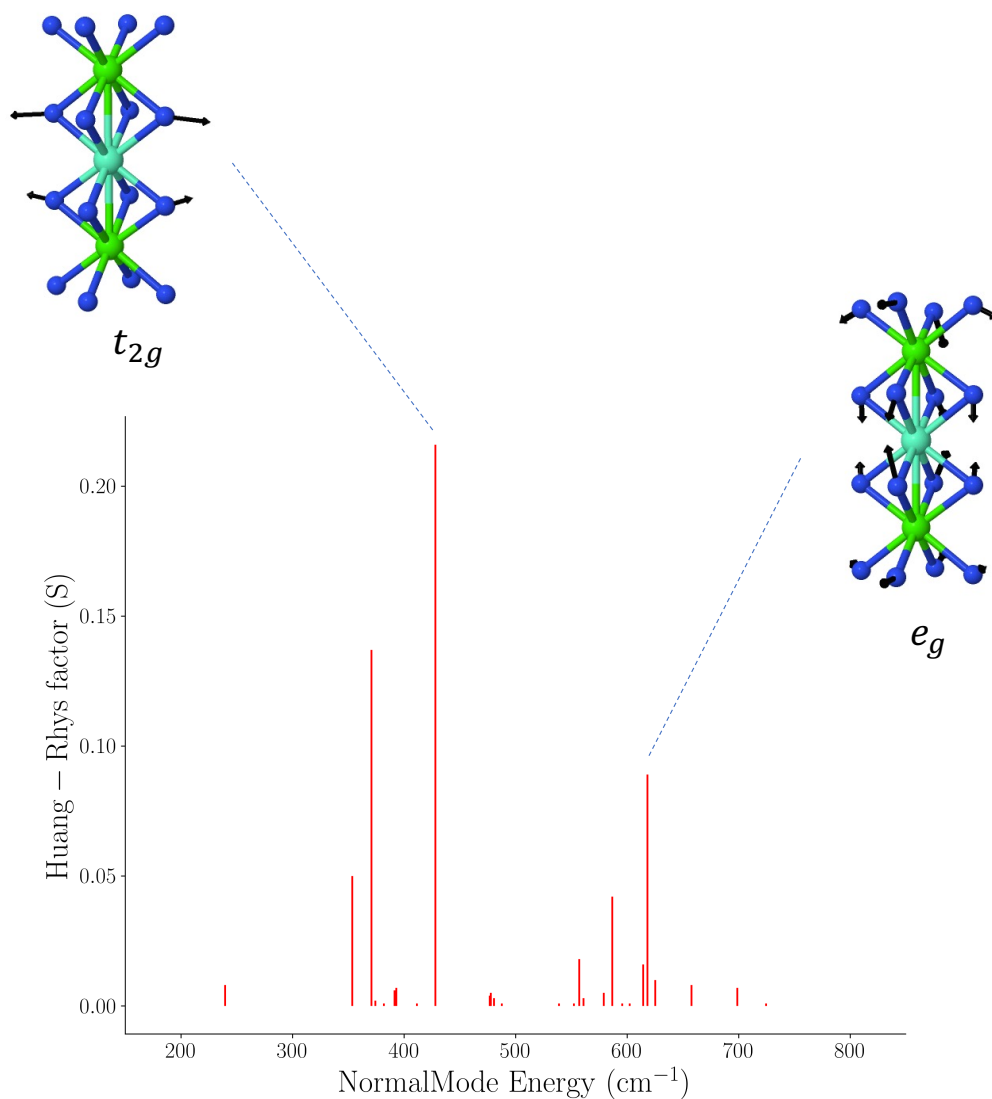


Figure A. 9. Huang-Rhys factors (S) distribution over the vibration degree of freedom of the emission transition in trimer model of CBLA2:Eu²⁺ doped at Ca²⁺ site. The highest contributing modes within the asymmetric and symmetric vibration regions (t_{2g} and e_g modes, respectively) are also visualized.

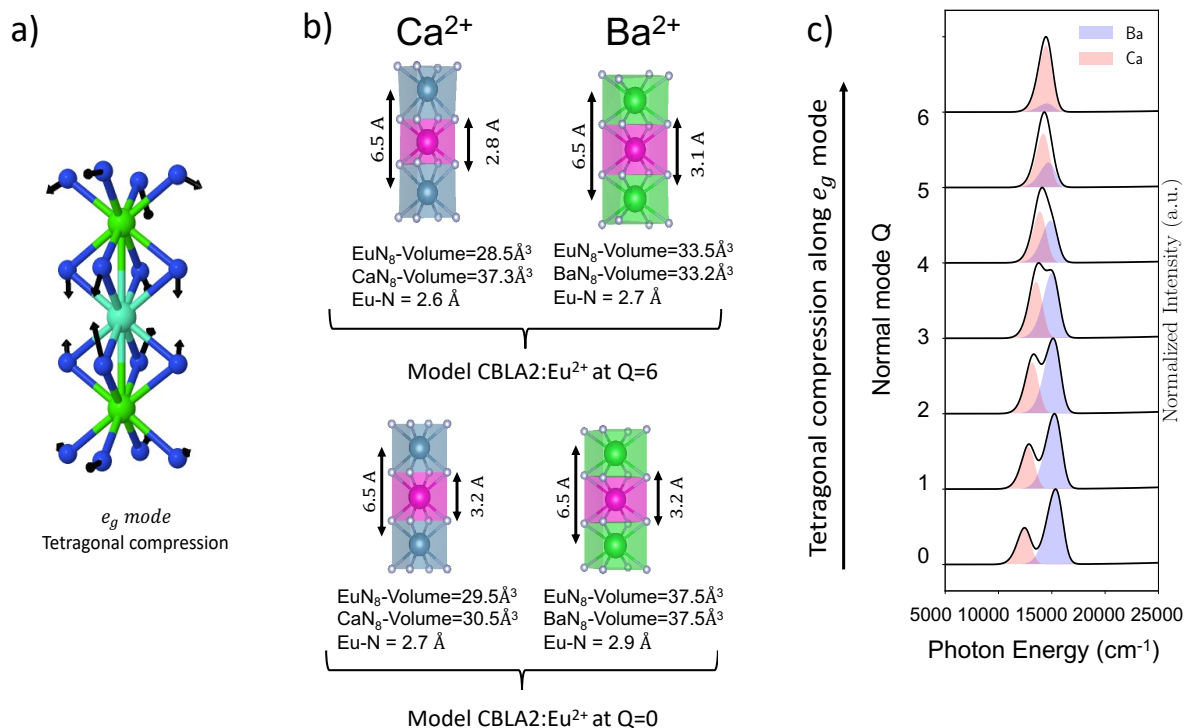


Figure A. 10. a) Illustration of the e_g vibrational mode leading the tetragonal compression pathway of the Eu²⁺ doped cuboids in CBLA2. b) The structures of the model CBLA2 along the tetragonal compression pathway at the equilibrium (Q=0) and at selected point (Q=12). c) The normalized ESD/TDDFT/PBE0 computed emission spectra of the model CBLA2:Eu²⁺ along the tetragonal distortion pathway.

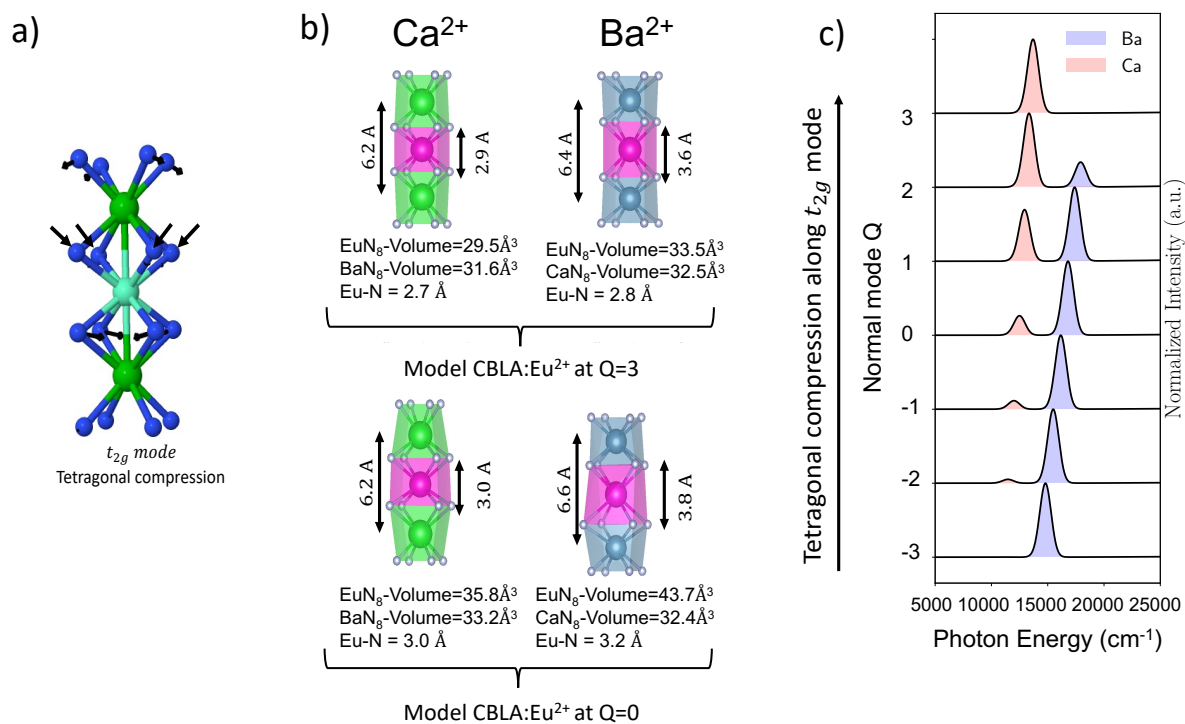


Figure A. 11. Illustration of the t_{2g} vibrational mode leading the tetragonal compression pathway of the Eu²⁺ doped cuboids in CBLA. b) The structures of the model CBLA along the tetragonal compression pathway at the equilibrium (Q=0) and at selected point (Q=12). c) The normalized ESD/TDDFT/PBE0 computed emission spectra of the model CBLA:Eu²⁺ along the tetragonal distortion pathway.

A.3. In-silico synthesis of CBLA Phosphor

The crystal structure of the hypothetical CBLA phosphor host was constructed based on the CBLA2 host's structure. This involved transforming the CBLA2 unit cell into a tetragonal ($I4/m$) space group, using VESTA software.[568] Then, the unit cell was primarily relaxed using CRYSTAL17 software,[569] with geometry optimization performed through the DFT/PBE0 functional employing a triple-zeta basis set for all elements. The BFGS scheme, with default thresholds for gradients and displacements, was adopted.[569]

The relaxed unit cell served as the basis for constructing the supercell structure, which was then used to prepare Eu^{2+} -doped trimer clusters at three potential doping sites ($\text{Ca}(1)^{2+}$, $\text{Ca}(2)^{2+}$, Ba^{2+}) in the CBLA host. The preparation of Eu^{2+} -doped trimer clusters followed the embedded cluster approach outlined in **Section 7.3**. Subsequently, using the ORCA 5.0 suite of programs, [354, 355, 411, 412] another geometry optimization, employing DFT/PBE0, [227, 234, 235] was conducted exclusively for the QC and HF regions of these clusters. The ECP and PC regions were held fixed during this process. Then it is followed by Hessian calculation.

Continuing with a consistent approach, all subsequent computations for doping energies and optical spectra were conducted using the same setup employed for the previously discussed phosphors, as detailed in **Sections 10.4** and **11.5**.

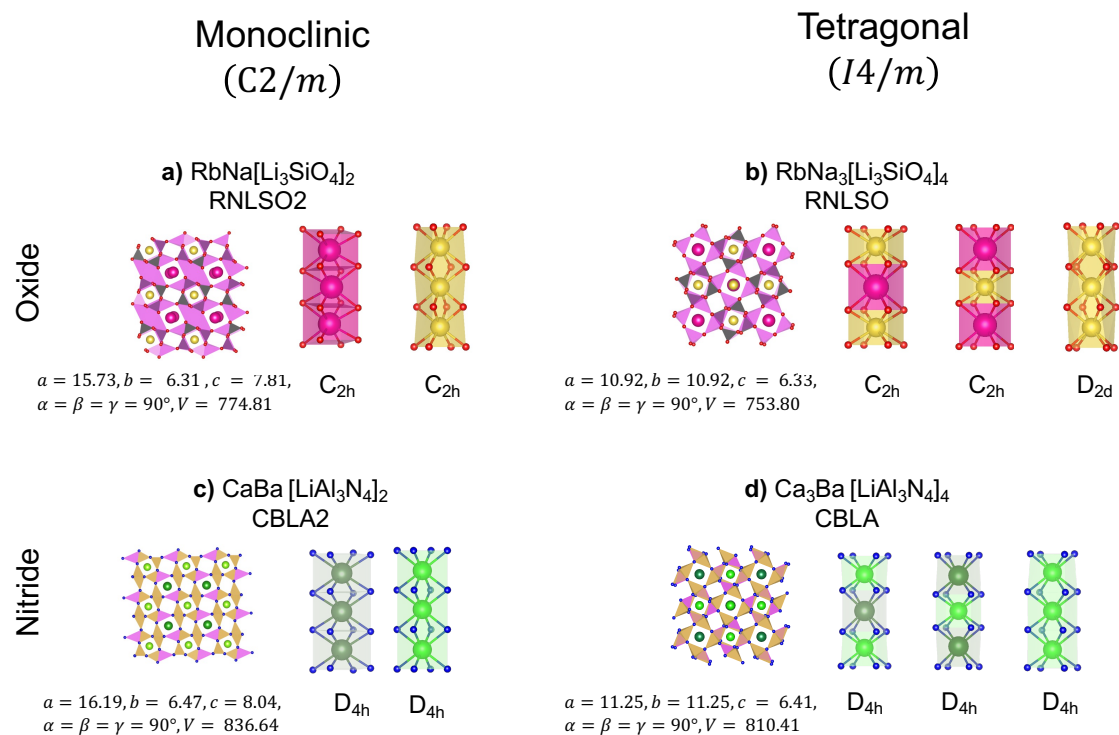


Figure A. 12. Space group, structural properties, and probable sites for Eu^{2+} doping for RNLSO2, RNLSO, CBLA2, and hypothetical CBLA Hosts.

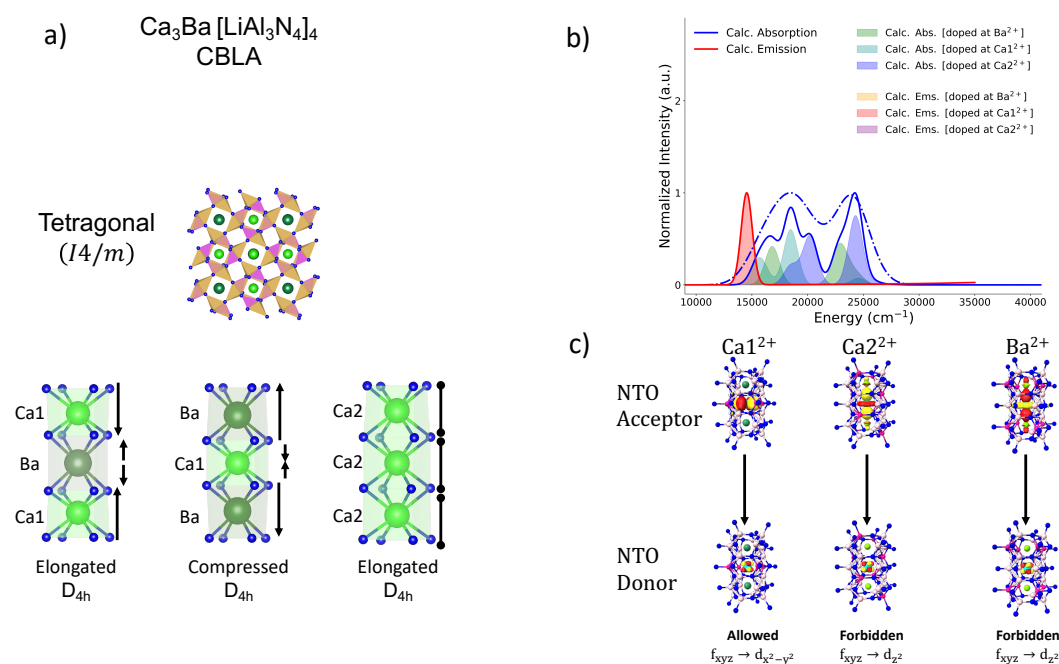


Figure A. 13. a) The crystalline structure optimized structure of CBLA and possible doping sites host ($\text{Ca}(1)^{2+}$, Ba^{2+} and $\text{Ca}(2)^{2+}$) and b) calculated TDDFT/PBE0 absorption (blue; solid and dashed lines plotted with gaussian broadening 1500, 3000 cm^{-1} , respectively) spectra and ESD/TDDFT/PBE0 calculated (red) emission spectra. Filled colored bands indicate individual contributions of the different Eu^{2+} -doped centers. c) The 1st transition responsible for emission upon relaxation for all the candidate Eu^{2+} -doped centers.

Table A. 8. Experimental versus predicted maximum emission energy positions and bandwidths according to the descriptors relations (1) and (2) for a given computed maximum absorption band maximum and the respective covalency factor ($5d \alpha^2$) and calculated Stokes Shift ΔS for previously studied (BMS, SMS, CLA, SALON, SLBO):Eu²⁺ and (RNLSO, RNLSO2, CBLA2, CBLA):Eu²⁺-doped phosphors at emitting centers.

Phosphor	Doping site	Experimental Emission Band			Calculated First Absorption band		Predicted Emission Band		
		Energy	Width	ΔS	Energy	Eu ²⁺ 5d	Energy	Width	ΔS
		(cm ⁻¹)	(cm ⁻¹)	(cm ⁻¹)	(cm ⁻¹)	α^2	(cm ⁻¹)	(cm ⁻¹)	(cm ⁻¹)
Ba[Mg ₃ SiN ₄]:Eu ²⁺ BMS	Ba ²⁺	14920	2015	3500	16000	0.64	14925	1950	2810
Sr[Mg ₃ SiN ₄]:Eu ²⁺ SMS	Sr ²⁺	16250	1150	750	18200	0.97	16260	1150	950
Ca[LiAl ₃ N ₄]:Eu ²⁺ CLA	Ca ²⁺	14980	1340	1000	16150	0.84	14970	1350	847
Sr[LiAl ₃ N ₄]:Eu ²⁺ SLA	Sr ²⁺	15380	1140	800	17200	0.96	15384	1160	840
Sr[Al ₂ Li ₂ O ₂ N ₂]:Eu ²⁺ SALON	Sr ²⁺	16300	1220	1100	18100	0.90	16286	1220	1150
<i>Continued in the next page</i>									

A. Additional Information to PART II

Phosphor	Doping site	Experimental Emission Band			Calculated First Absorption band		Predicted Emission Band		
		Energy (cm ⁻¹)	Width (cm ⁻¹)	ΔS (cm ⁻¹)	Energy (cm ⁻¹)	Eu ²⁺ 5d α^2	Energy (cm ⁻¹)	Width (cm ⁻¹)	ΔS (cm ⁻¹)
SrLi ₂ [Be ₄ O ₆]:Eu ²⁺ SLBO	Sr ²⁺	22000	1220	980	23800	0.95	21929	1170	750
RbNa ₃ [Li ₃ SiO ₄] ₄ :Eu ²⁺ RNLSO	Na(1) ⁺	21231	1015	--	23087	0.95	21968	1234	1120
RbNa[Li ₃ SiO ₄] ₂ :Eu ²⁺ RNLSO2	Na ⁺	19121	1465	--	20030	0.92	19367	1496	670
CaBa[LiAl ₃ N ₄] ₂ :Eu ²⁺ CBLA2	Ba ²⁺	15674	1191	--	17100	0.94	15484	1259	1570
	Ca ²⁺	12658	1450	--	14400	0.87	12970	1436	1310
Ca ₃ Ba[LiAl ₃ N ₄] ₄ :Eu ²⁺ CBLA	Ca(1) ²⁺	--	--	--	15642	0.91	14600	1220	1460
MAE(%)							0.01	0.04	0.16

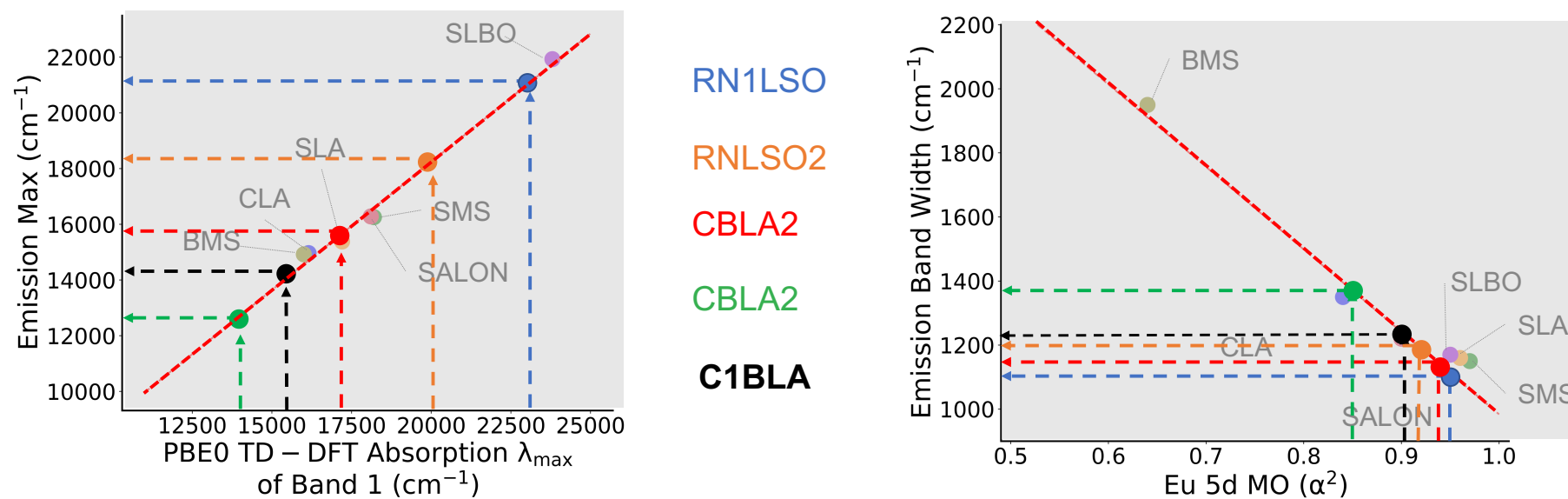


Figure A. 14. Using the previously defined descriptors to predict the luminescence band energy and bandwidth of the emitting centers of the studied (RNLSO:Eu²⁺ doped at Na(1)⁺ in blue, RNLSO2:Eu²⁺ doped at Na⁺ in orange, and CBLA2:Eu²⁺ doped at Ba²⁺ in red and Ca²⁺ in green) and hypothetical CBLA:Eu²⁺ doped at Ca(1)²⁺ in black.

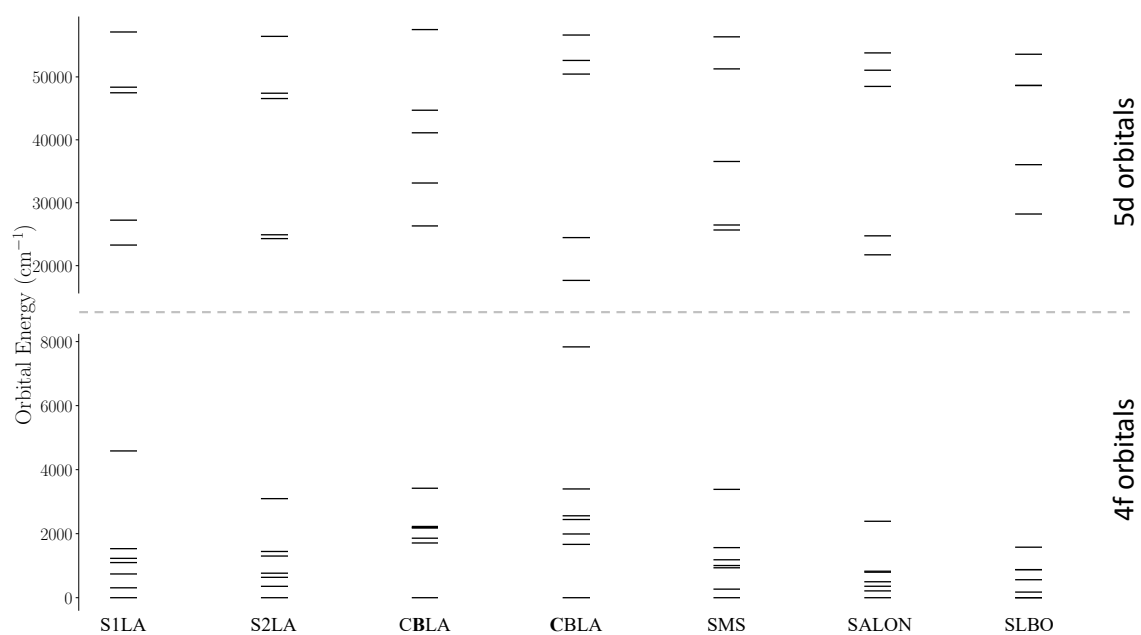


Figure A. 15. Energies (in cm^{-1}) of the 4f5d active orbitals after SA($^836, ^635$)-CASSCF(7,19) CI optimization, across the studied phosphors.

Table A. 9. Orbital configurations and population of the CAS at the doping sites of studied phosphors after SA(⁸36, ⁶35)-CASSCF(7,19) optimization. Atomic 5d orbitals contributing with < 5% and ligand (L – 2p) orbitals, in the active orbitals are omitted.

Phosphor	Doping site	SA-CASSCF CAS Compositions
SLA	Sr1 ²⁺	$4f^{6.04} (75\% 5d_{z^2})^{0.31} (65\% 5d_{x^2-y^2}/9\% 5d_{xy})^{0.23} (32\% 5d_{xz}/32\% 5d_{xy}/13\% 5d_{yz})^{0.16}$ $(62\% 5d_{yz}/11\% 5d_{xz})^{0.14} (38\% 5d_{xz}/34\% 5d_{xy}/6\% 5d_{x^2-y^2})^{0.11} 5f^{0.01}$
	Sr2 ²⁺	$4f^{6.04} (35\% 5d_{z^2}/35\% 5d_{x^2-y^2})^{0.27} (40\% 5d_{z^2}/30\% 5d_{x^2-y^2})^{0.26} (40\% 5d_{xy}/35\% 5d_{xz}/5\% 5d_{x^2-y^2})^{0.16}$ $(72\% 5d_{yz})^{0.14} (42\% 5d_{xz}/32\% 5d_{xy})^{0.11} 5f^{0.01}$
CBLA2	Ba ²⁺	$4f^{6.04} (75\% 5d_{z^2})^{0.27} (52\% \mathbf{5d_{xy}}/26\% 5d_{x^2-y^2})^{0.20} (62\% 5d_{xz}/22\% 5d_{yz})^{0.19}$ $(51\% 5d_{x^2-y^2}/20\% 5d_{xy})^{0.17} (62\% 5d_{yz}/21\% 5d_{xz})^{0.11} 5f^{0.01}$
	Ca ²⁺	$4f^{6.00} (32\% \mathbf{5d_{xy}}/26\% 5d_{x^2-y^2}/9\% 5d_{z^2})^{0.41} (60\% 5d_{z^2}/10\% 5d_{xy})^{0.26} (58\% 5d_{yz}/12\% 5d_{xz})^{0.11}$ $(44\% 5d_{x^2-y^2}/25\% 5d_{xy})^{0.11} (55\% 5d_{xz}/15\% 5d_{yz})^{0.10} 5f^{0.01}$
SMS	Sr ²⁺	$4f^{6.04} (75\% 5d_{z^2})^{0.26} (47\% 5d_{x^2-y^2}/28\% 5d_{xy})^{0.26} (39\% 5d_{xz}/17\% 5d_{xy}/9\% 5d_{x^2-y^2}/8\% 5d_{yz})^{0.19}$ $(52\% 5d_{yz}/22\% 5d_{xz})^{0.12} (32\% 5d_{xy}/20\% 5d_{yz}/18\% 5d_{x^2-y^2}/9\% 5d_{xz})^{0.11} 5f^{0.01}$
SALON	Sr ²⁺	$4f^{6.21} (77\% 5d_{z^2})^{0.23} (47\% 5d_{xy}/32\% 5d_{x^2-y^2})^{0.20} (49\% 5d_{yz}/35\% 5d_{xz})^{0.12}$ $(51\% 5d_{x^2-y^2}/32\% 5d_{xy})^{0.11} (49\% 5d_{xz}/33\% 5d_{yz})^{0.11} 5f^{0.02}$
SLBO	Sr ²⁺	$4f^{6.21} (45\% 5d_{x^2-y^2}/41\% 5d_{xy})^{0.20} (87\% 5d_{z^2})^{0.19} (51\% 5d_{xz}/34\% 5d_{yz})^{0.13} (51\% 5d_{yz}/34\% 5d_{xz})^{0.13}$ $(45\% 5d_{xy}/42\% 5d_{x^2-y^2})^{0.11} 5f^{0.02}$

A. Additional Information to PART II

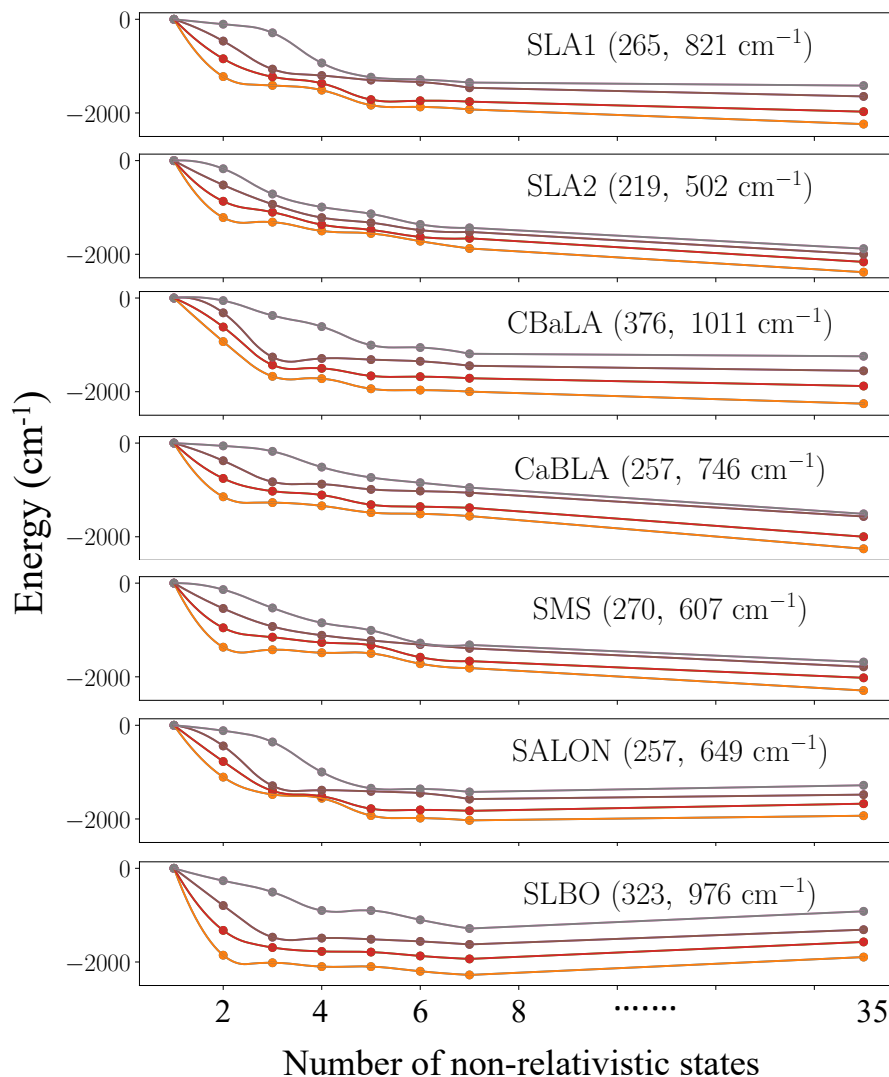


Figure A. 16. The effect of the number non-relativistic states considered in CASSC/NEVPT2/SOC calculation, on the lowest 4 KDs in terms of energy variation and splitting, across the studied phosphors. To facilitate comparison, all energies are normalized to the lowest KDs calculated with only one non-relativistic state for each corresponding case, across the studied phosphors. The energy splitting between the lowest two KDs and the total splitting in the four KDs (from the lowest to the highest KDs) after inclusion of 35 octet states are provided in parentheses for each case. Observations can be summarized as follows:

- 1) The predominant effect arises from, inclusion of 1st extra states ($2\ 4f \rightarrow 5d$ transitions), resulting in a substantial and perfectly equidistant separation. This is attributed to the fact that the lowest two transitions correspond to ($2\ 4f_{\pm m_l} \rightarrow 5d$ transitions).
- 2) Convergence of the energy levels is achieved at considering 7 states (lowest 7 $4f_{\pm m_l} \rightarrow 5d$ transitions, $m_l = 0, \pm 1, \pm 2, \pm 3$), with slight change afterwards.

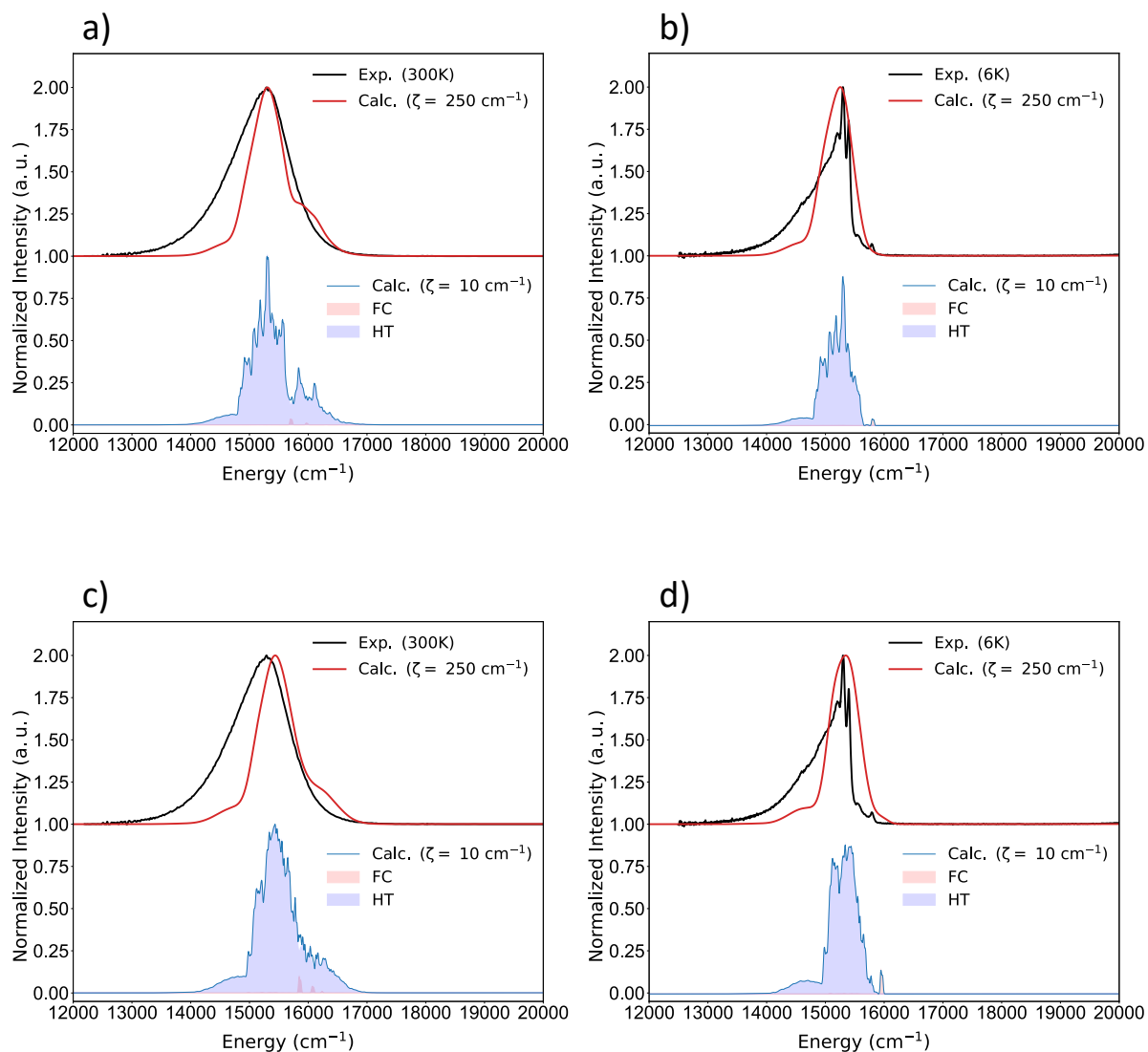


Figure A. 17. SLA:Eu²⁺ experimental (black) and calculated (Frank-Condon + Herzberg-Teller) luminescence spectra using gaussian broadening (ζ) with 10 (red) and 250 (blue) cm⁻¹ linewidth at a) 300K and b) 6K for SLA:Eu²⁺ doped at Sr1 site while c) 300K and d) 6K for SLA:Eu²⁺ doped at Sr2 site. Also, the total contribution of FC and HT are given in red and blue fill using $\zeta = 10$ cm⁻¹, respectively.

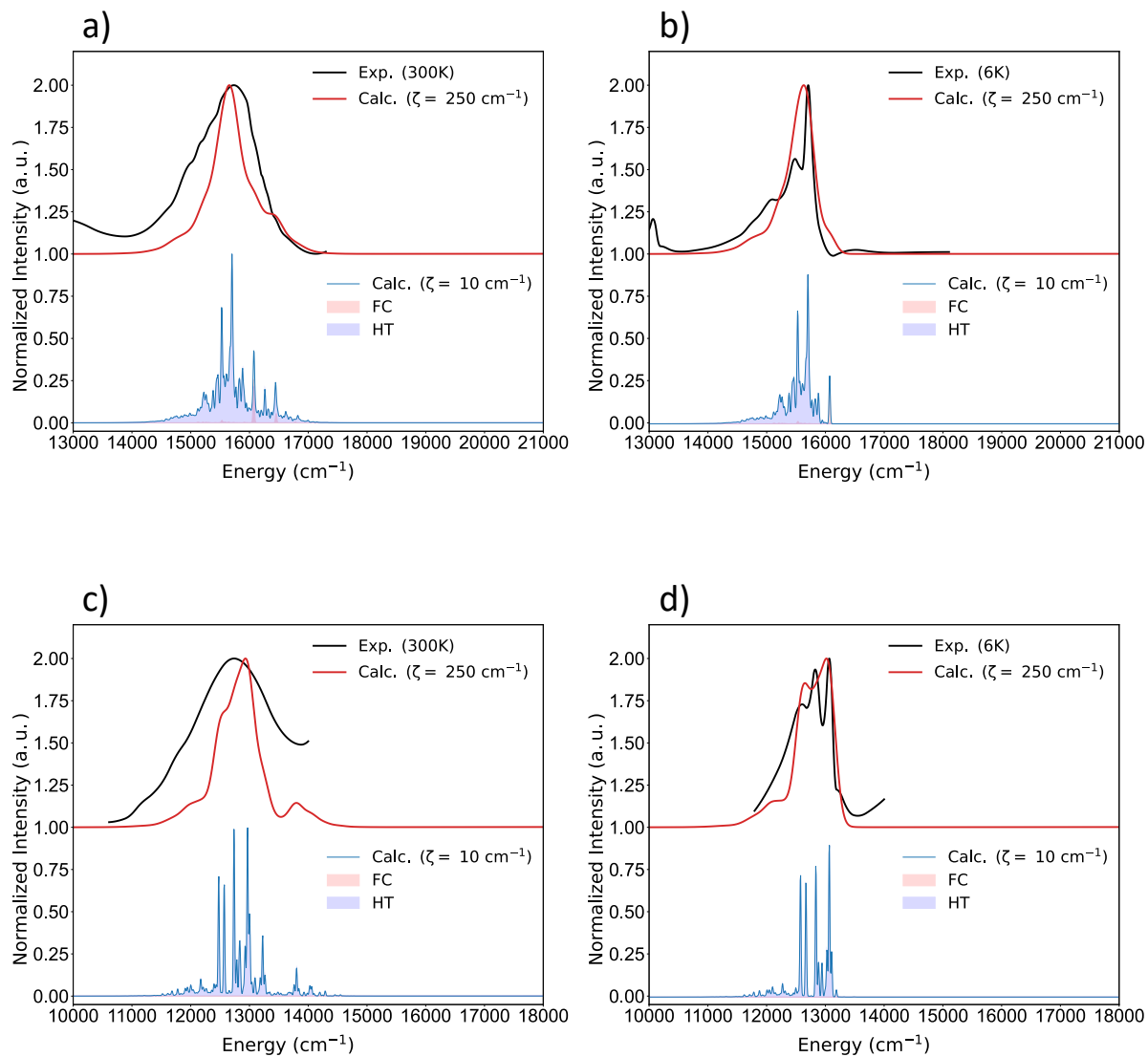


Figure A. 18. CBLA2:Eu²⁺ experimental (black) and calculated (Frank-Condon + Herzberg-Teller) luminescence spectra using gaussian broadening with 10 (red) and 250 (blue) cm⁻¹ linewidth at a) 300K and b) 6K for CBLA2:Eu²⁺ doped at Ba site while c) 300K and d) 6K for CBLA2:Eu²⁺ doped at Ca site. Also, the total contribution of FC and HT are given in red and blue fill using $\zeta = 10$ cm⁻¹, respectively.

B. Additional Information to PART III

Table B. 1. Calculated relevant structural parameters [bond distances in (Å) and angles in (°)], for PBE0 optimized structures for all the studied complexes (**1** and **2**), with available experimental data.[508]. The structure optimizations were conducted for the ground (S_0) state, first singlet (S_1), and first triplet (T_1) excited states. For each enantiomeric pair, the optimized structural parameters are identical. The halogen X is either Cl, or I, as depicted in the complex.

Complex	State	Re-X (Å)	Re-C _{carbene} (Å)	Re-N (Å)	Re-C _{ax-CO} (Å)	Re-C _{eq-CO} (Å)	X-Re-C _{ax-CO} (°)	N-C _{carbene-N} (°)	Helical angle (°)
1 C-Cl	exp.	2.51	2.12	2.20	1.91	1.95/1.92	176.65	106.72	--
	S_0	2.51	2.13	2.20	1.90	1.96/1.91	177.23	106.15	--
	T_1	2.45	2.11	2.09	1.95	1.98/1.98	173.00	106.87	--
	S_1	2.41	2.11	2.14	1.95	2.00/1.95	170.50	106.95	--
1 C-I	exp.	2.83	2.13	2.17	1.94	1.95/1.95	179.08	106.60	--
	S_0	2.85	2.13	2.20	1.90	1.96/1.92	178.67	106.20	--
	T_1	2.86	2.11	2.10	1.93	1.98/1.97	170.72	106.81	--
	S_1	2.77	2.11	2.15	1.94	2.00/1.94	164.20	106.95	--
2 M,A-Cl 2 P,C-Cl	exp.	Not Available							
	S_0	2.51	2.12	2.20	1.90	1.96/1.91	177.31	106.32	44.26
	T_1	2.51	2.11	2.20	1.90	1.96/1.91	177.67	106.49	44.25
	S_1	2.51	2.12	2.20	1.90	1.96/1.91	177.31	106.32	45.24
2 M,C-Cl 2 P,A-Cl	exp.	2.51	2.08	2.20	1.91	1.98/1.96	176.62	107.21	47.47
	S_0	2.51	2.12	2.20	1.91	1.96/1.91	177.39	106.43	44.09
	T_1	2.51	2.12	2.02	1.90	1.96/1.91	177.39	106.43	44.09
	S_1	2.51	2.13	2.21	1.90	1.96/1.91	176.94	106.25	45.42
2 M,A-I 2 P,C-I	exp.	Not Available							
	S_0	2.85	2.12	2.20	1.90	1.96/1.92	178.57	106.25	43.90
	T_1	2.85	2.11	2.20	1.90	1.96/1.92	178.84	106.46	44.88
	S_1	2.78	2.11	2.15	1.94	2.00/1.94	173.54	106.56	44.76
2 M,C-I 2 P,A-I	exp.	2.80	2.12	2.21	1.96	1.97/1.92	176.80	105.77	50.60
	S_0	2.81	2.12	2.20	1.90	1.96/1.92	178.36	106.21	45.69
	T_1	2.85	2.11	2.20	1.90	1.97/1.92	178.65	106.44	45.69
	S_1	2.85	2.12	2.20	1.90	1.96/1.92	178.36	106.21	44.55

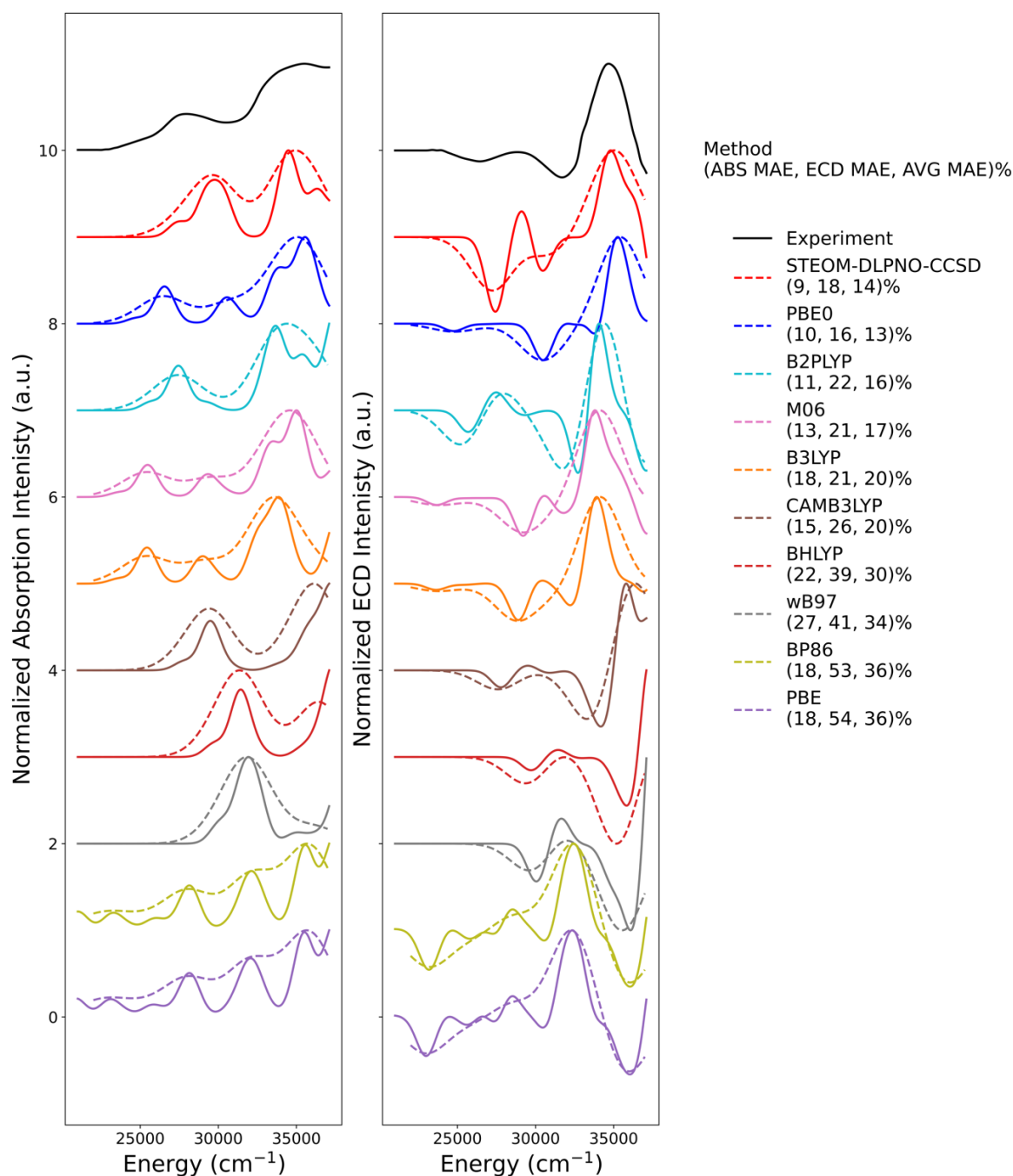


Figure B. 1. Experimental (black) vs. calculated non-relativistic STEOM-DLPNO-CCSD (red), non-relativistic TD-DFT/BP86 (olive), PBE (purple), BHLYP (pale red), PBE0 (blue), B3LYP (orange), M06 (pink), CAMB3LYP (brown), wB97 (gray), B2PLYP(cyan) ABS (left side) and ECD (right side) spectra of complex **1** A-Cl. Solid lines indicate constant Gaussian broadening of 1500 cm^{-1} while dotted lines indicate constant Gaussian broadening of 3000 cm^{-1} . Given in parenthesis are the %MAE errors with respect to experiment, for (ABS, ECD and their average).

Table B. 2. Calculated MAEs, from the experimental spectra, of all calculated spectra at different level of theory (STEOM-DLPNO-CCSD/SOC only for **1** A-Cl, as well as TD-DFT(PBE0 and B3LYP)/SOC for all studied complexes).

Complex	MAE = $\frac{ \text{Area}_{\text{Exp.}} - \text{Area}_{\text{Calc.}} }{\text{Area}_{\text{Exp.}}}$					
	STEOM-DLPNO-CCSD/SOC		PBE0/SOC		B3LYP/SOC	
	Absorption	ECD	Absorption	ECD	Absorption	ECD
1 A-Cl	0.04	0.02	0.14	0.22	0.35	0.44
1 C-Cl			0.14	0.24	0.36	0.43
1 A-I			0.28	0.35	0.32	0.40
1 C-I			0.24	0.36	0.31	0.41
2 M,A-Cl			0.08	0.15	0.12	0.34
2 P,C-Cl			0.08	0.15	0.12	0.33
2 M,C-Cl			0.07	0.12	0.11	0.23
2 P,A-Cl			0.07	0.09	0.11	0.24
2 M,A-I			0.06	0.11	0.16	0.30
2 P,C-I			0.07	0.12	0.15	0.32
2 M,C-I			0.11	0.23	0.18	0.35
2 P,A-I			0.11	0.17	0.18	0.35
Average MAE	0.04	0.02	0.12	0.19	0.21	0.34

B. Additional Information to PART III

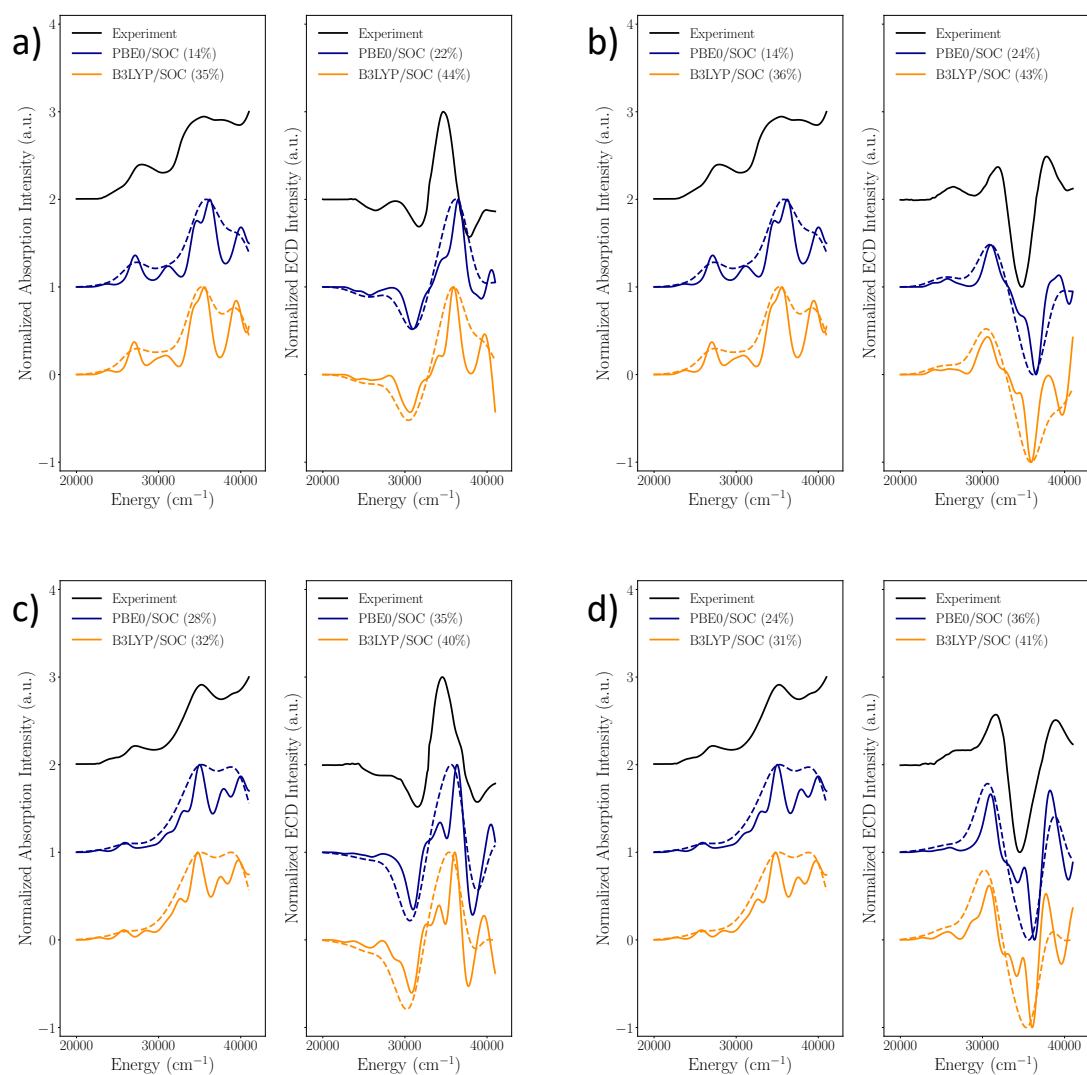


Figure B. 2. Experimental (black) versus calculated relativistically corrected Absorption and ECD spectra PBE0/TD-DFT (blue) and B3LYP/TD-DFT (orange) for non-helicene Complex 1 a) A-Cl b) C-Cl c) A-I and d) C-I. %MAE errors in comparison to experiment are provided in parenthesis. Solid lines indicate constant Gaussian broadening of 1500 cm⁻¹ while dotted lines indicate constant Gaussian broadening of 3000 cm⁻¹.

B. Additional Information to PART III

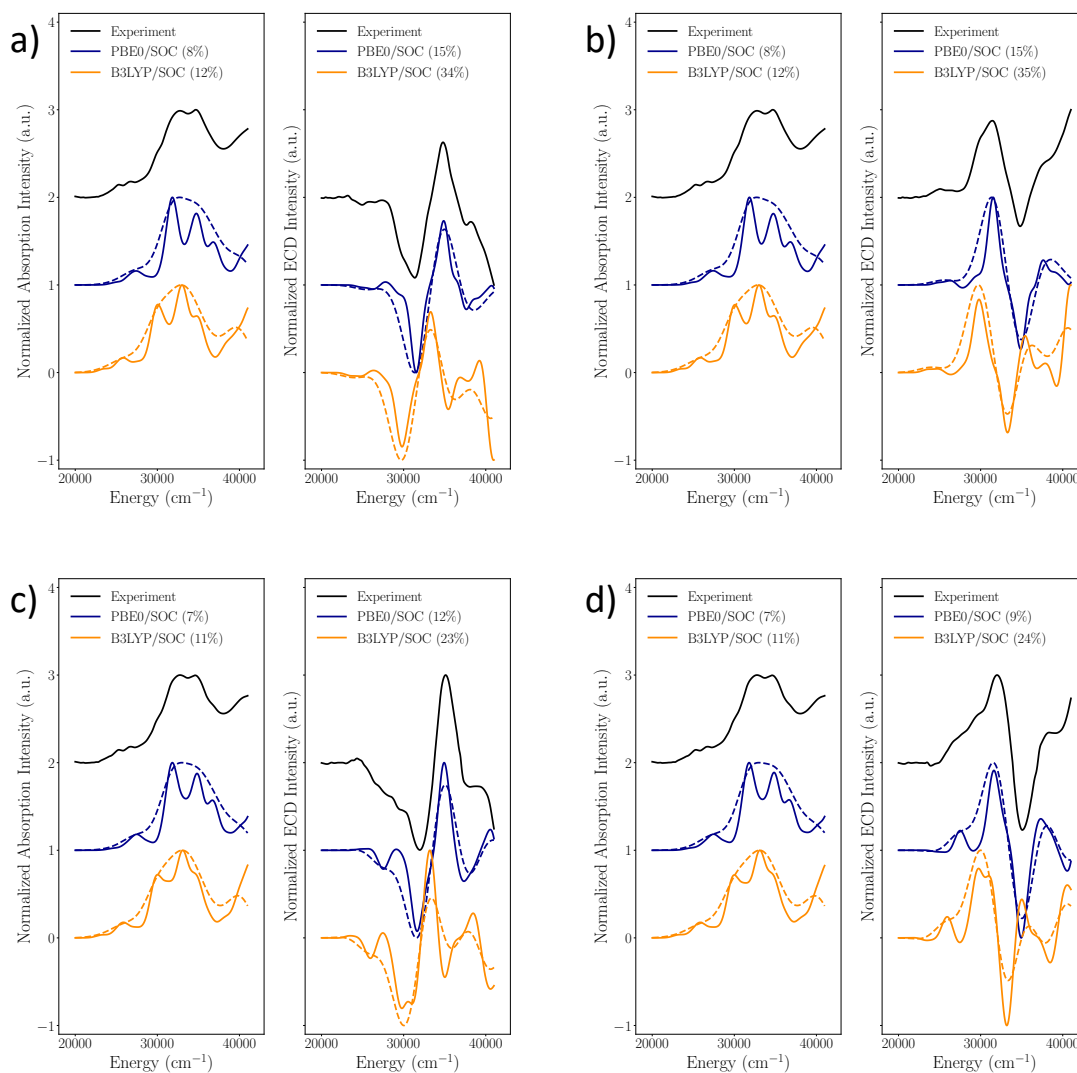


Figure B. 3. Experimental (black) versus calculated relativistically corrected Absorption and ECD spectra PBE0/TD-DFT (blue) and B3LYP/TD-DFT (orange) for helicene Complex **2** a) M,A-Cl b) P,C-Cl c) M,C-Cl d) P,A-Cl. %MAE errors in comparison to experiment are provided in parenthesis. Solid lines indicate constant Gaussian broadening of 1500 cm⁻¹ while dotted lines indicate constant Gaussian broadening of 3000 cm⁻¹.

B. Additional Information to PART III

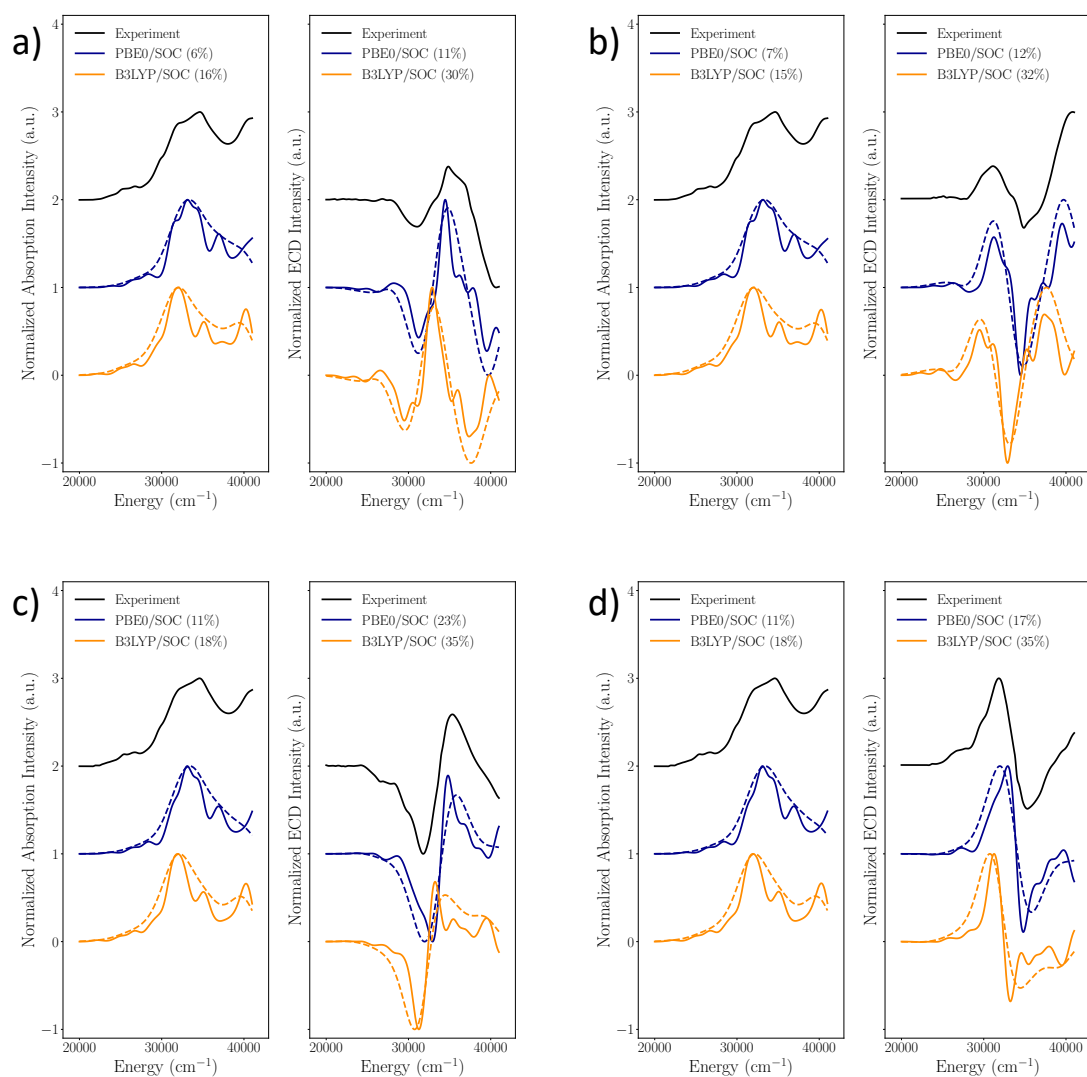


Figure B. 4. Experimental (black) versus calculated relativistically corrected Absorption and ECD spectra PBE0/TD-DFT (blue) and B3LYP/TD-DFT (orange) for helicene Complex **2** a) M,A-I b) P,C-I c) M,C-I d) P,A-I. %MAE errors in comparison to experiment are provided in parenthesis. Solid lines indicate constant Gaussian broadening of 1500 cm^{-1} while dotted lines indicate constant Gaussian broadening of 3000 cm^{-1} .

B. Additional Information to PART III

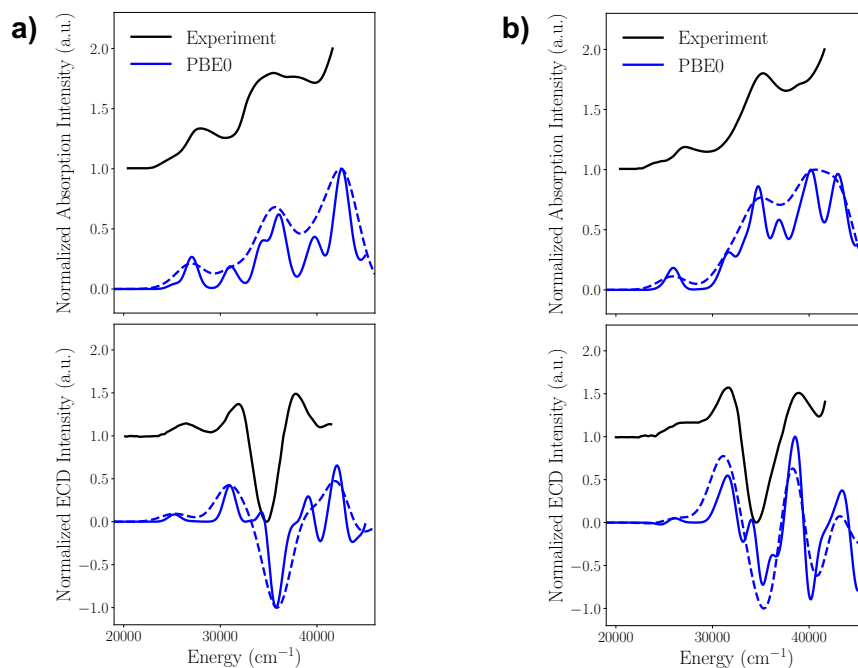


Figure B. 5. Experimental (black) PBE0/TD-DFT (blue) of Absorption and ECD spectra of non-helicene enantiomer a) **1** C-Cl and b) **1** C-I. Solid and dotted lines indicate constant Gaussian broadening of 1500 and 3000 cm⁻¹, respectively.

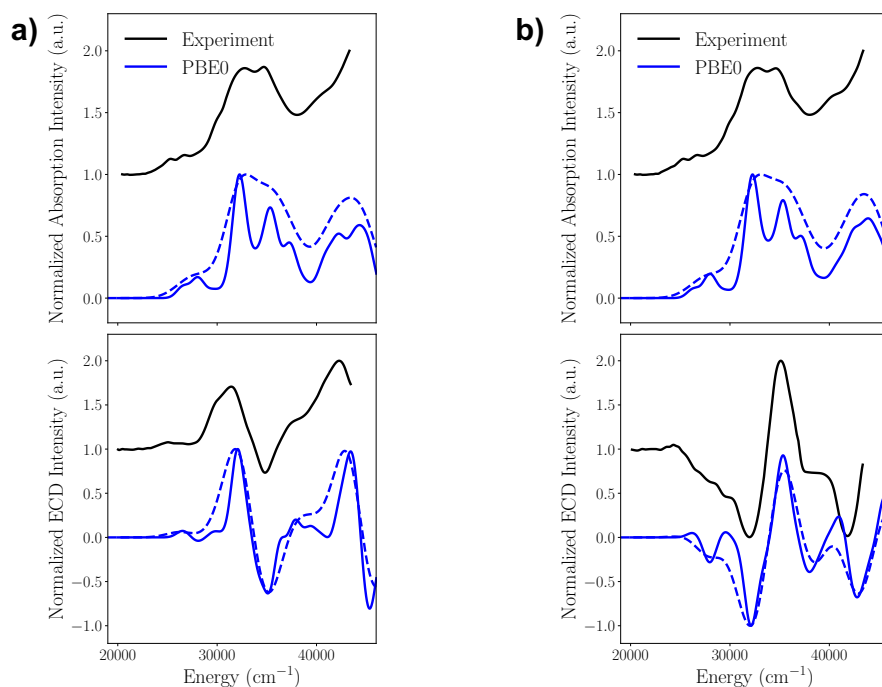


Figure B. 6. Experimental (black) PBE0/TD-DFT (blue) of Absorption and ECD spectra of helicene enantiomer a) **2** P,C-Cl and b) **2** M,C-Cl. Solid and dotted lines indicate constant Gaussian broadening of 1500 and 3000 cm⁻¹, respectively.

B. Additional Information to PART III

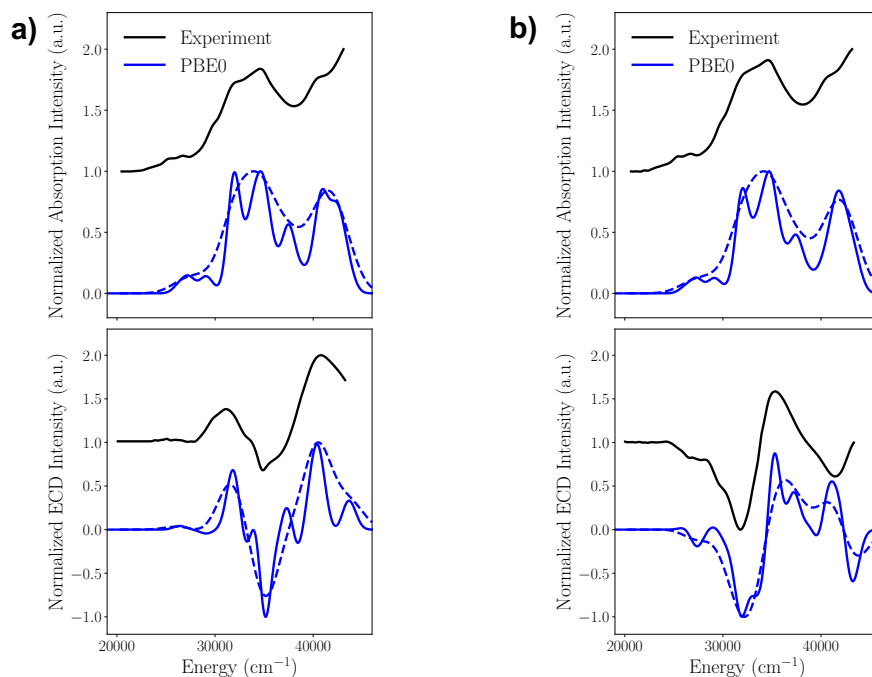


Figure B. 7. Experimental (black) PBE0/TD-DFT (blue) of Absorption and ECD spectra of non-helicene enantiomer a) a) **2** P,C-I and b) **2** M,C-I. Solid and dotted lines indicate constant Gaussian broadening of 1500 and 3000 cm^{-1} , respectively.

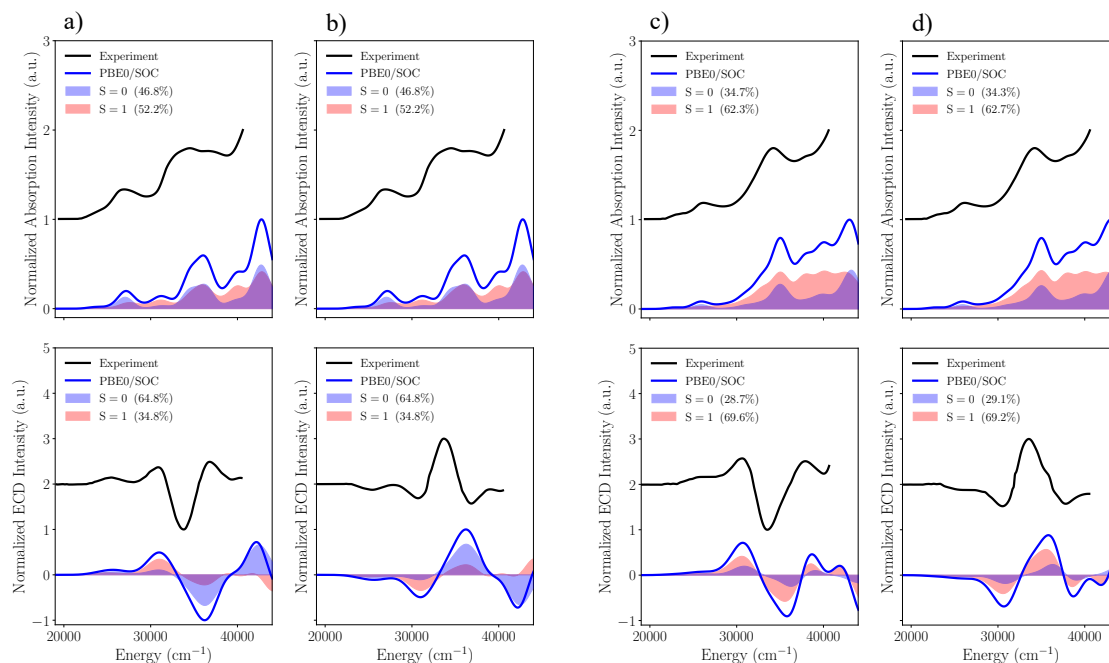


Figure B. 8. Experimental and Calculated relativistic absorption and CD spectra [PBE0/TD-DFT/SOC in blue] with singlet and triplet contributions in blue and red fill, respectively of non-helicene complex **1** as a) C-Cl b) A-Cl c) C-I d) A-I.

B. Additional Information to PART III

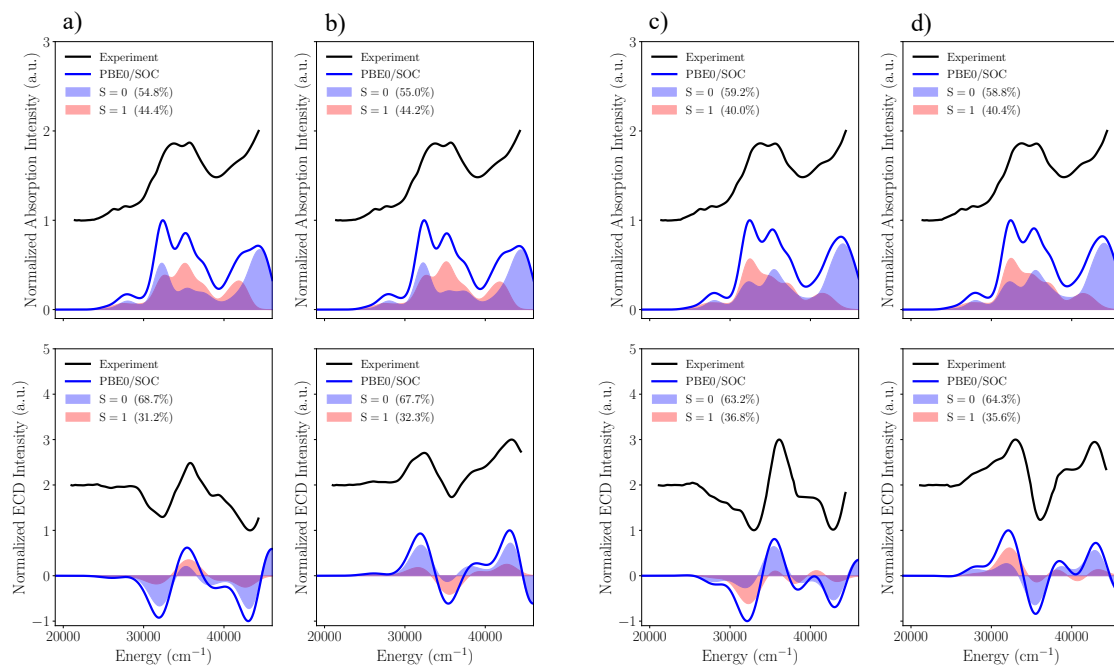


Figure B. 9. Experimental and Calculated relativistic absorption and CD spectra [PBE0/TD-DFT/SOC in blue] with singlet and triplet contributions in blue and red fill, respectively of Cl-substituted helicene complex **2** as a) M,A-Cl b) P,C-Cl c) M,C-I d) P,A-Cl.

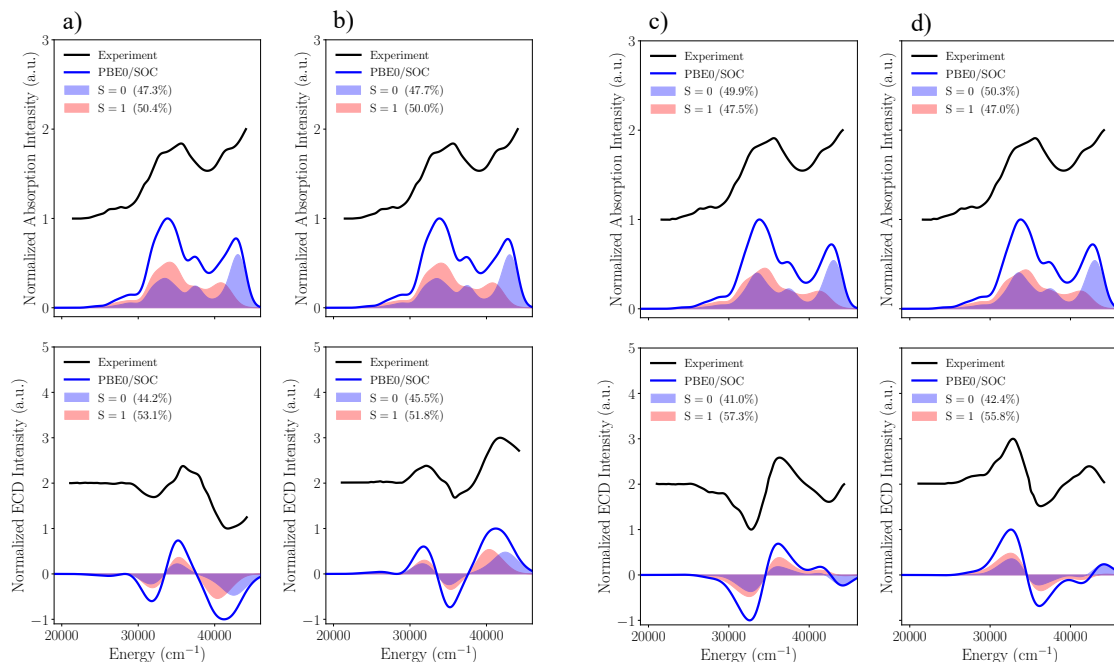


Figure B. 10. Experimental and Calculated relativistic absorption and CD spectra [PBE0/TD-DFT/SOC in blue] with singlet and triplet contributions in blue and red fill, respectively of Cl-substituted helicene complex **2** as a) M,A-Cl b) P,C-Cl c) M,C-I d) P,A-Cl.

B. Additional Information to PART III

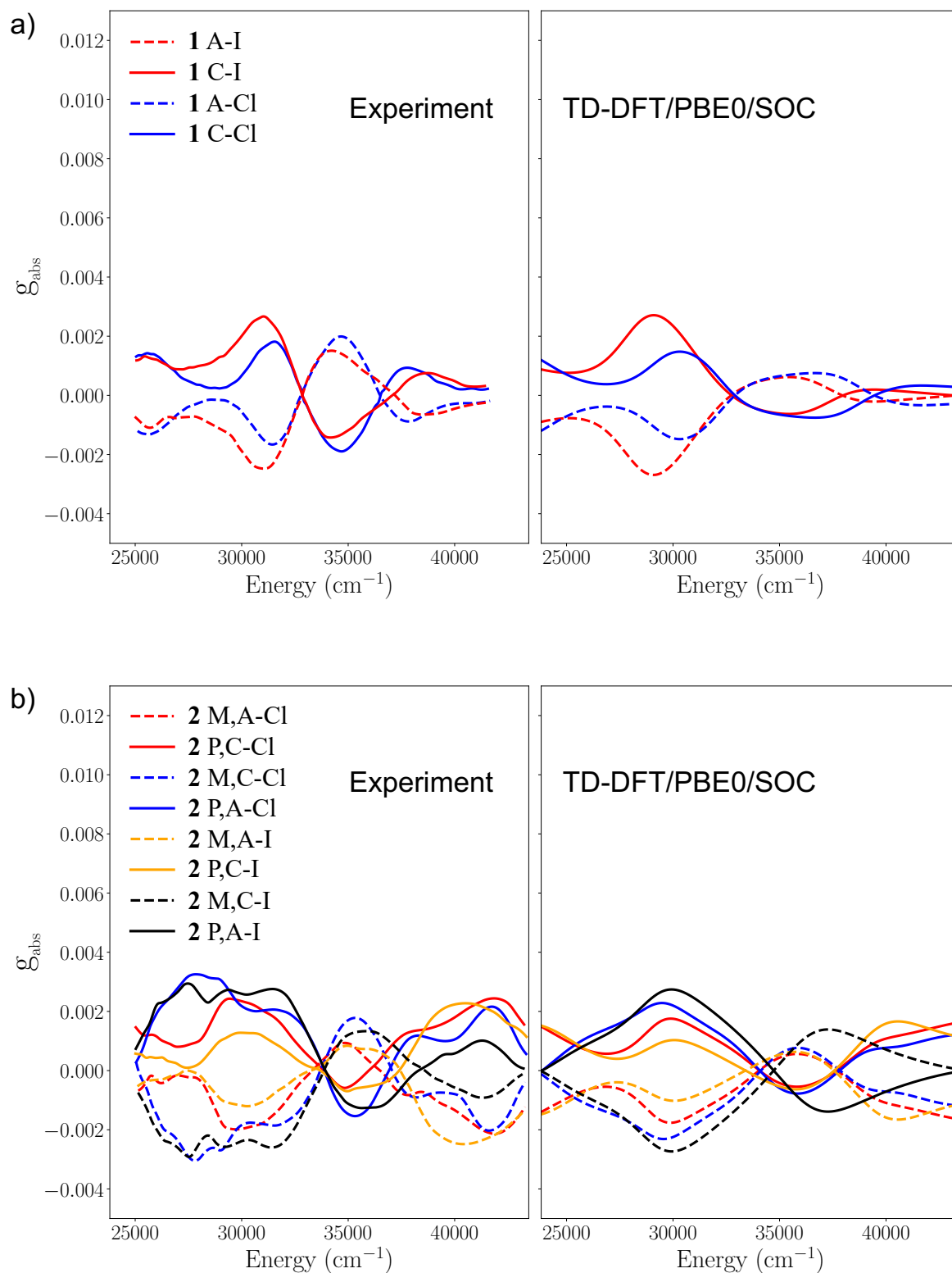


Figure B. 11. Experimental (left) versus calculated PBE0/TD-DFT/SOC g_{abs} of a) non-helicene diastereomeric structures **1** and b) Helicene diastereomeric structures **2**.

Table B. 3. Lowest 5 Singlet and Triplet SO-free states with corresponding transition energies (E in eV), oscillator strength (f), rotatory strength (R in 10^{40} cgs) and type of CT as extracted from NTO and TheoDORE analyses, calculated with TDDFT-PBE0 for complex **1** A-Cl.

States	E (eV)	$f(\times 10^{-3})$	R	NTO Character	TheoDORE Character
S ₁	3.255	16.40	8.44	MLCT/XLCT	MLCT _{pyr} /MLCT _{NHC} /XLCT/LLCT
S ₂	3.479	111.50	0.49	MLCT/XLCT	MLCT _{pyr} /MLCT _{NHC} /XLCT/LLCT
S ₃	3.707	2.20	-0.01	MLCT	MLCT _{pyr} /MLCT _{NHC} / LLCT
S ₄	3.969	75.70	35.3	LLCT	MLCT _{pyr} / XLCT/LLCT
S ₅	4.102	13.30	-4.25	LLCT	MLCT _{pyr} / XLCT/LLCT
T ₁	3.028	---	---		MLCT _{pyr} /MLCT _{NHC} /MLCT _{CO} /XLCT/LLCT _{pyr}
T ₂	3.149	---	---		MLCT _{pyr} /MLCT _{NHC} /MLCT _{CO} /XLCT/LLCT _{pyr}
T ₃	3.545	---	---		MLCT _{pyr} /MLCT _{NHC} /MLCT _{CO} /LLCT _{pyr}
T ₄	3.593	---	---		LC _{pyr} /LLCT _{pyr} /LC _{NHC}
T ₅	3.596	---	---		MLCT _{pyr} /LC _{NHC} /LLCT _{pyr}

Table B. 4. Lowest 5 Singlet and Triplet SO-free States with corresponding transition energies (E in eV), oscillator strength (f), rotatory strength (R in 10^{40} cgs) and type of CT as extracted from NTO and TheoDORE analyses, calculated with TDDFT-PBE0 for complex **1** A-I.

States	E (eV)	$f(\times 10^{-3})$	R	NTO Character	TheoDORE Character
S ₁	3.211	6.70	-4.05	MLCT/XLCT	XMLCT _{pyr} /MLCT _{pyr}
S ₂	3.344	55.90	7.37	MLCT/XLCT	XMLCT _{pyr} /MLCT _{pyr}
S ₃	3.709	1.90	-0.02	MLCT	MLCT _{pyr} /MLCT _{NHC} /MLCT _{CO}
S ₄	3.923	16.70	21.47	LLCT/XLCT	XLCT _{pyr} /MLCT _{pyr} /LLCT _{pyr}
S ₅	4.005	21.20	4.19	LLCT/XLCT	XLCT _{pyr} /LLCT _{pyr}
T ₁	3.022	---	---		XLCT _{pyr} /MLCT _{pyr} /MLCT _{NHC}
T ₂	3.092	---	---		XLCT _{pyr} /MLCT _{pyr} /MLCT _{NHC}
T ₃	3.481	---	---		LC _{NHC} /MLCT _{pyr} /LLCT _{pyr} /XLCT _{pyr}
T ₄	3.547	---	---		LC _{NHC} /MLCT _{pyr} /XLCT _{pyr} /LLCT _{pyr}
T ₅	3.595	---	---		XLCT _{pyr} /LC _{NHC} /LC _{pyr}

B. Additional Information to PART III

Table B. 5. Lowest 5 Singlet and Triplet SO-free States with corresponding transition energies (E in eV), oscillator strength (f), rotatory strength (R in 10^{40} cgs) and type of CT as extracted from NTO and TheoDORE analyses, calculated with TDDFT-PBE0 for complex **2** M,C-Cl.

States	E (eV)	$f(\times 10^{-3})$	R	NTO Character	TheoDORE Character
S ₁	3.142	44.70	16.69	MLCT/XLCT/ ILCT _{Helicene}	MLCT _{pyr,NHC,CO} /LC _{NHC} /LLCT _{pyr}
S ₂	3.346	114.80	-80.0	MLCT/XLCT/ ILCT _{Helicene}	MLCT _{pyr,NHC,CO} /LC _{NHC} /LLCT _{pyr} /XLCT _{pyr}
S ₃	3.513	18.20	13.6	ILCT _{Helicene}	LC _{NHC}
S ₄	3.568	16.60	15.94	ILCT _{Helicene}	LC _{NHC} /LLCT _{pyr} /MLCT _{pyr,NHC}
S ₅	3.618	2.90	- 14.01	ILCT _{Helicene}	MLCT _{pyr,NHC,CO} /LC _{NHC}
T ₁	2.333	---	---		LC _{NHC}
T ₂	2.878	---	---		LC _{NHC} /MLCT _{pyr,NHC,CO} /LLCT _{pyr}
T ₃	3.034	---	---		MLCT _{NHC,pyr,CO} /LLCT _{pyr} /XLCT _{pyr}
T ₄	3.073	---	---		LC _{NHC}
T ₅	3.209	---	---		LC _{NHC}

Table B. 6. Lowest 5 Singlet and Triplet SO-free States with corresponding transition energies (E in eV), oscillator strength (f), rotatory strength (R in 10^{40} cgs) and type of CT as extracted from NTO and TheoDORE analyses, calculated with TDDFT-PBE0 for complex **2** M,C-I.

States	E (eV)	$f(\times 10^{-3})$	R	NTO Character	TheoDORE Character
S ₁	3.126	29.60	8.65	MLCT/XLCT/ ILCT _{Helicene}	XLCT _{pyr} /MLCT _{pyr,NHC} /LC _{NHC}
S ₂	3.267	66.10	-51.37	MLCT/XLCT/ ILCT _{Helicene}	XLCT _{pyr} /MLCT _{pyr,NHC}
S ₃	3.477	62.30	9.25	ILCT _{Helicene}	LC _{NHC} /XLCT _{pyr} /LLCT _{pyr}
S ₄	3.552	9.50	4.94	ILCT _{Helicene}	LC _{NHC} /LLCT _{pyr}
S ₅	3.618	8.80	-23.51	ILCT _{Helicene}	LC _{NHC} /LLCT _{pyr} /MLCT _{NHC,pyr}
T ₁	2.331	---	---		LC _{NHC}
T ₂	2.892	---	---		LC _{NHC} /XLCT _{pyr}
T ₃	3.02	---	---		XLCT _{pyr} /MLCT _{NHC,pyr,CO}
T ₄	3.06	---	---		LC _{NHC}
T ₅	3.174	---	---		LC _{NHC}

Table B. 7. Lowest SOC corrected States (all states with energy $\leq 25000 \text{ cm}^{-1}$) with corresponding energies (E in cm^{-1}), oscillator strength (f), rotatory strength (R in 10^{40}cgs) and composition with respect to Ms characters, calculated with TDDFT/PBE0 for complex **1** C-Cl.

SOC States	E (eV)	$f(\times 10^{-3})$	R	Composition
0	0.000			99% $S_0(0)$
1	2.991	0.01	-0.00567	37% $T_1(-1)$ + 10% $T_2(-1)$ + 37% $T_1(1)$ + 10% $T_2(1)$
2	2.993	0.05	-0.07019	37% $T_1(-1)$ + 10% $T_2(-1)$ + 37% $T_1(1)$ + 10% $T_2(1)$
3	3.016	4.21	-0.30655	87% $T_1(0)$
4	3.098	5.33	2.98785	27% $S_1(0)$ + 64% $T_2(0)$
5	3.204	0.01	-0.01922	10% $T_1(-1)$ + 37% $T_2(-1)$ + 10% $T_1(1)$ + 37% $T_2(1)$
6	3.207	0.30	0.09311	10% $T_1(-1)$ + 38% $T_2(-1)$ + 10% $T_1(1)$ + 38% $T_2(1)$
7	3.312	10.73	5.4157	65% $S_1(0)$ + 30% $T_2(0)$
8	3.483	82.38	1.83379	71% $S_2(0)$ + 6% $T_1(0)$ + 5% $T_3(0)$ + 6% $T_4(-1)$ + 6% $T_4(1)$
9	3.564	0.00	0.00078	7% $T_3(0)$ + 6% $T_4(0)$ + 40% $T_3(-1)$ + 40% $T_3(1)$
10	3.568	0.06	-0.05746	7% $T_3(0)$ + 44% $T_3(-1)$ + 44% $T_3(1)$
11	3.573	7.16	-0.47547	7% $S_2(0)$ + 76% $T_3(0)$ + 7% $T_3(-1)$ + 7% $T_3(1)$
12	3.605	0.08	0.04653	19% $T_4(0)$ + 5% $T_5(0)$ + 29% $T_5(-1)$ + 29% $T_5(1)$
13	3.608	2.67	0.79317	65% $T_5(0)$ + 7% $T_4(-1)$ + 7% $T_4(1)$
14	3.614	0.28	0.07554	42% $T_5(-1)$ + 42% $T_5(1)$
15	3.648	1.34	0.22303	43% $T_4(0)$ + 14% $T_4(-1)$ + 9% $T_5(-1)$ + 14% $T_4(1)$ + 9% $T_5(1)$
16	3.653	1.10	-0.22302	21% $T_4(0)$ + 9% $T_5(0)$ + 25% $T_4(-1)$ + 7% $T_5(-1)$ + 25% $T_4(1)$ + 7% $T_5(1)$
17	3.658	8.69	-0.48791	10% $S_2(0)$ + 10% $T_5(0)$ + 35% $T_4(-1)$ + 35% $T_4(1)$
18	3.743	0.85	-0.24827	55% $S_3(0)$ + 12% $T_6(-1)$ + 7% $T_7(-1)$ + 12% $T_6(1)$ + 7% $T_7(1)$
19	3.751	0.75	-0.00221	10% $T_6(0)$ + 26% $T_6(-1)$ + 13% $T_7(-1)$ + 26% $T_6(1)$ + 13% $T_7(1)$
20	3.760	0.81	0.37078	35% $S_3(0)$ + 21% $T_6(-1)$ + 7% $T_7(-1)$ + 21% $T_6(1)$ + 7% $T_7(1)$

Table B. 8. Lowest SOC corrected States (all states with energy ≤ 25000 cm^{-1}) with corresponding energies (E in cm^{-1}), oscillator strength (f), rotatory strength (R in 10^{40}cgs) and composition with respect to Ms characters, calculated with TDDFT/PBE0 for complex **1** C-I.

SOC States	E (eV)	$f(\times 10^{-3})$	R	Composition
0	0.000			99% $S_0(0)$
1	2.893	0.06	0.07239	30% $T_1(-1)$ + 18% $T_2(-1)$ + 30% $T_1(1)$ + 18% $T_2(1)$
2	2.894	0.13	-0.04936	29% $T_1(-1)$ + 19% $T_2(-1)$ + 29% $T_1(1)$ + 19% $T_2(1)$
3	2.937	4.20	1.22106	16% $S_2(0)$ + 78% $T_1(0)$
4	2.962	2.17	0.0346	34% $S_1(0)$ + 60% $T_2(0)$
5	3.178	0.00	0.00794	18% $T_1(-1)$ + 29% $T_2(-1)$ + 18% $T_1(1)$ + 29% $T_2(1)$
6	3.192	3.95	2.31008	18% $T_1(-1)$ + 29% $T_2(-1)$ + 18% $T_1(1)$ + 29% $T_2(1)$
7	3.276	4.46	-1.52173	54% $S_1(0)$ + 33% $T_2(0)$
8	3.344	24.90	4.72195	65% $S_2(0)$ + 13% $T_1(0)$ + 8% $T_3(0)$
9	3.479	0.16	-0.02527	7% $T_4(0)$ + 38% $T_3(-1)$ + 38% $T_3(1)$
10	3.480	0.43	-0.07257	27% $T_3(0)$ + 24% $T_3(-1)$ + 9% $T_4(-1)$ + 24% $T_3(1)$ + 9% $T_4(1)$
11	3.509	5.32	-0.07696	6% $S_2(0)$ + 52% $T_3(0)$ + 17% $T_3(-1)$ + 17% $T_3(1)$
12	3.554	0.66	1.63165	45% $T_4(0)$ + 17% $T_4(-1)$ + 17% $T_4(1)$
13	3.566	0.06	-0.17033	20% $T_4(0)$ + 6% $T_5(0)$ + 7% $T_3(-1)$ + 22% $T_4(-1)$ + 7% $T_3(1)$ + 22% $T_4(1)$
14	3.577	2.62	-0.79556	7% $T_4(0)$ + 7% $T_3(-1)$ + 30% $T_4(-1)$ + 7% $T_3(1)$ + 30% $T_4(1)$
15	3.619	2.86	0.43404	41% $T_5(-1)$ + 41% $T_5(1)$
16	3.621	0.94	-0.28811	49% $T_5(0)$ + 15% $T_5(-1)$ + 15% $T_5(1)$
17	3.626	0.11	0.4212	7% $T_4(0)$ + 22% $T_5(0)$ + 23% $T_5(-1)$ + 23% $T_5(1)$
18	3.679	0.14	-0.2972	16% $T_6(-1)$ + 18% $T_7(-1)$ + 16% $T_6(1)$ + 18% $T_7(1)$
19	3.684	0.65	0.22927	11% $T_6(-1)$ + 22% $T_7(-1)$ + 5% $T_8(-1)$ + 11% $T_6(1)$ + 22% $T_7(1)$ + 5% $T_8(1)$
20	3.704	3.19	1.86317	6% $S_3(0)$ + 8% $S_5(0)$ + 27% $T_6(0)$ + 22% $T_7(0)$ + 6% $T_8(0)$

Table B. 9. Lowest SOC corrected States (all states with energy $\leq 25000 \text{ cm}^{-1}$) with corresponding energies (E in cm^{-1}), oscillator strength (f), rotatory strength (R in 10^{40}cgs) and composition with respect to Ms characters, calculated with TDDFT/PBE0 for complex **2** M,C-Cl.

SO-States	E (eV)	$f(\times 10^{-3})$	R	Composition
0	0.000			100% $S_0(0)$
1	2.343	0.001	0.00085	24% $T_1(0)$ + 38% $T_1(-1)$ + 38% $T_1(1)$
2	2.343	0.001	-0.00028	75% $T_1(0)$ + 12% $T_1(-1)$ + 12% $T_1(1)$
3	2.343	0.01	-0.00167	50% $T_1(-1)$ + 50% $T_1(1)$
4	2.858	0.01	-0.02337	42% $T_2(-1)$ + 42% $T_2(1)$
5	2.859	0.04	-0.14687	43% $T_2(-1)$ + 43% $T_2(1)$
6	2.869	1.35	-0.72987	92% $T_2(0)$
7	2.988	9.95	4.01739	23% $S_1(0)$ + 59% $T_3(0)$ + 9% $T_4(0)$
8	3.022	0.12	0.05051	33% $T_3(-1)$ + 9% $T_4(-1)$ + 33% $T_3(1)$ + 9% $T_4(1)$
9	3.023	0.07	-0.13635	34% $T_3(-1)$ + 8% $T_4(-1)$ + 34% $T_3(1)$ + 8% $T_4(1)$
10	3.060	1.45	-0.24603	6% $S_1(0)$ + 23% $T_3(0)$ + 63% $T_4(0)$
11	3.096	0.00	-0.00801	8% $T_3(-1)$ + 39% $T_4(-1)$ + 8% $T_3(1)$ + 39% $T_4(1)$
12	3.098	0.26	0.02747	9% $T_3(-1)$ + 38% $T_4(-1)$ + 9% $T_3(1)$ + 38% $T_4(1)$
13	3.155	11.65	4.2646	39% $S_1(0)$ + 7% $T_3(0)$ + 22% $T_4(0)$ + 25% $T_5(0)$
14	3.223	10.26	1.36976	8% $S_1(0)$ + 39% $T_5(0)$ + 21% $T_5(-1)$ + 21% $T_5(1)$
15	3.226	0.25	-0.01313	46% $T_5(-1)$ + 46% $T_5(1)$
16	3.229	18.91	1.49625	19% $S_1(0)$ + 24% $T_5(0)$ + 24% $T_5(-1)$ + 24% $T_5(1)$
17	3.301	4.67	-1.93373	91% $T_6(0)$
18	3.302	0.01	-0.00067	47% $T_6(-1)$ + 47% $T_6(1)$
19	3.302	0.26	-0.0516	50% $T_6(-1)$ + 50% $T_6(1)$
20	3.351	78.41	-55.9888	71% $S_2(0)$ + 8% $T_5(0)$

Table B. 10. Lowest SOC corrected States (all states with energy ≤ 25000 cm^{-1}) with corresponding energies (E in cm^{-1}), oscillator strength (f), rotatory strength (R in 10^{40}cgs) and composition with respect to Ms characters, calculated with TDDFT/PBE0 for complex **2** M,C-I.

SOC States	E (eV)	$f(\times 10^{-3})$	R	Composition
0	0.000			100% $S_0(0)$
1	2.347	0.001	0.00182	50% $T_1(-1)$ + 50% $T_1(1)$
2	2.347	0.03	0.00836	8% $T_1(0)$ + 46% $T_1(-1)$ + 46% $T_1(1)$
3	2.347	0.00	-0.00474	92% $T_1(0)$
4	2.818	0.08	-0.01383	30% $T_2(-1)$ + 12% $T_3(-1)$ + 30% $T_2(1)$ + 12% $T_3(1)$
5	2.818	0.06	-0.05205	30% $T_2(-1)$ + 13% $T_3(-1)$ + 30% $T_2(1)$ + 13% $T_3(1)$
6	2.845	2.04	0.10281	10% $S_2(0)$ + 79% $T_2(0)$
7	2.894	7.62	2.66297	34% $S_1(0)$ + 50% $T_3(0)$ + 9% $T_4(0)$
8	2.988	0.00	-0.00265	17% $T_2(-1)$ + 19% $T_3(-1)$ + 9% $T_4(-1)$ + 17% $T_2(1)$ + 19% $T_3(1)$ + 9% $T_4(1)$
9	2.990	0.77	0.00939	17% $T_2(-1)$ + 18% $T_3(-1)$ + 11% $T_4(-1)$ + 17% $T_2(1)$ + 18% $T_3(1)$ + 11% $T_4(1)$
10	3.020	1.12	-0.66316	8% $S_2(0)$ + 13% $T_2(0)$ + 20% $T_3(0)$ + 43% $T_4(0)$ + 7% $T_5(0)$
11	3.100	0.01	-0.02936	9% $T_3(-1)$ + 32% $T_4(-1)$ + 9% $T_3(1)$ + 32% $T_4(1)$
12	3.105	0.92	0.1013	9% $T_3(-1)$ + 33% $T_4(-1)$ + 6% $T_5(-1)$ + 9% $T_3(1)$ + 33% $T_4(1)$ + 6% $T_5(1)$
13	3.132	1.18	0.1671	10% $S_1(0)$ + 33% $T_4(0)$ + 37% $T_5(0)$
14	3.181	12.50	4.21576	20% $S_1(0)$ + 6% $S_2(0)$ + 8% $T_3(0)$ + 15% $T_5(0)$ + 16% $T_5(-1)$ + 16% $T_5(1)$
15	3.196	0.11	-0.04924	7% $T_5(0)$ + 7% $T_3(-1)$ + 35% $T_5(-1)$ + 7% $T_3(1)$ + 35% $T_5(1)$
16	3.222	17.25	-1.03966	22% $S_1(0)$ + 5% $S_2(0)$ + 11% $T_3(0)$ + 21% $T_5(-1)$ + 21% $T_5(1)$
17	3.286	12.60	-11.82175	36% $S_2(0)$ + 17% $T_5(0)$ + 15% $T_6(0)$ + 6% $T_6(-1)$ + 6% $T_6(1)$
18	3.305	0.00	-0.00045	38% $T_6(0)$ + 30% $T_6(-1)$ + 30% $T_6(1)$
19	3.305	0.62	-0.11969	49% $T_6(-1)$ + 49% $T_6(1)$
20	3.313	4.07	-4.48478	14% $S_2(0)$ + 45% $T_6(0)$ + 14% $T_6(-1)$ + 14% $T_6(1)$

B. Additional Information to PART III

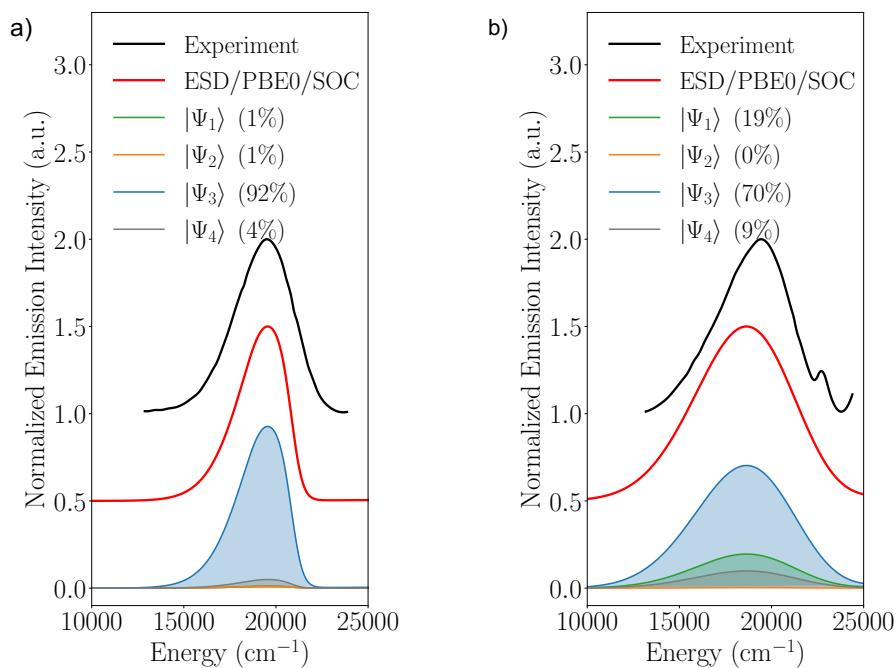


Figure B. 12. Experimental and calculated emission spectra (ESD/PBE0/TD-DFT/SOC) of non-helicene complex **1** a) C-Cl b) C-Cl.

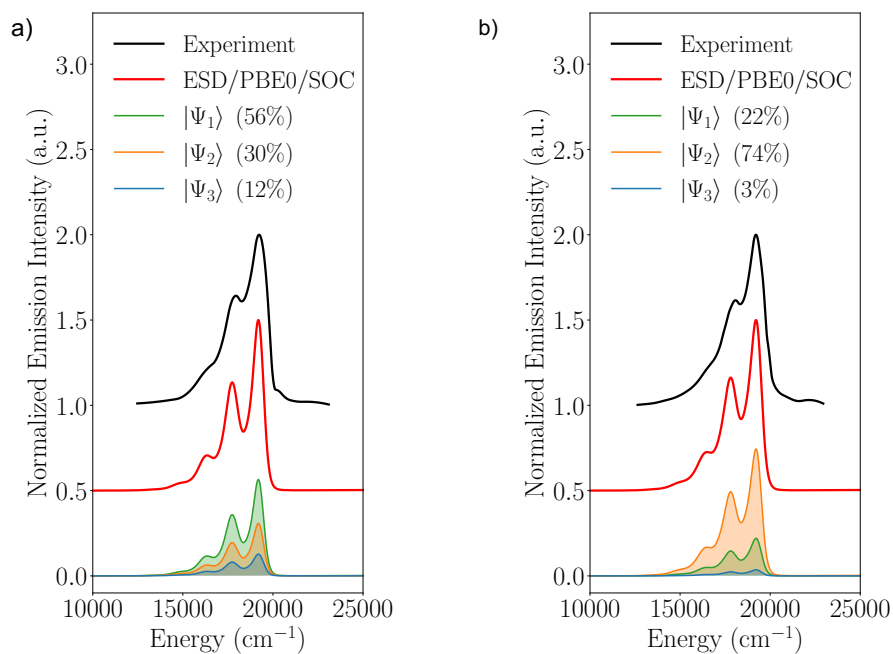


Figure B. 13. Experimental and calculated emission spectra (ESD/PBE0/TD-DFT/SOC) of helicene I-substituted complex **2** a) M,A-I b) P,A-I.

B. Additional Information to PART III

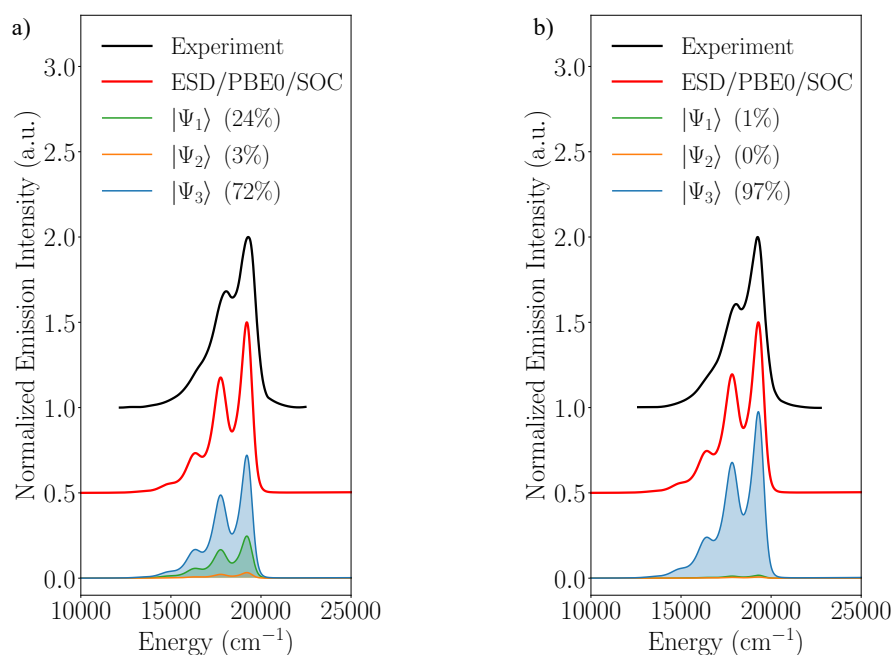


Figure B. 14. Experimental and calculated emission spectra (ESD/PBE0/TD-DFT/SOC) of helicene I-substituted complex **2** a) P,C-Cl b) M,C-Cl.

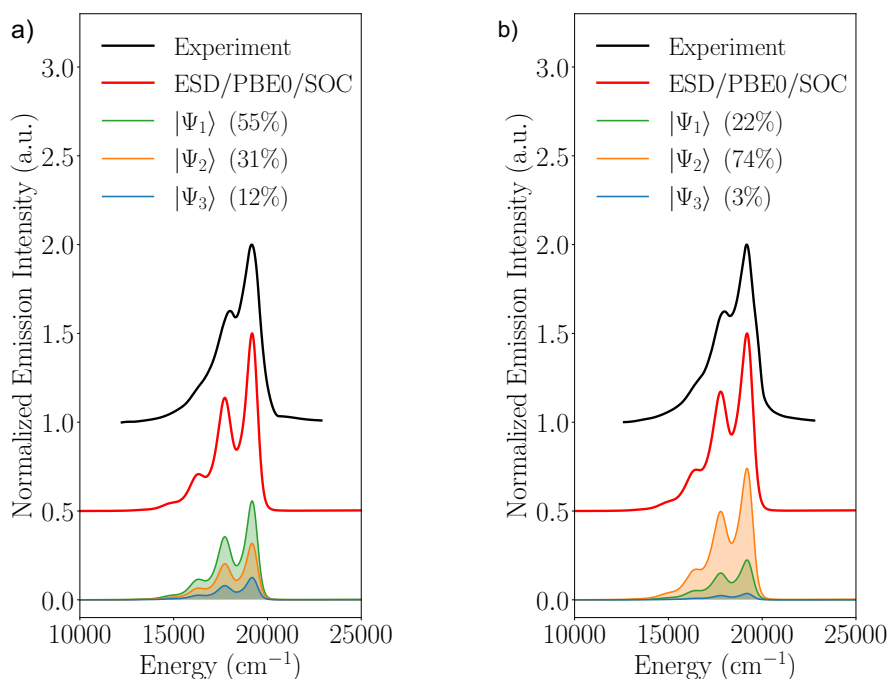


Figure B. 15. Experimental and calculated emission spectra (ESD/PBE0/TD-DFT/SOC) of helicene I-substituted complex **2** a) P,C-I b) M,C-I.

B. Additional Information to PART III

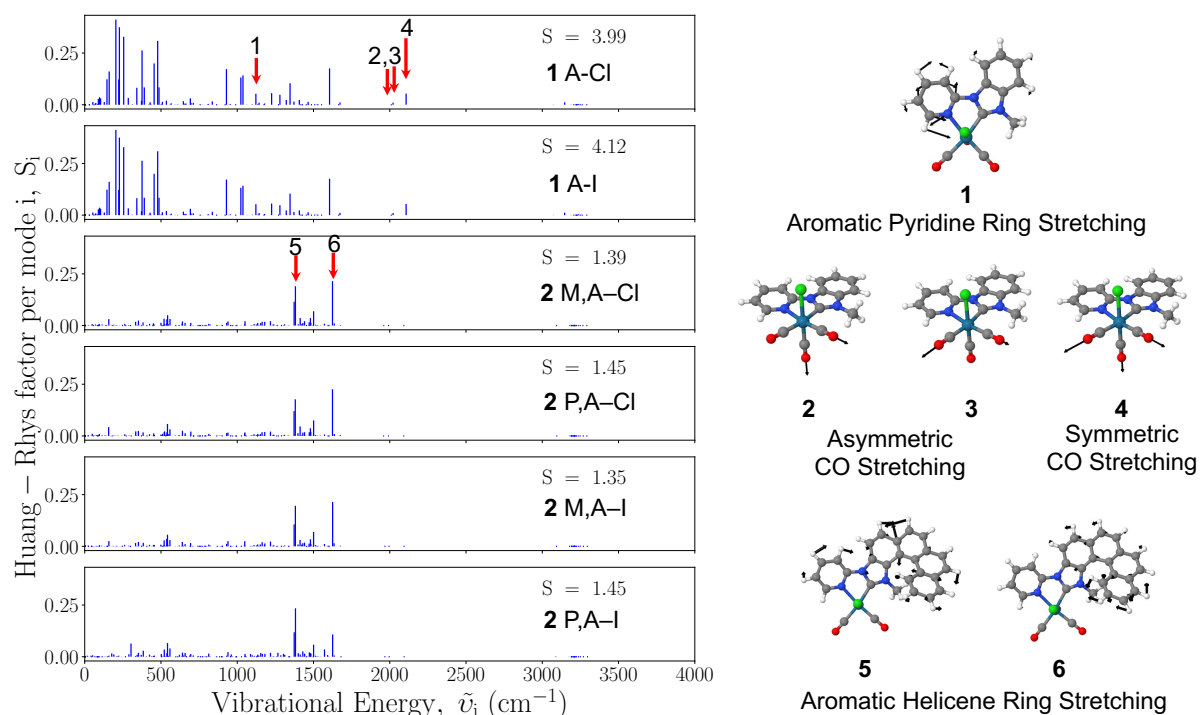


Figure B. 16. PBE0/TD-DFT computed Huang-Rhys factor (S_i) distribution over the entire set of the vibrational normal modes with energies ($\tilde{\nu}_i$ in wavenumbers, cm^{-1}) for a selected set of diastereomers **1** and **2**. The Huang-Rhys factor (S) of the phosphoresce relaxation transition (defined as $S = \sum_i S_i$) is shown in top right of each case. Red arrows indicate the selected vibrations modes (1-6) for the SA-CASSCF, SA-CASSCF/NEVPT2 and SA-CASSCF/QD-NEVPT2 PES scans. Modes 1-6 are visualized on the right.

B. Additional Information to PART III

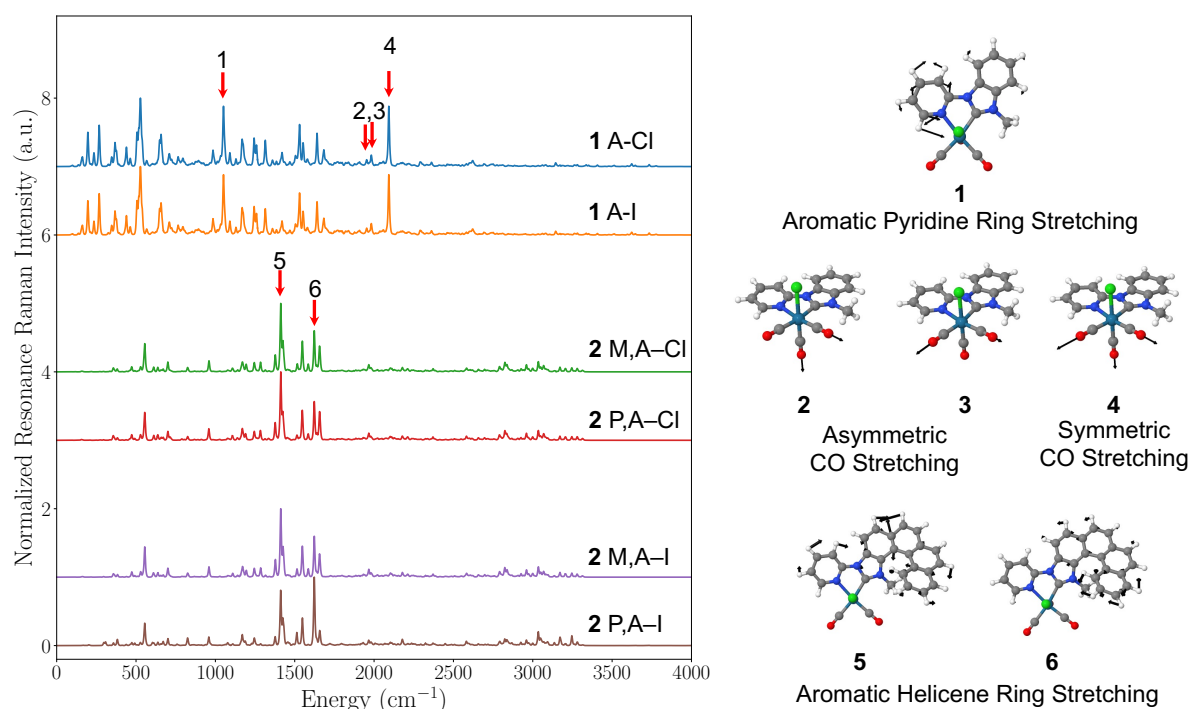


Figure B. 17. PBE0/TD-DFT computed resonance Raman (rR) spectra for a selected set of diastereomers **1** and **2**. The laser energy was set to the phosphorescence relaxation transition energies (2.30 eV and 2.65 eV) of diastereomers **1** and **2**, respectively. Red arrows indicate the selected vibrations modes (1-6) for the SA-CASSCF, SA-CASSCF/NEVPT2 and SA-CASSCF/QD-NEVPT2 PES scans. Modes 1-6 are visualized on the right.

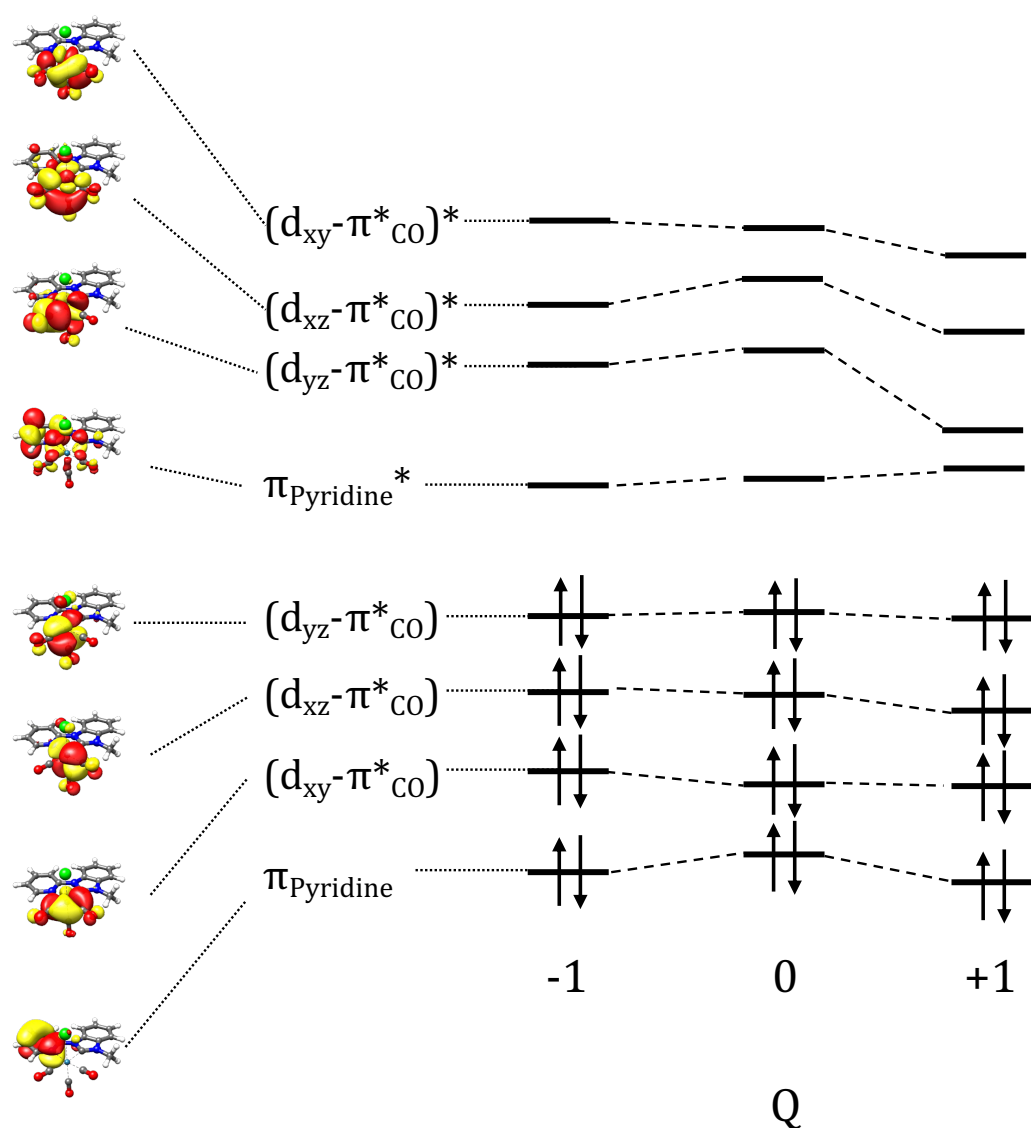


Figure B. 18. Molecular orbital diagram of CASSCF(8,8) orbitals along the asymmetric CO stretching mode's normal coordinate at $Q=-1, 0, 1$ (pointing to a step-before, at, and step-after the equilibrium geometry, respectively) for complex **1** A-Cl of the geometries.

B. Additional Information to PART III

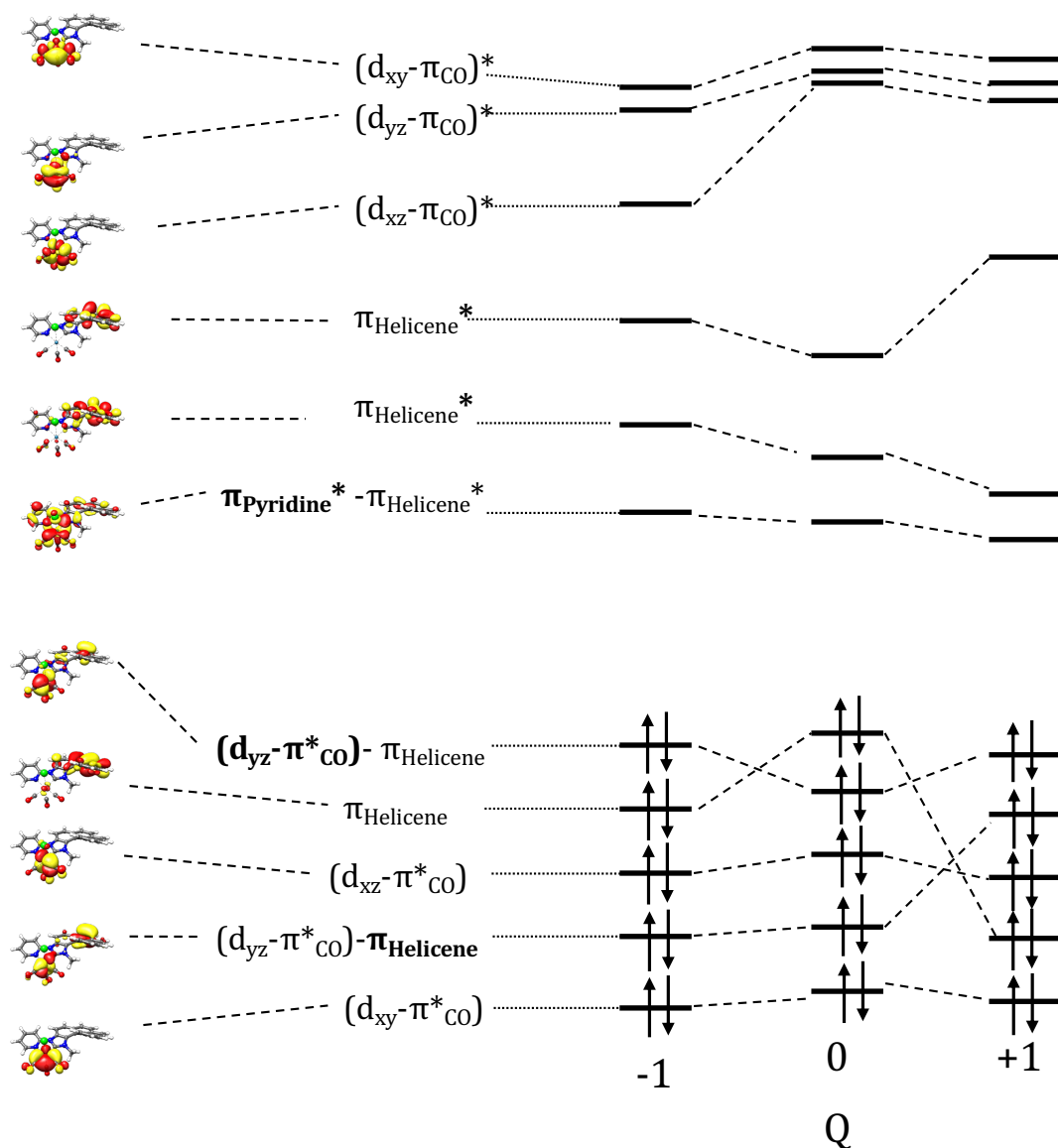


Figure B. 19. Molecular orbital diagram of CASSCF(10,11) orbitals along the asymmetric C=C ring stretching mode's normal coordinate at $Q=-1, 0, 1$ (pointing to a step-before, at, and step-after the equilibrium geometry, respectively) for complex 2 M,A-Cl of the geometries.

B. Additional Information to PART III

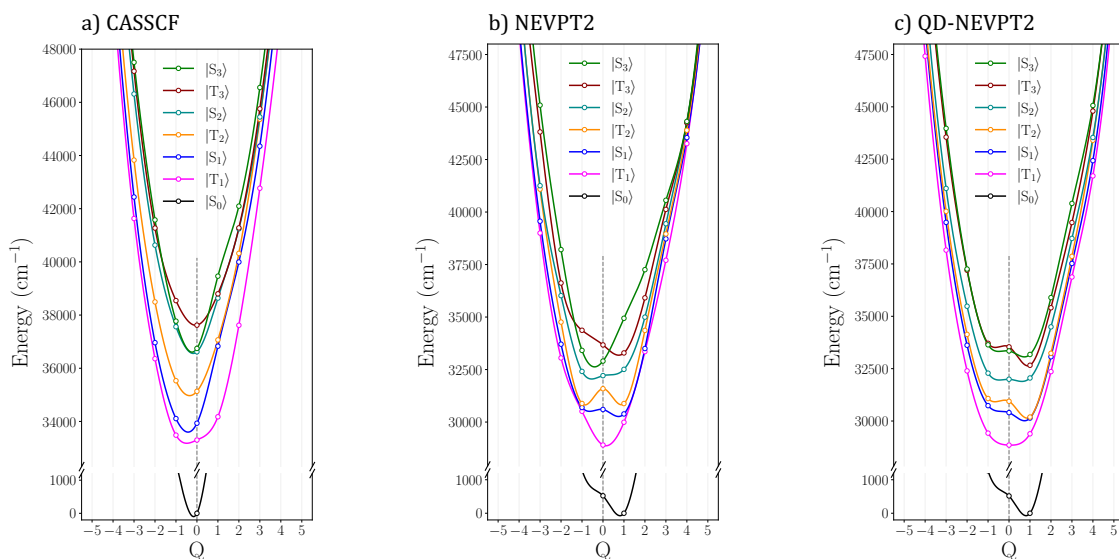


Figure B. 20. Computed non-relativistic PES complex **1** A-Cl along the asymmetric CO stretching mode's normal coordinate (Q) at different level of theory a) CASSCF(8,8) b) CASSCF/NEVPT2 c) CASSCF/QD-NEVPT2.

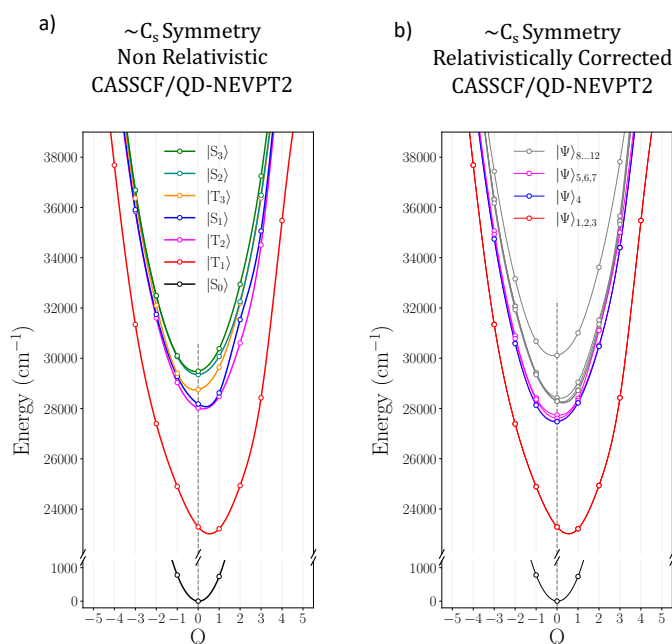


Figure B. 21. SA-CASSCF(10,11)/QD-NEVPT2 PES scan along a chosen modes representing antisymmetric stretching helicene vibrations for **2** M,A-I a) for the ‘actual’ C_s symmetry around Re(I) in the non-relativistic limit and b) for the ‘actual’ C_s symmetry around Re(I) including relativistic SOC corrections.

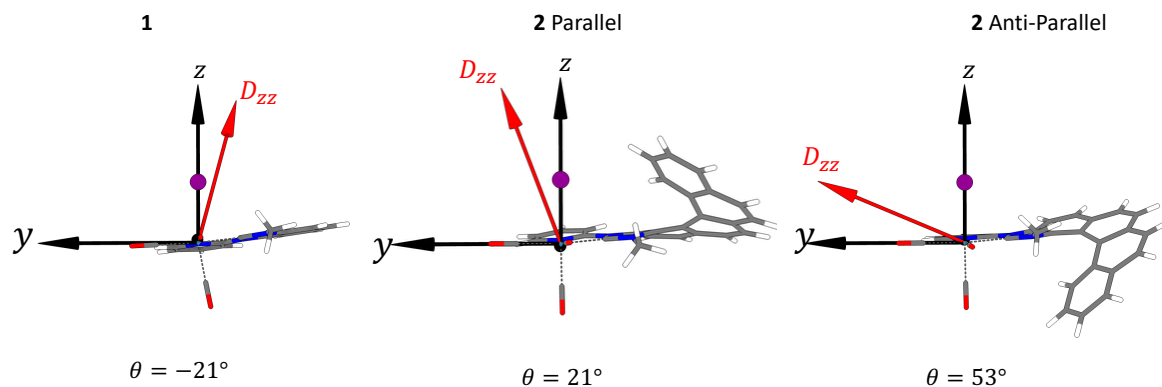


Figure B. 22. SA-CASSCF/QD-NEVPT2 computed D_{zz} magnetic vectors of excited state D tensors, based on the excited ZFS calculated employing the effective Hamiltonian of excited SOC $|\Psi_{1-3}\rangle$ states and its angle from the reference magnetic axis in the ground $|\Psi_0\rangle$ SOC state (aligned with z -axis) for a) complex **1 A-I**, b) ‘parallel’ complex **2 MA-I** and c) ‘anti-parallel’ complex **2 PA-I**

B. Additional Information to PART III

Table B. 11. Experimental and ESD/TD-DFT/PBE0+SOC calculated radiative and non-radiative relaxation rates and phosphorescence times (μs) at 295K. Relativistic ground and lowest excited SOC states with corresponding energies and composition with respect to M_S characters.

Complex	SOC State	SOC State Composition	Energy (cm ⁻¹)	k _r	k _r	t	k _r	k _r	k _{nr}	k _{nr}	Φ	t
				(s ⁻¹)	(s ⁻¹)	(μs)	(s ⁻¹)	(s ⁻¹)	(s ⁻¹)	(s ⁻¹)	(× 10 ²)	(μs)
				77K			295K					
2 M,A-I	Ψ ₀ ⟩	99% S ₀ (0)	0									
	Ψ ₁ ⟩	98% T ₁ (±1)	18880	202			277		34306			
	Ψ ₂ ⟩	17% T ₁ (0) + 82%	18880	110			151		18681			
		T ₁ (±1)			119	8395		163		20245	0.8	49
	Ψ ₃ ⟩	82% T ₁ (0) + 16%	18880	46			62		7747			
		T ₁ (±1)										
2 P,A-I	Ψ ₀ ⟩	99% S ₀ (0)	0									
	Ψ ₁ ⟩	98% T ₁ (±1)	18924	110			117		14559			
	Ψ ₂ ⟩	6% T ₁ (0) + 92% T ₁ (±1)	18924	372	166	6010	397	178	49223	22044	0.8	45
	Ψ ₃ ⟩	92% T ₁ (0)	18924	18			19		2352			
2 M,A-Cl	Ψ ₀ ⟩	99% S ₀ (0)	0									
	Ψ ₁ ⟩	73% T ₁ (0) + 26%	18853	108			102		915			
		T ₁ (±1)										
	Ψ ₂ ⟩	6% T ₁ (0) + 92% T ₁ (±1)	18853	15	151	6626	14	143	126	1284	10.0	701
	Ψ ₃ ⟩	20% T ₁ (0) + 78%	18853	330			312		2811			
		T ₁ (±1)										
Continued in the next page												

B. Additional Information to PART III

Complex	SOC State	SOC State Composition	Energy (cm ⁻¹)	k _r	k _r	t	k _r	k _r	k _{nr}	k _{nr}	Φ	t
				(s ⁻¹)	(s ⁻¹)	(μs)	(s ⁻¹)	(s ⁻¹)	(s ⁻¹)	(s ⁻¹)	(× 10 ²)	(μs)
				77K			295K					
2 P,A-Cl	Ψ ₀ ⟩	99% S ₀ (0)	0									
	Ψ ₁ ⟩	26% T ₁ (0) + 72% T ₁ (±1)	18881	9			13		200			
	Ψ ₂ ⟩	73% T ₁ (0) + 26% T ₁ (±1)	18881	4	184	5427	5	139	81	2171	6.0	433
	Ψ ₃ ⟩	98% T ₁ (±1)	18881	541			398		6231			
1 A-I	Ψ ₀ ⟩	99% S ₀ (0)	0									
	Ψ ₁ ⟩	58% T ₁ (±1) + 34% T ₂ (±1)	23324	394898			3629		2588374			
	Ψ ₂ ⟩	58% T ₁ (±1) + 36% T ₂ (±1)	23336	6543	227276	4.4	60	7368	42885	5.5× 10 ⁶	0.14	0.19
	Ψ ₃ ⟩	15% S ₂ (0) + 77% T ₁ (0)	23676	6532046			60025		42814694			
	Ψ ₄ ⟩	33% S ₁ (0) + 59% T ₂ (0)	23887				25643		18290541			
1 A-Cl	Ψ ₀ ⟩	99% S ₀ (0)	0									
	Ψ ₁ ⟩	72% T ₁ (±1) + 18% T ₂ (±1)	24123	88154			8314		407385			
	Ψ ₂ ⟩	74% T ₁ (±1) + 18% T ₂ (±1)	24143	80698	312500	3.2	7611	285714	372930	1.4× 10 ⁷	2.00	0.07
	Ψ ₃ ⟩	10% S ₂ (0) + 87% T ₁ (0)	24326	17354432			1636738		80200153			
	Ψ ₄ ⟩	26% S ₁ (0) + 63% T ₂ (0)	24990				2185367		107083000			

B. Additional Information to PART III

Table B. 12. Calculated versus available experimental normalized dissymmetry factors (g_{lum}) of CPL for complexes **2** and **1**. Electronic transition properties are given, in terms of transition electric dipole ($D = |\mu|^2$), magnetic dipole ($M = |m|^2$) and rotatory ($R = -|\mu||m|\cos\theta$) strengths. μ, m, θ° are transition electric and magnetic dipole moments and angle between them, respectively.

Complex	$D = \mu ^2$ / 10^{-40} $esu^2.cm^2$	$M = m ^2$ / 10^{-40} $erg^2.G^{-2}$	$R = - \mu m \cos\theta$ / 10^{-40} $esu.cm.erg.G^{-1}$	θ°	Calc. / 10^{-2} $g_{lum} = -4R/D \cdot M$	Exp. / 10^{-2} g_{lum}	Normalized Calc. g_{lum}	Normalized Exp. g_{lum}
2 M,A-I	212	0.0001	-0.0022	79	0.4	0.1	0.03	0.02
2 P,C-I	214	0.0001	0.0014	79	-0.3	-0.1	-0.02	-0.02
2 M,C-I	212	0.0002	0.1502	36	13.0	-4.5	-0.84	-0.90
2 P,A-I	216	0.0002	-0.1484	39	-12.9	4.5	0.83	0.90
2 M,A-Cl	102	0.0001	-0.0150	60	5.7	2	0.34	0.40
2 P,C-Cl	102	0.0001	0.0150	57	-5.7	-2	-0.35	-0.40
2 M,C-Cl	129	0.0001	0.0740	34	15.8	-5	-1.00	-1.00
2 P,A-Cl	137	0.0002	-0.0801	42	-15.5	5	1.00	1.00
1 A-Cl	45847	0.0252	3.2293	54	0.01	0.1	-0.001	-0.20
1 C-Cl	45847	0.0252	-3.2270	54	-0.01	-0.1	0.001	0.20

Table B. 13. SA-CASSCF/QD-NEVPT2 computed axial and rhombic excited state multiplet ZFS parameters (D (cm^{-1}) and E/D) at equilibrium and minimum energy geometries together with the respective axial and rhombic spin-vibronic coupling constants ξ_D (cm^{-1}) and ξ_E along a selected set of vibrational normal modes for A-Cl/I diastereomers **1** and **2**.

Complex	CAS (m,n)	Mode [†]	ZFS				Spin-Vibronic Coupling	
			Q _{eq.}		Q _{min.}		Axial coupling ξ_D	Rhombic Coupling ξ_E
			D	E/D	D	E/D		
1 A-Cl	(8,8)	1	-83.14	0.07	-248.29	0.10	-83.99	-7.56
		2	-85.14	0.01	-350.15	0.05	-121.83	-9.75
		3	-85.14	0.04	-319.15	0.08	-119.83	-9.59
		4	-86.75	0.08	-84.59	0.20	-119.04	-8.33
Total/Average			-84.72	0.05	-250.25	0.09	-110.63	-7.74
1 A-I	(8,8)	1	-318.01	0.01	-215.78	0.01	-95.27	-0.95
		2	-330.01	0.01	-354.23	0.01	-107.24	-1.07
		3	-324.01	0.01	-229.51	0.06	-102.62	-1.03
		4	-330.01	0.01	-312.94	0.02	-105.23	-1.05
Total/Average			-325.52	0.02	-277.52	0.02	-102.25	-1.02

Continued in the next page

B. Additional Information to PART III

Complex	CAS (m,n)	Mode [†]	ZFS				Spin-Vibronic Coupling	
			Q _{eq.}		Q _{min.}		Axial coupling ξ_D	Rhombic Coupling ξ_E
			D	E/D	D	E/D		
2 M,A-Cl	(10,11)	5	-5.54	0.27	-3.86	0.30	-20.05	-2.41
		6	-5.53	0.25	-4.40	0.23	-20.58	-2.12
Total/Average			-5.53	0.25	-4.13	0.25	-20.27	-2.23
2 P,A-Cl	(10,11)	5	-6.96	0.28	-4.32	0.29	-20.38	-4.89
		6	-4.97	0.21	-5.38	0.20	-30.90	-5.43
Total/Average			-4.96	0.24	-4.85	0.23	-30.14	-5.04
2 M,A-I	(10,11)	5	-4.92	0.18	-4.92	0.18	~0	0.00
		6	-3.56	0.24	-4.47	0.29	-1.35	-0.16
Total/Average			-4.24	0.21	-4.69	0.21	-1.35	-0.16
2 P,A-I	(10,11)	5	-5.92	0.16	-6.01	0.21	-0.22	-0.05
		6	-4.05	0.27	-4.24	0.23	-0.37	-0.08
Total/Average			-4.98	0.23	-5.12	0.22	-0.27	-0.06

[†]The modes are visualized in **Figures B.16** and **B.17**.

Bibliography

1. Glusac, K. What has light ever done for chemistry? *Nature Chem.*, **2016**. 8(8), 734-735.
2. Harvey, E.N., A history of luminescence from the earliest times until 1900. **1957**, Philadelphia: American Philosophical Society.
3. Cawte, A.D., Unrau, P.J., and Rueda, D.S. Live cell imaging of single RNA molecules with fluorogenic Mango II arrays. *Nat. Commun.*, **2020**. 11(1), 1283.
4. Thirumalai, J., Luminescence: An Outlook on the Phenomena and Their Applications. **2016**: BoD–Books on Demand.
5. Mockl, L., Lamb, D.C., and Brauchle, C. Super-resolved fluorescence microscopy: Nobel Prize in Chemistry 2014 for Eric Betzig, Stefan Hell, and William E. Moerner. *Angew. Chem. Int. Ed.*, **2014**. 53(51), 13972-7.
6. Choquet, D. The 2014 Nobel Prize in Chemistry: a large-scale prize for achievements on the nanoscale. *Neuron*, **2014**. 84(6), 1116-9.
7. Kraftmakher, Y. Nobel Prize for blue LEDs. *Eur. J. Phys.*, **2015**. 36(3), 035024.
8. Gibney, E. Blue LED wins physics Nobel. *Nature*, **2014**. 514(7521), 152-3.
9. Akasaki, I., Amano, H., Nakamura, S., and Nakamura, S. The nobel prize in physics 2014. *The Royal Swedish Academy of Science*, **2014**.
10. Armaroli, N. and Balzani, V. Solar Electricity and Solar Fuels: Status and Perspectives in the Context of the Energy Transition. *Chem. Eur. J.*, **2016**. 22(1), 32-57.
11. Shaner, M.R., Atwater, H.A., Lewis, N.S., and McFarland, E.W. A comparative technoeconomic analysis of renewable hydrogen production using solar energy. *Energy Environ. Sci.*, **2016**. 9(7), 2354-2371.
12. Costa, R.D., Orti, E., Bolink, H.J., Monti, F., Accorsi, G., and Armaroli, N. Luminescent ionic transition-metal complexes for light-emitting electrochemical cells. *Angew. Chem. Int. Ed.*, **2012**. 51(33), 8178-211.
13. Croce, R., Van Grondelle, R., Van Amerongen, H., and Van Stokkum, I., Light harvesting in photosynthesis. **2018**: CRC press.
14. Bopp, M.A., Jia, Y., Li, L., Cogdell, R.J., and Hochstrasser, R.M. Fluorescence and photobleaching dynamics of single light-harvesting complexes. *PNAS*, **1997**. 94(20), 10630-5.
15. Hariyani, S., Sójka, M., Setlur, A., and Brgoch, J. A guide to comprehensive phosphor discovery for solid-state lighting. *Nat. Rev. Mater.*, **2023**. 8(11), 759-775.

16. Fang, M.H., Bao, Z., Huang, W.T., and Liu, R.S. Evolutionary Generation of Phosphor Materials and Their Progress in Future Applications for Light-Emitting Diodes. *Chem. Rev.*, **2022**. 122(13), 11474-11513.
17. Zhao, M., Zhang, Q.Y., and Xia, Z.G. Narrow-band emitters in LED backlights for liquid-crystal displays. *Mater. Today*, **2020**. 40, 246-265.
18. Fang, M.H., Mariano, C.O.M., Chen, P.Y., Hu, S.F., and Liu, R.S. Cuboid-Size-Controlled Color-Tunable Eu-Doped Alkali–Lithosilicate Phosphors. *Chem. Mater.*, **2020**. 32(5), 1748-1759.
19. Li, S., Xie, R.-J., Takeda, T., and Hirosaki, N. Critical Review—Narrow-Band Nitride Phosphors for Wide Color-Gamut White LED Backlighting. *ECS J. Solid State Sci. Technol.*, **2017**. 7(1), R3064-R3078.
20. Leañó, J.L., Fang, M.-H., and Liu, R.-S. Critical Review—Narrow-Band Emission of Nitride Phosphors for Light-Emitting Diodes: Perspectives and Opportunities. *ECS J. Solid State Sci. Technol.*, **2017**. 7(1), R3111-R3133.
21. Zhao, Q., Huang, C., and Li, F. Phosphorescent heavy-metal complexes for bioimaging. *Chem. Soc. Rev.*, **2011**. 40(5), 2508-24.
22. Wolfbeis, O.S. An overview of nanoparticles commonly used in fluorescent bioimaging. *Chem. Soc. Rev.*, **2015**. 44(14), 4743-68.
23. Resch-Genger, U., Grabolle, M., Nitschke, R., and Nann, T., Nanocrystals and Nanoparticles Versus Molecular Fluorescent Labels as Reporters for Bioanalysis and the Life Sciences: A Critical Comparison, in *Advanced Fluorescence Reporters in Chemistry and Biology II*. **2010**. p. 3-40.
24. Papkovsky, D.B. and Dmitriev, R.I. Biological detection by optical oxygen sensing. *Chem. Soc. Rev.*, **2013**. 42(22), 8700-32.
25. Graf, C. and Rühl, E., Imaging techniques for probing nanoparticles in cells and skin, in *Biological Responses to Nanoscale Particles: Molecular and Cellular Aspects and Methodological Approaches*. **2019**. p. 213-239.
26. Zhang, K.Y., Yu, Q., Wei, H., Liu, S., Zhao, Q., and Huang, W. Long-Lived Emissive Probes for Time-Resolved Photoluminescence Bioimaging and Biosensing. *Chem. Rev.*, **2018**. 118(4), 1770-1839.
27. Long, Q.X., Liu, B.Z., Deng, H.J., Wu, G.C., Deng, K., Chen, Y.K., Liao, P., Qiu, J.F., Lin, Y., Cai, X.F., Wang, D.Q., Hu, Y., Ren, J.H., Tang, N., Xu, Y.Y., Yu, L.H., Mo, Z., Gong, F., Zhang, X.L., Tian, W.G., Hu, L., Zhang, X.X., Xiang, J.L., Du, H.X., Liu, H.W., Lang, C.H., Luo, X.H., Wu, S.B., Cui, X.P., Zhou, Z., Zhu, M.M., Wang, J., Xue, C.J., Li, X.F., Wang, L., Li, Z.J., Wang, K., Niu, C.C., Yang, Q.J., Tang, X.J., Zhang, Y., Liu, X.M., Li, J.J., Zhang, D.C., Zhang, F., Liu, P., Yuan, J., Li, Q., Hu, J.L., Chen, J., and Huang, A.L. Antibody responses to SARS-CoV-2 in patients with COVID-19. *Nat. Med.*, **2020**. 26(6), 845-848.
28. Zhu, S. and Wang, D. Photocatalysis: basic principles, diverse forms of implementations and emerging scientific opportunities. *Adv. Energy Mater.*, **2017**. 7(23), 1700841.
29. Beydoun, D., Amal, R., Low, G., and McEvoy, S. Role of nanoparticles in photocatalysis. *J. Nanopart. Res.*, **1999**. 1, 439-458.

30. Wang, L., Wang, X., Kohsei, T., Yoshimura, K.I., Izumi, M., Hirosaki, N., and Xie, R.J. Highly Efficient Narrow-Band Green and Red Phosphors Enabling Wider Color-Gamut LED Backlight for More Brilliant Displays. *Opt. Express*, **2015**. 23(22), 28707.
31. Walther, T. and Fry, E.S., Optics in remote sensing, in *Optics in Our Time*. **2016**, Springer, Cham. p. 201-222.
32. Xie, R.-J., Li, Y.Q., Hirosaki, N., and Yamamoto, H., Nitride phosphors and solid-state lighting. **2011**: Taylor & Francis Boca Raton, FL.
33. Qiao, J., Zhou, G., Zhou, Y., Zhang, Q., and Xia, Z. Divalent europium-doped near-infrared-emitting phosphor for light-emitting diodes. *Nat. Commun.*, **2019**. 10(1), 5267.
34. Duan, B.S., Wang, T., Zhu, N.N., An, X., He, Q.S., Zhu, X.Y., Liu, H.Z., Feng, W., and Yu, X. Li⁺ Ion Doping Induced Photoluminescence Enhancement and Anti-Thermal Quenching of LaOBr:Eu³⁺ Phosphor. *ECS J. Solid State Sci. Technol.*, **2023**. 12(2).
35. Wang, J., Lang, T.C., Cai, M.S., Jing, X.L., Peng, L.L., Qiang, Q.P., Yakovlev, N., Han, T., and Liu, B.T. Enhanced cyan emission via competitive site occupancy engineering in Sr₂SiO₄:Eu²⁺ phosphor for achieving full-spectrum LED lighting. *J. Lumin.*, **2023**. 254.
36. Xue, Y.L., Liang, Y.J., Dou, Y., Li, H.R., Wang, Q.K., Wu, X.D., and Han, Y.S. Optical tuning and energy transfer of single-phase white-emitting Y₃TaO₇:Bi³⁺, Eu³⁺ for ultraviolet converted pc-WLED with high chromatic stability. *J. Alloys Compd.*, **2023**. 940.
37. Zhao, J.W., Dong, J., Zhou, J., and Wang, L.S. Sr-substitution-guided Eu²⁺ site engineering of Ca₉Nd(PO₄)₇:Eu²⁺ for high-efficiency white light-emitting diodes. *Optik*, **2022**. 267.
38. Panigrahi, K. and Nag, A. Challenges and Strategies to Design Phosphors for Future White Light Emitting Diodes. *J. Phys. Chem. C*, **2022**. 126(20), 8553-8564.
39. Cao, M., Tian, J., Zhuang, W., Liu, R., Liu, Y., Chen, G., Zhou, G., Wang, L., and Wang, J. Multisite Cation Regulation of Broadband Cyan-Emitting (Ba_{1-x}Sr_x)₉Lu₂Si₆O₂₄/Eu²⁺ Phosphors for Full-Spectrum wLEDs. *Inorg. Chem.*, **2022**. 61(3), 1805-1815.
40. Yang, T., Ma, Z., Huang, S., Zhang, T., Zhao, K., Yin, L., Gu, Q., and Cao, P. Ultra-narrow-band blue-emitting K₂SrBa(PO₄)₂:Eu²⁺ phosphor with superior efficiency and thermal stability. *J. Alloys Compd.*, **2022**. 892, 10.
41. Shi, R., Zhang, X., Qiu, Z., Zhang, J., Liao, S., Zhou, W., Xu, X., Yu, L., and Lian, S. Composition and Antithermal Quenching of Noninteger Stoichiometric Eu²⁺-Doped Na-β-Alumina with Cyan Emission for Near-UV WLEDs. *Inorg. Chem.*, **2021**. 60(24), 19393-19401.
42. Zhao, J.W., Dong, J., Zhou, J., and Wang, L.S. Enhancing blue light absorption by Sm³⁺ Co-doping in Ca₉Nd(PO₄)₇: Eu³⁺ for white light-emitting diodes. *Mater. Res. Express*, **2021**. 8(9).
43. Bispo, A.G., Saraiva, L.F., Lima, S.A.M., Pires, A.M., and Davolos, M.R. Recent prospects on phosphor-converted LEDs for lighting, displays, phototherapy, and indoor farming. *J. Lumin.*, **2021**. 237.
44. Xie, R.J. Development of sialon phosphors and their applications to solid-state lighting. *J. Ceram. Soc. Jpn.*, **2020**. 128(10), 710-717.

45. Liu, S.Q., Liang, Y.J., Li, H.R., Zhang, W.L., Tu, D., and Chen, Y.J. Color tuning of β - $\text{Ca}_3(\text{PO}_4)_2$ -type phosphor with enhanced quantum efficiency via self-charge compensation for healthy and warm solid state lighting application. *Chem. Eng. J.*, **2020**. 390.
46. Luo, X.F. and Xie, R.J. Recent progress on discovery of novel phosphors for solid state lighting. *J. Rare Earths*, **2020**. 38(5), 464-473.
47. Dong, Q., Yang, J., Cui, J., Xu, F., Yang, F., Peng, J., Du, F., Ye, X., and Yang, S. A narrow-band ultra-bright green phosphor for LED-based applications. *Dalton Trans.*, **2020**. 49(6), 1935-1946.
48. Zhong, J.S., Li, J.N., Liu, M.J., Wang, K.Y., Zhu, Y.W., Li, X.Y., Ji, Z.G., and Chen, D.Q. Novel cyan-emitting $\text{KBaScSi}_2\text{O}_7:\text{Eu}^{2+}$ phosphors with ultrahigh quantum efficiency and excellent thermal stability for WLEDs. *J. Am. Ceram. Soc.*, **2019**. 102(12), 7376-7385.
49. Chen, H.R., Cai, C., Zhang, Z.W., Zhang, L., Lu, H.P., Xu, X., Bui, H.V., Qiu, K.H., and Yin, L.J. Enhancing the luminescent efficiency of $\text{Y}_3\text{Al}_5\text{O}_{12}:\text{Ce}^{3+}$ by coating graphitic carbon nitride: Toward white light-emitting diodes. *J. Alloys Compd.*, **2019**. 801, 10-18.
50. Hong, F., Cheng, H.M., Song, Y., Li, D., Liu, G.X., Yu, W.S., Wang, J.X., and Dong, X.T. Room-temperature synthesis, optimized photoluminescence and warm-white LED application of a highly efficient non-rare-earth red phosphor. *J. Alloys Compd.*, **2019**. 775, 1365-1375.
51. Han, B., Dai, Y.Z., Zhang, J., Liu, B.B., and Shi, H.Z. Development of near-ultraviolet-excitable single-phase white-light-emitting phosphor $\text{KBaY}(\text{BO}_3)_2:\text{Ce}^{3+}, \text{Dy}^{3+}$ for phosphor-converted white light-emitting-diodes. *Ceram. Int.*, **2018**. 44(12), 14803-14810.
52. Xu, H.B., Zhuang, W.D., Liu, R.H., Liu, Y.H., Zhou, T.L., Cho, Y., Gao, W., Yan, C.P., Hirotsaki, N., and Xie, R.J. Significantly enhanced photoluminescence and thermal stability of $\text{La}_3\text{Si}_8\text{N}_{11}\text{O}_4:\text{Ce}^{3+}, \text{Tb}^{3+}$ via the $\text{Ce}^{3+} \rightarrow \text{Tb}^{3+}$ energy transfer: a blue-green phosphor for ultraviolet LEDs. *RSC Adv.*, **2018**. 8(61), 35271-35279.
53. Tanaka, H., Inoue, Y., and Mori, T. Circularly Polarized Luminescence and Circular Dichroisms in Small Organic Molecules: Correlation between Excitation and Emission Dissymmetry Factors. *Chemphotochem*, **2018**. 2(5), 386-402.
54. Wu, Y., Li, M., Zheng, Z.G., Yu, Z.Q., and Zhu, W.H. Liquid Crystal Assembly for Ultra-dissymmetric Circularly Polarized Luminescence and Beyond. *J. Am. Chem. Soc.*, **2023**. 145(24), 12951-12966.
55. Zhan, X., Xu, F.F., Zhou, Z., Yan, Y., Yao, J., and Zhao, Y.S. 3D Laser Displays Based on Circularly Polarized Lasing from Cholesteric Liquid Crystal Arrays. *Adv. Mater.*, **2021**. 33(37), e2104418.
56. Sang, Y., Han, J., Zhao, T., Duan, P., and Liu, M. Circularly Polarized Luminescence in Nanoassemblies: Generation, Amplification, and Application. *Adv. Mater.*, **2020**. 32(41), e1900110.
57. Han, J.M., Guo, S., Lu, H., Liu, S.J., Zhao, Q., and Huang, W. Recent Progress on Circularly Polarized Luminescent Materials for Organic Optoelectronic Devices. *Adv. Optical Mater.*, **2018**. 6(17), 1800538.

58. Zhang, L., Qin, L., Wang, X., Cao, H., and Liu, M. Supramolecular chirality in self-assembled soft materials: regulation of chiral nanostructures and chiral functions. *Adv. Mater.*, **2014**. 26(40), 6959-64.
59. Li, M., Li, S.H., Zhang, D., Cai, M., Duan, L., Fung, M.K., and Chen, C.F. Stable Enantiomers Displaying Thermally Activated Delayed Fluorescence: Efficient OLEDs with Circularly Polarized Electroluminescence. *Angew. Chem. Int. Ed.*, **2018**. 57(11), 2889-2893.
60. MacKenzie, L.E. and Pal, R. Circularly polarized lanthanide luminescence for advanced security inks. *Nat. Rev. Chem.*, **2021**. 5(2), 109-124.
61. Yashima, E., Ousaka, N., Taura, D., Shimomura, K., Ikai, T., and Maeda, K. Supramolecular helical systems: helical assemblies of small molecules, foldamers, and polymers with chiral amplification and their functions. *Chem. Rev.*, **2016**. 116(22), 13752-13990.
62. Liu, M., Zhang, L., and Wang, T. Supramolecular Chirality in Self-Assembled Systems. *Chem. Rev.*, **2015**. 115(15), 7304-97.
63. Zhao, T., Han, J., Duan, P., and Liu, M. New Perspectives to Trigger and Modulate Circularly Polarized Luminescence of Complex and Aggregated Systems: Energy Transfer, Photon Upconversion, Charge Transfer, and Organic Radical. *Acc. Chem. Res.*, **2020**. 53(7), 1279-1292.
64. Song, F., Xu, Z., Zhang, Q., Zhao, Z., Zhang, H., Zhao, W., Qiu, Z., Qi, C., Zhang, H., and Sung, H.H. Highly efficient circularly polarized electroluminescence from aggregation-induced emission luminogens with amplified chirality and delayed fluorescence. *Adv. Funct. Mater.*, **2018**. 28(17), 1800051.
65. Chen, Z., Zhong, C., Han, J., Miao, J., Qi, Y., Zou, Y., Xie, G., Gong, S., and Yang, C. High-Performance Circularly Polarized Electroluminescence with Simultaneous Narrowband Emission, High Efficiency, and Large Dissymmetry Factor. *Adv. Mater.*, **2022**. 34(17), e2109147.
66. Yan, Z.P., Yuan, L., Zhang, Y., Mao, M.X., Liao, X.J., Ni, H.X., Wang, Z.H., An, Z., Zheng, Y.X., and Zuo, J.L. A Chiral Dual-Core Organoboron Structure Realizes Dual-Channel Enhanced Ultrapure Blue Emission and Highly Efficient Circularly Polarized Electroluminescence. *Adv. Mater.*, **2022**. 34(36), e2204253.
67. Zhang, D.W., Li, M., and Chen, C.F. Recent advances in circularly polarized electroluminescence based on organic light-emitting diodes. *Chem. Soc. Rev.*, **2020**. 49(5), 1331-1343.
68. Kim, J.-Y., Yeom, J., Zhao, G., Calcaterra, H., Munn, J., Zhang, P., and Kotov, N. Assembly of gold nanoparticles into chiral superstructures driven by circularly polarized light. *J. Am. Chem. Soc.*, **2019**. 141(30), 11739-11744.
69. Liu, D.Y., Li, H.Y., Han, R.P., Liu, H.L., and Zang, S.Q. Multiple Stimuli-Responsive Luminescent Chiral Hybrid Antimony Chlorides for Anti-Counterfeiting and Encryption Applications. *Angew. Chem. Int. Ed.*, **2023**. 62(36), e202307875.
70. Xue, C., Jiang, Y., Wang, H.X., Du, C., Xu, L., Li, T., and Liu, M. Excitation-Dependent Circularly Polarized Luminescence from Helical Assemblies Based on Tartaric Acid-Derived Acylhydrazones. *Angew. Chem. Int. Ed.*, **2022**. 61(29), e202205633.

71. Guo, Q., Zhang, M., Tong, Z., Zhao, S., Zhou, Y., Wang, Y., Jin, S., Zhang, J., Yao, H.B., Zhu, M., and Zhuang, T. Multimodal-Responsive Circularly Polarized Luminescence Security Materials. *J. Am. Chem. Soc.*, **2023**. 145(7), 4246-4253.
72. Hou, J., Toyoda, R., Meskers, S.C.J., and Feringa, B.L. Programming and Dynamic Control of the Circular Polarization of Luminescence from an Achiral Fluorescent Dye in a Liquid Crystal Host by Molecular Motors. *Angew. Chem. Int. Ed.*, **2022**. 61(41), e202206310.
73. Xu, M., Ma, C., Zhou, J., Liu, Y., Wu, X., Luo, S., Li, W., Yu, H., Wang, Y., and Chen, Z. Assembling semiconductor quantum dots in hierarchical photonic cellulose nanocrystal films: circularly polarized luminescent nanomaterials as optical coding labels. *J. Mater. Chem. C*, **2019**. 7(44), 13794-13802.
74. Joos, J.J., Smet, P.F., Seijo, L., and Barandiaran, Z. Insights into the complexity of the excited states of Eu-doped luminescent materials. *Inorg. Chem. Front.*, **2020**. 7(4), 871-888.
75. Lai, S., Zhao, M., Qiao, J., Molokeev, M.S., and Xia, Z. Data-Driven Photoluminescence Tuning in Eu(2+)-Doped Phosphors. *J Phys Chem Lett*, **2020**. 11(14), 5680-5685.
76. Li, S. and Xie, R.-J. Critical Review—Data-Driven Discovery of Novel Phosphors. *ECS J. Solid State Sci. Technol.*, **2019**. 9(1), 016013.
77. Wang, Y., Niu, D., Ouyang, G., and Liu, M. Double helical pi-aggregate nanoarchitectonics for amplified circularly polarized luminescence. *Nat. Commun.*, **2022**. 13(1), 1710.
78. Zhou, Y., Wang, Y., Song, Y., Zhao, S., Zhang, M., Li, G., Guo, Q., Tong, Z., Li, Z., Jin, S., Yao, H.B., Zhu, M., and Zhuang, T. Helical-caging enables single-emitted large asymmetric full-color circularly polarized luminescence. *Nat. Commun.*, **2024**. 15(1), 251.
79. Shafei, R., Hamano, A., Gourlaouen, C., Maganas, D., Takano, K., Daniel, C., and Neese, F. Theoretical spectroscopy for unraveling the intensity mechanism of the optical and photoluminescent spectra of chiral Re(I) transition metal complexes. *J. Chem. Phys.*, **2023**. 159(8), 084102.
80. Shafei, R., Maganas, D., Strobel, P.J., Schmidt, P.J., Schnick, W., and Neese, F. Electronic and Optical Properties of Eu²⁺-Activated Narrow-Band Phosphors for Phosphor-Converted Light-Emitting Diode Applications: Insights from a Theoretical Spectroscopy Perspective. *J. Am. Chem. Soc.*, **2022**. 144(18), 8038-8053.
81. Barone, V., Alessandrini, S., Biczysko, M., Cheeseman, J.R., Clary, D.C., McCoy, A.B., DiRisio, R.J., Neese, F., Melosso, M., and Puzzarini, C. Computational molecular spectroscopy. *Nat. Rev. Methods Primers*, **2021**. 1(1).
82. Grunenberg, J., Computational spectroscopy: methods, experiments and applications. **2011**: John Wiley & Sons.
83. Dittmer, A., Stoychev, G.L., Maganas, D., Auer, A.A., and Neese, F. Computation of NMR Shielding Constants for Solids Using an Embedded Cluster Approach with DFT, Double-Hybrid DFT, and MP2. *J. Chem. Theory Comput.*, **2020**. 16(11), 6950-6967.

84. Dittmer, A., Izsak, R., Neese, F., and Maganas, D. Accurate Band Gap Predictions of Semiconductors in the Framework of the Similarity Transformed Equation of Motion Coupled Cluster Theory. *Inorg. Chem.*, **2019**. 58(14), 9303-9315.
85. Maganas, D., Kowalska, J.K., Van Stappen, C., DeBeer, S., and Neese, F. Mechanism of L(2,3)-edge x-ray magnetic circular dichroism intensity from quantum chemical calculations and experiment-A case study on V(IV)/V(III) complexes. *J. Chem. Phys.*, **2020**. 152(11), 114107.
86. Neese, F., Atanasov, M., Bistoni, G., Maganas, D., and Ye, S. Chemistry and Quantum Mechanics in 2019: Give Us Insight and Numbers. *J. Am. Chem. Soc.*, **2019**. 141(7), 2814-2824.
87. Van Stappen, C., Maganas, D., DeBeer, S., Bill, E., and Neese, F. Investigations of the Magnetic and Spectroscopic Properties of V(III) and V(IV) Complexes. *Inorg. Chem.*, **2018**. 57(11), 6421-6438.
88. Maganas, D., DeBeer, S., and Neese, F. Pair Natural Orbital Restricted Open-Shell Configuration Interaction (PNO-ROCIS) Approach for Calculating X-ray Absorption Spectra of Large Chemical Systems. *J. Phys. Chem. A*, **2018**. 122(5), 1215-1227.
89. Maganas, D., DeBeer, S., and Neese, F. Restricted open-shell configuration interaction cluster calculations of the L-edge X-ray absorption study of TiO₂ and CaF₂ solids. *Inorg. Chem.*, **2014**. 53(13), 6374-85.
90. Tzima, T.D., Ferentinos, E., Maganas, D., Melissas, V.S., Sanakis, Y., and Kyritsis, P. Electronic and magnetic properties of the binuclear [Mn₂{(OPPh₂)₂N}₄] complex, as revealed by magnetometry, EPR and density functional broken-symmetry studies. *Polyhedron*, **2013**. 52, 706-712.
91. Maganas, D., Sottini, S., Kyritsis, P., Groenen, E.J., and Neese, F. Theoretical analysis of the spin Hamiltonian parameters in Co(II)S₄ complexes, using density functional theory and correlated ab initio methods. *Inorg. Chem.*, **2011**. 50(18), 8741-54.
92. Szabo, A. and Ostlund, N.S., Modern quantum chemistry: introduction to advanced electronic structure theory. **2012**: Courier Corporation.
93. Bersuker, I.B., Electronic structure and properties of transition metal compounds: introduction to the theory. **2010**: John Wiley & Sons.
94. McHale, J.L., Molecular spectroscopy. **2017**: CRC Press.
95. Atkins, P.W. and Friedman, R.S., Molecular quantum mechanics. **2011**: Oxford university press.
96. Barron, L.D., Molecular light scattering and optical activity. **2009**: Cambridge University Press.
97. Bersuker, I., The Jahn-Teller effect and vibronic interactions in modern chemistry. **2013**: Springer Science & Business Media.
98. Cotton, F.A., Chemical applications of group theory. **1991**: John Wiley & Sons.
99. Cowan, R.D., The theory of atomic structure and spectra. **1981**: Univ of California Press.
100. Cramer, C.J., Essentials of computational chemistry: theories and models. **2013**: John Wiley & Sons.

101. De Groote, J.Y., Jean, Y., Marsden, C., Marsden, C.T., de Physique Quantique Irsamc Colin Marsden, L., and Hoffmann, R., Molecular Orbitals of Transition Metal Complexes. **2005**: OUP Oxford.
102. Dirac, P.A.M., The principles of quantum mechanics. **1981**: Oxford university press.
103. Figgis, B.N. and Hitchman, M.A., Ligand field theory and its applications. **1999**.
104. Hänninen, P. and Härmä, H., Lanthanide luminescence: photophysical, analytical and biological aspects. Vol. 7. **2011**: Springer Science & Business Media.
105. Henderson, B. and Bartram, R.H., Crystal-field engineering of solid-state laser materials. **2005**.
106. Herzberg, G., Molecular spectra and molecular structure. **1945**: D. van Nostrand.
107. Jensen, F., Introduction to Computational Chemistry. **2017**: John wiley & sons.
108. Lakowicz, J.R. and Valeur, B., Principles of Fluorescence Spectroscopy. **2006**.
109. Levine, I.N., Busch, D.H., and Shull, H., Quantum chemistry. Vol. 6. **2009**: Pearson Prentice Hall Upper Saddle River, NJ.
110. McCreery, R.L., Raman spectroscopy for chemical analysis. **2005**: John Wiley & Sons.
111. Nafie, L.A., Vibrational optical activity: Principles and applications. **2011**: John Wiley & Sons.
112. Schatz, G.C. and Ratner, M.A., Quantum mechanics in chemistry. **2002**: Courier Corporation.
113. Smith, E. and Dent, G., Modern Raman spectroscopy: a practical approach. **2019**: John Wiley & Sons.
114. Solé, J., Bausa, L., and Jaque, D., An introduction to the optical spectroscopy of inorganic solids. **2005**: John Wiley & Sons.
115. Dittmer, A., Exploring Problems in Inorganic Solid-State Systems with Wavefunction-Based Molecular Spectroscopy Methods. **2023**, University of Bonn.
116. Maxwell, J.C. VIII. A dynamical theory of the electromagnetic field. *Philosophical transactions of the Royal Society of London*, **1865**(155), 459-512.
117. Ratner, M.A. and Schatz, G. Quantum Mechanics in Chemistry. **1993**.
118. Griffiths, D.J., Introduction to Electrodynamics 3rd ed. Vol. 7458. **1999**: Pearson Education Inc., New Jersey, Indian Reprint by Prentice Hall India.
119. Fox, M., Optical properties of solids. **2001**: Oxford University Press.
120. Strobel, P., Narrow-band emitting phosphors for solid-state lighting. **2018**, LMU.
121. Jenkins, R. and Snyder, R.L., Introduction to X-ray Powder Diffractometry (Volume 138). **1996**: Wiley Online Library.
122. Smyth, M.S. and Martin, J.H. x ray crystallography. *Mol. Pathol.*, **2000**. 53(1), 8-14.
123. Kasha, M. and McGlynn, S.P. Molecular Electronic Spectroscopy. *Annu. Rev. Phys. Chem.*, **1956**. 7(1), 403-424.
124. Wagatha, P., Weiler, V., Schmidt, P.J., and Schnick, W. Tailoring Emission Characteristics: Narrow-Band Red Luminescence from SLA to CaBa[Li₂Al₆N₈]:Eu²⁺. *Chem. Mater.*, **2018**. 30(21), 7885-7891.

125. Hoerder, G.J., Seibald, M., Baumann, D., Schroder, T., Peschke, S., Schmid, P.C., Tyborski, T., Pust, P., Stoll, I., Bergler, M., Patzig, C., Reissaus, S., Krause, M., Berthold, L., Hoche, T., Johrendt, D., and Huppertz, H. Sr[Li₂Al₂O₂N₂]:Eu²⁺-A high performance red phosphor to brighten the future. *Nat. Commun.*, **2019**. 10(1), 1824.
126. Strobel, P., Maak, C., Weiler, V., Schmidt, P.J., and Schnick, W. Ultra-Narrow-Band Blue-Emitting Oxoberyllates AELi₂[Be₄O₆]:Eu²⁺ (AE=Sr,Ba) Paving the Way to Efficient RGB pc-LEDs. *Angew. Chem. Int. Ed.*, **2018**. 57(28), 8739-8743.
127. Mosca, S., Conti, C., Stone, N., and Matousek, P. Spatially offset Raman spectroscopy. *Nat. Rev. Methods Primers*, **2021**. 1(1), 21.
128. Long, D.A., The Raman Effect: A Unified Treatment of the Theory of Raman Scattering by Molecules. **2002**: John Wiley & Sons Ltd.
129. Gardiner, D.J. Introduction to Raman scattering. *Practical Raman Spectroscopy*, **1989**, 1-12.
130. Clarke, R.J. and Oprysa, A. Fluorescence and light scattering. *J. Chem. Educ.*, **2004**. 81(5), 705-707.
131. Dalum, S. and Hedegård, P. Theory of Chiral Induced Spin Selectivity. *Nano Lett.*, **2019**. 19(8), 5253-5259.
132. Fay, T.P. and Limmer, D.T. Origin of Chirality Induced Spin Selectivity in Photoinduced Electron Transfer. *Nano Lett.*, **2021**. 21(15), 6696-6702.
133. Born, M. Nachrichten Akad. Wiss. Göttingen, Math. Physik Kl. II, Berlin, **1951**.
134. Liu, G., Electronic Energy Level Structure, in *Spectroscopic properties of rare earths in optical materials*, B. Jacquier, Editor. **2006**, Springer Science & Business Media.
135. Mauro, M., Aliprandi, A., Septiadi, D., Kehr, N.S., and De Cola, L. When self-assembly meets biology: luminescent platinum complexes for imaging applications. *Chem. Soc. Rev.*, **2014**. 43(12), 4144-4166.
136. Aravena, D., Atanasov, M., and Neese, F. Periodic Trends in Lanthanide Compounds through the Eyes of Multireference ab Initio Theory. *Inorg. Chem.*, **2016**. 55(9), 4457-69.
137. Jung, J., Atanasov, M., and Neese, F. Ab Initio Ligand-Field Theory Analysis and Covalency Trends in Actinide and Lanthanide Free Ions and Octahedral Complexes. *Inorg. Chem.*, **2017**. 56(15), 8802-8816.
138. Neese, F., Lang, L., Chilkuri, V.G., and an der Ruhr, M. Effective Hamiltonians in Chemistry. *Topology, Entanglement, and Strong Correlations, Modeling and Simulation*; Pavarini, E., Koch, E., Eds, **2020**.
139. Lang, L., Atanasov, M., and Neese, F. Improvement of Ab Initio Ligand Field Theory by Means of Multistate Perturbation Theory. *J. Phys. Chem. A*, **2020**. 124(5), 1025-1037.
140. Atanasov, M., Aravena, D., Suturina, E., Bill, E., Maganas, D., and Neese, F. First principles approach to the electronic structure, magnetic anisotropy and spin relaxation in mononuclear 3d-transition metal single molecule magnets. *Coord. Chem. Rev.*, **2015**. 289-290, 177-214.
141. Maganas, D., Roemelt, M., Havecker, M., Trunschke, A., Knop-Gericke, A., Schlögl, R., and Neese, F. First principles calculations of the structure and V L-edge X-ray

- absorption spectra of V_2O_5 using local pair natural orbital coupled cluster theory and spin-orbit coupled configuration interaction approaches. *Phys. Chem. Chem. Phys.*, **2013**. 15(19), 7260-76.
142. Maganas, D., Roemelt, M., Weyhermuller, T., Blume, R., Havecker, M., Knop-Gericke, A., DeBeer, S., Schlogl, R., and Neese, F. L-edge X-ray absorption study of mononuclear vanadium complexes and spectral predictions using a restricted open shell configuration interaction ansatz. *Phys. Chem. Chem. Phys.*, **2014**. 16(1), 264-76.
143. Roemelt, M. and Neese, F. Excited states of large open-shell molecules: an efficient, general, and spin-adapted approach based on a restricted open-shell ground state wave function. *J. Phys. Chem. A*, **2013**. 117(14), 3069-83.
144. Wu, S., Steffen, J., Hu, P., and Nooijen, M. Multireference equation of motion coupled cluster benchmark study of magnetic model systems. *Comput. Theor. Chem.*, **2018**. 1130, 160-174.
145. Liu, Z., Huntington, L.M., and Nooijen, M. Application of the multireference equation of motion coupled cluster method, including spin-orbit coupling, to the atomic spectra of Cr, Mn, Fe and Co. *Mol. Phys.*, **2015**. 113(19-20), 2999-3013.
146. Neese, F., Petrenko, T., Ganyushin, D., and Olbrich, G. Advanced aspects of ab initio theoretical optical spectroscopy of transition metal complexes: Multiplets, spin-orbit coupling and resonance Raman intensities. *Coord. Chem. Rev.*, **2007**. 251(3-4), 288-327.
147. Ganyushin, D. and Neese, F. First-principles calculations of zero-field splitting parameters. *J. Chem. Phys.*, **2006**. 125(2), 24103.
148. Neese, F. A spectroscopy oriented configuration interaction procedure. *J. Chem. Phys.*, **2003**. 119(18), 9428-9443.
149. Neese, F. Efficient and accurate approximations to the molecular spin-orbit coupling operator and their use in molecular g-tensor calculations. *J. Chem. Phys.*, **2005**. 122(3), 34107.
150. Neese, F. and Solomon, E.I. Calculation of Zero-Field Splittings, g-Values, and the Relativistic Nephelauxetic Effect in Transition Metal Complexes. Application to High-Spin Ferric Complexes. *Inorg. Chem.*, **1998**. 37(26), 6568-6582.
151. Abragam, A., Bleaney, B., Electron Paramagnetic Resonance of Transition Ions. **1986**, New York: Dover Publications.
152. Atherton, N.M., Principles of Electron Spin Resonance. Ellis Horwood PTR Prentice Hall ed. **1993**.
153. Telser, J., Goldfarb, D., and Stoll, S., EPR interactions—zero-field splittings, in *EPR Spectroscopy: Fundamentals and Methods*. **2018**. p. 29-62.
154. Boca, R. Zero-field splitting in metal complexes. *Coord. Chem. Rev.*, **2004**. 248(9-10), 757-815.
155. Neese, F., First Principles Approach to Spin-Hamiltonian Parameters, in *Multifrequency Electron Paramagnetic Resonance*, S.K. Misra, Editor. **2011**. p. 295-326.
156. R. McWeeny, Methods of Molecular Quantum Mechanics. **1992**, London: Academic.
157. McLaughlin, M.P., Retegan, M., Bill, E., Payne, T.M., Shafaat, H.S., Peña, S., Sudhamsu, J., Ensign, A.A., Crane, B.R., Neese, F., and Holland, P.L. Azurin as a

- Protein Scaffold for a Low-coordinate Nonheme Iron Site with a Small-molecule Binding Pocket. *J. Am. Chem. Soc.*, **2012**. 134(48), 19746-19757.
158. Retegan, M., Collomb, M.-N., Neese, F., and Duboc, C. A combined high-field EPR and quantum chemical study on a weakly ferromagnetically coupled dinuclear Mn(III) complex. A complete analysis of the EPR spectrum beyond the strong coupling limit. *Phys. Chem. Chem. Phys.*, **2013**. 15(1), 223-234.
 159. Atanasov, M., Ganyushin, D., Sivalingam, K., and Neese, F., A Modern First-Principles View on Ligand Field Theory Through the Eyes of Correlated Multireference Wavefunctions, in *Molecular Electronic Structures of Transition Metal Complexes II*, D.M.P. Mingos, P. Day, and J.P. Dahl, Editors. **2012**, Springer Berlin Heidelberg. p. 149-220.
 160. Maurice, R., Guihéry, N., Bastardis, R., and Graaf, C.d. Rigorous Extraction of the Anisotropic Multispin Hamiltonian in Bimetallic Complexes from the Exact Electronic Hamiltonian. *J. Chem. Theory Comput.*, **2010**. 6(3), 977-977.
 161. Maurice, R., Pradipto, A.M., Guihéry, N., Broer, R., and de Graaf, C. Antisymmetric Magnetic Interactions in Oxo-Bridged Copper(II) Bimetallic Systems. *J. Chem. Theory Comput.*, **2010**. 6(10), 3092-3101.
 162. Maurice, R., Vendier, L., and Costes, J.-P. Magnetic Anisotropy in NiII–YIII Binuclear Complexes: On the Importance of Both the First Coordination Sphere of the NiII Ion and the YIII Ion Belonging to the Second Coordination Sphere. *Inorg. Chem.*, **2011**. 50(21), 11075-11081.
 163. Becke, A.D. Density functionals for static, dynamical, and strong correlation. *J. Chem. Phys.*, **2013**. 138(7).
 164. Löwdin, P.O. Quantum theory of many-particle systems. I. Physical interpretations by means of density matrices, natural spin-orbitals, and convergence problems in the method of configurational interaction. *Phys. Rev.*, **1955**. 97(6), 1474.
 165. Löwdin, P.O. Correlation Problem in Many-Electron Quantum Mechanics I. Review of Different Approaches and Discussion of Some Current Ideas. *Adv. Chem. Phys.*, **1958**, 207-322.
 166. Sherrill, C.D. and Schaefer III, H.F., The configuration interaction method: Advances in highly correlated approaches, in *Advances in quantum chemistry*. **1999**, Elsevier. p. 143-269.
 167. Pople, J.A., Head-Gordon, M., and Raghavachari, K. Quadratic configuration interaction. A general technique for determining electron correlation energies. *J. Chem. Phys.*, **1987**. 87(10), 5968-5975.
 168. Buenker, R.J. and Peyerimhoff, S.D. Energy extrapolation in CI calculations. *Theoret. Chim. Acta.*, **1975**. 39, 217-228.
 169. Roos, B.O., Taylor, P.R., and Sigbahn, P.E.M. A complete active space SCF method (CASSCF) using a density matrix formulated super-CI approach. *Chem. Phys.*, **1980**. 48(2), 157-173.
 170. Olsen, J. The CASSCF method: A perspective and commentary. *Int. J. Quantum Chem.*, **2011**. 111(13), 3267-3272.
 171. Møller, C. and Plesset, M.S. Note on an approximation treatment for many-electron systems. *Phys. Rev.*, **1934**. 46(7), 618.

172. Head-Gordon, M., Pople, J.A., and Frisch, M.J. MP2 energy evaluation by direct methods. *Chem. Phys. Lett.*, **1988**. 153(6), 503-506.
173. Pople, J.A., Seeger, R., and Krishnan, R. Variational configuration interaction methods and comparison with perturbation theory. *Int. J. Quantum Chem.*, **1977**. 12(S11), 149-163.
174. Pople, J.A., Binkley, J.S., and Seeger, R. Theoretical models incorporating electron correlation. *Int. J. Quantum Chem.*, **1976**. 10(S10), 1-19.
175. Krishnan, R. and Pople, J.A. Approximate fourth-order perturbation theory of the electron correlation energy. *Int. J. Quantum Chem.*, **1978**. 14(1), 91-100.
176. Purvis III, G.D. and Bartlett, R.J. A full coupled-cluster singles and doubles model: The inclusion of disconnected triples. *J. Chem. Phys.*, **1982**. 76(4), 1910-1918.
177. Van Voorhis, T. and Head-Gordon, M. Two-body coupled cluster expansions. *J. Chem. Phys.*, **2001**. 115(11), 5033-5040.
178. Cremer, D. and He, Z. Analysis of coupled cluster methods: IV. Size-extensive quadratic CI methods—quadratic CI with triple and quadruple excitations. *Theoret. Claim. Acta.*, **1994**. 88, 47-67.
179. Schmidt, M.W. and Gordon, M.S. The construction and interpretation of MCSCF wavefunctions. *Annu. Rev. Phys. Chem.*, **1998**. 49, 233-66.
180. Levine, B.G., Durden, A.S., Esch, M.P., Liang, F., and Shu, Y. CAS without SCF—Why to use CASCI and where to get the orbitals. *J. Chem. Phys.*, **2021**. 154(9), 090902.
181. Ungur, L. and Chibotaru, L.F. Ab Initio Crystal Field for Lanthanides. *Chem. Eur. J.*, **2017**. 23(15), 3708-3718.
182. Singh, S.K., Eng, J., Atanasov, M., and Neese, F. Covalency and chemical bonding in transition metal complexes: An ab initio based ligand field perspective. *Coord. Chem. Rev.*, **2017**. 344, 2-25.
183. Atanasov, M., Ganyushin, D., Pantazis, D.A., Sivalingam, K., and Neese, F. Detailed Ab Initio First-Principles Study of the Magnetic Anisotropy in a Family of Trigonal Pyramidal Iron(II) Pyrrolide Complexes. *Inorg. Chem.*, **2011**. 50(16), 7460-7477.
184. Siegbahn, P.E.M., Almlöf, J., Heiberg, A., and Roos, B.O. The Complete Active Space Scf (CASSCF) Method in a Newton-Raphson Formulation with Application to the HNO Molecule. *J. Chem. Phys.*, **1981**. 74(4), 2384-2396.
185. Malmqvist, P.Å., Rendell, A., and Roos, B.O. The restricted active space self-consistent-field method, implemented with a split graph unitary group approach. *J. Phys. Chem.*, **1990**. 94(14), 5477-5482.
186. Olsen, J., Roos, B.O., Jørgensen, P., and Jensen, H.J.A. Determinant based configuration interaction algorithms for complete and restricted configuration interaction spaces. *J. Chem. Phys.*, **1988**. 89(4), 2185-2192.
187. Benavides-Riveros, C.L., Lathiotakis, N.N., and Marques, M.A.L. Towards a formal definition of static and dynamic electronic correlations. *Phys. Chem. Chem. Phys.*, **2017**. 19, 12655-12664.
188. Chilkuri, V.G. and Neese, F. Comparison of many-particle representations for selected-CI I: A tree based approach. *J. Comput. Chem.*, **2021**. 42(14), 982-1005.

189. Chilkuri, V.G. and Neese, F. Comparison of many-particle representations for selected configuration interaction: II. Numerical benchmark calculations. *J. Chem. Theory Comput.*, **2021**. 17(5), 2868-2885.
190. Sharma, S. and Chan, G.K. Spin-adapted density matrix renormalization group algorithms for quantum chemistry. *J. Chem. Phys.*, **2012**. 136(12).
191. Young, D.C., Computational Chemistry: A Practical Guide for Applying Techniques to Real World Problems. **2001**, New Jersey, U.S.: John Wiley & Sons, Inc.
192. Cremer, D. Møller–Plesset perturbation theory: From small molecule methods to methods for thousands of atoms. *Wiley Interdiscip. Rev. Comput. Mol. Sci.*, **2011**. 1(4), 509-530.
193. Angeli, C., Cimiraglia, R., Evangelisti, S., Leininger, T., and Malrieu, J.P. Introduction of n-electron valence states for multireference perturbation theory. *J. Chem. Phys.*, **2001**. 114(23), 10252-10264.
194. Angeli, C., Cimiraglia, R., and Malrieu, J.-P. n-electron valence state perturbation theory: A spinless formulation and an efficient implementation of the strongly contracted and of the partially contracted variants. *J. Chem. Phys.*, **2002**. 117(20), 9138-9153.
195. Angeli, C., Cimiraglia, R., and Malrieu, J.-P. N-electron valence state perturbation theory: a fast implementation of the strongly contracted variant. *Chem. Phys. Lett.*, **2001**. 350(3-4), 297-305.
196. Andersson, K., Malmqvist, P.A., Roos, B.O., Sadlej, A.J., and Wolinski, K. Second-order perturbation theory with a CASSCF reference function. *J. Phys. Chem.*, **1990**. 94(14), 5483-5488.
197. Andersson, K., Malmqvist, P.Å., and Roos, B.O. Second-order perturbation theory with a complete active space self-consistent field reference function. *J. Chem. Phys.*, **1992**. 96(2), 1218-1226.
198. Angeli, C., Borini, S., Cestari, M., and Cimiraglia, R. A quasidegenerate formulation of the second order n-electron valence state perturbation theory approach. *J. Chem. Phys.*, **2004**. 121(9), 4043-9.
199. Neese, F., Quantum chemistry and EPR parameters, in *EPR Spectroscopy: Fundamentals and Methods*. **2017**.
200. Bartlett, R.J. and Musiał, M. Coupled-cluster theory in quantum chemistry. *Rev. Mod. Phys.*, **2007**. 79(1), 291.
201. Riplinger, C. and Neese, F. An efficient and near linear scaling pair natural orbital based local coupled cluster method. *J. Chem. Phys.*, **2013**. 138(3), 034106.
202. Riplinger, C., Sandhoefer, B., Hansen, A., and Neese, F. Natural triple excitations in local coupled cluster calculations with pair natural orbitals. *J. Chem. Phys.*, **2013**. 139(13).
203. Pinski, P., Riplinger, C., Valeev, E.F., and Neese, F. Sparse maps—A systematic infrastructure for reduced-scaling electronic structure methods. I. An efficient and simple linear scaling local MP2 method that uses an intermediate basis of pair natural orbitals. *J. Chem. Phys.*, **2015**. 143(3).
204. Riplinger, C., Pinski, P., Becker, U., Valeev, E.F., and Neese, F. Sparse maps—A systematic infrastructure for reduced-scaling electronic structure methods. II. Linear

- scaling domain based pair natural orbital coupled cluster theory. *J. Chem. Phys.*, **2016**. 144(2).
205. Saitow, M., Becker, U., Riplinger, C., Valeev, E.F., and Neese, F. A new near-linear scaling, efficient and accurate, open-shell domain-based local pair natural orbital coupled cluster singles and doubles theory. *J. Chem. Phys.*, **2017**. 146(16), 164105.
 206. Emrich, K. An extension of the coupled cluster formalism to excited states (I). *Nucl. Phys. A*, **1981**. 351(3), 379-396.
 207. Ravi, M., Park, Y.C., Perera, A., and Bartlett, R.J. The intermediate state approach for doubly excited dark states in EOM-coupled-cluster theory. *J. Chem. Phys.*, **2022**. 156(20), 201102.
 208. Sekino, H. and Bartlett, R.J. A linear response, coupled-cluster theory for excitation energy. *Int. J. Quantum Chem.*, **1984**. 26(S18), 255-265.
 209. Comeau, D.C. and Bartlett, R.J. The equation-of-motion coupled-cluster method. Applications to open-and closed-shell reference states. *Chem. Phys. Lett.*, **1993**. 207(4-6), 414-423.
 210. Stanton, J.F. and Bartlett, R.J. The equation of motion coupled-cluster method. A systematic biorthogonal approach to molecular excitation energies, transition probabilities, and excited state properties. *J. Chem. Phys.*, **1993**. 98(9), 7029-7039.
 211. Nooijen, M. and Bartlett, R.J. Equation of motion coupled cluster method for electron attachment. *J. Chem. Phys.*, **1995**. 102(9), 3629-3647.
 212. Szalay, P.G., Watson, T., Perera, A., Lotrich, V.F., and Bartlett, R.J. Benchmark studies on the building blocks of DNA. 1. Superiority of coupled cluster methods in describing the excited states of nucleobases in the Franck–Condon region. *J. Phys. Chem. A*, **2012**. 116(25), 6702-6710.
 213. Huntington, L.M.J., Krupicka, M., Neese, F., and Izsak, R. Similarity transformed equation of motion coupled-cluster theory based on an unrestricted Hartree-Fock reference for applications to high-spin open-shell systems. *J Chem Phys*, **2017**. 147(17), 174104.
 214. Nooijen, M. and Bartlett, R.J. Similarity transformed equation-of-motion coupled-cluster theory: Details, examples, and comparisons. *J. Chem. Phys.*, **1997**. 107(17), 6812-6830.
 215. Laurent, A.D. and Jacquemin, D. TD-DFT benchmarks: A review. *Int. J. Quantum Chem.*, **2013**. 113(17), 2019-2039.
 216. Vlček, A. and Zális, S. Modeling of charge-transfer transitions and excited states in d^6 transition metal complexes by DFT techniques. *Coord. Chem. Rev.*, **2007**. 251(3), 258-287.
 217. Zangwill, A. The education of Walter Kohn and the creation of density functional theory. *Archive for history of exact sciences*, **2014**. 68, 775-848.
 218. Jones, R.O., Density functional theory: a personal view, in *Strongly correlated systems: Theoretical methods*. **2011**, Springer. p. 1-28.
 219. Cremer, D. Density functional theory: coverage of dynamic and non-dynamic electron correlation effects. *Mol. Phys.*, **2001**. 99(23), 1899-1940.

220. Hohenberg, P. and Kohn, W. Inhomogeneous electron gas. *Phys. Rev.*, **1964**. 136(3B), B864.
221. Kohn, W. and Sham, L.J. Self-Consistent Equations Including Exchange and Correlation Effects. *Phys. Rev.*, **1965**. 140(4A), A1133-A1138.
222. Burke, K. Perspective on density functional theory. *J. Chem. Phys.*, **2012**. 136(15).
223. Bao, J.L., Gagliardi, L., and Truhlar, D.G. Self-Interaction Error in Density Functional Theory: An Appraisal. *J. Phys. Chem. Lett.*, **2018**. 9(9), 2353-2358.
224. Perdew, J.P. and Schmidt, K. *Jacob's ladder of density functional approximations for the exchange-correlation energy*. in *AIP Conference Proceedings*. **2001**. American Institute of Physics.
225. Harrison, N. An introduction to density functional theory. *Nato Science Series Sub Series III Computer and Systems Sciences*, **2003**. 187, 45-70.
226. Perdew, J.P., Burke, K., and Wang, Y. Generalized gradient approximation for the exchange-correlation hole of a many-electron system. *Phys. Rev. B Condens. Matter.*, **1996**. 54(23), 16533-16539.
227. Perdew, J.P., Burke, K., and Ernzerhof, M. Generalized Gradient Approximation Made Simple. *Phys. Rev. Lett.*, **1996**. 77(18), 3865-3868.
228. Becke, A.D. Density-functional exchange-energy approximation with correct asymptotic behavior. *Phys. Rev. A*, **1988**. 38(6), 3098-3100.
229. Lee, C., Yang, W., and Parr, R.G. Development of the Colle-Salvetti correlation-energy formula into a functional of the electron density. *Phys. Rev. B*, **1988**. 37(2), 785.
230. Perdew, J.P. Density-functional approximation for the correlation energy of the inhomogeneous electron gas. *Phys. Rev. B Condens. Matter.*, **1986**. 33(12), 8822-8824.
231. Zhao, Y. and Truhlar, D.G. The M06 suite of density functionals for main group thermochemistry, thermochemical kinetics, noncovalent interactions, excited states, and transition elements: two new functionals and systematic testing of four M06-class functionals and 12 other functionals. *Theor. Chem. Acc.*, **2008**. 120(1), 215-241.
232. Tao, J., Perdew, J.P., Staroverov, V.N., and Scuseria, G.E. Climbing the density functional ladder: Nonempirical meta-generalized gradient approximation designed for molecules and solids. *Phys. Rev. Lett.*, **2003**. 91(14), 146401.
233. Becke, A.D. Density-functional thermochemistry. III. The role of exact exchange. *J. Chem. Phys.*, **1993**. 98(7), 5648-5652.
234. Adamo, C. and Barone, V. Toward reliable density functional methods without adjustable parameters: The PBE0 model. *J. Chem. Phys.*, **1999**. 110(13), 6158-6170.
235. Perdew, J.P., Ernzerhof, M., and Burke, K. Rationale for mixing exact exchange with density functional approximations. *J. Chem. Phys.*, **1996**. 105(22), 9982-9985.
236. Grimme, S. Semiempirical hybrid density functional with perturbative second-order correlation. *J. Chem. Phys.*, **2006**. 124(3), 034108.
237. Dreuw, A. and Head-Gordon, M. Single-reference ab initio methods for the calculation of excited states of large molecules. *Chem. Rev.*, **2005**. 105(11), 4009-37.
238. Casida, M.E. Time-dependent density-functional theory for molecules and solids. *J. Mol. Struct.*, **2009**. 914, 3-18.

239. González, L., Escudero, D., and Serrano-Andrés, L. Progress and Challenges in the Calculation of Electronic Excited States. *ChemPhysChem*, **2012**. 13(1), 28-51.
240. Jaffé, H.H. and Miller, A.L. The fates of electronic excitation energy. *J. Chem. Educ.*, **1966**. 43(9), 469.
241. Penfold, T.J., Gindensperger, E., Daniel, C., and Marian, C.M. Spin-Vibronic Mechanism for Intersystem Crossing. *Chem. Rev.*, **2018**. 118(15), 6975-7025.
242. Gómez, S., Galván, I.F., Lindh, R., and González, L., Motivation and Basic Concepts, in *Quantum Chemistry and Dynamics of Excited States*. **2020**. p. 1-12.
243. Shafei, R., Strobel, P.J., Schmidt, P.J., Maganas, D., Schnick, W., and Neese, F. A theoretical spectroscopy study of the photoluminescence properties of narrow band Eu²⁺-doped phosphors containing multiple candidate doping centers. Prediction of an unprecedented narrow band red phosphor. *Phys. Chem. Chem. Phys.*, **2024**. 26(7), 6277-6291.
244. Kato, T., Haruta, N., and Sato, T., Definitions and Derivations, in *Vibronic Coupling Density: Understanding Molecular Deformation*. **2021**, Springer Singapore: Singapore. p. 69-113.
245. Krempel, S., Winterstetter, M., Plöhn, H., and Domcke, W. Path-integral treatment of multi-mode vibronic coupling. *J. Chem. Phys.*, **1994**. 100(2), 926-937.
246. Kundu, S., Roy, P.P., Fleming, G.R., and Makri, N. Franck-Condon and Herzberg-Teller Signatures in Molecular Absorption and Emission Spectra. *J. Phys. Chem. B*, **2022**. 126(15), 2899-2911.
247. Franck, J. and Dymond, E. Elementary processes of photochemical reactions. *Transactions of the Faraday Society*, **1926**. 21(February), 536-542.
248. Condon, E. The theory of complex spectra. *Phys. Rev.*, **1930**. 36(7), 1121.
249. Condon, E. A theory of intensity distribution in band systems. *Phys. Rev.*, **1926**. 28(6), 1182.
250. Herzberg, G. and Teller, E. Schwingungsstruktur der Elektronenübergänge bei mehratomigen Molekülen. *Z. Phys. Chem.*, **1933**. 21(1), 410-446.
251. Baiardi, A., Bloino, J., and Barone, V. General Time Dependent Approach to Vibronic Spectroscopy Including Franck-Condon, Herzberg-Teller, and Duschinsky Effects. *J. Chem. Theory Comput.*, **2013**. 9(9), 4097-115.
252. Jahn, H.A., Teller, E., and Donnan, F.G. Stability of polyatomic molecules in degenerate electronic states - I—Orbital degeneracy. *Proc. R. Soc. Lond. A - Mathematical and Physical Sciences*, **1937**. 161(905), 220-235.
253. Maganas, D., Kristiansen, P., Duda, L.C., Knop-Gericke, A., DeBeer, S., Schlögl, R., and Neese, F. Combined Experimental and Ab Initio Multireference Configuration Interaction Study of the Resonant Inelastic X-ray Scattering Spectrum of CO₂. *J. Phys. Chem. C*, **2014**. 118(35), 20163-20175.
254. Atanasov, M., Zadrozny, J.M., Long, J.R., and Neese, F. A theoretical analysis of chemical bonding, vibronic coupling, and magnetic anisotropy in linear iron(II) complexes with single-molecule magnet behavior. *Chem. Sci.*, **2013**. 4(1), 139-156.

255. Bersuker, I.B. The Jahn-Teller and Pseudo-Jahn-Teller Effects: A Unique and Only Source of Spontaneous Symmetry Breaking in Atomic Matter. *Symmetry*, **2021**. 13(9), 1577.
256. Worth, G.A. and Cederbaum, L.S. Beyond Born-Oppenheimer: molecular dynamics through a conical intersection. *Annu. Rev. Phys. Chem.*, **2004**. 55, 127-58.
257. Ham, F.S. Dynamical Jahn-Teller effect in paramagnetic resonance spectra: Orbital reduction factors and partial quenching of spin-orbit interaction. *Phys. Rev.*, **1965**. 138(6A), A1727.
258. Habitz, P. and Schwarz, W.H.E. Vibronic and Spin-Orbit Splitting in Spectra of Systems Exhibiting Jahn-Teller-Effect. *Theoret. Claim. Acta.*, **1973**. 28(3), 267-282.
259. Streltsov, S.V., Temnikov, F.V., Kugel, K.I., and Khomskii, D.I. Interplay of the Jahn-Teller effect and spin-orbit coupling: The case of trigonal vibrations. *Phys. Rev. B*, **2022**. 105(20), 205142.
260. Streltsov, S.V. and Khomskii, D.I. Jahn-Teller Effect and Spin-Orbit Coupling: Friends or Foes? *Phys. Rev. X*, **2020**. 10(3), 031043.
261. Berova, N., Nakanishi, K., and Woody, R.W., Circular dichroism: principles and applications. **2000**: John Wiley & Sons.
262. Kelvin, W.T.B., Baltimore lectures on molecular dynamics and the wave theory of light. **1904**: CJ Clay and Sons.
263. Micali, N., Engelkamp, H., Van Rhee, P., Christianen, P., Scolaro, L.M., and Maan, J. Selection of supramolecular chirality by application of rotational and magnetic forces. *Nature Chem.*, **2012**. 4(3), 201-207.
264. Hsu, E.C. and Holzwarth, G. Vibrational circular dichroism observed in crystalline α -NiSO₄·6H₂O and α -ZnSeO₄·6H₂O between 1900 and 5000 cm⁻¹. *J. Chem. Phys.*, **1973**. 59(9), 4678-4685.
265. Kuwata-Gonokami, M., Saito, N., Ino, Y., Kauranen, M., Jefimovs, K., Vallius, T., Turunen, J., and Svirko, Y. Giant optical activity in quasi-two-dimensional planar nanostructures. *Phys. Rev. Lett.*, **2005**. 95(22), 227401.
266. Hendry, E., Carpy, T., Johnston, J., Popland, M., Mikhaylovskiy, R., Lapthorn, A., Kelly, S., Barron, L., Gadegaard, N., and Kadodwala, M. Ultrasensitive detection and characterization of biomolecules using superchiral fields. *Nature Nanotech.*, **2010**. 5(11), 783-787.
267. Peacock, R.D. and Stewart, B. Natural Circular Dichroism in X-ray Spectroscopy. *J. Phys. Chem. B*, **2001**. 105(2), 351-360.
268. Foglia, N.O., Maganas, D., and Neese, F. Going beyond the electric-dipole approximation in the calculation of absorption and (magnetic) circular dichroism spectra including scalar relativistic and spin-orbit coupling effects. *J. Chem. Phys.*, **2022**. 157(8), 084120.
269. List, N.H., Saue, T., and Norman, P. Rotationally averaged linear absorption spectra beyond the electric-dipole approximation. *Mol. Phys.*, **2017**. 115(1-2), 63-74.
270. Bernadotte, S., Atkins, A.J., and Jacob, C.R. Origin-independent calculation of quadrupole intensities in X-ray spectroscopy. *J. Chem. Phys.*, **2012**. 137(20), 204106.

271. Neese, F. and Solomon, E.I. MCD C-Term Signs, Saturation Behavior, and Determination of Band Polarizations in Randomly Oriented Systems with Spin $S \geq 1/2$. Applications to $S = 1/2$ and $S = 5/2$. *Inorg. Chem.*, **1999**. 38(8), 1847-1865.
272. Ganyushin, D. and Neese, F. First-principles calculations of magnetic circular dichroism spectra. *J. Chem. Phys.*, **2008**. 128(11), 114117.
273. de Souza, B., Neese, F., and Izsak, R. On the theoretical prediction of fluorescence rates from first principles using the path integral approach. *J. Chem. Phys.*, **2018**. 148(3), 034104.
274. de Souza, B., Farias, G., Neese, F., and Izsak, R. Predicting Phosphorescence Rates of Light Organic Molecules Using Time-Dependent Density Functional Theory and the Path Integral Approach to Dynamics. *J. Chem. Theory Comput.*, **2019**. 15(3), 1896-1904.
275. de Souza, B., Farias, G., Neese, F., and Izsak, R. Efficient simulation of overtones and combination bands in resonant Raman spectra. *J. Chem. Phys.*, **2019**. 150(21), 214102.
276. Ianconescu, R. and Pollak, E. Photoinduced cooling of polyatomic molecules in an electronically excited state in the presence of Dushinskii rotations. *J. Phys. Chem. A*, **2004**. 108(39), 7778-7784.
277. Tatchen, J. and Pollak, E. Ab initio spectroscopy and photoinduced cooling of the trans-stilbene molecule. *J. Chem. Phys.*, **2008**. 128(16), 164303.
278. Niu, Y., Peng, Q., Deng, C., Gao, X., and Shuai, Z. Theory of excited state decays and optical spectra: application to polyatomic molecules. *J. Phys. Chem. A*, **2010**. 114(30), 7817-31.
279. Peng, Q., Niu, Y.L., Deng, C.M., and Shuai, Z.G. Vibration correlation function formalism of radiative and non-radiative rates for complex molecules. *Chem. Phys.*, **2010**. 370(1-3), 215-222.
280. Improta, R., Scalmani, G., Frisch, M.J., and Barone, V. Toward effective and reliable fluorescence energies in solution by a new state specific polarizable continuum model time dependent density functional theory approach. *J. Chem. Phys.*, **2007**. 127(7), 074504.
281. Barone, V., Bloino, J., Biczysko, M., and Santoro, F. Fully Integrated Approach to Compute Vibrationally Resolved Optical Spectra: From Small Molecules to Macrosystems. *J. Chem. Theory Comput.*, **2009**. 5(3), 540-54.
282. Liu, Y., Cerezo, J., Mazzeo, G., Lin, N., Zhao, X., Longhi, G., Abbate, S., and Santoro, F. Vibronic Coupling Explains the Different Shape of Electronic Circular Dichroism and of Circularly Polarized Luminescence Spectra of Hexahelicenes. *J. Chem. Theory Comput.*, **2016**. 12(6), 2799-819.
283. Mori, K., Goumans, T.P., van Lenthe, E., and Wang, F. Predicting phosphorescent lifetimes and zero-field splitting of organometallic complexes with time-dependent density functional theory including spin-orbit coupling. *Phys. Chem. Chem. Phys.*, **2014**. 16(28), 14523-30.
284. Englman, R. and Jortner, J. The energy gap law for radiationless transitions in large molecules. *Mol. Phys.*, **1970**. 18(2), 145-164.
285. Baryshnikov, G., Minaev, B., and Agren, H. Theory and Calculation of the Phosphorescence Phenomenon. *Chem. Rev.*, **2017**. 117(9), 6500-6537.

286. Mishra, K.C. and Collins, J. Formulation of radiative and nonradiative transitions of a polyatomic system within the crude adiabatic approximation. *Optical Materials: X*, **2022**. 15, 100190.
287. Tomasi, J., Mennucci, B., and Cammi, R. Quantum mechanical continuum solvation models. *Chem. Rev.*, **2005**. 105(8), 2999-3094.
288. Marini, A., Munoz-Losa, A., Biancardi, A., and Mennucci, B. What is solvatochromism? *J. Phys. Chem. B*, **2010**. 114(51), 17128-35.
289. Rauh, R.D. and Leermakers, P.A. Solvent effects upon the phosphorescence lifetimes and photoreactivity of butyrophenone. *J. Am. Chem. Soc.*, **1968**. 90(9), 2246-2249.
290. Reichardt, C., Solvent and Solvent Effects in Organic Chemistry. **2002**.
291. Cossiello, R.F., Akcelrud, L., and Atvars, D.Z. Solvent and molecular weight effects on fluorescence emission of MEH-PPV. *Journal of the Brazilian Chemical Society*, **2005**. 16(1), 74-86.
292. Suppan, P. and Ghoneim, N., Solvatochromism. **1997**: Royal Society of Chemistry.
293. Stufkens, D.J. and Vlcek, A. Ligand-dependent excited state behaviour of Re(I) and Ru(II) carbonyl-diimine complexes. *Coord. Chem. Rev.*, **1998**. 177(1), 127-179.
294. Kumar, A., Sun, S.-S., and Lees, A.J., Photophysics and Photochemistry of Organometallic Rhenium Diimine Complexes, in *Photophysics of Organometallics*, A.J. Lees, Editor. **2009**, Springer Berlin Heidelberg: Berlin, Heidelberg. p. 37-71.
295. Lees, A.J., Photophysics of organometallics. Vol. 29. **2010**: Springer Science & Business Media.
296. Vaughan, J.G., Reid, B.L., Ramchandani, S., Wright, P.J., Muzzioli, S., Skelton, B.W., Raiteri, P., Brown, D.H., Stagni, S., and Massi, M. The photochemistry of rhenium(I) tricarbonyl N-heterocyclic carbene complexes. *Dalton Trans.*, **2013**. 42(39), 14100-14.
297. Thompson, D.W., Ito, A., and Meyer, T.J. $[\text{Ru}(\text{bpy})_3]^{2+*}$ and other remarkable metal-to-ligand charge transfer (MLCT) excited states*. *Pure Appl. Chem.*, **2013**. 85(7), 1257-1305.
298. Kleinschmidt, M., van Wullen, C., and Marian, C.M. Intersystem-crossing and phosphorescence rates in *fac*-Ir(III)(ppy)₃: a theoretical study involving multi-reference configuration interaction wavefunctions. *J. Chem. Phys.*, **2015**. 142(9), 094301.
299. Mohammed, O.F., Kwon, O.H., Othon, C.M., and Zewail, A.H. Charge transfer assisted by collective hydrogen-bonding dynamics. *Angew. Chem. Int. Ed.*, **2009**. 48(34), 6251-6.
300. Nishiya, T., Yamauchi, S., Hirota, N., Baba, M., and Hanazaki, I. Fluorescence studies of intramolecularly hydrogen-bonded o-hydroxyacetophenone, salicylamide, and related molecules. *J. Phys. Chem.*, **1986**. 90(22), 5730-5735.
301. Furstenberg, A. and Vauthey, E. Excited-state dynamics of the fluorescent probe Lucifer Yellow in liquid solutions and in heterogeneous media. *Photochem. Photobiol. Sci.*, **2005**. 4(3), 260-7.
302. Krystkowiak, E., Dobek, K., and Maciejewski, A. Origin of the strong effect of protic solvents on the emission spectra, quantum yield of fluorescence and fluorescence lifetime of 4-aminophthalimide. *J. Photochem. Photobiol. A: Chem*, **2006**. 184(3), 250-264.

303. Sherin, P.S., Grilj, J., Tsentalovich, Y.P., and Vauthey, E. Ultrafast excited-state dynamics of kynurenine, a UV filter of the human eye. *J. Phys. Chem. B*, **2009**. 113(14), 4953-62.
304. Cossi, M. and Barone, V. Time-dependent density functional theory for molecules in liquid solutions. *J. Chem. Phys.*, **2001**. 115(10), 4708-4717.
305. Vreven, T. and Morokuma, K. The ONIOM (our own N-layered integrated molecular orbital + molecular mechanics) method for the first singlet excited (S 1) state photoisomerization path of a retinal protonated Schiff base. *J. Chem. Phys.*, **2000**. 113(8), 2969-2975.
306. Gao, J. and Truhlar, D.G. Quantum mechanical methods for enzyme kinetics. *Annu. Rev. Phys. Chem.*, **2002**. 53(1), 467-505.
307. Chipot, C. and Pohorille, A., Free energy calculations. Vol. 86. **2007**: Springer.
308. Cammi, R. and Mennucci, B. Linear response theory for the polarizable continuum model. *J. Chem. Phys.*, **1999**. 110(20), 9877-9886.
309. Larsson, P. and Lindahl, E. A high-performance parallel-generalized born implementation enabled by tabulated interaction rescaling. *J. Comput. Chem.*, **2010**. 31(14), 2593-2600.
310. Zhang, H., Tan, T., and van der Spoel, D. Generalized Born and Explicit Solvent Models for Free Energy Calculations in Organic Solvents: Cyclodextrin Dimerization. *J. Chem. Theory Comput.*, **2015**. 11(11), 5103-5113.
311. Zhang, J., Zhang, H., Wu, T., Wang, Q., and van der Spoel, D. Comparison of Implicit and Explicit Solvent Models for the Calculation of Solvation Free Energy in Organic Solvents. *J. Chem. Theory Comput.*, **2017**. 13(3), 1034-1043.
312. Barone, V. and Cossi, M. Quantum calculation of molecular energies and energy gradients in solution by a conductor solvent model. *J. Phys. Chem. A*, **1998**. 102(11), 1995-2001.
313. Marenich, A.V., Cramer, C.J., and Truhlar, D.G. Universal solvation model based on solute electron density and on a continuum model of the solvent defined by the bulk dielectric constant and atomic surface tensions. *J. Phys. Chem. B*, **2009**. 113(18), 6378-6396.
314. Warshel, A. and Levitt, M. Theoretical studies of enzymic reactions: dielectric, electrostatic and steric stabilization of the carbonium ion in the reaction of lysozyme. *J. Mol. Biol.*, **1976**. 103(2), 227-249.
315. York, D.M. and Karplus, M. A smooth solvation potential based on the conductor-like screening model. *J. Phys. Chem. A*, **1999**. 103(50), 11060-11079.
316. Garcia-Ratés, M. and Neese, F. Effect of the Solute Cavity on the Solvation Energy and its Derivatives within the Framework of the Gaussian Charge Scheme. *J. Comput. Chem.*, **2020**. 41(9), 922-939.
317. Lange, A.W. and Herbert, J.M. A smooth, nonsingular, and faithful discretization scheme for polarizable continuum models: The switching/Gaussian approach. *J. Chem. Phys.*, **2010**. 133(24).
318. Garcia-Ratés, M. and Neese, F. Efficient implementation of the analytical second derivatives of hartree-fock and hybrid DFT energies within the framework of the

- conductor-like polarizable continuum model. *J. Comput. Chem.*, **2019**. 40(20), 1816-1828.
319. Cramer, C.J. and Truhlar, D.G. Implicit solvation models: equilibria, structure, spectra, and dynamics. *Chem. Rev.*, **1999**. 99, 2161-2200.
 320. Ponder, J.W. and Case, D.A. Force fields for protein simulations. *Adv. Protein Chem.*, **2003**. 66, 27-85.
 321. Sousa, C., Tosoni, S., and Illas, F. Theoretical approaches to excited-state-related phenomena in oxide surfaces. *Chem. Rev.*, **2013**. 113(6), 4456-95.
 322. Maganas, D., Trunschke, A., Schlogl, R., and Neese, F. A unified view on heterogeneous and homogeneous catalysts through a combination of spectroscopy and quantum chemistry. *Faraday Discuss.*, **2016**. 188, 181-97.
 323. Kubas, A., Berger, D., Oberhofer, H., Maganas, D., Reuter, K., and Neese, F. Surface Adsorption Energetics Studied with "Gold Standard" Wave-Function-Based Ab Initio Methods: Small-Molecule Binding to TiO₂(110). *J. Phys. Chem. Let.*, **2016**. 7(20), 4207-4212.
 324. Lang, P.F. Is a Metal "Ions in a Sea of Delocalized Electrons?". *J. Chem. Educ.*, **2018**. 95(10), 1787-1793.
 325. Staemmler, V., The Cluster Approach for the Adsorption of Small Molecules on Oxide Surfaces, in *Theoretical Aspects of Transition Metal Catalysis*. **2005**. p. 219-256.
 326. Pust, P., Wochnik, A.S., Baumann, E., Schmidt, P.J., Wiechert, D., Scheu, C., and Schnick, W. Ca[LiAl₃N₄]:Eu²⁺—A Narrow-Band Red-Emitting Nitridolithoaluminate. *Chem. Mater.*, **2014**. 26(11), 3544-3549.
 327. Schmiechen, S., Schneider, H., Wagatha, P., Hecht, C., Schmidt, P.J., and Schnick, W. Toward New Phosphors for Application in Illumination-Grade White pc-LEDs: The Nitridomagnesosilicates Ca[Mg₃SiN₄]:Ce³⁺, Sr[Mg₃SiN₄]:Eu²⁺, and Eu[Mg₃SiN₄]. *Chem. Mater.*, **2014**. 26(8), 2712-2719.
 328. Schmiechen, S., Strobel, P., Hecht, C., Reith, T., Siegert, M., Schmidt, P.J., Huppertz, P., Wiechert, D., and Schnick, W. Nitridomagnesosilicate Ba[Mg₃SiN₄]:Eu²⁺ and Structure–Property Relations of Similar Narrow-Band Red Nitride Phosphors. *Chem. Mater.*, **2015**. 27(5), 1780-1785.
 329. Pust, P., Weiler, V., Hecht, C., Tucks, A., Wochnik, A.S., Henss, A.K., Wiechert, D., Scheu, C., Schmidt, P.J., and Schnick, W. Narrow-band red-emitting Sr[LiAl₃N₄]:Eu²⁺ as a next-generation LED-phosphor material. *Nat. Mater.*, **2014**. 13(9), 891-6.
 330. Liao, M., Mu, Z., Wang, Q., Zhang, X., Dong, H., Wen, M., and Wu, F. Understanding the cyan-emitting phosphor RbNa(Li₃SiO₄)₂: Eu²⁺ by providing Rb ion vacancies. *J. Alloys Compd.*, **2020**. 837.
 331. Liao, H., Zhao, M., Molokeev, M.S., Liu, Q., and Xia, Z. Learning from a Mineral Structure toward an Ultra-Narrow-Band Blue-Emitting Silicate Phosphor RbNa₃(Li₃SiO₄)₄:Eu²⁺. *Angew. Chem. Int. Ed.*, **2018**. 57(36), 11728-11731.
 332. Shannon, R.D. Revised effective ionic radii and systematic studies of interatomic distances in halides and chalcogenides. *Acta Cryst. section A*, **1976**. 32(5), 751-767.
 333. Izsak, R., Riplinger, C., Blunt, N.S., de Souza, B., Holzmann, N., Crawford, O., Camps, J., Neese, F., and Schopf, P. Quantum computing in pharma: A multilayer embedding approach for near future applications. *J. Comput. Chem.*, **2023**. 44(3), 406-421.

334. Petit, J., Lannoo, M., and Allan, G. Calculation of the optical properties of the isolated dangling bond in silicon. *Solid State Commun.*, **1986**. 60(11), 861-865.
335. Assmann, J. and Mönch, W. Optical properties of dangling-bond states at cleaved silicon surfaces. *Surf. Sci.*, **1980**. 99(1), 34-44.
336. Wadt, W.R. and Hay, P.J. Ab initio effective core potentials for molecular calculations. Potentials for main group elements Na to Bi. *J. Chem. Phys.*, **1985**. 82(1), 284-298.
337. Hay, P.J. and Wadt, W.R. Ab initio effective core potentials for molecular calculations. Potentials for the transition metal atoms Sc to Hg. *J. Chem. Phys.*, **1985**. 82(1), 270-283.
338. Hay, P.J. and Wadt, W.R. Ab initio effective core potentials for molecular calculations. Potentials for K to Au including the outermost core orbitals. *J. Chem. Phys.*, **1985**. 82(1), 299-310.
339. Dunning, T.H. and Hay, P.J., Gaussian Basis Sets for Molecular Calculations, in *Methods of Electronic Structure Theory*, H.F. Schaefer, Editor. **1977**, Springer US: Boston, MA. p. 1-27.
340. Fuentealba, P., Preuss, H., and Stoll, H. A proper account of core-polarization with pseudopotentials: single valence-electron alkali compounds. *Chem. Phys. Lett.*, **1982**. 89(5), 418-422.
341. Kaupp, M., Schleyer, P.v.R., Stoll, H., and Preuss, H. The question of bending of the alkaline earth dihalides MX_2 (M= beryllium, magnesium, calcium, strontium, barium; X= fluorine, chlorine, bromine, iodine). An ab initio pseudopotential study. *J. Am. Chem. Soc.*, **1991**. 113(16), 6012-6020.
342. Bergner, A., Dolg, M., Küchle, W., Stoll, H., and Preuß, H. Ab initio energy-adjusted pseudopotentials for elements of groups 13–17. *Mol. Phys.*, **1993**. 80(6), 1431-1441.
343. Leininger, T., Nicklass, A., Küchle, W., Stoll, H., Dolg, M., and Bergner, A. The accuracy of the pseudopotential approximation: Non-frozen-core effects for spectroscopic constants of alkali fluorides XF (X= K, Rb, Cs). *Chem. Phys. Lett.*, **1996**. 255(4-6), 274-280.
344. Mulliken, R.S. Electronic population analysis on LCAO–MO molecular wave functions. I. *J. Chem. Phys.*, **1955**. 23(10), 1833-1840.
345. Mulliken, R. Electronic population analysis on LCAO-MO molecular wave functions. III. Effects of hybridization on overlap and gross AO populations. *J. Chem. Phys.*, **1955**. 23(12), 2338-2342.
346. Mulliken, R.S. Electronic Population Analysis on LCAO–MO Molecular Wave Functions. II. Overlap Populations, Bond Orders, and Covalent Bond Energies. *J. Chem. Phys.*, **1955**. 23(10), 1841-1846.
347. Mulliken, R. Electronic population analysis on LCAO-MO molecular wave functions. IV. Bonding and antibonding in LCAO and valence-bond theories. *J. Chem. Phys.*, **1955**. 23(12), 2343-2346.
348. Cusachs, L.C. and Politzer, P. On the problem of defining the charge on an atom in a molecule. *Chem. Phys. Lett.*, **1968**. 1(11), 529-531.
349. Löwdin, P.O. On the non-orthogonality problem connected with the use of atomic wave functions in the theory of molecules and crystals. *J. Chem. Phys.*, **1950**. 18(3), 365-375.

350. Hirshfeld, F.L. Bonded-atom fragments for describing molecular charge densities. *Theoret. Claim. Acta.*, **1977**. 44, 129-138.
351. Cox, S. and Williams, D. Representation of the molecular electrostatic potential by a net atomic charge model. *J. Comput. Chem.*, **1981**. 2(3), 304-323.
352. Wiberg, K.B. and Rablen, P.R. Comparison of Atomic Charges Derived Via Different Procedures. *J. Comput. Chem.*, **1993**. 14(12), 1504-1518.
353. Breneman, C.M. and Wiberg, K.B. Determining atom-centered monopoles from molecular electrostatic potentials. The need for high sampling density in formamide conformational analysis. *J. Comput. Chem.*, **1990**. 11(3), 361-373.
354. Neese, F. Software update: The ORCA program system—Version 5.0. *Wiley Interdiscip. Rev. Comput. Mol. Sci.*, **2022**. 12(5), e1606.
355. Neese, F., Wennmohs, F., Becker, U., and Riplinger, C. The ORCA quantum chemistry program package. *J. Chem. Phys.*, **2020**. 152(22), 224108.
356. OECD, World Energy Outlook 2023. **2023**, Paris.
357. Pust, P., Schmidt, P.J., and Schnick, W. A revolution in lighting. *Nat. Mater.*, **2015**. 14(5), 454-8.
358. Hoerder, G.J., Seibald, M., Baumann, D., Schroder, T., Peschke, S., Schmid, P.C., Tyborski, T., Pust, P., Stoll, I., Bergler, M., Patzig, C., Reissaus, S., Krause, M., Berthold, L., Hoche, T., Johrendt, D., and Huppertz, H. Sr[Li₂Al₂O₂N₂]:Eu²⁺-A high performance red phosphor to brighten the future. *Nat. Commun.*, **2019**. 10.
359. Zhou, X.Q., Qiao, J.W., and Xia, Z.G. Learning from Mineral Structures toward New Luminescence Materials for Light-Emitting Diode Applications. *Chem. Mater.*, **2021**. 33(4), 1083-1098.
360. Zhao, M., Liao, H., Molokeev, M.S., Zhou, Y., Zhang, Q., Liu, Q., and Xia, Z. Emerging ultra-narrow-band cyan-emitting phosphor for white LEDs with enhanced color rendition. *Light Sci. Appl.*, **2019**. 8, 38.
361. Liao, H., Zhao, M., Zhou, Y., Molokeev, M.S., Liu, Q., Zhang, Q., and Xia, Z. Polyhedron transformation toward stable narrow-band green phosphors for wide-color-gamut liquid crystal display. *Adv. Funct. Mater.*, **2019**. 29(30), 1901988.
362. Zhao, M., Liao, H., Ning, L., Zhang, Q., Liu, Q., and Xia, Z. Next-generation narrow-band green-emitting RbLi (Li₃SiO₄)₂:Eu²⁺ phosphor for backlight display application. *Adv. Mater.*, **2018**. 30(38), 1802489.
363. Bispo, A.G., Morais, A.J.D., Calado, C.M.S., Mazali, I.O., and Sigoli, F.A. Lanthanide-doped luminescent perovskites: A review of synthesis, properties, and applications. *J. Lumin.*, **2022**. 252.
364. Zhuo, Y., Mansouri Tehrani, A., Oliynyk, A.O., Duke, A.C., and Brgoch, J. Identifying an efficient, thermally robust inorganic phosphor host via machine learning. *Nat. Commun.*, **2018**. 9(1), 4377.
365. Wang, Z., Chu, I.-H., Zhou, F., and Ong, S.P. Electronic Structure Descriptor for the Discovery of Narrow-Band Red-Emitting Phosphors. *Chem. Mater.*, **2016**. 28(11), 4024-4031.

366. Tolhurst, T.M., Schmiechen, S., Pust, P., Schmidt, P.J., Schnick, W., and Moewes, A. Electronic Structure, Bandgap, and Thermal Quenching of $\text{Sr}[\text{Mg}_3\text{SiN}_4]:\text{Eu}^{2+}$ in Comparison to $\text{Sr}[\text{LiAl}_3\text{N}_4]:\text{Eu}^{2+}$. *Adv. Optical Mater.*, **2016**. 4(4), 584-591.
367. Tolhurst, T.M., Boyko, T.D., Pust, P., Johnson, N.W., Schnick, W., and Moewes, A. Investigations of the Electronic Structure and Bandgap of the Next-Generation LED-Phosphor $\text{Sr}[\text{LiAl}_3\text{N}_4]:\text{Eu}^{2+}$ -Experiment and Calculations. *Adv. Optical Mater.*, **2015**. 3(4), 546-550.
368. Zeuner, M., Hintze, F., and Schnick, W. Low Temperature Precursor Route for Highly Efficient Spherically Shaped LED-Phosphors $\text{M}_2\text{Si}_5\text{N}_8:\text{Eu}^{2+}$ (M = Eu, Sr, Ba). *Chem. Mater.*, **2009**. 21, 336.
369. Hecht, C., Stadler, F., Schmidt, P.J., auf der G nne, J.S., Baumann, V., and Schnick, W. $\text{SrAlSi}_4\text{N}_7:\text{Eu}^{2+}$ —a Nitridoalumosilicate Phosphor for Warm White Light (pc)LEDs with Edge-Sharing Tetrahedra. *Chem. Mater.*, **2009**. 21, 1595.
370. Mueller-Mach, R., Mueller, G., Krames, M.R., H ppe, H.A., Stadler, F., Schnick, W., Juestel, T., and Schmidt, P. Highly efficient all-nitride phosphor-converted white light emitting diode. *Phys. Status Solidi A*, **2005**. 202(9), 1727-1732.
371. Tolhurst, T.M., Strobel, P., Schmidt, P.J., Schnick, W., and Moewes, A. Direct Measurements of Energy Levels and Correlation with Thermal Quenching Behavior in Nitride Phosphors. *Chem. Mater.*, **2017**. 29(18), 7976-7983.
372. Zhao, M., Yang, Z., Ning, L., and Xia, Z. Tailoring of White Luminescence in a $\text{NaLi}_3\text{SiO}_4:\text{Eu}^{2+}$ Phosphor Containing Broad-Band Defect-Induced Charge-Transfer Emission. *Adv. Mater.*, **2021**. 33(29), e2101428.
373. Ruegenberg, F., Seibald, M., Baumann, D., Peschke, S., Philipp, F., and Huppertz, H. $\text{Rb}[\text{Li}_5\text{Si}_2\text{O}_7]$ - A Latecomer in the Family of Alkali Lithosilicates Hiding a Green-Emitting Lithosilicate. *Chem. Eur. J.*, **2021**. 27(45), 11701-11706.
374. Wimmer, D.S., Seibald, M., Baumann, D., Peschke, S., Wurst, K., Heymann, G., Dutzler, D., Garcia-Fuente, A., Urland, W., and Huppertz, H. Novel Narrow Band Cyan-Green Phosphor $\text{LiK}_7[\text{Li}_3\text{SiO}_4]_8:\text{Eu}^{2+}$ with Enhanced Suppression of Second Broad Band Emission. *Eur. J. Inorg. Chem.*, **2021**. 2021(43), 4470-4481.
375. Ruegenberg, F., Garc a-Fuente, A., Seibald, M., Baumann, D., Peschke, S., Urland, W., Meijerink, A., Huppertz, H., and Suta, M. Chasing Down the Eu^{2+} Ions: The Delicate Structure–Property Relationships in the Ultra-Narrow Band Phosphor $\text{K}_{1.6}\text{Na}_{2.1}\text{Li}_{0.3}[\text{Li}_3\text{SiO}_4]_4:\text{Eu}^{2+}$. *Adv. Optical Mater.*, **2021**. 9(24).
376. Liao, M., Wang, Q., Lin, Q., Xiong, M., Zhang, X., Dong, H., Lin, Z., Wen, M., Zhu, D., Mu, Z., and Wu, F. Na Replaces Rb towards High-Performance Narrow-Band Green Phosphors for Backlight Display Applications. *Adv. Optical Mater.*, **2021**. 9(17).
377. Uheda, K., Hirosaki, N., Yamamoto, Y., Naito, A., Nakajima, T., and Yamamoto, H. Luminescence properties of a red phosphor, $\text{CaAlSiN}_3:\text{Eu}^{2+}$, for white light-emitting diodes. *Electrochem. Solid-State Lett.*, **2006**. 9(4), H22-H25.
378. Schubert, E.F. and Kim, J.K. Solid-state light sources getting smart. *Science*, **2005**. 308(5726), 1274-8.
379. Pimputkar, S., Speck, J.S., DenBaars, S.P., and Nakamura, S. Prospects for LED lighting. *Nat. Photon.*, **2009**. 3(4), 179-181.

380. Wang, Y., Wang, Z., Wei, G., Yang, Y., He, S., Li, J., Shi, Y., Li, R., Suo, H., and Li, P. Efficient near-infrared broadband garnet phosphor for pc-LED and its application to vascular visualization and night vision. *Opt. Express*, **2022**. 30(16), 28550-28558.
381. Xiao, H., Zhang, J., Zhang, L., Wu, H., Wu, H., Pan, G., Liu, F., and Zhang, J. Cr³⁺ Activated Garnet Phosphor with Efficient Blue to Far-Red Conversion for pc-LED. *Adv. Optical Mater.*, **2021**. 9(20), 2101134.
382. Saikia, S., Joshi, A., Arfin, H., Badola, S., Saha, S., and Nag, A. Sb³⁺–Er³⁺-Codoped Cs₂NaInCl₆ for Emitting Blue and Short-Wave Infrared Radiation. *Angew. Chem. Int. Ed.*, **2022**. 61(32), e202201628.
383. Schmidt, P.J., Hintze, F.C., Pust, P.A.H., Weiler, V., Hecht, C.S., Schmiechen, S.F., Schnick, W., and Wiechert, D.U., *Phosphors, such as new narrow-band red emitting phosphors for solid state lighting*. 2017, Google Patents.
384. Pust, P., Hintze, F., Hecht, C., Weiler, V., Locher, A., Zitnanska, D., Harm, S., Wiechert, D., Schmidt, P.J., and Schnick, W. Group (III) Nitrides M[Mg₂Al₂N₄] (M = Ca, Sr, Ba, Eu) and Ba[Mg₂Ga₂N₄]—Structural Relation and Nontypical Luminescence Properties of Eu²⁺ Doped Samples. *Chem. Mater.*, **2014**. 26(21), 6113-6119.
385. Seibald, M., Baumann, D., Fiedler, T., Lange, S., Huppertz, H., Dutzler, D., Schroeder, T., Bichler, D., Plundrich, G., and Peschke, S. Luminophore And Process For Producing A Luminophore. *Patent WO2018/029299*, **2016**.
386. Zhang, Y., Yang, X., Zhao, S.N., Zhai, Y., Pang, X., and Lin, J. Recent Developments of Microscopic Study for Lanthanide and Manganese Doped Luminescent Materials. *Small*, **2022**. 18(50), e2205014.
387. Anh, N.D.Q., Le, P.X., and Lee, H.-Y. Selection of a Remote Phosphor Configuration to Enhance the Color Quality of White LEDs. *Current Optics and Photonics*, **2019**. 3(1), 78-85.
388. Ahn, Y.N., Kim, K.D., Anoop, G., Kim, G.S., and Yoo, J.S. Design of highly efficient phosphor-converted white light-emitting diodes with color rendering indices (R₁ – R₁₅) ≥ 95 for artificial lighting. *Sci. Rep.*, **2019**. 9(1), 16848.
389. Khan, S.A., Khan, N.Z., Sohail, M., Ahmed, J., Alhokbany, N., Alshehri, S.M., Xu, X., Zhu, J., and Agathopoulos, S. Modern aspects of strategies for developing single-phase broadly tunable white light-emitting phosphors. *J. Mater. Chem. C*, **2021**. 9(38), 13041-13071.
390. Zhuo, Y., Mansouri Tehrani, A., Oliynyk, A.O., Duke, A.C., and Brgoch, J. Identifying an efficient, thermally robust inorganic phosphor host via machine learning. *Nat. Commun.*, **2018**. 9(1), 4377.
391. Strobel, P., Schmiechen, S., Siegert, M., Tücks, A., Schmidt, P.J., and Schnick, W. Narrow-Band Green Emitting Nitridolithoalumosilicate Ba[Li₂(Al₂Si₂)N₆]:Eu²⁺ with Framework Topology whj for LED/LCD-Backlighting Applications. *Chem. Mater.*, **2015**. 27(17), 6109-6115.
392. Barandiarán, Z. and Seijo, L. Radial correlation effects on interconfigurational excitations at the end of the lanthanide series: A restricted active space second order perturbation study of Yb²⁺ and SrCl₂:Yb²⁺. *J. Chem. Phys.*, **2013**. 138(7).
393. Freeman, A.J. and Watson, R.E. Theoretical Investigation of Some Magnetic and Spectroscopic Properties of Rare-Earth Ions. *Phys. Rev.*, **1962**. 127(6), 2058-2075.

394. Koch, E., Multiplets and Spin-Orbit Coupling, in *Topology, Entanglement, and Strong Correlations*. **2020**, Forschungszentrum Jülich GmbH, Institute for Advanced Simulation.
395. Angeli, C. and Cimiraglia, R. Multireference perturbation configuration interaction V. Third-order energy contributions in the Moller-Plesset and Epstein-Nesbet partitions. *Theor. Chem. Acc.*, **2002**. 107(5), 313-317.
396. Neese, F. Importance of Direct Spin-Spin Coupling and Spin-Flip Excitations for the Zero-Field Splittings of Transition Metal Complexes: A Case Study. *J. Am. Chem. Soc.*, **2006**. 128(31), 10213-10222.
397. Pantazis, D.A., Chen, X.Y., Landis, C.R., and Neese, F. All-Electron Scalar Relativistic Basis Sets for Third-Row Transition Metal Atoms. *J. Chem. Theory Comput.*, **2008**. 4(6), 908-19.
398. Pantazis, D.A. and Neese, F. All-Electron Scalar Relativistic Basis Sets for the Lanthanides. *J. Chem. Theory Comput.*, **2009**. 5(9), 2229-38.
399. Pantazis, D.A. and Neese, F. All-Electron Scalar Relativistic Basis Sets for the Actinides. *J. Chem. Theory Comput.*, **2011**. 7(3), 677-684.
400. Pantazis, D.A. and Neese, F. All-electron scalar relativistic basis sets for the 6p elements. *Theor. Chem. Acc.*, **2012**. 131(11), 1292.
401. Douglas, M. and Kroll, N.M. Quantum electrodynamical corrections to the fine structure of helium. *Ann. Phys.*, **1974**. 82(1), 89-155.
402. Hess, B.A. Relativistic electronic-structure calculations employing a two-component no-pair formalism with external-field projection operators. *Phys. Rev. A*, **1986**. 33(6), 3742-3748.
403. Visscher, L. and Dyall, K.G. Dirac-Fock Atomic Electronic Structure Calculations Using Different Nuclear Charge Distributions. *At. Data Nucl. Data Tables*, **1997**. 67(2), 207-224.
404. Freitag, L., Knecht, S., Keller, S.F., Delcey, M.G., Aquilante, F., Pedersen, T.B., Lindh, R., Reiher, M., and González, L. Orbital entanglement and CASSCF analysis of the Ru-NO bond in a Ruthenium nitrosyl complex. *Phys. Chem. Chem. Phys.*, **2015**. 17(22), 14383-92.
405. Martin, W., Zalubas, R., and Hagan, L., Atomic energy levels-The rare-Earth elements. NSRDS-NBS 60. **1978**.
406. Schäfer, A., Horn, H., and Ahlrichs, R. Fully optimized contracted Gaussian basis sets for atoms Li to Kr. *J. Chem. Phys.*, **1992**. 97(4), 2571-2577.
407. Weigend, F. and Ahlrichs, R. Balanced basis sets of split valence, triple zeta valence and quadruple zeta valence quality for H to Rn: Design and assessment of accuracy. *Phys. Chem. Chem. Phys.*, **2005**. 7(18), 3297-305.
408. Wen, F. Crystal field analysis of the 8-coordinated cubic environment in optical materials. *Results in Optics*, **2021**. 3, 100056.
409. Schmiechen, S., Strobel, P., Hecht, C., Reith, T., Siegert, M., Schmidt, P.J., Huppertz, P., Wiechert, D., and Schnick, W. Nitridomagnesosilicate Ba[Mg₃SiN₄]:Eu²⁺ and Structure-Property Relations of Similar Narrow-Band Red Nitride Phosphors. *Chem. Mater.*, **2015**. 27(5), 1780-1785.

410. Wang, W., Tao, M.X., Liu, Y.X., Wei, Y., Xing, G.C., Dang, P.P., Lin, J., and Li, G.G. Photoluminescence Control of UC₄C₄-Type Phosphors with Superior Luminous Efficiency and High Color Purity via Controlling Site Selection of Eu²⁺ Activators. *Chem. Mater.*, **2019**. 31(21), 9200-9210.
411. Neese, F. The ORCA program system. *WIREs. Comput. Mol. Sci.*, **2012**. 2(1), 73-78.
412. Neese, F. Software update: the ORCA program system, version 4.0. *Wiley Interdiscip. Rev. Comput. Mol. Sci.*, **2018**. 8(1).
413. Eichkorn, K., Treutler, O., Öhm, H., Häser, M., and Ahlrichs, R. Auxiliary basis sets to approximate Coulomb potentials. *Chem. Phys. Lett.*, **1995**. 240(4), 283-290.
414. Neese, F., Wennmohs, F., Hansen, A., and Becker, U. Efficient, approximate and parallel Hartree–Fock and hybrid DFT calculations. A ‘chain-of-spheres’ algorithm for the Hartree–Fock exchange. *Chem. Phys.*, **2009**. 356(1–3), 98-109.
415. Helmich-Paris, B., de Souza, B., Neese, F., and Izsak, R. An improved chain of spheres for exchange algorithm. *J. Chem. Phys.*, **2021**. 155(10), 104109.
416. Demel, O., Pittner, J., and Neese, F. A Local Pair Natural Orbital-Based Multireference Mukherjee's Coupled Cluster Method. *J. Chem. Theory Comput.*, **2015**. 11(7), 3104-14.
417. Liakos, D.G. and Neese, F. Domain Based Pair Natural Orbital Coupled Cluster Studies on Linear and Folded Alkane Chains. *J. Chem. Theory Comput.*, **2015**. 11(5), 2137-43.
418. Dutta, A.K., Neese, F., and Izsak, R. Towards a pair natural orbital coupled cluster method for excited states. *J. Chem. Phys.*, **2016**. 145(3), 034102.
419. Dutta, A.K., Nooijen, M., Neese, F., and Izsak, R. Exploring the Accuracy of a Low Scaling Similarity Transformed Equation of Motion Method for Vertical Excitation Energies. *J. Chem. Theory Comput.*, **2018**. 14(1), 72-91.
420. Hirata, S. and Head-Gordon, M. Time-dependent density functional theory within the Tamm–Dancoff approximation. *Chem. Phys. Lett.*, **1999**. 314(3), 291-299.
421. Kubas, A., Berger, D., Oberhofer, H., Maganas, D., Reuter, K., and Neese, F. Surface Adsorption Energetics Studied with “Gold Standard” Wave-Function-Based Ab Initio Methods: Small-Molecule Binding to TiO₂(110). *J. Phys. Chem. Let.*, **2016**. 7, 4207-4212.
422. Weber, J. and Schmedt auf der Günne, J. Calculation of NMR Parameters in Ionic Solids by an Improved Self-Consistent Embedded Cluster Method. *Phys. Chem. Chem. Phys.*, **2010**. 12, 583-603.
423. Lindon, J.C. In Vivo NMR Methods. *Encyclopedia of Spectroscopy and Spectrometry*, **1999**.
424. Bühl, M., Malkin, V.G., and Kaupp, M., Calculation of NMR and EPR Parameters, Theory and Applications. **2004**.
425. Bühl, M. and van Mourik, T. NMR Spectroscopy: Quantum-Chemical Calculations. *Wiley Interdiscip. Rev. Comput. Mol. Sci.*, **2011**. 1, 634-647.
426. Grimme, S., Bannwarth, C., Dohm, S., Hansen, A., Pisarek, J., Pracht, P., Seibert, J., and Neese, F. Fully Automated Quantum-Chemistry-Based Computation of Spin–Spin-Coupled Nuclear Magnetic Resonance Spectra. *Angew. Chem. Int. Ed.*, **2017**. 56, 14763-14769.

427. Helgaker, T., Jaszuński, M., and Ruud, K. Ab Initio Methods for the Calculation of NMR Shielding and Indirect Spin–Spin Coupling Constants. *Chem. Rev.*, **1999**. 99, 293-352.
428. Roemelt, M., Maganas, D., DeBeer, S., and Neese, F. A combined DFT and restricted open-shell configuration interaction method including spin-orbit coupling: application to transition metal L-edge X-ray absorption spectroscopy. *J. Chem. Phys.*, **2013**. 138, 204101.
429. Amachraa, M., Wang, Z., Chen, C., Hariyani, S., Tang, H., Brgoch, J., and Ong, S.P. Predicting Thermal Quenching in Inorganic Phosphors. *Chem. Mater.*, **2020**. 32(14), 6256-6265.
430. Lin, Y.-C., Bettinelli, M., Sharma, S.K., Redlich, B., Speghini, A., and Karlsson, M. Unraveling the impact of different thermal quenching routes on the luminescence efficiency of the $\text{Y}_3\text{Al}_5\text{O}_{12}:\text{Ce}^{3+}$ phosphor for white light emitting diodes. *J. Mater. Chem. C*, **2020**. 8(40), 14015-14027.
431. Duke, A.C., Finley, E., Hermus, M., and Brgoch, J. Yellow-green luminescence and extreme thermal quenching in the $\text{Sr}_6\text{M}_2\text{Al}_4\text{O}_{15}:\text{Eu}^{2+}$ (M = Y, Lu, Sc) phosphor series. *Solid State Sci.*, **2016**. 60, 108-113.
432. Ha, J., Wang, Z., Novitskaya, E., Hirata, G.A., Graeve, O.A., Ong, S.P., and McKittrick, J. An integrated first principles and experimental investigation of the relationship between structural rigidity and quantum efficiency in phosphors for solid state lighting. *J. Lumin.*, **2016**. 179, 297-305.
433. de Jong, M., Seijo, L., Meijerink, A., and Rabouw, F.T. Resolving the ambiguity in the relation between Stokes shift and Huang–Rhys parameter. *Phys. Chem. Chem. Phys.*, **2015**. 17(26), 16959-16969.
434. Huang, K., Rhys, A., and Mott, N.F. Theory of light absorption and non-radiative transitions in F-centres. *Proc. R. Soc. Lond. A - Mathematical and Physical Sciences*, **1950**. 204(1078), 406-423.
435. Zhuo, Y., Mansouri Tehrani, A., and Brgoch, J. Predicting the Band Gaps of Inorganic Solids by Machine Learning. *J. Phys. Chem. Lett.*, **2018**. 9(7), 1668-1673.
436. Neese, F. Metal and ligand hyperfine couplings in transition metal complexes: The effect of spin–orbit coupling as studied by coupled perturbed Kohn–Sham theory. *J. Chem. Phys.*, **2003**. 118(9), 3939-3948.
437. Neese, F., Hedman, B., Hodgson, K.O., and Solomon, E.I. Relationship between the Dipole Strength of Ligand Pre-Edge Transitions and Metal–Ligand Covalency. *Inorg. Chem.*, **1999**. 38(21), 4854-4860.
438. Strobel, P., Weiler, V., Schmidt, P.J., and Schnick, W. $\text{Sr}[\text{BeSi}_2\text{N}_4]:\text{Eu}^{2+}/\text{Ce}^{3+}$ and $\text{Eu}[\text{BeSi}_2\text{N}_4]$: Nontypical Luminescence in Highly Condensed Nitridoberyllsilicates. *Chem. Eur. J.*, **2018**. 24(28), 7243-7249.
439. Wang, X., Huang, X., Zhao, M., Tanner, P.A., Zhou, X., and Ning, L. Role of the Rigid Host Structure in Narrow-Band Green Emission of Eu^{2+} in $\text{Rb}_2\text{Na}_2(\text{Li}_3\text{SiO}_4)_4$: Insights into Electron–Phonon Coupling. *Inorg. Chem.*, **2022**. 61(19), 7617-7623.
440. Bouquiaux, J., Ponce, S., Jia, Y.C., Miglio, A., Mikami, M., and Gonze, X. A First-Principles Explanation of the Luminescent Line Shape of $\text{SrLiAl}_3\text{N}_4:\text{Eu}^{2+}$ Phosphor for Light-Emitting Diode Applications. *Chem. Mater.*, **2023**. 35(14), 5353-5361.

441. Yanai, T., Tew, D.P., and Handy, N.C. A new hybrid exchange–correlation functional using the Coulomb-attenuating method (CAM-B3LYP). *Chem. Phys. Lett.*, **2004**. 393(1), 51-57.
442. Casanova-Páez, M., Dardis, M.B., and Goerigk, L. ω B2PLYP and ω B2GPPLYP: The First Two Double-Hybrid Density Functionals with Long-Range Correction Optimized for Excitation Energies. *J. Chem. Theory Comput.*, **2019**. 15(9), 4735-4744.
443. Guo, Y., Riplinger, C., Liakos, D.G., Becker, U., Saitow, M., and Neese, F. Linear scaling perturbative triples correction approximations for open-shell domain-based local pair natural orbital coupled cluster singles and doubles theory [DLPNO-CCSD(T_0/T)]. *J. Chem. Phys.*, **2020**. 152(2), 024116.
444. Neese, F. Prediction of molecular properties and molecular spectroscopy with density functional theory: From fundamental theory to exchange-coupling. *Coord. Chem. Rev.*, **2009**. 253(5-6), 526-563.
445. Suturina, E.A., Maganas, D., Bill, E., Atanasov, M., and Neese, F. Magneto-Structural Correlations in a Series of Pseudotetrahedral $[\text{Co}^{\text{II}}(\text{XR})_4]^{2-}$ Single Molecule Magnets: An ab Initio Ligand Field Study. *Inorg. Chem.*, **2015**. 54(20), 9948-61.
446. Jiang, S.D., Maganas, D., Levesanos, N., Ferentinos, E., Haas, S., Thirunavukkuarasu, K., Krzystek, J., Dressel, M., Bogani, L., Neese, F., and Kyritsis, P. Direct Observation of Very Large Zero-Field Splitting in a Tetrahedral Ni(II)Se₄ Coordination Complex. *J. Am. Chem. Soc.*, **2015**. 137(40), 12923-8.
447. Aiga, F., Hiramatsu, R., and Ishida, K. Ab initio theoretical study of 4f→5d transitions in Eu²⁺-doped CaF₂. *J. Lumin.*, **2014**. 145, 951-955.
448. Ning, L., Huang, X., Huang, Y., and Tanner, P.A. Origin of the green persistent luminescence of Eu-doped SrAl₂O₄ from a multiconfigurational ab initio study of 4f⁷→4f⁶5d¹ transitions. *J. Mater. Chem. C*, **2018**. 6(25), 6637-6640.
449. Azam, S., Khan, S.A., and Goumri-Said, S. Exploring the optoelectronic properties of Nitrido-magneso-silicates: Ca[Mg₃SiN₄], Sr[Mg₃SiN₄], and Eu[Mg₃SiN₄]. *Semicond. Sci. Technol.*, **2017**. 32(5), 055017.
450. Ruegenberg, F., García-Fuente, A., Seibald, M., Baumann, D., Hoerder, G., Fiedler, T., Urland, W., Huppertz, H., Meijerink, A., and Suta, M. Mixed Microscopic Eu²⁺ Occupancies in the Next-Generation Red LED Phosphor Sr[Li₂Al₂O₂N₂]:Eu²⁺ (SALON:Eu²⁺). *Adv. Optical Mater.*, **2023**. 11(9), 2202732.
451. Xu, L., Wang, X., Wang, W., Sun, M., Choi, W.J., Kim, J.Y., Hao, C., Li, S., Qu, A., Lu, M., Wu, X., Colombari, F.M., Gomes, W.R., Blanco, A.L., de Moura, A.F., Guo, X., Kuang, H., Kotov, N.A., and Xu, C. Enantiomer-dependent immunological response to chiral nanoparticles. *Nature*, **2022**. 601(7893), 366-373.
452. Shibayev, P.P. and Pergolizzi, R.G. The effect of circularly polarized light on the growth of plants. *Int. J. Bot.*, **2011**. 7, 113-117.
453. Biet, T., Cauchy, T., Sun, Q., Ding, J., Hauser, A., Oulevey, P., Burgi, T., Jacquemin, D., Vanthuyne, N., Crassous, J., and Avarvari, N. Triplet state CPL active helicene-dithiolene platinum bipyridine complexes. *Chem. Commun.*, **2017**. 53(66), 9210-9213.
454. Baron, E., Goldhahn, R., Deppe, M., As, D.J., and Feneberg, M. Photoluminescence Line-Shape Analysis of Highly n-Type Doped Zincblende GaN. *Phys. Status Solidi B*, **2020**. 257(4), 1900522.

455. Egidi, F., Fusè, M., Baiardi, A., Bloino, J., Li, X., and Barone, V. Computational simulation of vibrationally resolved spectra for spin-forbidden transitions. *Chirality*, **2018**. 30(7), 850-865.
456. Longhi, G., Castiglioni, E., Koshoubu, J., Mazzeo, G., and Abbate, S. Circularly Polarized Luminescence: A Review of Experimental and Theoretical Aspects. *Chirality*, **2016**. 28(10), 696-707.
457. Richardson, F.S. and Riehl, J.P. Circularly polarized luminescence spectroscopy. *Chem. Rev.*, **1977**. 77(6), 773-792.
458. Riehl, J.P. and Coruh, N. Circularly Polarized Luminescence from Eu(III) as a Probe of Metal-Ion Binding-Sites in Calcium-Binding Proteins. *Eur. J. Solid State Inorg. Chem.*, **1991**. 28, 263-266.
459. Riehl, J.P. and Richardson, F.S. Circularly polarized luminescence spectroscopy. *Chem. Rev.*, **1986**. 86(1), 1-16.
460. Kaminski, M., Cukras, J., Pecul, M., Rizzo, A., and Coriani, S. A computational protocol for the study of circularly polarized phosphorescence and circular dichroism in spin-forbidden absorption. *Phys. Chem. Chem. Phys.*, **2015**. 17(29), 19079-86.
461. McAlexander, H.R. and Crawford, T.D. Simulation of circularly polarized luminescence spectra using coupled cluster theory. *J. Chem. Phys.*, **2015**. 142(15), 154101.
462. Ludowieg, H.D., Srebro-Hooper, M., Crassous, J., and Autschbach, J. Optical Activity of Spin-Forbidden Electronic Transitions in Metal Complexes from Time-Dependent Density Functional Theory with Spin-Orbit Coupling. *ChemistryOpen*, **2022**. 11(5), e202200020.
463. Mayorga Burrezo, P., Jimenez, V.G., Blasi, D., Ratera, I., Campana, A.G., and Veciana, J. Organic Free Radicals as Circularly Polarized Luminescence Emitters. *Angew. Chem. Int. Ed.*, **2019**. 58(45), 16282-16288.
464. Fujiki, M. and Yoshimoto, S. Time-evolved, far-red, circularly polarised luminescent polymer aggregates endowed with sacrificial helical Si-Si bond polymers. *Mater. Chem. Front.*, **2017**. 1(9), 1773-1785.
465. Ghidinelli, S., Abbate, S., Mazzeo, G., Paolesse, R., Pomarico, G., and Longhi, G. MCD and MCPL Characterization of Luminescent Si(IV) and P(V) Tritolylcorroles: The Role of Coordination Number. *ACS Omega*, **2021**. 6(40), 26659-26671.
466. Schulte, T.R., Holstein, J.J., Krause, L., Michel, R., Stalke, D., Sakuda, E., Umakoshi, K., Longhi, G., Abbate, S., and Clever, G.H. Chiral-at-Metal Phosphorescent Square-Planar Pt(II)-Complexes from an Achiral Organometallic Ligand. *J. Am. Chem. Soc.*, **2017**. 139(20), 6863-6866.
467. Zhao, F., Zhao, J.Y., Wang, Y., Liu, H.T., Shang, Q.H., Wang, N., Yin, X.D., Zheng, X.Y., and Chen, P.K. [5]Helicene-based chiral triarylboranes with large luminescence dissymmetry factors over a 10^{-2} level: synthesis and design strategy via isomeric tuning of steric substitutions. *Dalton Trans.*, **2022**. 51(16), 6226-6234.
468. Wang, X.Z., Sun, M.Y., Huang, Z.J., Xie, M., Huang, R.S., Lu, H.H., Zhao, Z.J., Zhou, X.P., and Li, D. Turn-On Circularly Polarized Luminescence in Metal-Organic Frameworks. *Adv. Optical Mater.*, **2021**. 9(23).

469. Mori, T., Frontiers of Circularly Polarized Luminescence Chemistry of Isolated Small Organic Molecules, in *Circularly Polarized Luminescence of Isolated Small Organic Molecules*, T. Mori, Editor. **2020**, Springer Singapore: Singapore. p. 1-10.
470. Gendron, F., Moore Ii, B., Cador, O., Pointillart, F., Autschbach, J., and Le Guennic, B. Ab Initio Study of Circular Dichroism and Circularly Polarized Luminescence of Spin-Allowed and Spin-Forbidden Transitions: From Organic Ketones to Lanthanide Complexes. *J. Chem. Theory Comput.*, **2019**. 15(7), 4140-4155.
471. Lee, E., Ju, H., Park, I.H., Jung, J.H., Ikeda, M., Kuwahara, S., Habata, Y., and Lee, S.S. pseudo[1]Catenane-Type Pillar[5]thiacrown Whose Planar Chiral Inversion is Triggered by Metal Cation and Controlled by Anion. *J. Am. Chem. Soc.*, **2018**. 140(30), 9669-9677.
472. OuYang, J. and Crassous, J. Chiral multifunctional molecules based on organometallic helicenenes: Recent advances. *Coord. Chem. Rev.*, **2018**. 376, 533-547.
473. Pescitelli, G., Ludeke, S., Chamayou, A.C., Marolt, M., Justus, V., Gorecki, M., Arrico, L., Di Bari, L., Islam, M.A., Gruber, I., Enamullah, M., and Janiak, C. Broad-Range Spectral Analysis for Chiral Metal Coordination Compounds: (Chiro)optical Superspectrum of Cobalt(II) Complexes. *Inorg. Chem.*, **2018**. 57(21), 13397-13408.
474. Pop, F. and Avarvari, N. Chiral metal-dithiolene complexes. *Coord. Chem. Rev.*, **2017**. 346, 20-31.
475. Richards, C.J. and Arthurs, R.A. Catalyst Optimisation for Asymmetric Synthesis by Ligand Chirality Element Addition: A Perspective on Stereochemical Cooperativity. *Chem. Eur. J.*, **2017**. 23(48), 11460-11478.
476. Sharma, S., Chauhan, M., Jamsheera, A., Tabassum, S., and Arjmand, F. Chiral transition metal complexes: Synthetic approach and biological applications. *Inorg. Chim. Acta*, **2017**. 458, 8-27.
477. Wu, T., You, X.Z., and Bour, P. Applications of chiroptical spectroscopy to coordination compounds. *Coord. Chem. Rev.*, **2015**. 284, 1-18.
478. Zhang, Y., Guo, J., Shi, L., Zhu, Y., Hou, K., Zheng, Y., and Tang, Z. Tunable chiral metal organic frameworks toward visible light-driven asymmetric catalysis. *Sci. Adv.*, **2017**. 3(8), e1701162.
479. Chen, B.H., Zhao, Z.M., and Morris, S.M. Chiral switches bring new twist to photonics. *Nat. Photon.*, **2022**. 16(3), 174-175.
480. Montali, A., Bastiaansen, C., Smith, P., and Weder, C. Polarizing energy transfer in photoluminescent materials for display applications. *Nature*, **1998**. 392(6673), 261-264.
481. Ma, J.-L., Peng, Q., and Zhao, C.-H. Circularly Polarized Luminescence Switching in Small Organic Molecules. *Chem. Eur. J.*, **2019**. 25(68), 15441-15454.
482. Avello, M.G., de la Torre, M.C., Guerrero-Martinez, A., Sierra, M.A., Gornitzka, H., and Hemmert, C. Chiral-at-Metal BODIPY-Based Iridium(III) Complexes: Synthesis and Luminescence Properties. *Eur. J. Inorg. Chem.*, **2020**. 2020(42), 4045-4053.
483. Avello, M.G., Frutos, M., de la Torre, M.C., Viso, A., Velado, M., de la Pradilla, R.F., Sierra, M.A., Gornitzka, H., and Hemmert, C. Chiral Sulfur Functional Groups as Definers of the Chirality at the Metal in Ir and Rh Half-Sandwich Complexes: A Combined CD/X-ray Study. *Chem. Eur. J.*, **2017**. 23(58), 14523-14531.

484. Bhaskararao, B. and Sunoj, R.B. Asymmetric Dual Chiral Catalysis using Iridium Phosphoramidites and Diarylprolinol Silyl Ethers: Insights into Stereodivergence. *ACS Catal.*, **2017**. 7(10), 6675-6685.
485. Dieckmann, M., Jang, Y.S., and Cramer, N. Chiral cyclopentadienyl iridium(III) complexes promote enantioselective cycloisomerizations giving fused cyclopropanes. *Angew. Chem. Int. Ed.*, **2015**. 54(41), 12149-52.
486. Fliedel, C., Labande, A., Manoury, E., and Poli, R. Chiral N-heterocyclic carbene ligands with additional chelating group(s) applied to homogeneous metal-mediated asymmetric catalysis. *Coord. Chem. Rev.*, **2019**. 394, 65-103.
487. Grell, Y., Demirel, N., Harms, K., and Meggers, E. Chiral Bis(oxazoline) Ligands as C₂-Symmetric Chiral Auxiliaries for the Synthesis of Enantiomerically Pure Bis-Cyclometalated Rhodium(III) Complexes. *Organometallics*, **2019**. 38(19), 3852-3859.
488. Hellou, N., Jahier-Diallo, C., Basle, O., Srebro-Hooper, M., Toupet, L., Roisnel, T., Caytan, E., Roussel, C., Vanthuyne, N., Autschbach, J., Mauduit, M., and Crassous, J. Electronic and chiroptical properties of chiral cycloiridiated complexes bearing helicenic NHC ligands. *Chem. Commun.*, **2016**. 52(59), 9243-6.
489. Loxq, P., Manoury, E., Poli, R., Deydier, E., and Labande, A. Synthesis of axially chiral biaryl compounds by asymmetric catalytic reactions with transition metals. *Coord. Chem. Rev.*, **2016**. 308, 131-190.
490. Melcher, M.C., Rolim Alves da Silva, B., Ivsic, T., and Strand, D. Chiral Discrimination in Rhodium(I) Catalysis by 2,5-Disubstituted 1,3a,4,6a-Tetrahydropentalene Ligands-More Than Just a Twist of the Olefins? *ACS Omega*, **2018**. 3(3), 3622-3630.
491. Mendola, D., Saleh, N., Hellou, N., Vanthuyne, N., Roussel, C., Toupet, L., Castiglione, F., Melone, F., Caronna, T., Fontana, F., Marti-Rujas, J., Parisini, E., Malpezzi, L., Mele, A., and Crassous, J. Synthesis and Structural Properties of Aza[n]helicene Platinum Complexes: Control of Cis and Trans Stereochemistry. *Inorg. Chem.*, **2016**. 55(5), 2009-17.
492. Shen, C.S., He, X.Y., Toupet, L., Norel, L., Rigaut, S., and Crassous, J. Dual Redox and Optical Control of Chiroptical Activity in Photochromic Dithienylethenes Decorated with Hexahelicene and Bis-Ethynyl-Ruthenium Units. *Organometallics*, **2018**. 37(5), 697-705.
493. Wang, C., Zheng, Y., Huo, H., Rose, P., Zhang, L., Harms, K., Hilt, G., and Meggers, E. Merger of visible light induced oxidation and enantioselective alkylation with a chiral iridium catalyst. *Chem. Eur. J.*, **2015**. 21(20), 7355-9.
494. Ye, B. and Cramer, N. Chiral Cyclopentadienyls: Enabling Ligands for Asymmetric Rh(III)-Catalyzed C-H Functionalizations. *Acc. Chem. Res.*, **2015**. 48(5), 1308-18.
495. Shen, C., Srebro-Hooper, M., Weymuth, T., Krausbeck, F., Navarrete, J.T.L., Ramirez, F.J., Nieto-Ortega, B., Casado, J., Reiher, M., Autschbach, J., and Crassous, J. Redox-Active Chiroptical Switching in Mono- and Bis-Iron Ethynylcarbo[6]helicenes Studied by Electronic and Vibrational Circular Dichroism and Resonance Raman Optical Activity. *Chem. Eur. J.*, **2018**. 24(56), 15067-15079.
496. Shen, X., Li, Y., Wen, Z., Cao, S., Hou, X., and Gong, L. A chiral nickel DBFOX complex as a bifunctional catalyst for visible-light-promoted asymmetric photoredox reactions. *Chem. Sci.*, **2018**. 9(20), 4562-4568.

497. Le Gal, Y., Vacher, A., Dorcet, V., Fourmigué, M., Crassous, J., and Lorcy, D. The near infra red (NIR) chiroptical properties of nickel dithiolene complexes. *New J. Chem.*, **2015**. 39(1), 122-129.
498. Shen, C., Loas, G., Srebro-Hooper, M., Vanthuyne, N., Toupet, L., Cador, O., Paul, F., Lopez Navarrete, J.T., Ramirez, F.J., Nieto-Ortega, B., Casado, J., Autschbach, J., Vallet, M., and Crassous, J. Iron Alkynyl Helicenes: Redox-Trigged Chiroptical Tuning in the IR and Near-IR Spectral Regions and Suitable for Telecommunications Applications. *Angew. Chem. Int. Ed.*, **2016**. 55(28), 8062-6.
499. Berardozi, R., Badetti, E., Carmo Dos Santos, N.A., Wurst, K., Licini, G., Pescitelli, G., Zonta, C., and Di Bari, L. Co(ii)-induced giant vibrational CD provides a new design of methods for rapid and sensitive chirality recognition. *Chem. Commun.*, **2016**. 52(54), 8428-31.
500. Pescitelli, G., Ludeke, S., Gorecki, M., and Di Bari, L. Symmetry-Dependent Vibrational Circular Dichroism Enhancement in Co(II) Salicylaldiminato Complexes. *J. Phys. Chem. Lett.*, **2019**. 10(3), 650-654.
501. Saha, B., Petrovic, A.G., Dhamija, A., Berova, N., and Rath, S.P. Complexation of Chiral Zinc(II) Porphyrin Tweezer with Achiral Aliphatic Diamines Revisited: Molecular Dynamics, Electronic CD, and ¹H NMR Analysis. *Inorg. Chem.*, **2019**. 58(17), 11420-11438.
502. Cantrell, W.R., Richter-Addo, G.B., and Gladysz, J.A. Syntheses of cyclic imine complexes of the chiral rhenium Lewis acid [(v⁵-C₅H₅) Re(NO)(PPh₃)]⁺ by hydride ion abstraction from amido complexes. *J. Organomet. Chem.*, **1994**. 472(1), 195-204.
503. Simonneau, A., Bideau, F.L., Mirebeau, J.H., Marrot, J., and Jaouen, G. Review on Bioorganometallic Chemistry and New Outcomes in the Synthesis and Substitution of Tetracarbonyl(pyrrolylimine) Complexes of Rhenium with Organophosphorus Ligands. *Curr. Top. Med. Chem.*, **2017**. 17(25), 2807-2819.
504. Zhou, Y.H., Li, J., Wu, T., Zhao, X.P., Xu, Q.L., Li, X.L., Yu, M.B., Wang, L.L., Sun, P., and Zhen, Y.X. Photoluminescent and ferroelectric properties of a chiral rhenium(I) complex based on the chiral (-)-4,5-pinene-2,2'-bipyridine ligand. *Inorg. Chem. Commun.*, **2013**. 29, 18-21.
505. Álvarez, C.M., Carrillo, R., García-Rodríguez, R., and Miguel, D. Stereoselective Aldol addition to Rhenium (I) complexes and reversible dimerization with epimerization of the metal center. *Chem. Eur. J.*, **2013**. 19(25), 8285-8293.
506. Medcraft, C., Wolf, R., and Schnell, M. High-resolution spectroscopy of the chiral metal complex [CpRe(CH₃)(CO)(NO)]: a potential candidate for probing parity violation. *Angew. Chem. Int. Ed.*, **2014**. 53(43), 11656-11659.
507. Saleh, N., Srebro, M., Reynaldo, T., Vanthuyne, N., Toupet, L., Chang, V.Y., Muller, G., Williams, J.A., Roussel, C., Autschbach, J., and Crassous, J. enantio-Enriched CPL-active helicene-bipyridine-rhenium complexes. *Chem. Commun.*, **2015**. 51(18), 3754-7.
508. Gauthier, E.S., Abella, L., Hellou, N., Darquie, B., Caytan, E., Roisnel, T., Vanthuyne, N., Favereau, L., Srebro-Hooper, M., Williams, J.A.G., Autschbach, J., and Crassous, J. Long-Lived Circularly Polarized Phosphorescence in Helicene-NHC Rhenium(I) Complexes: The Influence of Helicene, Halogen, and Stereochemistry on Emission Properties. *Angew. Chem. Int. Ed.*, **2020**. 59(22), 8394-8400.

509. Zhang, Y.P. and Zheng, Y.X. Frontiers in chiral phosphorescent complexes for circularly polarized electroluminescence. *Dalton Trans.*, **2022**. 51(26), 9966-9970.
510. McDonnell, U., Kerchoffs, J.M., Castineiras, R.P., Hicks, M.R., Hotze, A.C., Hannon, M.J., and Rodger, A. Synthesis and cytotoxicity of dinuclear complexes containing ruthenium(II) bipyridyl units linked by a bis(pyridylimine) ligand. *Dalton Trans.*, **2008**(5), 667-75.
511. Schnable, D., Schley, N.D., and Ung, G. Circularly Polarized Luminescence from Uranyl Improves Resolution of Electronic Transitions. *J. Am. Chem. Soc.*, **2022**. 144(24), 10718-10722.
512. Tsurui, M., Kitagawa, Y., Fushimi, K., Gon, M., Tanaka, K., and Hasegawa, Y. Electronic strain effect on Eu(III) complexes for enhanced circularly polarized luminescence. *Dalton Trans.*, **2020**. 49(16), 5352-5361.
513. Walsh, K.M., Pressler, K., Crane, M.J., and Gamelin, D.R. Ferromagnetism and Spin-Polarized Luminescence in Lead-Free CsEuCl₃ Perovskite Nanocrystals and Thin Films. *ACS Nano*, **2022**. 16(2), 2569-2576.
514. Andrushchenko, V. Eu³⁺ as a luminescence probe in DNA studies: Structural and conformational implications. *Spectrochim. Acta. A Mol. Biomol. Spectrosc.*, **2019**. 213, 456-462.
515. Saleh, N., Moore, B., 2nd, Srebro, M., Vanthuyne, N., Toupet, L., Williams, J.A., Roussel, C., Deol, K.K., Muller, G., Autschbach, J., and Crassous, J. Acid/base-triggered switching of circularly polarized luminescence and electronic circular dichroism in organic and organometallic helices. *Chem. Eur. J.*, **2015**. 21(4), 1673-81.
516. Jia, J., Wang, Y., Feng, L., and Zhao, X. Theoretical Analysis on the Importance of Achiral Unidentate Ligands to Electronic Circular Dichroism of cis-Bis(ethylenediamine) Cobalt(III) Complexes. *Inorg. Chem.*, **2016**. 55(14), 6949-60.
517. Wang, Y., Wang, Y., Wang, J., Liu, Y., and Yang, Y. Theoretical analysis of the individual contributions of chiral arrays to the chiroptical properties of tris-diamine ruthenium chelates. *J. Am. Chem. Soc.*, **2009**. 131(25), 8839-47.
518. Saha, B., Petrovic, A.G., Dhamija, A., Berova, N., and Rath, S.P. Complexation of Chiral Zinc(II) Porphyrin Tweezer with Achiral Aliphatic Diamines Revisited: Molecular Dynamics, Electronic CD, and ¹H NMR Analysis. *Inorg. Chem.*, **2019**. 58(17), 11420-11438.
519. van Horn, M., Saue, T., and List, N.H. Probing chirality across the electromagnetic spectrum with the full semi-classical light-matter interaction. *J. Chem. Phys.*, **2022**. 156(5), 054113.
520. Gendron, F., Moore II, B., Cador, O., Pointillart, F., Autschbach, J., and Le Guennic, B. Ab Initio Study of Circular Dichroism and Circularly Polarized Luminescence of Spin-Allowed and Spin-Forbidden Transitions: From Organic Ketones to Lanthanide Complexes. *J. Chem. Theory Comput.*, **2019**. 15(7), 4140-4155.
521. Caspar, J.V. and Meyer, T.J. Application of the energy gap law to nonradiative, excited-state decay. *J. Phys. Chem.*, **1983**. 87(6), 952-957.

522. Kober, E.M., Marshall, J.L., Dressick, W.J., Sullivan, B.P., Caspar, J.V., and Meyer, T.J. Synthetic control of excited states. Nonchromophoric ligand variations in polypyridyl complexes of osmium (II). *Inorg. Chem.*, **1985**. 24(18), 2755-2763.
523. Arima, D., Niihori, Y., and Mitsui, M. Unravelling the origin of dual photoluminescence in Au₂Cu₆ clusters by triplet sensitization and photon upconversion. *J. Mater. Chem. C*, **2022**. 10(12), 4597-4606.
524. Dakua, K.K., Rajak, K., and Mishra, S. Spin-vibronic coupling in the quantum dynamics of a Fe(III) trigonal-bipyramidal complex. *J. Chem. Phys.*, **2022**. 156(13), 134103.
525. Feng, J., Reponen, A.P.M., Romanov, A.S., Linnolahti, M., Bochmann, M., Greenham, N.C., Penfold, T., and Credgington, D. Influence of Heavy Atom Effect on the Photophysics of Coinage Metal Carbene-Metal-Amide Emitters. *Adv. Funct. Mater.*, **2021**. 31(1), 2005438.
526. Foller, J., Ganter, C., Steffen, A., and Marian, C.M. Computer-Aided Design of Luminescent Linear N-Heterocyclic Carbene Copper(I) Pyridine Complexes. *Inorg. Chem.*, **2019**. 58(9), 5446-5456.
527. Fumanal, M., Gindensperger, E., and Daniel, C. Ligand substitution and conformational effects on the ultrafast luminescent decay of [Re(CO)₃(phen)(L)]⁺ (L = imidazole, pyridine): non-adiabatic quantum dynamics. *Phys. Chem. Chem. Phys.*, **2018**. 20(2), 1134-1141.
528. Fumanal, M., Gindensperger, E., and Daniel, C. Ultrafast Intersystem Crossing vs Internal Conversion in alpha-Diimine Transition Metal Complexes: Quantum Evidence. *J. Phys. Chem. Lett.*, **2018**. 9(17), 5189-5195.
529. Harabuchi, Y., Eng, J., Gindensperger, E., Taketsugu, T., Maeda, S., and Daniel, C. Exploring the Mechanism of Ultrafast Intersystem Crossing in Rhenium(I) Carbonyl Bipyridine Halide Complexes: Key Vibrational Modes and Spin-Vibronic Quantum Dynamics. *J. Chem. Theory Comput.*, **2016**. 12(5), 2335-45.
530. Kitzmann, W.R., Moll, J., and Heinze, K. Spin-flip luminescence. *Photochem. Photobiol. Sci.*, **2022**. 21(7), 1309-1331.
531. Eng, J., Gourlaouen, C., Gindensperger, E., and Daniel, C. Spin-vibronic quantum dynamics for ultrafast excited-state processes. *Acc. Chem. Res.*, **2015**. 48(3), 809-17.
532. Mai, S., Plasser, F., Pabst, M., Neese, F., Kohn, A., and Gonzalez, L. Surface hopping dynamics including intersystem crossing using the algebraic diagrammatic construction method. *J. Chem. Phys.*, **2017**. 147(18), 184109.
533. Moseley, D.H., Stavretis, S.E., Thirunavukkuarasu, K., Ozerov, M., Cheng, Y., Daemen, L.L., Ludwig, J., Lu, Z., Smirnov, D., Brown, C.M., Pandey, A., Ramirez-Cuesta, A.J., Lamb, A.C., Atanasov, M., Bill, E., Neese, F., and Xue, Z.L. Spin-phonon couplings in transition metal complexes with slow magnetic relaxation. *Nat. Commun.*, **2018**. 9(1), 2572.
534. Chakarawet, K., Atanasov, M., Ellis, J.E., Lukens, W.W., Jr., Young, V.G., Jr., Chatterjee, R., Neese, F., and Long, J.R. Effect of Spin-Orbit Coupling on Phonon-Mediated Magnetic Relaxation in a Series of Zero-Valent Vanadium, Niobium, and Tantalum Isocyanide Complexes. *Inorg. Chem.*, **2021**. 60(23), 18553-18560.

535. Vacher, M., Kunnus, K., Delcey, M.G., Gaffney, K.J., and Lundberg, M. Origin of core-to-core x-ray emission spectroscopy sensitivity to structural dynamics. *Struct. Dyn.*, **2020**. 7(4), 044102.
536. Savchenko, V., Brumboiu, I.E., Kimberg, V., Odelius, M., Krasnov, P., Liu, J.C., Rubensson, J.E., Bjorneholm, O., Sathe, C., Grasjo, J., Dong, M., Pietzsch, A., Fohlisch, A., Schmitt, T., McNally, D., Lu, X., Polyutov, S.P., Norman, P., Iannuzzi, M., Gel'mukhanov, F., and Ekholm, V. Vibrational resonant inelastic X-ray scattering in liquid acetic acid: a ruler for molecular chain lengths. *Sci. Rep.*, **2021**. 11(1), 4098.
537. Gel'mukhanov, F., Odelius, M., Polyutov, S.P., Föhlisch, A., and Kimberg, V. Dynamics of resonant x-ray and Auger scattering. *Rev. Mod. Phys.*, **2021**. 93(3), 035001.
538. Zobel, J.P. and Gonzalez, L. The Quest to Simulate Excited-State Dynamics of Transition Metal Complexes. *JACS Au*, **2021**. 1(8), 1116-1140.
539. Chizallet, C., Costentin, G., Lauron-Pernot, H., Krafft, J.M., Che, M., Delbecq, F., and Sautet, P. Assignment of Photoluminescence Spectra of MgO Powders: TD-DFT Cluster Calculations Combined to Experiments. Part II. Hydroxylation Effects. *J. Phys. Chem. C*, **2008**. 112(49), 19710-19717.
540. Shinsuphan, N., Kongsuk, S., and Amornkitbamrung, V. The Photoluminescence Properties of the Alkali Metals Functionalized Adamantane Studied by Using Linear-Response Time-Dependent Density Functional Theory (TD-DFT) Calculations. *Advanced Materials Research*, **2015**. 1131, 117-122.
541. Yu, Y. and McCluskey, M.D. Classification of Semiconductors Using Photoluminescence Spectroscopy and Machine Learning. *Appl. Spectrosc.*, **2022**. 76(2), 228-234.
542. Joung, J.F., Han, M., Hwang, J., Jeong, M., Choi, D.H., and Park, S. Deep Learning Optical Spectroscopy Based on Experimental Database: Potential Applications to Molecular Design. *JACS Au*, **2021**. 1(4), 427-438.
543. Ashalley, E., Acheampong, K., Besteiro, L.V., Yu, P., Neogi, A., Govorov, A.O., and Wang, Z.M. Multitask deep-learning-based design of chiral plasmonic metamaterials. *Photonics Res.*, **2020**. 8(7), 1213-1225.
544. Ju, C.W., Bai, H., Li, B., and Liu, R. Machine Learning Enables Highly Accurate Predictions of Photophysical Properties of Organic Fluorescent Materials: Emission Wavelengths and Quantum Yields. *J. Chem. Inf. Model.*, **2021**. 61(3), 1053-1065.
545. Kubas, A., Noak, J., Trunschke, A., Schlögl, R., Neese, F., and Maganas, D. A combined experimental and theoretical spectroscopic protocol for determination of the structure of heterogeneous catalysts: developing the information content of the resonance Raman spectra of M1 MoVO_x. *Chem. Sci.*, **2017**. 8(9), 6338-6353.
546. Stephens, P.J. Magnetic Circular Dichroism. *Annu. Rev. Phys. Chem.*, **1974**. 25, 201-232.
547. Cahn, R.S., Ingold, C., and Prelog, V. Specification of Molecular Chirality. *Angew. Chem. Int. Ed.*, **1966**. 5(4), 385-415.
548. Cahn, R. An introduction to the sequence rule: a system for the specification of absolute configuration. *J. Chem. Educ.*, **1964**. 41(3), 116.
549. Neese, F. The ORCA program system. *Wiley Interdiscip. Rev. Comput. Mol. Sci.*, **2011**. 2(1), 73-78.

550. Neese, F. Software update: the ORCA program system, version 4.0. *Wiley Interdiscip. Rev. Comput. Mol. Sci.*, **2017**. 8(1).
551. Grimme, S., Antony, J., Ehrlich, S., and Krieg, H. A consistent and accurate ab initio parametrization of density functional dispersion correction (DFT-D) for the 94 elements H-Pu. *J. Chem. Phys.*, **2010**. 132(15), 154104.
552. Grimme, S., Ehrlich, S., and Goerigk, L. Effect of the damping function in dispersion corrected density functional theory. *J. Comput. Chem.*, **2011**. 32(7), 1456-65.
553. Schäfer, A., Huber, C., and Ahlrichs, R. Fully optimized contracted Gaussian basis sets of triple zeta valence quality for atoms Li to Kr. *J. Chem. Phys.*, **1994**. 100(8), 5829-5835.
554. Feyereisen, M., Fitzgerald, G., and Komornicki, A. Use of approximate integrals in ab initio theory. An application in MP2 energy calculations. *Chem. Phys. Lett.*, **1993**. 208(5-6), 359-363.
555. Kendall, R.A. and Fruchtl, H.A. The impact of the resolution of the identity approximate integral method on modern ab initio algorithm development. *Theor. Chem. Acc.*, **1997**. 97(1-4), 158-163.
556. Truong, T.N. and Stefanovich, E.V. A New Method for Incorporating Solvent Effect into the Classical, Ab-Initio Molecular-Orbital and Density-Functional Theory Frameworks for Arbitrary Shape Cavity. *Chem. Phys. Lett.*, **1995**. 240(4), 253-260.
557. Dutta, A.K., Neese, F., and Izsak, R. Speeding up equation of motion coupled cluster theory with the chain of spheres approximation. *J. Chem. Phys.*, **2016**. 144(3), 034102.
558. Becke, A.D. A new mixing of Hartree-Fock and local density-functional theories. *J. Chem. Phys.*, **1993**. 98(2), 1372-1377.
559. Stephens, P.J., Devlin, F.J., Chabalowski, C.F., and Frisch, M.J. Ab initio calculation of vibrational absorption and circular dichroism spectra using density functional force fields. *J. Phys. Chem.*, **1994**. 98(45), 11623-11627.
560. Chai, J.-D. and Head-Gordon, M. Systematic optimization of long-range corrected hybrid density functionals. *J. Chem. Phys.*, **2008**. 128(8).
561. Plasser, F. TheoDORÉ: A toolbox for a detailed and automated analysis of electronic excited state computations. *J. Chem. Phys.*, **2020**. 152(8), 084108.
562. Vlček, A. Ultrafast excited-state processes in Re(I) carbonyl-diimine complexes: From excitation to photochemistry. *Photophysics of Organometallics*, **2010**, 115-158.
563. Liard, D.J., Busby, M., Matousek, P., Towrie, M., and Vlček, A. Picosecond Relaxation of 3MLCT Excited States of $[\text{Re}(\text{Etpy})(\text{CO})_3(\text{dmb})]^+$ and $[\text{Re}(\text{Cl})(\text{CO})_3(\text{bpy})]$ as Revealed by Time-Resolved Resonance Raman, UV-vis, and IR Absorption Spectroscopy. *J. Phys. Chem. A*, **2004**. 108(13), 2363-2369.
564. Bach, C., Willner, H., Aubke, F., Wang, C., Rettig, S.J., and Trotter, J. Cationic Iridium (III) Carbonyl Complexes: $[\text{Ir}(\text{CO})_6]^{3+}$ and $[\text{Ir}(\text{CO})_5\text{Cl}]^{2+}$. *Angew. Chem. Int. Ed.*, **1996**. 35(17), 1974-1976.
565. Maganas, D., DeBeer, S., and Neese, F. A Restricted Open Configuration Interaction with Singles Method To Calculate Valence-to-Core Resonant X-ray Emission Spectra: A Case Study. *Inorg. Chem.*, **2017**. 56(19), 11819-11836.

Bibliography

- 566. Ye, S., Kupper, C., Meyer, S., Andris, E., Navrátil, R., Krahe, O., Mondal, B., Atanasov, M., Bill, E., Roithová, J., Meyer, F., and Neese, F. Magnetic Circular Dichroism Evidence for an Unusual Electronic Structure of a Tetracarbene–Oxoiron(IV) Complex. *J. Am. Chem. Soc.*, **2016**. 138(43), 14312-14325.
- 567. Badger, R.M. The relation between the internuclear distances and force constants of molecules and its application to polyatomic molecules. *J. Chem. Phys.*, **1935**. 3(11), 710-714.
- 568. Momma, K. and Izumi, F. VESTA 3 for three-dimensional visualization of crystal, volumetric and morphology data. *J. Appl. Cryst.*, **2011**. 44(6), 1272-1276.
- 569. Dovesi, R., Erba, A., Orlando, R., Zicovich-Wilson, C.M., Civalleri, B., Maschio, L., Rérat, M., Casassa, S., Baima, J., Salustro, S., and Kirtman, B. Quantum-mechanical condensed matter simulations with CRYSTAL. *Wiley Interdiscip. Rev. Comput. Mol. Sci.*, **2018**. 8(4), e1360.